Project No. 12-113

Proposed Modifications to AASHTO Cross-Frame Analysis and Design

APPENDIX F

PHASE III SUMMARY

Table of Contents

Table of Contents i
Table of Figures iv
Table of Tables xi
F1 Introduction 1
F2 Task 11 Workload Management 3
F3 Fatigue Loading Study 5
F3.1 Preparation and Modeling Approach 6
F3.1.1 Unified Modeling Technique 6
F3.1.2 Analytical Testing Matrix 13
F3.1.3 Load Application 19
F3.1.4 Mesh Sensitivity 20
F3.1.5 Postprocessing Critical Cross-Frames 22
F3.1.6 Automation and Scripts 26
F3.1.7 Data Visualization 27
F3.1.8 Influence-Surface Results 29
F3.2 Fatigue Study – AASHTO Design Loads 49
F3.2.1 Postprocessing Procedure 50
F3.2.2 Governing Cross-Frame Member 55
F3.2.3 Governing Lane Passage 67
F3.2.4 Cycles per Truck Passage 69
F3.2.5 Impact of Bridge Parameters 75
F3.2.6 Design Parameters 89
F3.3 Fatigue Study - Weigh-In-Motion Records 95
F3.3.1 WIM Records and Record Filtering 96
F3.3.2 Application of WIM Traffic Streams to Analytical Testing Matrix 101
F3.3.3 Comparative Study using Primary Member Calibration Data 120
F3.3.4 Multiple Presence Study 123
F3.3.5 Reliability Studies using Published Resistance Data 133
F3.3.6 Revisiting AASHTO Fatigue Design 138
F3.4 Major Outcomes 140
F4 R-Factor Study 142
F4.1 Member-Level Studies 144
F4.1.1 Simplified Model 145

F4.1.2 Analytical Results 150
F4.1.3 Comparison to Experimental Results 152
F4.2 Panel-Level Studies 154
F4.2.1 Panel-Level Modeling Approach 155
F4.2.2 Parametric Study Results 158
F4.2.3 Spot-Check Results 165
F4.3 System-Level Studies 169
F4.3.1 Preliminary Study 170
F4.3.2 Spot-Check Models 172
F4.3.3 Parametric Study 196
F4.4 Major Outcomes 200
F5 Commercial Design Software Study 202
F5.1 Overall Process 202
F5.2 Equivalent Beam Approach for Cross-Frames 206
F5.3 Approaches for Improving 2D Analyses 208
F5.4 Comparative Results 212
F5.4.1 Sample Influence-Line Results 212
F5.4.2 Postprocessing Error 218
F5.4.3 Parametric Study 232
F5.4.4 Alternative 2D Postprocessing Procedure 235
F5.5 Major Outcomes 238
F6 Stability Study 239
F6.1 Bracing Strength Requirements 240
F6.1.1 Background 241
F6.1.2 Parametric Finite-Element Study 242
F6.1.3 Pertinent Results 249
F6.2 Bracing Stiffness Requirements 257
F6.2.1 Background 257
F6.2.2 Parametric Finite-Element Study 258
F6.2.3 Pertinent Results 261
F6.3 Negative Bending and Moment Gradient Factors 267
F6.3.1 Background 267
F6.3.2 Parametric Finite-Element Study 271
F6.3.3 Pertinent Results 280
F6.4 Major Outcomes 287
References 288

F7 Analytical Testing Matrix 290

Table of Figures

Figure F3-1: Common cross-frame modeling approaches in 3D FEA models 7
Figure F3-2: Final selected modeling technique for truss-element cross-frames 8
Figure F3-3: Screenshot showing a sample 3D FEA model built in the Fatigue Loading Study (top view) 12
Figure F3-4: Screenshot showing a sample 3D FEA model built in the Fatigue Loading Study (bottom view) 13
Figure F3-5: Schematic demonstrating the independent parameters and constants used in the Fatigue Loading Study (plan view) 15
Figure F3-6: Schematic demonstrating the independent parameters and constants used in the Fatigue Loading Study (cross-section view) 16
Figure F3-7: Example bridge demonstrating the staggered cross-frame layout considered in the Fatigue Loading Study 16
Figure F3-8: Response of a cross-frame diagonal in sample skewed bridge to demonstrate effects of loading grid discretization 20
Figure F3-9: Response of cross-frame in sample normal bridge to demonstrate effects of shell element mesh 21
Figure F3-10: Comparison of influence-surface plots for axial force response of cross-frame diagonal near intermediate support with (left) no skew and (right) 60-degree skew 24
Figure F3-11: Critical cross-frames to be evaluated for sample bridges: (top) single-span with skewed supports, (middle) two-span continuous with skewed supports, and (bottom) three-span continuous with normal supports 26
Figure F3-12: Screenshot of interactive Excel-based graphical interface showing influence-surface results 28
Figure F3-13: Screenshot of interactive Excel-based graphical interface showing displacement results 29
Figure F3-14: Screenshot of interactive Excel-based graphical interface showing bridge parameters, framing plan, and cross-section views 29
Figure F3-15: Comparison of influence-surface plots (axial-force response) of cross-frame bottom strut near (left) maximum dead load moment region and (right) skewed intermediate support 33
Figure F3-16: Comparison of influence-surface plots (axial-force response) of cross-frame (left) diagonal 1 and (right) diagonal 2 maximum dead load moment region 34
Figure F3-17: Comparison of influence-surface plots (axial-force response) of midspan cross-frame bottom strut with a (left) 6-foot girder spacing and (right) 10-foot girder spacing 35
Figure F3-18: Comparison of influence-surface plots (axial-force response) of cross-frame bottom strut with (left) 8-inch concrete deck and (right) 10-inch concrete deck 36
Figure F3-19: Comparison of influence-surface plots (axial-force response) of cross-frame diagonal 2 near intermediate support of (left) straight bridge and (right) curved bridge (R = 750 ft) 37
Figure F3-20: Comparison of influence-surface plots (axial-force response) of cross-frame diagonal 2 near intermediate support of bridge with (left) contiguous and (right) staggered layout 38
Figure F3-21: Sample influence-surface plots demonstrating the development of a “hotspot” graph for a bottom strut in bridge with (top) 60-degree, (middle) 30-degree, and (bottom) no skew 43
Figure F3-22: Hotspot graph showing the position of the applied load that maximizes tension in the cross-frame diagonal of interest (near intermediate support) for various degrees of support skewness 45
Figure F3-23: Hotspot graph showing the position of the applied load that maximizes tension in the cross-frame diagonal of interest (near end support) for various degrees of support skewness 46

Figure F3-24: Hotspot graph showing the position of the applied load that maximizes tension in the cross-frame diagonal of interest (in interior bay near maximum positive dead load moment region) for various degrees of support skewness 47
Figure F3-25: Hotspot graph showing the position of the applied load that maximizes tension in the cross-frame diagonal of interest (in end bay near maximum positive dead load moment region) for various degrees of support skewness 48
Figure F3-26: AASHTO fatigue truck (adapted from AASHTO LRFD) 50
Figure F3-27: Sample data showing the development of influence-line plots from an influence-surface . 52
Figure F3-28: Governing unfactored fatigue design force for every cross-frame member in sample straight and normal bridge 58
Figure F3-29: Governing unfactored fatigue design force for every cross-frame member in sample straight and skewed bridge 59
Figure F3-30: Governing unfactored fatigue design force for every cross-frame member in sample horizontally curved bridge 60
Figure F3-31: Sample data set (cross-frame D2 at M-E of straight, normal bridges) demonstrating the development of the box-and-whiskers plot 62
Figure F3-32: Unfactored design force ranges compiled for every cross-frame member evaluated 63
Figure F3-33: Bar graph illustrating the most common critical cross-frame members under AASHTO fatigue loading criteria 65
Figure F3-34: Common deformation pattern observed in cross-frame panels due to an applied live load 66
Figure F3-35: Bar graph presenting the critical lane position associated with the governing cross-frame member 68
Figure F3-36: Average number of secondary force cycles measured from critical lane passage 71
Figure F3-37: Sample influence-line plots demonstrating typical number of cycles per truck passage for different cross-frame members 73
Figure F3-38: Sample data demonstrating the impacts of bridge curvature on cross-frame force demands 76
Figure F3-39: Spectrum of unfactored design forces highlighting the impacts of bridge curvature 78
Figure F3-40: Relative stiffness of transverse load distribution mechanisms 79
Figure F3-41: Unfactored design force spectra demonstrating the impacts of general bridge geometry and girder layout 80
Figure F3-42: Unfactored design force spectra demonstrating the impacts of support skewness 82
Figure F3-43: Unfactored design force spectra demonstrating the impacts of bridge curvature 83
Figure F3-44: Unfactored design force spectra demonstrating the impacts of cross-frame type and layout 84
Figure F3-45: Unfactored design force spectra demonstrating the impacts of deck parameters 85
Figure F3-46: Sample influence-line data demonstrating the impacts of girder stiffness and bridge barriers on the axial-force response of cross-frames 89
Figure F3-47: Governing fatigue stress ranges for all bridges in Fatigue Loading Study 92
Figure F3-48: Fatigue II demand-to-capacity ratios for two extreme traffic conditions 93
Figure F3-49: Fatigue II demand-to-capacity ratios for various bridge types (Houston I-10 traffic) 94
Figure F3-50: CDF of GVWs from FHWA 2014 Data (excluding light vehicles) 100
Figure F3-51: CDF of GVWs from SHRP 2 R19B WIM Data, adapted from Modjeski and Masters (2015) 100
Figure F3-52: Sample load event history showing three vehicles back to back 102
Figure F3-53: Illustration of worst-case truck position to maximize cross-frame force effects 103
Figure F3-54: Illustration of realistic truck position in drive lane 104
Figure F3-55: Illustration showing distribution of vehicle transverse location within 12-foot design lane for a 30-foot wide bridge 105

Figure F3-56: Illustration showing selection of 99.99th percentile stress range 106
Figure F3-57: Summary of Fatigue I normalized 99.99% stress ranges ($SR_{99.99\%}$) for 18 WIM records and 20 sites prior to truncating the lower stress ranges (i.e., removing stress ranges less than 25% CAFL).. 108
Figure F3-58: Summary of Fatigue I normalized 99.99% stress ranges ($SR_{99.99\%}$) for 18 WIM records and 20 sites after truncating the lower stress ranges (i.e., removing stress ranges less than 25% CAFL). 109
Figure F3-59: CDF of Fatigue I normalized 99.99th percentile stress ranges for 18 WIM records and 20 bridge sites prior to truncating the lower stress ranges (i.e., removing stress ranges less than 25% CAFL. 110
Figure F3-60: CDF of Fatigue I normalized 99.99th percentile stress ranges for 18 WIM records and 20 bridge sites after truncating the lower stress ranges (i.e., removing stress ranges less than 25% CAFL). A best fit line is demonstrated via linear regression. 111
Figure F3-61: Summary of Fatigue II normalized effective stress ranges (S_{re}) for 18 WIM records and 20 sites prior to truncating the lower stress ranges (i.e., removing stress ranges less than 25% CAFL)..... 113
Figure F3-62: Summary of Fatigue II normalized effective stress ranges (S_{re}) for 18 WIM records and 20 sites after truncating the lower stress ranges (i.e., removing stress ranges less than 25% CAFL). 114
Figure F3-63: Summary of Fatigue II damage ratios for 18 WIM records and 20 sites prior to truncating the lower stress ranges (i.e., removing stress ranges less than 25% CAFL)..... 116
Figure F3-64: Summary of Fatigue II damage ratios for 18 WIM records and 20 sites after truncating the lower stress ranges (i.e., removing stress ranges less than 25% CAFL)..... 117
Figure F3-65: CDF of maximum Fatigue II damage ratios for 18 WIM records and 20 bridge sites prior to truncating the lower stress ranges (i.e., removing stress ranges less than 25% CAFL)..... 118
Figure F3-66: CDF of maximum Fatigue II damage ratios for 18 WIM records and 20 bridge sites after truncating the lower stress ranges (i.e., removing stress ranges less than 25% CAFL). A best fit line is demonstrated via linear regression..... 119
Figure F3-67: Illustration of an adjacent lanes (truck-passing-truck) scenario; negative and positive clear distances indicate the passing truck's front axle is ahead or behind the drive lane truck's rear axle, respectively. 123
Figure F3-68: Histogram from two-lane WIM records, showing the clear distance between a passing truck and the drive lane truck (Indiana US 31 NB)..... 125
Figure F3-69: Histogram from two-lane WIM records, showing the clear distance between a passing truck and the drive lane truck (Indiana US 31 SB) 125
Figure F3-70: Histogram from two-lane WIM records, showing the clear distance between a passing truck and the drive lane truck (Tennessee IH 40 EB) 126
Figure F3-71: Histogram from two-lane WIM records, showing the clear distance between a passing truck and the drive lane truck (Tennessee IH 40 WB)..... 126
Figure F3-72: Histogram from two-lane WIM records, showing the clear distance between a passing truck and the drive lane truck (Virginia US 29)..... 127
Figure F3-73: Histogram from two-lane WIM records, showing GVW of a passing truck (Indiana US 31 NB)..... 127
Figure F3-74: Histogram from two-lane WIM records, showing GVW of a passing truck (Indiana US 31 SB) 128
Figure F3-75: Histogram from two-lane WIM records, showing GVW of a passing truck (Tennessee IH 40 EB) 128
Figure F3-76: Histogram from two-lane WIM records, showing GVW of a passing truck (Tennessee IH 40 WB)..... 129
Figure F3-77: Histogram from two-lane WIM records, showing GVW of a passing truck (Virginia US 29) 129
Figure F3-78: Histogram from two-lane WIM records, showing the ratio of the passing lane GVW to the drive lane GVW (Indiana US 31 NB)..... 130

Figure F3-79: Histogram from two-lane WIM records, showing the ratio of the passing lane GVW to the drive lane GVW (Indiana US 31 SB) 130
Figure F3-80: Histogram from two-lane WIM records, showing the ratio of the passing lane GVW to the drive lane GVW (Tennessee IH 40 EB) 131
Figure F3-81: Histogram from two-lane WIM records, showing the ratio of the passing lane GVW to the drive lane GVW (Tennessee IH 40 WB) 131
Figure F3-82: Histogram from two-lane WIM records, showing the ratio of the passing lane GVW to the drive lane GVW (Virginia US 29) 132
Figure F3-83: Fatigue II demand-to-capacity ratios for various bridge types (Houston I-10 traffic) using reduced load factors 139
Figure F4-1: Types of cross-frame deformation caused by relative moment of adjacent girders 143
Figure F4-2: Assumed eccentric load path through a cross-frame member along both orthogonal axes (left) and the corresponding, typical 3D modeling simplification (right) 146
Figure F4-3: Assumed analytical model to represent the eccentric end connections (left) versus the modeling approach commonly used to represent cross-frame members (right) 148
Figure F4-4: Assumed Whitmore section to determine effective height and length connection and gusset plates 148
Figure F4-5: Out-of-plane stiffness of connection plate for (left) real conditions and (right) idealized conditions 149
Figure F4-6: Scaled view demonstrating the in-plane restraint provided by the connection (and/or gusset plate) 150
Figure F4-7: Stiffness modification factor derived as a function of the gusset plate flexural stiffness 151
Figure F4-8: Stiffness modification factor derived as a function of the angle length 152
Figure F4-9: Eccentrically loaded single-angle specimen (McDonald and Frank 2009) 153
Figure F4-10: Sample static test conducted on single-angle specimen (McDonald and Frank 2009) 153
Figure F4-11: Laboratory cross-frame stiffness test from Wang (2013) and associated FEA model developed by the RT 155
Figure F4-12: Computation of cross-frame stiffness from laboratory test and FEA analysis 156
Figure F4-13: Surface-to-surface (left) and edge-to-edge (right) connections in cross-frame members 157
Figure F4-14: Truss-element (left) and shell-element (right) panel models used in panel-level studies 158
Figure F4-15: Three loading cases considered in the panel-level FEA parametric study 160
Figure F4-16: Sample deflected shapes corresponding to the various loading conditions considered 161
Figure F4-17: Assumed orientation of cross-frame members for differential-rotation loading 162
Figure F4-18: Computed stiffness modification factors for various loading conditions and angle thicknesses 164
Figure F4-19: Connection details for 9-, 8-, and 7-inch wide connection plates 166
Figure F4-20: Loading cases considered in the X-frame spot check 166
Figure F4-21: Loading cases and deflected shapes considered in K-frame spot check 168
Figure F4-22: Shell- (top) and truss-element (bottom) models used in the system-level parametric study 170
Figure F4-23: Various cross-frame modeling approaches considered in system-level studies 173
Figure F4-24: Sample cross-frame panel and the corresponding eccentric-beam models 178
Figure F4-25: Sample calculation of effective section properties for the various eccentric-beam modeling approaches 179
Figure F4-26: Close-up view of eccentric-beam approach for cross-frames in 3D FEA models 184
Figure F4-27: Example data from two-span, continuous skewed bridge demonstrating the predicted cross-frame design force range from the truss-element approach (using various R-factors) and the shell-element approach 186

Figure F4-28: Sample data set (truss-element models with R = 0.5) demonstrating the development of the box-and-whiskers plot in Figure F4-29 188
Figure F4-29: Box-and-whiskers plot indicating the overall level of accuracy for a given R-factor (1/2-inch gusset plate) 188
Figure F4-30: Box-and-whiskers plot indicating the overall level of accuracy for a given R-factor (1-inch gusset plate) 189
Figure F4-31: Example data from two-span, continuous skewed bridge demonstrating the predicted cross-frame design force range from the truss-element approach (using various R-factors), the shell-element approach, and the refined eccentric-beam element 191
Figure F4-32: Box-and-whiskers plot indicating the overall level of accuracy for the eccentric-beam modeling approach compared to the truss-element approach (1/2-inch gusset plate) 192
Figure F4-33: Box-and-whiskers plot indicating the overall level of accuracy for the eccentric-beam modeling approach compared to the truss-element approach (1-inch gusset plate) 193
Figure F4-34: Example data demonstrating the predicted cross-frame force range for the various the eccentric-beam models (same bridges as Figure F4-31) 194
Figure F4-35: Cross-frame panels investigated as part of the system-level study 197
Figure F4-36: Box-and-whiskers plot indicating the overall level of accuracy for a given R-factor (1/4-inch gusset plate) 198
Figure F4-37: Box-and-whiskers plot indicating the overall level of accuracy for a given R-factor (1/2-inch gusset plate) 198
Figure F4-38: Box-and-whiskers plot indicating the overall level of accuracy for a given R-factor (3/4-inch gusset plate) 199
Figure F5-1: Screenshot of the various analysis methods considered in the study 206
Figure F5-2: General process for equivalent beam approach to analyzing cross-frames 207
Figure F5-3: General process for improved 2D grillage analysis 211
Figure F5-4: General process for improved 2D PEB analysis 211
Figure F5-5: Comparison of analysis methods for three select cross-frame members in a straight bridge with normal supports 214
Figure F5-6: Comparison of analysis methods for three select cross-frame members in a straight bridge with skewed supports 215
Figure F5-7: Comparison of analysis methods for three select cross-frame members in a curved bridge with skewed supports 216
Figure F5-8: Sample 2D PEB and 3D cross-frame results for straight bridge with normal supports (noncomposite and composite) under static load 220
Figure F5-9: Sample 2D PEB and 3D cross-frame results for straight bridge with normal supports (noncomposite and composite) under static load 221
Figure F5-10: Idealized deformation pattern of noncomposite (left) and composite (right) systems 222
Figure F5-11: Total cross-frame shear force as a function of concrete deck modulus (Bridge 253-3) 225
Figure F5-12: Total cross-frame shear force as a function of concrete deck modulus (Bridge 1181-2) 226
Figure F5-13: Total cross-frame shear force as a function of concrete deck modulus (Bridge 1181-4) 226
Figure F5-14: Total cross-frame shear force as a function of concrete deck modulus (Bridge 909-2) 227
Figure F5-15: Shear force distribution as a function of concrete deck modulus for the three sample bridges with X-type cross-frames 228
Figure F5-16: Force couple distribution as a function of concrete deck modulus for the four sample bridges 229
Figure F5-17: Analysis error as a function of concrete deck modulus for the four sample bridges 231
Figure F5-18: Box-and-whiskers plot demonstrating the range of analysis error obtained from the Commercial Design Software Study (all cross-frame member types) 233

Figure F5-19: Box-and-whiskers plot demonstrating the range of analysis error obtained from the Commercial Design Software Study (bottom struts versus diagonals) 233
Figure F5-20: Box-and-whiskers plot demonstrating the range of analysis error obtained for different bridge geometries (bottom struts only) 234
Figure F5-21: Alternative postprocessing procedure demonstrated through Load Case 1 on Bridge 253-3 237
Figure F6-1: Types of stability bracing for columns, frames, and frames (Helwig and Yura 2015) 240
Figure F6-2: Geometry and boundary conditions of twin-girder systems 243
Figure F6-3: Elastic, perfectly plastic stress-strain relationship assumed in the FEA studies 244
Figure F6-4: Cross-sections considered in the parametric study 244
Figure F6-5: Various loading conditions (n = 3 intermediate brace locations illustrated) 246
Figure F6-6: Assumed initial imperfection shape used in the brace strength study 247
Figure F6-7: An example demonstrating how brace moments were distributed to the struts and diagonal members (left) and the corresponding buckled shape (right) 249
Figure F6-8: Brace moments under varying material yield limits (Cross-section 2 with uniform moment loading and 5 intermediate braces) 250
Figure F6-9: Brace moments as a function of applied bending moment (under uniform-moment loading) 251
Figure F6-10: Brace moments as a function of applied bending moment (under transverse loading) 253
Figure F6-11: Brace moments as a function of reverse-curvature bending (Cross-section 1; n = 5; mid-height loading) 256
Figure F6-12: Geometry and boundary conditions used for bracing stiffness model 259
Figure F6-13: Assumed initial imperfection in the bracing stiffness model (similar to Figure F6-6) 260
Figure F6-14: Girder cross-sectional twist as a function of applied uniform moment for various brace stiffness values (n = 1, cross-section 2, and top flange loading) 261
Figure F6-15: Girder cross-sectional twist as a function of girder spacing (twin-girder system, Cross-section 2, top flange loading) 262
Figure F6-16: Girder cross-sectional twist as a function of number of girders (10-foot girder spacing, Cross-section 2, top flange loading) 263
Figure F6-17: Girder cross-sectional twist as a function of applied uniform moment for various brace stiffness values (twin-girder system) 264
Figure F6-18: Web-distortional buckling of composite girder in negative moment regions (Yura 2001) 268
Figure F6-19: General layout and boundary conditions used in the parametric FEA model 272
Figure F6-20: Typical cross-section used in the parametric study and an example showing how a simply-supported nonprismatic girder with flange transitions is developed 275
Figure F6-21: Flange transitions considered in the parametric study 276
Figure F6-22: Flange transition cases for simply-supported condition with different intermediate bracing schemes 277
Figure F6-23: Moment gradients considered in the parametric study 278
Figure F6-24: Applied loading scheme for simply-supported condition with different intermediate bracing schemes 279
Figure F6-25: FEA results compared to the AISC approximate solution (Eqs. F6.12 and F6.13) for various span-to-depth ratios and moment gradient cases I-0 and E-0 280
Figure F6-26: FEA results compared to the AISC approximate solution (Eqs. F6.12 and F6.13) for various I_y multipliers and moment gradient cases S-0, S-1, I-0, I-1, E-0, and E-1 281
Figure F6-27: FEA results compared to the AISC approximate solution (Eqs. F6.12 and F6.13) for various transition locations and moment gradient cases S-0, S-1, I-0, I-1, E-0, and E-1 282
Figure F6-28: FEA results compared to the AISC approximate solution (Eqs. F6.12 and F6.13) for various transition locations and moment gradient cases I-2 and E-2 283

Figure F6-29: Evaluating the accuracy of Eqs. F6.12 and F6.13 for all prismatic beams in the parametric study 284
Figure F6-30: Evaluating the accuracy of Eqs. F6.12 and F6.13 for all nonprismatic beams in the parametric study 285
Figure F6-31: Schematic of special moment gradient cases in which R_m term requires modification 286

Table of Tables

Table F2-1: Overview of Task 11 work breakdown 3
Table F3-1: Comparison of analytical and measured girder deflections at line 4 for critical load cases (Bridge 1) 9
Table F3-2: Comparison of analytical and measured cross-frame axial forces for critical load cases (Bridge 1) 9
Table F3-3: Comparison of analytical and measured girder deflections for critical load cases (Bridge 2) 10
Table F3-4: Comparison of analytical and measured cross-frame axial forces for critical load cases (Bridge 2) 10
Table F3-5: Comparison of analytical and measured girder deflections at line 11 for critical load cases (Bridge 3) 11
Table F3-6: Comparison of analytical and measured cross-frame axial forces for critical load cases (Bridge 3) 11
Table F3-7: Parameters considered in development of analytical testing matrix 17
Table F3-8: Range of values used for independent variables in Fatigue Loading Study 18
Table F3-9: Constant values used in Fatigue Loading Study 18
Table F3-10: Independent variables describing sample influence-surface plots 32
Table F3-11: Sample hotspot data points to demonstrate the normalization process (Figure F3-21) 43
Table F3-12: Sample data demonstrating the process of determining factored, fatigue design stress ranges in cross-frames 55
Table F3-13: Independent variables describing sample bridges in Figure F3-28, Figure F3-29, and Figure F3-30 56
Table F3-14: Independent variables describing sample bridges in Figure F3-37 72
Table F3-15: Independent variables describing sample bridges in Figure F3-38 77
Table F3-16: Summary of trends and observations from Figure F3-41 through Figure F3-45 87
Table F3-17: Independent variables describing sample bridges in Figure F3-46 88
Table F3-18: Sample demonstration of factored fatigue resistances 91
Table F3-19: SPS sites from which weigh-in-motion data was obtained by FHWA 97
Table F3-20: SPS sites from which weigh-in-motion data was obtained by FHWA 99
Table F3-21: Comparison of statistical parameters obtained for the Fatigue I stress ranges by two methods. 111
Table F3-22: Comparison of statistical parameters obtained for the Fatigue II damage ratios by two methods. 119
Table F3-23: Fatigue I and II parameters published in the SHRP 2 R19B for positive bending of a simply-supported 200-foot long bridge. The statistical summary of the parameters is not taken from the SHRP 2 R19B report 121
Table F3-24: Fatigue I and II parameters using 18 WIM records for positive bending of a simply-supported 200-foot long bridge. 122
Table F3-25: Summary of Multiple Presence Statistics for Adjacent Lane Loaded 133
Table F3-26: Statistical parameters for resistance as calculated from SHRP 2 R19B (Kulicki et al. 2015). 134
Table F3-27: Statistical parameters describing the load effects in cross-frames for Fatigue I and II limit states 135
Table F3-28: Reliability of cross-frames for Fatigue I and II limit states using new load factors 137
Table F3-29: Reliability of cross-frames for Fatigue I and II limit states using adjustment factor of 0.65 to existing load factors. 137
Table F4-1: Parameters considered in the analytical-model parametric study 151

Table F4-2: Parameters of test specimens studied (McDonald and Frank 2009) 154
Table F4-3: Comparison of experimental results and analytical solution..... 154
Table F4-4: Cross-frame stiffness from laboratory test and Abaqus analysis 157
Table F4-5: Parameters considered in the panel-level parametric study 159
Table F4-6: Sample computed cross-frame stiffnesses and modification factors for various loading cases 163
Table F4-7: Cross-frame geometries considered in connection-plate spot-check studies 166
Table F4-8: Computed modification factors for different connection plate lengths (configuration Case 1 in Table F4-7)..... 167
Table F4-9: Computed modification factors for different connection plate lengths (configuration Case 2 in Table F4-7)..... 167
Table F4-10: Computed modification factors for different connection plate lengths (configuration Case 3 in Table F4-7) 167
Table F4-11: Sample computed cross-frame stiffness for K-frame subjected to various load cases..... 169
Table F4-12: Range of values considered for preliminary system-level study..... 171
Table F4-13: Predicted cross-frame forces for critical bottom strut and diagonal in straight bridge with 5-foot girder spacing using various stiffness reduction factors..... 172
Table F4-14: Predicted cross-frame forces for critical bottom strut and diagonal in straight bridge with 15-foot girder spacing using various stiffness reduction factors..... 172
Table F4-10: Independent variables describing 20 representative bridges in system-level R-Factor Study (straight bridges) 175
Table F4-11: Independent variables describing 20 representative bridges in system-level R-Factor Study (curved bridges) 176
Table F4-17: Parameters considered in the preliminary system-level parametric study 196
Table F4-18: R-factor results from system-level parametric study..... 199
Table F5-1: Parameters considered in the analytical-model parametric study 205
Table F5-2: Summary of improved analysis techniques for 2D models..... 212
Table F6-1: Variation of Eq. F6.2 as a function of the number of braces..... 242
Table F6-2: Computed brace forces for various girder moments 249
Table F6-3: Summary of strength requirements of torsional bracing for different cross sections and load conditions..... 254
Table F6-4: Summary of stiffness requirements of torsional bracing for different cross sections and load conditions..... 266

CHAPTER F1

Introduction

The final report of NCHRP Project 12-113 succinctly summarizes the key outcomes of the research for practicing engineers. As such, many of the detailed results were not included in the body of the main document for clarity. The intent of this appendix is to provide a more comprehensive overview of the work completed in Phase II of the project. Similarly, Appendix D and E expand on Phase II and III of the project, respectively. For reference, Phase III is comprised of the following tasks, which were previously identified in main body of the final report as well as the project Request for Proposals (RFP):

- Task 11: Execute Part 2 of the analytical program as described in Task 3. Perform parametric studies on cross-frame forces related to live-load induced fatigue.
- Task 12: Based on the analytical and experimental investigations, develop specification and commentary language for proposed changes to AASHTO LRFD including design examples and flowcharts.
- Task 13: Prepare Interim Report No. 3 that documents and summarizes the results of Tasks 11 and 12 no later than 15 months after approval of Phase II.

For reference, Part 2 of the analytical program includes the following items, as outlined in the project RFP:

a. Analytical and loading studies (finite element analyses) to investigate appropriate fatigue stress ranges for evaluation of cross-frames for right, skewed, and curved bridges, and Fatigue I and II;

b. The influence of girder spacing, cross-frame stiffness and spacing (including staggered), and deck thickness;

c. Parametric modeling studies to investigate the effective stiffness of cross-frames, including the effects of connection details and the connection plate stiffness on cross-frame member stiffness reduction;

d. Evaluation of commercial software programs and their ability to accurately predict cross-frame forces for various bridge geometries, as well as the geometry and configuration of cross-frames;

e. Development of stability bracing requirements for steel I-girders during construction and in-service extending available solutions to include bottom flanges in compression in multi-span continuous bridges with nonprismatic girders. The analytical studies should include evaluation of how to combine stability bracing strength requirements with consideration of other loads such as wind, construction, etc.

This appendix primarily outlines the procedures used to accomplish Tasks 11, as well as presents pertinent results. An emphasis is placed on the five subtasks listed above (Part 2 of the analytical program) in the context of the three major research studies: (i) *fatigue loading criteria*, (ii) *analysis procedures*, and (iii) *stability bracing requirements*. Task 12 is covered extensively in the main body of the report. Thus, it is not detailed herein.

The appendix is organized in a traditional report format and is divided into seven distinct chapters. Following this introductory chapter and is divided into nine chapters. Following this introduction, Chapter F2 outlines the workload plan related to Task 11, which includes a detailed description of analytical studies conducted. The various analytical studies, which address different components of the five subtasks of Task 11, serve as the organization of Chapters F3, F4, F5, and F6. Chapter F3 summarizes the findings of the Fatigue Loading Study, which investigates the appropriate fatigue loading criteria for cross-frame systems. Chapter F4 summarizes the R-Factor Study, which addresses the impact of eccentric end connections on cross-frame stiffness in refined analyses; Chapter F5 outlines the Commercial Design Software Study, which investigates the accuracy of simplified three-dimensional (3D) and two-dimensional (2D) modeling techniques at predicting cross-frame response. Chapter F6 summarizes the findings of the Stability Study, for which the stability bracing requirements of cross-frames are evaluated. Finally, a supplementary chapter is included at the end to provide the reader with the additional reference material. In Chapter F7, the full analytical testing matrix is summarized.

CHAPTER F2

Task 11 Workload Management

As outlined in Chapter F1, the scope of Task 11 includes five subtasks. The results from each of these subtasks ultimately dictate the proposed modifications to AASHTO LRFD documented in the main body of the report and Appendix A. Prior to conducting any of these studies, the RT identified a work plan that best accomplishes the subtasks in a timely and efficient manner. This section outlines how the RT divided the work among the team and the various software platforms, as summarized in Table F2-1. For simplicity, the five subtasks are abbreviated as Parts "a" through "e" based on the order in which they are presented in Chapter F1.

Table F2-1: Overview of Task 11 work breakdown

Subtask	Overview	Model	Software
a	Fatigue loading studies	Fatigue Loading Study	Abaqus
b	Influence of bridge geometry and cross-frame details		
c	Cross-frame stiffness reduction	R-Factor Study	Abaqus
d	Commercial software evaluation	Commercial Design Software Study	Software A, Software B
e	Stability bracing requirements	Stability Study	Abaqus

As presented in Table F2-1, the five subtasks are addressed through a series of four individual analytical studies. Parts a and b, which are best described as evaluating the effects of bridge geometry, cross-frame layout, and cross-frame type on the expected live load-induced force ranges in critical cross-frames, were performed together via a parametric study in Abaqus. This parametric study is abbreviated as the "Fatigue Loading Study" herein. The Fatigue Loading Study addresses the first of the three major research focuses: (i) *fatigue loading criteria*.

Part c, related to cross-frame stiffness and eccentric connections, was also accomplished in a standalone parametric study in Abaqus. This is referred to as the "R-Factor Study." Part d draws comparisons between representative commercially available software programs (Software A and Software B) and validated models in Abaqus. By performing the commercial software studies on a 2D model (Software B) and a 3D FEA model (Software A), the RT can properly evaluate the effects of common modeling approaches on cross-frame force predictions. This is referred to as the "Commercial Design Software Study" herein. Both the R-Factor Study and the Commercial Design Software Study address the second of the three major research focuses: (ii) *analysis techniques*.

Before addressing Part e, there are two important notes to make with respect to the Commercial Design Software Study. First, no references to the specific commercial software packages are made throughout this appendix to avoid promoting a specific brand. As such, the two programs studied extensively are generically referred to as Software A and B based on the discussion in Appendix D, the Phase I summary. Second, the term "commercial software program" must be clearly defined. The term "commercial" can refer to any program available to the public with a one-time or annual fee. Thus, Abaqus, a general-use FEA program, represents a "commercial" program, as do Software A and Software B. However, the focus of the Commercial Design Software Study is on those commercially available programs specifically designed for and marketed as a bridge design tool. Abaqus, although a commercial program, is not specifically suited for bridge design, whereas Software A and B are.

Part e, which involves the stability bracing component to the project, was performed independently of the other studies and is identified as the "Stability Study" in this appendix. The Stability Study investigates the stiffness and strength requirements for cross-frames, which act as torsional braces for I-girders. This study addresses the final of the three major research focuses: (iii) *stability bracing requirements*.

As discussed in introductory section, subsequent Chapters F3 through F6 summarize the procedures and results of each of the four studies introduced in this chapter. The proposed modifications to AASHTO LRFD are ultimately based on the findings of each study, which are outlined in the main body of the report and Appendix A.

CHAPTER F3

Fatigue Loading Study

As introduced in the preceding sections, the Fatigue Loading Study is intended to investigate two major questions concerning load-induced fatigue design of cross-frame systems: (i) the influence of bridge geometry (e.g. support skew, girder depth) and cross-frame details (e.g. cross-frame layout) on fatigue force effects and (ii) the appropriate fatigue stress ranges for evaluation of cross-frames in right, skewed, and curved bridge. The RT obtained preliminary answers to these questions from the field experiments conducted during Phase II and documented in Appendix E. However, the instrumented bridges represent only three unique geometries subjected to local traffic conditions in the greater Houston area. In order to adequately assess the AASHTO fatigue loading criteria, a more expansive study is required.

Based on the lessons learned from the modeling validation process in Phase II, the RT developed and conducted a robust, finite element parametric study. The parametric study effectively improves the depth of knowledge by expanding the breadth of the data set (i.e., by investigating a variety of bridge configurations and traffic conditions beyond the three instrumented structures in Houston). In total, 4,104 unique bridge geometries were studied including various girder and cross-frame layouts, girder cross-sections, and cross-frame details. The 4,104-model data set is intended to reasonably represent a wide variety of steel I-girder bridges currently in service in the United States. The details of the 4,104-model matrix are discussed in the subsequent sections.

To address the major objectives of the Fatigue Loading Study outlined above, the RT focused its efforts on three major tasks. First, a unified modeling approach was developed to analyze the various bridge structures (i.e., right, skewed, and curved bridges) in a consistent and repeatable manner. Second, the RT implemented the current fatigue design criteria on the full set of bridges considered in the study. The cross-frames of the representative bridges were effectively "designed" for AASHTO LRFD 9th Edition fatigue provisions. Lastly, the RT implemented measured weigh-in-motion (WIM) data from different US states on a subset of the bridges considered in the study.

The observations and findings of each successive task are then used to address the two major objectives of the study. By comparing the load-induced force and displacement response of cross-frames in a variety of bridge types, the influence of bridge geometry and cross-frame details can be evaluated. For example, the influence of girder spacing on the force demands in cross-frame elements can be studied. By comparing the fatigue "design" forces with the force effects due to real traffic patterns (i.e., via WIM records), a realistic approximation of actual fatigue stress ranges can be assessed. The appropriateness of current AASHTO LRFD fatigue design criteria such as critical load position and Fatigue I and II load factors (which have been calibrated for longitudinal girders only) can be evaluated with respect to cross-frame systems.

This chapter addresses the methodology and results pertaining to these major tasks. Following this introduction, the modeling approach adopted in the Fatigue Loading Study is outlined (Section F3.1). Pertinent results related to the structural analysis and the current fatigue design loading are then presented (F3.2), as well as the methodology and results related to the WIM study (F3.3). Major outcomes are summarized in Section F3.3.5, for which serve as the basis for the proposed modifications discussed in the main body of the report and Appendix A.

F3.1 Preparation and Modeling Approach

Preliminary work and preparation are critical for any comprehensive parametric study, analytical or experimental. The RT has learned this through past experiences, typically with scaled member- or panel-level studies. Preparation is especially important for the Fatigue Loading Study, which parametrically considered entire bridge structures in refined 3D analyses.

As such, the RT dedicated its efforts in the early stages of Phase III to prepare for and expedite the large-scale analytical study. Due to the wide range of parameters considered, the RT first developed an ordered process that systematically conducted the analyses and processed the results. Specifically, the RT focused on the balance between computational efforts, project schedule, and modeling accuracy. For a parametric study of this size, it was not feasible to evaluate every permutation of every critical parameter given limitations to computational resources and time. With computational constraints in the forefront of the discussion, the RT conducted preliminary analyses to establish expectations and develop a reasonable scope. In particular, the seven tasks below were performed prior to conducting the Fatigue Loading Study to help narrow the focus and limit the required computational time:

- Adopt a consistent modeling technique for cross-frame elements;
- Develop a reasonable analytical testing matrix for purposes of the Fatigue Loading Study;
- Refine the applied loading approach;
- Conduct mesh sensitivity studies to optimize computational efforts;
- Streamline post-processing efforts by evaluating only critical cross-frames;
- Develop Python scripts to automate the modeling process; and
- Develop Excel-based macros for processing the FEA results.

Each of these preliminary tasks were important in developing a robust and defensible study. Each task is addressed independently herein; the seven tasks serve as subsections Section F3.1.1 through Section F3.1.7. Sample results are then presented in Section F3.1.8.

F3.1.1 Unified Modeling Technique

As documented in subsequent sections of the appendix, there are numerous ways that designers commonly model bridge superstructures and specifically cross-frame elements, ranging from sophisticated to overly simplified. Fundamentally, there are 2D and 3D modeling approaches for steel I-girder bridges. For each approach, there are several widely regarded methods to modeling cross-frames. This section does not address and compare every modeling technique. Rather, a unified modeling approach that is both repeatable and justifiable is explored for use in the Fatigue Loading Study. For information regarding simplified 2D and 3D modeling techniques, refer to Chapter F5 of this appendix (Commercial Design Software Study).

Because they generally produce more reliable cross-frame results, only 3D models were considered for use in the Fatigue Loading Study. Most 3D models, either from commercial software packages or high-fidelity FEA software, employ the same basic modeling strategies for the concrete deck and girders. The deck and girders are generally modeled as a collection of thin shell elements, and composite action is simulated by vertically offsetting and restraining relative movement between nodes in the top flange and deck shells. The modeling strategies for cross-frames and diaphragms often vary. To simplify the discussions, there are two major approaches to modeling cross-frame elements in 3D analysis models: (i) modeling cross-frames with shell elements and (ii) modeling cross-frames as pin-ended truss elements.

In the first alternative, each component of the cross-frame panel is explicitly modeled with a shell element: connection plates, gusset plates, cross-frame members (typically single angles), and fill plates commonly found at the intersection of diagonals in X-frames. The eccentricity caused by the offset between each

component and the weld restraints are also explicitly considered. These models are simply referred to as shell-element models in this section.

The second alternative, which is more common in design practice, simplifies the cross-frames as pin-ended truss elements. Therefore, the eccentric load path and the stiffness contributions of connection and gusset plates are neglected. While many past studies simply focused on the use of the cross-sectional area of the cross-frame members, Wang (2013) demonstrated the impact of the eccentric connection that could be handled with the stiffness modification factor, *R*. In this study, the R-factor was utilized to account for the reduction in the cross-frame stiffness by either modifying the area or the elastic modulus. These types of models are referred to as truss-element models in this section. Each modeling technique is presented schematically in Figure F3-1.

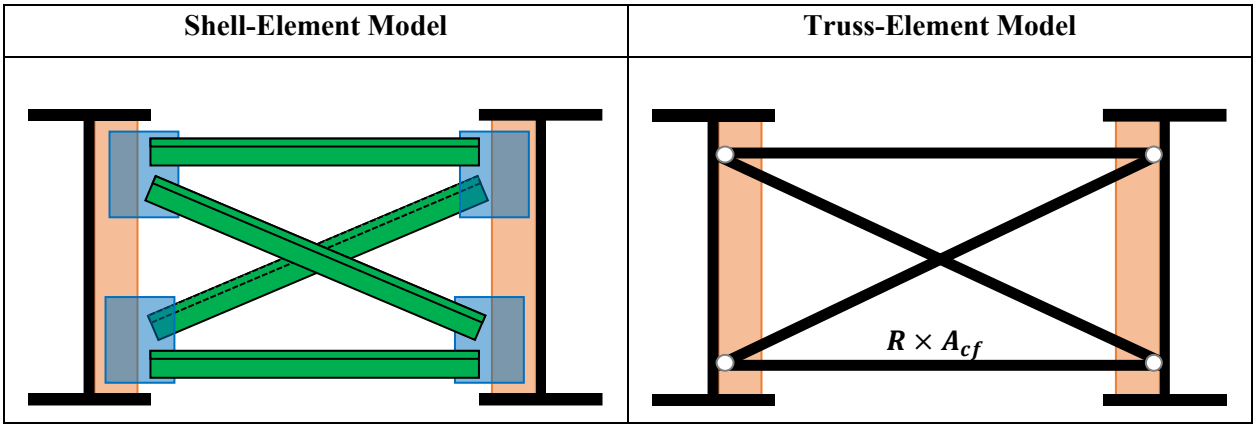

Figure F3-1: Common cross-frame modeling approaches in 3D FEA models

Both 3D modeling techniques (shell-element and truss-element models) were investigated for use in the Fatigue Loading Study. Explicitly modeling the cross-frames as shell elements is the more accurate approach. However, this refined technique (especially with a fine mesh) rapidly increases the computational demands and run time.

As documented in the main body of the report and Appendix E, the RT employed shell-element modeling techniques when performing preliminary and validation studies on the three instrumented bridges in Houston, Texas (TX). For purposes of those initial validation studies, the RT was less concerned about computational efforts and more concerned about representing the three instrumented bridges with the highest precision possible. The primary objective was to achieve good agreement between the measured data and the analytical results, regardless of computational demands.

The Fatigue Loading Study, however, investigates over 4,000 different models using general-purpose FEA program Abaqus. Thus, computational demands become more critical with such a large-scale parametric study. After conducting trial analyses, the RT deemed the shell-element modeling approach too computationally intensive. The RT also learned that the shell-element models provide only marginal improvement on the predicted cross-frame behavior when compared to the truss-element models; this trend is further discussed in Chapter F5. To balance computational speed, project schedule, and modeling accuracy, the RT elected to perform the Fatigue Loading Study with truss-element models.

To better understand the behavior, the RT explored several different nuances to the truss-element modeling approach. The RT performed studies in Abaqus to determine which modeling technique for truss-element cross-frames produces the most accurate results relative to the validated, shell-element models. The following parameters were evaluated:

- The inclusion of the connection plate versus excluding the connection plate;

- In models with the connection plate, the impact of terminating the truss element at the edge of the shell versus passing the truss element through the plate and connecting directly to the web shell; and
- The inclination angle of the diagonal (i.e., changes in the working line of the cross-frame depending on the termination point).

Although not explicitly shown in this appendix, the RT considered various combinations of the parameters listed above. Ultimately, the modeling technique illustrated in Figure F3-2 was adopted by the RT, given the good agreement to the shell-element models. Based on these studies, the RT arrived at the following conclusions:

- Without the connection plates, cross-frame forces are greatly affected by web distortion caused by the concentrated forces acting on an unstiffened, flexible web (i.e., assuming the cross-frame truss element does not connect the web-flange juncture);
- Terminating the cross-frame truss member at the edge of or in the middle of the connection plate affected the force distribution in the cross-frame members;
- Adjusting the inclination angles of the diagonals such that the struts and diagonals share a common node generally yielded the best correlation with the shell-element models.

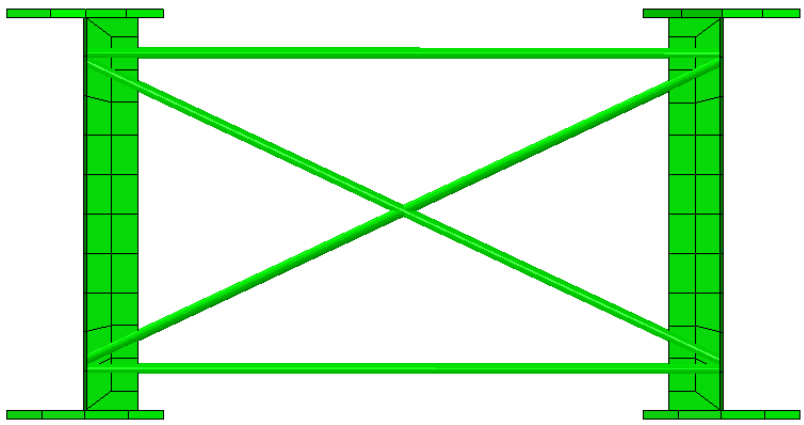

Figure F3-2: Final selected modeling technique for truss-element cross-frames

With a method selected, the RT verified the accuracy of the truss-element modeling approaches and its simplifications before conducting the large-scale parametric study. To do so, the RT reproduced the three validated models (i.e., the instrumented bridges in Houston) but replaced shell-element cross-frames with truss-element cross-frames (as presented in Figure F3-2). The stiffness of the cross-frame truss elements were then modified in accordance with the R-factors derived by previous University of Texas research (Battistini, Wang and Helwig, et al. 2016). Table F3-1 through Table F3-6 present comparative girder deflection and cross-frame results for the three instrumented bridges.

Measured data and analytical results from the validated shell-element and truss-element models are tabulated for critical static load cases. Table F3-1 and Table F3-2 correspond to Bridge 1 results (straight bridge with normal supports), Table F3-3 and Table F3-4 to Bridge 2 (straight bridge with skewed supports), and Table F3-5 and Table F3-6 to Bridge 3 (curved bridge). Similar to the format presented in Appendix E, the ten largest force and deflection magnitudes are presented and compared in these tables. Reaching good agreement with critical measurements was deemed more important than assessing error on small force and deflection magnitudes. For clarity, the geometries of Bridges 1, 2, and 3, as well as the instrumentation plans and load tests, are not included in this appendix. For additional information regarding the field experiments including the truck positions and the load case numbers, refer to Appendix E.

Table F3-1: Comparison of analytical and measured girder deflections at line 4 for critical load cases (Bridge 1)

Load Case	Girder No.	Vertical Deflections (in)		
		Measured	Analytical – Shell Element	Analytical – Truss Element
1	G1	1.48	1.48	1.48
1	G2	1.12	1.09	1.09
2	G1	1.44	1.38	1.37
2	G2	1.06	1.06	1.06
4	G4	1.17	1.08	1.08
4	G5	1.44	1.45	1.44
5	G4	0.93	0.88	0.88
5	G5	0.88	0.91	0.91
6	G4	1.05	0.93	0.93
6	G5	1.29	1.21	1.20

Table F3-2: Comparison of analytical and measured cross-frame axial forces for critical load cases (Bridge 1)

Load Case	Cross-Frame No.	Axial Force (kips)		
		Measured	Analytical – Shell Element	Analytical – Truss Element
3	CF-3	5.03	5.53	5.43
3	CF-4	5.68	8.99	8.34
3	CF-7	7.67	8.77	7.97
3	CF-8	6.41	9.50	8.60
3	CF-9	7.45	8.14	7.70
3	CF-12	5.37	6.19	5.97
7	CF-4	4.37	6.65	6.04
7	CF-7	4.58	5.13	4.66
7	CF-9	5.09	5.97	5.54
7	CF-16	6.74	5.49	6.67

Table F3-3: Comparison of analytical and measured girder deflections for critical load cases (Bridge 2)

Load Case	Girder No.	Vertical Deflections (in)		
		Measured	Analytical – Shell Element	Analytical – Truss Element
1	G23-Line 4	0.28	0.27	0.24
1	G24-Line 6	0.14	0.12	0.10
2	G23-Line 4	0.31	0.34	0.31
2	G24-Line 6	0.15	0.15	0.13
2	G21-Line 6	0.14	0.14	0.12
3	G18-Line 6	0.18	0.16	0.17
4	G23-Line 4	0.23	0.23	0.21
4	G21-Line 6	0.18	0.15	0.14
6	G18-Line 6	0.20	0.22	0.23
7	G14-Line 8	0.24	0.36	0.33

Table F3-4: Comparison of analytical and measured cross-frame axial forces for critical load cases (Bridge 2)

Load Case	Cross-Frame No.	Axial Force (kips)		
		Measured	Analytical – Shell Element	Analytical – Truss Element
2	CF-2	-6.18	-7.29	-4.78
2	CF-3	-4.33	-5.47	-4.02
2	CF-4	-6.12	-7.24	-4.44
3	CF-9	6.45	6.87	5.37
3	CF-11	9.25	10.11	7.39
4	CF-7	8.73	10.20	7.64
4	CF-10	6.93	7.26	5.73
5	CF-8	5.77	5.63	3.90
5	CF-9	6.33	6.99	5.58
5	CF-10	5.87	5.77	4.08

Table F3-5: Comparison of analytical and measured girder deflections at line 11 for critical load cases (Bridge 3)

Load Case	Girder No.	Vertical Deflections (in)		
		Measured	Analytical – Shell Element	Analytical – Truss Element
1	G4	0.88	0.89	0.89
2	G1	0.87	0.91	0.91
3	G1	1.50	1.68	1.69
3	G2	1.17	1.24	1.25
4	G1	1.92	2.14	2.15
4	G2	1.36	1.48	1.48
6	G1	1.17	1.26	1.26
6	G2	0.83	0.87	0.88
7	G1	1.23	1.37	1.37
7	G2	1.00	1.10	1.11

Table F3-6: Comparison of analytical and measured cross-frame axial forces for critical load cases (Bridge 3)

Load Case	Cross-Frame No.	Axial Force (kips)		
		Measured	Analytical – Shell Element	Analytical – Truss Element
1	CF-13	-3.75	-3.91	-3.93
1	CF-14	3.74	4.35	4.40
2	CF-10	-4.30	-5.38	-5.54
2	CF-11	3.66	5.35	5.46
2	CF-14	4.50	4.99	4.96
3	CF-10	-5.93	-7.55	-7.44
3	CF-11	4.84	7.49	7.46
4	CF-10	-5.03	-6.14	-5.72
4	CF-16	-3.66	-4.32	-3.79
7	CF-10	-4.29	-5.30	-5.15

From these tables, it is apparent that modeling cross-frames as truss elements with a stiffness modification factor generally had little impact on the predicted girder and cross-frame behavior when compared to the validated shell-element models and measured data. Predicted girder deflections are nearly identical for all cases, meaning the global stiffness of the superstructure is largely unaffected by the cross-frame modeling approach. More importantly, predicted force effects in the cross-frames from truss-element models are generally within 10% of the shell-element model with a few exceptions, and the sign is always correct.

Larger discrepancies, however, were observed in the Bridge 2 cross-frame results. The cross-frame force effects were consistently underpredicted in the truss-element model. As previously discussed, the R-factor expressions developed by Battistini et al. (2016) were used in the development of these preliminary truss-element models. The cross-frame aspect ratio of Bridge 2 (ratio of girder spacing to cross-frame height) is

large relative to the ratios of Bridges 1 and 3, given the short span lengths and shallow girder depths. Consequently, the assigned R-factor was 0.46, which was significantly lower than the factor assigned to Bridges 1 and 3. Based on the R-Factor Study documented in Chapter F4, the larger discrepancies in cross-frame forces are likely due to the modification factor, not the inherent error associated with the truss-element modeling simplifications. As such, the truss-element approach was deemed suitable for the Fatigue Loading Study. Note that a detailed discussion on the Battistini et al. formulation and the appropriate R-factor is provided in the subsequent chapter.

Based on the findings above, the RT adopted the truss-element modeling approach for the Fatigue Loading Study. It offered reasonably accurate solutions and minimized computational efforts. Aside from the discussions above, the RT also implemented the lessons learned from the validation study in Phase II. During the validation phase of the project, the RT gained valuable insight on the variables and modeling assumptions that were most critical to producing reliable results. The RT identified the following variables as the most important: (i) elastic stiffness of concrete deck and barriers, (ii) spring stiffness of bearing supports, and (iii) presence of concrete rails (especially in curved bridges). These key parameters were considered accordingly in the parametric study.

Lastly, a first-order, elastic analysis was conducted for all cases which is consistent with common design practice and AASHTO LRFD recommendations. This assumption is reasonable, particularly for fatigue loading conditions that are more representative of service-level load magnitudes. The RT performed supplementary FEA studies that considered second-order effects and initial imperfections in cross-frame members but found negligible impacts on force demands. Thus, first-order, elastic analyses were deemed suitable for the Fatigue Loading Study.

For reference, a screenshot of a sample 3D FEA model produced during the Fatigue Loading Study is presented in Figure F3-3 (isometric view from top) and Figure F3-4 (isometric view from underneath). The sample bridge is a two-span, continuous system with a trapezoidal support skew layout (60, 0, and -60 degrees, respectively) and seven girders across the width. Note the deck shell elements are discretized according to the loading grid (Section F3.1.4), as well as the projected outline of the top flange widths. Discontinuous, concrete barriers with joints spaced at 20 feet on center are also included in the FEA model.

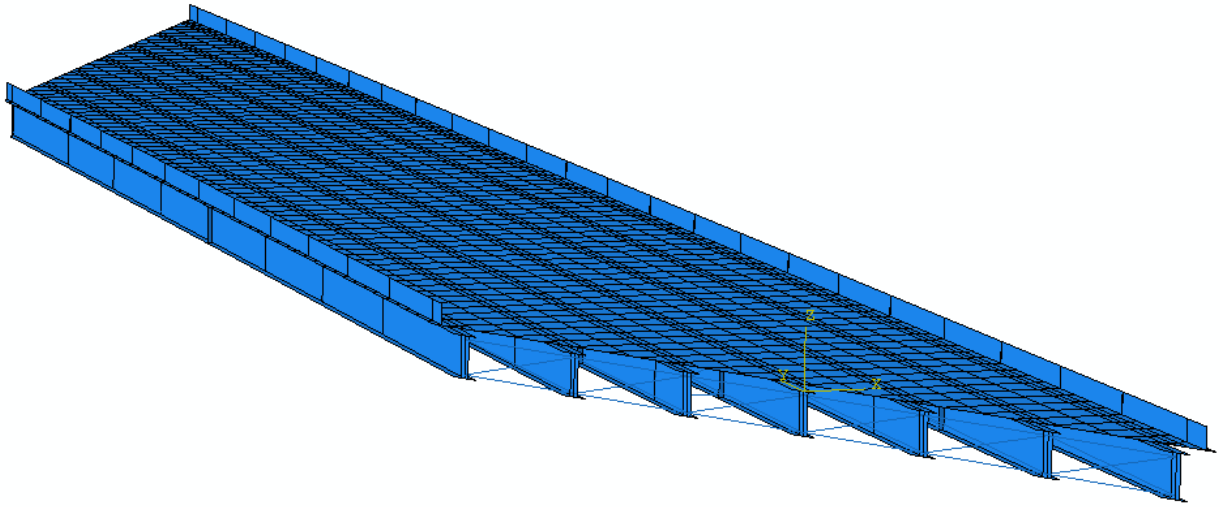

Figure F3-3: Screenshot showing a sample 3D FEA model built in the Fatigue Loading Study (top view)

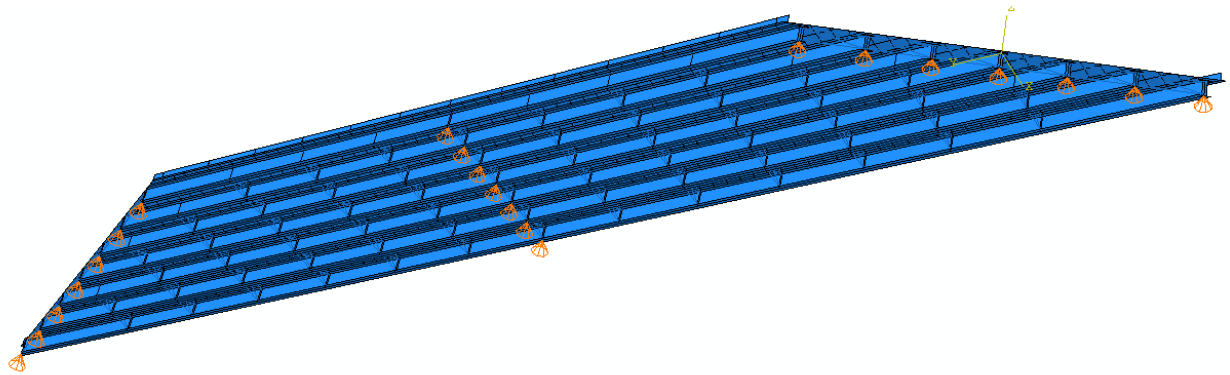

Figure F3-4: Screenshot showing a sample 3D FEA model built in the Fatigue Loading Study (bottom view)

F3.1.2 Analytical Testing Matrix

As previously stated, the range of bridges considered in the study (referred to as the analytical texting matrix hereafter) must represent the common range of steel I-girder bridges currently in service. Developing a testing matrix that represents the thousands of steel I-girder bridges in the US is challenging. There are many different parameters that potentially impact the behavior and response of its cross-frames, and conducting every permutation of every parameter is not feasible given the size. Thus, the RT spent considerable time developing a testing matrix that covers only the most pertinent cases but still balances accurate results and the project schedule.

To accomplish this, the RT began by outlining all possible parameters and categorized them as independent or dependent parameters; independent parameters were then further classified as either constants or variables. Table F3-7 provides a comprehensive breakdown of all parameters considered in the development of the testing matrix. Parameters are divided into four categories: overall geometry, girder cross-section, cross-frame detail, and materials. The proper designation (independent parameter, independent constant, or dependent parameter) is also shown. Dependent variables, although not actively used in the development of the FEA models, are important values that are commonly used to describe the geometry of a bridge and the cross-section proportions of I-girders; hence, they are included in the table for reference. These variables are simply a function of other independent variables and constants. For example, the span length is a function of the girder depth and the span-to-depth ratio of the bridge.

Table F3-8 and Table F3-9 describe the range of variable(s) considered for independent variables and constants, respectively. Note that the list of parameters assumes that the truss-element modeling approach described in the previous subsection is implemented; thus, parameters related to cross-frame details such as gusset plate dimensions are not considered in the Fatigue Loading Study, but are considered in the R-Factor Study instead. For further clarification, Figure F3-5, Figure F3-6, and Figure F3-7 are provided to graphically illustrate some key parameters defined in the tables. Figure F3-5 and Figure F3-6 represent only one example bridge (horizontally curved with parallel support skews and contiguous lines of cross-frames); however, the parameter definitions are consistent across all bridge geometries considered. Figure F3-7 demonstrates an example of a staggered cross-frame layout considered in the study.

There are several key discussion points from these figures and tables. The following bulleted items outline each of those important aspects:

- The differentiation between independent variables and constants is based on prioritization of the parameters, the information gained from the validation studies, data collected from the industry survey, and common bridge design practice. For example, the presence of a concrete barrier was

deemed important based on the validation studies in Phase II. However, for purposes of the Phase III parametric study, the RT elected to simply maintain constant dimensions and parameters for barriers rather than evaluating variable dimensions.

- In the same vein, overhang dimensions were taken as a uniform 3 feet (measured from the centerline of the fascia girder to the outer edge of the deck as shown in Figure F3-6) to simplify the calculations. For bridges with a wider girder spacing, overhang lengths are commonly greater than 3 feet. As is discussed later in Chapter F3, fatigue forces in cross-frames are often maximized by truck passages where a wheel line rides along the overhang portion of the deck. It was found, however, that force effects in a cross-frame member due to an "overhang" live load are generally linearly dependent on the outer wheel distance to the centerline of the fascia girders. In other words, the force effects can effectively be extrapolated to consider wider overhang widths. A similar procedure was utilized in the WIM study, documented in Section F3.3.
- The radius of curvature values reported are based on the centerline of the bridge, as demonstrated in Figure F3-5. Span lengths are also taken about the centerline of the bridge regardless of support skew angles. Span lengths in horizontally curved structures are taken as the arc lengths along the centerline, as is traditionally done in practice.
- Staggered cross-frame layouts were considered in the study, but skewed cross-frames were not. For skewed bridges, cross-frames were either: (i) contiguous lines normal to the longitudinal girders (Figure F3-5) or (ii) discontinuous lines that run parallel to the support skew angle but frame normally into the girders (Figure F3-7). Because both support skew angles considered in the study (30 and 60 degrees) exceed 20 degrees, skewed cross-frames parallel to the support skew were not considered in accordance with AASHTO Article 6.7.4.2. The impact of support skews up to 20 degrees are also considered minimal.
- Lean-on braces were instrumented and studied as part of Phase II. However, these bracing systems and their load-induced behavior were not explicitly considered in the study, as it extended beyond the scope of NCHRP 12-113.
- In general, the RT ensured AASHTO Article 6.7.4.2 was satisfied for the layout of cross-frames. In particular, the cross-frame depth was selected to exceed 75% of the plate girder depth to preclude any significant web distortional effects. The vertical offset between the inside face of the flange and the centerline of the cross-frame member was uniformly taken as 6 inches, which is consistent with common design practice. Additionally, the cross-frame layout rules near obtuse and acute corners of skewed bridges were enforced per AASHTO Article C6.7.4.2. As demonstrated in Figure F3-5, intermediate cross-frames near end and intermediate supports are omitted when the distance along the girder between the cross-frame connection and the support is less than $0.4L_b$, where L_b is taken as the typical cross-frame spacing.
- A constant stiffness modification factor (R-factor) is assumed for all cross-frame systems, regardless of its assumed geometry and connection details. As briefly demonstrated in Section F3.1.1 for instrumented Bridge 2, assigning inappropriate R-factors (either too large or too small) can result in discrepancies in the results. Because the focus of the Fatigue Loading Study is not stiffness modification factors, the RT elected to normalize the effects of eccentric load paths for all cross-frame systems in the 4,104-model parametric study. That way, any potential variability associated with the R-factors is eliminated; the relative impact is then consistent across all bridge models. A uniform factor of 0.60 was selected, as it was shown to be a relatively "average" value in preliminary R-factor studies.
- To maintain the tight project schedule, the decision to use R = 0.6 was made early in Phase III, several months before the final results were obtained from the R-Factor Study (i.e., proposed R = 0.75). Clearly, consistently larger cross-frame force effects would have been determined, had the parametric study been conducted with the larger R-factor. As noted in Chapter F4, an increase in R-factor from 0.60 to 0.75 would only increase those predicted force effects about 5 to 7%. As

such, it was justified that this slight deviation did not warrant a "re-run" of the parametric study or that any major conclusions outlined herein were affected.

- Only single-angle sections for cross-frame members have been considered in the study. Single angles are the most common sections used to construct intermediate cross-frame panels, as was confirmed during the industry survey performed and documented in Appendix D. Single-angle sections are also most critical in terms of eccentric end connection effects. The connection of single angles to connection or gusset plates (typically welds or bolts along only one leg) have an inherent flexibility that is extensively addressed in Section F4, the R-Factor Study. Tee sections (WT sections) are often used instead of angle sections but are generally stiffer and less affected by eccentric load paths. Consequently, only two single-angle sections were considered (L4x4x3/8 and L5x5x1/2) to maintain a manageable scope.
- The span lengths of multi-span bridges were always taken as equal to simplify the analysis and postprocessing of data.
- The girder sections of each bridge were evaluated with respect to proportion limits (AASHTO Article 6.10.2) and strength limit states (6.10.6). In other words, the RT ensured that the full set of bridges represent "real" structures that have been properly designed and detailed. In most cases, the demand-to-capacity ratios of the preliminary designs were below unity for grade 50 steel (F_y = 50 ksi), resulting in a "safe" design. However, several of the more flexible systems resulted in "unconservative" strength designs for grade 50 steel. These cases represent bridges that potentially utilize higher grades of steel (F_y > 50 ksi).
- Aside from the parameters listed in the tables, the RT also conducted "spot checks," particularly for the parameters taken as constants. The RT primarily investigated different flange dimensions and the removal of bridge barriers. Several models were reproduced identically, except for increased flange dimensions with or without barriers. This procedure was done to evaluate the effects of stiff and/or nonprismatic girder sections, as well as models that neglect the bridge rail/barrier which is commonplace in design practice. Thus, a full study of these parameters was not performed in the same manner as the independent variables, but the spot checks still verify the general effect on cross-frame forces.

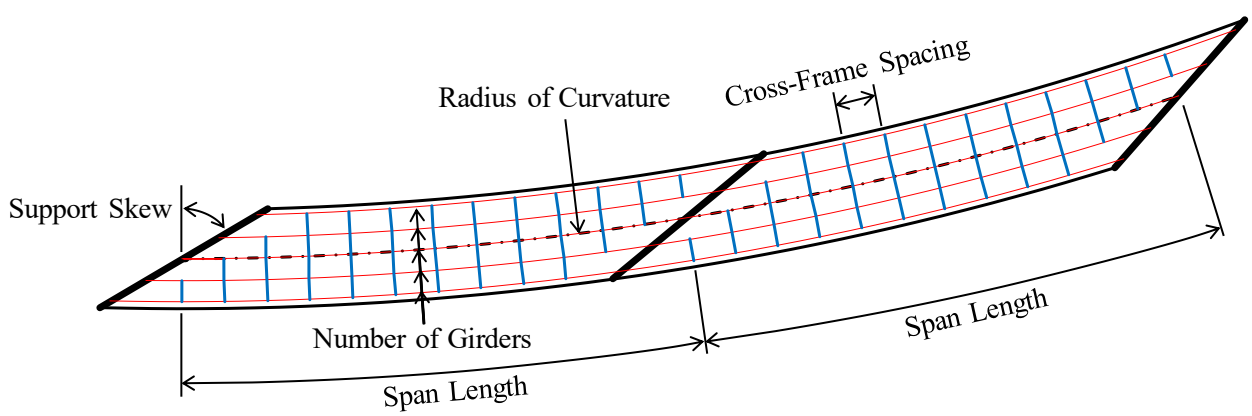

Figure F3-5: Schematic demonstrating the independent parameters and constants used in the Fatigue Loading Study (plan view)

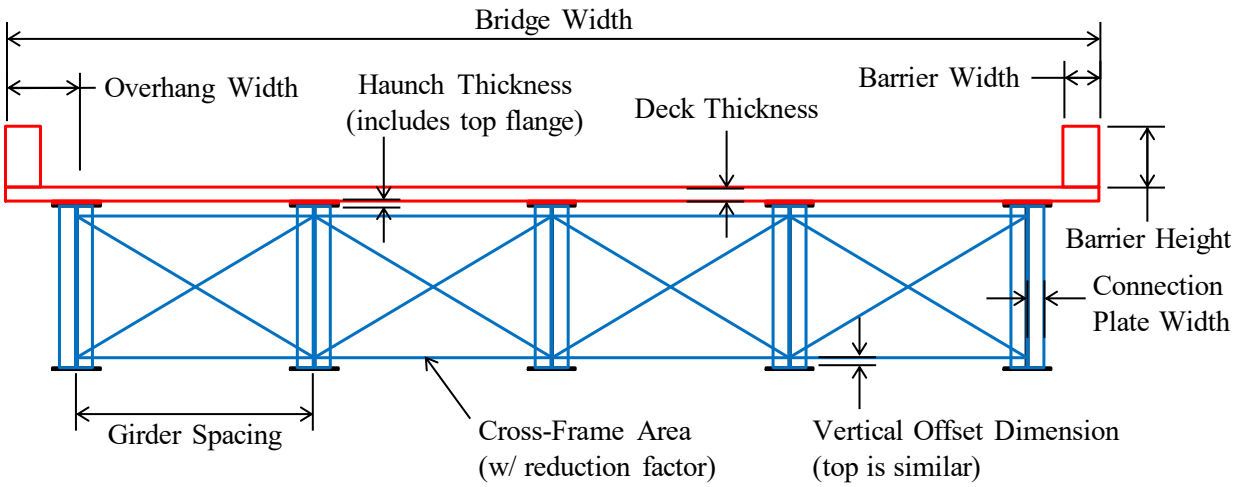

Figure F3-6: Schematic demonstrating the independent parameters and constants used in the Fatigue Loading Study (cross-section view)

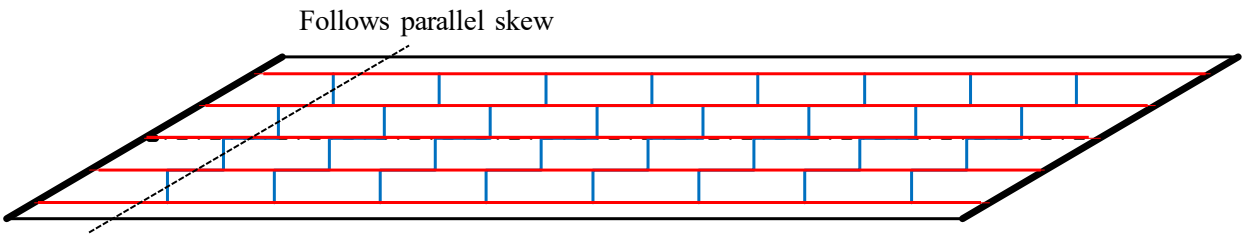

Figure F3-7: Example bridge demonstrating the staggered cross-frame layout considered in the Fatigue Loading Study

Table F3-7: Parameters considered in development of analytical testing matrix

Parameters and Type							
Geometry	**Type**	**Cross-Section**	**Type**	**Cross-Frame Detail**	**Type**	**Material**	**Type**
No. spans	IND	Web depth	IND	Cross-frame type	IND	Concrete modulus	IND
L/d ratio	IND	Deck thickness	IND	Cross-frame area	IND	Steel modulus	CON
Girder spacing	IND	Web slenderness	CON	Connection plate width	CON		
No. girders	IND	Top flange width	CON	Conn. plate thickness	CON		
Support skew	IND	Bottom flange width	CON	Vertical offset dimension	CON		
Radius of curvature	IND	Flange slenderness	CON	Modification factor	CON		
Cross-frame spacing	IND	Degree of monosymmetry	CON				
Cross-frame layout	IND	Flange transitions	CON				
Barrier joint spacing	CON	Haunch thickness	CON				
Overhang width	CON	Barrier thickness	CON				
Span length	DEP	Barrier height	CON				
Bridge width	DEP	Bearing stiffness	CON				
Skew index	DEP	Web thickness	DEP				
Curvature index	DEP	Top flange thickness	DEP				
		Bottom flange thickness	DEP				

Note: IND = independent variable, CON = constant value, DEP = dependent variable

Table F3-8: Range of values used for independent variables in Fatigue Loading Study

Parameter	Range of Values
No. spans	{1, 2, 3}
L/d ratio	{25, 30, 35}
Girder spacing [ft]	{6, 8, 10}
No. girders	{3, 5, 7}
Support skew	{0, 30, 60}; {Parallel, Trapezoidal}
Radius of curvature [ft]	{Infinite, 1500, 750}
Cross-frame spacing [ft]	{20, 30}
Cross-frame layout	{Contiguous, Staggered}
Web depth [in]	{72, 96}
Deck thickness [in]	{8, 10}
Cross-frame type	{X, K}
Cross-frame area [in^2]	{2.86, 4.79}; {L4x4x3/8, L5x5x1/2}
Concrete modulus [ksi]	{3600, 5000}

Table F3-9: Constant values used in Fatigue Loading Study

Parameter	Value
Barrier joint spacing [ft]	20
Overhang width [ft]	3
Web slenderness	128
Top flange width [in]	24
Bottom flange width [in]	24
Flange slenderness	8
Degree of monosymmetry	0.5
Flange transitions	None
Haunch thickness [in]	3 (Including flange)
Barrier thickness [in]	18
Barrier height [in]	36
Bearing stiffness	As-validated
Connection plate width [in]	8
Connection plate thickness [in]	0.5
Vertical offset dimension [in]	6
Stiffness modification factor	0.6
Steel modulus [ksi]	29000

Based on the parameters outlined in Table F3-8 and Table F3-9, it is apparent that conducting every permutation of every parameter is not feasible given computational constraints. Every permutation would result in a parametric study matrix of over 100,000 models. Instead, the RT filtered the matrix to consider only the most critical cases. The desired number of models was computed as a function of the project

schedule and the run/post-processing time required for any given model. In total, the RT filtered the matrix down to the most critical 4,104 models.

To do so, rules were established to eliminate permutations deemed unnecessary or less important than others. Many of these rules were based on current AASHTO provisions with regards to geometric limits. For example, AASHTO Article 2.5.2.6.3 recommendations were implemented to establish reasonable bounds on the span-to-depth-ratios considered in the study. For straight, simply-supported bridges, the *L/d* ratio was limited to 30; for straight, continuous bridges, the ratio was limited to 35. Similarly, curved bridges were limited to *L/d* ratios of 25 (simply-supported) and 30 (continuous). The comprehensive list of every bridge is provided Chapter F7 and includes the parameters used to build the superstructures.

F3.1.3 Load Application

As previously documented, the objective of the Fatigue Loading Study is to evaluate a variety of bridge geometries and the response of its cross-frames under various loading conditions. Therefore, it is imperative to develop an analytical model that accurately represents the applied loading in an efficient manner. Current AASHTO fatigue loading criteria require that the fatigue truck be positioned in all transverse and longitudinal positions across the bridge deck to maximize the stress ranges in the detail under consideration (Article 3.6.1.4.3). In terms of the FEA model, this type of loading can be applied in one of two ways: (i) directly applying the moving truck loads to the deck surface or (ii) performing an influence-surface analysis where a static 1-kip load is applied to a predefined grid of load positions.

Both alternatives involve a series of static load cases that can be computationally intensive and time-consuming. In the first alternative, the response of cross-frames is evaluated directly for specific moving trucks. In the second alternative, the output is independent of any specific truck configuration such that realistic trucks can be evaluated externally of the Abaqus FEA model. Both approaches ultimately arrive at the same results, but the level of efficiency is drastically different. The influence-surface approach offers more flexibility and computational savings by limiting the demands on Abaqus. Thus, it is the preferred choice.

Influence-surface analysis was generated in Abaqus by applying a unit point load across a defined grid of load positions. The loading grid extended over the entire width (in-to-in dimension of the barriers) and length of the bridge to capture the full influence. For bridges with skewed end supports, the loading grid extended to the acute angle of the bridge deck. To capture the effects of a realistic truck passage instead of a static unit load, an Excel program and script were developed to simulate these effects. This procedure is detailed in Section F3.2 of the appendix.

Similar to the discussion in Section F3.1.1, modeling decisions for large-scale parametric studies are often about balancing computational efficiency and modeling accuracy. In terms of accuracy, it is important that the critical loading position is captured by the specified loading grid. Recall from the measured data reported in Appendix E that the induced axial force in a cross-frame member can be highly sensitive to load position, which heightens the importance of the assumed grid.

Thus, the RT spent considerable time determining the appropriate discretization size (i.e., how often the unit load is applied longitudinally and transversely). The RT conducted a preliminary study in Software A, which has built-in influence-surface functionality, to understand the effects of loading grid discretization.

Figure F3-8 presents an example of the analysis performed in this initial study. For a three-girder, two-span continuous, straight bridge with skewed end supports, an influence-surface analysis was performed for two cases: (i) with a fine loading mesh (1-ft longitudinal and 1-ft transverse) and (ii) with a coarse loading mesh (5-ft longitudinal and 4-ft transverse). The girders were spaced at 8 feet on center in this example; hence, the 4-ft transverse discretization size in the second case corresponded to a grid at the girder lines and the midpoint between girder lines (i.e., midpoint of each cross-frame bay).

Figure F3-8 presents the influence-line results for a cross-frame diagonal near the intermediate skewed support (as highlighted in the figure). The bridge is subjected to the AASHTO fatigue truck driving over the centerline of the bridge. It is evident that the predicted axial force response of the cross-frame is not significantly affected by the loading grid assumed. For this example, the largest difference in the predicted maximum force range was less than 4% when a coarse mesh was applied. The RT performed similar analyses on other bridge geometries and cross-frame members, and the results were comparable. This was the case for both longitudinal and transverse variations in truck location. For straight bridges with normal supports, the discrepancy observed was generally less than 1%.

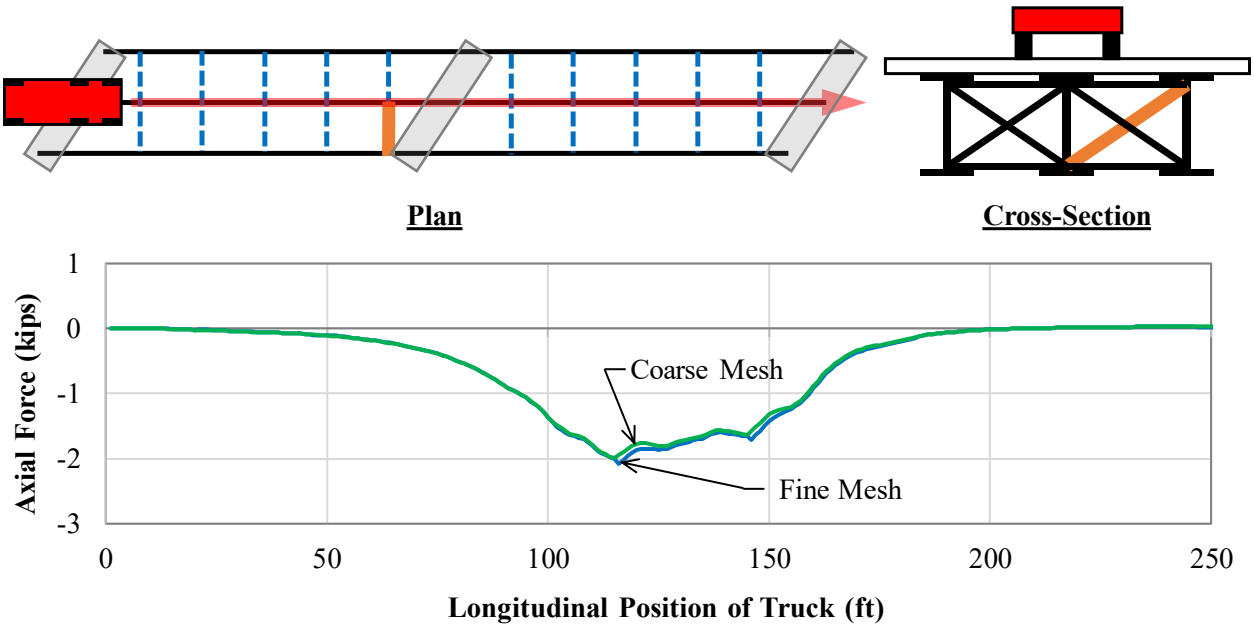

Figure F3-8: Response of a cross-frame diagonal in sample skewed bridge to demonstrate effects of loading grid discretization

The behavior in Figure F3-8 is realized largely because the transverse load influence on cross-frame forces is approximately linear between the adjacent girders and the midpoint of each cross-frame bay. Thus, adding additional load points on an already linear response is unnecessary, especially since linear interpolation is performed in the calculation of these responses.

The RT optimized the applied loading grid by assigning load points at every 5 feet longitudinally and at the following transverse locations: at each girder line, midpoint of every cross-frame bay, and at each deck edge (1 foot outboard from the centerline of the fascia girder). Thus, every bridge analysis included between approximately 217 to 1,905 static load cases; the number of static load cases depended on the bridge length and width. For context, over 3.6 million load cases were performed as part of the Fatigue Loading Study despite the coarse loading grid adopted.

For curved bridges, the 5-foot longitudinal grid spacing was based on the arc length of the bridge centerline. Therefore, the true distance along the inner radius of the curve is less than 5 feet, and the true distance along the outer radius is greater than 5 feet.

F3.1.4 Mesh Sensitivity

In addition to the sensitivity of the loading grid mesh, the sensitivity of the finite-element model mesh was also extensively studied prior to conducting the Fatigue Loading Study. During the validation stage of Phase

II, a fine mesh was used to accurately represent the real conditions of each instrumented bridge. Fine element meshes potentially offer more accurate solutions but at the cost of increased computation time and storage. Acknowledging that computation speed is of the utmost importance for obtaining the necessary data from the Fatigue Loading Study, the RT studied the effects of a coarser mesh on the predicted response of cross-frame members.

The RT conducted several preliminary tests in which the same model was run twice, once with a fine mesh and the other with a coarse mesh. For the fine mesh, the girder constructed of flange and web shells was meshed at 6 inches, and the deck shell was meshed at 12 inches. For the coarse mesh, the respective shell meshes were quadrupled. Note the deck mesh specified is in addition to the loading grid discussed in the preceding subsection, as the unit loads must be applied at a defined node. The predicted cross-frame force effects were then compared between the two models.

Similar to Figure F3-8, Figure F3-9 presents the influence-line results for a cross-frame diagonal near the maximum positive dead load moment region of a two-span continuous, straight bridge with normal supports. The bridge was subjected to the AASHTO fatigue truck driving over the first interior girder line, as illustrated in the figure. It is observed that the response predicted by the coarse mesh model was nearly identical to the predicted response of the fine mesh model (less than a 1% discrepancy in stress range). The results for other models evaluated were similar.

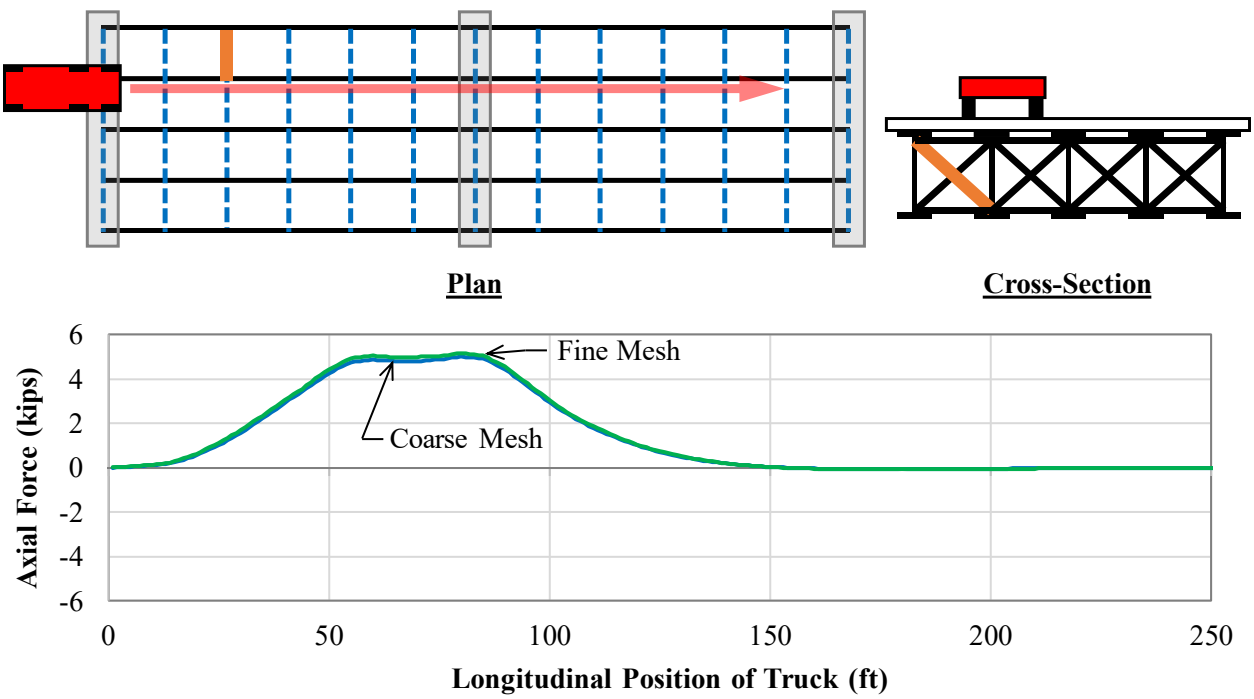

Figure F3-9: Response of cross-frame in sample normal bridge to demonstrate effects of shell element mesh

Given that cross-frame forces were not found to be overly sensitive to shell element mesh size and localized stresses are not important to the study at hand, a coarse mesh was adopted leading to a more efficient parametric study. The girder shells were meshed at 24 inches (i.e., three to four shells along the depth of the web), and the deck shells were meshed at 48 inches (in addition to the loading grid). Girder flanges were partitioned along the web such that two shells across the flange width were considered. Quadrilateral meshes were typically used, except at extreme cases near skewed ends. In those cases, special care was taken to ensure reasonable aspect ratios (i.e., within 3 to 5).

F3.1.5 Postprocessing Critical Cross-Frames

As outlined in previous subsections, executing a large-scale parametric study must balance accurate solutions with computational demands. This discussion is important for model development (e.g. element mesh size) but is equally important for postprocessing of output. The field experimental data demonstrated that force demands in cross-frames are highly dependent on several items including load position, bridge geometry (e.g. radius of curvature and support skew angle), and location of the cross-frame in relation to the supports and deck edges.

Depending on these parameters, the stresses/forces induced in cross-frames along the length and width vary and, as a result, certain cross-frames will be critical for fatigue.. Rather than evaluating the forces in every cross-frame from every model in the Fatigue Loading Study, it is more reasonable to evaluate only the most critical members. This, in turn, simplifies the postprocessing required and reduces computational efforts in Abaqus. For context, the 4,104-model Fatigue Loading Study included over 200,000 cross-frame panels and over 900,000 cross-frame members (top strut, bottom strut, diagonals). Processing the results of nearly a million cross-frame members was not feasible given the schedule constraints of the project.

Even if every cross-frame is not evaluated, the objective is still to evaluate the most critical cross-frames for each bridge. Knowing that force effects are likely dependent on load position, bridge geometry, and location on the span, identifying the critical cross-frame for all 4,104 unique bridges is challenging. Thus, the RT took a more systematic approach to determine the most likely "critical" cross-frames for a given bridge. Prior to the Fatigue Loading Study, the RT conducted a preliminary parametric study to answer the two following questions:

1. Where is the most critical cross-frame typically located along the length and width of a bridge (for normal, skewed, and/or curved bridges)?
2. What is the influence of the transverse and longitudinal load position on the force effects in these critical cross-frames?

The preliminary parametric study implemented only the most extreme geometric conditions listed in Table F3-8. By investigating the effects of extreme parameters, the RT felt confident that the general trends across the entire data set would be revealed. The RT conducted an influence-surface analysis in accordance with Section F3.1.3 and studied how applied loads are generally distributed through highly skewed and highly curved bridge structures.

In terms of the first question posed above, the RT found that the location of the critical cross-frame (based on maximum stress/force ranges) largely depends on the presence of a support skew. For bridges with normal supports (straight or horizontally curved), the most critical cross-frame members tended to be diagonal and bottom strut members near the location of maximum positive dead load moment on the span (i.e., midspan of a simply-supported bridge and approximately $0.35L$ to $0.40L$ of end spans of continuous units). For bridges with skewed supports (30 degrees or more), cross-frames near end or intermediate supports of skewed bridges showed the most substantial force effects relative to other cross-frames on the bridge.

For the second question, the RT observed that cross-frames are significantly more sensitive to transverse position of load compared to longitudinal position of load. In general, the force effects in cross-frames are maximized when the load is positioned directly over the cross-frame of interest (i.e., just to the left or right of the cross-frame panel of interest), and the differential deflection of adjacent girders is maximized. This same behavior was observed and documented extensively in Appendix E for all three instrumented bridges.

However, cross-frames in skewed systems tend to have a more complex response to load position. When compared to straight bridges with normal supports, support skew and curvature generally broaden the longitudinal load influence as evidenced by the results of the preliminary parametric study. An example of this is demonstrated by the influence-surface results in Figure F3-10. As is discussed further in Section

F3.1.8, influence-surface results are best displayed as color contour plots where the x- (longitudinal) and y-coordinates (transverse) represent the spatial coordinates of the applied load on the deck surface and the z-axis (color intensity) represents the corresponding magnitude of the force effect.

Note that the framing plan for each bridge in Figure F3-10 is overlaid on the color contour plot. Girder lines and cross-frames are shown with thin green lines; supports are represented as bolded and dashed black lines. The cross-frame of interest, for which the influence-surface results are presented, are bolded.

The contour plot in Figure F3-10 demonstrates the axial-force response of a select diagonal cross-frame member near the intermediate support. The diagonal that frames into the top flange of the first interior girder from the left (i.e., “left” corresponding to negative values about the y-axis) is displayed. Two different influence-surface results are provided: a two-span, straight bridge with normal supports and an otherwise identical bridge (e.g. same deck thickness, girder spacing, etc.) with 60-degree support skews. Thus, the only discernible differences between the bridges are the support skew and the cross-frame layout at the skews. Note that the x- and y-coordinates are not to scale; the transverse (y-axis) is scaled up for easier viewing.

The color intensity on the plots corresponds to the axial force induced in the cross-frame member due to a 1-kip load positioned at a given spatial coordinate on the deck surface. Thus, the color intensity is specified in units of kips of axial force per kips of applied load on the deck (i.e., kips/kip). For loads applied in the "red" area on the plot, the compression force in the diagonal is maximized. For loads in the "blue" area, the tension force in the diagonal is maximized. Load positions in the grey area have negligible influence on the axial-force response in that cross-frame member. As an example, a value of +0.1 kips/kip at a given location on the deck (representing a critical tensile load position) means that a 1-kip load applied there results in 0.1 kips of axial tension in the cross-frame diagonal of interest.

From Figure F3-10, it is obvious that the longitudinal load influence of the skewed bridge is broadened relative to the normal bridge. In fact, there is strong tensile load influence along the outer “right” edge of the bridge deck (i.e., a blue area), which is not present for the straight bridge. The overall magnitudes at the critical load positions are also slightly higher in the skewed system, as expected.

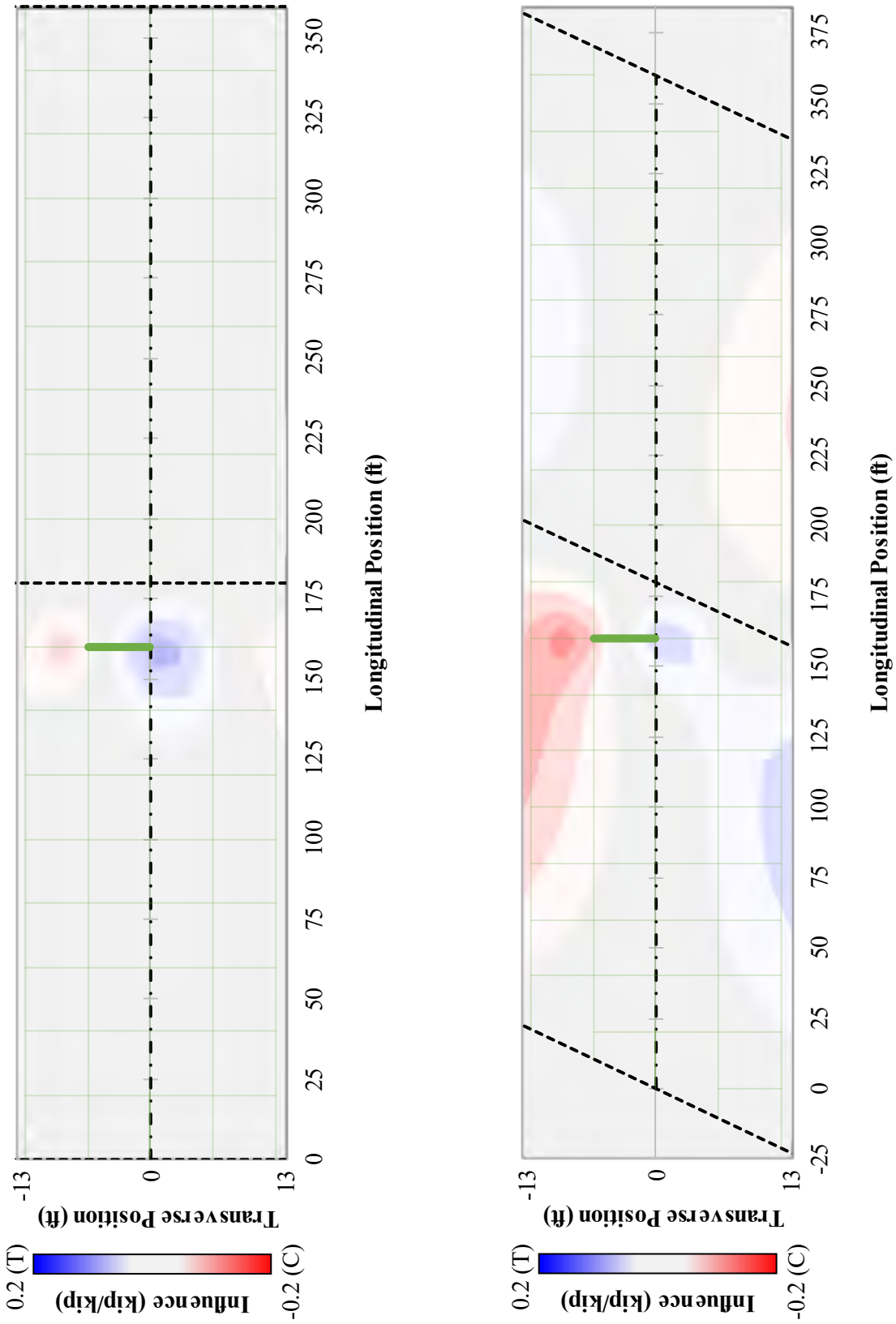

Figure F3-10: Comparison of influence-surface plots for axial force response of cross-frame diagonal near intermediate support with (left) no skew and (right) 60-degree skew

Based on the findings of this preliminary parametric study, the RT decided to preselect cross-frames to evaluate prior to running the full parametric study. Given the unique geometries and cross-frame layouts, the selected cross-frames are not in the exact same location for each bridge. Rather, the RT selected general locations/regions that are consistent across all 4,104 models. For those specified regions, the RT wanted to investigate the complex load paths near skewed supports, as well as the localized load effects away from the supports. Thus, the four general locations/regions, which apply equally to both straight and curved bridges, included:

- Edge cross-frame bay closest to maximum positive dead load moment;
- Interior cross-frame bay closest to maximum positive dead load moment;
- Interior cross-frame bay nearest to the end support (skewed or non-skewed); and
- Interior cross-frame bay nearest to the intermediate support (skewed or non-skewed).

To maximize differential girder displacements at skewed supports (end or intermediate), interior cross-frames are to be evaluated instead of the edge cross-frames; in these instances, one end of the cross-frame panel frames into a girder in close proximity to a bearing support where vertical displacement is restrained. The effects of deck overhang loading can be prominent, particularly in the edge bays near the maximum dead load moment region; therefore, both an interior and edge bay are selected in these regions. For bridges with only three girders, the other end bay is evaluated in lieu of the nonexistent interior bay. For simply-supported spans with no intermediate support lines, the cross-frame results at the opposite end support (similar to what is reported for the third location) were evaluated in lieu of a cross-frame near an intermediate support.

Note that all members of the selected cross-frames were evaluated as part of the parametric study (i.e., top strut, diagonals, bottom struts for both X- and K-type frames). Thus, the RT evaluated 16 cross-frame members per model for bridges with X-type cross-frames (4 cross-frames * 4 members per cross-frame = 16 members) and 20 cross-frame members for bridges with K-type cross-frames (4 cross-frames * 5 members per cross-frame = 20 members). In total, the influence-surface of 68,352 cross-frame members were analyzed as part of the Fatigue Loading Study (compared to the over 900,000 members available from which to choose). By only evaluating the most critical cross-frames for each model iteration, more efficient computational efforts are realized.

A representative sketch is provided in Figure F3-11, showing the critical cross-frames to be evaluated for single-span, two-span continuous, and three-span continuous straight bridges. Note that these figures are simply schematic and not drawn to scale. In addition, only intermediate cross-frames are illustrated; cross-frames at end and intermediate supports are hidden for clarity, as these are not the focus of the Fatigue Loading Study.

In Figure F3-11, the single- and two-span bridges are presented with skewed supports. The three-span bridge is presented with normal supports. For all three-span bridges considered in the study (which only represent 72 of the 4,104 bridges in the matrix), only cross-frames in the interior span are evaluated. The behavior in the end spans are assumed to be fairly consistent with the behavior of the two-span bridges. Still, the general layout of the critical cross-frame regions in the interior span is consistent with the single- and two-span bridges.

Given that a small percentage are evaluated for each bridge, the RT acknowledges that the most critical cross-frame for a given bridge may not be included in the predetermined list of four. However, the variation between the most critical cross-frame and the largest of the four cross-frames evaluated in the study is relatively small. Based on the analysis performed, the RT feels confident that, even if the critical cross-frame is “missed” by the postprocessing methodology, the four cross-frames considered are still among the most critical. Therefore, the design stress/force range determined from the four select cross-frames will only be marginally smaller than the “true” range based on every intermediate cross-frame. This assertion is

examined further in Section F3.2.2.

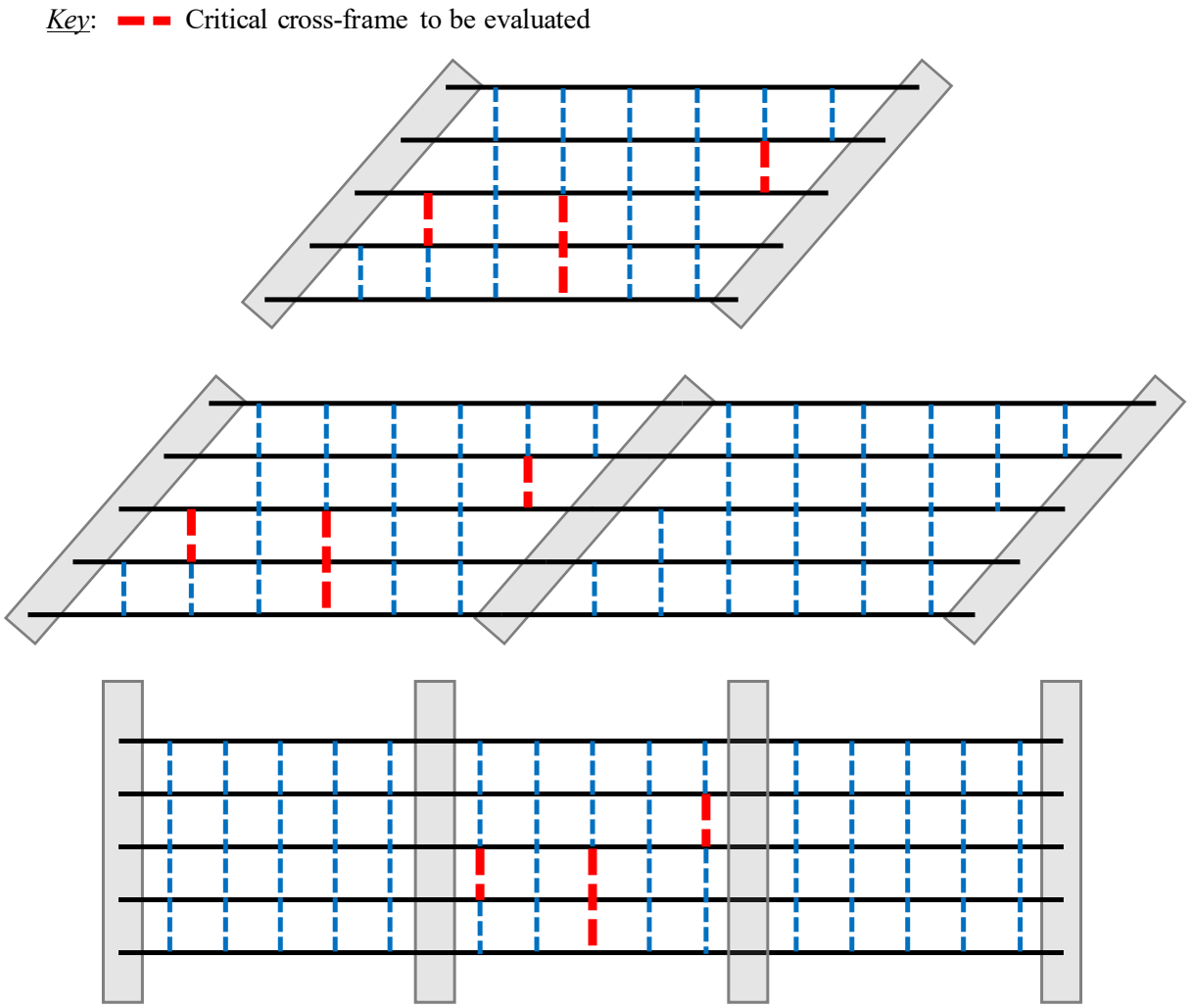

Figure F3-11: Critical cross-frames to be evaluated for sample bridges: (top) single-span with skewed supports, (middle) two-span continuous with skewed supports, and (bottom) three-span continuous with normal supports

F3.1.6 Automation and Scripts

Despite the efforts to limit the computational demands, conducting a large-scale parametric study with 4,104 unique bridge models was still time-consuming. To expedite the process and maintain the project schedule, the RT developed Python scripts to automate the large-scale calculations. The Python scripts were designed to perform the following tasks: (i) build the 3D FEA models for all geometries (Section F3.1.2) and apply the appropriate loading grid in Abaqus (Sections F3.1.1, F3.1.3, and F3.1.4), (ii) run the simulated influence-surface analysis, (iii) output the axial force and displacement response of the preselected cross-frame members of interest (Section F3.1.5), and (iv) create summarized output files of all pertinent data. The summarized output files tabulated the influence-surface results for every critical cross-frame member.

For each load position in the influence-surface analysis, the following data was collected and stored in the raw output files: axial member forces and "corner" displacements of the four select cross-frames panels. The corner displacements represent the vertical and transverse deflections of the four "corners" that

comprise a cross-frame panel. These displacements, when plotted together, illustrate the deformation patterns undergone by the panel when subjected to live load traffic.

The Python script was designed to operate off the Linux-based Texas Advanced Computing Center (TACC) server. TACC offers extremely fast computation times and the ability to run simultaneous jobs. The RT developed two independent scripts (straight and curved) that are capable of building all bridge geometries in the 4,104-model parametric study. Once the summarized data files were obtained from the TACC computers, further postprocessing was performed in an external Excel program, which is documented in the next subsection.

F3.1.7 Data Visualization

As outlined in the previous subsections, the analysis procedure was designed to record the axial force and displacements of four critical cross-frames for 4,104 unique bridges. For each bridge, between 217 and 1,905 static load cases (depending on bridge length and width) were evaluated per model to develop an influence-surface profile of the entire deck surface. A single output file contained all pertinent data for every bridge; thus, a total of 4,104 output files were created during the Fatigue Loading Study.

Due to the overwhelming amount of data produced from the parametric study, the RT identified a need to view and evaluate data in an organized manner. Accessing every output file and processing individually was simply not feasible. An Excel-based "data visualization" workbook was developed as a centralized tool to view all data obtained from the finite element models. The workbook was designed to run a series of calculations and macros that eliminate the need to store all data in one comprehensive file. This, in turn, significantly reduces the necessary memory and computational time.

The interactive, Excel-based workbook, besides organizing the output file structure, serves several basic functions. These functions, which are driven from a set of user inputs, are as follows:

- Display the influence surface for the axial-force response of cross-frames in the form of a color contour plot;
- Display the global and localized displacement of the cross-frame panel of interest, where localized displacement implies that the rigid-body motion of the superstructure is removed (see the discussion on load-induced deformation patterns in Chapter F4);
- Simulate the passage of any given truck(s) along the length of the influence surface to develop an influence-line plot; and
- Tabulate all relevant parameters describing the geometry and details of the superstructure, as well as provide a framing plan and cross-section view for reference.

An example of these features are presented in Figure F3-12, Figure F3-13, and Figure F3-14. These figures display a screenshot of the interactive workbook for an example bridge (simply-supported, straight bridge with normal supports). Note that the influence-line plot shown in Figure F3-13, a process that is summarized in Section F3.2, is based on the AASHTO fatigue truck traversing the bridge about its centerline. This lane position represents the critical loading for the cross-frame member of interest. The results presented in Sections F3.1.8 and F3.2 were largely developed from the Excel-based workbook.

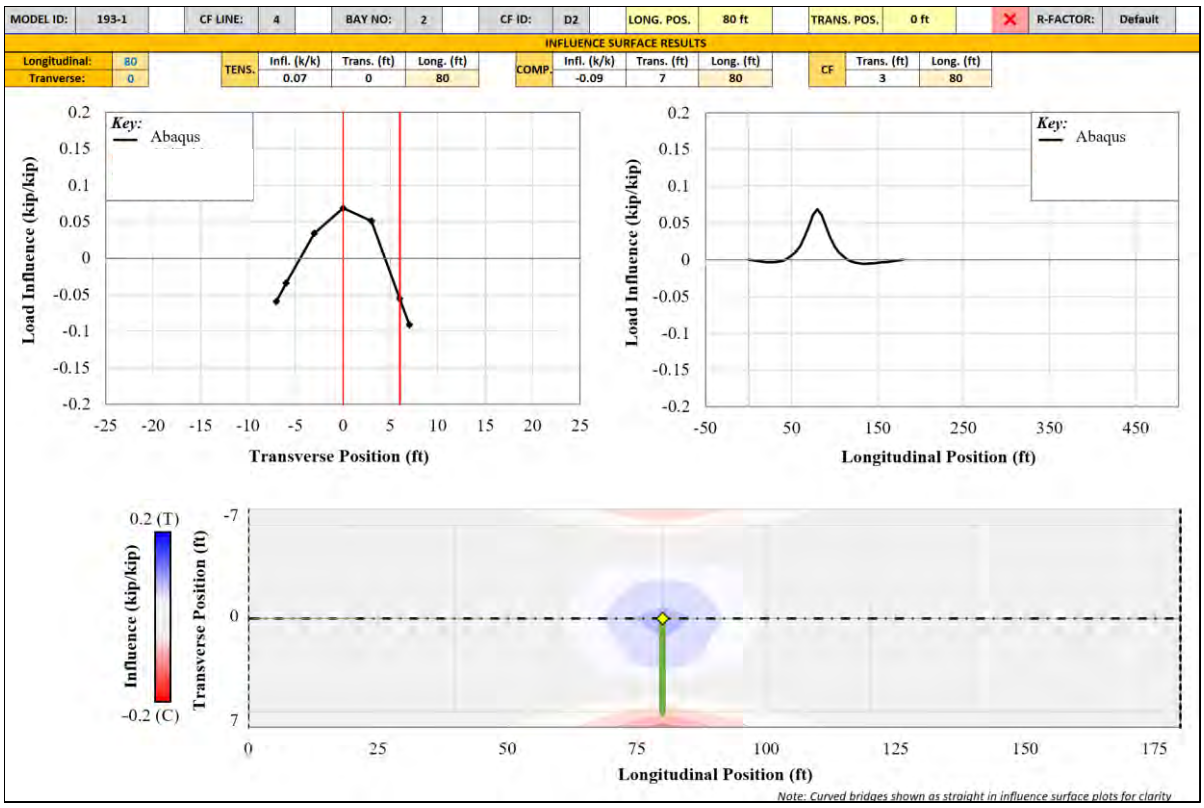

Figure F3-12: Screenshot of interactive Excel-based graphical interface showing influence-surface results

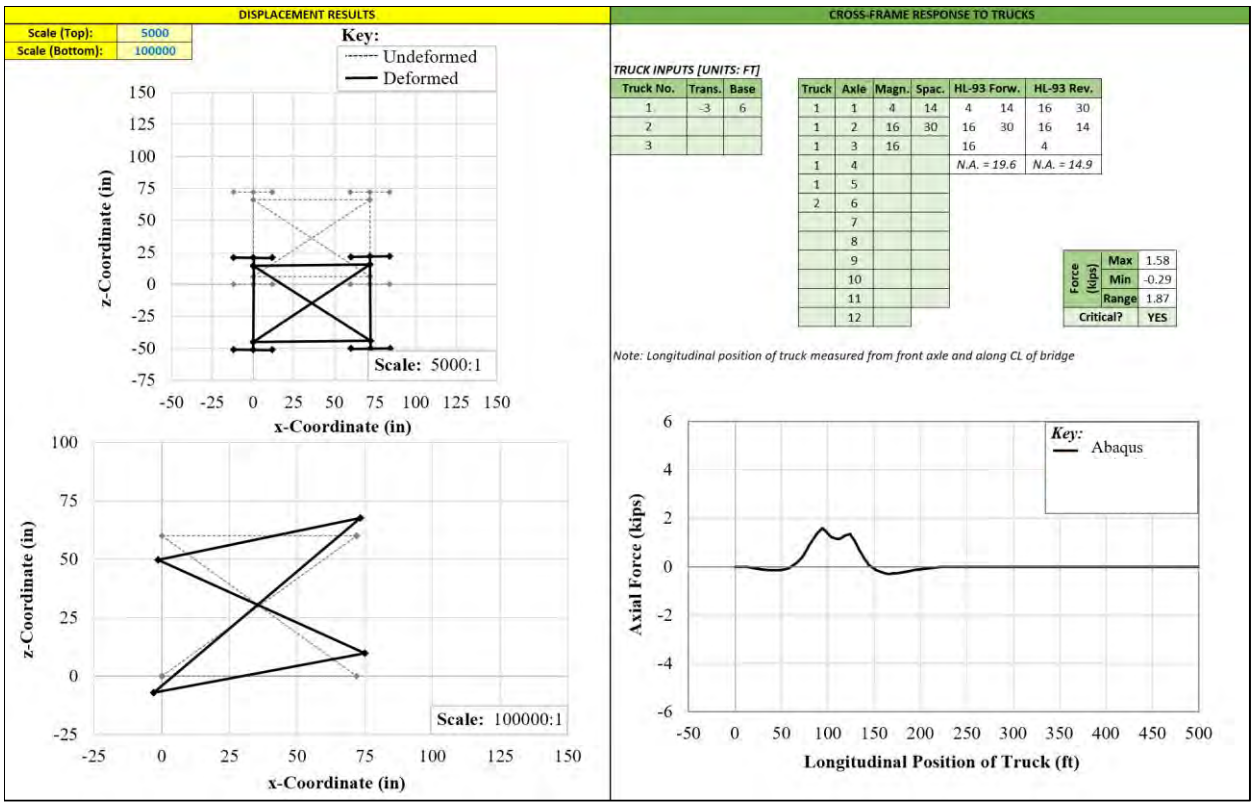

Figure F3-13: Screenshot of interactive Excel-based graphical interface showing displacement results

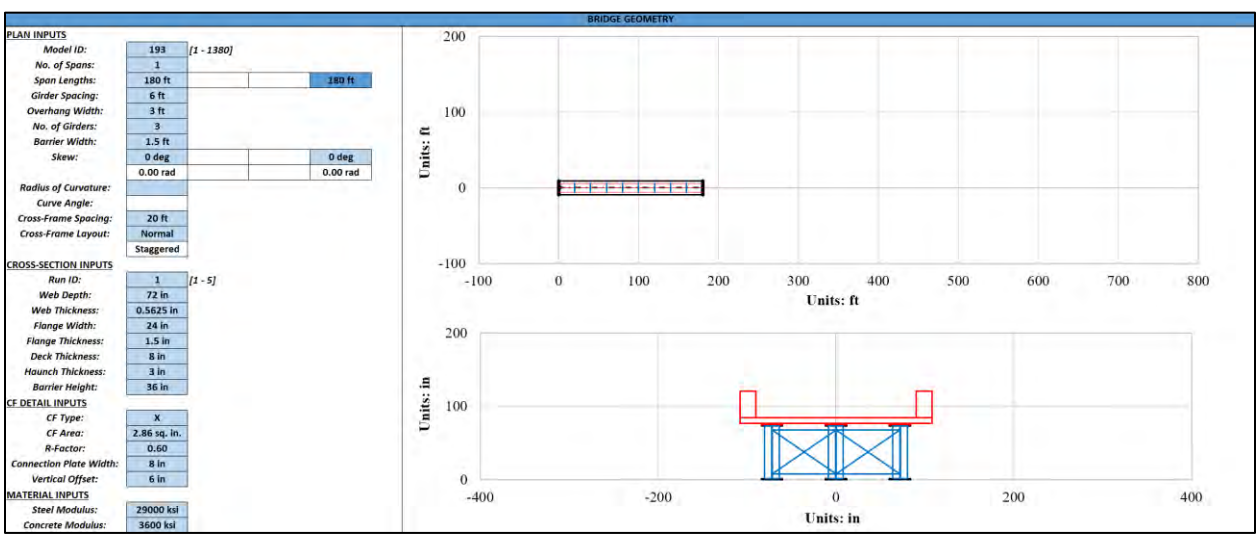

Figure F3-14: Screenshot of interactive Excel-based graphical interface showing bridge parameters, framing plan, and cross-section views

F3.1.8 Influence-Surface Results

In total, the RT produced over 65,000 influence-surface plots from the Fatigue Loading Study. As

previously discussed, presenting all results is not feasible given its sheer volume. Instead, this subsection is dedicated to showing additional influence-surface examples, similar to Figure F3-10 and Figure F3-12, as well as methods to graphically compile and present data from the full data set. As such, Section F3.1.8.1 presents six additional influence-surface figures and commentary, and Section F3.1.8.2 outlines the general trends and observations of the full data set.

F3.1.8.1 Influence-Surface Results

As stated above, six different comparative examples are provided in this section (Figure F3-15 through Figure F3-20). The sample data, which were selected to generally represent the full data set, demonstrate how to interpret the plots and introduce key trends and observations. Similar to Figure F3-10, these influence-surface results are depicted as color contours. Each figure demonstrates a key observation about how a particular parameter affects (i) the overall transverse and longitudinal load influence and (ii) the force demands in critical cross-frames.

The general transverse and longitudinal load influence is illustrated by the "distribution of color intensities" across the bridge width and length. For example, straight bridges with normal supports typically have localized load-influence effects, meaning the color intensities are centralized around the cross-frame panel of interest. The relative force demands, in contrast, are indicated by the magnitudes of the color intensities. Although the 1-kip loads applied to the deck surface have no physical meaning, larger load-influence magnitudes correlate to larger force/stress ranges when design loads and real WIM loads are applied. The evaluation of the bridges with respect to these realsitic loads is addressed in Sections F3.2 and F3.3, respectively.

In each figure, two different influence surfaces for the axial-force response of a cross-frame member are presented. The "left" and "right" influence-surface plots in each figure correspond to nearly identical bridges, except for one key parameter. That one parameter is isolated such that the differences in the load influence are solely attributed to it.

Table F3-10 summarizes all the independent variables that describe the bridge geometry, cross-frame layout, and cross-frame details of each case. In this sample data, a variety of bridge conditions are highlighted (e.g. straight bridge with normal support, straight bridge with skewed supports, and horizontally curved bridges). As identified above, each figure compares nearly identical conditions between the "left" and "right" plots; therefore, many of the values in the table remain unchanged. The key parameter that is isolated and evaluated for a given figure is bolded. For example, Figure F3-17 evaluates the axial-force response of a cross-frame member due to increasing the deck thickness from 8 to 10 inches; the balance of the parameters in that figure are identical between "left" and "right" plots. The following list summarizes the key parameter that is evaluated for each figure:

- Figure F3-15: demonstrates that the location of the cross-frame panel relative to skewed supports has a significant impact on load distribution and force demands in cross-frame members;
- Figure F3-16: demonstrates the sensitivity of transverse load influence for different cross-frame members in the same panel;
- Figure F3-17: demonstrates the impact of girder spacing on the force demands in critical cross-frames;
- Figure F3-18: demonstrates the impact of deck thickness on the force demands in critical cross-frames;
- Figure F3-19: demonstrates the impact of bridge curvature on the load distribution and force demands in critical cross-frames; and
- Figure F3-20: demonstrates that cross-frame layout (contiguous line of cross-frames versus a discontinuous, staggered layout) has significant effects on the force demands in critical cross-

frames.

Note that diagonal 1 (D1) refers to the cross-frame diagonal that frames into the top of the "left" girder, where left and right directions correspond to the upstation view; diagonal 2 (D2) represents the other diagonal member. This notation is carried out through the rest of the appendix.

These six comparative figures represent a very small portion of the full data set. The sample results are not intended to be comprehensive, but rather highlight key attributes with respect to cross-frame behavior. For more information regarding the construction of Figure F3-16 through Figure F3-20 (namely axes definitions, scaling, and units), refer to the detailed discussion in Section F3.1.5.

Table F3-10: Independent variables describing sample influence-surface plots

Parameter	Figure F3-15		Figure F3-16		Figure F3-17		Figure F3-18		Figure F3-19		Figure F3-20	
	Left	**Right**	**Left**	**Right**	**Left**	**Right**	**Left**	**Right**	**Left**	**Right**	**Left**	**Right**
Model ID	1181-1	1181-1	1181-1	1181-1	205-1	253-1	1173-2	1173-3	749-1	755-1	749-1	751-1
CF location[a]	**IS**	**M-I**	M-I	M-I	M-I	M-I	M-I	M-I	IS	IS	IS	IS
CF member[b]	BS	BS	**D1**	**D2**	BS	BS	BS	BS	D2	D2	D2	D2
No. spans	2	2	2	2	1	1	2	2	2	2	2	2
L/d ratio	35	35	35	35	30	30	35	35	30	30	30	30
Girder spacing [ft]	8	8	8	8	**6**	**10**	8	8	8	8	8	8
No. girders	5	5	5	5	5	5	3	3	5	5	5	5
Support skew [deg.][c]	60	60	60	60	0	0	60,0,-60	60,0,-60	60	60	60	60
Radius of curvature [ft]	Infinite	Infinite	Infinite	Infinite	Infinite	Infinite	Infinite	Infinite	**Infinite**	**750**	Infinite	Infinite
Cross-frame spacing [ft]	20	20	20	20	20	20	20	20	20	20	20	20
Cross-frame layout[d]	Cont.	Cont.	Cont.	Cont.	Cont.	Cont.	Cont.	Cont.	Cont.	Cont.	**Cont.**	**Stag.**
Web depth [in]	72	72	72	72	72	72	72	72	72	72	72	72
Deck thickness [in]	8	8	8	8	8	8	**8**	**10**	8	8	8	8
Cross-frame type	X	X	X	X	X	X	X	X	X	X	X	X
Cross-frame area [in^2]	2.86	2.86	2.86	2.86	2.86	2.86	2.86	2.86	2.86	2.86	2.86	2.86
Concrete modulus [ksi]	3600	3600	3600	3600	3600	3600	5000	5000	3600	3600	3600	3600

Notes:
[a] IS = intermediate support, M-I = maximum positive dead load moment region; interior bay
[b] BS = bottom strut, D1 = diagonal 1, D2 = diagonal 2
[c] Models 1173-2 and 1173-3 have trapezoidal support skew layout, rest of models have parallel skew
[d] Cont. = contiguous line of cross-frames, Stag. = staggered line of cross-frames

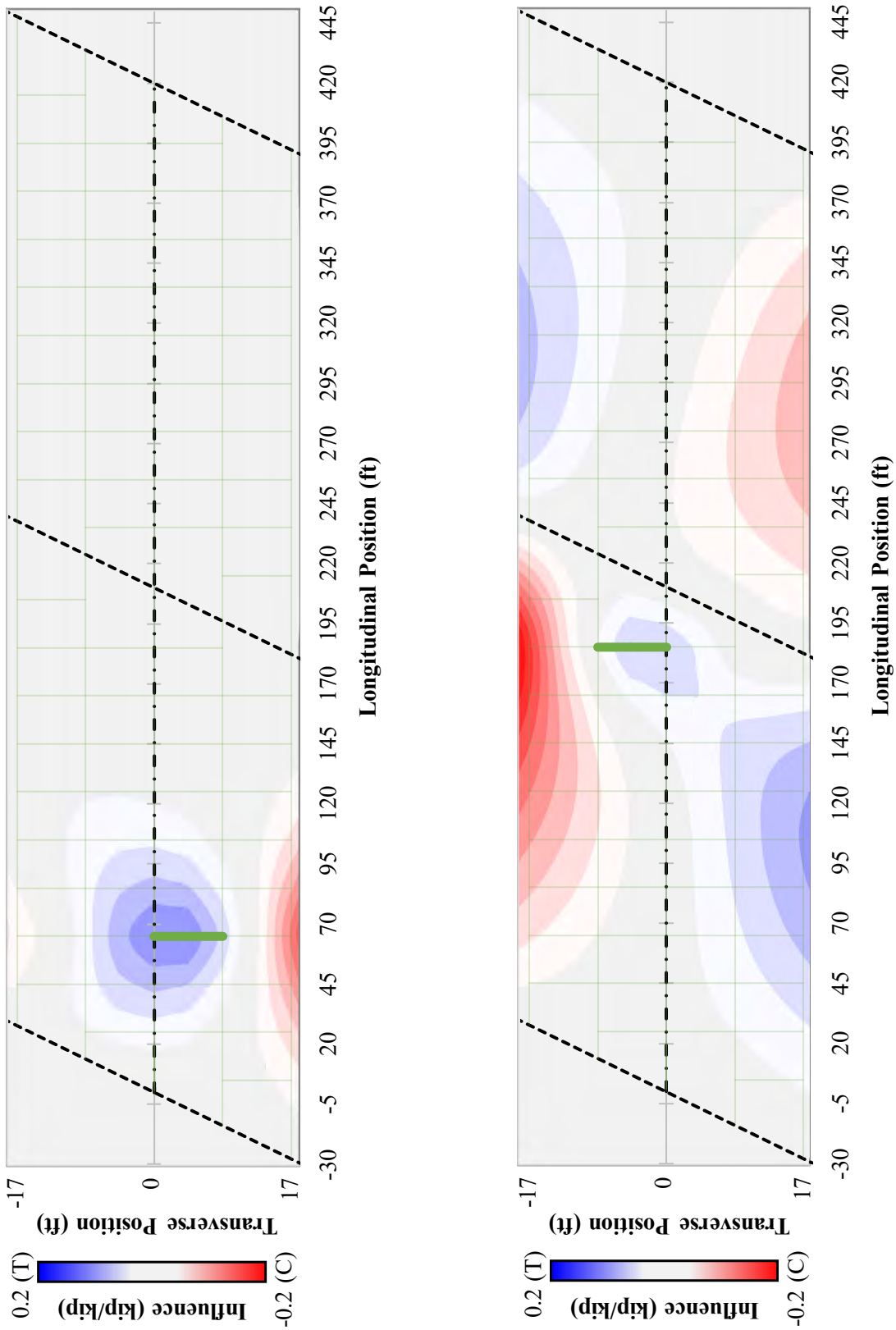

Figure F3-15: Comparison of influence-surface plots (axial-force response) of cross-frame bottom strut near (left) maximum dead load moment region and (right) skewed intermediate support

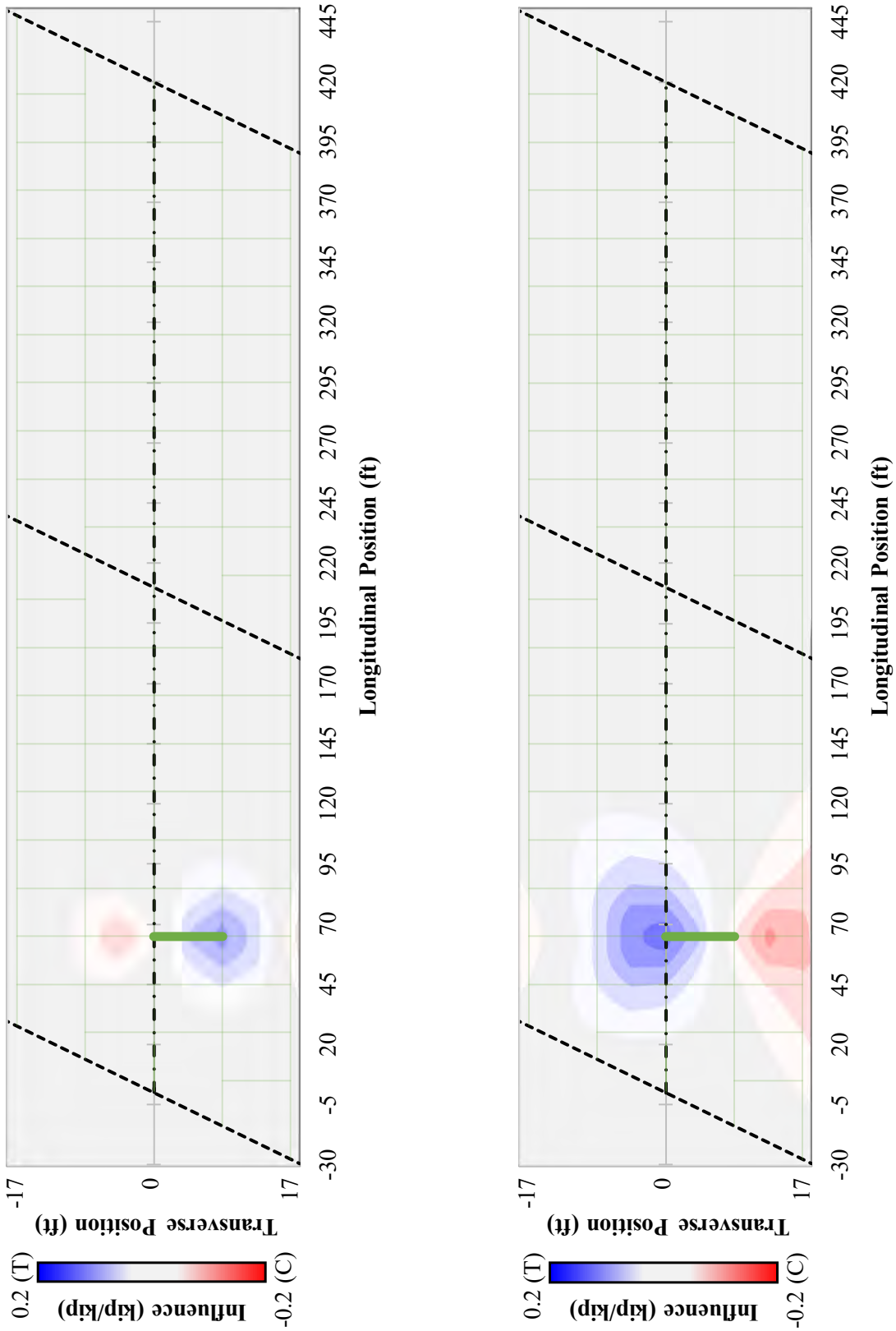

Figure F3-16: Comparison of influence-surface plots (axial-force response) of cross-frame (left) diagonal 1 and (right) diagonal 2 maximum dead load moment region

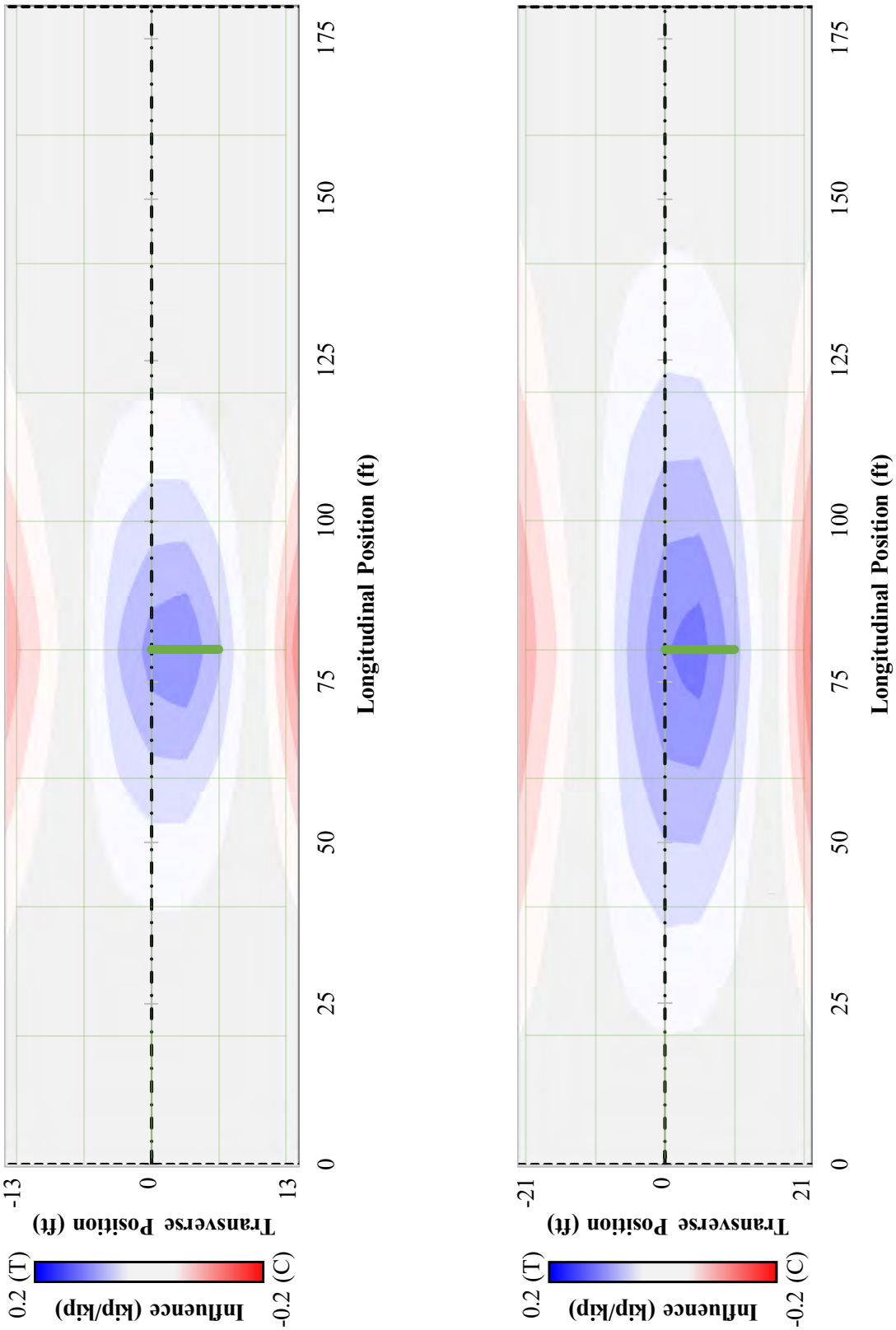

Figure F3-17: Comparison of influence-surface plots (axial-force response) of midspan cross-frame bottom strut with a (left) 6-foot girder spacing and (right) 10-foot girder spacing

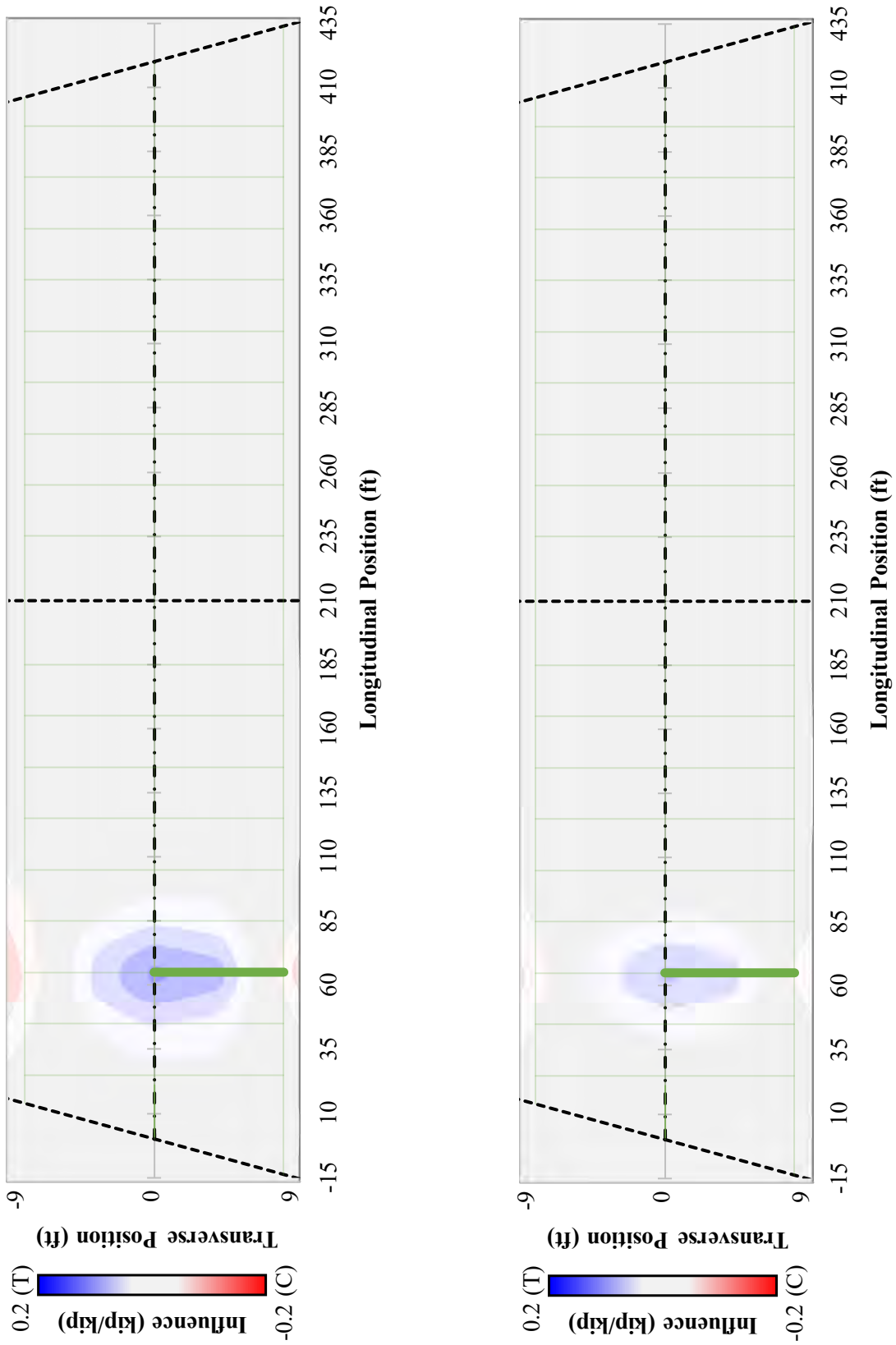

Figure F3-18: Comparison of influence-surface plots (axial-force response) of cross-frame bottom strut with (left) 8-inch concrete deck and (right) 10-inch concrete deck

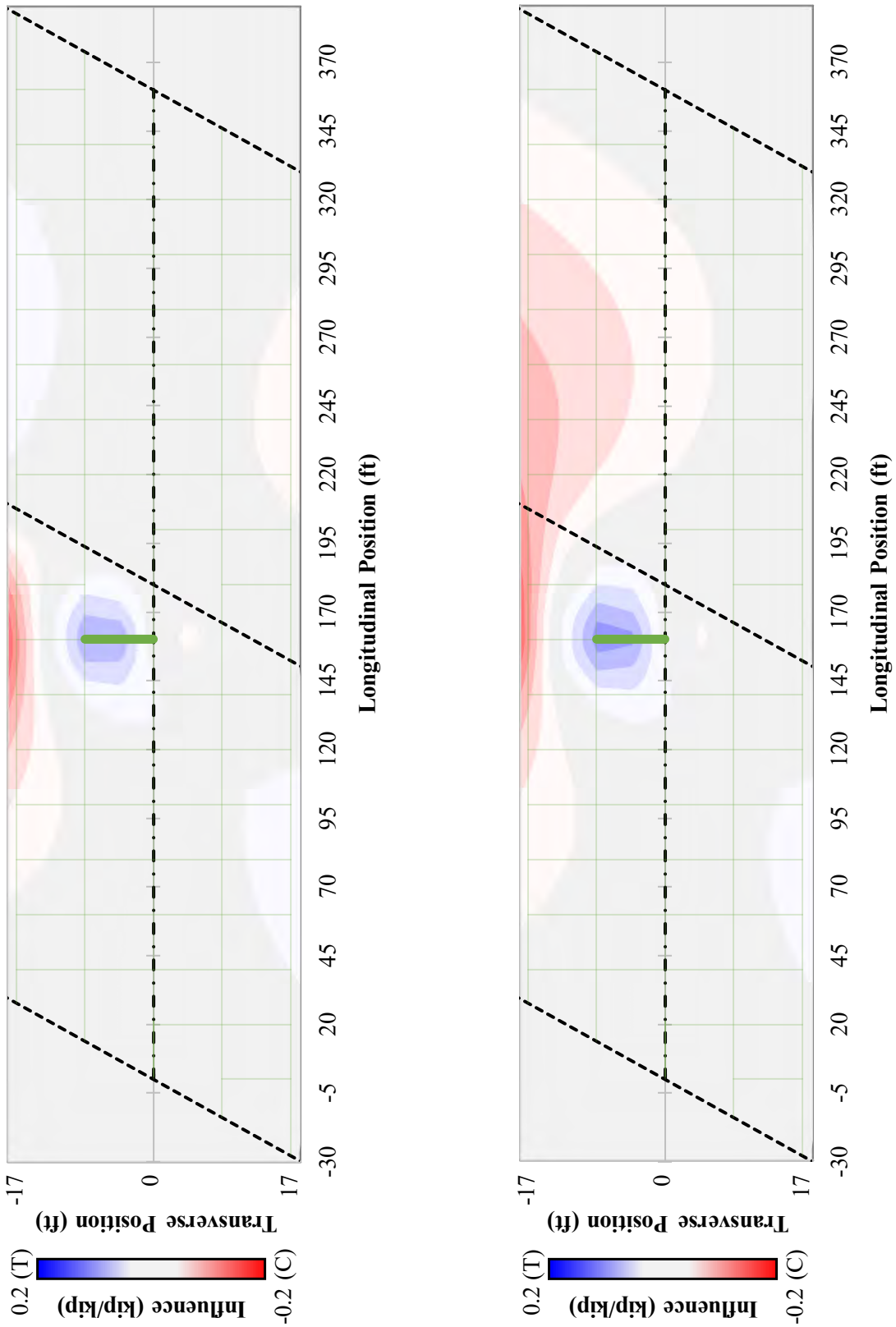

Figure F3-19: Comparison of influence-surface plots (axial-force response) of cross-frame diagonal 2 near intermediate support of (left) straight bridge and (right) curved bridge (R = 750 ft)

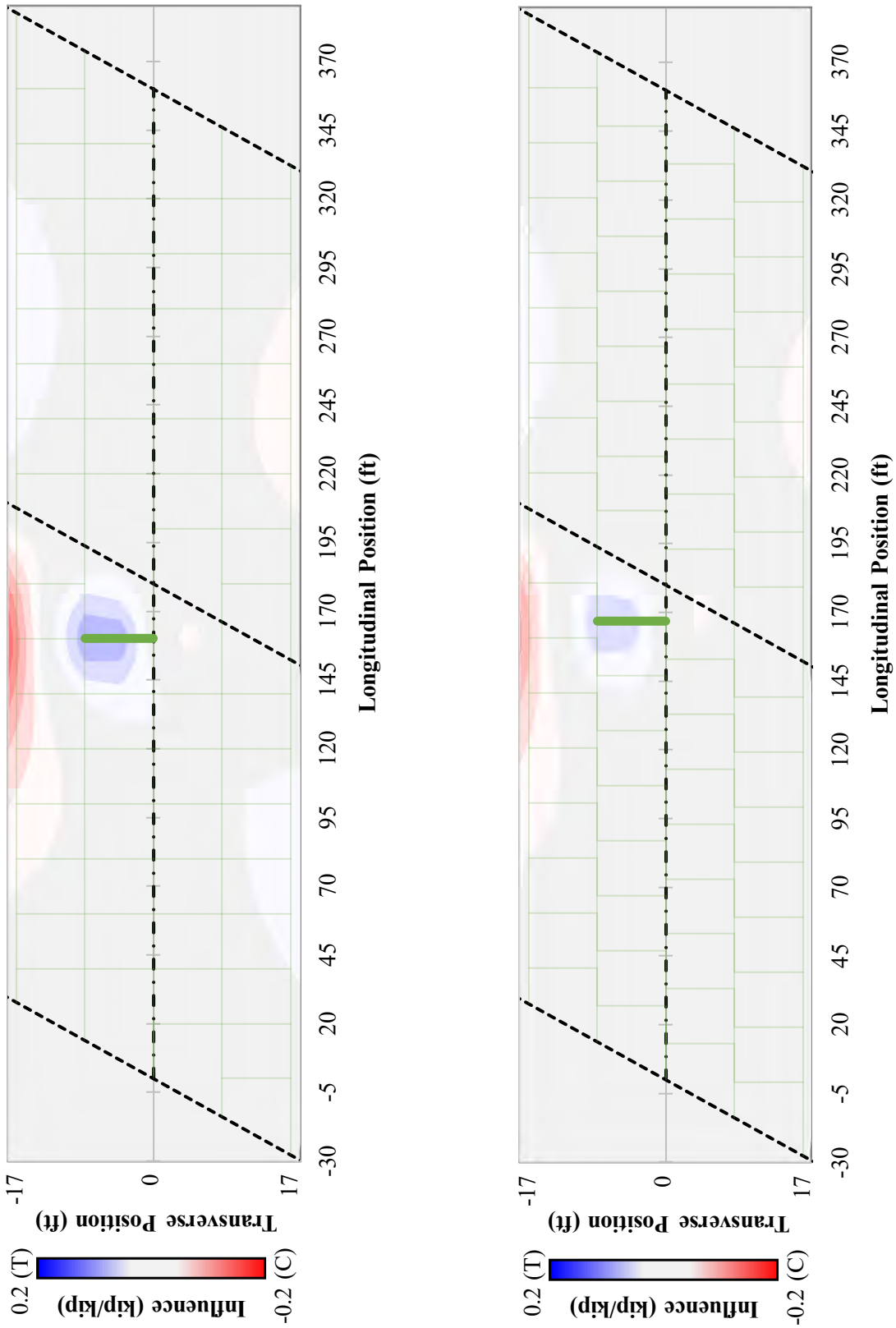

Figure F3-20: Comparison of influence-surface plots (axial-force response) of cross-frame diagonal 2 near intermediate support of bridge with (left) contiguous and (right) staggered layout

From Figure F3-15, the following observations can be made about load influence with respect to cross-frame location relative to skewed supports:

- **Overall load influence and distribution**: The load influence is more complex and broadened for cross-frames near skewed (intermediate or end) supports than for cross-frames near the maximum positive dead load moment region.

  The supports generally have little effect on the response of cross-frames near midspan, skewed or not. This is reflected in the left plot. The longitudinal load influence is localized (i.e., the influence is negligible when the load is positioned beyond 50 feet longitudinally from the cross-frame panel). Conversely, the transverse load influence is highly sensitive. A load applied just to the left of the bay maximizes tension; a load applied along the right barrier maximizes compression. Similar observations were made from the field experimental results documented in Appendix E.

  In the right plot, the response is much more complex. Compression is maximized in the bottom strut of interest when the load is applied along the left barrier at the same longitudinal position of the panel (i.e., +180 ft according to the longitudinal x-coordinate system). Tension, however, is maximized when the load is applied along the right barrier 70 feet downstation from the panel (+110 ft). There are also significant load influences on the adjacent spans, which is not observed in the right plot.

- **Cross-frame force demands**: In general, the force demands (i.e., the load influence magnitudes) are higher for the bottom strut near the intermediate support. Therefore, cross-frames near supports in skewed systems tend to govern fatigue design, which is consistent with field performance in many older bridges where out-of-plane cracking has been observed. Relative displacements (rotation and deflection) between adjacent girders and global torsional effects on the superstructure are maximized at those locations. As will be documented in subsequent sections, this behavior is fairly consistent for all heavily skewed bridges.

From Figure F3-16, the following observations can be made about load influence with respect to different members in a cross-frame panel:

- **Overall load influence and distribution**: Similar to the left plot of Figure F3-15, the longitudinal influence is localized about the cross-frame panel of interest, but the transverse influence is highly sensitive. This is generally true for cross-frames not in the vicinity of skewed supports.

  For diagonal 1 (left plot), tension is maximized when the load is applied just to the right of the bay. For diagonal 2 (right plot), tension is maximized when the load is applied to the left. This behavior is consistent with a simple truss analysis of the isolated cross-frame panel, when loaded vertically along either side.

- **Cross-frame force demands**: In this particular case, force demands in diagonal 2 exceed that of diagonal 1. This behavior is generally bridge-specific, meaning the critical member (bottom strut, diagonal 1, or diagonal 2) depends on the overall geometry.

From Figure F3-17, the following observations can be made about load influence with respect to girder spacing:

- **Overall load influence and distribution**: In this simple span with normal supports, the general shape of the influence-surface response is consistent with Figure F3-16 (i.e., longitudinal influence is localized; transverse influence is sensitive).

- **Cross-frame force demands**: For the bridge with a 10-foot girder spacing, the force demands in the bottom strut of interest increased. This is reflected by the difference in color intensities between the left and right plots. The RT has observed that cross-frames not only restrain relative displacement of adjacent girders, but they also effectively act as floorbeams in composite systems. In other words, the bottom strut is analogous to the tensile flange of a floorbeam, and the concrete deck is analogous to the compressive flange. Thus, wider girder spacing generally correlates to larger force demands in cross-frame members, particularly in bottom struts. Located near the neutral axis of this composite system, the top strut generally has the smallest force demands in a cross-frame panel. Refer to Chapter F4 for a detailed discussion on the different load-induced deformation patterns in cross-frame systems.

From Figure F3-18, the following observations can be made about load influence with respect to concrete deck thickness:

- **Overall load influence and distribution**: Despite the trapezoidal skew effects, the same behavior is observed for the cross-frame of interest near the maximum positive dead load moment region as in Figure F3-16 and Figure F3-17.

- **Cross-frame force demands**: Cross-frame force demands are greater for the bridge with an 8-inch composite deck than for the bridge with a 10-inch deck. Load-induced displacement between adjacent girders is restrained by two unique systems: (i) flexure of the concrete deck and (ii) the cross-frame system. The relative difference between the transverse stiffness of the deck and the stiffness of the cross-frame system largely dictates the force demands on the cross-frame members. Thus, by increasing its thickness from 8 inches to 10 inches, the concrete deck becomes stiffer, which has two major outcomes. First, in highly indeterminate systems like multi-girder bridges, stiffer elements attract larger shares of force, thereby shedding load away from the cross-frames. Second, a stiffer concrete deck implies a stiffer composite superstructure, which in turn implies less load-induced girder displacements. Less differential girder displacements generally result in smaller cross-frame force demands. This behavior is reflected in the influence-surface results in Figure F3-18.

From Figure F3-19, the following observations can be made about load influence with respect to bridge curvature:

- **Overall load influence and distribution**: With respect to cross-frames near the skewed support, both the horizontally curved (right plot) and straight systems (left) have unique load influence distributions. In both cases, applying load in the opposite span can have impacts on the cross-frame diagonal of interest. In the curved bridge, however, there are significant compression force demands in the cross-frame diagonal due to loads applied along the inner radius of the curve (i.e., along transverse coordinate -17); this behavior is not observed in the straight system. Inner-radius loads on curved systems generate an additional torsional response of the bridge superstructure, which amplify cross-frame force demands.

- **Cross-frame force demands**: The critical force demands in the cross-frame diagonal of interest (both tension and compression) are higher for the curved system.

From Figure F3-20, the following observations can be made about load influence with respect to cross-frame layout in skewed superstructures:

- **Overall load influence and distribution**: The overall load influence plot is generally unchanged with the staggered layout when compared to the contiguous layout. In other words, the critical load positions for tension and compression are the same for both left and right plots.

- **Cross-frame force demands**: As outlined in Section F3.1.2, staggered cross-frame layouts are often utilized in skewed bridge construction to increase the inherent flexibility of transverse load distribution, lessen force demands in cross-frame members, and potentially alleviate lateral bending stresses in girder flanges. These beneficial effects are demonstrated in the right plot of Figure F3-20. The overall load influence magnitudes are decreased by introducing a staggered, discontinuous cross-frame layout.

To summarize, the important observations from Figure F3-15 through Figure F3-20 are as follows:

- The critical load position for a given cross-frame member is highly variable and depends on a number of parameters including cross-frame location, support skew, and bridge curvature;
- Similarly, the governing cross-frame member (i.e., highest force demands) in a given bridge depends on the same set of parameters; and
- The force demands in critical cross-frame members also vary substantially and depend on many parameters including but not limited to cross-frame location, support skew, bridge curvature, deck thickness, and girder spacing. The force demands on cross-frames (with respect to realistic truck traffic) are addressed in Sections F3.2 and F3.3.

These figures, although a small sample set, provide a fairly representative overview of the major trends and observations from the full data set. Influence-surface plots are useful visual tools as demonstrated with Figure F3-15 through Figure F3-20. However, evaluating over 65,000 plots in an efficient and meaningful way is virtually impossible given the number of parameters investigated and the variability in the response. In order to assess the correlation between truck placement, fatigue stresses, and the parameters studied, additional processing of the data is necessary. Thus, the RT investigated different ways to present the full set of data in a concise, organized fashion as is documented in the next subsection.

F3.1.8.2 Compiled Data

The RT explored several methods to systematically evaluate the trends observed from the full set of influence-surface results. Ultimately, "hotspot" graphs were deemed the most efficient way to determine critical load positions and magnitudes for the 4,104 unique bridges. Hotspot plots, much like influence-surface plots, illustrate the longitudinal and transverse position of load application that maximizes tension or compression in a specific cross-frame member. Hotspot plots, however, differ from influence-surface plots in two major ways. First, a "hotspot" plot isolates and presents only the load position for which axial force in the cross-frame is largest. In contrast, an influence-surface plot presents the relative influence at all locations on the deck surface, regardless of magnitude. Second, a hotspot graph incorporates the comprehensive data set into one concise plot. Thus, each unique bridge represents a singular data point, for which the critical load position was recorded. With hotspot graphs, the trends introduced in the preceding section for select bridge examples can then be validated for the full data set.

To fully understand and interpret hotspot graphs, an example of the process is provided herein for reference. Figure F3-21 presents the influence-surface plots for three bridges analyzed in the parametric study. The influence-surface results correspond to the axial-force response of cross-frame diagonal 1 near the intermediate support. The cross-frame of interest is bolded for clarity.

The parameters of these three bridges (bridge IDs 1091-1, 1083-1, and 1077-1) are identical, except for the support skew angle and the corresponding cross-frame layout near the skewed supports. Each bridge is horizontally curved with a 750-foot radius about the centerline of the bridge; note that the influence-surface plots are "straightened out" for clarity. The bridges consist of five girders across the width spaced at 10 feet on center, which are braced by X-type cross-frames spaced typically at 20 feet on center. The top plot (1091-1) is for a support skew of 60 degrees, the middle plot (1083-1) for a support skew of 30 degrees,

and the bottom plot (1077-1) for zero skew.

In each respective plot, the coordinates of the cross-frame centroid and the load application that maximizes tension in the cross-frame of interest are depicted. Note that similar coordinates for the critical compression load can and have been recorded but are not shown for clarity here. The cross-frame centroid is the same for all three bridges {220, -5}, but the critical load position is not. For the bridge with 60-degree support skews, the critical load position is along the left barrier on the opposite span {285, -21}. For the bridge with 30-degree skews, the critical position is along the right barrier near midspan of the first span {120, 21}. For the bridge with no support skew, the response is localized; the critical position is just to the right of the cross-frame panel {215, 0}.

In order to evaluate every bridge in the analytical testing matrix, the coordinate systems are normalized given the wide range of bridge lengths, widths, and cross-frame layouts considered. This process is demonstrated in Table F3-11. The cross-frame centroids are set at {0,0}, and the distance between the critical load position and the cross-frame centroid is normalized by the respective span length and width, which are 240 feet and 46 feet (measured out-to-out of deck) in Figure F3-21. For example, the normalized, critical longitudinal load position for the bridge with 60-degree skews is taken as 65 feet (i.e., 285 – 220 = 65) divided by 240 feet, equating to 0.27 (i.e., 65 / 240 = 0.27). This process was repeated and tabulated for all coordinate points in Table F3-11.

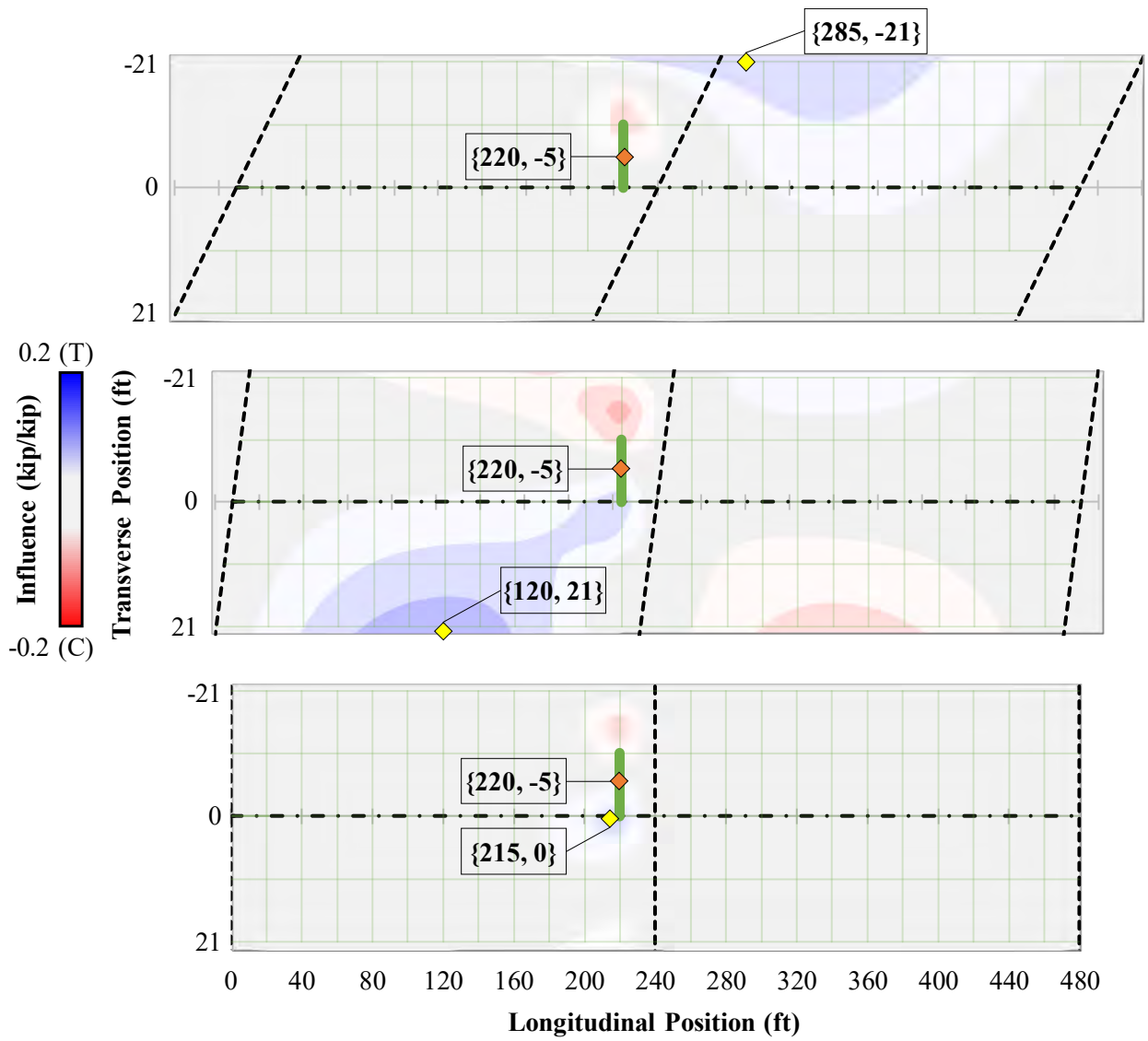

Figure F3-21: Sample influence-surface plots demonstrating the development of a "hotspot" graph for a bottom strut in bridge with (top) 60-degree, (middle) 30-degree, and (bottom) no skew

Table F3-11: Sample hotspot data points to demonstrate the normalization process (Figure F3-21)

Plot	Model ID	Support Skew (deg)	Cross-Frame ID	Cross-Frame Centroid		Tensile Hotspot	
				Actual	Normalized	Actual	Normalized
Top	1091-1	60	D1; IS	{220, -5}	{0, 0}	{285, -21}	{0.27, -0.35}
Middle	1083-1	30	D1; IS	{220, -5}	{0, 0}	{120, 21}	{-0.42, 0.56}
Bottom	1077-1	0	D1; IS	{220, -5}	{0, 0}	{215, 0}	{-0.02, 0.11}

Notes:
Span length = 240 ft; Total bridge width = 46 ft
IS = intermediate support, D1 = diagonal 1

In the development of the hotspot graphs, the normalized coordinates in Table F3-11 represent just three data points among thousands. In other words, the process outlined in Figure F3-21 and Table F3-11 was repeated for every evaluated cross-frame member in every bridge, leading to 68,352 data points (i.e., normalized longitudinal and transverse coordinates); those data points are then superimposed on a normalized coordinate system to illustrate the critical load position for every cross-frame member studied. From this, the general trends in global bridge response and localized cross-frame behavior can be examined. Additionally, the RT can filter the full data set to study the effects of a particular parameter on the hotspot results. In general though, it was discovered that only support skew significantly impacts the critical load positions in cross-frames. Parameters such as deck thickness and girder spacing generally only impact force magnitudes, not critical load positions.

The RT prepared several hotspot graphs (Figure F3-22 through Figure F3-25) that analyze the effects of support skew on critical load position. For each figure, the general location of the cross-frame member is studied independently. Figure F3-22 specifically evaluates cross-frame members near intermediate supports, as outlined in Section F3.1.5; these cross-frame panels are identified as IS (intermediate support) cross-frames. Figure F3-23 evaluates cross-frames near the end support (ES). Figure F3-24 evaluates cross-frames in an interior bay near the maximum positive dead load moment region (M-I), and Figure F3-25 evaluates cross-frames in an exterior bay of the same region (M-E).

In each of these figures, bottom struts and both diagonals (diagonal 1 and 2) are also examined independently. Top struts have been neglected given that force demands in these members have been shown to be insignificant compared to the other members. For reference, the three data points highlighted in Figure F3-21 are presented in Figure F3-22.

In addition to the example and notes provided above, there are several items to consider when evaluating hotspot graphs (Figure F3-22 through Figure F3-25):

- As outlined in the Figure F3-21 example, the cross-frame centroid is presented at coordinate {0, 0} on the normalized plot. This allows the RT to directly compare the results, regardless of where the cross-frame is located on a given bridge geometry.
- The data points relative to the {0, 0} location are normalized in the same manner, regardless if the critical load position exists on the opposite span. Therefore, in theory, normalized longitudinal positions greater than 1.0 are possible. In reality, though, no data points in that range were observed as the longitudinal influence is generally localized about the cross-frame of interest in most cases.
- A reference sketch is also provided in the figure to clarify the relative position of the cross-frame; the results for the bolded cross-frame panel location are plotted. Note that the exact location of the cross-frame, the number of girders, the number of spans, the support skew angle, and the radius of curvature in the sketch are for visual reference only; the bridge geometries of the various data points likely differ from the representative sketch.
- Hotspot graphs can be developed for the load position maximizing axial tension in the cross-frame member as well as the load position maximizing axial compression. Because axial tension is more critical for fatigue evaluation, only the axial tension case is plotted.
- The color of the data point relates to a specific parameter; in this case, the figures compare the results between bridges with support skew angles of 0, 30, and 60 degrees, respectively. Thus, data points colored red correspond to all models in the analytical testing matrix with normal supports; similarly, data points colored blue and green correspond to all models with support skews of 30 degrees and 60 degrees, respectively. The scatter in the data for each skew angle is related to the remaining parameters (e.g. deck thickness), which are different for each model in the specific data set.
- The size of the hotspot is a function of the frequency of occurrence and relative magnitude of the load influence. For example, if many data points share the same coordinate on the normalized grid,

then the resulting hotspot will be larger; conversely, if only one data point has a unique coordinate, then the resulting hotspot will be smaller in size.

- As noted above, similar plots can be generated for different isolated parameters (i.e., other than support skewness). The RT evaluated other parameters but has found that the correlation between load position and skew angle is the strongest. For instance, there is little to no correlation observed between the critical loading position and deck thickness. Thus, only support skewness is evaluated in depth in this appendix.

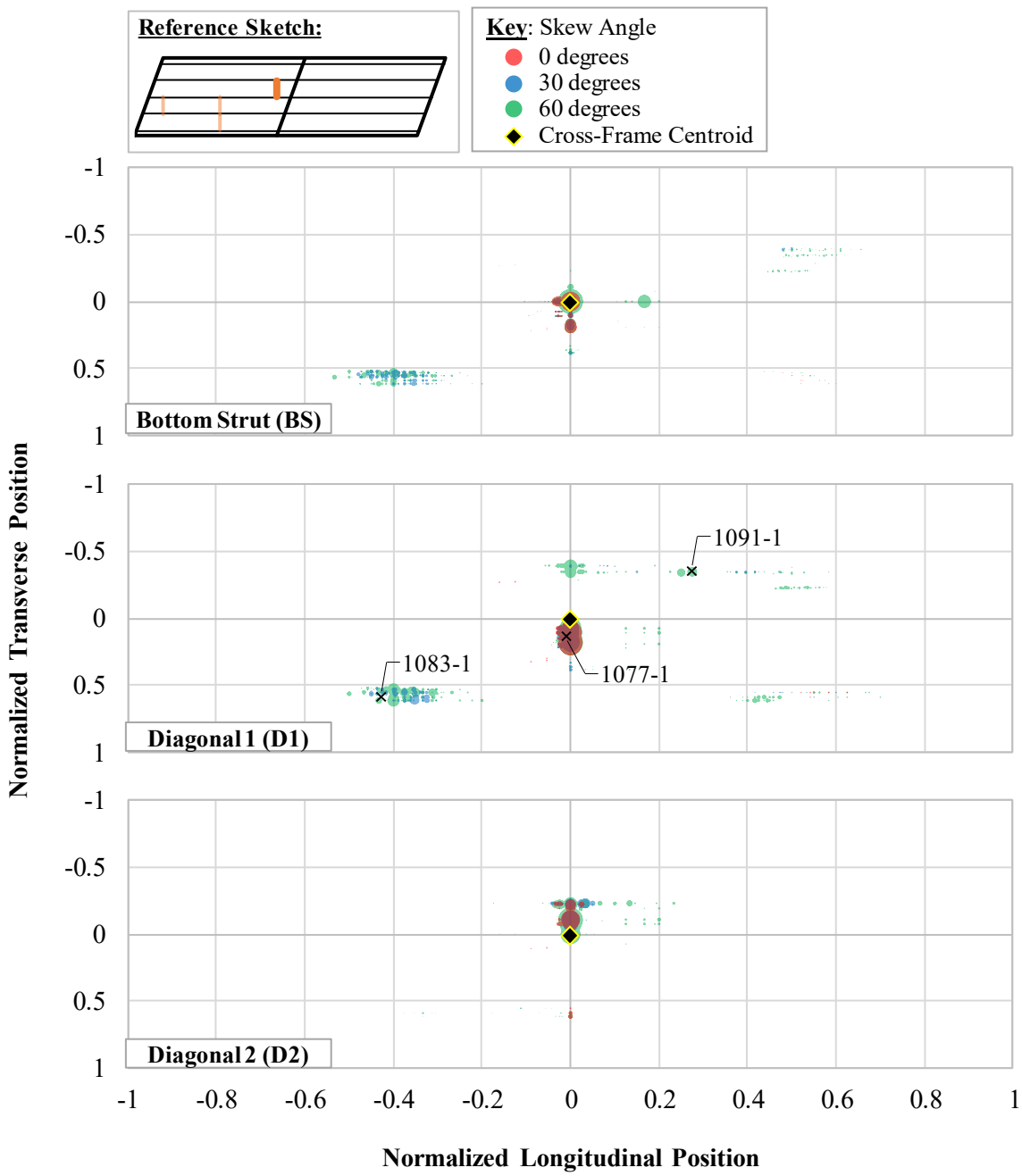

Figure F3-22: Hotspot graph showing the position of the applied load that maximizes tension in the cross-frame diagonal of interest (near intermediate support) for various degrees of support

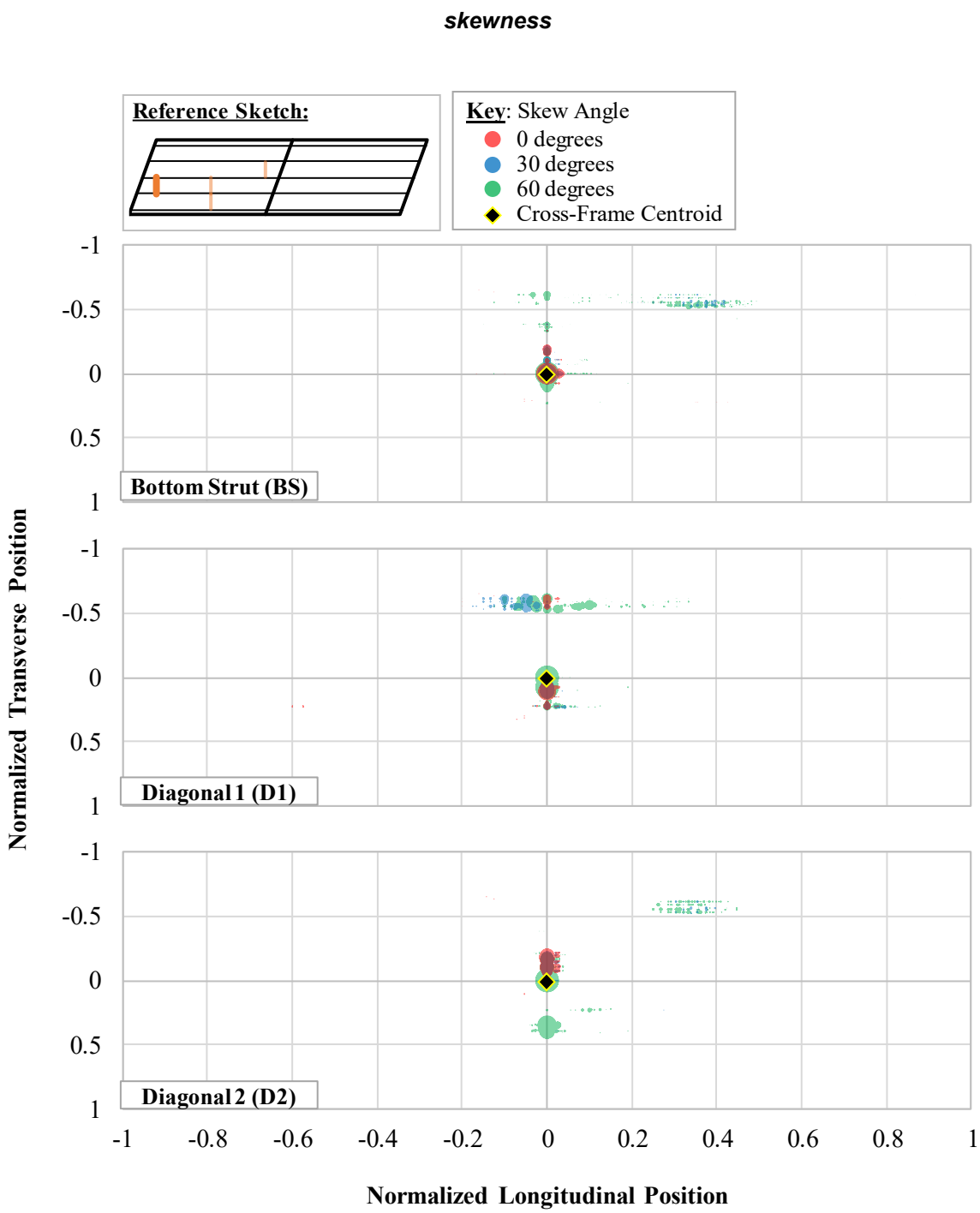

Figure F3-23: Hotspot graph showing the position of the applied load that maximizes tension in the cross-frame diagonal of interest (near end support) for various degrees of support skewness

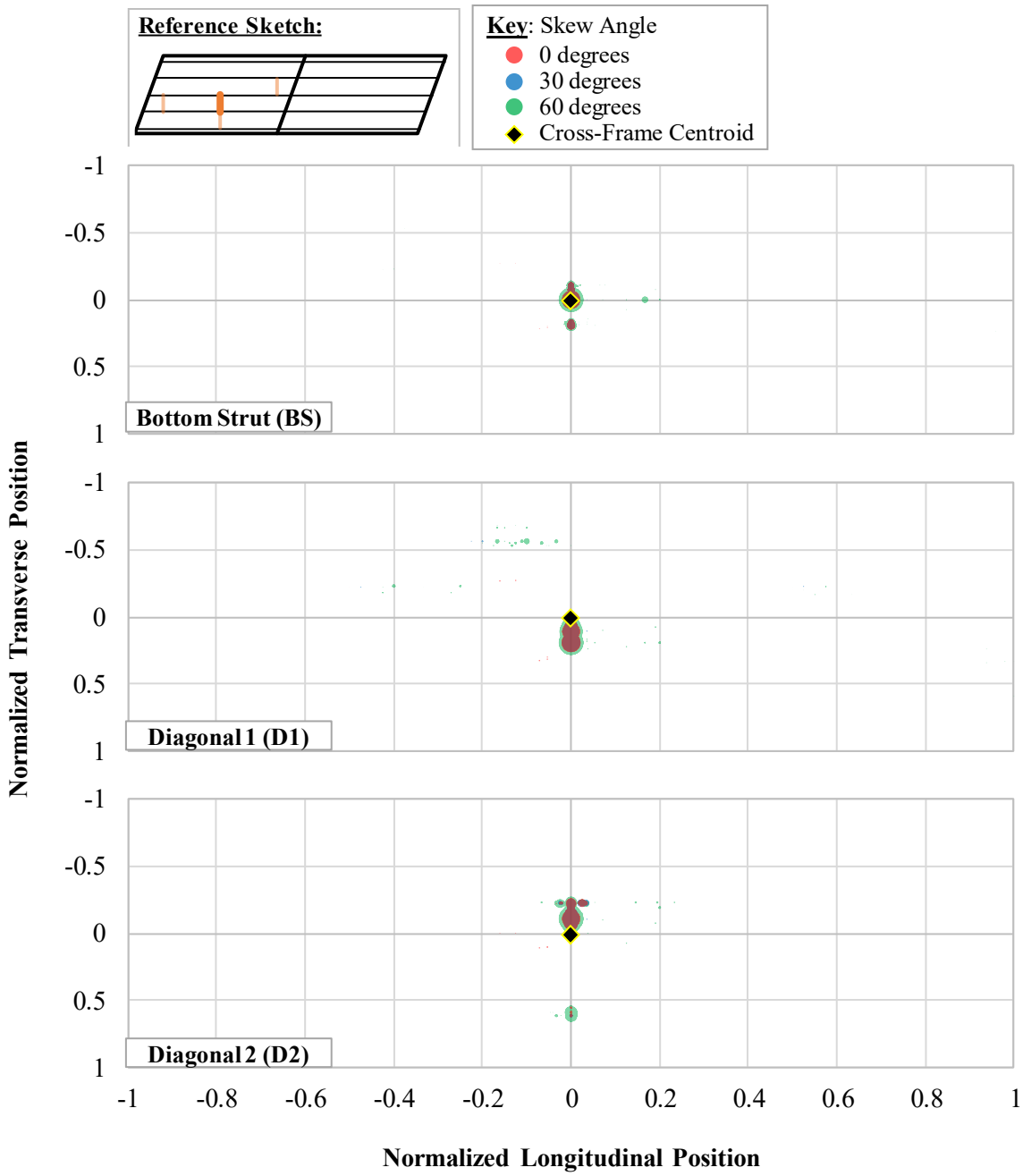

Figure F3-24: Hotspot graph showing the position of the applied load that maximizes tension in the cross-frame diagonal of interest (in interior bay near maximum positive dead load moment region) for various degrees of support skewness

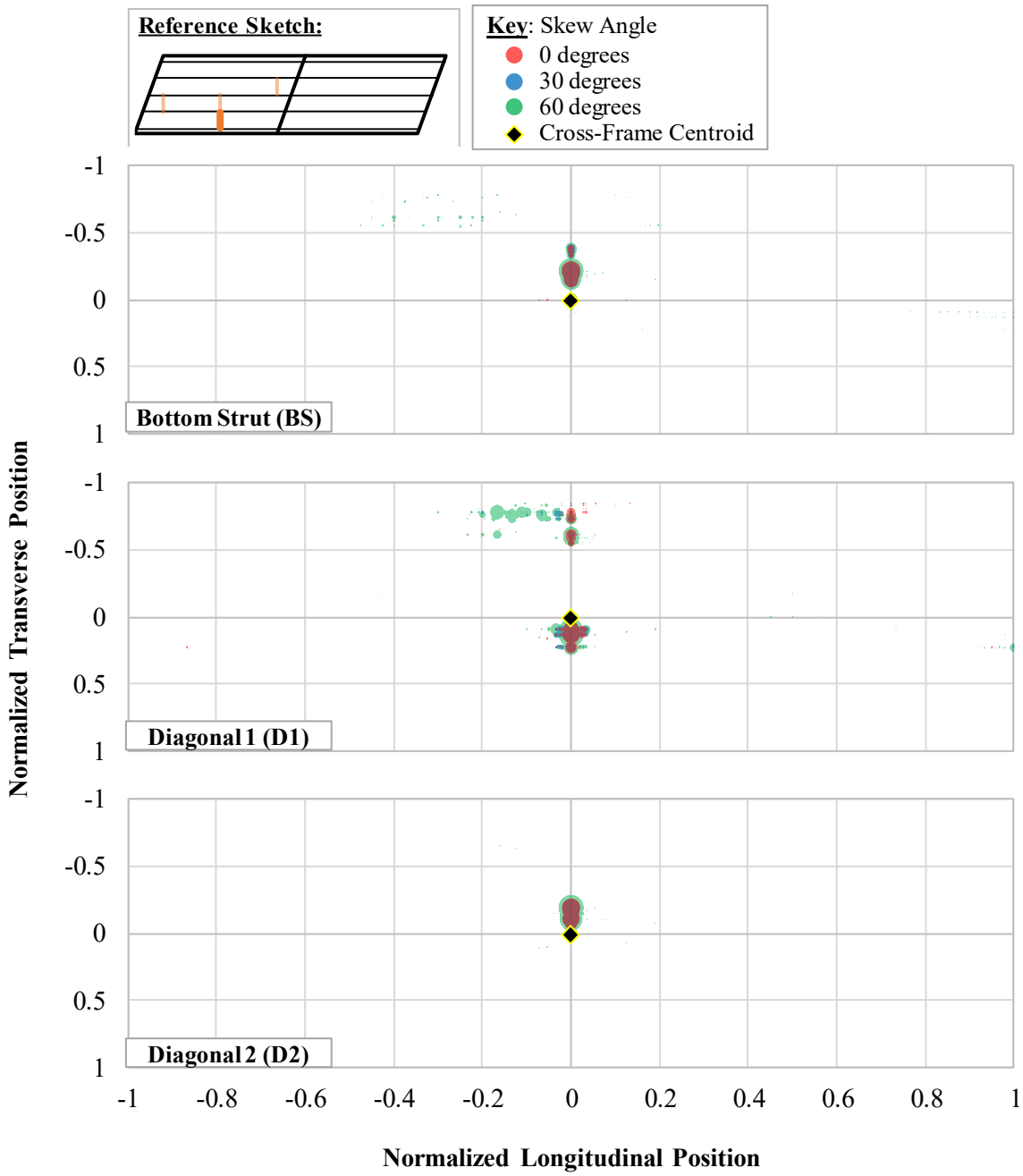

Figure F3-25: Hotspot graph showing the position of the applied load that maximizes tension in the cross-frame diagonal of interest (in end bay near maximum positive dead load moment region) for various degrees of support skewness

From Figure F3-22 and Figure F3-23, the following observations can be made about critical load position with respect to cross-frames near intermediate and end supports:

- For bridges with normal supports, loads applied near coordinate {0, 0} (i.e., directly above the cross-frame) generally maximize axial tension in bottom struts. Loads applied just to the right of the cross-frame panel (i.e., near coordinate 0, 0.1) maximize tension in diagonal 1, and loads to the left (i.e., near coordinate 0, -0.1) maximize tension in diagonal 2. Therefore, it can be concluded

that the load influence and response of cross-frames in non-skewed bridges is highly localized, even in the vicinity of supports.

- For bridges with skewed supports, the load influence for cross-frames near supports is much more scattered. For example, the axial tension in many of the bottom strut members at intermediate supports was maximized when load was applied along the opposite bridge railing at a distance 30 to 50 feet downstation. In these scenarios, the torsional response of the superstructure at the skewed support is maximized, which engages the nearby cross-frames.

From Figure F3-24 and Figure F3-25, the following observations can be made about critical load position with respect to cross-frames near the maximum positive dead load moment region (i.e., midspan of single-span bridges and approximately 0.35*L* from the end support in continuous spans):

- In general, the response of the cross-frames to load position is highly localized, similar to the non-skewed bridge cases presented in Figure F3-22 and Figure F3-23. Therefore, it can be concluded that support skew does not significantly impact the response of cross-frames near midspan.
- For diagonal 1 members in interior and edge bays of the bridge, some scatter is observed. These cases correspond to horizontally curved bridges. Axial force demands in these diagonal members (along the outer radius) are maximized by loads applied along the inner radius, which induces an additional torque on the superstructure. The applied load is eccentric to the chord of the curved geometry (i.e., straight line distance between the start and end points of the bridge centerline).

In general, the trends observed from the hotspot graphs are consistent with the sample influence-surface plots presented previously. For straight bridges with normal supports, the response of cross-frames to applied loads on a composite deck is fairly predictable. However, introducing curvature to the bridge layout and especially support skews often complicates the anticipated response.

While Section F3.1.8 examined static unit loading for purposes of generating influence-surface and hotspot plots, Sections F3.2 and F3.3 introduce more realistic traffic loads. The behavioral trends observed from the influence-surface and hotspot graphs, although based on a unit load, are very important when understanding the response of cross-frames to live loads. With that in mind, Section F3.2 utilizes the over 65,000 influence-surface plots to examine the appropriateness of current AASHTO fatigue loading criteria on the 4,104 unique bridge geometries. Section F3.3 expands on that analysis and investigates the effects of measured WIM traffic streams.

F3.2 Fatigue Study – AASHTO Design Loads

As outlined in Section F3.1, the primary goals of the Fatigue Loading Study are twofold: (i) to examine the influence of bridge geometry and cross-frame details on fatigue force effects and (ii) to investigate the appropriate fatigue stress ranges for the evaluation of cross-frames. Although the unit loads outlined in Section F3.1.8 highlight key trends in the behavioral response of cross-frame systems, these questions can only be answered by evaluating the response under realistic traffic loads. This section focuses on current AASHTO design loads, and Section F3.3 focuses on the use of recent WIM records. By comparing the cross-frame response to each set of live loads, the RT can then examine Fatigue I and II load factors as well as critical lane positions. That is to say, Section F3.2 assesses the "state of load-induced fatigue" in cross-frame systems based on current design practice, whereas Section F3.3 offers a "reality check" by implementing real traffic.

In terms of the first objective, the RT applied fatigue loading in accordance with current AASHTO LRFD Specifications. The single AASHTO fatigue truck (Figure F3-26) was positioned in all transverse and longitudinal directions to maximize the stress/force range in the cross-frame member of interest (Article 3.6.1.4.3). Those maximum force ranges were then compared for the various bridge geometries, such that the impact of each parameter with respect to cross-frame force effects could be evaluated. The overall

postprocessing procedure is outlined in Section F3.2.1, and pertinent results are shown in Sections F3.2.2 through F3.2.5.

In terms of the second objective, the RT sought to effectively "design" the cross-frames in each of the 4,104 bridges for the fatigue limit state, which involved a detailed study of the factored loading criteria and the factored resistance criteria. By establishing the design criteria for each of the 4,104 representative bridge structures, the RT can assess the accuracy and appropriateness of the current Fatigue I and II load criteria with respect to real WIM data. Section F3.2.6 outlines this process.

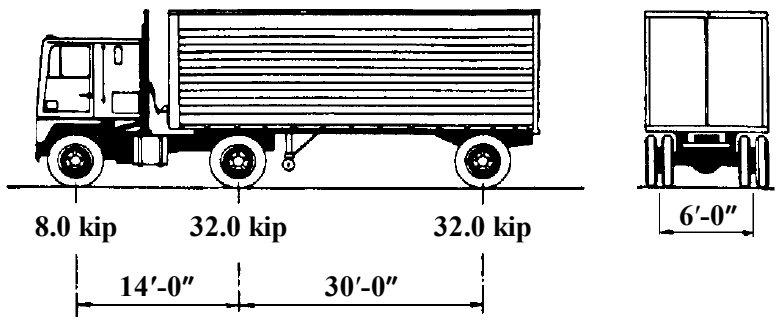

Figure F3-26: AASHTO fatigue truck (adapted from AASHTO LRFD)

In relation to the two primary objectives of the Fatigue Loading Study, the RT sought answers to specific questions regarding the response of cross-frames to AASHTO and WIM loading. The questions, along with the subsection dedicated to answering said question, are listed below:

1. Which cross-frame member (e.g. bottom struts versus diagonals; midspan cross-frames versus cross-frames near supports) typically governs the fatigue design [Section F3.2.2]?
2. Which lane position typically maximizes the force range in critical cross-frame members [F3.2.3]?
3. How many secondary cycles are typically generated for a given fatigue truck passage (i.e., constant *n* in AASHTO Table F6.6.1.2.5-2) [F3.2.4]?
4. How do various parameters (e.g. girder spacing) impact the maximum force ranges observed in cross-frames [F3.2.5]?
5. How do the design force ranges (based on current AASHTO fatigue loading) compare to code-specified fatigue resistances [F3.2.6]?
6. How do the design force ranges (based on current AASHTO fatigue loading) compare to force ranges determined from WIM data [F3.3]?

As illustrated in the list above, the subsections herein address each one of these questions as they pertain to the two primary objectives of the Fatigue Loading Study, following an introductory section explaining the means and methods.

F3.2.1 Postprocessing Procedure

As introduced in preceding subsection, the objectives of the Fatigue Loading Study are to examine the impact of bridge geometry and details on fatigue force effects in cross-frames and to investigate the appropriate fatigue stress ranges. To do so, the RT implemented current AASHTO fatigue loading criteria on the 4,104 unique bridge models. As discussed in Section F3.1.3, the RT explored two different procedures for applying said loading criteria. Ultimately, the RT elected to conduct an influence-surface analysis in Abaqus (i.e., a grid of unit loads) and consider moving loads via an external Excel program (Section F3.1.7). Through a series of bilinear interpolation calculations and superposition, the influence-

surface plots are used to develop influence-influence line plots, for which the axial-force response of the cross-frame due to the passing truck is demonstrated.

AASHTO Article 3.6.1.3.4 states that "a single design truck shall be positioned transversely and longitudinally to maximize stress range at the detail under consideration, regardless of the position of traffic or design lanes on the deck." To satisfy this requirement, a single AASHTO fatigue truck (Figure F3-26) was effectively "run" along the entire length of the influence-surface in a specified lane (i.e., the transverse position was held fixed for the entire longitudinal passage, so "zig-zag" loads were not considered). Then, different lane passages were considered by repeating the process above in 1-foot transverse increments in both the forward and backward directions (i.e., truck traversing upstation and downstation). Therefore, the total number of lane iterations for a given bridge was a function of the inside-to-inside dimension between the barriers and the transverse wheel spacing of the fatigue truck (6 feet). At deck overhangs, a 1-foot clear distance between the centerline of the outermost wheel line and the inside face of the barrier was maintained. Especially for fatigue evaluation, consideration of trucks driving in close proximity to the barrier (within 1 foot) is not considered necessary as it is an infrequent occurrence in most cases; for completeness, these extreme loading conditions are considered in the study.

An example of this procedure is presented in Figure F3-27. The sample influence-surface plot corresponds to diagonal 1 near the intermediate, skewed support of bridge 1181-1, which was previously presented in Figure F3-15. For information regarding the bridge geometry and cross-frame details, refer to Table F3-10. The AASHTO fatigue truck was "run" across the influence-surface in the upstation direction for three distinct lane positions: left wheel line 1-foot from the left barrier, centerline of bridge, and right wheel line 1-foot from the right barrier. Note that in the actual analyses of this influence-surface, this process was completed 58 total times [i.e. (35 one-foot increments between the barriers) – (6-foot wheel line spacing) = 29 available lane positions; (29 lanes) * (2 traffic directions) = 58 influence-lines developed].

The x-axis of the influence line plots corresponds to the longitudinal position of the front truck axle relative to the coordinate system established in the color contour plot. Therefore at skewed ends, the truck is introduced to the deck surface at different x-coordinates, as is reflected in the figures.

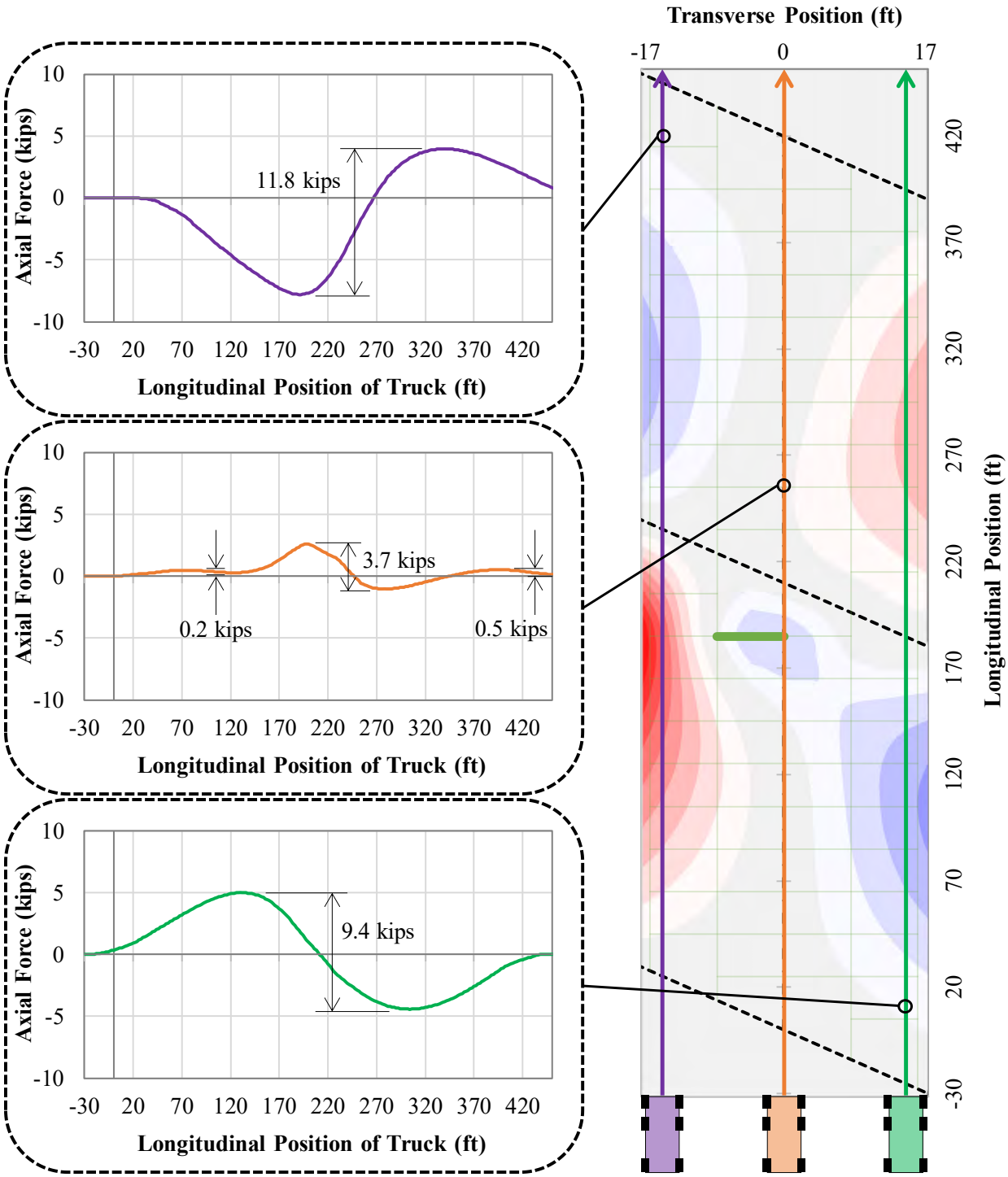

Figure F3-27: Sample data showing the development of influence-line plots from an influence-surface

As presented in the figure, the axial-force response of the cross-frame varies significantly for each truck passage. When traversing the bridge along the left barrier, the fatigue truck enters the deck surface at a longitudinal coordinate of about +20 ft; this is reflected in the influence-line plot, as the response is zero

force until +20 on the x-axis. Once on the bridge deck, the truck then passes the critical "compression zone" of the influence surface (i.e., red area) in the first span and then a "tensile zone" in the back span (i.e., blue area). This behavior is also reflected in the corresponding influence-line plot, as the cross-frame diagonal experiences compression force followed by tension force, resulting in substantial force cycle (11.8 kips).

For the fatigue truck passing along the right barrier, the truck enters the deck surface at approximately -30 ft on the coordinate system. Similar to the left-barrier passage, a large force reversal is also observed, except in the opposite order. The cross-frame diagonal is loaded in tension as the truck traverses the first span and in compression as the truck traverses the back span. The result is one primary force cycle with a magnitude of 9.4 kips.

For the truck passing along the centerline of the bridge, the force magnitudes are smaller, but the response is more complex. Whereas the other two truck passages resulted in one primary force cycle, the centerline passage results in additional secondary cycles of lesser magnitude. The primary cycle (3.7 kips) and the two secondary cycles (0.5 kips and 0.2 kips) are illustrated on the figure.

Given the permanent stress states in the cross-frames of these representative bridges are unknown (e.g., locked-in fit-up forces, dead loads, residual stresses), only live load force/stress cycles entirely in tension or subject to reversal, regardless of how small the tension component is, are considered. The RT recognizes that this assumption is typically only valid when the Fatigue I factored tensile component exceeds the compressive stress due to unfactored permanent loads, or the permanent loads are tensile in nature. To simplify the analysis, the tensile component is always considered to be large enough to propagate a crack. Thus, truck passages that induce a purely compressive force/stress cycle with no tensile component are disregarded from the evaluation, as they are not a fatigue-sensitive loading condition. Also note that, since the primary focus of this study is related to the fatigue limit state, dead loads and locked-in stresses are not explicitly addressed herein.

Again, in the actual analysis of this influence-surface, the process outlined in Figure F3-27 was repeated 55 more times to consider all transverse lane positions in both traffic directions. This computationally intensive procedure was then performed for all 68,352 influence-surface plots obtained from 4,104 bridge models in Abaqus, which resulted in over 3 million influence-line plots similar to the three examples in Figure F3-27.

Ultimately, a script was developed to automate these moving-load simulations. The script was designed to perform rainflow counting on the various influence-line plots (i.e., axial-force time histories), and the following output was recorded for each cross-frame member: (i) the transverse position of the AASHTO fatigue truck that maximizes the force range, (ii) the magnitude of the primary force cycle caused by the critical lane passage, and (iii) the number and magnitude of any secondary cycles caused by that same critical lane passage.

The maximum force range for a given cross-frame member would then represent the *unfactored design force* for which the engineer evaluates the Fatigue I or II limit state. Thus, for a bridge with X-type cross-frames, unfactored design loads for 16 different cross-frame members (Section F3.1.5) were determined; for bridges with K-type cross-frames, unfactored design loads for 20 members were determined. The results presented in Section F3.2.2 are based on the data at this point in postprocessing. In other words, each cross-frame is evaluated independently to study the effects of cross-frame location with respect to force demands.

For purposes of Section F3.2.5 which examines the data with respect to fatigue design, the RT considered only the governing cross-frame member for each bridge (i.e., the cross-frame member with the largest unfactored design force range). This implies that the design of every cross-frame member on a bridge is based on the most critical case, which is typically done in practice. The RT acknowledges that compression capacity in diagonals and struts can very depending on member lengths, such that the design of those member types shall be done independently. However, to facilitate bridge-to-bridge comparisons, the RT

felt it was easier and justifiable to only examine the most critical member, regardless of type. The findings outlined herein would be largely unchanged had non-critical members been evaluated in the same context.

Those singular design force ranges are then factored in accordance with AASHTO LRFD Specifications. As stated in Section F3.1.5, the governing force range presented herein assumes that the critical cross-frame member of the 16 (or 20) evaluated is, in fact, the "true" critical member. Based on supplementary studies, even if the "true" cross-frame member is not among the 16 or 20 selected, the unfactored design force reported herein is typically within a few percent of the value obtained from the governing member, which is deemed acceptable. This assertion is evaluated through a series of example bridge results in the subsequent section.

For the example in Figure F3-27, the process of determining factored design criteria is summarized in Table F3-12. The table presents the same data illustrated in the figure, including the primary force range induced in the cross-frame diagonal of interest by three different transverse lane passages (i.e., 11.8, 3.7, and 9.4 kips). The governing, unfactored design force range for every cross-frame member and for every considered truck passage happened to coincide with the left-barrier case. Thus, the unfactored design force range for all intermediate cross-frames in this bridge is taken as 11.8 kips (based on the critical bottom strut near the intermediate support). For different bridge geometries and cross-frame layouts, the critical cross-frame member and its design force range would obviously vary.

With the unfactored force range established, the fatigue limit state on this type of detail is generally worked in terms of axial stress on the cross-section. In accordance with AASHTO Table F6.6.1.2.3-1 (7.2), the stress range must be calculated based on the effective net area of the angle member to consider shear lag effects. Because the weld lengths of the angle-to-gusset connections in the study are unknown, the RT based its shear lag factor, *U*, on standard TxDOT cross-frame details. Using an average value for typical welded connection details, a *U* factor of 0.76 was applied uniformly to all bridges in the parametric study. This approach was adopted in the development of Table F3-12 to produce a net effective area of 2.17 in^2 (based on L4x4x3/8 single-angle section). Note that the stiffness modification factor does not factor into this equation, as *R*-factors are only considered in the structural analysis.

In addition to the shear lag factor, the dynamic load allowance (1.15 for fatigue limit state in accordance with AASHTO Article 3.6.2) and appropriate Fatigue I and II load factors (1.75 and 0.80, respectively, per Article 3.4.1) are also considered. Thus, the governing, factored design stress range for this example bridge is 9.5 and 4.3 ksi for Fatigue I and II, respectively.

Table F3-12: Sample data demonstrating the process of determining factored, fatigue design stress ranges in cross-frames

Model ID	Cross-Frame ID[a]	Trans. Lane Passage[b]	Force Range (kips)	Governing, Unfactored Force Range (kips)[c]	Governing, Factored Design Stress Range (ksi)[d]	
					Fatigue I	Fatigue II
1181-1	BS; IS	-17	11.8	11.8	9.5	4.3
		-3	3.7			
		+11	9.4			

Notes:
[a]IS = intermediate support, BS = bottom strut
[b]Values corresponds to the transverse position of the left wheel line relative to the coordinate system established in the influence-surface plot (e.g. +11 corresponds to truck passage along right barrier)
[c]Although only one cross-frame member and three lane positions shown, value is based on 16 different cross-frame members with 58 different truck passages each
[d]Force range is divided by effective area of cross-frame angle (considering shear lag effects)

These factored design stress ranges can then be compared to factored resistances in accordance with AASHTO to examine the criticality of load-induced fatigue LRFD (Section F3.2.6) or measured WIM traffic to assess the accuracy of current design loading criteria (Section F3.3).

F3.2.2 Governing Cross-Frame Member

To answer the first question posed (*which cross-frame member typically governs the fatigue design?*), the RT examined the unfactored design force for each selected cross-frame member in the 4,104 unique bridges. In other words, the procedure outlined in Section F3.2.1 was used to determine the critical lane passage and the corresponding force range induced in all 68,352 cross-frame members evaluated. Those design forces were then compiled on a bridge-by-bridge basis to examine which cross-frame would govern the "design" (i.e., the cross-frame with the largest force range recorded).

Before evaluating the entire 4,104-model matrix, it is important to examine the accuracy of the preselected cross-frame member assumption (per Section F3.1.5). As discussed above, it was assumed that the 16 to 20 selected cross-frame members were among the most critical cross-frame members in each bridge studied based on preliminary analysis. To validate this assertion, several of the 4,104 bridges in the Fatigue Loading Study matrix were evaluated in full, and three sample bridges are presented herein. In other words, the unfactored, design force ranges were determined for every intermediate cross-frame member rather than just the 16 preselected members. The three representative bridges examined included a straight bridge with normal supports, a straight bridge with skewed supports, and a horizontally curved bridge. The parameters describing the geometry and cross-frame layout are summarized in Table F3-13.

Table F3-13: Independent variables describing sample bridges in Figure F3-28, Figure F3-29, and Figure F3-30

Parameter	Value		
	Figure F3-28	**Figure F3-29**	**Figure F3-30**
Model ID	277-2	1181-2	909-2
No. spans	1	2	2
L/d ratio	30	35	30
Girder spacing [ft]	6	8	6
No. girders	5	5	5
Support skew [deg.]	0	60	0
Radius of curvature [ft]	Infinite	Infinite	750
Cross-frame spacing [ft]	20	20	20
Cross-frame layout	Contiguous	Contiguous	Contiguous
Web depth [in]	96	72	96
Deck thickness [in]	8	8	8
Cross-frame type	X	X	X
Cross-frame area [in^2]	2.86	2.86	2.86
Concrete modulus [ksi]	5000	5000	5000

In accordance with Section F3.2.1, influence surfaces were developed and unfactored design force ranges (i.e., total force range considering reversal) were computed for every cross-frame member in the three representative bridges. The respective results are summarized graphically in Figure F3-28 (straight bridge with normal supports), Figure F3-29 (straight bridge with skewed supports), and Figure F3-30 (curved bridge with normal supports). The governing design force range is superimposed on the corresponding framing plan, which is generally not to scale (note that the curved bridge 909-2 is depicted as a straight bridge for clarity in Figure F3-30). Top strut, diagonal, and bottom strut results are also presented separately for clarity. Note that only the results for intermediate cross-frame members are presented; that is to say, cross-frame members at supports are not provided as this is not the scope of the project.

The cross-frames in the framing plan are color-coordinated based on the relative force range magnitude of a specific member. Cross-frame members colored light grey have minimal fatigue force demands, whereas members colored in dark red represent the most critical in a particular bridge. Furthermore, bolded force range values indicate that the specific cross-frame member represents one of the preselected 16 members outlined above.

The governing force range for each member corresponds to a specific transverse truck (AASHTO fatigue truck) position. In many cases, that corresponding lane position differs for each of the results presented in the figures. In other words, Figure F3-28 though Figure F3-30 inherently consider the critical truck position, despite not explicitly demonstrated in the plots.

Several of the cross-frame members are designated with dashed lines instead of a governing force range. In these cases, there was no truck passage that induced a tensile component to the force range (i.e., every lane passage resulted in a fully compressive force response). As outlined in Section F3.2.1, these loading conditions were disregarded in the context of the fatigue limit state.

In assessing the results in Figure F3-28 though Figure F3-30, the following observations can be made:

- For the straight and normal bridge (Figure F3-28), the "true" critical cross-frame member was an interior-bay bottom strut that was a few cross-frame lines away from midspan. The governing, unfactored fatigue force demand for this specific member is 3.25 kips. In contrast, the maximum design force considering only the 16 preselected cross-frame members is 3.12 kips, which is within 3% of the "true" value. Thus, the "true" critical member was not actively considered in the assumed set of cross-frame panels evaluated; however, the results presented in subsequent sections are still pertinent and valid given the marginal relative difference between the design force ranges.
- For the skewed bridge (Figure F3-29), the "true" critical cross-frame member was an interior-bay diagonal near the intermediate skewed support, which was not actively considered in the preselected set. The design force corresponding to this member is 10.7 kips. Conversely, the assumed, preselected cross-frame members produced a governing design force of 10.4 kips, which is still within 3% of the "true" value.
- For the curved bridge (Figure F3-30), the "true" critical cross-frame member was an interior-bay bottom strut member near midspan, a few cross-frame lines away from the assumed critical location. However, the preselected cross-frame members produced a governing design force of 6.35 kips, which is still within 10% of the "true" value (7.10 kips).

As discussed above, the results in Figure F3-28 though Figure F3-30 represent just three examples. In many other cases, the "true" cross-frame member was captured in the preselected list of cross-frames. For cases in which the "true" critical member was not actively considered (as shown above), the relative difference in the governing design force was less than 10%, which the RT deemed acceptable given the substantial benefits in the required computational efforts. Consequently, the RT felt confident advancing the studies further based on this observation.

Unfactored Fatigue Design Forces (kips)

Top Struts				Diagonal 1				Diagonal 2				Bottom Struts			
0.98	**0.99**	0.99	0.98	2.09	**1.65**	1.17	0.70	0.70	**1.17**	1.65	2.09	1.13	**2.43**	2.43	1.13
0.98	1.23	1.23	0.98	2.57	2.08	1.19	0.91	0.91	1.19	2.08	2.57	1.47	3.20	3.20	1.47
0.93	1.28	1.28	0.93	2.59	2.11	1.20	1.02	1.02	1.20	2.11	2.59	1.55	3.25	3.25	1.55
0.88	1.30	1.30	0.88	2.50	2.08	1.22	1.05	1.05	1.22	2.08	2.50	1.58	3.21	3.21	1.58
0.83	1.31	1.31	0.83	2.41	2.04	1.22	1.06	1.06	1.22	2.04	2.41	1.59	3.16	3.16	1.59
0.79	1.31	**1.31**	**0.79**	2.33	2.02	**1.22**	**1.06**	1.06	1.22	**2.02**	**2.33**	1.59	3.12	**3.12**	**1.59**
0.83	1.31	1.31	0.83	2.41	2.04	1.22	1.06	1.06	1.22	2.04	2.41	1.59	3.16	3.16	1.59
0.88	1.30	1.30	0.88	2.50	2.08	1.22	1.05	1.05	1.22	2.08	2.50	1.58	3.21	3.21	1.58
0.93	1.28	1.28	0.93	2.59	2.11	1.20	1.02	1.02	1.20	2.11	2.59	1.55	3.25	3.25	1.55
0.98	1.23	1.23	0.98	2.57	2.08	1.19	0.91	0.91	1.19	2.08	2.57	1.47	3.20	3.20	1.47
0.98	0.99	**0.99**	0.98	2.08	1.65	**1.17**	0.70	0.70	1.17	**1.65**	2.08	1.12	2.43	**2.43**	1.12

Figure F3-28: Governing unfactored fatigue design force for every cross-frame member in sample straight and normal bridge

Unfactored Fatigue Design Forces (kips)

Top Struts

0.58			
1.28	1.59	3.26	
1.34	1.82	2.36	2.07
1.40	1.88	1.90	1.90
1.49	1.87	1.84	1.79
1.54	1.86	1.81	1.80
1.64	1.89	1.83	1.77
1.91	2.07	1.83	1.66
2.32	2.54	1.86	1.49
	3.89	2.49	1.47
			1.42
1.42			
1.47	**2.49**	3.89	
1.49	1.86	2.54	2.32
1.66	1.83	2.07	1.91
1.77	1.83	1.89	1.64
1.80	1.81	1.86	1.54
1.79	1.84	1.87	1.49
1.90	1.90	**1.88**	**1.40**
2.07	2.36	1.82	1.34
	3.26	**1.59**	1.28
			0.58

Diagonal 1

0.45			
5.99	6.53	2.74	
3.32	6.21	3.80	3.69
3.92	4.37	2.93	2.25
4.24	4.15	2.69	1.12
4.36	4.07	2.65	1.27
4.71	4.12	2.65	1.54
5.77	4.14	2.68	2.26
9.91	5.79	2.86	3.62
	10.7	2.61	4.25
			0.60
1.64			
7.37	**7.68**	3.14	
5.83	7.55	4.19	4.41
3.84	4.85	3.36	3.20
4.16	4.17	2.76	1.67
4.25	4.07	2.65	1.32
4.46	4.11	2.61	1.07
5.03	4.18	**2.61**	**1.65**
8.19	4.15	2.85	2.77
	9.17	**2.77**	3.31
			0.45

Diagonal 2

0.45			
3.31	2.77	9.17	
2.77	2.85	4.15	8.19
1.65	2.61	4.18	5.03
1.07	2.61	4.11	4.46
1.32	2.65	4.07	4.25
1.67	2.76	4.17	4.16
3.20	3.36	4.85	3.84
4.41	4.19	7.55	5.83
	3.14	7.68	7.37
			1.64
0.60			
4.25	**2.61**	10.7	
3.62	2.86	5.79	9.91
2.26	2.68	4.14	5.77
1.54	2.65	4.12	4.71
1.27	2.65	4.07	4.36
1.12	2.69	4.15	4.24
2.25	2.93	**4.37**	**3.92**
3.69	3.80	6.21	3.32
	2.74	**6.53**	5.99
			0.45

Bottom Struts

--			
2.25	8.36	5.76	
1.90	6.38	8.02	4.94
2.16	4.77	5.18	2.38
2.28	4.73	4.75	2.27
2.33	4.69	4.64	2.13
2.51	4.91	4.70	2.10
2.82	5.95	5.05	1.94
5.92	9.97	7.92	2.85
	7.21	10.4	3.71
			0.62
0.62			
3.71	**10.4**	7.21	
2.85	7.92	9.97	5.92
1.94	5.05	5.95	2.82
2.10	4.70	4.91	2.51
2.13	4.64	4.69	2.33
2.27	4.75	4.73	2.28
2.38	5.18	**4.77**	**2.16**
4.94	8.02	6.38	1.90
	5.76	**8.36**	2.25
			--

Figure F3-29: Governing unfactored fatigue design force for every cross-frame member in sample straight and skewed bridge

Unfactored Fatigue Design Forces (kips)

Top Struts				Diagonal 1				Diagonal 2				Bottom Struts			
1.05	0.99	0.99	1.08	1.70	1.56	1.56	--	1.44	1.92	2.33	2.44	1.43	2.56	3.01	2.10
1.22	1.20	1.15	1.11	2.17	2.57	1.86	2.40	2.11	2.61	3.15	3.41	2.37	4.45	4.56	3.00
1.27	1.21	1.15	1.35	3.52	3.07	3.09	4.19	2.51	2.99	3.44	3.88	3.19	5.74	5.56	3.71
1.30	1.18	1.12	1.48	4.07	3.41	3.43	4.59	2.86	3.24	3.60	4.14	3.74	6.59	6.35	4.29
1.29	1.15	1.08	1.50	4.30	3.61	3.61	4.80	3.01	3.33	3.68	4.24	4.00	7.00	6.76	4.60
1.27	1.12	1.08	1.50	4.33	3.66	3.66	4.84	3.05	3.38	3.70	4.26	4.05	7.10	6.86	4.67
1.26	1.16	1.10	1.50	4.23	3.58	3.59	4.77	3.00	3.33	3.67	4.22	3.98	6.94	6.69	4.55
1.26	1.18	1.12	1.46	4.04	3.40	3.39	4.54	2.77	3.19	3.57	4.11	3.62	6.40	6.19	4.20
1.25	1.18	1.12	1.42	3.63	3.07	3.07	4.19	2.56	2.98	3.41	3.93	3.21	5.70	5.50	3.71
1.24	1.15	1.10	1.34	3.05	2.62	2.66	3.69	2.13	2.67	3.12	3.59	2.44	4.55	4.45	3.02
1.09	0.96	0.92	1.18	2.05	1.87	2.05	2.81	1.58	2.13	2.35	2.76	1.55	2.90	2.90	2.00
1.09	**0.96**	0.92	1.18	2.05	**1.87**	2.05	2.81	1.58	**2.13**	2.35	2.76	1.55	**2.90**	2.90	2.00
1.24	1.15	1.10	1.34	3.05	2.62	2.66	3.69	2.13	2.67	3.12	3.59	2.44	4.55	4.45	3.02
1.25	1.18	1.12	1.42	3.63	3.07	3.07	4.19	2.56	2.98	3.41	3.93	3.21	5.70	5.50	3.71
1.26	1.18	1.12	1.46	4.04	3.40	3.39	4.54	2.77	3.19	3.57	4.11	3.62	6.40	6.19	4.20
1.26	1.16	1.10	1.50	4.23	3.58	3.59	4.77	3.00	3.33	3.67	4.22	3.98	6.94	6.69	4.55
1.27	1.12	1.08	1.50	4.33	3.66	3.66	4.84	3.05	3.38	3.70	4.26	4.05	7.10	6.86	4.67
1.29	1.15	1.08	1.50	4.30	3.61	3.61	4.80	3.01	3.33	3.68	4.24	4.00	7.00	6.76	4.60
1.30	1.18	**1.12**	**1.48**	4.07	3.41	**3.43**	**4.59**	2.86	3.24	**3.60**	**4.14**	3.74	6.59	**6.35**	**4.29**
1.27	1.21	1.15	1.35	3.52	3.07	3.09	4.19	2.51	2.99	3.44	3.88	3.19	5.74	5.56	3.71
1.22	1.20	1.15	1.11	2.17	2.57	1.86	2.40	2.11	2.61	3.15	3.41	2.37	4.45	4.56	3.00
1.05	0.99	**0.99**	1.08	1.70	1.56	**1.56**	--	1.44	1.92	**2.33**	2.44	1.43	2.56	**3.01**	2.09

Figure F3-30: Governing unfactored fatigue design force for every cross-frame member in sample horizontally curved bridge

With the assumptions established in Section F3.1.5 validated, the next step is to evaluate the entire Fatigue Loading Study data set. First, Figure F3-32 compiles the unfactored design force ranges for all 68,352 cross-frames studied in the form of a box-and-whiskers plots. Each box-and-whiskers component is organized by cross-frame location and then further by cross-frame member. Thus, each figure presents the results of 16 different types of cross-frame members. For the sake of clarity, cross-frame identification is abbreviated in all subsequent figures. As far as cross-frame location, "ES" represents the cross-frame panel near the end support (colored in red), "M-I" the interior bay near the maximum positive dead load moment region (blue), "M-E" the edge bay near the maximum positive dead load moment region (green), and "IS" near the intermediate support (purple). Refer to Section F3.1.5 for more information on these general locations.

In terms of the cross-frame members, "TS" represents top strut members, "D1" for diagonal 1 (diagonal framing into the top flange of the left girder where left is based on the coordinate system previously established), "D2" for diagonal 2, and "BS" for bottom struts. Note that for K-type cross-frames, there are two independent bottom strut members. For purposes of the results hereafter, only the governing member is presented.

The plots are also organized by bridge type to illustrate the effects of support skew and bridge curvature on the cross-frame response. Data labeled as "straight, normal" was generated from all bridges with no bridge curvature (i.e., infinite radius of curvature) and zero support skew. Data labeled as "straight, skewed" was generated from bridges with no bridge curvature, but support skews of 30 and 60 degrees collectively. Similarly, data labeled as "curved" was generated from bridges with a radius of curvature of 1500 feet or 750 feet collectively.

To fully understand and interpret the box and whiskers plot, there are additional items to consider:

- The box-and-whiskers are a graphical means to present scatter in a large data set (i.e., a discrete probability density function). In other words, each box-and-whiskers represents the results of all bridges and cross-frames that satisfy the applied filters. For example, the box-and-whiskers labeled "D2" under the "M-E" category in the "Straight, Normal" graph represents the compiled design force ranges for all diagonal 2 members evaluated near the maximum positive dead load moment region (edge bay) of straight and normal bridges. In total, 312 data points (corresponding to the unfactored design force ranges for 312 unique, straight and normal bridges) are represented. The transformation from a probability density function to a box-and-whiskers plot is demonstrated graphically in Figure F3-31 for the example above.
- For each box-and-whiskers plot, six key statistical parameters are displayed: (i) the minimum value in the data set, (ii) the first quartile or the 25th percentile, (iii) the second quartile or the median value, (iv) the third quartile of the 75th percentile, (v) the maximum value, and (vi) the mean value. The max and min values are represented by the whiskers, the quartile values are represented by the bounds of the box, and the "X" represents the mean. An example is presented in Figure F3-31 for clarity.
- The critical lane passage that corresponds to the design force ranges presented are different for each data point. In this figure, only the magnitudes of the design force ranges are of interest. The critical lane positions are covered in a subsequent section.
- A reference sketch is also provided in the figure to clarify the relative position of the cross-frame considered; the results for the bolded and color-coded cross-frame locations are plotted. Note that the exact location of the cross-frame, the number of girders, the number of spans, the support skew angle, and the radius of curvature in the sketch are for visual reference only; the bridge geometries of the various data points may differ from the representative sketch.

By presenting the box-and-whiskers side-by-side, the RT can evaluate which cross-frame members generally experience the largest force ranges due to the passage of the AASHTO fatigue truck in its critical

lane. By examining the results independently for bridge types, the RT can evaluate the impacts of support skewness and bridge curvature on which cross-frame members are critical.

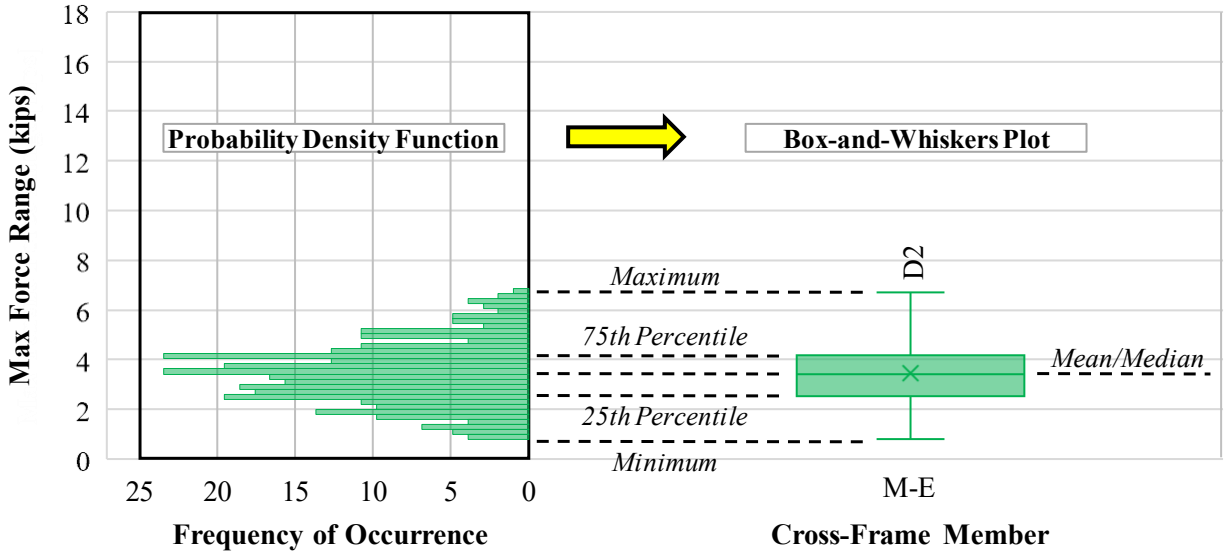

Figure F3-31: Sample data set (cross-frame D2 at M-E of straight, normal bridges) demonstrating the development of the box-and-whiskers plot

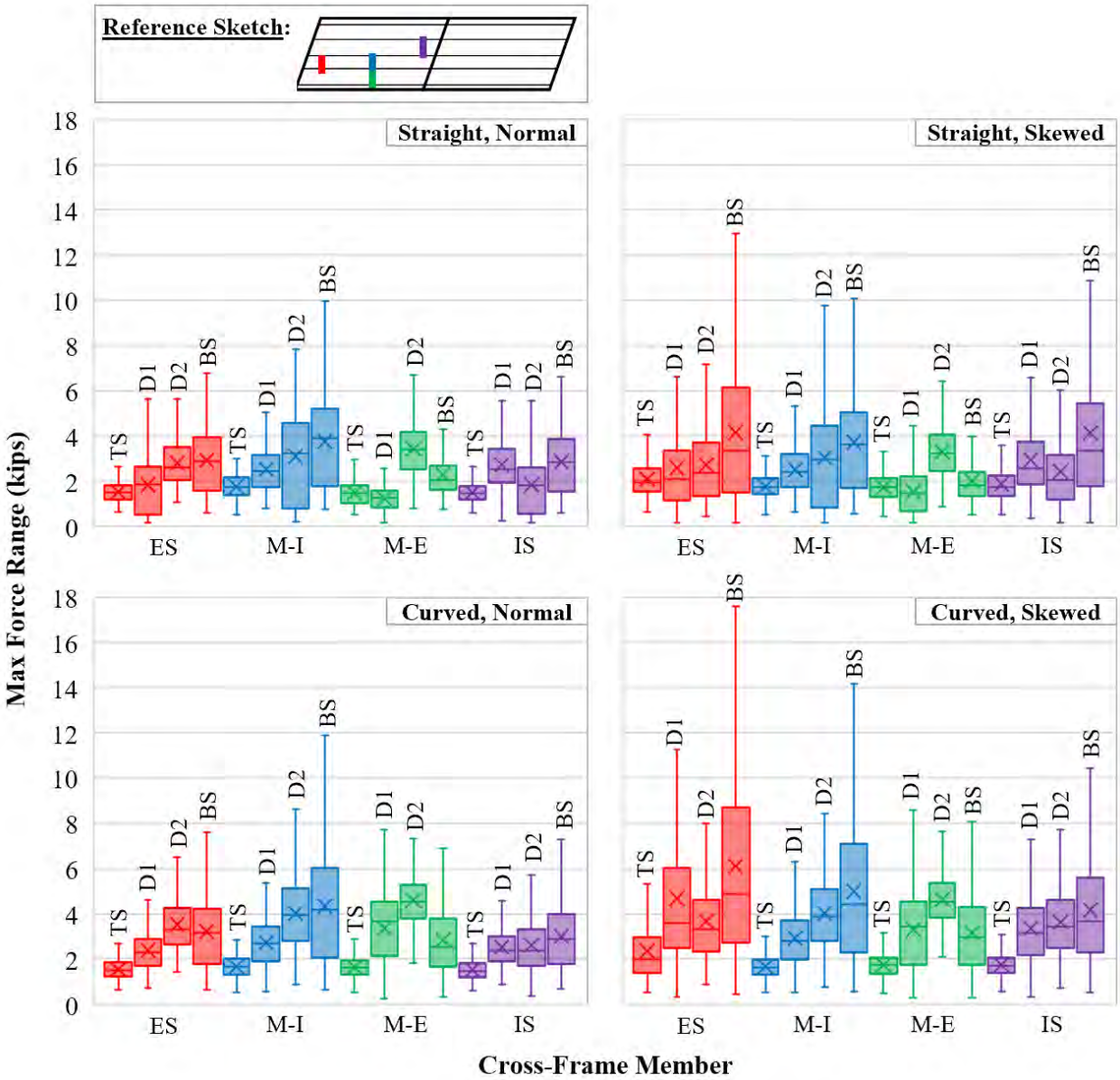

Figure F3-32: Unfactored design force ranges compiled for every cross-frame member evaluated

From Figure F3-32, the following observations can be made about governing cross-frame members:

- There is substantial variability observed in all box-and-whiskers presented. For example, the design forces for bottom struts near end supports of curved and skewed bridges range from a minimum of about 0.5 kips to a maximum of nearly 18 kips. This scatter is attributed to the large number of bridge parameters which are inherently considered in the results.
- Top strut members, as anticipated, generally have the lowest force demands observed.
- The force ranges observed in skewed and/or curved bridges are generally greater than equivalent straight and normal bridges, particularly in bottom strut and diagonal members near skewed supports. For example, the mean force range for bottom struts at end supports increases from 3 kips for straight and normal bridges to over 4 kips for straight and skewed bridges.
- This same relationship is not as impactful for cross-frames not in the vicinity of supports (i.e., near

the maximum positive dead load moment region). As highlighted in Section F3.1.8.2, cross-frames in these regions are less impacted by the effects of support skew.

- In general, bottom strut members near M-I regions (interior bay near maximum positive dead load moment region) have the largest design force ranges for non-skewed (straight or curved) bridges. The maximum, 75th percentile, and mean values are all largest for this condition.
- For skewed bridges, the bottom strut members near end supports tend to have the largest force demands, but there is still significant scatter.

Figure F3-33 expands on Figure F3-32 by evaluating only the cross-frame member with the largest force demands in each bridge. For all 4,104 bridges, the RT recorded the governing cross-frame member based on location and member type; then, the number of occurrences for each were compiled. Thus, top struts are not expected to make a significant impact on Figure F3-33, given the relatively low force demands observed, regardless of bridge type.

Similar to Figure F3-32, Figure F3-33 presents the results of straight/normal, straight/skewed, curved/normal, and curved/skewed bridges independently. However, instead of presenting the maximum force ranges along the y-axis, this figure presents the probability of occurrence (i.e., the number of times a specific cross-frame member produced the largest design force range in a bridge). The probability of occurrence is calculated with respect to the number of bridges in each type (e.g. 312 straight and normal bridges). For example, the bottom strut in the interior bay near the maximum positive dead load moment region governed the cross-frame fatigue design of over 55% of the 312 straight and normal bridges evaluated; in contrast, the top strut near the end support never governed (0% probability of occurrence).

Given that the figures are inherently related, it is anticipated that the critical cross-frames observed in Figure F3-32 are also observed in Figure F3-33.

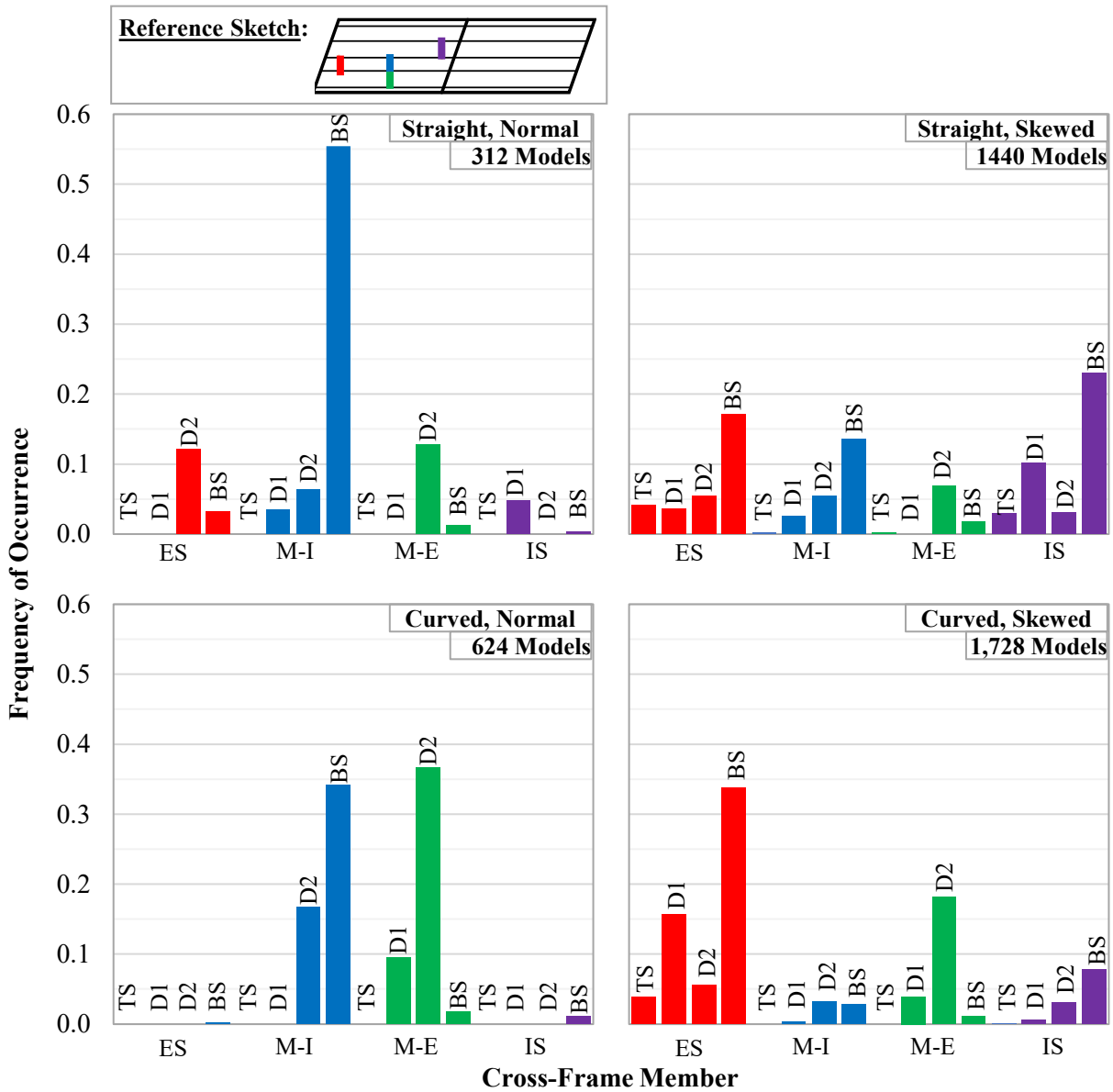

Figure F3-33: Bar graph illustrating the most common critical cross-frame members under AASHTO fatigue loading criteria

From Figure F3-33, the following observations can be made about governing cross-frame members:

- For non-skewed bridges, bottom struts and diagonals near the maximum positive dead load moment region tend to produce the largest force demands. This is particularly evident in the plot for curved and normal bridges, where fatigue design was governed by these specific members for nearly all 624 cases.
- For skewed bridges, the response is more variable. However, cross-frames near skewed supports (both end and intermediate) have much larger probabilities of occurrence when compared to non-skewed bridges. For example, bottom struts near end supports governed cross-frame fatigue design in nearly 35% of all curved, skewed bridges, whereas 0% governed for similar curved, straight bridges.

From all the data obtained from this study, it is apparent that bottom strut members tend to be the most critical in terms of fatigue force demands. In past studies that focused on stability bracing applications, top and bottom struts were assumed zero-force members (i.e., adjacent girders rotating equally). But for cross-frames in composite systems and subjected to live loads, bottom struts are often engaged. In many cases, the cross-frame acts like a floorbeam system to distribute loads from girder-to-girder. Under a truck load, adjacent girders have differential rotation. The bottom strut is analogous to the bottom tension flange of a composite floorbeam, the concrete deck is the top compression flange, and the top strut is in close proximity to the composite neutral axis. This behavior is illustrated schematically in Figure F3-34.

At skewed supports, the global, torsional response of the superstructure tends to engage the nearby bottom struts. Contiguous lines of cross-frame panels act like a stiff, closed section that resists the torsional moments on the bridge cross-section. Chapter F4, the R-Factor Study, addresses the various deformation patterns observed in cross-frames.

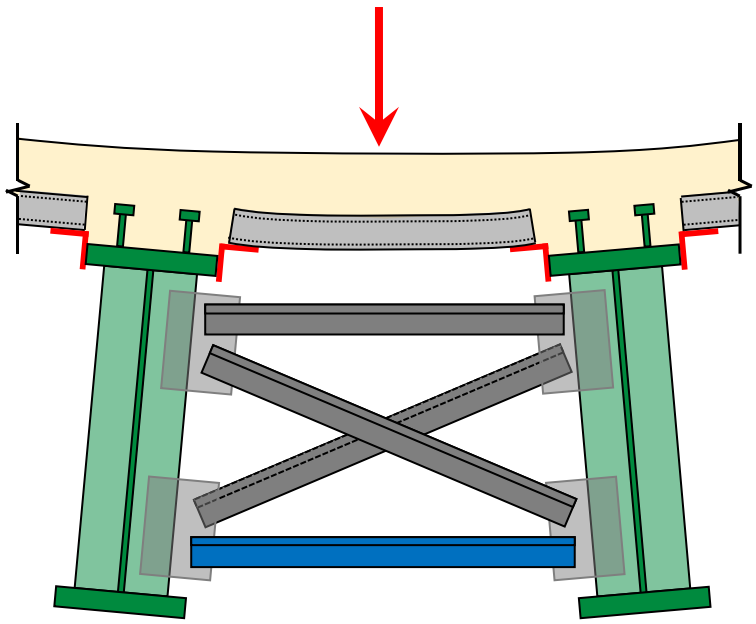

Figure F3-34: Common deformation pattern observed in cross-frame panels due to an applied live load

Even with these discernible trends, there is still significant variability in cross-frame response. The governing cross-frame member is still a function of many bridge parameters, albeit support skew and curvature are the most important. Given a random bridge geometry, the critical cross-frame panel could likely be identified within reasonable limits before any analysis is performed (i.e., based on the general rules of thumb previously documented). Still, it is recommended that the critical cross-frame is not "missed" by taking a shortcut. Rather, conducting an influence-surface analysis and performing a comprehensive design of all intermediate cross-frames in the bridge ensures a fully vetted design.

Many commercial software packages have the built-in functionality to analyze and design all cross-frames for design loads. If the program does not automatically address this, manually developing a spreadsheet to evaluate each cross-frame due to AASHTO fatigue loading criteria is possible.

F3.2.3 Governing Lane Passage

Where Section F3.2.2 evaluates which cross-frame members govern for common bridge types, the section herein addresses the lane position corresponding to those critically-loaded members. The second question (*which lane position typically maximizes the force range in critical cross-frame members*?) is examined. As is currently documented in AASHTO LRFD Article 3.6.1.4.3, bridge designers must consider all transverse and longitudinal truck positions when evaluating details and components for the fatigue limit state. Other than a 1-foot clear distance from the inside face of the bridge barrier, AASHTO fatigue truck passages must be evaluated in all possible transverse lanes, forward and backward: a provision that is included primarily due to the uncertainty in future lane striping and/or bridge widening. Therefore, without assurance that the traffic lanes are to remain unchanged throughout the service life a bridge, the designer must take the conservative approach.

As documented previously, the AASHTO fatigue truck was "run" over all 4,104 bridges in numerous transverse lane positions. Using 1-foot increments, between approximately 20 and 120 lane passages were considered for each bridge depending on the width. Given the number of lane passages and cross-frame members studied, drawing concise and meaningful conclusions on the data is challenging. In the evaluation of the data, however, the RT observed that many of the critical cross-frame members were governed by truck passages along the inside faces of the barriers (i.e., centerline of the wheel line within 1 foot of the closest barrier).

Thus, to simplify the discussions in this section, lane passages are grouped as either "overhang" loads or "non-overhang" loads. Overhang loads represent truck passages where one of the transverse wheel lines is applied outboard of the fascia girder centerline; these load cases include "left" and "right" overhang loads, as well as both the forward and backward directions. Non-overhang loads represent truck passages for which both wheel lines are within the centerlines of the fascia girders.

Overhang loads, as defined above, occur on a much less frequent basis for bridges in service. Although critical load cases for strength limit states, truck drivers are likely less inclined to drive within a few feet of the barrier (i.e., along the overhanging portion of the deck). As such, overhang loads are less representative of the fatigue limit state, which focuses heavily on "everyday" loading. Non-overhang loads, on the other hand, are much more representative.

With that said, the focus of this section is to identify the types of bridges most commonly governed by overhang load cases. Assuming the designer is uncertain about future lane striping and/or bridge widening, these special bridge types are the most affected by the conservative language in Article 3.6.1.4.3. Again, this section only addresses current AASHTO fatigue loading conditions; Section F3.3 studies the response of cross-frames to WIM streams applied in various lane positions.

Figure F3-35 compiles the lane position associated with the results presented in Figure F3-33. For each of the 4,104 unique bridges, the critical lane passage corresponding to the governing cross-frame was recorded and was later categorized as an overhang or non-overhang load based on the definition above. The tallied results are presented in the form of a bar graph in Figure F3-35, where the y-axis represents the probability of occurrence with respect to the number of bridges in each type (e.g. 312 straight and normal bridges). Each of the bars are then further characterized as overhang and non-overhang loading conditions.

The figure independently evaluates bridge types, similar to Figure F3-33, but does not explicitly present data from individual member types (i.e., bottom struts, diagonals, top struts). Instead, any of the governing cross-frame members from Figure F3-33, regardless of member type, are grouped based on their general location in the framing plan (i.e., ES, M-I, M-E, and IS).

To clarify the intent of the figure, take the straight, normal data set as an example. For all 312 straight and normal bridges evaluated, the governing cross-frame was located in an interior bay near the maximum positive dead load moment region on 204 occasions (65%). Of those 204 occasions, the critical cross-frame

member was always governed by a non-overhang load (i.e., 100% non-overhang and 0% overhang). This is reflected in the "M-I" bar in the straight, normal portion of Figure F3-35.

A more interesting example is the "IS" case of the straight and skewed data set. In total, 1,440 straight and skewed bridges were analyzed in the Fatigue Loading Study. Of those 1,440 bridges, 565 were governed by cross-frame members near the intermediate support (39%). Of those 565 cases, 514 were governed by overhang lane passages and only 51 by non-overhang loads.

From Figure F3-35, the RT can identify which bridge types are most commonly impacted by these infrequent overhang loads.

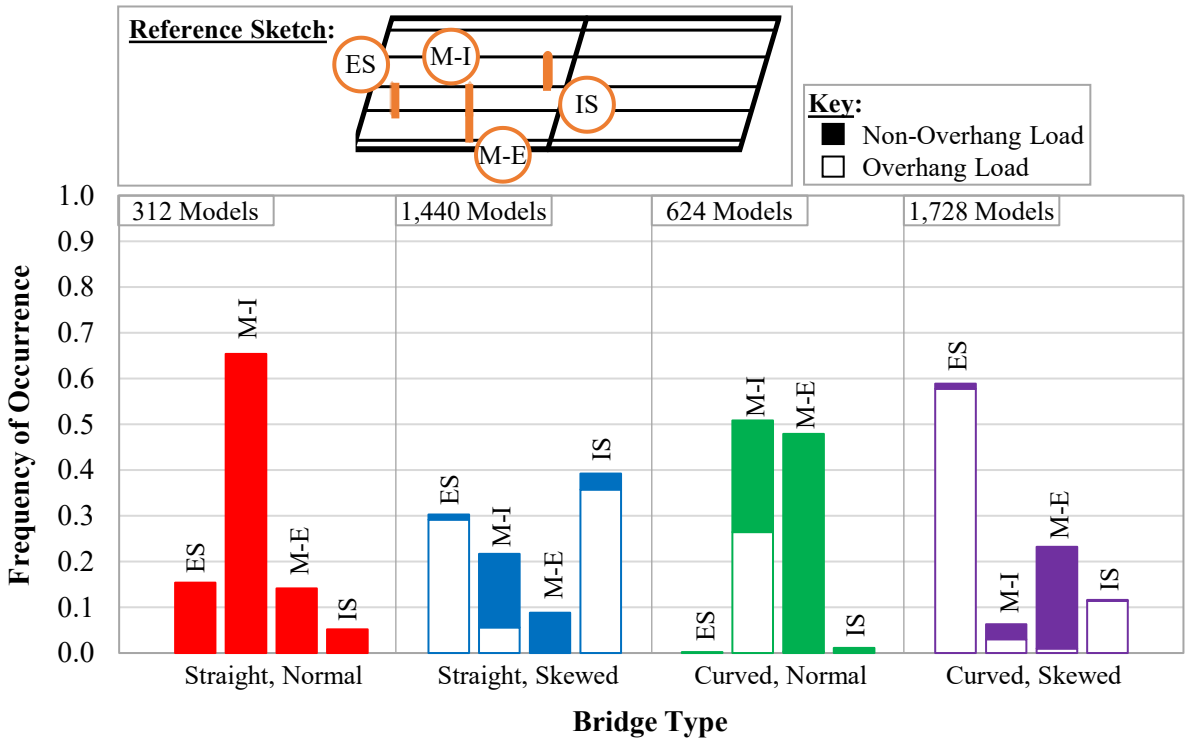

Figure F3-35: Bar graph presenting the critical lane position associated with the governing cross-frame member

From Figure F3-35, the following observations can be made about bridge type and critical lane passages:

- Non-overhang loads, although not overly descriptive, generally correspond to "localized" load effects. In other words, the force effects in the critical cross-frame were maximized by a truck passing just to the left or right of the panel, similar to the trends observed in the influence-surface plots.
- For non-skewed bridges, the critical cross-frame members are almost always governed by non-overhang loads. In fact, the forces in critical cross-frame members in straight, normal bridges were maximized 100% of the time by non-overhang loads. The exception to this rule is M-I cross-frames in curved bridges (interior bay near the maximum positive dead load moment region), who were often governed by truck passages along the outer radius of the curve. Thus, it can be concluded that cross-frame fatigue design in bridges without support skews are largely governed by truck passages in close transverse proximity to the panel.
- For skewed bridges, the overhang loads represent a large percentage of the critical truck passages,

particularly for "ES" and "IS" cross-frames. As previously documented, cross-frames near end and intermediate supports often govern the fatigue design of all cross-frames in skewed framing plans. The torsional response of the superstructure and the corresponding girder rotations often heavily engage the bottoms struts and diagonals in these areas. As such, loads that maximize the induced torque on the bridge cross-section are often critical. For straight bridges, the critical loads correspond to those applied along either deck edge where the moment arm about the bridge centroid is largest. For curved bridges, those loads correspond to either the inner or outer radius about the straight-line chord of the curved segment.

It is evident that force demands in cross-frames of skewed bridges, especially those near the end or intermediate supports, are sensitive to overhang loads. Because these cases are rather infrequent, basing a fatigue limit state design on an overhang truck passage could potentially result in overly conservative design loads. With that in mind, overhang and non-overhang truck passages are evaluated in the context of measured WIM data in Section F3.3, where the appropriate lane position for AASHTO implementation is examined in greater depth.

F3.2.4 Cycles per Truck Passage

As shown in the example in Figure F3-27, cross-frames often respond to a truck passage with more than one stress or force cycle. Although Sections F3.2.2 and F3.2.3 only focus on the primary cycle as it largely governs the design, the smaller secondary cycles can potentially have an impact on the performance of a fatigue detail.

The nominal resistance of a fatigue detail is a function of three key metrics: (i) the magnitudes of the load-induced stress cycles, S_r, (ii) the number of stress cycles over the service life, N, and (iii) the detail and its proneness to fatigue damage (related to variable, A). The resistance, in terms of number of cycles, has been shown to be inversely proportional to the cube of the stress range magnitude, as shown by the following expression:

$$N_f = \frac{A}{{S_r}^3} \qquad \textit{F3.1}$$

where: N_f = number of cycles at constant-amplitude stress range, S_r, until failure; A = fatigue detail category constant per AASHTO (ksi^3); and S_r = constant-amplitude stress range magnitude (ksi).

The expression above, which forms the basis of the S-N curves provided in AASHTO LRFD, is based on a constant-amplitude stress range. Like many other real structures, bridge components are often subjected to variable stress cycles at non-uniform time intervals due to the variability in the truck population and the passing lane positions. And in some instances, a passing truck can induce multiple stress cycles in an element, which further complicates the behavior.

AASHTO specifications, like many other design codes, have adopted simplified methodologies to handle these sources of variability. First, variable stress cycles are considered in the development of the fatigue loading criteria. The AASHTO fatigue truck and the corresponding load factors have been calibrated to represent the response of a bridge component to the entire variable truck population (Modjeski and Masters 2015). For instance, the Fatigue II load factors in conjunction with the fatigue truck (Figure F3-26) are intended to produce the effective stress range of the full traffic spectrum (with an appropriate reliability index). The effective stress range relates the damage caused by the "real" variable-amplitude stress cycles to a singular, constant-amplitude stress cycle of equal cycle count.

Second, the number of stress cycles over the service life of the bridge is estimated by two independent measures: (i) the single-lane average daily truck traffic ($ADTT_{SL}$) and (ii) the number of stress cycles per

truck passage. In other words, the designer estimates the projected number of trucks to traverse the bridge in the critical lane in one direction over the 75-year (or more) service life; then, the designer relates total number of stress cycles to total number of trucks via AASHTO Table F6.6.1.2.5-2. The values in that table, *n*, are intended to represent the average number of stress cycles incurred for each passing truck. For simple span girders, *n* is to be taken as 1.0. For orthotropic deck plate connections, *n* is taken as 5 given the cycles induced by each individual wheel. Currently, Table F6.6.1.2.5-2 provides no guidance on cross-frame members specifically, other than the ambiguous designation for "transverse members." The *n*-value should not only take the number of additional cycles into consideration, but also the variable stress magnitudes of each secondary cycle. For instance, a secondary stress cycle that is small in amplitude compared to the primary cycle will have negligible impact on the accumulated fatigue damage, given the relationship between stress range and number of cycles.

Thus, this section is dedicated to evaluating the *n*-value for cross-frame members based on current AASHTO fatigue loading, answering the question: *how many secondary cycles are typically generated for a given fatigue truck passage?* In Section F3.3, a similar exercise is to be performed for WIM data.

To address that question, Figure F3-36 expands on the results presented in Figure F3-32. Figure F3-32 presented the unfactored, design force range for every cross-frame member evaluated in all 4,104 bridges (based on the governing lane passage); however, only the primary cycle was reported in those plots. Although not shown, the RT not only recorded the primary cycle but also any additional secondary cycles incurred during that critical truck passage for every data point in Figure F3-32. The number of secondary cycles, as well as their stress/force range magnitudes, were compiled. Figure F3-36 presents the results in terms of cycle counts (neglecting the stress magnitudes of secondary cycles, for now).

Figure F3-36 is organized and presented similarly to Figure F3-33 in that cross-frame member types and locations are evaluated independently. Along the y-axis, the average number of cycles for each critical lane passage is reported. For example, top struts near end supports (TS bar under IS category) in straight, normal bridges saw nearly 1.9 cycles per critical truck passage on average. In other words, a secondary cycle was observed in nearly 90% of the 312 cases studied. In contrast, D1 members in M-I regions (i.e., diagonal cross-frame member in an interior bay near the maximum positive dead load moment region) of curved, normal bridges averaged 1.0 cycles per critical truck passage. Thus, a secondary cycle was never observed in the 624 cases.

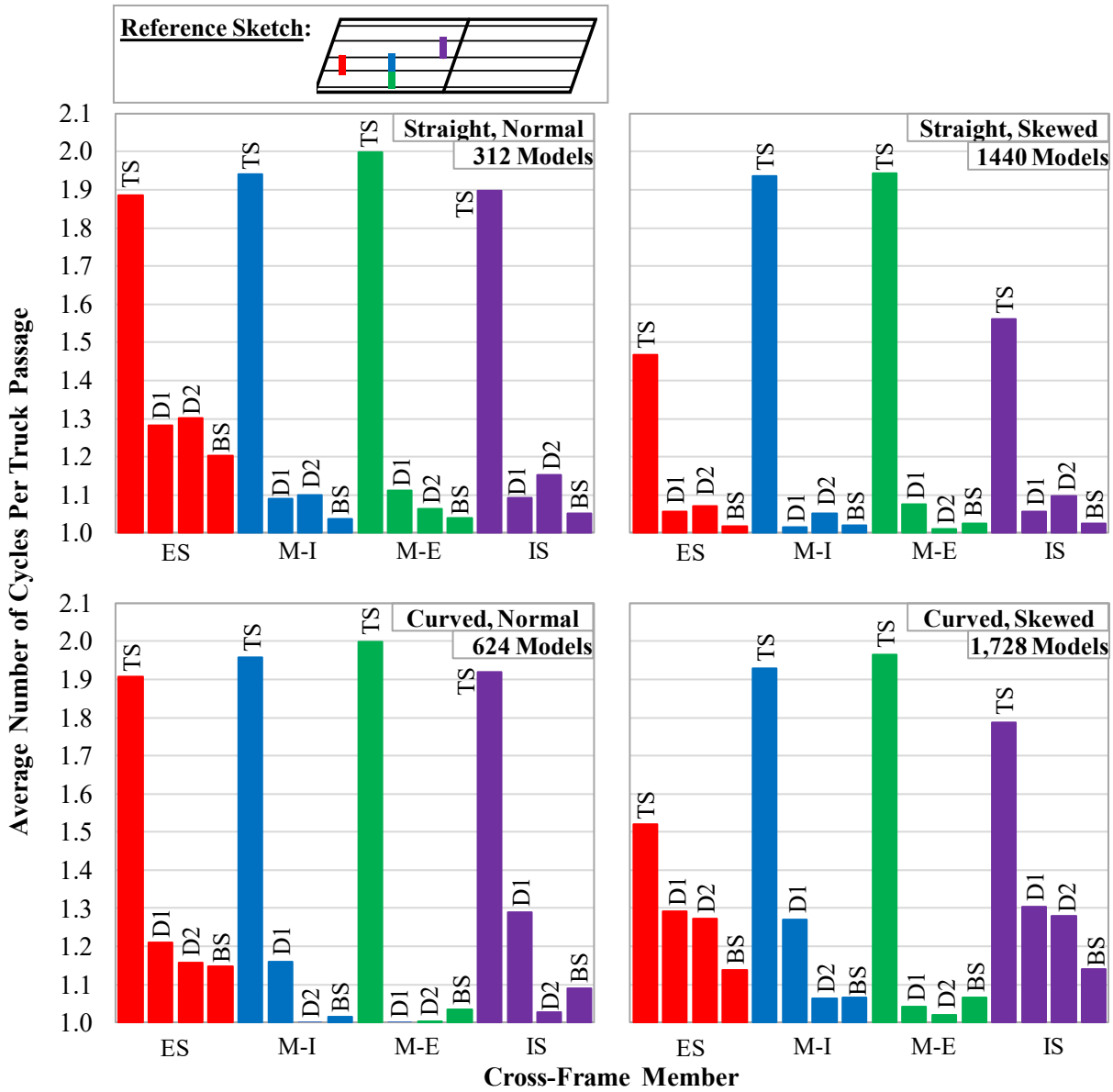

Figure F3-36: Average number of secondary force cycles measured from critical lane passage

From Figure F3-36, the following observations can be made about secondary force cycles:

- In general, top struts are the only cross-frame members that see significant secondary cycles, regardless of bridge type. In most cases, the average number of cycles per critical truck passage is between 1.5 and 2.0. However, it is important to note that the stress magnitudes of these members are typically small when compared to bottom struts and diagonals such that this observed behavior is less impactful.
- For bottom struts and diagonals, the average number of cycles per truck passage never exceeded 1.3. Thus, when the AASHTO fatigue truck traverses the bridge, regardless of skew angle or curvature, bottom struts and diagonals generally only experience one primary cycle.

Figure F3-37 illustrates this behavior through an example. For a straight bridge with skewed supports, the axial force response of every member in a cross-frame panel near the skewed support (as a function of the truck position on the bridge) is presented for an AASHTO fatigue truck passage along the "left" barrier. This loading condition happens to govern the design of all four cross-frame members presented here. Refer to Table F3-14 for the pertinent parameters that describe the geometry of the bridge and the layout of the cross-frames. Note that the plan sketch of the bridge in Figure F3-37 is not to scale.

From the sample data in Figure F3-37, it is evident that the top strut experiences three force cycles during the truck passage (2.95, 0.48, and 0.40 kips). Diagonal 2 experiences two independent cycles, but the magnitude of the secondary cycle is extremely small compared to the primary cycle. The bottom strut and diagonal 1 experience only one cycle for the given truck passage; both members are subjected to a full force reversal. As such, these sample results are consistent with the comprehensive data set presented previously.

Table F3-14: Independent variables describing sample bridges in Figure F3-37

Parameter	Value
Model ID	1059-1
No. spans	2
L/d ratio	30
Girder spacing [ft]	10
No. girders	3
Support skew [deg.]	60
Radius of curvature [ft]	Infinite
Cross-frame spacing [ft]	20
Cross-frame layout	Staggered
Web depth [in]	96
Deck thickness [in]	8
Cross-frame type	X
Cross-frame area [in^2]	2.86
Concrete modulus [ksi]	3600

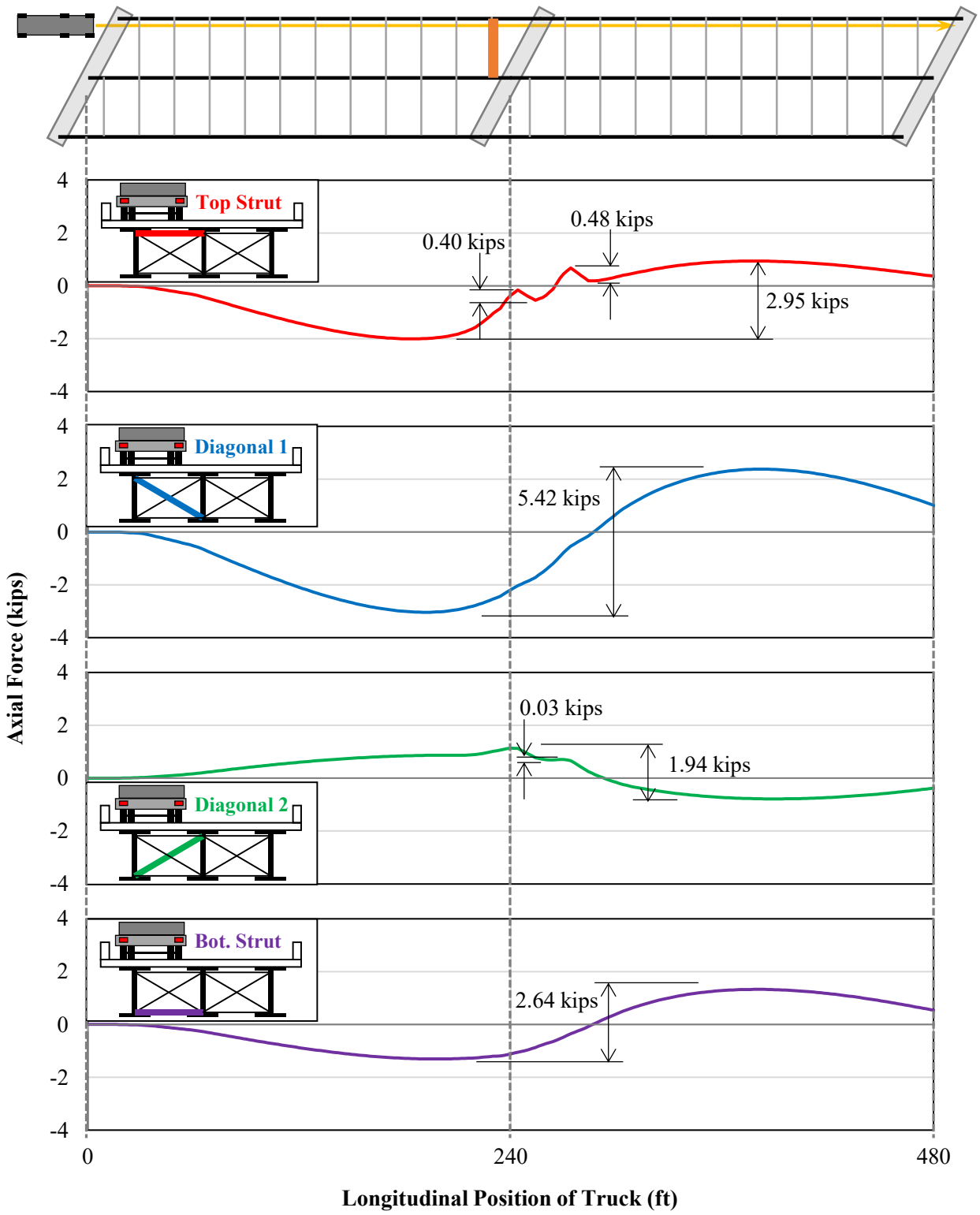

Figure F3-37: Sample influence-line plots demonstrating typical number of cycles per truck passage for different cross-frame members

As introduced above, producing a secondary stress cycle is only meaningful to damage accumulation if the stress magnitude is significant. To relate the secondary stress cycle magnitudes with the primary stress cycle magnitude, Palmgren-Miner's rule (Miner 1945) is employed. Palmgren-Miner's rule is a cumulative damage theory adopted by AASHTO. It demonstrates that fatigue damage is the summation of all cycles of varying amplitude and that larger magnitudes produce proportionally higher damage than smaller magnitudes. It is generically represented by the following expression:

$$D = \sum_{j=1}^{k} \frac{n_j}{N_{f,j}} \qquad \textit{F3.2}$$

where: D = damage accumulation index; n_j = number of cycles measured within jth stress range, $S_{r,j}$ (stress range spectrum); and $N_{f,j}$ = number of cycles at jth stress range, $S_{r,j}$, that would initiate failure.

Thus, the RT examined the additional damage accumulated by the secondary cycle(s) and compared it to the damage accumulated by just the primary cycle, a ratio defined as *DI* herein (damage increase index). The damage increase index practically ranges from 1.0 to 2.0. A value of unity represents no additional damage is accumulated by secondary cycles. A value of two represents the case in which the damage associated with the secondary cycle equals the damage of the primary cycle (i.e., equal stress magnitudes). This relationship is demonstrated mathematically by the progression of the following expressions:

$$DI = \frac{D_p + D_s}{D_p} = 1 + \frac{D_s}{D_p} \qquad \textit{F3.3}$$

$$DI = 1 + \frac{\sum_{s=1}^{k}\left[\frac{n_s}{\left(\frac{A}{{S_{r,s}}^3}\right)}\right]}{\frac{n_p}{\left(\frac{A}{{S_{r,p}}^3}\right)}} = 1 + \frac{\sum_{s=1}^{k}\left[1 * {S_{r,s}}^3\right]}{1 * {S_{r,p}}^3} \qquad \textit{F3.4}$$

$$DI = 1 + \frac{\sum_{s=1}^{k}\left[{S_{r,s}}^3\right]}{{S_{r,p}}^3} \qquad \textit{F3.5}$$

where: DI = damage increase index defined above; D_s = damage accumulated by secondary stress cycles (if any) of variable magnitude, $S_{r,s}$; D_p = damage accumulated by primary stress cycle of magnitude, $S_{r,p}$; n_s = number of secondary stress cycles at specific variable magnitude, $S_{r,s}$; and n_p = number of primary cycles at magnitude, $S_{r,p}$, taken as unity.

Based on this expression, the increase in damage accumulation due to a secondary stress cycle(s) is related to the sum of the secondary stress magnitudes cubed divided by the primary stress cycle cubed. To demonstrate the relationship, a simple example is provided. In the majority of the cases observed from the parametric study, the magnitude of the secondary stress cycle was approximately 20% of the primary cycle magnitude on average. Using the expressions above, considering the contribution of the secondary cycles mathematically results in a damage increase of less than 1% (i.e., $DI = 1 + 0.2^3 = 1.008$). This procedure was performed on every cross-frame member evaluated in the 4,104-model study, and the percent increase was always less than 1%.

Thus, it can be concluded that secondary stress cycles in the response of cross-frames, if any, are typically inconsequential in terms of fatigue damage accumulation under the current design loading criteria. As noted previously, the RTevaluated these same effects for WIM data in Section F3.3. Based on those findings, a recommendation for the *n*-value in AASHTO Table F6.6.1.2.5-2 can be made.

F3.2.5 Impact of Bridge Parameters

As shown in the preceding subsections, there is significant variability in load-induced cross-frame response. This was particularly evident in Figure F3-33, which presented the governing force demand in every cross-frame member evaluated in the 4,104-model matrix. The variability in the response is attributed to one or many of the parameters that comprise the bridge structures. This section herein examines the impacts of these parameters on the force effects in critical cross-frame members, thereby answering the following question: *how do various parameters impact the maximum force ranges observed in cross-frames?*

Before evaluating the effects of each parameter, Figure F3-38 presents one isolated example for reference. In this plot, the response of a diagonal cross-frame member near the maximum positive dead load moment region is illustrated for three different bridge structures. The influence-line shown corresponds to a passing AASHTO fatigue truck, whose left wheel line is positioned 5 feet from the bridge centerline. Therefore, the truck passes just to the left of the cross-frame panel of interest, as depicted in the framing plan sketch in Figure F3-38.

The three bridges share identical parameters except for curvature: straight, 1500-ft radius, and 750-ft radius. Thus, any differences in the cross-frame response can be attributed directly to the introduction of a curved layout. The pertinent parameters that describe the framing geometry and cross-frame layout are summarized in Table F3-15 for reference. Note that the model identification and the bridge radii are bolded, as these vary from bridge to bridge.

Based on this sample data, it is evident that the force demand in the cross-frame member of interest increases as the bridge radius decreases (or its curvature increases). The resulting force range from the passing truck increases 10% when a 1500-ft radius is introduced and an additional 9% when the radius is halved to 750 feet. The general response of the cross-frame is the same, except for the magnitudes. Thus, based on this limited data set, it could be stated that bridge curvature is positively correlated to cross-frame force demands (i.e., bridge radius is negatively correlated).

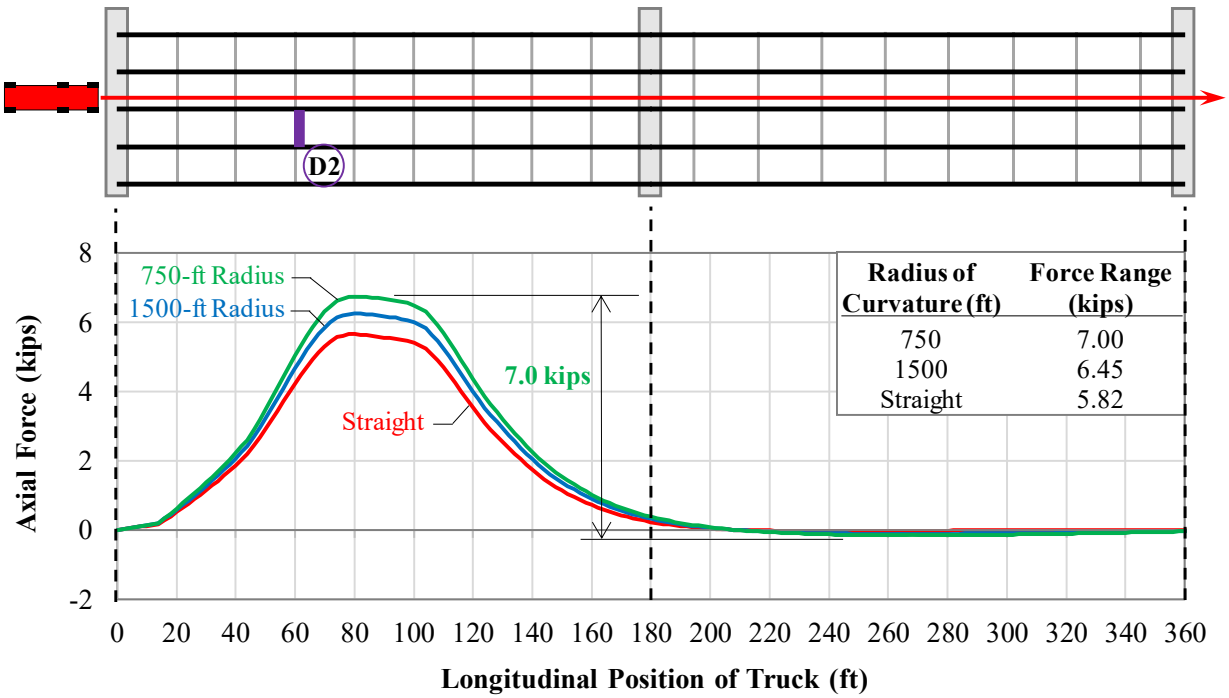

Figure F3-38: Sample data demonstrating the impacts of bridge curvature on cross-frame force demands

Figure F3-38 represents three of potentially millions of data points. Similarly, the response could have been presented for different lane positions, different cross-frame members, and different bridges altogether. As discussed in Sections F3.2.2 and F3.2.3, evaluating only the critical cross-frame member and the governing lane position for each bridge is often more valuable than evaluating every individual case. Ultimately, the engineer is more concerned with how a bridge parameter impacts the overall fatigue design of cross-frames, not the localized effects on non-governing members which are deemed less important. Therefore, the results presented hereafter correspond to the governing cross-frame members and lane positions only (i.e., the unfactored design forces).

Table F3-15: Independent variables describing sample bridges in Figure F3-38

Parameter	Value		
	Straight Bridge (Red)	**Curved Bridge (Blue)**	**Curved Bridge (Green)**
Model ID	**821-1**	**823-1**	**825-1**
CF location[a]	M-I	M-I	M-I
CF member[b]	D2	D2	D2
No. spans	2	2	2
L/d ratio	30	30	30
Girder spacing [ft]	10	10	10
No. girders	5	5	5
Support skew [deg.]	0	0	0
Radius of curvature [ft]	**Infinite**	**1500**	**750**
Cross-frame spacing [ft]	20	20	20
Cross-frame layout	Contiguous	Contiguous	Contiguous
Web depth [in]	72	72	72
Deck thickness [in]	8	8	8
Cross-frame type	X	X	X
Cross-frame area [in^2]	2.86	2.86	2.86
Concrete modulus [ksi]	3600	3600	3600

Notes:
[a]M-I = interior bay near maximum positive dead load moment region
[b]D2 = diagonal 2; framing into top flange of "left" girder

Expanding on Figure F3-38, Figure F3-39 presents the full set of unfactored design forces with respect to bridge curvature. Each box-and-whiskers plot (left figure) represents the spectrum of design forces for every bridge with an infinite radius of curvature, a 1500-foot radius, and a 750-foot radius, respectively. This plot is similar to those presented in Figure F3-33. In the right figure, the same data is presented in the form of three line graphs, representing the mean of each data set as well as the 95th and 5th percentile values. The respective percentile lines give an indication where 90% of the data set is populated. The left plot presents x-axis in terms of radius of curvature, and the right plot presents it in terms of curvature (i.e., the inverse of the radius) to clarify the scale.

The three examples provided in Figure F3-38 are also graphed on Figure F3-39 for reference. Note that the diagonal member and lane position illustrated for Figure F3-38 happen to represent governing design conditions, such that there are directly applicable to the results in Figure F3-39. The three sample data points are close to the respective mean values of the data sets.

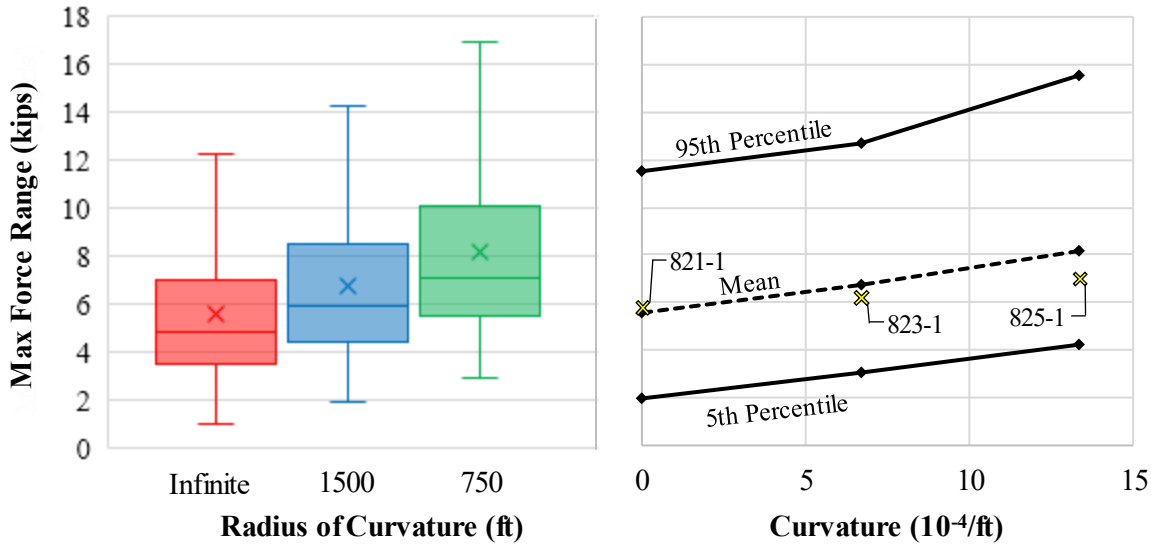

Figure F3-39: Spectrum of unfactored design forces highlighting the impacts of bridge curvature

Figure F3-39, like Figure F3-38, shows a correlation between radius of curvature and fatigue force demands in cross-frames. Whereas Figure F3-38 displays that trend for singular data points, Figure F3-39 displays that same trend over a broader data set that includes a wide variety of bridge geometries. Thus, it can be concluded that Figure F3-39 confirms the trend while expanding the breadth of results.

Figure F3-41 through Figure F3-45 presents the trends observed for all pertinent parameters investigated. Figure F3-41 specifically investigates the impact of parameters related to the overall geometry of the framing plan (i.e., number of spans, span-to-depth ratio, girder spacing, and number of girders). Figure F3-42 investigates parameters related to the support skew (i.e., skew angle, skew type, and skew index). Figure F3-43 investigates parameters related to the bridge curvature (i.e., horizontal curvature and connectivity index). Figure F3-44 investigates parameters related to cross-frames (i.e., spacing, cross-sectional area, layout, and type), and Figure F3-45 investigates parameters related to the concrete deck (i.e., deck thickness, concrete modulus, and relative deck-to-cross-frame stiffness). The parameters studied, except skew index, connectivity index, and deck-to-cross-frame stiffness ratio, represent the independent variables summarized in Table F3-8.

Skew (I_s) and connectivity (I_c) indexes are respective measures of bridge skewness and curvature, as defined in the AASHTO G13.1 Guidelines for Steel Bridge Analysis (2014). These indexes are used to categorize bridge geometries for purposes of recommended analysis practices. Bridges with larger skew and connectivity indexes require more advanced analysis procedures, either improved 2D or 3D techniques. The skew and connectivity indexes are defined by the following expressions:

$$I_s = \frac{w tan\theta}{L_s} \qquad F3.6$$

$$I_c = \frac{15000}{R(n_{cf} + 1)m} \qquad F3.7$$

where: I_s, I_c = skew index and connectivity index, respectively; w = width of bridge, measured between the centerlines of the fascia girders; θ = largest skew angle on bridge, relative to the axis normal to the longitudinal girders; L_s = span length at the bridge centerline; R = minimum radius of the horizontal

curvature; n_{cf} = number of intermediate cross-frames in the span; m = constant; taken as 1 for simple-span bridges and 2 for continuous-span bridges. As the equations show, the skew index increases for shorter, wider spans with larger skew angles. Similarly, the connectivity index increases for tighter curves (i.e., smaller radius of curvature) and fewer cross-frames connecting the girders together.

The relative deck-to-cross-frame stiffness quantifies and compares the stiffness of the two primary transverse load-distribution mechanisms: the concrete deck and the cross-frames (X-type or K-type). Figure F3-40 depicts the deformed shape assumed in the development of this stiffness ratio and the appropriate stiffness expression (Helwig and Yura 2015). Note that the cross-frames are assumed to deform due to uniform rotation of adjacent girders for the sake of simplicity. For a more detailed investigation of realistic load-induced deformed patterns of cross-frames, refer to Chapter F4.

Load Distribution Mechanism	Stiffness (kip-in/rad)
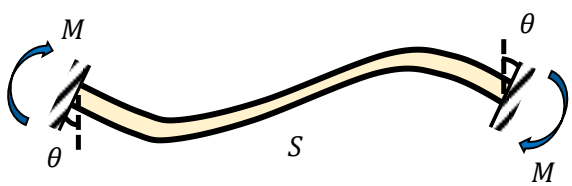	$\beta_{deck} = \frac{M}{\theta} = \frac{6E_c I_{deck}}{S}$
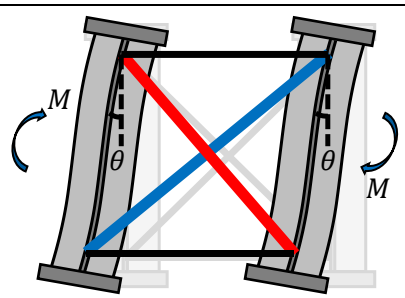	$\beta_{cf,x} = \frac{M}{\theta} = \frac{E_s A_{cf} S^2 {h_b}^2}{{L_d}^3}$
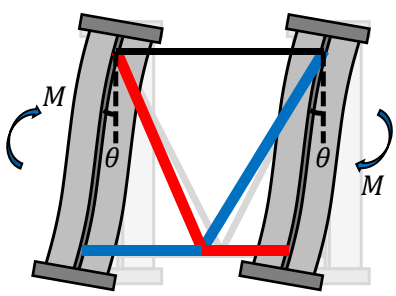	$\beta_{cf,k} = \frac{M}{\theta} = \frac{2E_s A_{cf} S^2 {h_b}^2}{8{L_d}^3 + S^3}$

Figure F3-40: Relative stiffness of transverse load distribution mechanisms

From the equations presented in Figure F3-40, the following expressions illustrate the relative stiffness ratio between the concrete deck and the cross-frame (X-type and K-type):

$$\frac{\beta_{deck}}{\beta_{cf,x}} = \frac{\frac{6E_c I_{deck}}{S}}{\frac{E_s A_{cf} S^2 {h_b}^2}{{L_d}^3}} \qquad F3.8$$

$$\frac{\beta_{deck}}{\beta_{cf,k}} = \frac{\frac{6E_c I_{deck}}{S}}{\frac{2E_s A_{cf} S^2 {h_b}^2}{8{L_d}^3 + S^3}} \qquad F3.9$$

where: $\beta_{deck}, \beta_{cf,x}, \beta_{cf,k}$ = rotational stiffness of concrete deck, X-type cross-frames, and K-type cross-frames, respectively; E_c, E_s = modulus of elasticity of concrete and steel, respectively; S, h_b, L_s = girder spacing, depth of cross-frame, and length of diagonal member, respectively; I_{deck} = moment of inertia of the concrete deck about the longitudinal axis of the bridge, taken as $\frac{1}{12} s_{cf} {t_{deck}}^3$ where the effective width is the typical cross-frame spacing; and A_{cf} = cross-sectional area of the cross-frame member, which is assumed the same for diagonals and struts.

Increasing ratios represent cases for which the concrete deck is significantly stiffer than the cross-frame. For example, a 10-inch concrete deck with 5,000-ksi modulus relative to a 6-foot deep cross-frame with L4x4x3/8 angle sections would result in a large stiffness ratio.

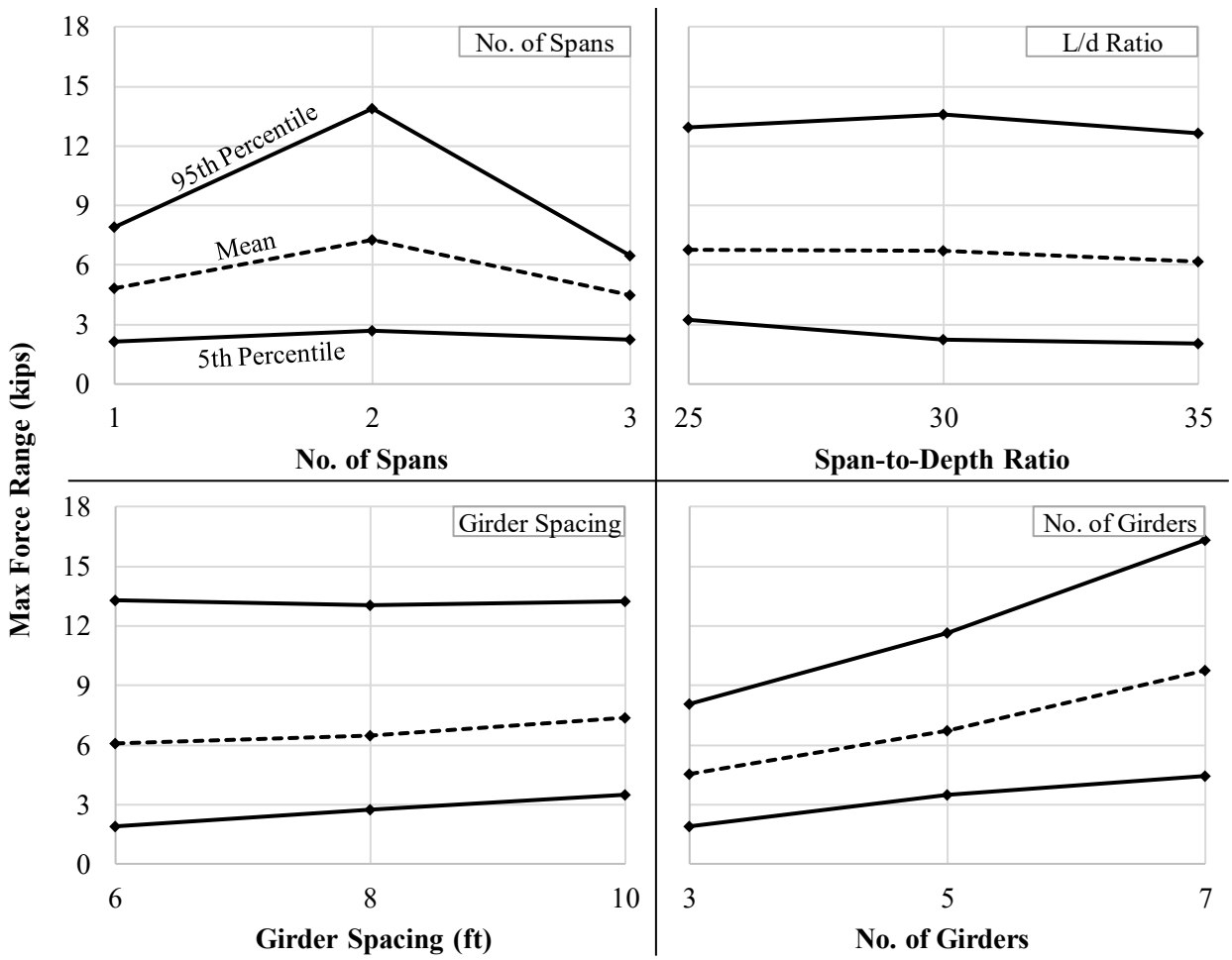

Figure F3-41: Unfactored design force spectra demonstrating the impacts of general bridge geometry and girder layout

From Figure F3-41, the following observations can be made about cross-frame force demands and bridge

parameters related to overall geometry:

- **Number of spans**: In general, two-span continuous bridges result in higher cross-frame forces than simple-span conditions. The mean value of the data sets increased by 50% when introducing a second span. This is attributed to the fact that skewed supports greatly impact cross-frame forces near intermediate supports, as well as the potential amplification in force range due to back span loading (as shown in Figure F3-27). The governing design forces for the three-span bridges is substantially lower than the two-span bridges. However, recall that only straight bridges were considered for the three-span conditions for simplicity and that only cross-frames from the middle span were evaluated. Thus, the apparent reduction in cross-frame force demands are a product of those factors.
- **Span-to-depth ratio**: The mean value of the data set slightly decreases as the span-to-depth ratio increases, particularly for L/d ratios of 35. Thus, a slight negative correlation is observed (i.e., a correlation coefficient of -0.05). However, recall that only straight, two-span bridges were considered for bridges with L/d = 35. Thus, it is anticipated that the results are affected slightly given the impacts of skew angle on force demands.
- **Girder spacing**: A positive correlation is observed between cross-frame force demands and girder spacing (correlation coefficient of +0.16) based on the mean of the data sets, whereas the scatter in the data is fairly consistent. On average, a 1-foot increase in girder spacing results in a 5% increase in the governing design force effect. This is mostly attributed to the floorbeam effects documented in Section F3.2.2 and Figure F3-34. These results are consistent with the results in Figure F3-17.
- **Number of girders**: There is an obvious positive correlation between number of girders (i.e., bridge width) and cross-frame force demands; the observed correlation coefficient is +0.60. A more variable response was also observed as the number of girders increased, as evidenced by the distance between the 95th and 5th percentile lines. On average, increasing the overall width of the bridge results in a 30% increase in the governing force effect. These trends are attributed to the overhang truck loads outlined in Section F3.2.3. Eccentric loading and torque on a straight or curved system are amplified for wider bridges, which in turn amplifies the cross-frame response.

Key statistics and metrics for the results presented in Figure F3-41 are summarized in Table F3-16.

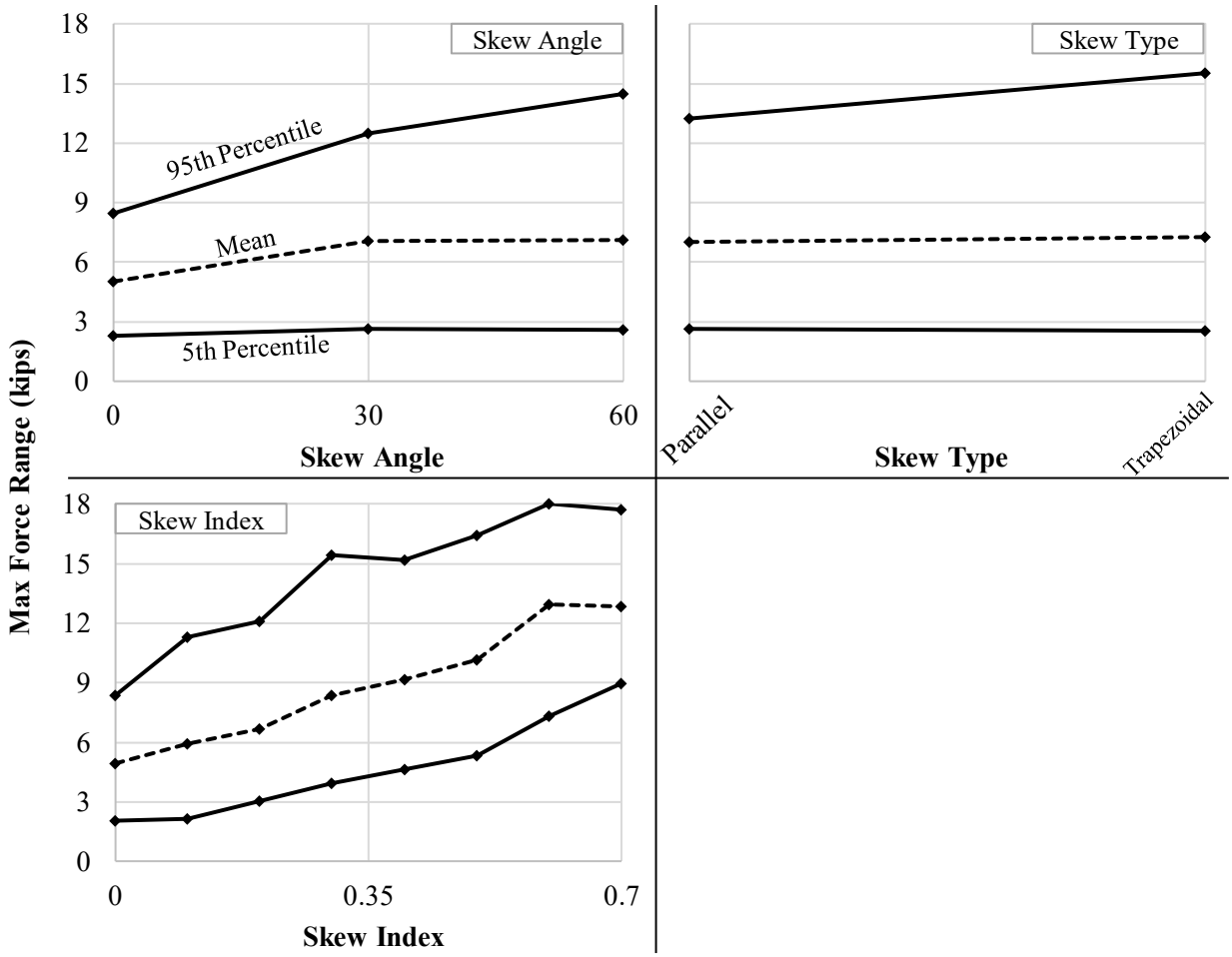

Figure F3-42: Unfactored design force spectra demonstrating the impacts of support skewness

From Figure F3-42, the following observations can be made about cross-frame force demands and bridge parameters related to support skew:

- **Skew angle**: Governing cross-frame force effects were shown to increase as the support skew angle increased, particularly when comparing results for bridges with zero and 30-degree skew angles. A +0.23 correlation coefficient was obtained from the data set, indicating a slight positive correlation. Assuming a linear dependency, an approximate 6% increase in cross-frame force effects can be anticipated for every additional 10 degrees of maximum support skew.
- **Skew type**: A marginal increase in the mean values is observed when evaluating and comparing bridges with parallel and trapezoidal skew layouts. Trapezoidal skew layouts generally result in variable-length girders across the width of the span, which in turn affects the transverse and longitudinal stiffness. This is particularly true for curved systems if the trapezoidal layout increases the length of the fascia girder along the outer radius.
- **Skew index**: As introduced above, skew index is a metric commonly used to describe the overall framing plan of a skewed system. It is evident from the results that skew index substantially impacts the response of cross-frames. A +0.52 correlation coefficient was obtained, indicating a strong, positive relationship between skew index and cross-frame force effects. In simpler terms, a +0.1 increase in skew index generally results in a 25% increase in the critical cross-frame force demand.

Key statistics and metrics for the results presented in Figure F3-42 are also summarized in Table F3-16.

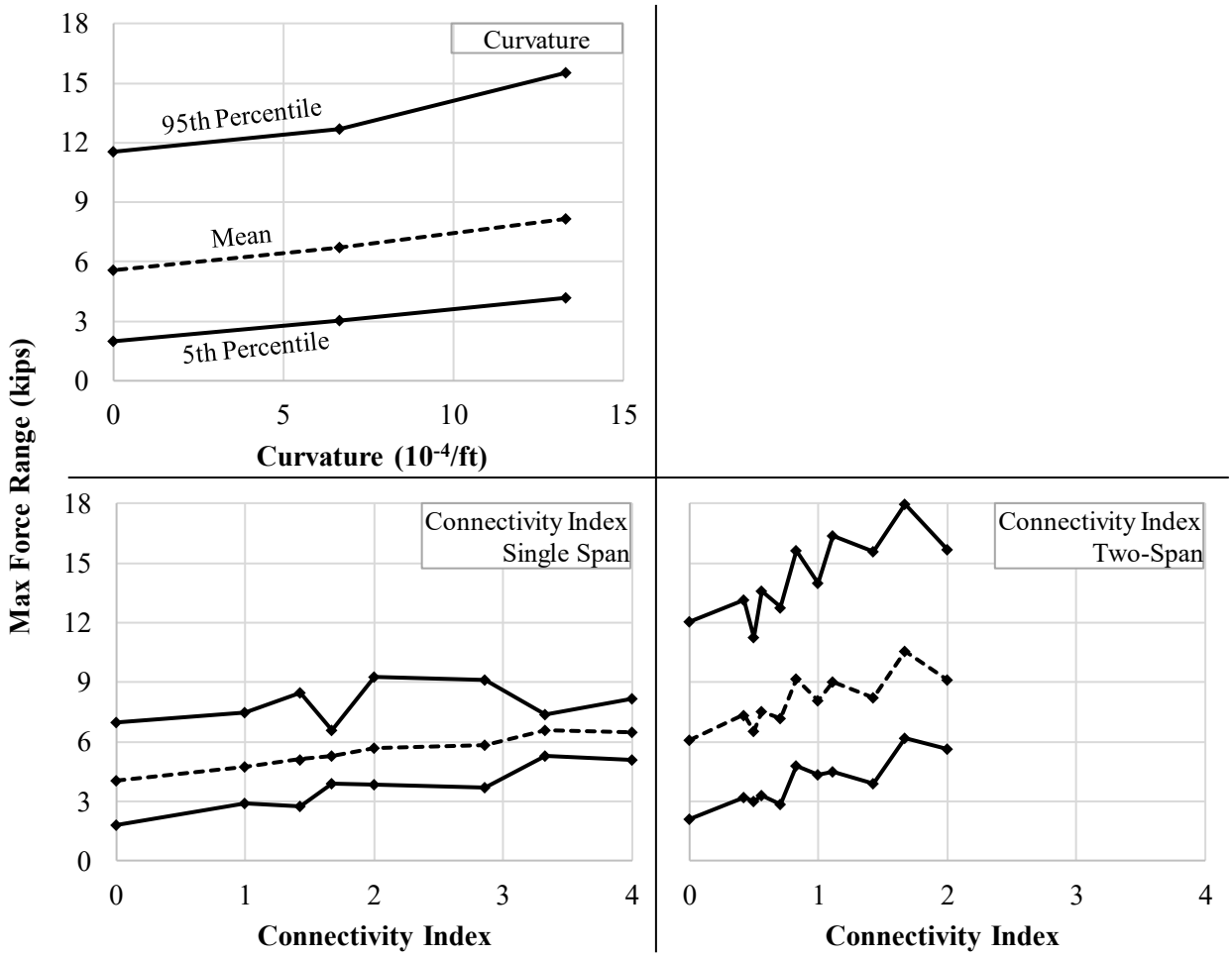

Figure F3-43: Unfactored design force spectra demonstrating the impacts of bridge curvature

From Figure F3-43, the following observations can be made about cross-frame force demands and bridge parameters related to horizontal curvature:

- **Curvature**: A positive correlation is observed between bridge curvature and cross-frame force effects (i.e., correlation coefficient of +0.32). On average, an increase in curvature of 10^{-4}/ft results in an increase of 3% for the governing cross-frame force effect. This trend has been introduced previously with Figure F3-19 and Figure F3-39.
- **Connectivity index**: As introduced above, connectivity index is a metric commonly used to describe the overall geometry of a curved system and its cross-frames. The connectivity index results for single-span and continuous-span bridges are presented independently. In both cases, a positive correlation is observed; a +0.44 and +0.33 correlation coefficient were obtained for the respective conditions. Thus, an increasing connectivity index (i.e., tighter radius and fewer cross-frames) results in higher cross-frame forces on average. The abrupt changes in these figures are attributed to other parameters that describe the bridge geometry.

Key statistics and metrics for the results presented in Figure F3-43 are also summarized in Table F3-16.

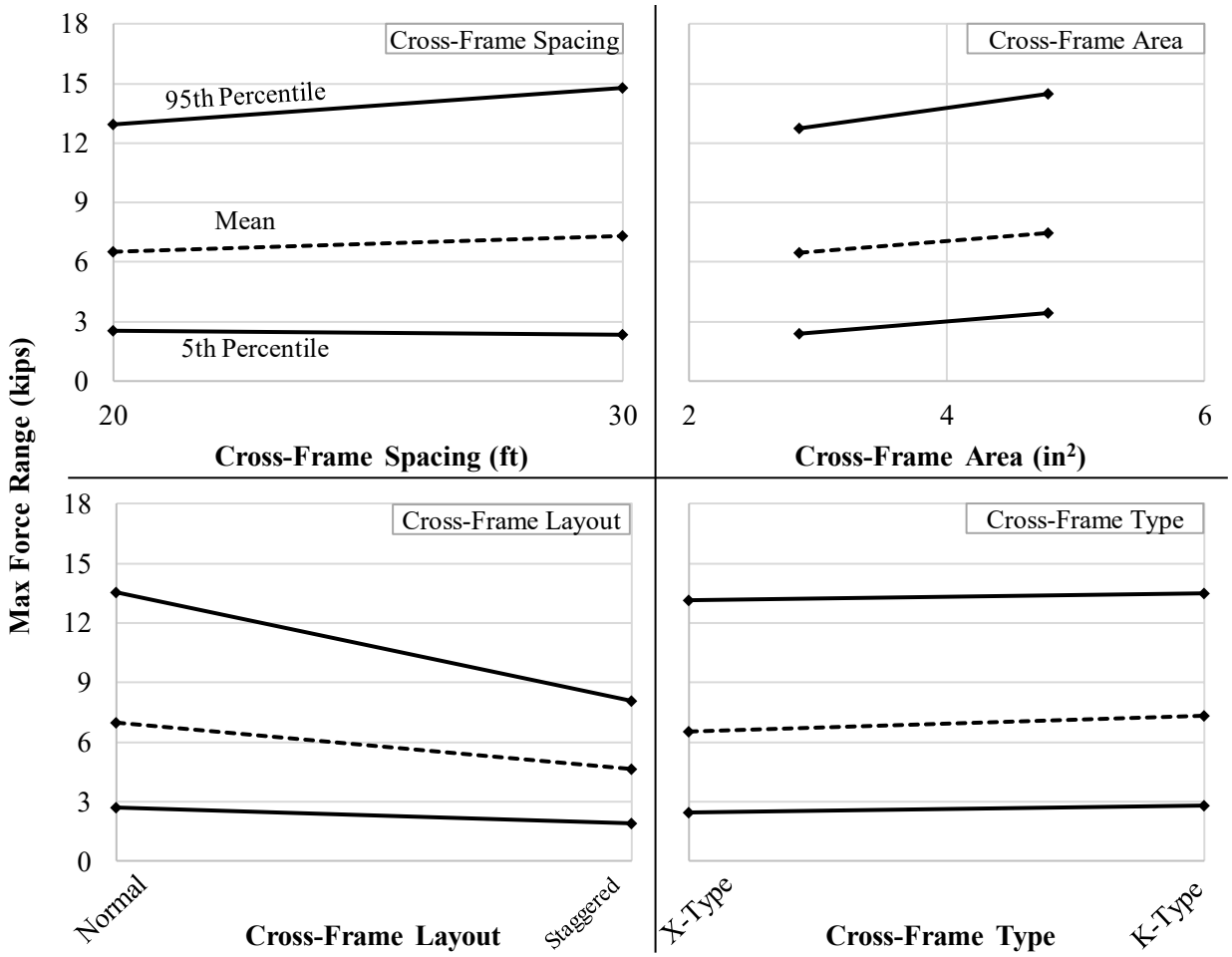

Figure F3-44: Unfactored design force spectra demonstrating the impacts of cross-frame type and layout

From Figure F3-44, the following observations can be made about cross-frame force demands and cross-frame parameters:

- **Cross-frame spacing**: A slight positive correlation is observed between governing cross-frame forces and cross-frame spacing; a +0.09 correlation coefficient was obtained. On average, cross-frame design forces were 13% higher when spaced at 30 feet.
- **Cross-frame area**: Similar to cross-frame spacing, a positive +0.11 correlation coefficient was determined for cross-frame area (i.e., L4x4x3/8 versus L5x5x1/2 single angle sections). In other words, using a larger cross-frame member increases the capacity but also increases the inherent stiffness. An increased stiffness then attracts more force in highly indeterminate systems like steel bridge superstructures (11% increase on average for the angle sections studied). Despite the small axial forces, it should be noted that the smaller L4x4x3/8 often resulted in smaller axial stresses, which is important from a fatigue perspective. This relationship is evaluated in more detail later.
- **Cross-frame layout**: Staggering the cross-frame layout in skewed bridges significantly reduces the governing design force in cross-frames (35% on average). This trend is attributed to the stiffness reduction associated with a discontinuous line of cross-frames. These results are consistent with the sample influence-surface plot presented in Figure F3-20.

- **Cross-frame type**: Despite typically being more flexible than X-type cross-frames (Figure F3-40), K-type cross-frames resulted in higher force demands (12% on average). This trend is attributed to the steeper inclination angle of the diagonal member in K-type frames, which inherently increases the forces throughout the truss system.

Key statistics and metrics for the results presented in Figure F3-44 are also summarized in Table F3-16.

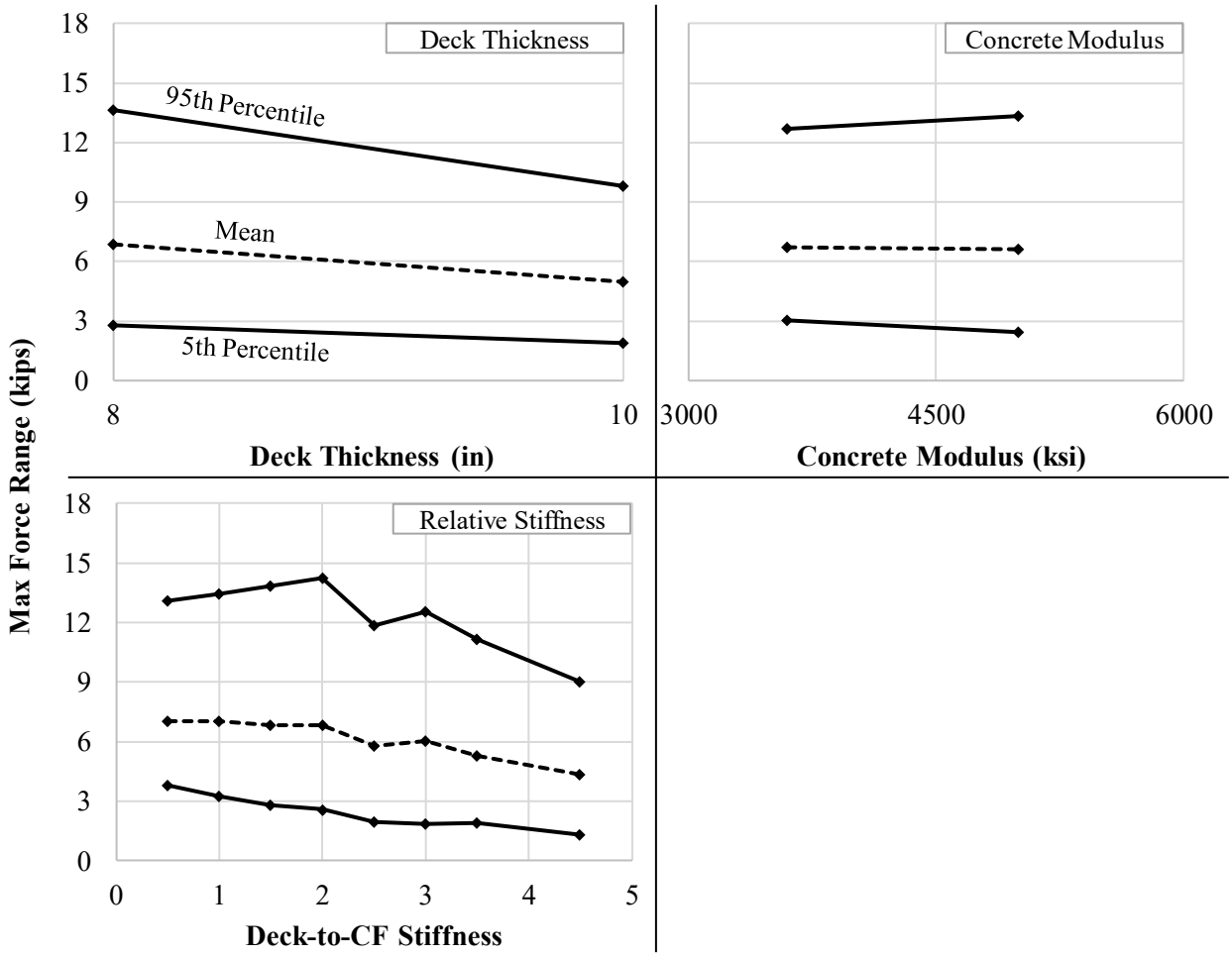

Figure F3-45: Unfactored design force spectra demonstrating the impacts of deck parameters

From Figure F3-45, the following observations can be made about cross-frame force demands and bridge parameters related to the concrete deck:

- **Deck thickness**: Deck thickness and cross-frame force effects are negatively correlated (-0.22 correlation coefficient). On average, a 1-inch increase in deck thickness results in a 14% decrease in force demands. This is attributed to the transverse load distribution effects outlined in Figure F3-40. A reduction in deck thickness often indicates that the cross-frames will attract a higher proportion of the load distribution, which increases member force effects. These results are consistent with the sample influence-surface plot presented in Figure F3-18.
- **Concrete modulus**: The mean values of the data sets show little correlation with the cross-frame force effects. In broader terms, the stiffness of the composite concrete deck had less impact on the load-distribution than its thickness. Given that the flexural stiffness of the deck is linearly proportional to the modulus and proportionally cubed to the deck thickness, the results are

reasonable. The scatter in the 5,000-ksi data set was greater than the 3,600 ksi data set. This trend is attributed to the fact that 3,432 bridge models were evaluated with 5,000-ksi-modulus concrete, and only 672 bridges models with 3,600-ksi-modulus concrete.

- **Deck-to-cross-frame stiffness**: As the stiffness of the concrete deck increases relative to the cross-frame stiffness, the corresponding cross-frame forces decrease. Consequently, a -0.20 correlation coefficient was observed. This trend is consistent with the results and commentary provided for deck thickness.

As documented previously, key statistics and metrics for the preceding results are summarized and tabulated in Table F3-16. The calculated coefficients of correlation are reported, as necessary. General rules of thumb are also included, which provide the reader context on how a particular parameter impacts the force magnitudes in simple terms. For each rule of thumb, a percent change (positive or negative) is tabulated with respect to a unit increase in the respective parameter. For example, an approximate 5 percent increase in the governing design force was observed for every 1-foot increase in girder spacing. It is acknowledged that these general rules of thumb are not mathematically exact but are intended to give a general approximation of the observed behavior and trends.

From Table F3-16, it is evident that the skew and connectivity indexes are good indicators of anticipated force effects in cross-frame members, as is the number of girders across the superstructure width. In simple terms, multi-span skewed and/or horizontally curved bridges with wide bridge decks are most susceptible to increased force demands in cross-frames. This statement is examined in greater detail in the next subsection, for which the bridges are “designed” with respect to assumed traffic conditions and AASHTO fatigue resistance criteria.

Table F3-16: Summary of trends and observations from Figure F3-41 through Figure F3-45

Category	Parameter		Coefficient of Correlation	General Rule of Thumb[a]	
				% Change	Per Unit Increase
Overall geometry	Number of spans[a]		+0.26	+50%	1 span
	Span-to-depth ratio		-0.05	N/A	
	Girder spacing		+0.16	+5%	1 foot
	Number of girders		+0.60	+30%	1 girder
Support skewness	Skew angle		+0.23	+1%	10 degrees
	Skew type		--	+13%[c]	
	Skew index		+0.52	+25%	0.1 units
Horizontal curvature	Curvature		+0.32	+3%	10^{-4}/ft
	Connectivity index	1 Span	+0.44	+15%	1 unit
		2 Spans	+0.33	+30%	1 unit
Cross-frame details	Spacing		+0.09	+13%	10 feet
	Area		+0.11	+8%	1 in^2
	Layout		--	-33%[d]	
	Type		--	+12%[e]	
Deck details	Deck thickness		-0.22	-14%	1 inch
	Concrete modulus		-0.01	N/A	
	Relative stiffness		-0.20	-10%	1 unit

Notes:
[a]General rules of thumb are based on the parameter limits and should not be extrapolated beyond those limits
[b]Correlation corresponds to one- and two-span bridges only
[c]Percent increases corresponds to trapezoidal skews versus parallel skews
[d]Percent decreases corresponds to contiguous versus discontinuous cross-frame layouts
[e]Percent increase corresponds to X-type versus K-type cross-frames

In addition to the primary variables investigated above, the RT also examined the effects of different flange dimensions and the removal of bridge barriers through several "spot check" models. These "spot check" parameters, although important, were deprioritized in the development of the analytical testing matrix due to time constraints. Consequently, only a cursory evaluation of these parameters is provided herein to demonstrate the general impacts; an example is presented in Figure F3-46.

Figure F3-46 presents the influence-line response of two cross-frame members in a horizontally curved bridge with 60-degree skewed supports in a trapezoidal layout, as depicted in the framing plan (note: framing plan is not to scale). The AASHTO fatigue truck traverses the bridge along the outer radius of the curve, where the centerline of the right wheel is at a transverse position 1-foot outboard of the fascia girder centerline. The response of diagonal 1 near the end support (D1; ES) and the bottom strut near the maximum positive dead load moment region (BS; M-I) are depicted. Note that the specified lane position and diagonal member correspond to the governing fatigue conditions on this bridge (i.e., results in the maximum cross-frame force range). Pertinent parameters that describe the geometry and cross-frame layout of the bridge are summarized in Table F3-17 for reference.

For each cross-frame member, three different responses are shown for various combinations of the two "spot check" parameters: (i) 1.5-inch flange thickness with barriers (i.e., the normal assumptions from Table F3-9), (ii) 3-inch flange thickness with barriers, and (iii) 1.5-inch flange thickness without barriers. By doubling the flange thickness from 1.5 inches to 3 inches, the noncomposite (steel only) moment of inertia increases by 90%, and the effective composite girder stiffness increases by 60%. By increasing the stiffness of the superstructure, it is anticipated that girder displacements decrease and thereby reducing cross-frame force demands.

Also recall that the removal of bridge barriers is not studying a typical physical condition, as bridges are seldom constructed without barriers, but rather a typical analysis assumption. It was observed during the validation process of Phase II that the presence of discontinuous bridge barriers impacted the predicted cross-frame force effects in narrow, curved systems. These effects are studied herein for another, representative curved structure. It is anticipated that removing the barrier (i.e., another load-carrying mechanism) in turn increases the force demands on the critical cross-frames.

Table F3-17: Independent variables describing sample bridges in Figure F3-46

Parameter	Value	
	Diagonal (Blue)	**Bottom Strut (Green)**
Model ID	761-2	761-2
CF location[a]	**ES**	**M-I**
CF member[b]	**D1**	**BS**
No. spans	2	2
L/d ratio	30	30
Girder spacing [ft]	8	8
No. girders	5	5
Support skew [deg.]	60, 0, -60	60, 0, -60
Radius of curvature [ft]	1500	1500
Cross-frame spacing [ft]	20	20
Cross-frame layout	Contiguous	Contiguous
Web depth [in]	72	72
Deck thickness [in]	8	8
Cross-frame type	X	X
Cross-frame area [in^2]	2.86	2.86
Concrete modulus [ksi]	5000	5000

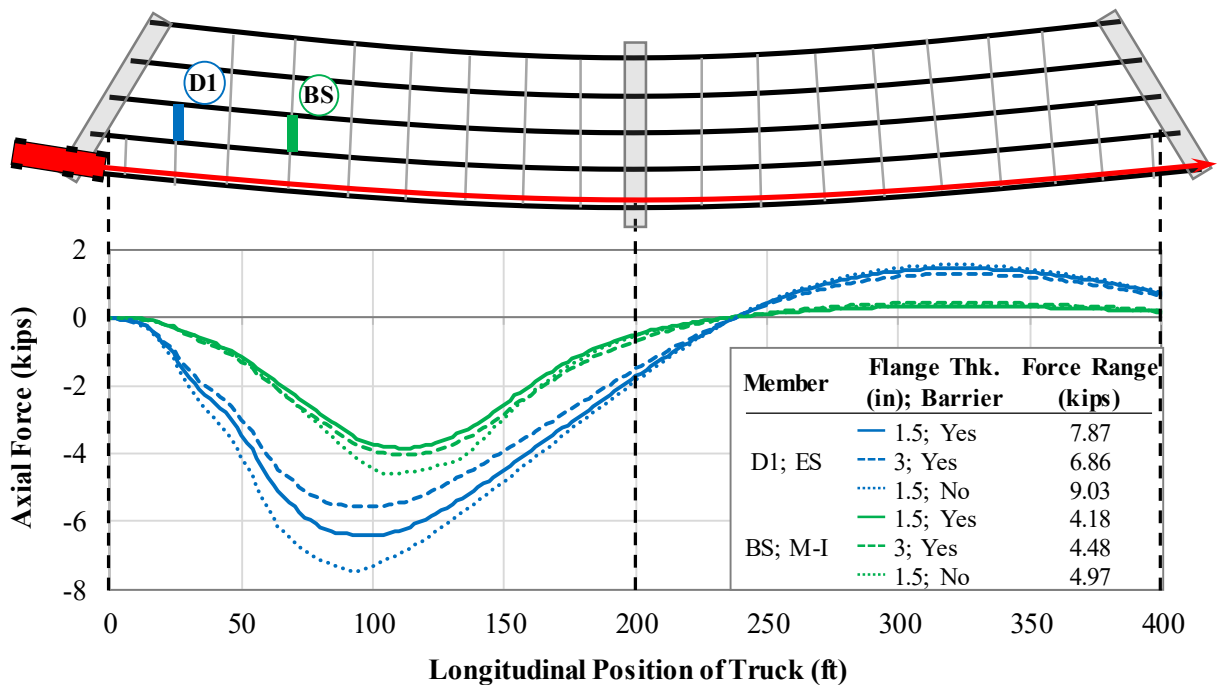

Figure F3-46: Sample influence-line data demonstrating the impacts of girder stiffness and bridge barriers on the axial-force response of cross-frames

From Figure F3-46, the following observations can be made about cross-frame force demands and the "spot check" parameters:

- **Girder stiffness**: For the governing diagonal member near the end support (D1; ES), increasing the composite stiffness of the entire superstructure resulted in a 13% reduction in the unfactored, fatigue design force. For the non-critical bottom strut member, the stiffer system actually resulted in a slight 7% increase in the axial force demand. Given that the governing diagonal 1 member is of more importance, it is evident that a dramatic change in girder stiffness (60% increase) still only results in a moderate change in the cross-frame force demands (13% reduction). Based on this upper-bound condition evaluated, a similar conclusion can be made for nonprismatic sections, which are commonly found in steel I-girder bridges.
- **Presence of barriers**: Removing the discontinuous bridge barriers resulted in a 15% and 19% increase for the governing diagonal and bottom strut members of interest, respectively. The general response (i.e., compression when loaded on the primary span and tension when loaded on the back span) is the same.

As documented in Appendix E, these effects are less impactful for straight and/or wider, more redundant systems. Thus, the bridge presented in Figure F3-46 represents a critical condition for the presence of bridge barriers in the analysis model. In terms of bridge design, it is recommended to include the contributions of the discontinuous bridge barrier for the most accurate results. However, neglecting the barrier, which is commonly done in practice, will result in a conservative estimate of the cross-frame design forces and is therefore acceptable.

F3.2.6 Design Parameters

Now that unfactored, design force ranges have been established for all 4,104 representative bridge structures, the next step is to evaluate factored, design stresses with respect to current AASHTO resistance

criteria (this section) and measured WIM traffic streams (Section F3.3). The following question posed in Section F3.2 can subsequently be answered: *how do the design force ranges (based on current AASHTO fatigue loading) compare to code-specified fatigue resistances*?

Given that AASHTO fatigue design typically works in terms of factored stress ranges, the unfactored, design force ranges presented in Section F3.2.5 were converted based on the procedures outlined in Section F3.2.1 and Table F3-12. Recall that shear lag effects, dynamic load allowance, and appropriate load factors were also assigned.

Once the factored stress ranges are determined, the next step is to estimate the factored fatigue resistance of the critical details. As suggested in AASHTO, both load-induced (6.6.1.2) and distortion-induced (6.6.1.3) fatigue shall be considered in design; however, given that the focus of NCHRP Project 12-113 is load-induced fatigue of cross-frames, only Article 6.6.1.2 is examined. For single-angle members connected to connection plates along one leg with fillet welds, the detail is designated as an E' category per AASHTO Table F6.6.1.2.3-1(7.2). The E' designation corresponds to a threshold stress range, ΔF_{TH}, (constant-amplitude fatigue limit) of 2.6 ksi and a constant used to describe the slope of the S-N curve, A, of 3.9×10^8 ksi^3.

Per Article 6.6.1.2.3, the fatigue detail of interest must then be evaluated for only one limit state, Fatigue I or II. The appropriate limit state is directly related to the projected traffic conditions on the bridge. In accordance with Article 6.6.1.2.3, if the single-lane Average Daily Truck Traffic ($ADTT_{SL}$) is less than or equal to the applicable value (the 75-year $ADTT_{SL}$ equivalent to infinite life) in Table F6.6.1.2.3-2, then the member may be designed for finite-life (Fatigue II). If the projected $ADTT_{SL}$ exceeds the tabulated value, then the member shall be designed for infinite-life (Fatigue I). For both cases, a factored resistance is computed in terms of a stress range magnitude. However, for Fatigue II, that factored fatigue resistance is inherently a function of both stress magnitude <u>and</u> frequency of load occurrence.

The 4,104 bridges considered in this study, however, are not representative of any particular location or traffic conditions. As such, the RT elected to investigate different representative traffic conditions to bound the problem. In other words, the RT effectively constructed these "fictional" bridges along different highway corridors in Texas, both in rural areas with low traffic volumes and congested, urban areas with high traffic volumes. Rather than utilize measured WIM data (Section F3.3) at this stage, the RT utilized ADT maps readily available on the TxDOT website (Texas Department of Transportation 2020), as well as simplifying assumptions recommended by AASHTO Article C3.6.1.4.2. Two extreme traffic conditions are studied for purposes of this analysis, and each is summarized in Table F3-18 below. A state highway system in rural Llano, TX and a heavily trafficked corridor in Houston, TX are used as the extreme conditions, but the general process is identical for other highway systems in other states.

The table summarizes all pertinent traffic parameters, including the average daily traffic (*ADT*), the class of highway (in accordance with AASHTO Table FC3.6.1.4.2-1), assumed number of directions, and assumed number of lanes. As documented above, the ADT was determined based on maps available on the TxDOT website. The class of highway (i.e., other rural and urban interstate) were based on simple observations of the roadways. The number of directions was assumed based the current traffic conditions of nearby bridges in Llano and Houston, respectively. Rural bridges in locations such as Llano, TX commonly serve two direction of traffic, whereas bridges operating along major highway systems often serve for only one direction of traffic (i.e., one, independent bridge per direction). The number of design lanes is variable and depends on the available roadway width of each bridge in the 4,104-model matrix. To simplify the discussions, design lanes were developed in accordance with Article 3.6.1.1.1.

The balance of the table summarizes all constants and factors used to determine the critical $ADTT_{SL}$ value. Again, the RT elected to utilize the simplifying assumptions provided in the commentary for cases in which data from traffic engineers is unavailable for these sites. By adopting this approach, the conservative design procedures in this subsection can be compared directly to the measured WIM data in Section F3.3. Table

F3-18 logically organizes this information in order of the design process. First, the bidirectional factor (percentage of traffic in critical direction), fraction of trucks factor (percentage of trucks among the ADT values), and lane factor (percentage of trucks in critical lane) are established.

Next, the governing $ADTT_{SL}$ value for each extreme condition (i.e., low volume and high volume conditions) are derived and compared to the threshold value in Table F6.6.1.2.3-2. Note that the total number of projected stress cycle ranges over the assumed 75-year service life, N, is assumed based on n = 1 (i.e., one stress cycle per truck passage) from the findings of Section F3.2.4. Also note that for the majority of E' details, Fatigue II will govern as shown in these examples.

Finally, AASHTO Eqs. 6.6.1.2.5-2 and 6.6.1.2.5-3 are implemented to determine the nominal fatigue resistance for cross-frame in each of these two traffic conditions. Note the resistance factors are taken as unity for the fatigue limit state in AASHTO LRFD. For the low-volume case, the factored fatigue resistance is equivalent to 4.27 ksi; for the high-volume case, the resistance is 1.68 ksi. The Houston, TX traffic condition results in a lower resistance to account for the significantly higher truck traffic volume anticipated.

Table F3-18: Sample demonstration of factored fatigue resistances

Parameter	Value	
	Low Volume	**High Volume**
Location	Llano, TX	Houston, TX
Highway system	TX-152	I-10 at I-610 Loop
Average daily traffic (*ADT*)	2,216	343,211
Class of highway	Other Rural	Urban Interstate
Assumed number of directions	2	1
Assumed number of lanes	2[a]	2[a]
Assumed number of lanes per direction	1	2
Bidirectional factor (C3.6.1.4.2)	0.55	1.0
Fraction of trucks (Table FC3.6.1.4.2-1)	0.15	0.15
Lane factor, *p* (Table F3.6.1.4.2-1)	1	1
Single-lane average daily traffic (ADT_{SL})[b]	1,218	20,000
Single-lane average daily truck traffic ($ADTT_{SL}$)[c]	182	3,000
Table F6.6.1.2.3-2 threshold	8,485	8,485
Governing fatigue category (6.6.1.2.3)	Fatigue II	Fatigue II
Projected number of stress range cycles over 75-year life (Eq. 6.6.1.2.5-3)	4.98×10^6	82.1×10^6
Factored fatigue resistance (ΔF_n) (Eq. 6.6.1.2.5-2)	4.27 ksi	1.68 ksi

Notes:
[a]The number of lanes is variable and depends on the available bridge width; an example (2 lanes) is shown in this table for clarity
[b]The single-lane ADT is equivalent to the product of the *ADT*, bidirectional factor, and lane factor; per AASHTO Article C3.6.1.4.2, *ADT* is physically limited to about 20,000 vehicles per lane per day under normal conditions
[c]The single-lane *ADTT* is equivalent to the product of ADT_{SL} and the fraction of truck factor

The process demonstrated in Table F3-18 for two-lane bridges was then repeated for bridges of all roadway widths (i.e., different number of design lanes across the width). The factored resistances are then compared to the factored design stresses in accordance with AASHTO Article 6.6.1.2.1. The results hereafter outline that procedure. Figure F3-47 presents the factored Fatigue II stress ranges that govern the design of all 4,104 representative bridges in the form of a histogram. The stress ranges were categorized in 0.1-ksi bins, and the counts were summed. These stress range values were determined in accordance with current AASHTO fatigue loading criteria and load factors, as demonstrated in the preceding subsections.

For reference, the factored designs stresses for the three instrumented bridges (based on analytical procedures outlined in Appendix E), as well as the measured effective stress ranges are also included. Recall that the Fatigue II load effects derived from AASHTO LRFD are synonymous with the effective stress range of the truck population; as such, a direct comparison can be made between the two entities. By comparing analytical and experimental results of instrumented Bridges 1, 2, and 3, a few key observations are established.

First, the governing design stress ranges for Bridges 1 and 2 are close to the mean response (2.35 ksi), and the stress range for Bridge 3 is in the lower tail of the spectrum. Second and more importantly, it is evident that the analytical results generally exceed the measured results by a considerable margin. This is a preliminary indication that the AASHTO fatigue model may be conservative when compared to real loading conditions experienced by the instrumented bridges in the context of cross-frame behavior. This assertion is verified for a wider range of bridges herein; but note that the physical evidence from measured data, rather than just relying entirely on analytical data, strengthens this observation.

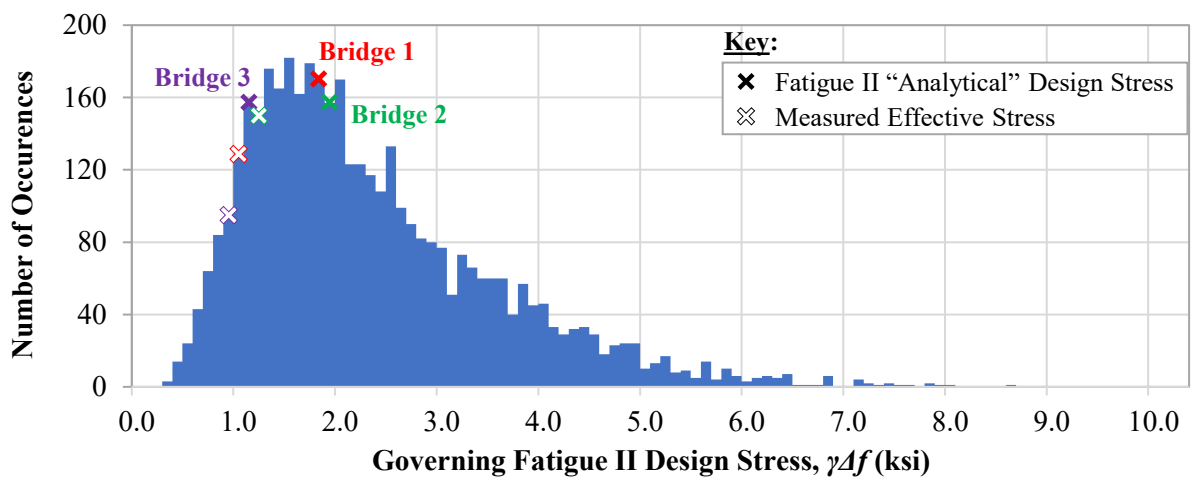

Figure F3-47: Governing fatigue stress ranges for all bridges in Fatigue Loading Study

Figure F3-48 illustrates the governing demand-to-capacity ratio (i.e., $\Delta F_n / \gamma\Delta f$) with respect to the Fatigue II limit state. The factored stress ranges from Figure F3-47 are compared to the factored resistances computed based on the sample procedure in Table F3-18. Demand-to-capacity (D/C) ratios below unity indicate designs in conformance with AASHTO LRFD, whereas ratios exceeding unity represent designs in violation of AASHTO LRFD. As outlined previously, it is assumed that the design of all intermediate cross-frame members is governed by the critical, maximum case. Thus, any bridge exceeding a D/C of 1.0 means that one (i.e., the critical cross-frame member) or more members are inadequate in terms of Fatigue II design criteria.

Figure F3-48 presents D/C histograms for the two extreme traffic conditions: rural Ranch Road 152 in Llano, TX and urban I-10 in Houston, TX. For each individual histogram, the factored demands are

identical; however, the factored capacities differ based on the large disparities in projected truck traffic volumes.

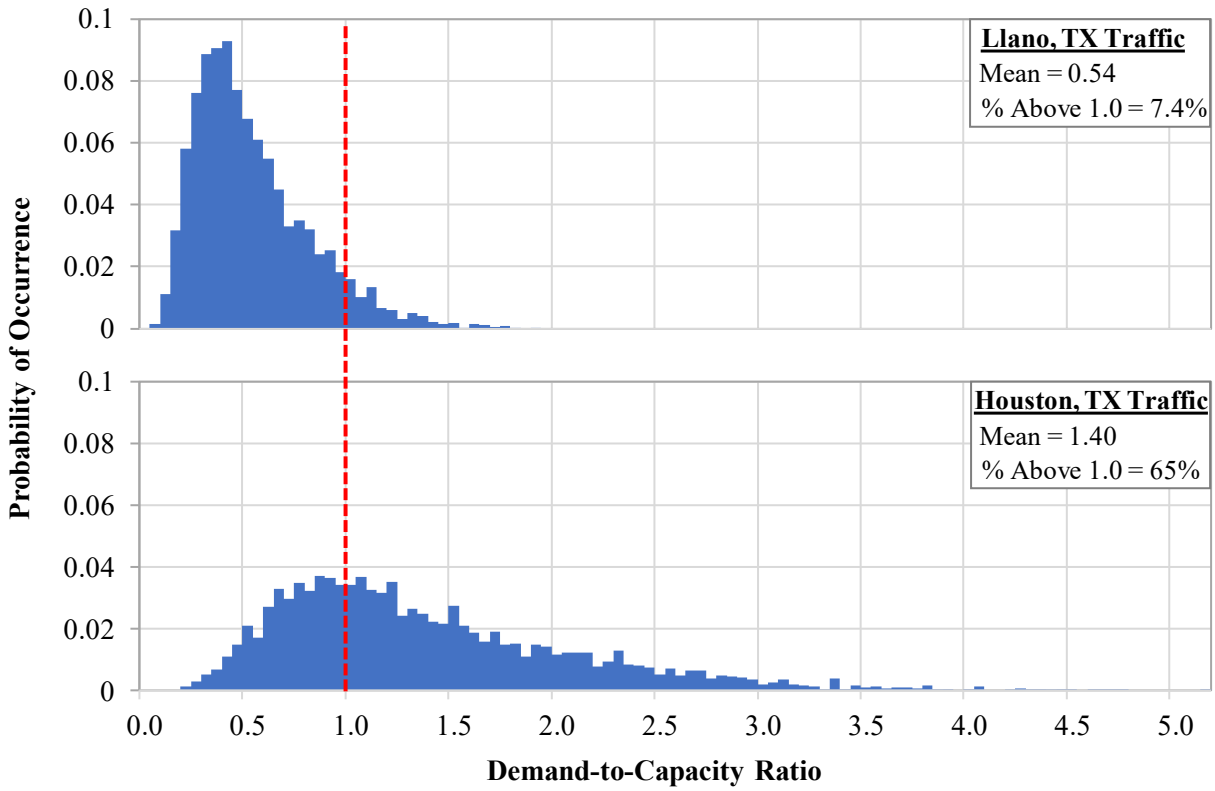

Figure F3-48: Fatigue II demand-to-capacity ratios for two extreme traffic conditions

From Figure F3-48, it is apparent that the projected traffic conditions have a significant impact on the results. For the low-volume conditions, the results indicate that the majority of the 4,104 bridges are conservative in terms of cross-frame fatigue design. In fact, the average D/C ratio was 0.54, which implies substantial reserve capacity for the majority of bridges. Only 7.4% of the models exceeded a D/C ratio of unity.

In contrast, the results indicate a more severe trend for the high-volume conditions. On average, the D/C ratios exceeded 1.0 (mean of 1.40), and 65% of the bridges resulted in an unconservative design. If these bridges were to be implemented for a real construction project, modifications to the cross-frame properties (e.g. increase cross-sectional area) or layout (e.g. use discontinuous cross-frame layout in heavily skewed bridges) would likely be required to bring the design in conformance with AASHTO LRFD. To expand further on Figure F3-48, Figure F3-49 highlights the differences between straight and curved bridges, as well as bridges with normal and skewed supports. The full histogram related to the Houston, TX traffic in Figure F3-48 is broken down into four bridge types: straight bridge with normal supports, straight bridge with skewed supports, curved bridge with normal supports, and curved bridge with skewed supports. Each subset histogram is overlaid on the full histogram to demonstrate how bridge curvature and support skewness affects the D/C ratios.

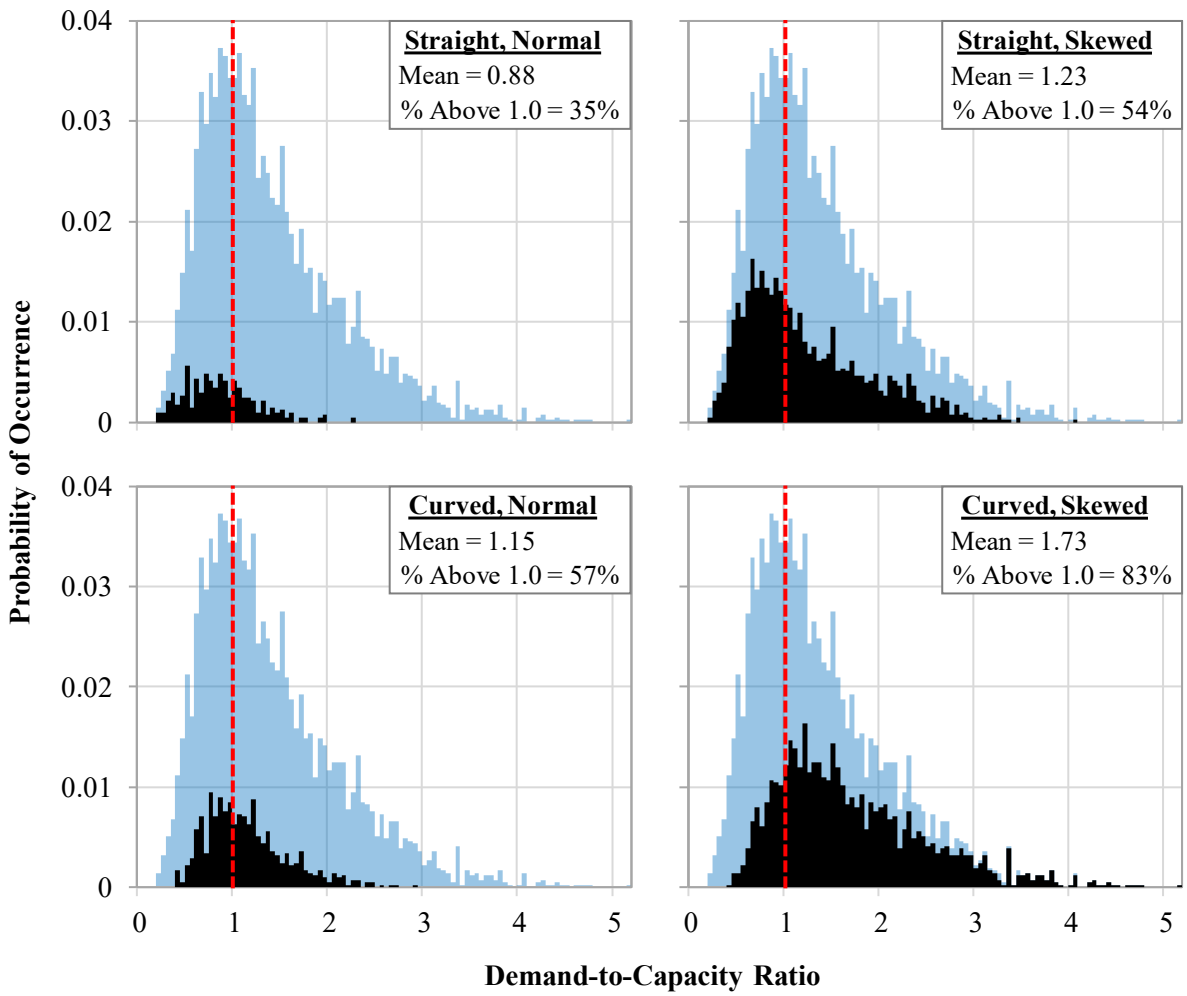

Figure F3-49: Fatigue II demand-to-capacity ratios for various bridge types (Houston I-10 traffic)

The average D/C ratio increases when skewed supports and/or horizontal curvature are introduced. For instance, the mean D/C for straight, normal bridges is 0.88; that value increases to 1.23 for straight, skewed bridges and 1.15 for curved, normal bridges. A similar trend is observed for the percent unconservative metric.

In broader terms, the results from Figure F3-48 and Figure F3-49 suggest the following:

- For roadways with low truck traffic, load-induced fatigue does not appear to be a major concern for the 4,104-model bridge sample (which represents the most common bridge conditions in the US) according to AASHTO 9th Edition criteria.
- For bridges serving heavy truck traffic, current AASHTO criteria indicate a potential load-induced fatigue problem.

Development of appropriate design criteria for cross-frames, like other structural elements, requires achieving acceptable structural safety but must also consider economy. As learned from the industry survey documented in Appendix D, load-induced fatigue problems in cross-frame members have been seldom found by bridge owners. Of the 57 survey respondents, 15 indicated that they have experienced issues related to load-induced fatigue cracking, whereas 39 indicated no such issues. Of the 15 respondents

reporting past load-induced fatigue cracking, many described more distortional-induced cracks than load-induced.

Thus, experience has shown that cross-frames are largely satisfying structural safety requirements in terms of load induced fatigue. A question of interest then is whether further economies are possible in cross-frame design, while still providing adequate structural safety? The absence of observed load induced fatigue failures does not necessarily imply the current AASHTO LRFD design criteria are overly conservative and wasteful from a cost perspective. Nonetheless, with a goal of developing improved design criteria for cross-frames, the question of whether current AASHTO LRFD design criteria for load induced fatigue of cross-frames are too conservative is important to examine. The analysis presented earlier in this section provides at least some indication that AASHTO LRFD may be too conservative and merits closer scrutiny.

When considering whether AASHTO LRFD may be too conservative for load induced fatigue design of cross-frames, the following three factors may be considered:

1. **The AASHTO fatigue resistance model is potentially too conservative (ΔF_n is too low)**. The resistance model primarily consists of detail category E′ and its associated constants (Table F6.6.1.2.3-1).
2. **3D FEA models perhaps consistently produce overly conservative force predictions**. Among many modeling assumptions, the primary focus is the stiffness modification factors (R-factors) for cross-frames in 3D models (Article C4.6.3.3.4).
3. **The AASHTO fatigue loading model is potentially too conservative ($\gamma\Delta f$ is too high)**. The loading model comprehensively consists of the following: fatigue truck (Article 3.6.1.4.1; Figure F3-26), truck positioning (Article 3.6.1.4.3; Article C6.6.1.2.1), dynamic load allowance (Article 3.6.2), load factors (Article 3.4.1), and shear lag factor (Table F6.6.1.2.3-1, 7.2).

Note that, by simply listing it, the RT is not advocating that changes to the design specifications are necessary for all items above. The list is intended to be comprehensive in nature and identify all possible sources. For instance, The RT is not suggesting that welded cross-frame connections be reclassified as a higher fatigue category. As noted in the main body of the report, fatigue resistance is beyond the scope of the project and is not discussed further.

Instead, the RT narrowed its efforts to examining the modeling approach (stiffness modification and simplified analysis techniques) and the fatigue loading model in Chapter F4, Chapter F5, and Section F3.3, respectively. Chapter F4 studies the accuracy of the current R-factor approach (0.65AE per AASHTO Article C4.6.3.3.4) and the assumed approach in the Fatigue Loading Study (0.60AE). Chapter F5 explores the limitations of simplified 2D modeling approaches, and Section F3.3 examines the loading model (primarily the fatigue truck, truck positioning, and load factors) with respect to WIM data.

F3.3 Fatigue Study - Weigh-In-Motion Records

As introduced at the beginning of Chapter F3, the Fatigue Loading Study investigates the appropriate fatigue stress ranges for the evaluation of cross-frames in right, skewed, and curved bridges. In total, 4,104 unique bridge geometries were studied, including various girder and cross-frame layouts, girder cross-sections, and cross-frame details. The 4,104-model data set is intended to represent a wide variety of steel I-girder bridges currently in service in the US. Previous sections discussed the use of the AASHTO design load (i.e., the fatigue design truck) and the design implications related to cross-frame force effects using this model data set. This section discusses the results of study for which the RT used measured WIM data obtained from sites throughout the US and applied this traffic data to a subset of the model data set. In other words, critical cross-frames in a representative set of bridge systems are evaluated for a variety of realistic traffic conditions, expanding on the studies in Section F3.2 which focus solely on current design procedures.

This study of WIM data provides an indication on the appropriateness of the current AASHTO LRFD Fatigue I and II load factors for the design of cross-frames.These load factors were developed primarily for girders, and not for cross-frames. Thus, a question under consideration is whether the AASHTO LRFD load factors of 1.75 for Fatigue I (infinite life) and 0.80 for Fatigue II (finite life) appear to be reasonable for cross-frames. An additional issue of interest in this study of WIM data is whether multiple presence should be considered in the fatigue evaluation of cross-frames.

The following subsections discuss various tasks the RT performed related to the measured WIM records. Section F3.3.1 summarizes the WIM data set and record filtering. Section F3.3.2 discusses the application of WIM traffic streams to a subset of 20 models obtained from the 4,104 model data set. Section F3.3.3 discusses the application of this project's WIM traffic streams to a bridge configuration studied in the SHRP 2 R19B study in order to compare this project's WIM data and analytical methods (i.e., computing scripts, filtering, rainflow counting techniques, etc.) to girder force effects published in the R19B project. Section F3.3.4 outlines a study in order to consider the effects of multiple presence on cross-frame force effects using multi-lane WIM records. Section F3.3.5 summarizes a stochastic simulation using the Monte Carlo technique in order to study the effects of using the statistical parameters developed in Section F3.3.2, along with published resistance parameters (Modjeski and Masters 2015), in the context of structural reliability. Finally, Section F3.3.6 revisits AASHTO fatigue design given the load factors developed in this study.

F3.3.1 WIM Records and Record Filtering

The RT obtained high-resolution WIM records from the Federal Highway Administration (FHWA) for 16 specific pavement study (SPS) sites across the US. The records are summarized in Table F3-19, and generally include a full year worth of measurements (collected in 2014). The record timestamps are reported with 0.01-second measurement resolution. Table F3-19 includes the SPS identification and site ID, the WIM sensor type, the number of days missing from the record (if any), and number of lanes recorded. Note that the SPS identification refers to a special materials focus of the Long-Term Pavement Performance program (Al-Qadi et al. 2016). For example, SPS-1 is a strategic study of structural factors for flexible pavements, and SPS-5 is a rehabilitation of asphalt concrete pavements. In total, the unfiltered records include approximately 46 million vehicle records from 16 sites over 15 states. Since some sites have multiple lanes, the records include 23 one-lane records.

Table F3-19: SPS sites from which weigh-in-motion data was obtained by FHWA

State	Road & Site ID	SPS ID	Sensor Type	Number of Days Missing[a]	Number of Lanes Recorded
AR	I-30, 050200	SPS-1	Bending plate	--	1
AZ	I-10, 040200	SPS-2	Bending plate	23	1
CA	SR-99, 060200	SPS-1	Bending plate	2	1
CO	I-76, 080200	SPS-2	Bending plate	--	1
IL	I-57, 170600	SPS-1	Bending plate	8	1
IN	US-31, 180600	SPS-1	Quartz	--	4
KS	I-70, 200200	SPS-1	Bending plate	--	1
LA	US-171, 220100	SPS-1	Quartz	--	1
MD	US-15, 240500	SPS-1	Bending plate	14	1
MN	US-2, 270500	SPS-035	Quartz		1
NM	I-25, 350100	SPS-1	Quartz	4	1
NM	I-10, 350500	SPS-2	Quartz	6	1
PA	I-80, 420600	SPS-158	Quartz	90	1
TN	I-40, 470600	SPS-1	Quartz	97	4
VA	US-29, 510100	SPS-1	Bending plate	--	2
WI	SH-29, 550100	SPS-1	Bending plate	--	1

[a]Data was collected at all sites from January 2014 through December 2014; value indicates the number of days missing from the full-year data set

Consistent with SHRP 2 Project R19B (Modjeski and Masters 2015), the RT applied a set of filtering techniques to this data set in an attempt to eliminate questionable records (i.e., unrealistic geometry or erroneous data) and apparent permit vehicles or illegally loaded vehicles. Many of these filters were based on NCHRP 12-76 (Sivakumar et al. 2011). Accordingly, the following filtering criteria were used:

- Records were eliminated when axle weight were less than 2 kips or greater than 70 kips (based on NCHRP 12-76);
- Records were eliminated when first axle spacing was less than 5 feet (based on NCHRP 12-76);
- Records were eliminated when any axle spacing was less than 3.4 feet (based on NCHRP 12-76);
- Records were eliminated when the gross vehicle weight (GVW) varies from the sum of the axle weights by more than 10 percent (based on NCHRP 12-76);
- Records were eliminated when the length of the truck varies from the sum of the spacing between axles by more than 1 foot (based on NCHRP 12-76);
- Records were eliminated when the steering axle is less than 6 kips (based on NCHRP 12-76);
- Records were eliminated when the sum of the axle spacing lengths is less than 7 feet (based on Pelphrey et al. (2008));
- Records were eliminated when the vehicle speed was less than 10 mph or greater than 100 mph (based on NCHRP 12-76);

- Records were eliminated when the GVW was greater than 50 kips with total number of axles less than three;
- Records were eliminated when the steering axle weights were more than 35 kips; and
- Records were eliminated when the individual axle weights were more than 45 kips.

After the above filtering was applied, the records still contained lightweight vehicle records (i.e., GVWs less than 20 kips). These entries are traditionally eliminated in fatigue studies, since previous research has indicated that light vehicles have negligible effects on the accumulated fatigue damage in a member or detail (Connor and Fisher 2006). To be consistent with well-established previous studies, these lightweight traffic records were removed to form a final set of WIM records to be used for the fatigue study herein (White (2020) conducted multiple sensitivity studies, in which these lightweight were retained in order to study the impact on force effects). In summary, the final set of records included the following filtering lightweight vehicle criteria:

- Records were eliminated when the assigned FHWA vehicle classification was less than Class 3 or greater than Class 14 (i.e., to filter out passenger cars, motorcycles, etc.);
- Records were eliminated when the GVW was less than 20 kips.

Table F3-20 provides a summary of WIM records prior to any filtering, as well as total number of vehicle records and average daily traffic counts for each SPS site before and after removing lightweight vehicles.

The records used for the fatigue study contain approximately 11 million truck measurements after all appropriate filters. Figure F3-50 shows the cumulative distribution functions (CDFs) of GVWs captured by the WIM sensors for all SPS sites. The GVWs are shown as a normal probability plot, in which the horizontal axis is GVW (in kips), and the vertical axis is the standard normal variable (i.e., axis values are "Z-values" indicating the number of standard deviations the GVW value is from the mean). A normal probability plot can be used to determine how well the data represents a normal distribution; nonlinear data sets indicate departures from normality. As clearly shown, the GVW populations are not normally distributed.

As also noted in the SHRP 2 Project R19B, the irregularity of the CDFs is a result of different types of vehicles within the WIM traffic streams (e.g., variety of vehicle lengths, payload, etc.). The mean GVWs for the 11 million truck records range from 40 to 62 kips, with a max GVW of 220 kips. As shown in Figure F3-51, the shape of the CDFs appears to be generally consistent with the CDFs of WIM data used in the SHRP 2 R19B project, which are recreated by the RT with the same filters described above. Thus, the 2014 data obtained from FHWA was deemed acceptable given its good agreement with the SHRP 2 R19B data.

Table F3-20: SPS sites from which weigh-in-motion data was obtained by FHWA

State	Initial Number of Records (Before Filtering)	Records Including Light Vehicles		Records After Removing Light Vehicles	
		Total Number of Records	Lane ADT	Total Number of Truck Records	Lane ADTT
AR	3,529,952	3,414,934	9,356	1,704,481	4,670
AZ	2,711,532	2,626,954	7,704	1,227,567	3,600
CA	4,873,640	4,779,602	13,167	1,380,075	3,802
CO	1,675,744	1,645,722	4,509	352,198	965
IL	2,807,183	2,707,469	7,584	798,935	2,238
IN (Lane 1)	1,886,428	1,865,543	5,111	370,241	1,014
IN (Lane 2)	500,621	471,291	1,302	21,340	59
IN (Lane 3)	1,843,395	1,802,053	4,937	360,458	988
IN (Lane 4)	548,382	524,003	1,460	20,158	56
KS	2,312,975	2,262,526	6,199	436,913	1,197
LA	1,734,519	1,722,311	4,719	76,547	210
MD	3,040,831	3,005,933	8,564	108,881	310
MN	864,803	857,522	2,349	52,757	145
NM1	1,018,250	1,005,887	2,786	147,077	407
NM2	1,675,090	1,609,947	4,485	892,295	2,486
PA	2,292,235	2,251,316	8,187	873,903	3,178
TN (Lane 1)	2,792,715	2,120,750	7,913	550,858	2,055
TN (Lane 2)	1,945,926	1,842,295	6,874	118,000	440
TN (Lane 3)	2,042,591	1,942,114	7,247	191,330	714
TN (Lane 4)	2,757,569	2,690,197	10,038	1,182,136	4,411
VA (Lane 1)	1,462,016	1,445,614	3,961	224,928	616
VA (Lane 2)	438,126	430,438	1,179	19,300	53
WI	1,468,798	1,358,660	5,435	120,079	480
Total	**46,223,321**	**44,383,081**		**11,230,457**	

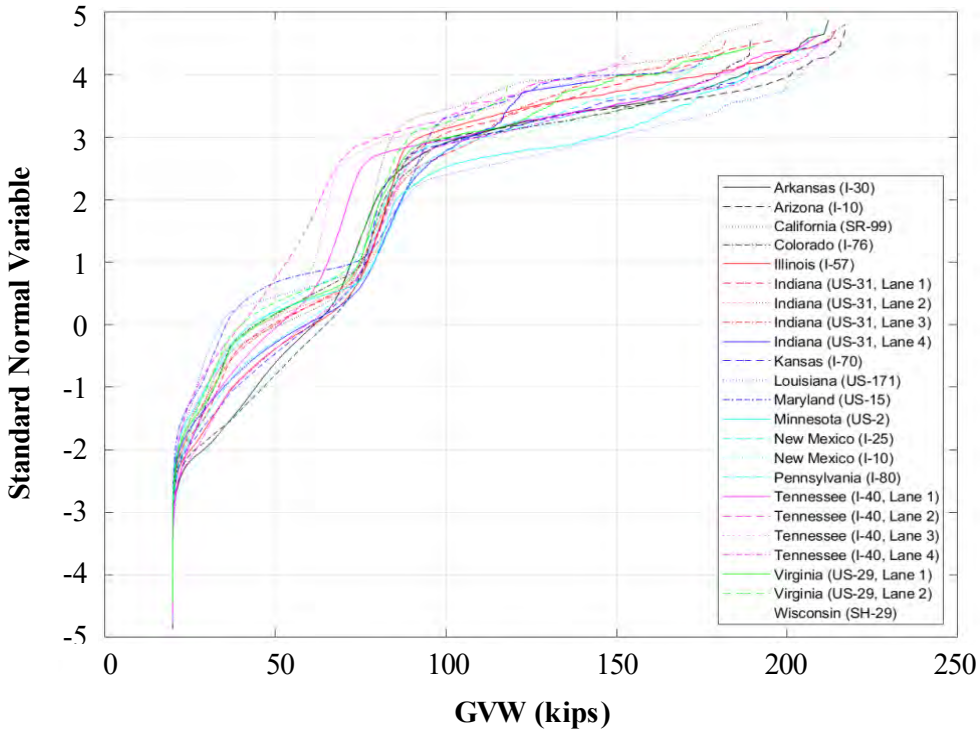

Figure F3-50: CDF of GVWs from FHWA 2014 Data (excluding light vehicles)

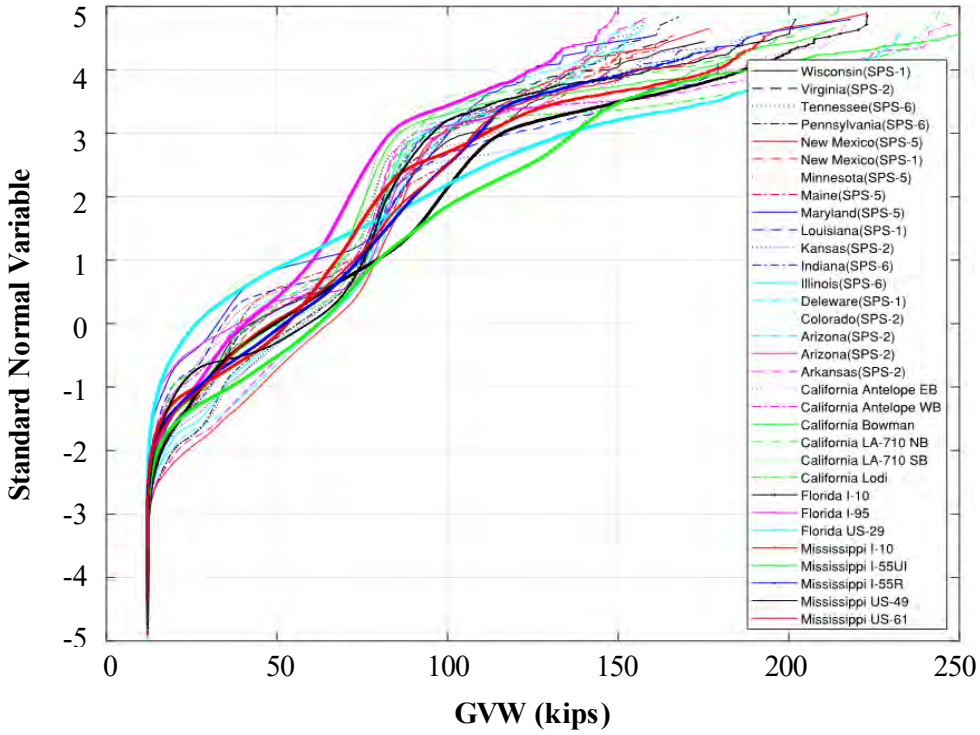

Figure F3-51: CDF of GVWs from SHRP 2 R19B WIM Data, adapted from Modjeski and Masters (2015)

F3.3.2 Application of WIM Traffic Streams to Analytical Testing Matrix

In order to estimate real live load force effects on cross-frame members, the RT applied the filtered WIM traffic streams to a subset of the analytical testing matrix discussed in Section F3.1.2. As the computational effort is significant (discussed in the next section), approximately 20 models were selected from the 4,104 model data set. While the models were somewhat arbitrarily selected, the RT attempted to choose models that would likely represent extreme cross-frame force effects based on our preliminary studies applying the AASHTO design load to the entire 4,104-model data set. Note that these representative 20 bridges are the same bridges used in the spot-check for the R-Factor Study outlined in Section F4.3.2 and the Commercial Design Software Study outlined in F5.4. For more information regarding the geometric and cross-frame parameters of these bridges, refer to Section F4.3.2.

In the following, Section F3.3.2.1 describes the automated scripts that the RT created to apply WIM traffic streams on influence surfaces obtained for each of the 20 bridge models and to extract specific information for evaluating fatigue stress ranges. Section F3.3.2.2 discusses the use of all WIM sites on all 20 bridge models when WIM traffic streams are located in realistic drive lanes.

F3.3.2.1 Automated Scripts

As previously discussed, the WIM data were filtered to eliminate questionable records (i.e., unrealistic geometry or erroneous data) and apparent permit or illegally loaded vehicles. Additionally, the data filtered lightweight vehicles (i.e., GVWs less than 20 kips). Using MATLAB, a script was developed to read and format the entire FHWA database. Since the axle tracks (i.e., the distance between the centerline of two roadwheels on the same axle) are not recorded in the WIM records, the RT set all axle tracks to 6 feet and assumed that the weight of each axle is evenly distributed between the driver and passenger side wheels.

The RT created scripts to perform the following basic load configuration routines:

Load Configuration 1 - Single Traffic Stream: This routine steps a stream of user-defined WIM traffic along an influence surface (chosen by the user) at 1-foot longitudinal intervals in any user-defined transverse position (also 1-foot intervals). In general, this procedure is similar to that described in Section F3.2.1, except that this analysis involves much more complex loading conditions (rather than a single AASHTO fatigue truck). The script uses a cluster analysis to include the effects of groups of vehicles in the same traffic stream, provided that any wheel of the following truck is on the bridge during the time window in which the leading vehicle is still on the bridge. Time windows are calculated based on the respective vehicle speeds.

Load Configuration 2 - Two Traffic Streams: Similar to Load Position 1, a user-defined WIM traffic stream is stepped along a user-defined bridge deck in a user-defined transverse position. The script uses a cluster analysis to include the effects of groups of vehicles in any adjacent user-defined transverse position, provided any tire on the following truck is on the bridge during the time window in which the leading vehicle is still on the bridge. Again, time windows are calculated based on the respective vehicle speeds.

Load Configuration 3 - Realistic Meandering Traffic Stream: This routine systemically steps a stream of user-defined WIM traffic along a user-defined influence surface at 1-foot longitudinal intervals in any user-defined 12-foot wide lane position. The routine randomly selects a transverse position (within the 12-foot wide lane) for each vehicle record based on a user-defined distribution, such that effects of lane meandering are considered due to cross-frames being highly sensitive to transverse position. This script uses a cluster analysis to include the effects of groups of vehicles, provided any of a following vehicle's tires are on the bridge during the time window that a leading vehicle is still on the bridge. Time windows are calculated based on the respective vehicle speeds.

Recalling that the influence-surface output from Abaqus provides results that are relatively sparsely gridded (Section F3.1.3), the scripts use bi-linear interpolation methods to re-mesh the influence surfaces to a 1-foot by 1-foot grid. This procedure is identical to that described in Section F3.2.1 for the single AASHTO fatigue truck.

The output of each load configuration routine above includes the following:

- A sample load event history (see Figure F3-52);
- The total number of stress cycles (using rainflow counting techniques);
- The average number of cycles per passage;
- The maximum stress and stress cycle recorded;
- The equivalent stress range using the Palmgren-Miner damage accumulation model (i.e., stress range corresponding to the Fatigue II limit state as referenced in Section F3.2.4); and
- The lowest stress range of the top 0.01% of all stress ranges (i.e., the 99.99th percentile criteria corresponding to the Fatigue I limit state which was detailed in Appendix E).

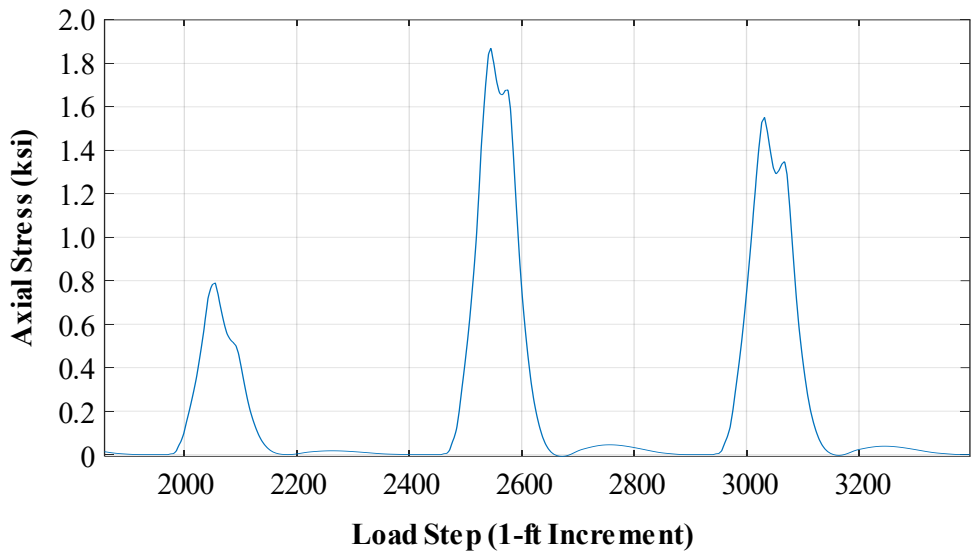

Figure F3-52: Sample load event history showing three vehicles back to back

For calculating the total number of stress cycles, the RT included counting half-cycles in addition to full cycles, which is consistent with previous research on load factor calibration (Modjeski and Masters 2015). The RT created a rainflow counting script that is consistent with ASTM E1049-85 (2017): "*Standard Practices for Cycle Counting in Fatigue Analysis*."

Past research has indicated that eliminating smaller stress cycles of a variable-amplitude loading source has negligible effect on the damage accumulated in a fatigue detail. Connor and Fisher (2006) showed that stress cycle magnitudes less than 25% of the constant amplitude fatigue limit (CAFL) generally have little impact on the long-term fatigue performance, which was outlined in Appendix E. To study the effects of this lower stress range truncation on cross-frames, the RT compiled the results of each loading iteration (as listed above) for two different conditions: (i) including the effects of stress magnitudes less than 25% of the CAFL and (ii) filtering out those effects. For the purposes of this study, a detail category E' is assumed based on the results of McDonald and Frank (2009) and AASHTO Table F6.6.1.2.3-1(7.2). The corresponding CAFL value for this detail is 2.6 ksi; thus, all stress cycles less than 0.65 ksi are truncated when the filter is applied.

Each of the routines discussed in the previous section systematically and sequentially applies a defined traffic stream (e.g., Virginia US-29 Lane 1) in a specific load configuration over the influence surface corresponding to one cross-frame member in one of the 20 representative bridges. Based on preliminary results applying the AASHTO design load to the 4,104 bridge models, the RT selected 16 to 20 cross-frames for each bridge that are assumed to include a governing, critical cross-frame for the design of that particular bridge. Using a subset of 20 models, this results in more than 320 influence surfaces for consideration.

For each influence surface, the user can define any 1-foot transverse lane position for a particular traffic stream. Since bridge widths of the 20 models range from 30 to 45 feet, this results in 25 to 41 possible transverse positions for selection (incorporating the 6-foot transverse width between wheel lines), resulting in approximately 8,000 to 13,000 iterations for unique transverse load positions. Considering the computational time for each iteration (depending on the total number of vehicle entries and bridge length) varies from several minutes to multiple hours and considering this does not consider other variables (such as adjacent lanes containing vehicles or the inclusion of passenger vehicles, etc.), the number of potential iterations becomes unmanageable. For this reason, the studies presented in this appendix were obtained by positioning the WIM traffic stream in a realistic drive lane, rather than a worst-case drive lane. This is further explained in the following sections.

A worst-case lane position to maximize force effects in a cross-frame is determined by stepping the WIM stream over every available transverse lane. There are two primary issues with this approach. First, the computational time required for each iteration of the WIM traffic streams is extensive. Second, based on preliminary studies conducted by the RT, the worst lane position is often when the truck is positioned at the edge of the deck (i.e., the right tire of a truck is positioned along the deck edge where a traffic barrier would be placed). Using the influence surface shown in Figure F3-10 as an example, the most critical lane position to maximize tension in the cross-frame shown is when the truck is positioned as close to the deck edge as possible. This is illustrated in Figure F3-53. This discussion is similar to that described in Section F3.2.3 with respect to "overhang" and "non-overhang" loads.

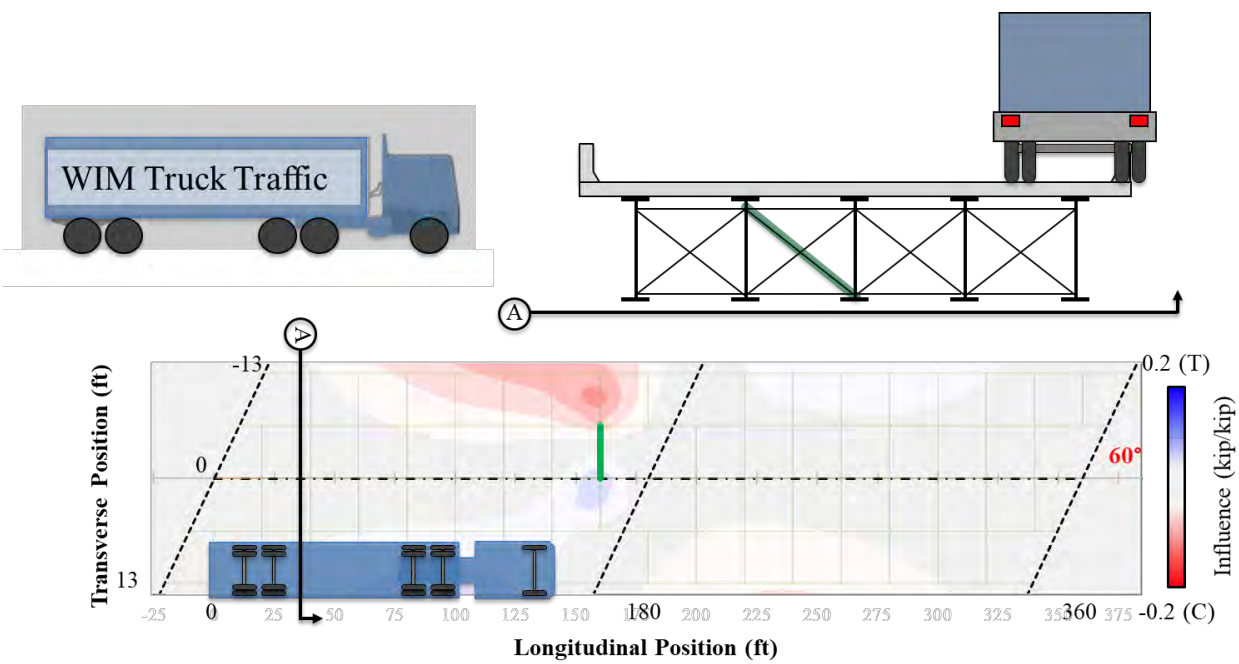

Figure F3-53: Illustration of worst-case truck position to maximize cross-frame force effects

As a worst-case lane position would lead to unnecessary conservatism, the RT opted for defining a realistic lane position based on the actual bridge width and recommendations from AASHTO Article 3.6.1.1.1. As illustrated in Figure F3-54, using the same influence surface from the previous example, this realistic truck position does not produce the largest tensile stress range for the selected cross-frame; however, this position would be consistent with realistic loading and lane striping on the bridge.

With that in mind, the RT deemed Loading Configuration 3 more pertinent than Configuration 1 with respect to fatigue design. As such, the focus of the next subsection is on realistic traffic streams as opposed to considering all possible lane positions (i.e., "overhang" loads).

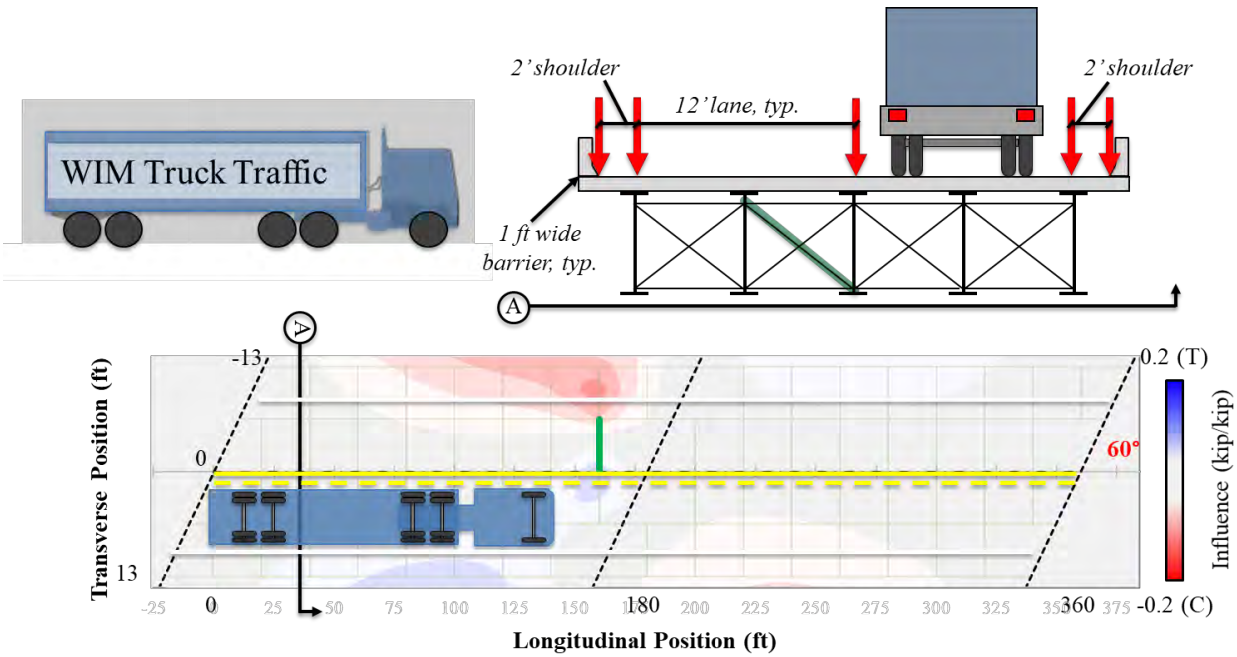

Figure F3-54: Illustration of realistic truck position in drive lane

For the actual location of each 6-foot vehicle track width (i.e., transverse distance between left and right wheel lines) within the realistic lane, the RT assumed a distribution for which the vehicle is located in the center of the lane 55% of the time; 30% of the time, the vehicle is located plus or minus 1 foot of the lane centerline; 10% of the time, the vehicle is located plus or minus 2 feet of the lane centerline; and 5% of the time, the vehicle is riding along one of the lane edges. This is illustrated in Figure F3-55 for a sample 30-foot wide bridge, although the procedure is the same for different bridge widths and lane configurations. The intent of this assumed distribution is to consider the inherent variability in driving ability and consistency.

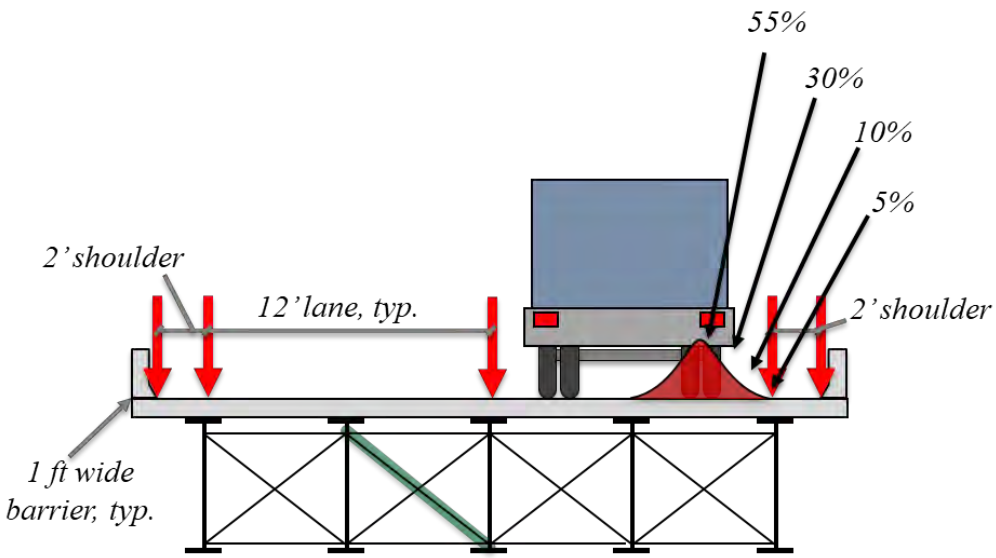

Figure F3-55: Illustration showing distribution of vehicle transverse location within 12-foot design lane for a 30-foot wide bridge

F3.3.2.2 WIM Drive Lane Truck Traffic Positioned in Realistic Drive Lanes

The following subsections describe the analysis and results from applying all obtained WIM sites to the 20 select bridges using Load Configuration 3 (i.e., Realistic Meandering Traffic Stream). The results herein are from one arbitrary drive lane (i.e., the analysis does not consider that traffic could be flowing the opposite direction). The symmetry of the bridge is assumed to produce similar maximum effects for one of the 16 to 20 critical cross-frames selected per bridge. This assumption was investigated at the conclusion of this study, when selected bridges and WIM records were chosen in order to run the WIM records on a bridge deck surface rotated by 180 degrees (i.e., traffic was located on the drive lane nearest the opposite edge of the bridge). The results of this spot check indicated there was very little difference in maximum force effects for fatigue for the bridges and WIM records selected.

The traffic streams for the following studies used the filtered records (i.e., excluding vehicles with GVW less than 20 kips) and a drive lane defined by AASHTO Article 3.6.1.1.1 and the assumed vehicle position distribution discussed in Section F3.3.2.1. The same procedure was done for the unfactored AASHTO fatigue truck, and the comparisons of maximum and effective stress ranges provide insight on the accuracy of current Fatigue I and II load factors with respect to cross-frame design.

In other words, all WIM-related results were normalized to the maximum stress range produced by applying the unfactored AASHTO design load (i.e., HS-20) to the same bridge in all possible transverse positions within the clear distance of the barriers. Note that the following results do not include an impact factor, since the WIM stations attempt to correct for dynamic effects and relate measured drive-by weights to static weights. It may be prudent to include a portion of the typical 0.15 impact factor (AASHTO Article 3.6.2.1) in subsequent studies, since the effects of bridge dynamics are not accounted for explicitly in this finite-element analysis.

F3.3.2.2.1 Fatigue I Stress Ranges (Normalized to Fatigue Truck)

The governing Fatigue I stress range calculated for all WIM sites was determined based on 99.99th percentile criteria. This stress range corresponds to the lowest magnitude of the top 0.01% of all stress ranges recorded (for the governing cross-frame for each bridge given the defined lane position). Figure

F3-56 illustrates the selection of the Fatigue I stress range from a CDF of stress ranges for a given cross-frame. In this figure, the stress range corresponding to the largest stress range recorded is approximately 7 ksi; however, the lowest stress range within the top 0.01 percent stress ranges is shown to be 5.15 ksi. Thus, 5.15 ksi is considered the maximum stress for which AASHTO Fatigue I load criteria is evaluated.

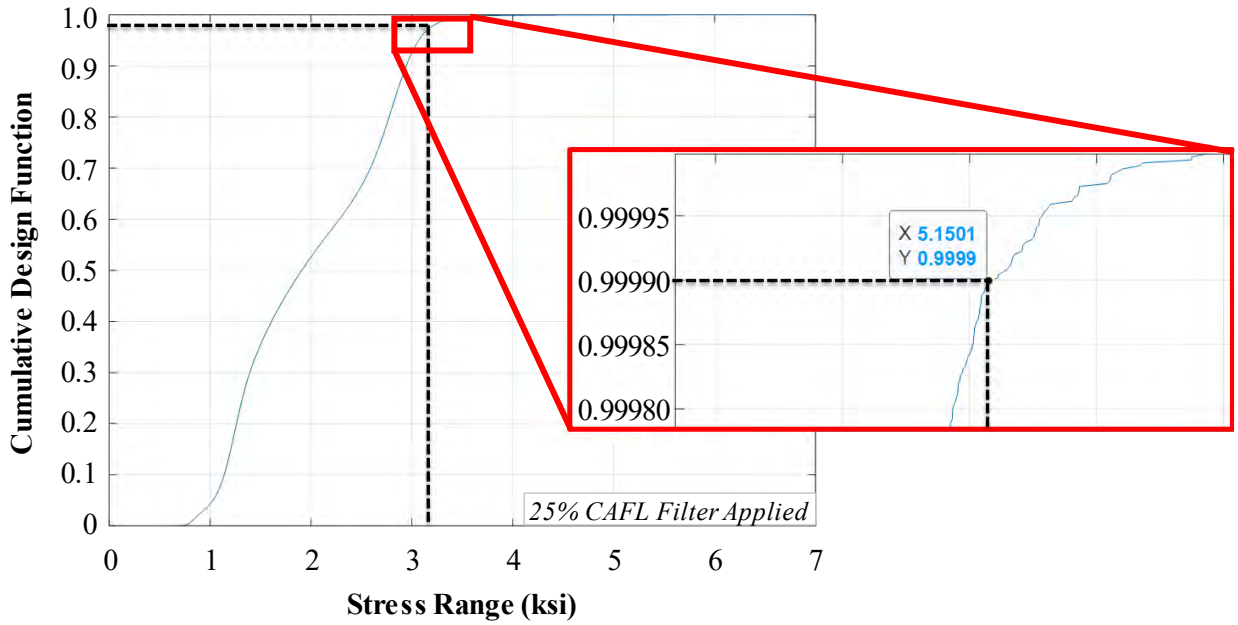

Figure F3-56: Illustration showing selection of 99.99th percentile stress range

Once all Fatigue I stress ranges were calculated for each WIM site and each bridge (i.e., one value per bridge per WIM record), the stress ranges were normalized to the largest stress range produced by applying the unfactored AASHTO design load (i.e., the fatigue truck) to the same bridge in all possible transverse positions within the clear distance of the barriers. Note that the positioning of the fatigue truck to create the largest stress range does not necessarily correspond to the location of the WIM traffic stream - this is consistent with the a typical design approach, where the bridge (and its cross-frames) is designed based on the maximum stress range produced by locating the fatigue truck in the critical position between the barriers (in accordance to AASHTO Article 3.6.1.4.3).

The Fatigue I stress ranges and biases[1] were calculated for each of the 20 bridges using all WIM site records, as well as the arithmetic mean of all stress ranges produced by the 18 WIM site records, and the "mean plus 1.5 standard deviations" of all stress ranges produced by the 18 WIM site records (the standard deviation is calculated for the distribution of all stress ranges produced by the 18 WIM site records). As documented in the SHRP 2 R19B report, the value associated with the "mean plus 1.5 standard deviations" was taken as both the bias of the data (R19B states this was a conservative measure, since it was unknown how accurately the WIM records used in the project reflected truck traffic across the nation), as well as an appropriate load factor. This resulted in a proposed load factor of 2.0 for Fatigue I; however, the load factor adopted in the 8th Edition of AASHTO LRFD was 1.75. Based on discussions with the authors of the R19B report and a review of the AASHTO T-14, T-5, and T-10 committee agenda items prior to the AASHTO revision, the value of 1.75 was achieved by using the arithmetic mean of the normalized stress ranges produced by the WIM site records (i.e., the bias and load factor are both taken to be equal to the mean bias

[1] "Load bias" refers to the ratio between the actual load effects to the design load effects (i.e., the WIM load effects divided by the load effects caused by the fatigue design truck).

value). This was rationalized by acknowledging conservatism inherent in the resistance data for Fatigue I and the fact that the WIM data reviewed was deemed to be sufficiently abundant to represent national traffic loads.

Figure F3-57 and Figure F3-58 summarize the ratios of the 99.99th percentile WIM stress ranges for each of the 20 bridges divided by the unfactored fatigue truck stress range for each bridge, before and after applying a stress range filter of 0.65 ksi (i.e., 0.25*CAFL for detail category E′), respectively. For both of these figures, each bin value represents the average of all Fatigue I stress ranges for all WIM sites applied to the identified bridge (as explained in the preceding paragraph). A solid line in each figure represents the arithmetic mean of all Fatigue I stress ranges for all WIM sites applied to the identified bridge. A dashed line in each figure represents the mean value of all "mean plus 1.5 standard deviations" (i.e., the mean plus 1.5 standard deviation for all values represented by the individual bars). Consistent with the approach that led to the recent AASHTO LRFD revisions, the arithmetic mean value of all Fatigue I stress ranges for all WIM sites would correspond to an appropriate Fatigue I load factor for cross-frames. In other words, the stress ranges produced by the unfactored fatigue truck must be amplified by this factor to produce an equivalent 99.99th percentile stress range that represents the 99.99th percentile load effects caused by the WIM traffic streams. Without consideration of material fatigue resistances (and therefore the reliability index), the mean values associated with the solid lines in Figure F3-57 and Figure F3-58 imply an appropriate load factor for the Fatigue I limit state is between 1.01 (with no stress range filtering) and 1.25 (with stress range filtering), respectively. The coefficients of variation associated with these values were calculated to be 0.23 and 0.20, respectively. Both of these load factors are less than the current Fatigue I load factor of 1.75, which indicates a potential source of conservatism in the design load criteria. Note that while the SHRP 2 Project R19B report indicates the revised load factor was developed using the lightweight vehicle filtering, the report does not indicate whether the researchers truncated lower stress cycles directly.

Recall from Section F3.3.1 that the GVWs for the WIM records are not normal; rather, many WIM sites appear to have multi-modal distributions that likely correspond to natural groupings of different vehicle types and payload. Rather than use the arithmetic mean of Fatigue I stress ranges, it is prudent to plot all normalized Fatigue I stress ranges on a normal probability plot to assess the normality of these maximum stress ranges. Figure F3-59 represents a CDF of the normalized stress ranges plotted on a normal probability plot prior to truncating the stresses below 25% CAFL, and Figure F3-60 represents the same data after truncating stresses below 25% CAFL.

It is apparent that the distribution of normalized Fatigue I stress ranges prior to truncating the stresses is not normal; however, the Fatigue I stress ranges after removal of these lower stresses can be adequately described as normal distributions. By applying a best-fit line (e.g., via linear regression analysis or manually) to the CDF of a normal distribution, the mean of the normal distribution corresponds to the horizontal axis value when the best fit line equals zero on the vertical axis (i.e., the standard normal variable is zero for a normal distribution). Additionally, the standard deviations of the data sets can be approximated by the inverse of the slope of the best fit line. Table F3-21 compares the standard deviations and means obtained by the direct arithmetic calculation (represented in Figure F3-57 and Figure F3-58) and the normal probability plot approach. For the truncated data, the normal probability plot approach involved performing a linear regression analysis on the entire CDF. For the data prior to truncation, the normal probability plot approach involved applying a best fit line to the higher stress range values that demonstrate a linear behavior. Fitting a line to the upper tail of the CDF allows emphasis to be placed on the higher stress ranges that will tend to govern in the Fatigue I case.

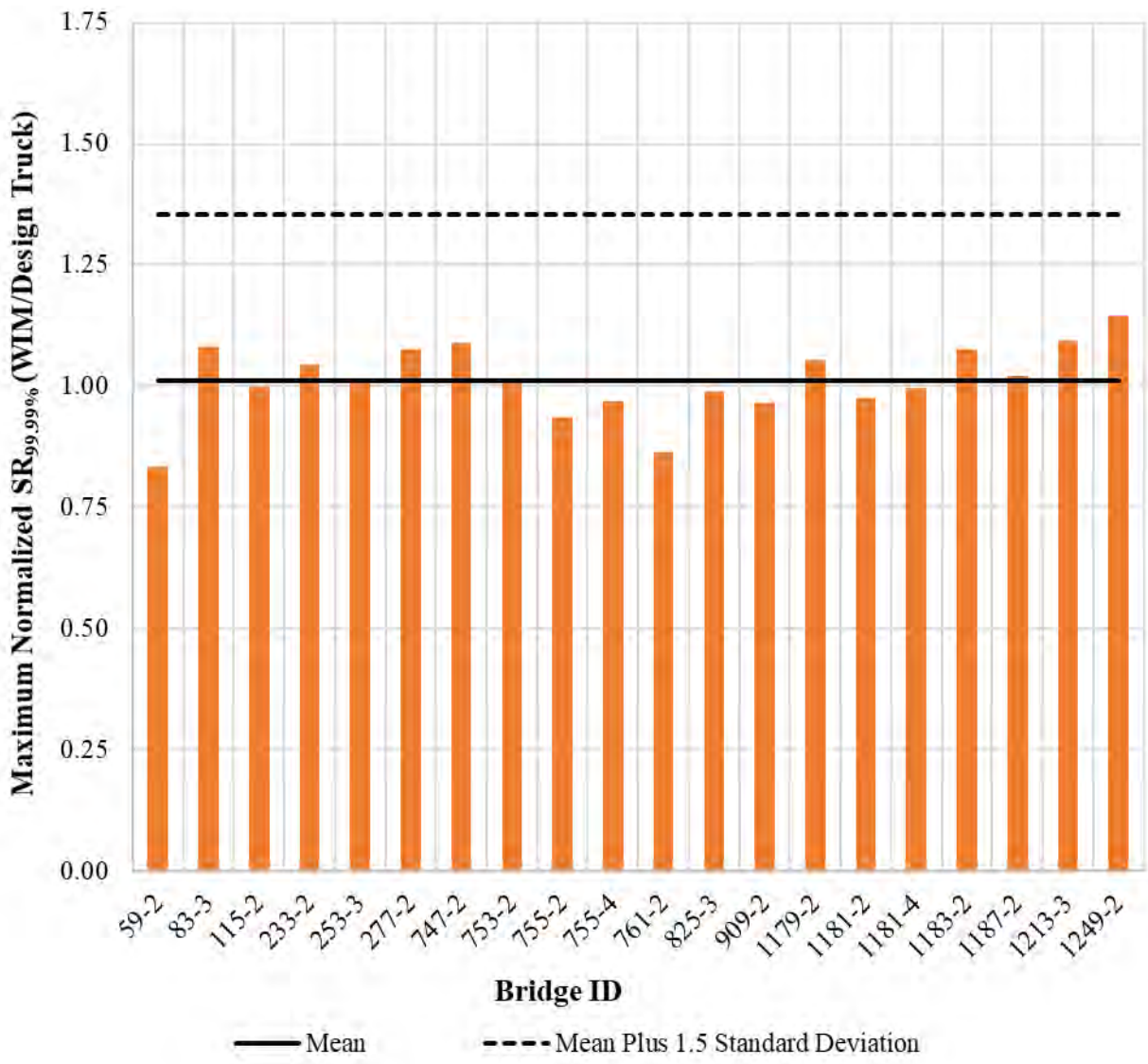

Figure F3-57: Summary of Fatigue I normalized 99.99% stress ranges ($SR_{99.99\%}$) for 18 WIM records and 20 sites prior to truncating the lower stress ranges (i.e., removing stress ranges less than 25% CAFL).

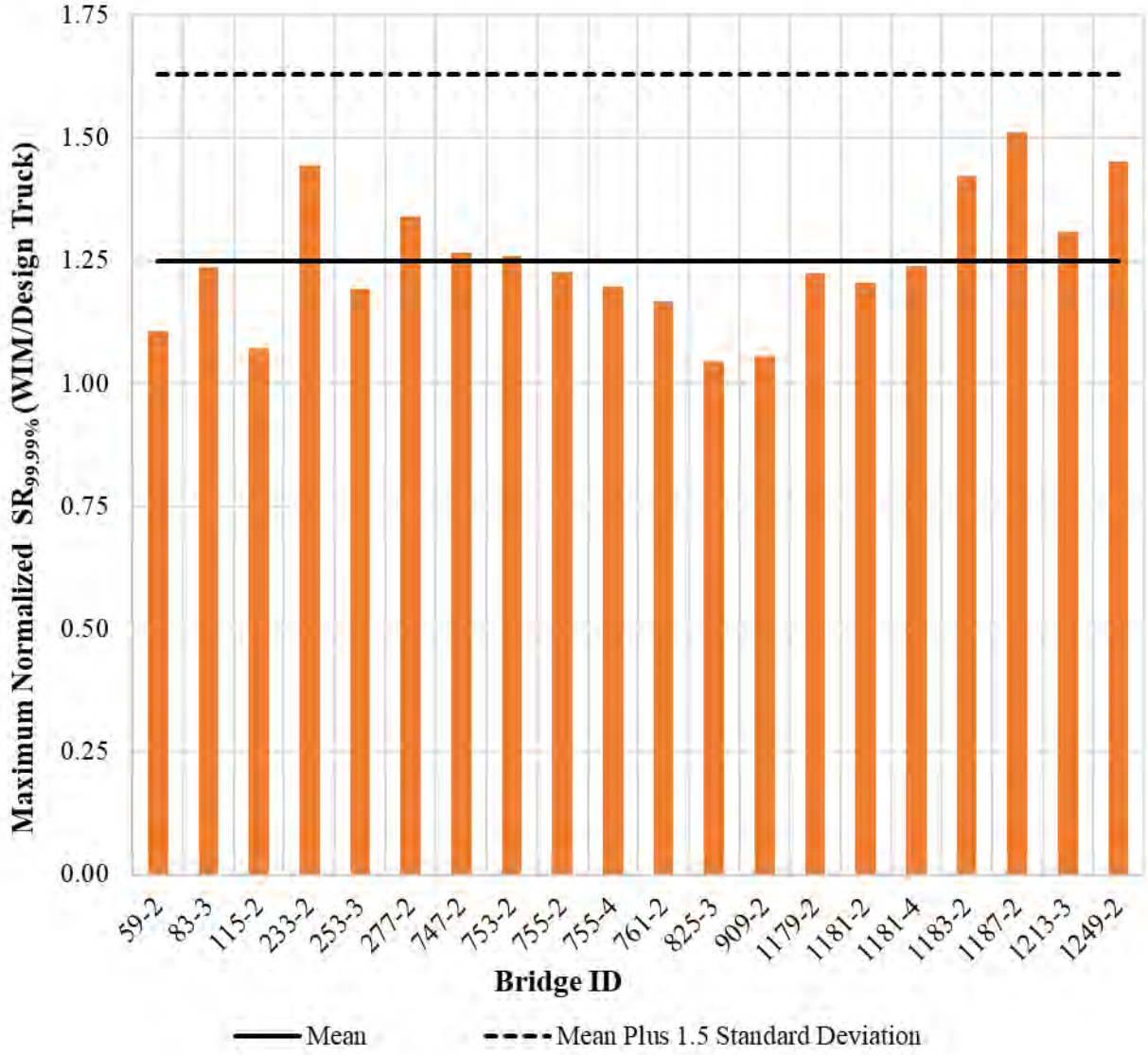

Figure F3-58: Summary of Fatigue I normalized 99.99% stress ranges ($SR_{99.99\%}$) for 18 WIM records and 20 sites after truncating the lower stress ranges (i.e., removing stress ranges less than 25% CAFL).

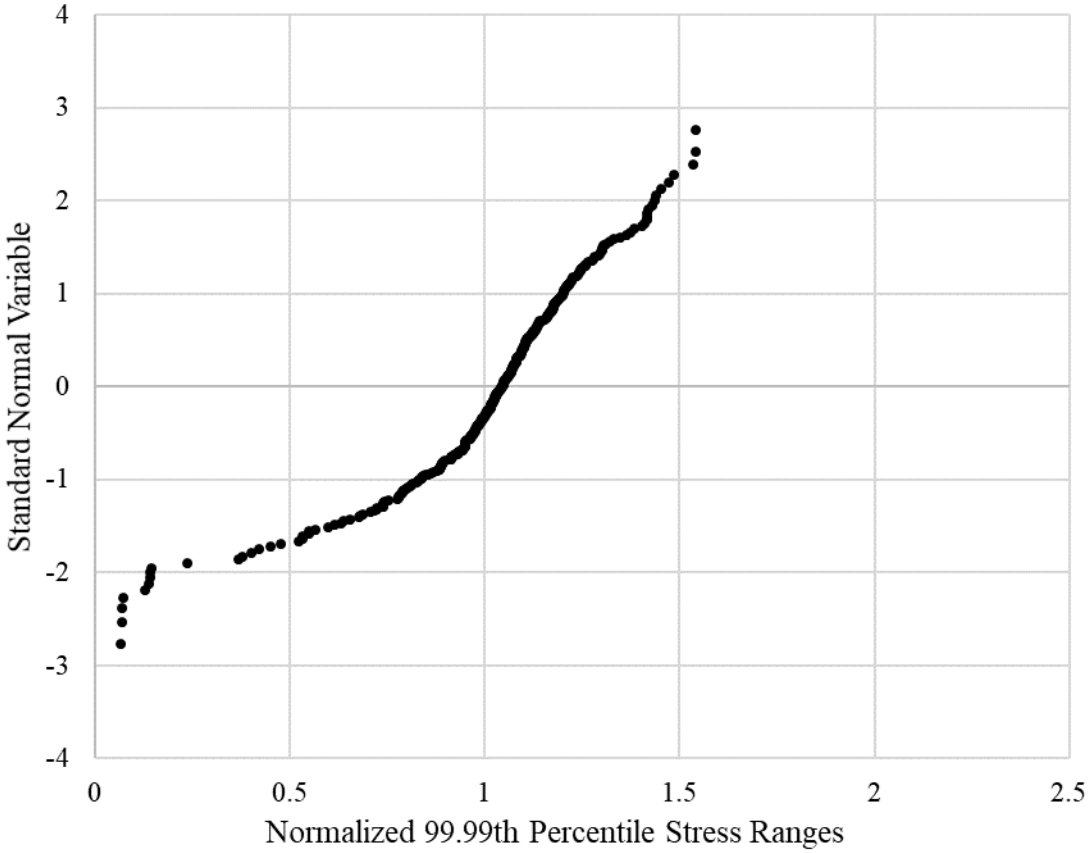

Figure F3-59: CDF of Fatigue I normalized 99.99th percentile stress ranges for 18 WIM records and 20 bridge sites prior to truncating the lower stress ranges (i.e., removing stress ranges less than 25% CAFL.

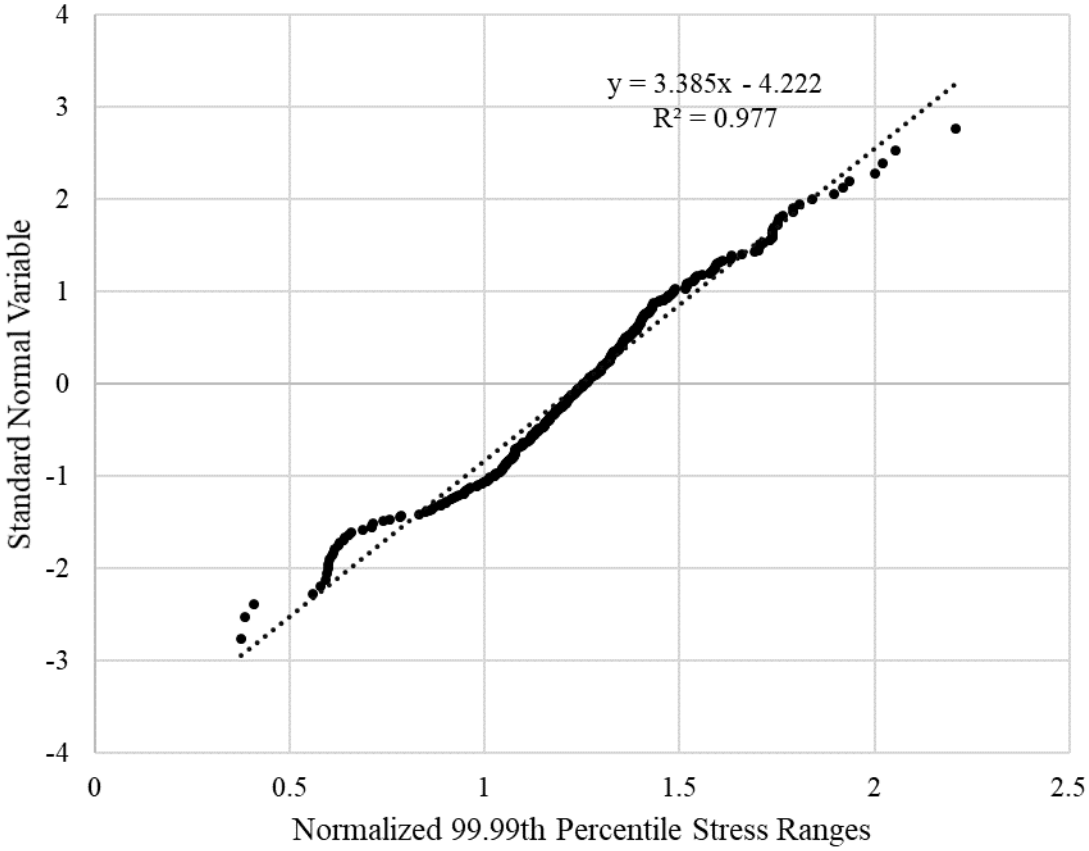

Figure F3-60: CDF of Fatigue I normalized 99.99th percentile stress ranges for 18 WIM records and 20 bridge sites after truncating the lower stress ranges (i.e., removing stress ranges less than 25% CAFL). A best fit line is demonstrated via linear regression.

Table F3-21: Comparison of statistical parameters obtained for the Fatigue I stress ranges by two methods.

		Mean	Coefficient of Variation	Mean Plus 1 Standard Deviation	Mean Plus 1.5 Standard Deviations
Prior to Removing Stresses Below 25% CAFL	Value Obtained by Direct Calculation	1.01	0.23	1.24	1.35
	Value Obtained from Normal Probability Plot	1.04	0.17	1.22	1.31
After Removing Stresses Below 25% CAFL	Value Obtained by Direct Calculation	1.25	0.20	1.50	1.63
	Value Obtained from Normal Probability Plot	1.25	0.24	1.54	1.69

F3.3.2.2.2 Fatigue II Stress Ranges (Normalized to Fatigue Truck)

Similar to the Fatigue I stress ranges, the governing Fatigue II stress ranges calculated for all WIM sites were determined based on the maximum effective stress range for all 16 to 20 cross-frames for each bridge. In other words, one critical cross-frame produced WIM stress ranges that exceeded the remainder of the cross-frames in the bridge and thus served as the governing case. In contrast to Section F3.3.2.2.1, the effective stress range of the cross-frames with respect to WIM loading was computed instead of the 99.99th percentile value. Recall that the Fatigue II limit state is more representative of the effective or "average" effect of the traffic population. These effects are generally characterized by the effective stress range (or equivalent stress range) of the variable-amplitude response.

Recall from Section F3.2.4 that the number of stress cycles can be expressed to be inversely proportional to the cube of the stress range magnitude. Using the same relationship, the effective stress range can be expressed mathematically by the following equation:

$$S_{re} = \left(\frac{A}{N_R}\right)^{\frac{1}{3}} \qquad F3.10$$

where: N_R = number of cycles at the effective stress range, S_{re}, until failure; and S_{re} = effective stress range (ksi).

In the equation above, the effective stress range, S_{re}, represents the fatigue damage caused by WIM traffic and is determined using Palmgren-Miner's rule using rainflow counting techniques on real stress cycles. The effective stress range mathematically characterizes a variable-amplitude response in terms of a constant-amplitude stress range of equal cycle count. Refer to Appendix E for a more detailed description of this calculation as in pertains to the Fatigue II limit state.

Once all Fatigue II stress ranges were calculated for each WIM site and each bridge using Eq. F3.10, the stress ranges were then normalized to the largest stress range produced by applying the unfactored fatigue truck to the same bridge in all possible transverse positions within the clear distance of the barriers (similar to Section F3.3.2.2.1 for Fatigue I criteria). Note that the positioning of the fatigue truck to create the largest stress range did not necessarily correspond to the location of the WIM traffic stream, which is consistent with the typical design approach.

Figure F3-61 and Figure F3-62 summarize the ratios of the effective stresses ranges from the WIM traffic streams divided by the unfactored fatigue truck stress range for each bridge, both before and after applying the 0.25*CAFL filter. The dashed and solid horizontal lines in Figure F3-61 are similar to those previously described for Figure F3-57. Using the effective stress range as the metric for comparison, the appropriate load factor for Fatigue II in the context of these 20 representative bridges is 0.55 (with CAFL filter) and 0.34 (without filter) based on the "mean plus 1.5 standard deviations" criteria used by SHRP 2 R19B (resulting in the load factor for Fatigue II that was adopted by AASHTO LRFD). The coefficients of variation associated with these values were calculated to be 0.10 and 0.17, respectively. Note that an appropriate load factor (without consideration of material resistances, and therefore the reliability index) would consider the actual damage accumulation given the effective stress range (discussed in the next section).

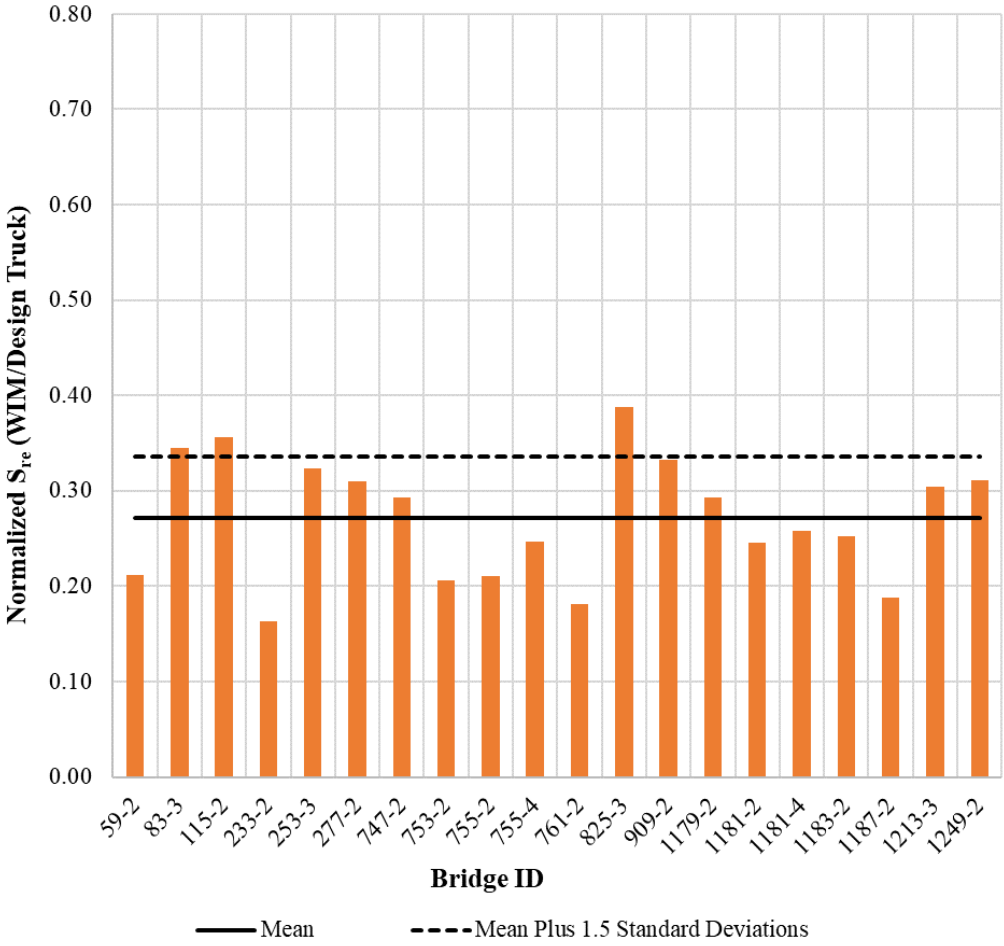

Figure F3-61: Summary of Fatigue II normalized effective stress ranges (S_{re}) for 18 WIM records and 20 sites prior to truncating the lower stress ranges (i.e., removing stress ranges less than 25% CAFL).

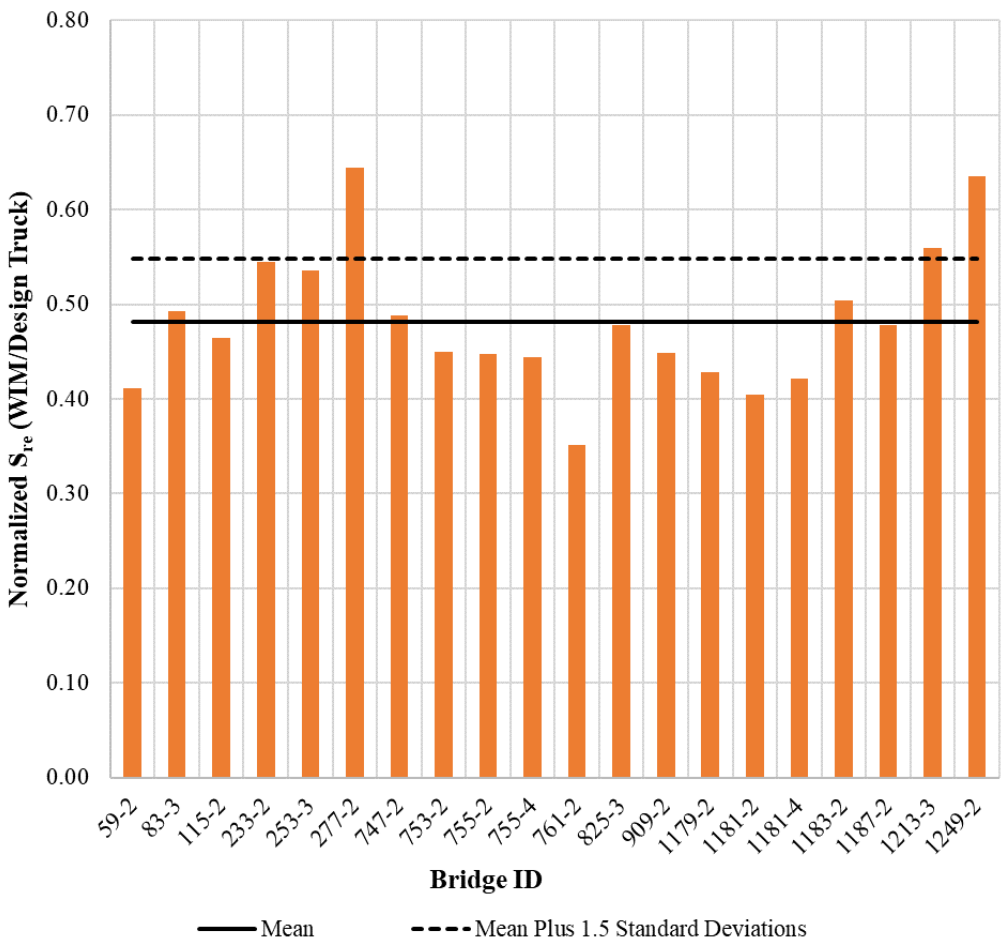

Figure F3-62: Summary of Fatigue II normalized effective stress ranges (S_{re}) for 18 WIM records and 20 sites after truncating the lower stress ranges (i.e., removing stress ranges less than 25% CAFL).

F3.3.2.2.3 Fatigue II Damage Ratios (Normalized to Fatigue Truck)

Similar to the previous section, the Fatigue II design criteria can also be evaluated in terms of accumulated damage, as opposed to simply the effective stress range of the truck population spectra. The accumulated damage metric is similar but inherently considers both the variable stress range magnitudes and the number of cycles. Thus, the total damage accumulated by the various WIM streams on the critical, governing cross-frame members is compared to the damage accumulated by the AASHTO fatigue truck (based on AASHTO criteria for the relationship between number of trucks and number of cycles).

With that in mind, the fatigue damage caused by the AASHTO design load can by expressed by the following equation (in terms of stress range, similar to F3.10):

$$S = \left(\frac{A}{N}\right)^{\frac{1}{3}} \qquad F3.11$$

where: N = number of design cycles calculated from AASHTO Table F6.6.1.2.5-2, and S = governing design stress range caused by the AASHTO fatigue truck (ksi). For this project, the number of design cycles

per truck was taken as 1, which is consistent with the analytical modeling and experimental analyses discussed in previous sections.

The boundaries of fatigue damage caused by the WIM traffic stream and the fatigue design truck can be related by equating Eqs F3.12 and F3.13 to form Eq. F3.14:

$$1 = \left(\frac{A}{N_R}\right)^{\frac{1}{3}} * \frac{1}{S_{re}} \qquad F3.12$$

$$1 = \left(\frac{A}{N}\right)^{\frac{1}{3}} * \frac{1}{S} \qquad F3.13$$

$$\left(\frac{A}{N_R}\right)^{\frac{1}{3}} * \frac{1}{S_{re}} = \left(\frac{A}{N}\right)^{\frac{1}{3}} * \frac{1}{S} \qquad F3.14$$

Eq. F3.14 can be rearranged to form the ratio of actual (WIM) fatigue damage to the fatigue damage caused by the design truck. Consistent with SHRP 2 Project R19B studies, we will define this ratio, λ, as the "fatigue damage ratio":

$$\lambda = \frac{\left(\frac{A}{N_R}\right)^{\frac{1}{3}} * \frac{1}{S_{re}}}{\left(\frac{A}{N}\right)^{\frac{1}{3}} * \frac{1}{S}} = \sqrt[3]{\frac{N_R}{N}} * \frac{S_{re}}{S} \qquad F3.15$$

Values of λ less than one indicate that the damage accumulated by the WIM data is less than that of the assumed values based on AASHTO design criteria (i.e., the design criteria is overly conservative); the opposite is true to values of λ larger than one. Figure F3-63 and Figure F3-64 summarize the fatigue damage ratios of the WIM traffic streams for each representative bridge, before and after applying a stress range filter of 0.65 ksi, respectively. Figure F3-63 and Figure F3-64 are similar to Figure F3-57 and Figure F3-61 with respect to the definition of the dashed and solid horizontal lines.

Without consideration of material resistances (and therefore the reliability index), the value associated with the "mean plus 1.5 standard deviations" implies that an appropriate load factor for the Fatigue II limit state is 0.49 with no stress range filtering, and a load factor of 0.47 with the 0.25*CAFL filter. The coefficients of variation associated with these values were calculated to be 0.16 and 0.19, respectively. Both load factors are significantly less than the 0.80 load factor currently specified in AASHTO LRFD for Fatigue II. The use of the "mean plus 1.5 standard deviations" as an indicator of an appropriate load factor is consistent with research documented in SHRP 2 Project R19B (Modjeski and Masters 2015) and the subsequent development of the 0.8 load factor for Fatigue II. This suggests that the 0.8 load factor may be conservative for cross-frames.

Similar to the comparison made in Section F3.3.2.2.1, the fatigue damage ratios for all WIM records and all bridges were plotted on a normal probability plot to assess the normality of the damage ratios. Figure F3-65 represents a CDF of the fatigue damage ratios plotted on a normal probability plot prior to truncating the stresses below 25% CAFL, and Figure F3-66 represents the same data after truncating stresses below 25% CAFL.

It is apparent that both distributions of Fatigue II damage ratios can be adequately described as normal distributions. By performing a linear regression analysis on the normalized values as described in Section F3.3.2.2.1, the mean and standard deviations of the distributions are calculated. Table F3-22 compares the

standard deviations and means obtained by the direct arithmetic calculation (represented in Figure F3-63 and Figure F3-64) and the normal probability plot approach.

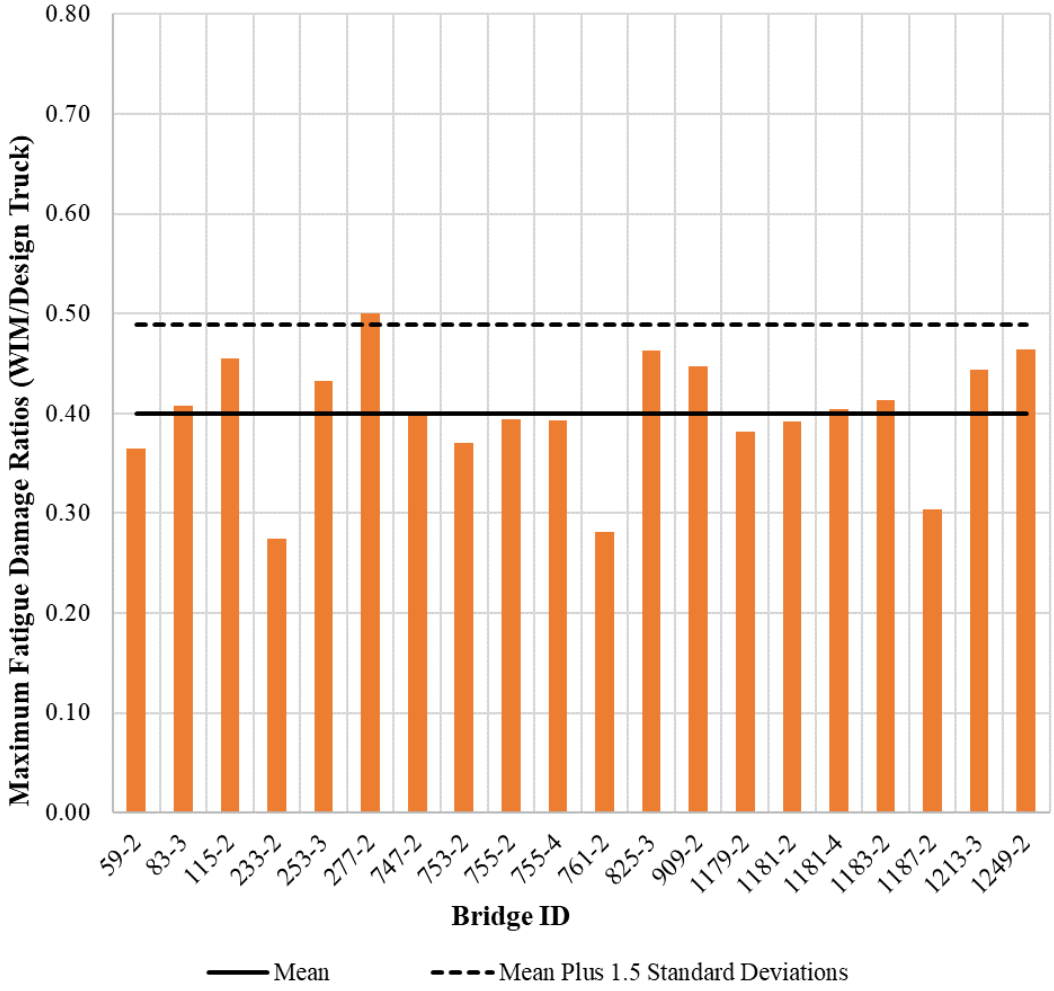

Figure F3-63: Summary of Fatigue II damage ratios for 18 WIM records and 20 sites prior to truncating the lower stress ranges (i.e., removing stress ranges less than 25% CAFL).

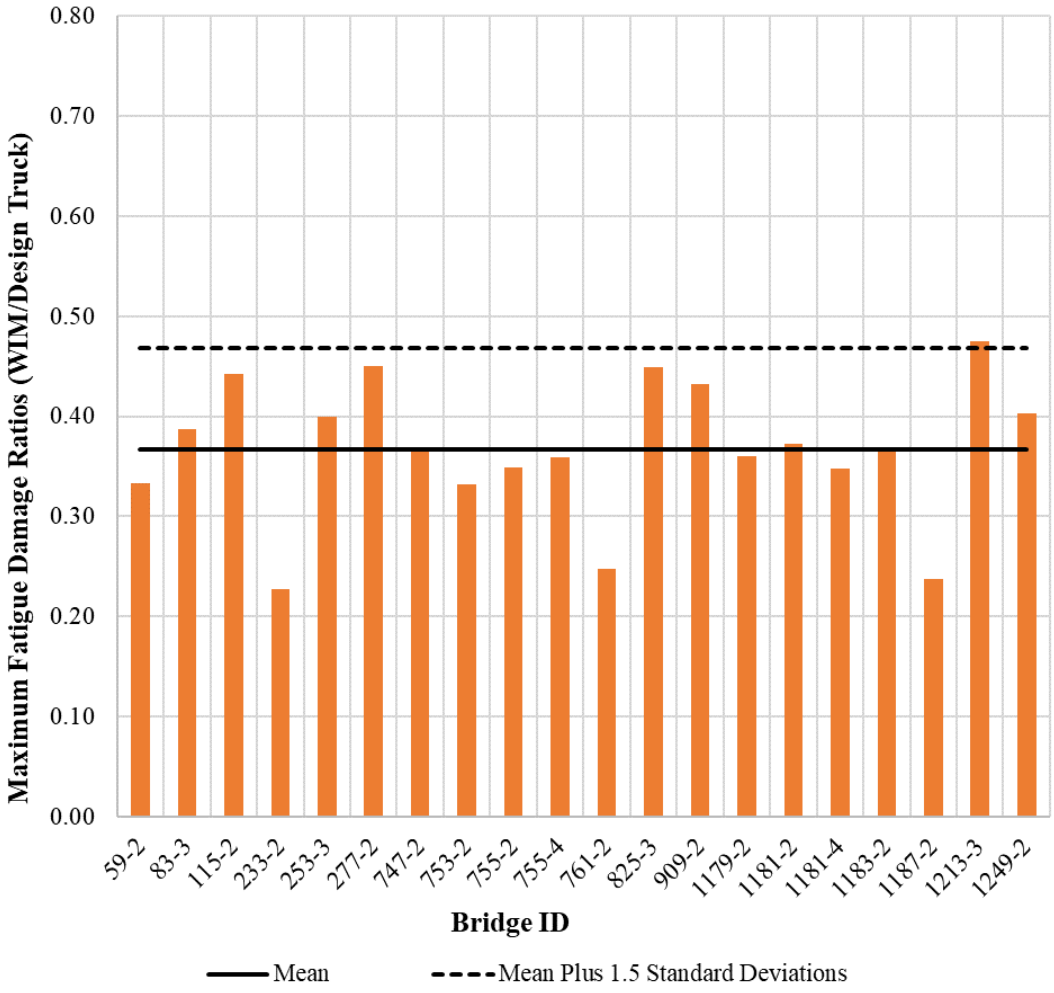

Figure F3-64: Summary of Fatigue II damage ratios for 18 WIM records and 20 sites after truncating the lower stress ranges (i.e., removing stress ranges less than 25% CAFL).

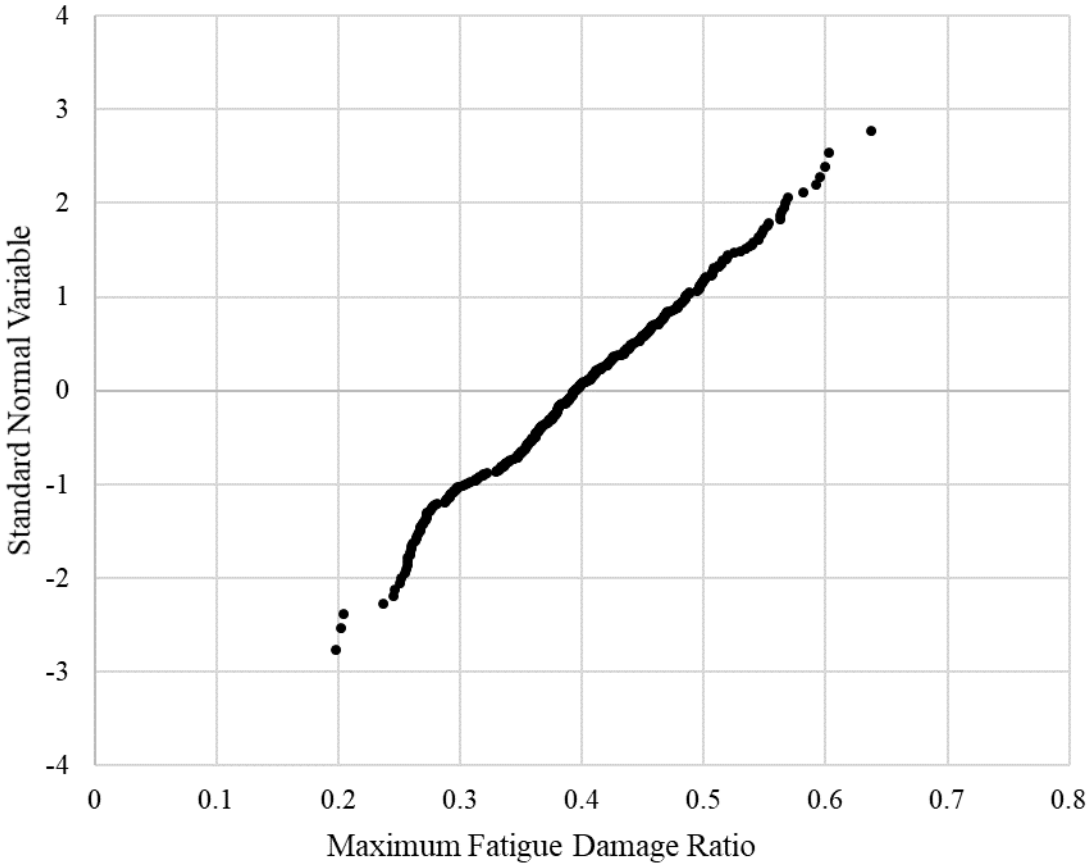

Figure F3-65: CDF of maximum Fatigue II damage ratios for 18 WIM records and 20 bridge sites prior to truncating the lower stress ranges (i.e., removing stress ranges less than 25% CAFL).

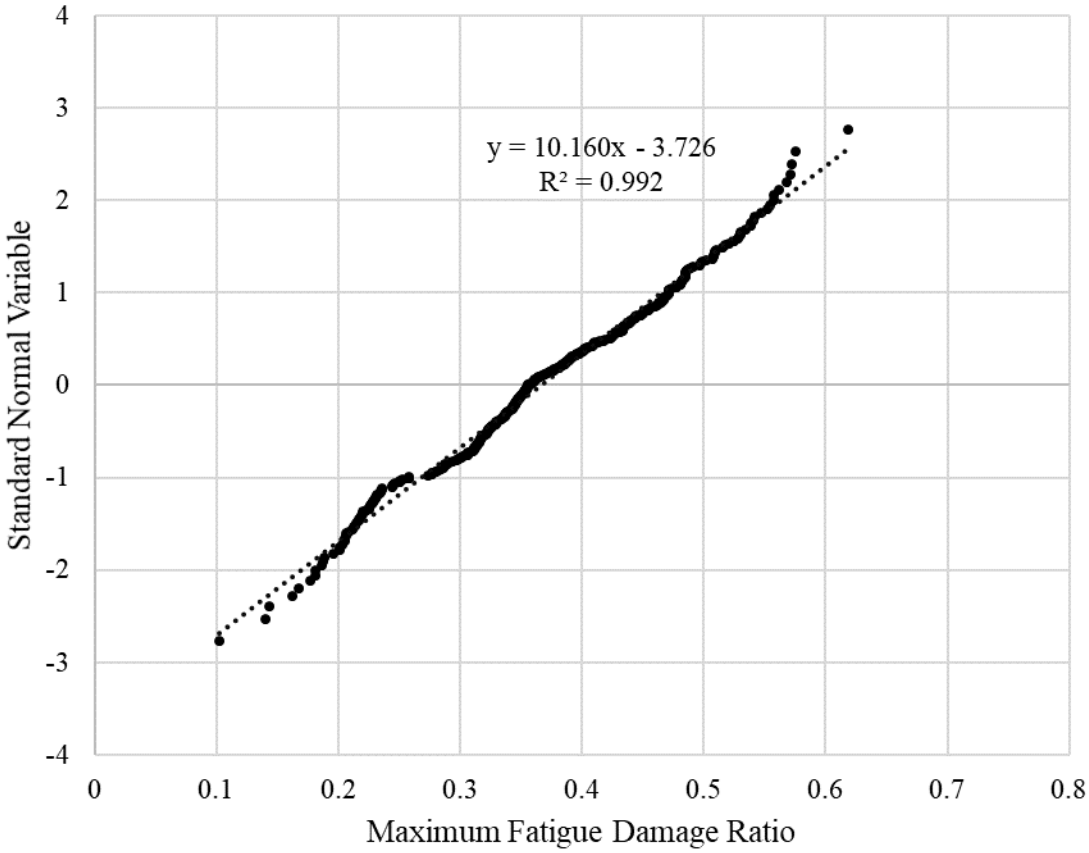

Figure F3-66: CDF of maximum Fatigue II damage ratios for 18 WIM records and 20 bridge sites after truncating the lower stress ranges (i.e., removing stress ranges less than 25% CAFL). A best fit line is demonstrated via linear regression.

Table F3-22: Comparison of statistical parameters obtained for the Fatigue II damage ratios by two methods.

		Mean	Coefficient of Variation	Mean Plus 1 Standard Deviation	Mean Plus 1.5 Standard Deviations
Prior to Removing Stresses Below 25% CAFL	Value Obtained by Direct Calculation	0.40	0.16	0.46	0.49
	Value Obtained from Normal Probability Plot	0.40	0.21	0.48	0.53
After Removing Stresses Below 25% CAFL	Value Obtained by Direct Calculation	0.37	0.19	0.43	0.47
	Value Obtained from Normal Probability Plot	0.37	0.27	0.47	0.51

F3.3.3 Comparative Study using Primary Member Calibration Data

The calibration of the current AASHTO LRFD load factors for the Fatigue I and II limit states was based entirely on the moment responses of primary girders to WIM traffic streams as described in the project report for SHRP 2 R19B. In order to directly compare the results of the advanced Fatigue I and Fatigue II WIM analyses discussed in the preceding sections to the results obtained by the SHRP 2 R19B project, the automated scripts discussed in Section F3.3.2.1 were modified to simulate the WIM traffic streams over a bridge in order to calculate the Fatigue I and II parameters (i.e., the maximum 99.99th percentile stress range and the maximum fatigue damage ratio). The published data in the SHRP 2 R19B report includes primary girder force effects for simply supported bridges (positive bending moment at midspan) and two-span continuous bridges (negative bending moment at the interior support and positive bending moment at 0.4 times the span length); in addition, the published data provides these bending moment values for 30, 60, 90, 120, and 200 foot long spans. For this comparative study, a simply supported bridge was chosen from the 20-model subset with a span length of 200 feet (i.e., this is the only simply supported bridge with a common span length for direct comparison). It is important to note that the WIM traffic streams used in this comparison are distinctly different WIM records than those used in the SHRP 2 R19B calibration.

The Fatigue I and II parameters published in the SHRP 2 R19B report for positive bending moment at midspan for a 200-foot long simply supported bridge are summarized in Table F3-23, and include 15 WIM records. At the bottom of this table, the statistical parameters for this data set are provided, including the mean of the Fatigue I and II parameters, the "mean plus 1 standard deviation" of the Fatigue I and II parameters, and the "mean plus 1.5 standard deviations" of the Fatigue I and II parameters.

Instead of calculating stress ranges in individual cross-frames due to a moving load fixed to a transverse position or range of positions, the automated scripts were modified to calculate the maximum positive bending moment at midspan of the selected bridge using a 1-dimensional influence line. In order to maintain consistency with the approach to cross-frames, the process used to filter WIM records, obtain the load history, perform cycle counts, and calculate the various results is exactly the same as done with cross-frames. Besides the use of completely different WIM records, another primary difference between the two simulation approaches involves the level of detail in modeling the fatigue design truck. The SHRP 2 study used the fatigue design truck footprint as specified in AASHTO LRFD Article 3.6.1.2.2 (i.e., the individual axle loads are taken as clustered point loads - an 8 kip steering axle followed by two 32 kip axles, spaced at 14 and 30 feet, respectively); this study uses the refined design truck footprint as specified in AASHTO LRFD Article 3.6.1.4.1 (i.e., the individual axle loads are modeled in greater detail as an 8 kip steering axle followed by four 16 kip axles, spaced at 12, 4, 26, and 4 feet, respectively). In the comparison study, the automated scripts also include a 10% dynamic load allowance, since it appears that the SHRP 2 study considers this in the published data.

Table F3-23: Fatigue I and II parameters published in the SHRP 2 R19B for positive bending of a simply-supported 200-foot long bridge. The statistical summary of the parameters is not taken from the SHRP 2 R19B report.

WIM Record Details		Fatigue I Parameters		Fatigue II Parameters		
Site	**No. of Vehicles**	**99.99th Percentile Moment Cycle (kip-ft)**	**99.99th Percentile Moment Cycle Normalized to AASHTO Fatigue Truck (kip-ft)**	**Equivalent Moment (kip-ft)**	**Equivalent Moment (kip-ft) Normalized to the AASHTO Fatigue Truck**	**Fatigue Damage Ratio**
New Mexico	26,501	5,640	1.84	2,594	0.85	0.85
Arizona	1,391,098	4,711	1.54	2,601	0.85	0.85
Arkansas	1,642,334	5,066	1.65	2,555	0.83	0.83
Colorado	326,017	4,854	1.58	2,311	0.75	0.76
Delaware	175,889	5,735	1.87	2,424	0.79	0.79
Illinois	821,809	5,033	1.64	2,533	0.83	0.83
Kansas	456,881	6,083	1.99	2,525	0.82	0.83
Louisiana	70,831	6,616	2.16	2,319	0.76	0.76
Maine	172,333	5,549	1.81	2,206	0.72	0.72
Maryland	124,474	5,061	1.65	1,983	0.65	0.65
Minnesota	47,794	6,225	2.03	2,220	0.72	0.72
Pennsylvania	1,458,818	5,291	1.73	2,469	0.81	0.81
Tennessee	1,583,151	4,906	1.60	2,418	0.79	0.79
Virginia	237,804	5,055	1.65	2,356	0.77	0.77
Wisconsin	209,239	5,396	1.76	2,350	0.77	0.77
Total Count	**8,744,973**	***Mean***	***1.77***		***Mean***	***0.78***
		Mean + 1SD	***1.95***		***Mean + 1SD***	***0.84***
		Mean + 1.5SD	***2.04***		***Mean + 1.5SD***	***0.87***

The results of the comparative study are summarized in Table F3-24 and represent the application of all 18 WIM site records used in this study to the selected bridge. At the bottom of this table, the statistical parameters for this data set are provided, including the mean of the Fatigue I and II parameters, the "mean plus 1 standard deviation" of the Fatigue I and II parameters, and the "mean plus 1.5 standard deviations" of the Fatigue I and II parameters. The good agreement between the responses provides confidence in the modeling approach (i.e., automated scripts), the fatigue parameter calculations (e.g., rainflow counting methodology), as well as the general force effects caused by two different WIM data sets.

Table F3-24: Fatigue I and II parameters using 18 WIM records for positive bending of a simply-supported 200-foot long bridge.

WIM Record Details		Fatigue I Parameters		Fatigue II Parameters		
Site	**No. of Vehicles**	**99.99th Percentile Moment Cycle (kip-ft)**	**99.99th Percentile Moment Cycle Normalized to AASHTO Fatigue Truck (kip-ft)**	**Equivalent Moment (kip-ft)**	**Equivalent Moment (kip-ft) Normalized to the AASHTO Fatigue Truck**	**Fatigue Damage Ratio**
Arizona	1,227,567	6,133	2.00	2,568	0.84	0.84
Arkansas	1,704,481	6,667	2.17	2,727	0.89	0.87
California	1,380,075	4,881	1.59	2,480	0.81	0.81
Colorado	352,198	6,700	2.18	2,405	0.78	0.79
Illinois	798,935	6,061	1.98	2,628	0.86	0.85
Indiana L1	370,241	5,858	1.91	2,525	0.82	0.82
Indiana L3	21,340	5,158	1.68	2,500	0.82	0.82
Indiana L4	360,458	5,525	1.80	2,499	0.82	0.82
Indiana L2	20,158	5,510	1.80	2,695	0.88	0.88
Kansas	436,913	6,294	2.05	2,609	0.85	0.85
Louisiana	76,547	7,326	2.39	2,421	0.79	0.79
Maryland	108,881	5,286	1.72	2,274	0.74	0.73
Minnesota	52,757	7,162	2.34	2,550	0.83	0.83
New Mexico	147,077	5,925	1.93	2,348	0.77	0.76
New Mexico	892,295	7,033	2.29	2,708	0.88	0.88
Pennsylvania	873,903	6,439	2.10	2,623	0.86	0.78
Tennessee L1	550,858	6,750	2.20	2,246	0.73	0.66
Tennessee L2	118,000	4,844	1.58	1,845	0.60	0.54
Tennessee L3	191,330	4,890	1.59	2,106	0.69	0.62
Tennessee L4	1,182,136	6,423	2.09	2,609	0.85	0.77
Virginia L1	224,928	5,700	1.86	2,405	0.78	0.79
Virginia L2	19,300	4,641	1.51	2,286	0.75	0.75
Wisconsin	120,079	6,349	2.07	2,497	0.81	0.82
Total Count	**11,230,457**	***Mean***	***1.95***		***Mean***	***0.79***
		Mean + 1SD	***2.21***		***Mean + 1SD***	***0.87***
		Mean + 1.5SD	***2.34***		***Mean + 1.5SD***	***0.91***

F3.3.4 Multiple Presence Study

The obtained WIM records include multi-lane records for three sites. As two of the sites (Indiana US 31 and Tennessee IH 40) include two lanes of traffic in two directions, the RT obtained a total of five two-lane data sets. With the availability of this higher resolution multi-lane data, the RT performed a study on the WIM records to better understand the statistical parameters surrounding multiple presence. This was performed using a cluster analysis to consider if a bridge may be loaded with other truck traffic during a primary drive lane load event (i.e., passage of one or more axles of a vehicle). The cluster analysis is performed based on the time stamps of the individual truck events, the lengths of the individual trucks, and the speed of the individual trucks. Since bridge lengths vary, the following study incorporates multiple presence load events that occur within a plus or minus 1000-foot window of the primary drive lane load event.

The RT developed a script to determine how many times a second truck is in a lane adjacent to the primary drive lane truck (i.e., a second truck is passing or is being passed by the truck in the drive lane, anywhere along an arbitrary length of 1000 feet). This scenario is illustrated schematically in Figure F3-67. Clear distances are measured from the rear axle of the drive lane truck to the front axle of the passing lane truck. Positive values indicate the passing lane truck's front axles are "behind" the drive lane truck's rear axles, and negative values indicate the passing lane truck's front axles are "ahead of" the drive lane truck's rear axles. This provides a smooth, continuous function of clear distances, with increasing clear distances (positive or negative) indicating a larger separation between vehicles

Note that a clear distance of zero corresponds to a staggered configuration, which was deemed critical to cross-frame force effects in the 7th Edition AASHTO LRFD Specifications. This provision has since been removed beginning with the 8th Edition, citing too infrequent occurrences. This study herein evaluates the frequency of occurrence in the context of cross-frame response.

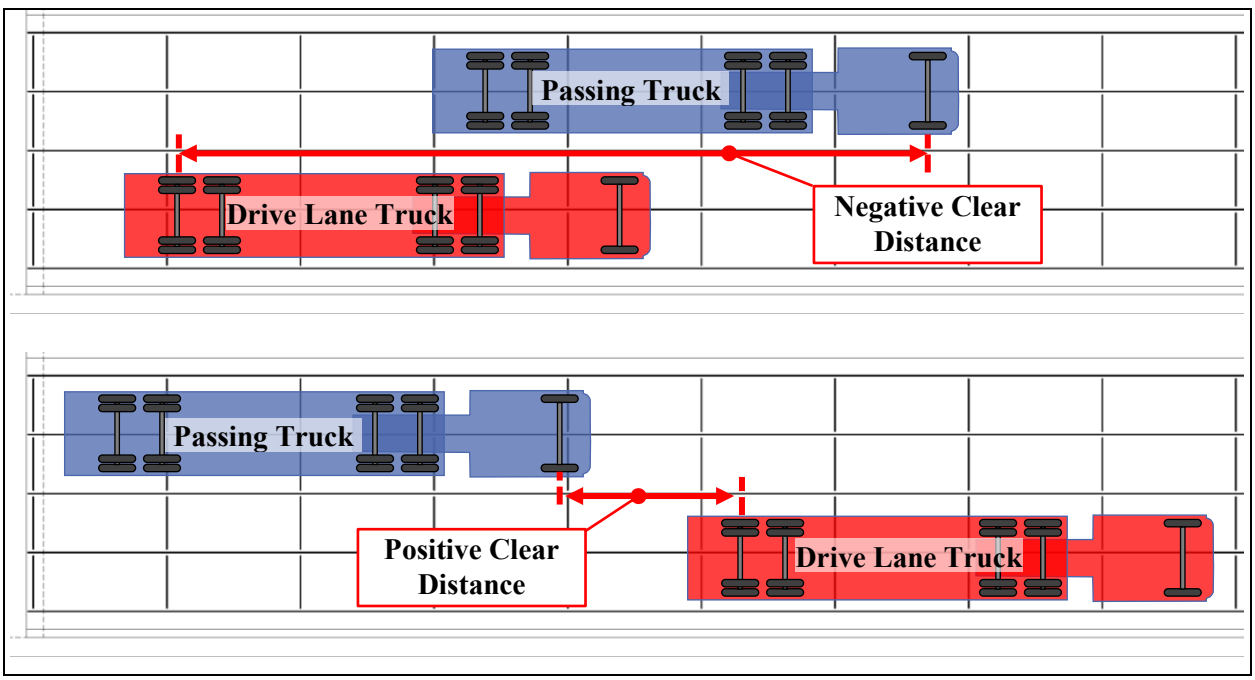

Figure F3-67: Illustration of an adjacent lanes (truck-passing-truck) scenario; negative and positive clear distances indicate the passing truck's front axle is ahead or behind the drive lane truck's rear axle, respectively.

The results of this adjacent lane scenario are summarized in Figure F3-68 through Figure F3-82, which provide histograms illustrating various aspects of multiple presence studied. For various load position parameters (e.g., clear distance between drive-lane and passing truck), the number of occurrences for each multi-lane WIM site is compiled and plotted. Specifically, Figure F3-68 through Figure F3-72 illustrate the clear distances between passing lane trucks and drive lane trucks, Figure F3-73 through Figure F3-77 illustrate the spectrum of GVW for passing lane trucks, and Figure F3-78 through Figure F3-82 illustrate the ratio of passing lane truck GVW to drive lane truck GVW. Note that the occurrences on the primary vertical axis for these histograms are the number of total occurrences for the year's worth of data. This value should be taken into context with the total Annual Truck Traffic (ATT) for the specific site. Table F3-25 summarizes how often (for the year of data considered) any truck was within a certain window of the drive lane truck, relative to the total volume of traffic in the drive lane for each specific site.

Based on these results, it is evident that a passing truck in close proximity to a drive lane truck is a rare occurrence. The frequency of occurrence is less than the assumptions used in the original calibration studies (Nowak 1999). The largest frequency of occurrence is demonstrated by the Tennessee IH40 WB data, where approximately 30% of traffic is accompanied by another vehicle located with a headway distance of less than 1000 feet, and 1.8% of traffic is accompanied by another vehicle located with a headway distance less than 20 feet. For the most critical passing lane position for cross-frames (one directly behind another, or zero clear distance), the largest frequency of occurrence is demonstrated to be 0.03%. Recalling that cross-frame forces generally reduce rapidly as a truck moves away from the cross-frame in the longitudinal direction, it is apparent that, for cross-frames, the largest frequency of occurrence for passing vehicles occurring simultaneously is appreciably low (i.e., larger headway distances generally do not result in superimposed cross-frame forces). Another observation is that the distribution of the passing lane truck's GVW appears to be bi-modal for several sites, with the heavier truck mode being equal or heavier to the drive lane truck's GVW. Sensitivity studies were conducted by White (2020) that explicitly accounted for the cross-frame force effects caused by passing lane vehicles, and the effects on the accumulated fatigue damage was found to be negligible.

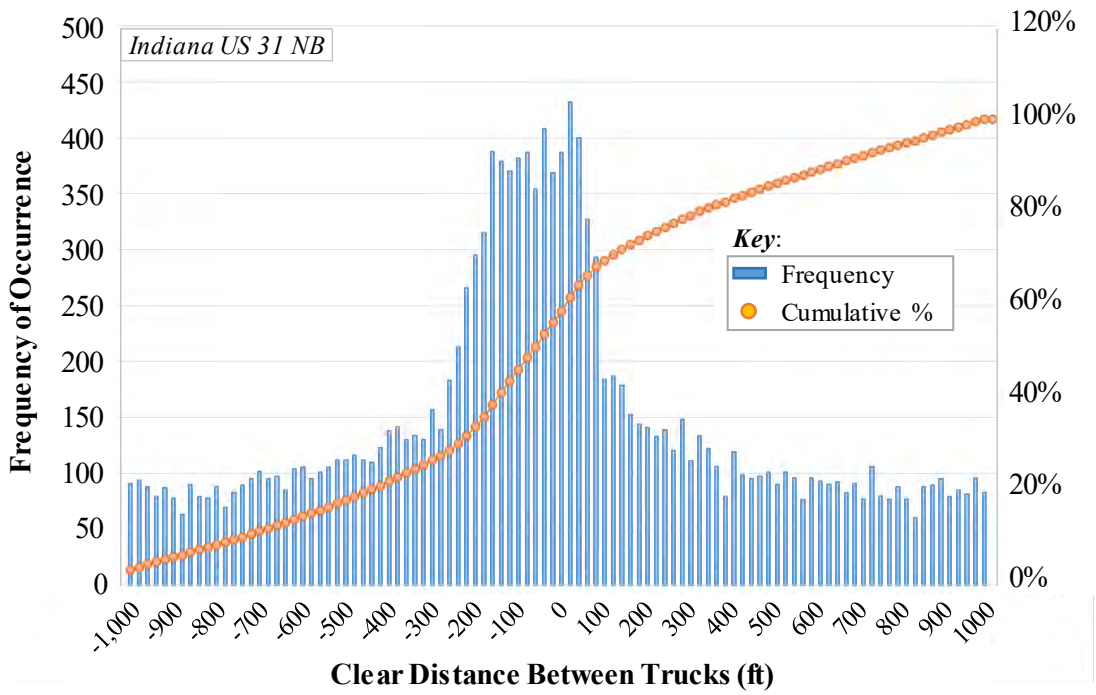

Figure F3-68: Histogram from two-lane WIM records, showing the clear distance between a passing truck and the drive lane truck (Indiana US 31 NB)

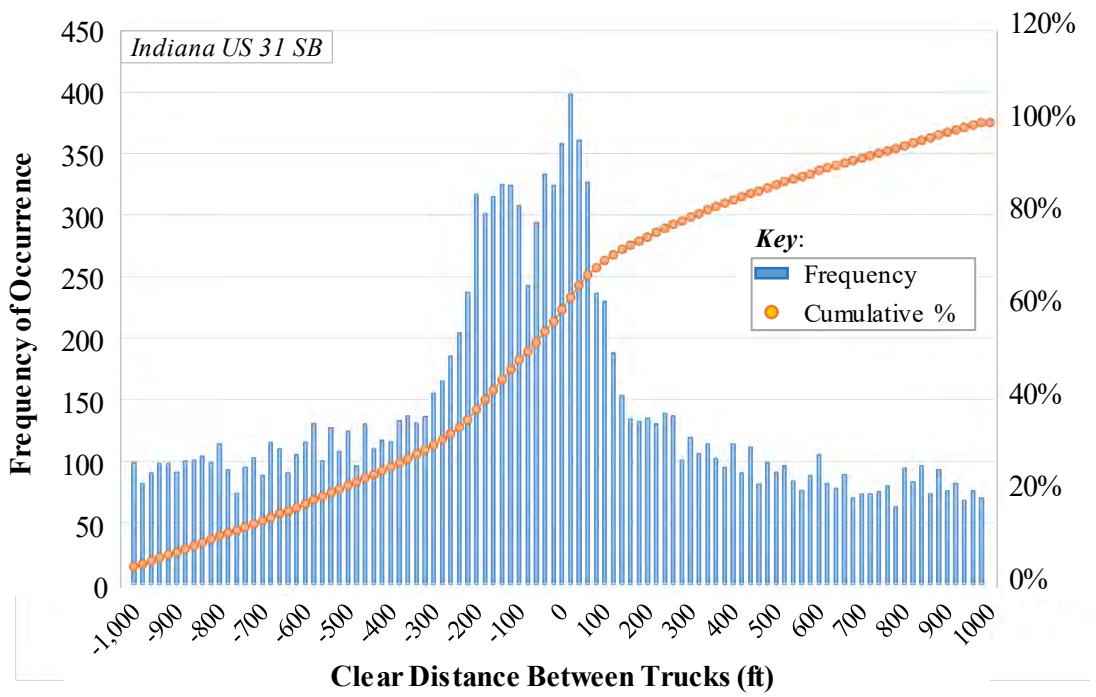

Figure F3-69: Histogram from two-lane WIM records, showing the clear distance between a passing truck and the drive lane truck (Indiana US 31 SB)

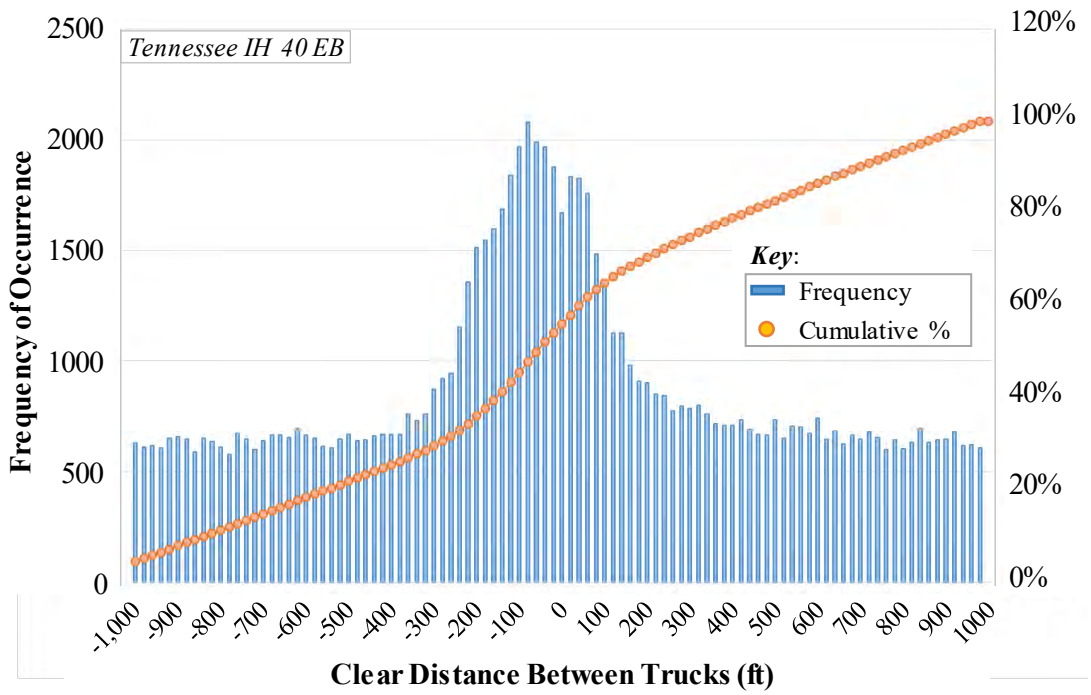

Figure F3-70: Histogram from two-lane WIM records, showing the clear distance between a passing truck and the drive lane truck (Tennessee IH 40 EB)

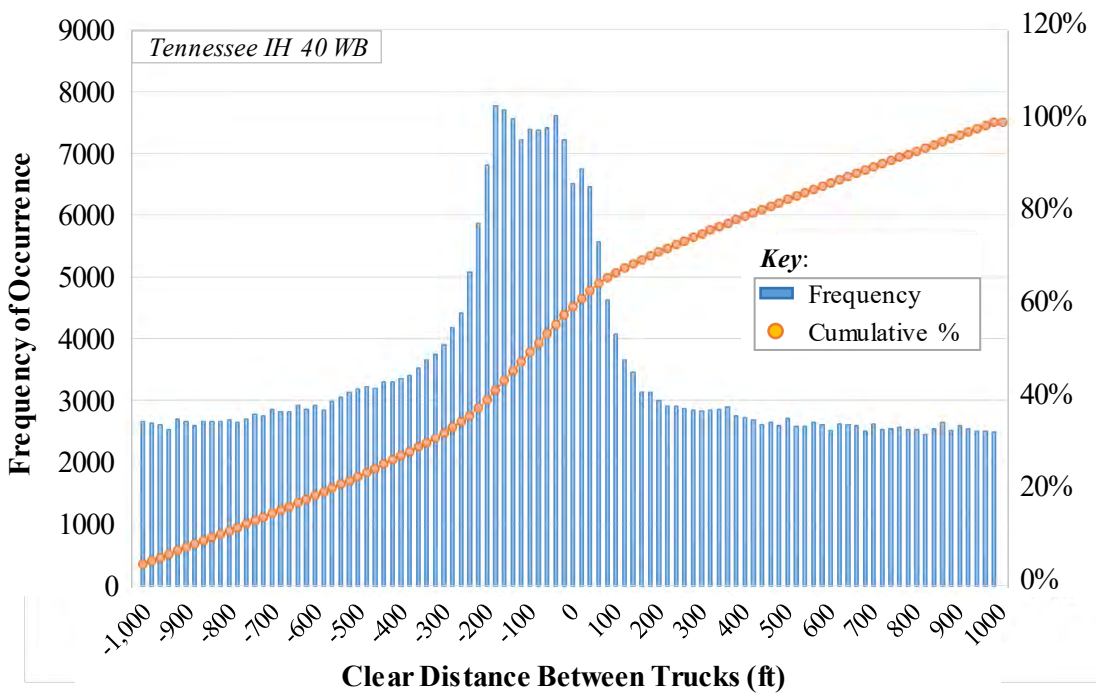

Figure F3-71: Histogram from two-lane WIM records, showing the clear distance between a passing truck and the drive lane truck (Tennessee IH 40 WB)

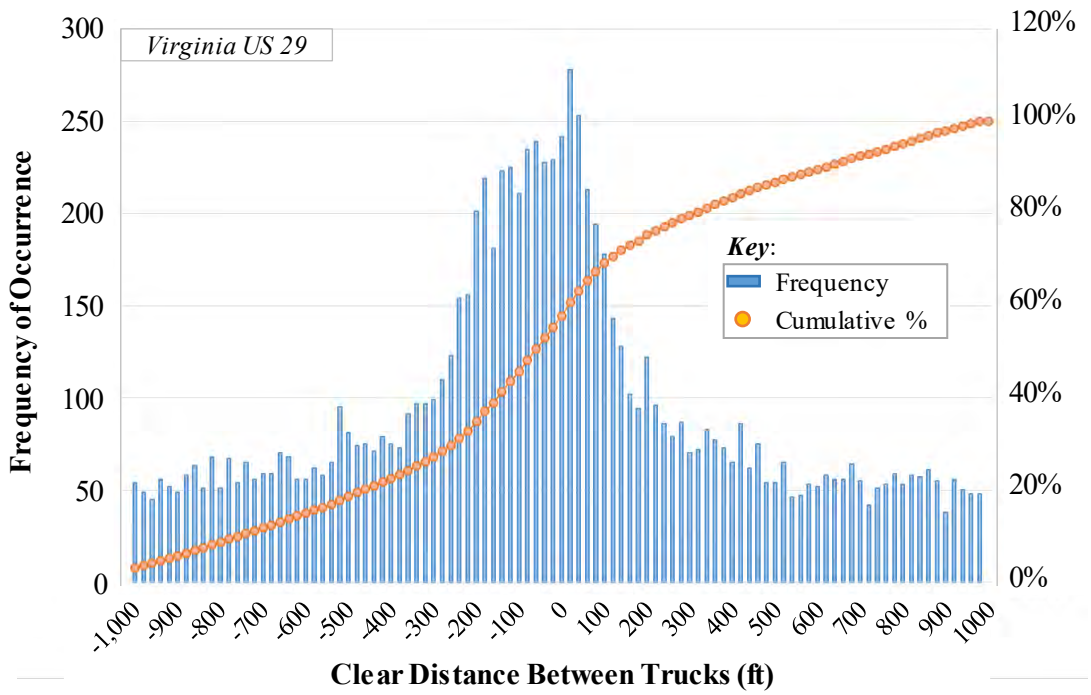

Figure F3-72: Histogram from two-lane WIM records, showing the clear distance between a passing truck and the drive lane truck (Virginia US 29)

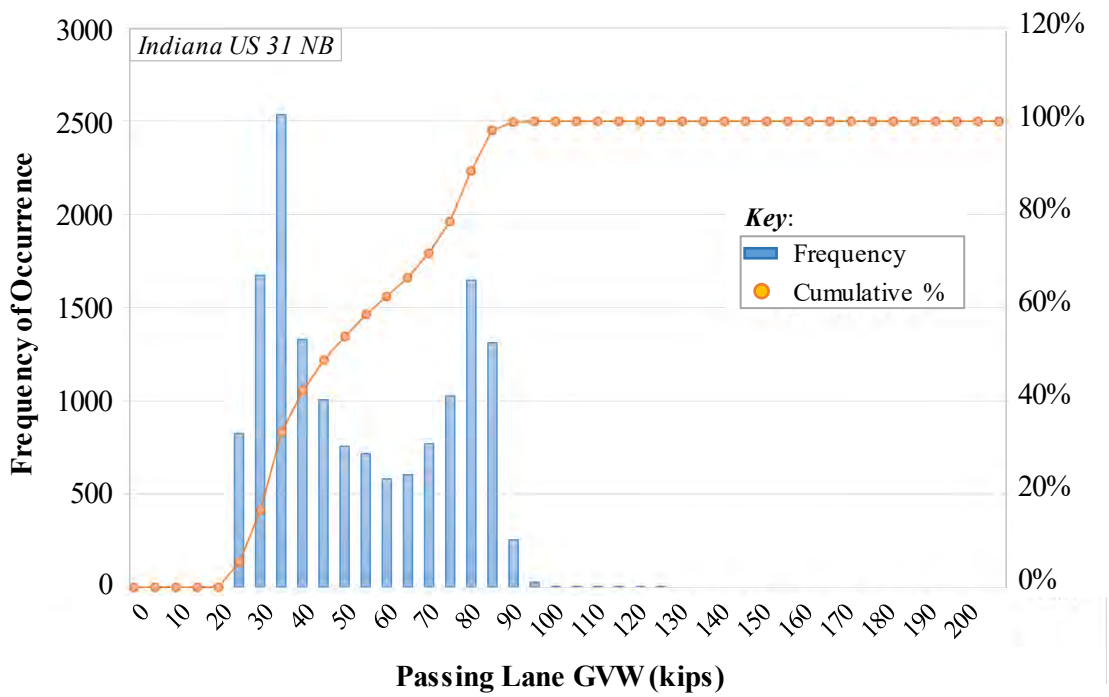

Figure F3-73: Histogram from two-lane WIM records, showing GVW of a passing truck (Indiana US 31 NB)

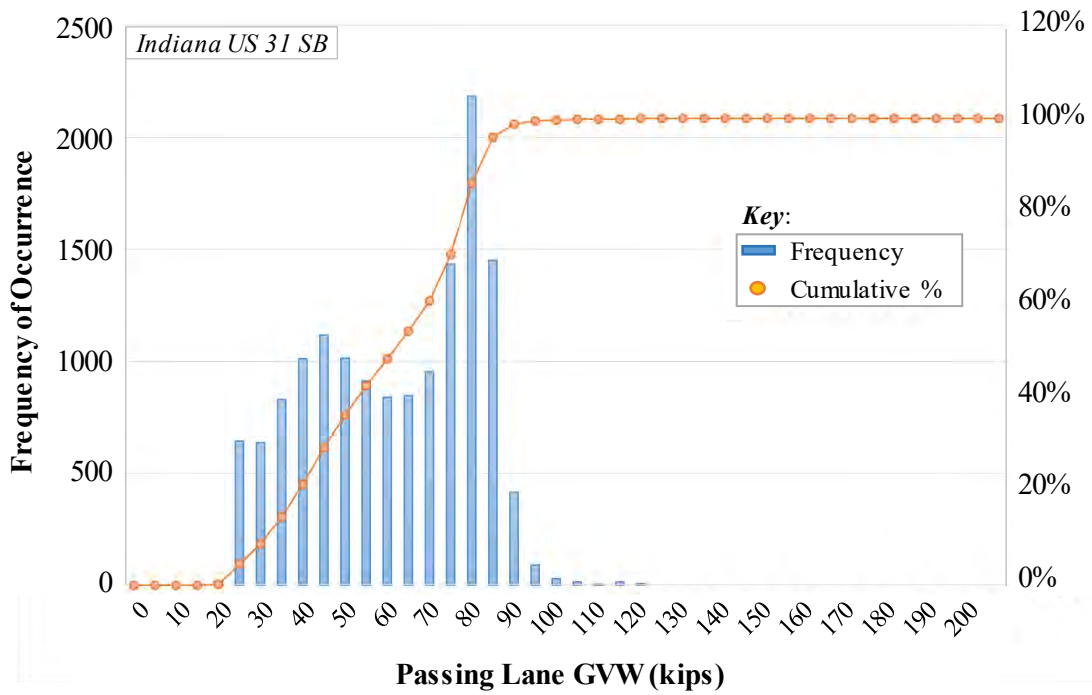

Figure F3-74: Histogram from two-lane WIM records, showing GVW of a passing truck (Indiana US 31 SB)

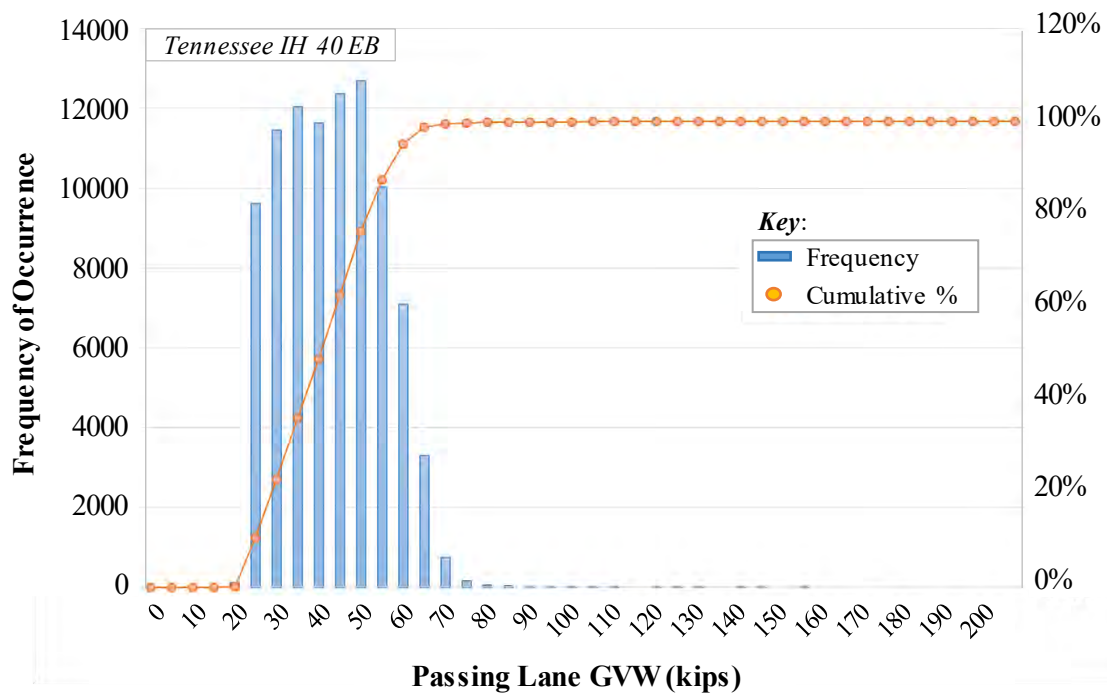

Figure F3-75: Histogram from two-lane WIM records, showing GVW of a passing truck (Tennessee IH 40 EB)

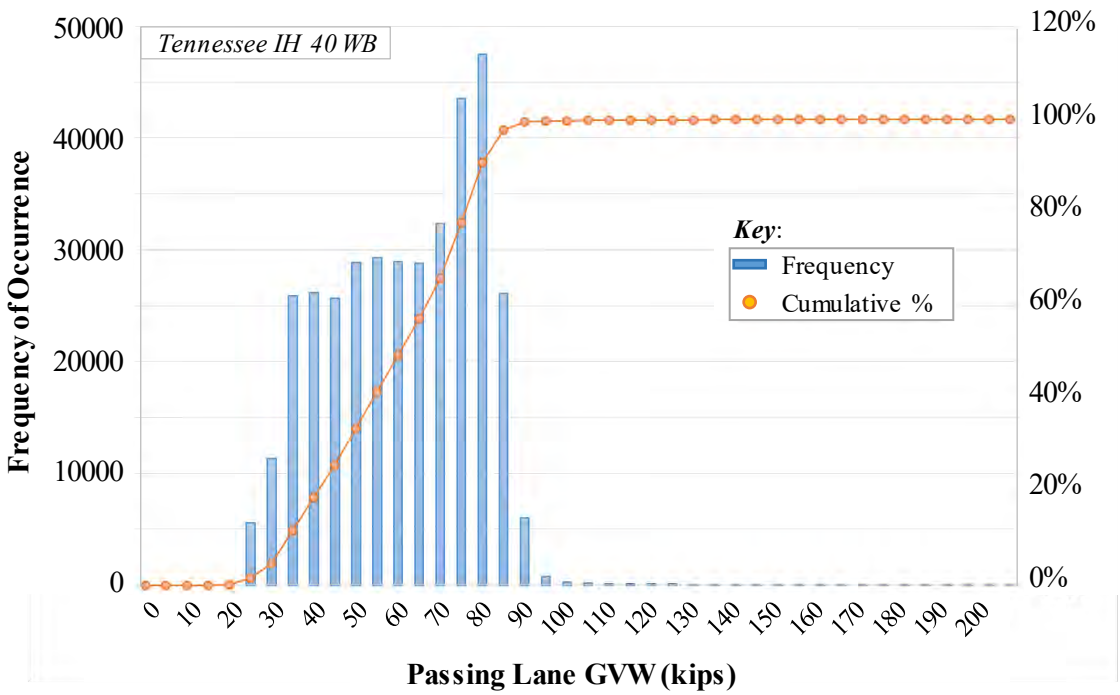

Figure F3-76: Histogram from two-lane WIM records, showing GVW of a passing truck (Tennessee IH 40 WB)

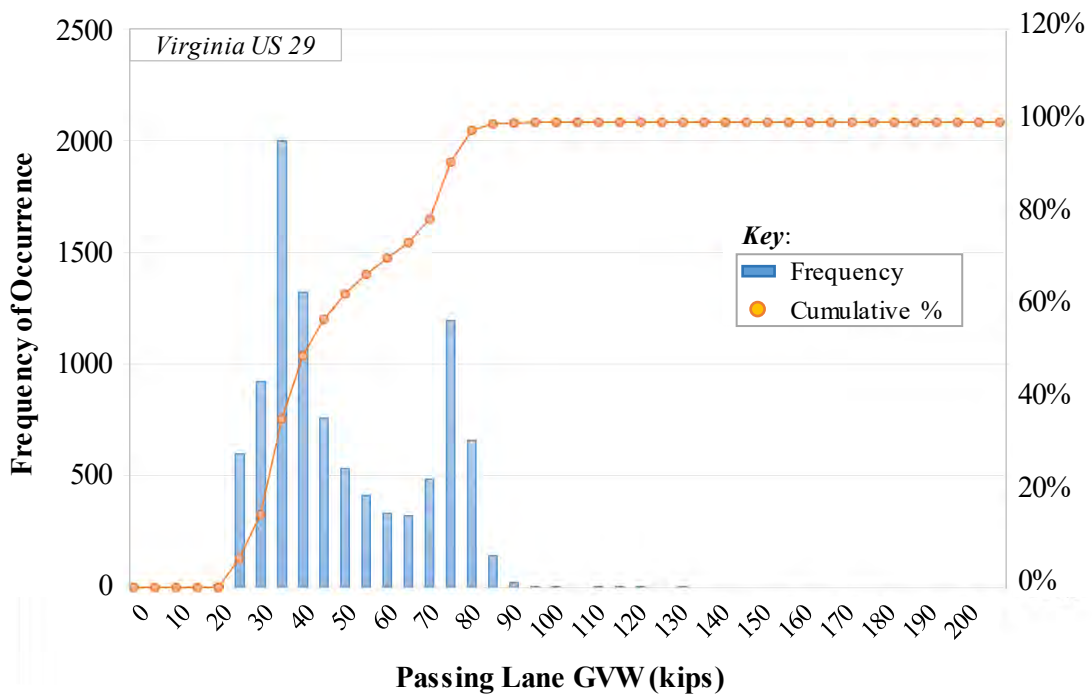

Figure F3-77: Histogram from two-lane WIM records, showing GVW of a passing truck (Virginia US 29)

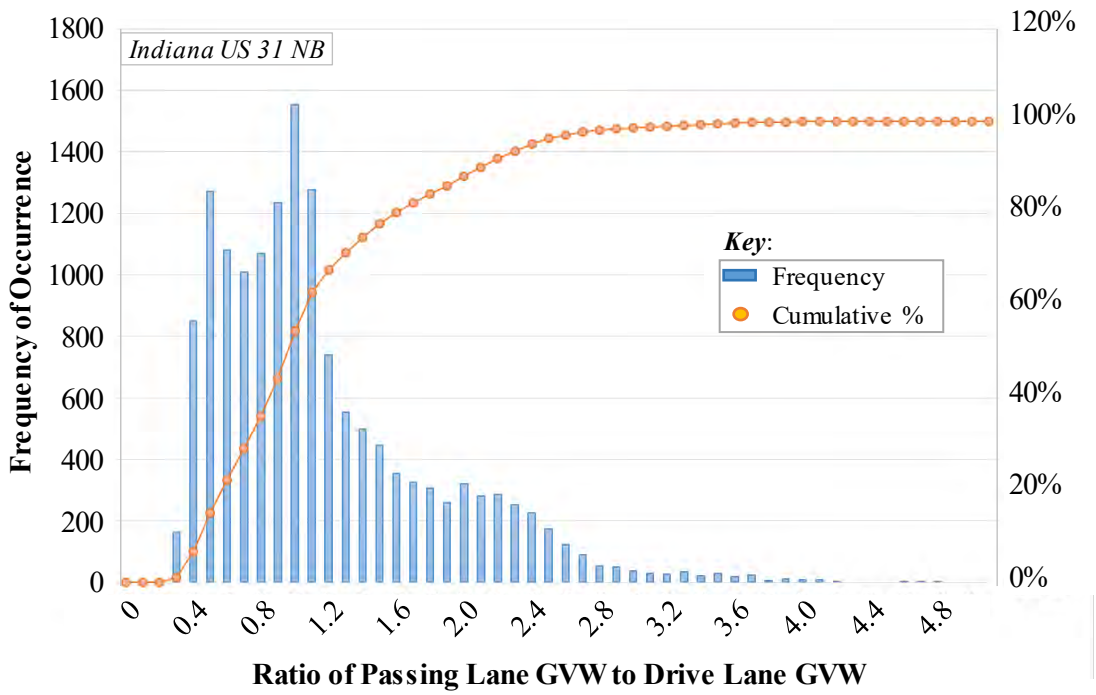

Figure F3-78: Histogram from two-lane WIM records, showing the ratio of the passing lane GVW to the drive lane GVW (Indiana US 31 NB)

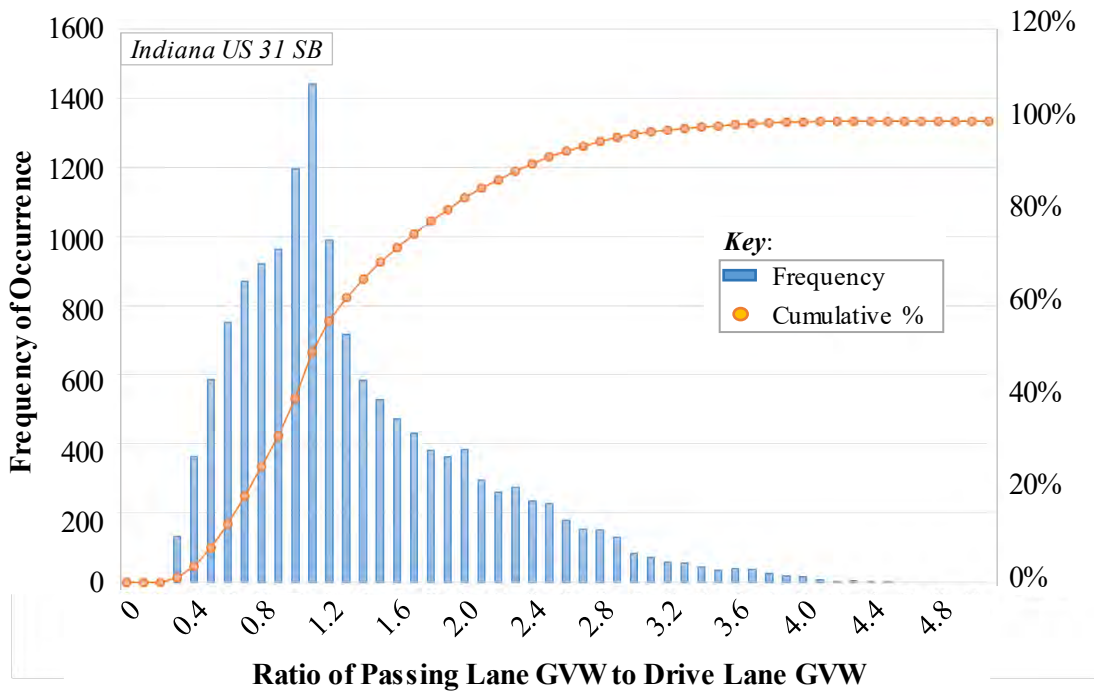

Figure F3-79: Histogram from two-lane WIM records, showing the ratio of the passing lane GVW to the drive lane GVW (Indiana US 31 SB)

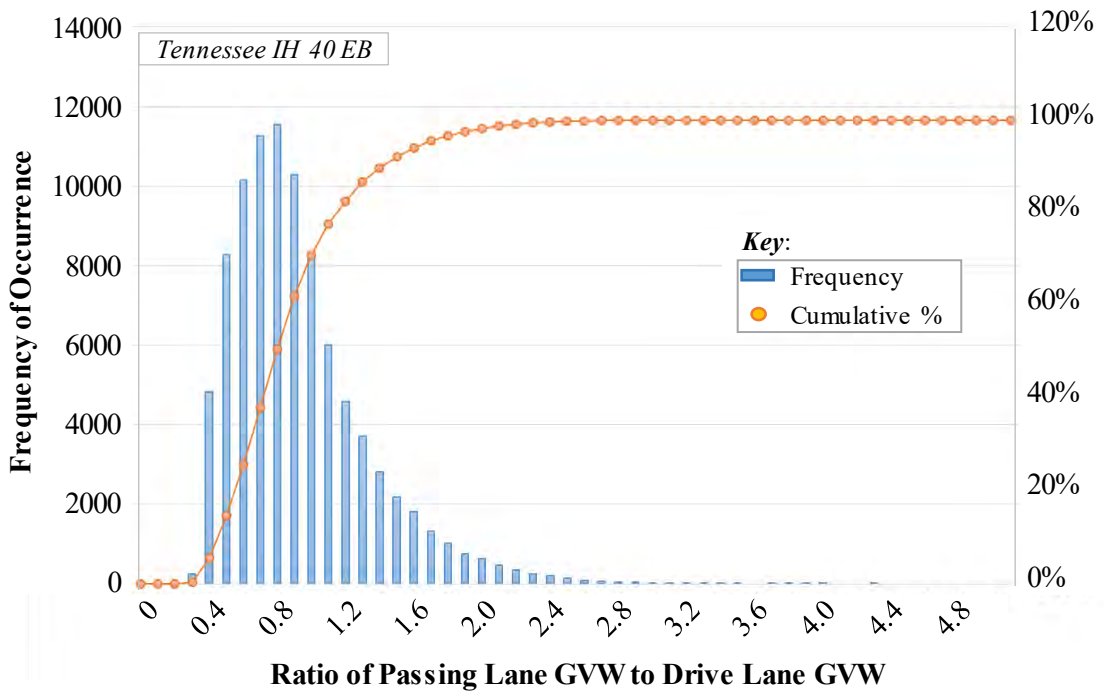

Figure F3-80: Histogram from two-lane WIM records, showing the ratio of the passing lane GVW to the drive lane GVW (Tennessee IH 40 EB)

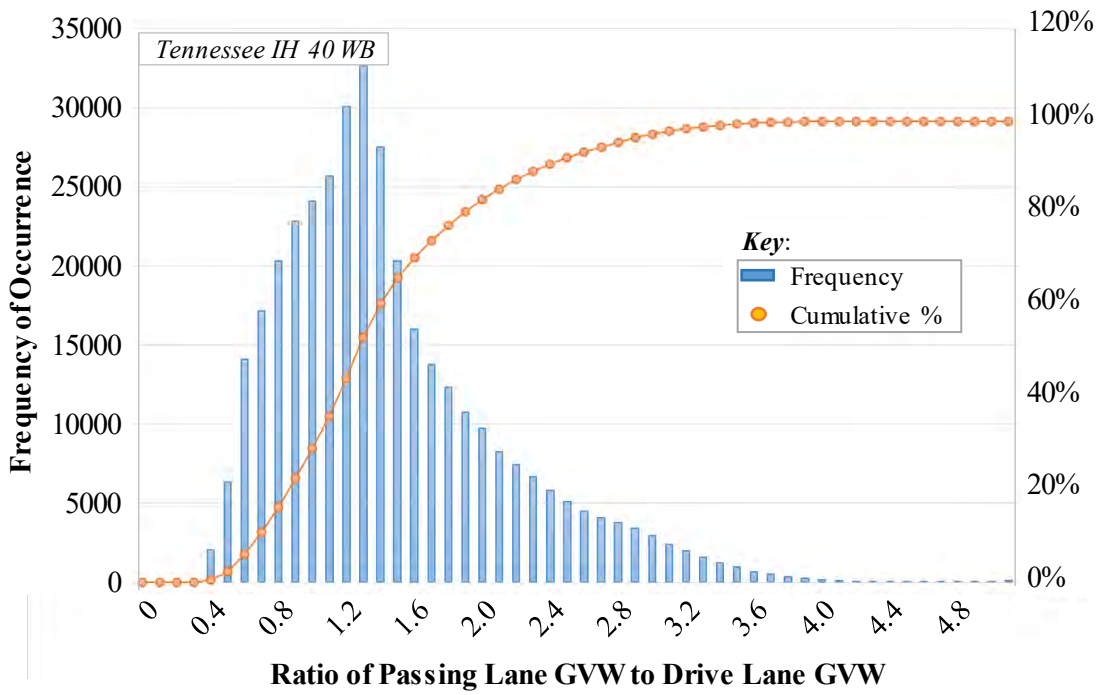

Figure F3-81: Histogram from two-lane WIM records, showing the ratio of the passing lane GVW to the drive lane GVW (Tennessee IH 40 WB)

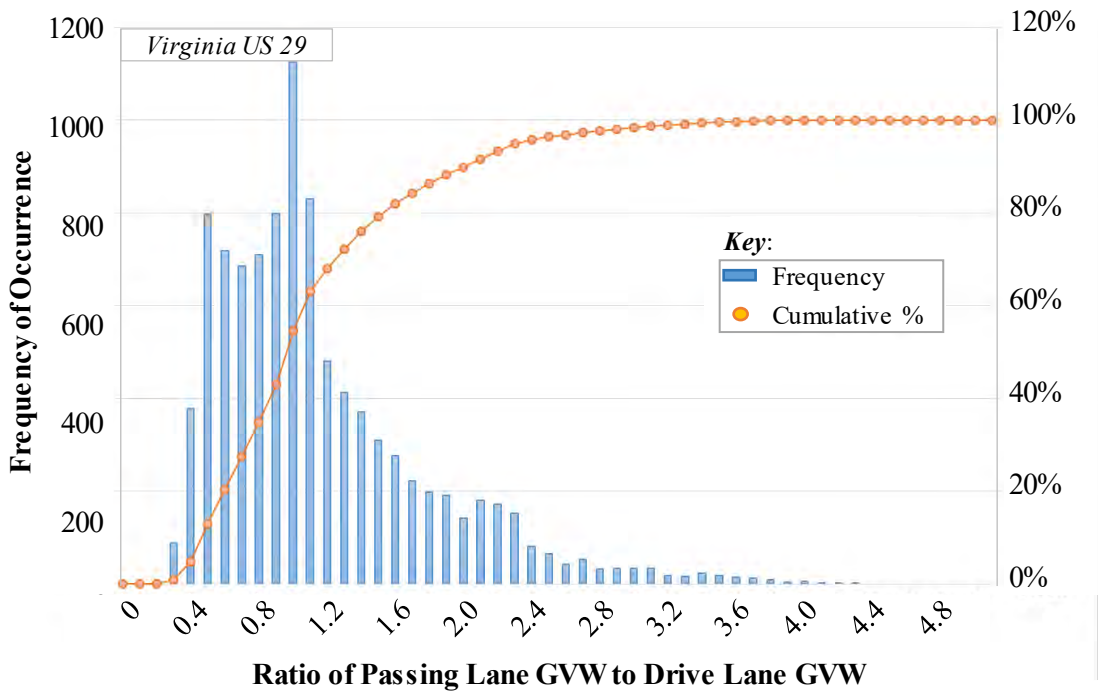

Figure F3-82: Histogram from two-lane WIM records, showing the ratio of the passing lane GVW to the drive lane GVW (Virginia US 29)

F3.3.4.1 Comparison of Statistical Parameters with Literature

The RT understands that the assumptions of multiple presence in original calibration studies (Nowak 1999) were initially based on engineering judgement and visual observations of truck traffic with unknown weights. These initial assumptions were that a "side by side" scenario (i.e., adjacent lane loaded with a passing truck in general alignment with the drive lane truck) occurred once every 15 load events. More recent studies have shown this assumption to be excessively conservative (Sivakumar et al. 2007). The research presented in the SHRP 2 R19B project attempted to verify certain statistical assumptions of multiple presence; however, the WIM records used in these studies have a time resolution of 1 second. At 70 miles per hour, plus or minus 1 second is equivalent to approximately plus or minus 100 feet. Since, at this resolution it is impossible to determine if another truck is even on the same span as the truck in question, higher-resolution data is essential to evaluate the frequency of occurrence of multiple presence. At 70 miles per hour, the 0.01 second resolution data the RT obtained from the FHWA will generally provide a resolution of plus or minus 1 foot.

Table F3-25: Summary of Multiple Presence Statistics for Adjacent Lane Loaded

WIM Site	Frequency of Occurrence within Clear Distance Window, Relative to Drive Lane Annual Truck Traffic (ATT) [a]				
	+/- 1000 ft	+/- 280 ft	+/- 50 ft	+/- 20 ft	+/- 0 ft
Indiana US 31 NB	4.0%	2.1%	0.5%	0.3%	0.01%
Indiana US 31 SB	4.2%	2.2%	0.5%	0.3%	0.00%
Tennessee IH 40 EB	16.0%	7.4%	1.7%	1.0%	0.02%
Tennessee IH 40 WB	29.9%	13.2%	3.0%	1.8%	0.03%
Virginia US 29	3.9%	2.0%	0.5%	0.3%	0.01%

[a]*Reference Figure F3-67 for illustration of positive and negative clear distances.*

F3.3.5 Reliability Studies using Published Resistance Data

This section discusses the implications of using the load statistics developed in Section F3.3.2.2 for fatigue of cross-frames in steel I-girder bridges in the context of a reliability-based design. Using these statistical characterizations of the total load effect, it is possible to compare this to the statistical characterization of fatigue resistance provided in the literature (Kulicki et al. 2015). Stochastic models can be implemented that utilize these characterizations of load and resistance to provide an indication of reliability, given a specific choice of design parameters.

The reliability study discussed in this section is performed via Monte Carlo simulation, in which values of load and resistance are obtained through a randomly determined process using the distribution parameters for load and resistance.

F3.3.5.1.1 Statistical Characterization of Available Resistance Data for Cross-Frames

The SHRP 2 R19B project's calibration of AASHTO LRFD's fatigue limit states (Kulicki et al. 2015) required a review of the resistance data originally collected by Keating and Fisher (1986). As part of the calibration, the R19B research required key statistical parameters from this data, which was not previously characterized. Because the original resistance studies only reported the relationship between stress ranges and number of cycles to failure, and each specimen group tested was often tested over small increments of stress ranges and limited in number, this made it difficult to fit one statistical distribution to the available data. By relating the constant amplitude stress ranges for a given test specimen to an effective constant amplitude stress range, the R19B project calculated a fatigue damage parameter, S_{fi}, which is defined as:

$$S_{fi} = (N * S_{ri}^3)^{\frac{1}{3}} \qquad \textit{F3.16}$$

where: N = number of cycles; and S_{ri} = constant amplitude stress range for a group of cycles (ksi).

The distribution of this fatigue damage parameter for each of the detail categories was then used to calculate the statistical parameters for that detail category. Table F3-26 summarizes the statistical parameters R19B developed for all eight detail categories. Note that the design value used to calculate the bias was obtained by taking the cube root of the constant, A, for the respective detail category found in AASHTO Table 6.6.1.2.5-1 (2015).

For the purposes of this study, the statistical parameters developed by Kulicki et al. (2015) are assumed to accurately represent the various fatigue categories. While this study will consider all detail categories, the category E' is of particularly importance to cross-frames, since most cross-frame members consist of single angle welded connections which are defined as a Category E' detail.

Table F3-26: Statistical parameters for resistance as calculated from SHRP 2 R19B (Kulicki et al. 2015).

Category	Standard Deviation	CV	Bias, λ	Measured Fatigue Parameter	Design Fatigue Parameter
A	1000.0	0.24	1.43	4,167.40	2,924
B	666.7	0.22	1.34	3,077.47	2,289
B'	250.0	0.11	1.28	2,336.10	1,827
C and C'	454.6	0.21	1.35	2,210.77	1,638
D	185.2	0.10	1.36	1,773.69	1,300
E	140.9	0.12	1.17	1,207.41	1,032
E'	232.6	0.20	1.56	1,1140.28	730

F3.3.5.1.2 Stochastic Simulation via the Monte Carlo Technique

The statistical parameters describing the load effects in cross-frames for the Fatigue I and II limit states was discussed in Section F3.3.2.2. For Fatigue I, the mean of all 99.99th percentile stress ranges implies an appropriate load factor for the Fatigue I limit state design of cross-frames falls between 1.01 (prior to 25% CAFL filtering) to 1.25 (after 25% CAFL filtering), as summarized in Table F3-21. These values bound a more appropriate load factor for fatigue design of cross-frames. Since the Fatigue I limit state is intended to represent the maximum stress ranges produced by the general truck population, and the truncated stresses were predominantly caused by the truck population (i.e., lightweight vehicles were discarded and the resulting records should be primarily truck traffic), it is most likely appropriate to rely on the records obtained prior to the truncation of the 25% CAFL stresses as a realistic population for examining the top 99.99% stress ranges. In other words, truncating lower stress ranges that are experienced in cross-frames by truck traffic artificially increases the 99.99th percentile of the realistic force effect spectrum. For Fatigue II, the "mean plus 1.5 standard deviations" (for normal distributions, "mean plus 1.5 standard deviations" includes approximately 93% of the population) implies an appropriate load factor for the Fatigue II limit state design of cross-frames falls between 0.49 to 0.53 (prior to 25% CAFL filtering) and 0.47 to 0.51 (after 25% CAFL filtering), as summarized in Table F3-22. These values bound a more appropriate Fatigue II load factor for design of cross-frames. The truncation of 25% CAFL stresses was an exercise to study the overall effects of this simplification when performed on truck traffic (i.e., passenger vehicles are already removed, so this truncation is primarily affecting stress ranges caused by truck traffic). While this approach may be warranted when collecting rainflow data during in-service monitoring to preserve data storage and

increase computational efficiency, for this study, the truncation of stresses removes data considered to accurately represent truck traffic. Therefore, for the reliability study, the values obtained without filtering will be used. The statistical parameters describing the load effects in cross-frames for the Fatigue I and II limit states used for additional reliability study are repeated in Table F3-27 for convenience.

Table F3-27: Statistical parameters describing the load effects in cross-frames for Fatigue I and II limit states.

Limit State	Coefficient of Variation of Load	Bias for Load Data	Load Factor
Fatigue I	0.26	1.01	1.01
Fatigue II	0.21	0.40	0.53

A Monte Carlo simulation was performed using the statistical summaries for resistance and cross-frame force effects previously described. For the simulation, a total of 10,000 samples were randomly generated from the distributions of load and resistance described by the statistical parameters. The following procedure was used in the development of this simulation:

1. **Define the nominal loads and nominal resistance**. For the purposes of this Monte Carlo simulation, this can merely be the relationship of nominal values per AASHTO LRFD (i.e., it is desirable to obtain a measure of reliability at the limit state failure boundary, where an element is allowed to be designed to be *just sufficient* for given a load). For both limit states, the relationship follows the generalized limit state, using the appropriate recommended load factors:

$$\gamma(\Delta f) \leq (\Delta F)_n \qquad \text{F3.17}$$

For Fatigue I, this relationship is as follows:

$$1.01 * (Q_N + IM) = R_n \qquad \text{F3.18}$$

For Fatigue II, this relationship is as follows:

$$0.53 * (Q_N + IM) = R_n \qquad \text{F3.19}$$

Note the inclusion of the dynamic allowance factor per AASHTO LRFD. This is equivalent to 1.15 of the fatigue stress range.

2. **Choose a selection of ADTTs.** In design, a member is first checked for infinite life (Fatigue I) using AASHTO LRFD Table 6.6.1.2.3-2. If the ADTT is equal to or below the value for the specific category, the member passes Fatigue I (infinite life) and only requires a check for Fatigue II. If the ADTT is above the value indicated for the specific category, then only the Fatigue I limit state is checked. For this step in the simulation, it is important to capture realistic ADTTs that fall above and below the thresholds that differentiate between requiring a Fatigue I or Fatigue II limit state check. In this manner, each detail category can be adequately sampled. The choice of ADTT ranges for consideration was balanced against how many failures were observed: for a Monte Carlo simulation, it is important to have a sufficient number of failures; otherwise, the sample size should be increased. For this study, the following range of ADTTs was chosen: 100, 1,000, 1,500, 2,500, 5,000, and 10,000.

3. **Perform the Monte Carlo simulation**. For the load effect being investigated, Q_N, define the associated resistance, R_N, through the relationship in Step 1. Then, for each ADTT in Step 2, a Monte Carlo simulation is performed by randomly selecting from these load and resistance distributions using the statistical parameters describing these distributions in Table F3-27. Note that the load effect chosen is arbitrary - the important consideration is that the relationship between load and resistance is maintained. It is necessary to generate a uniformly distributed random number, u_i, for randomly selecting nominal loads and resistances. The random number should be in the domain: $0 \leq u_i \leq 1$. The number of values generated, N, should generally be sufficient for at least 10 failures to occur. For this study, the number of values generated, N, is taken as 10,000 (i.e., 10,000 random values for each random value calculated). For each of the N randomly selected values, the following steps are taken:
    a. Iteratively sample from the load and resistance distributions. An individual sample (Q_i for load and R_i for resistance) is calculated by randomly selecting a value on either side of the mean, (μ_Q for load and μ_R for resistance). The location of this value relative to the mean is calculated by calculating the inverse normal distribution value associated with the uniformly distributed random number ($\phi^{-1}(u_{Qi})$ for load and $\phi^{-1}(u_{Ri})$ for resistance). This is performed by the following equation for live load:

$$Q_i = \mu_Q + \sigma_Q \phi^{-1}(u_{Qi}) \qquad \text{F3.20}$$

    and a similar equation for resistance:

$$R_i = \mu_R + \sigma_R \phi^{-1}(u_{Ri}) \qquad \text{F3.21}$$

    b. Calculate and store the evaluation of the limit state function: $G_i = R_i - Q_i$.
2. **Rank the limit state function values.** Rank the individual values calculated for the limit state function above in ascending order, and for each value i, calculate the individual probability of the occurrence, p_i, per Eq. F3.22 and the corresponding value of the inverse standard normal distribution ($\phi^{-1}(p_i)$).

$$p_i = \frac{i}{i + N} \qquad \text{F3.22}$$

4. **Create a cumulative distribution plot (CDF) of the limit state function results**. This is done by plotting the inverse standard normal distribution values, $\phi^{-1}(p_i)$ versus the corresponding, ranked individual values, G_i.
5. **Calculate the reliability index, $\boldsymbol{\beta}$**. This value can be obtained from the CDF above by taking the negative value of the CDF function where $G = 0$.

The simulation described above was performed for the cross-frame statistics in Table F3-27 for each detail category. The resulting reliability indices are shown in Table F3-28. Based on the reliability analysis performed, the resulting reliability indices for the Fatigue II limit state for cross-frames using the load factors developed in Section F3.3.2.2 generally exceed the target reliability assumed inherent within the AASHTO LRFD code ($\beta = 1$) as presented in the SHRP 2 R19B study. The resulting reliability indices for the Fatigue I limit state for cross frames varies, with several detail categories less than 1.

Table F3-28: Reliability of cross-frames for Fatigue I and II limit states using new load factors.

Detail Category	Reliability Index	
	Fatigue I	Fatigue II
A	1.01	1.77
B	0.88	1.74
B’	0.98	2.47
C	0.93	1.82
C’	0.93	1.82
D	1.27	2.89
E	0.60	1.95
E’	1.41	2.31

In order to obtain a reliability index close to the assumed target reliability of 1, adjustments to resistance factors are preferred. As an alternative to altering the resistance factors (or the associated changes in constant amplitude fatigue thresholds, $(\Delta F)_{TH}$, for Fatigue I, or detail constants, A, for Fatigue II) it is also possible to increase the load factor for fatigue such that the minimum target reliability of 1 is achieved for each category. Additionally, as an alternative to introducing two new load factors for the fatigue limit state for cross-frames, it is possible to apply a single adjustment factor to the existing load factors. Using an adjustment factor of 0.65 applied to the Fatigue I load factor of 1.75 (i.e., a resultant load factor for cross-frames of 1.14 for Fatigue I) and the Fatigue II load factor of 0.8 (i.e., a resultant load factor for cross-frames of 0.52), the resulting reliability indices are calculated via Monte Carlo simulation and shown in Table F3-29. Each detail category satisfies the minimum assumed target reliability of 1.

Table F3-29: Reliability of cross-frames for Fatigue I and II limit states using adjustment factor of 0.65 to existing load factors.

Detail Category	Reliability Index	
	Fatigue I	Fatigue II
A	1.32	1.74
B	1.22	1.70
B’	1.49	2.39
C	1.29	1.79
C’	1.30	1.77
D	1.82	2.81
E	1.08	1.87
E’	1.77	2.25

F3.3.6 Revisiting AASHTO Fatigue Design

Based on the fact that reduced cross-frame-specific load factors have been proposed to eliminate a source of conservatism observed in the fatigue loading model, it is worthwhile revisiting Figure F3-49. Recall that Figure F3-49 evaluated the fatigue design performance of cross-frames in each of the 4,104 bridges studied. Based on those results, it was apparent that current AASHTO design criteria indicate a potential load-induced fatigue problem in common cross-frame configurations, despite the lack of physical evidence in constructed superstructures across the US. As such, Figure F3-49 is replicated in Figure F3-83 with two notable exceptions.

First, the Fatigue II load factors inherently built into the force demands (i.e., the numerator of the D/C ratio) are reduced from 0.80 to 0.52 based on the recommendations outlined in the previous sections. Note that the resistance model (i.e., the denominator in the D/C ratio) remains unchanged. The second major exception is in how skewed and curved bridges are organized and presented. Rather than simply grouping the bridges based on the presence of support skew and/or horizontal curvature, the indexes developed in NCHRP Report 725 (White, et al. 2012) are adopted.

Thus, each bridge in the 4,104-model data set are grouped based on the skew and connectivity index (previously defined in Eqs. F3.6 and F3.7) bounds established in NCHRP Report 725. For instance, heavily curved bridges are differentiated from moderately curved bridges by $I_c > 1$ and $I_c \leq 1$, respectively. By organizing the figure in this manner, the criticality of a particular bridge type in terms of load-induced fatigue forces in cross-frames can be clearly delineated. It is also important to note that Figure F3-83 only investigates fatigue performance in the 4,104 bridges with respect to the high-volume truck traffic in Houston, TX. The results for low-volume Llano traffic would be much less severe.

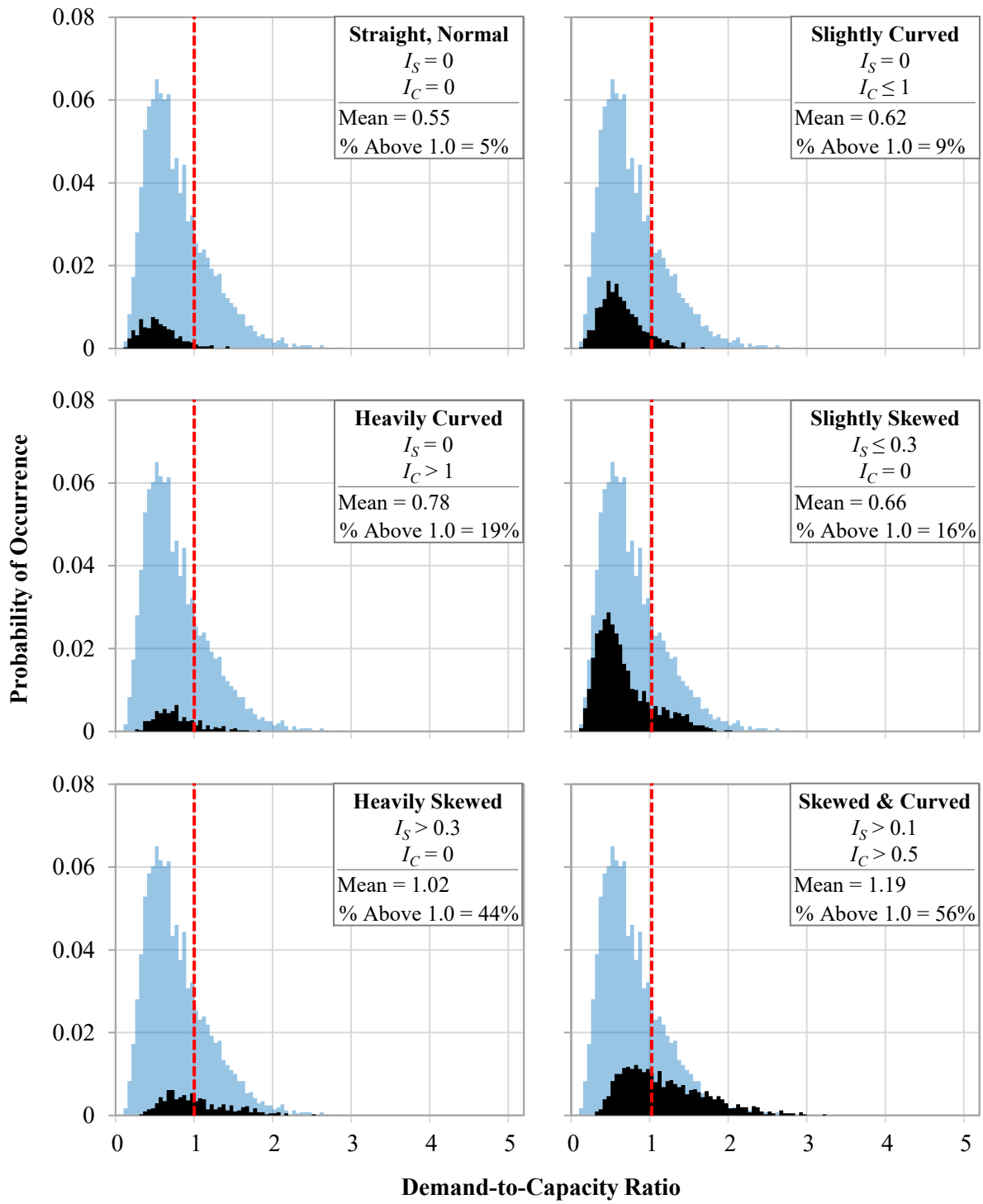

Figure F3-83: Fatigue II demand-to-capacity ratios for various bridge types (Houston I-10 traffic) using reduced load factors

With consideration of the proposed cross-frame-specific load factors and I-10 Houston traffic, the following observations can be made from Figure F3-83:

- In straight bridges with normal supports, the average D/C ratio was 0.55, where only 5% of the 312 qualifying bridges exceeded unity. This indicates that load-induced fatigue forces are generally not substantial in these bridge types, which also implies that conducting a 2D or 3D refined analysis to obtain live load force effects in cross-frames is likely not warranted. This observation is consistent with the current AASHTO LRFD design approach.
- For moderately curved bridges ($I_c \leq 1$) the mean D/C ratio (0.62) increased slightly compared to straight bridges, and only 9% of the qualifying data points exceeded unity. This indicates that moderately curved bridges with normal supports are not likely candidates for significant load-induced fatigue cracking. In contrast, heavily curved bridges ($I_c > 1$) showed an increase in mean D/C ratio to 0.78 and an increase in percent exceeding unity to 19%. Thus, it is recommended that cross-frames in bridges with a connectivity index exceeding 1.0 be analyzed for fatigue loads via a 2D or 3D analysis model, as discussed in Chapters F4 and F5.
- It is evident that support skew affects cross-frame force demands more significantly than horizontal curvature. Slightly skewed bridges ($I_s \leq 0.3$) and heavily skewed bridges ($I_s > 0.3$) produced mean D/C ratios of 0.66 and 1.02, respectively. Additional statistical analysis showed that that obtaining fatigue loads and designing for load-induced fatigue is likely critical for cross-frames in bridges with a skew index exceeding 0.15.
- For bridges with both support skew and horizontal curvature (i.e., $I_c > 0.5$ and $I_s > 0.1$), the mean D/C reported was 1.19, which indicates a significant load-induced fatigue issue even with the reduced load factors. Consequently, these bridges would likely need to be redesigned or the cross-frames reconfigured to mitigate the fatigue force demands. A refined 2D and 3D analysis would be required to accurately obtain those design forces.

F3.4 Major Outcomes

Based on the results of the Fatigue Loading Study presented in the preceding subsections, there are several major conclusions that can be drawn with respect to the appropriate fatigue stress ranges in cross-frame systems:

- Cross-frames are sensitive to transverse truck placement (i.e., to the left or right of the panel). For cross-frames near the maximum positive dead load moment region, the longitudinal load influence tends to be localized (i.e., truck loading beyond 50 feet longitudinally of the cross-frame of interest tends to produce negligible force effects). For cross-frames in straight or curved girder systems near skewed end or intermediate supports, the load influence response is significantly broadened. In other words, loading in adjacent spans or along the opposite deck edge (i.e., right lane loading maximize force effects in a cross-frame on the left side of the bridge) can produce substantial cross-frame forces. In general terms, the influence of load position is highly variable and difficult to predict unless an influence-surface analysis is conducted.
- Similarly, critical lane position also depends on a variety of parameters. In general, truck passages along the outer edges of the deck (i.e., overhang loads) tend to maximize cross-frame forces in skewed and curved bridges, but not in straight, normal bridges (i.e., load applies net torque on superstructure which engages cross-frames). Additionally, cross-frame response is generally linearly dependent on the location of applied load and the centerline of the fascia girder. That is to say, wheel loads that are 3 feet outboard of the fascia girder produce larger force demands on critical cross-frame members than loads that are 1 foot outboard.
- In terms of implementation into AASHTO LRFD, the results of this study indicate that the current specification language in Article 3.6.1.4.3a ("*a single design truck shall be positioned transversely and longitudinally to maximize stress range at the detail under consideration*") is the best way to ensure the critical load position is considered by the designer.

- The governing cross-frame in a given bridge depends on many variables including girder spacing, support skew, and lane positions. In general, bottom struts tend to govern most bridges, as cross-frames tend to act as composite "floorbeams" when distributing applied live loads transversely to adjacent girders. With that in mind, the response is likely too variable to pinpoint which cross-frames are critical without some refined, load-surface analysis (i.e., to examine all possible truck positions and cross-frame force effects).
- The correlation between specific variables and cross-frame fatigue design forces was obtained. In general, the following parameters are positively correlated with cross-frame forces (i.e., increase in parameter results in increase in cross-frame force): girder spacing/number of girders (bridge width), skew angle/index, bridge curvature/connectivity index, cross-frame spacing, cross-frame area. Deck thickness was the only parameter that was negatively correlated with regard to cross-frame forces. Despite the distinct correlations indicated, substantial variability was still observed in these results given that each bridge considered was a function of 13 different independent variables. These general rules-of-thumb, though, can potentially be utilized by engineers to mitigate cross-frame forces in the design phase of a project. In other words, the engineer can potentially avoid an iterative "chase-your-tail" design problem (e.g., increase the size of the cross-frame member to accommodate the design forces, re-analyze, and redesign for larger forces in the second pass) by adjusting other key parameters. For instance, using discontinuous, staggered cross-frame layout is a practical and economical solution, whereas increasing the deck thickness or decreasing girder spacing has significant impacts on the rest of the design.
- The WIM study confirmed that the dual truck event initially considered in the 7th Ed. AASHTO Specifications is a rare occurrence. As such, the current load criteria (i.e., a single design truck positioned in all longitudinal and transverse positions) is more appropriate.
- From the fatigue truck study, it was concluded that an apparent disconnect is present between the reality of load-induced fatigue problems in the US and the current design criteria. In addition to the analysis procedures (evaluated in the Chapter F4), the RT explored the Fatigue I and II load factors in the context of cross-frames through an analysis of WIM data. By analyzing a small subset of the Fatigue Loading Study matrix, it was determined that current load factors are likely overly conservative for cross-frame design. This is largely attributed to the fact that current design criteria requires <u>all</u> possible lane positions be considered in accordance with AASHTO Article 3.6.1.4.3a, regardless of design lanes or actual lane striping. A more realistic scenario is to consider only "drive lanes" (i.e., lanes within the limits of the fascia girders, for which the large majority of truck traffic traverses).
- In implementing the reduced cross-frame-specific load factors proposed, it was observed that load-induced fatigue problems are likely only an issue in skewed and/or curved bridges, for which $I_c > 1$, $I_s > 0.15$, or $I_c > 0.5$ & $I_s > 0.1$. For bridges that do not fall into one of these categories, a refined 2D or 3D analysis is likely not required.

The RT drafted proposed modifications to AASHTO LRFD with regards to appropriate fatigue stress ranges in cross-frames based on the findings listed above. Refer to the main body of the report and Appendix A for the proposed language and commentary.

CHAPTER F4

R-Factor Study

The primary objective of the R-Factor Study is to parametrically investigate the effective stiffness of cross-frames considering the effects of the connection details. As outlined previously in Section F3.1.1, engineers often prefer 3D models over 2D models when analyzing bridge superstructures, particularly for complex systems with support skews and/or horizontal curvature. 3D models are utilized to obtain accurate design forces for all structural elements under live loads, including cross-frames. These refined finite element analyses, which are often comprised of thin shell elements and beam elements, can be quite involved and complex. However, engineers often simplify the modeling approach of the cross-frame systems, given the level of geometric complexity (i.e., the eccentric load path created by the connection plates, gusset plates, and cross-frame members).

Rather than explicitly model each component and load eccentricity of the cross-frame with shell elements, engineers typically simplify them as pin-ended truss elements capable of only resisting axial force. In this simplified approach, the eccentric load path and the stiffness contributions of gusset and connection plates are neglected. The actual stiffness of the cross-frame system is instead simulated through a simple modification factor (commonly referred to as R-factor) assigned to the cross-sectional area of the truss element or the elastic modulus of the material. Refer to Figure F3-1 for a graphical depiction of this widely used modeling approach.

Current 9th Edition AASHTO LRFD Specifications (2020) recommend the use of a simple modification factor. In lieu of a more accurate analysis, an R-factor of 0.65 is to be applied to the axial stiffness of the cross-frame elements (*AE*) in the analysis model per Article C4.6.3.3.4. This recommendation, based on the work conducted by Battistini et al. (2016) at the University of Texas, is valid for equal leg single angles, unequal leg single angles connected to the long leg, and flange-connected tee-section cross-frame members.

Battistini et al. developed a more precise, regression-based expression that determines the appropriate R-factor as a function of the cross-frame geometry. Similar to the codified 0.65 factor, this expression imposes a reduced axial stiffness on cross-frame members in structural analysis programs to account for the eccentricity of its end connections. There are two forms of the equation depending on if the cross-frame is an X-type or K-type frame. For reference, the respective X-type and K-type equations are provided below:

$$R_x = 1.062 - 0.087\frac{S}{h_b} - 0.159\bar{y} - 0.403t \qquad \textit{F4.1}$$

$$R_K = 0.943 - 0.042\left(\frac{S}{h_b}\right) - 0.048\bar{y} - 0.420t \qquad \textit{F4.2}$$

where: S = girder spacing; h_b = height of the cross-frame; $\bar{y}$ = distance between the face of the connected leg and the neutral axis of the angle section; and t = angle leg thickness. For systems with larger connection eccentricities ($y, \bar{t}$) and smaller aspect ratios (S/h_b), the corresponding cross-frame stiffness is significantly reduced, which is reflected by a smaller resulting R-factor. From these expressions, typical R-factors for

cross-frames with single angle members generally range from 0.4 to 0.8 depending on the member sizes and geometry.

It is important to note that these equations were derived for stability-related conditions and deformations. More specifically, the stiffness reduction formulas were developed for noncomposite bridge girders undergoing lateral-torsional displacements as they buckle – or twist in the case of horizontally curved girders. Battistini et al. showed that these equations produce stiffness approximations that are often within a few percent of the actual stiffness for this specific condition.

In the present study, however, the RT investigated a different condition for a bridge girder: an in-service composite system subjected to moving live loads. From the Fatigue Loading Study, the RT observed that the deformation response of cross-frames is quite different for live load traffic than for the stability-related conditions during construction assumed in the development of Eqs. F4.1 and F4.2. It was demonstrated that the response is not only a function of the overall bridge geometry but also the load position, especially in skewed systems.

Intuitively, the relative movement of the corners of a cross-frame dictates the axial force demands in each member. It was observed that any load-induced deformed shape is a combination of the following responses between adjacent girders framing into a common cross-frame: (i) uniform rotation, (ii) differential vertical displacement, and (iii) differential rotation. These deformations are presented schematically in Figure F4-1. The cross-frame will also undergo rigid-body motion as the entire superstructure displaces under applied load. However, rigid-body motion does not induce strains and stresses on cross-frame members; thus, displacements due to rigid-body motion are not important to understanding cross-frame behavior.

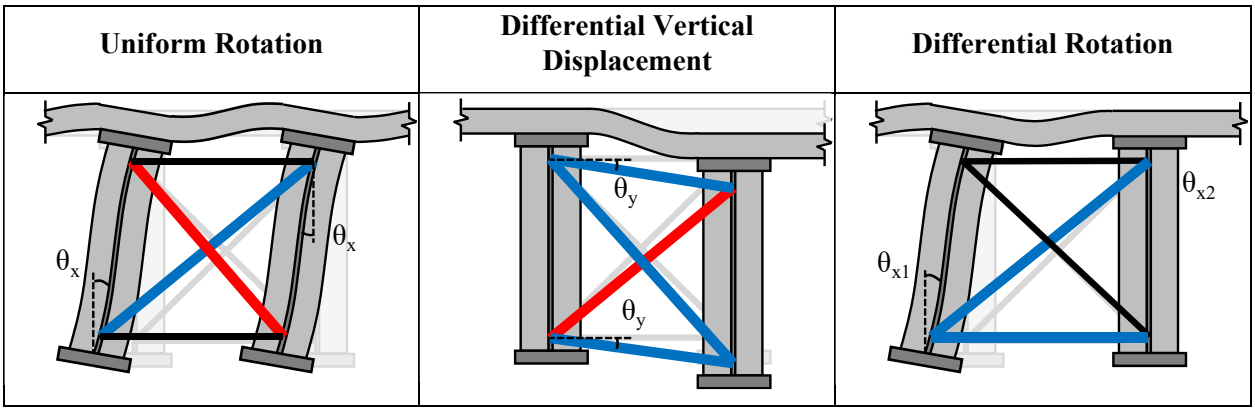

Figure F4-1: Types of cross-frame deformation caused by relative moment of adjacent girders

Eqs. F4.1 and F4.2 were based on the uniform rotation pattern, for which the top and bottom struts are zero-force members in X-type frames and the top strut is a zero-force member in K-type frames. Additionally, the contribution from the composite deck is neglected. For the uniform rotation condition, a simple equation has been derived to calculate the stiffness of an X-type and K-type cross-frame, respectively (Yura 2001):

$$\beta_{b,x} = \frac{A_D E S^2 h_b^2}{L_D^3} \qquad F4.3$$

$$\beta_{b,k} = \frac{2ES^2 h_b^2}{\frac{8L_D^3}{A_D} + \frac{S^3}{A_S}} \qquad F4.4$$

where: A_D = cross-sectional area of the diagonals; A_S = cross-sectional area of the struts (if different than the diagonals); E = modulus of elasticity; and L_D = length of the diagonal members.

For a cross-frame in a composite system subjected to traffic loads, the deformed shape is more complicated, and Eqs. F4.3 and F4.4 do not necessarily apply.

Given the variability of load-induced cross-frame response in composite systems, the RT decided to explore more generalized solutions beyond the regression-based solutions developed by Battistini et al. In order to investigate the stiffness response of cross-frames in these more generalized conditions, the RT conducted a series of three-dimensional analyses in Abaqus and approximate hand calculations. To extend the breadth and depth of knowledge on the effects of eccentric end connections, three different model-scale conditions were identified and evaluated, which include: (i) member-level, (ii) panel-level, and (iii) system-level studies. The work of each successive study builds on the previous one, and each individual study serves as the outline for Chapter F4 herein.

Member-level studies computationally investigate the fundamental behavior of axial-loaded sections with eccentric end connections. The effects of bending on the axial stiffness of an individual cross-frame member are studied. Although WT sections are also used, the focus of the present study was on single angle sections, as they are most impacted by eccentric load paths and are the most common section used for intermediate cross-frame systems in the US.

The knowledge gained from the member-level studies are then extended to panel-level studies. Panel-level studies analyze isolated cross-frame panels consisting of the various diagonal and strut members, as well as various gusset and connection plates. Panels are subjected to the deformations presented schematically in Figure F4-1. From the member- and panel-level studies, the RT developed a better understanding of cross-frame behavior in a noncomposite system.

The objective of the system-level study is to demonstrate how the behavior of cross-frames is affected when serving as a small part of a larger composite system. The RT conducted a parametric study consisting of full 3D bridge models that assess the accuracy of these approximate R-factors. In this parametric study, the RT conducted several iterations of the same bridge model including cross-frames modeled as shell elements (representing the most accurate solution) and cross-frames modeled as truss elements with different stiffness modification factors. For simplicity, the former will be simply referred to as shell-element models in this section, and the latter as truss-element models. By comparing the results from each model, the sensitivity of the predicted cross-frame forces relative to the stiffness modifications can be evaluated. In addition to the R-factor approach, the RT also proposed and explored an alternative for modeling cross-frame elements in 3D models: as an *eccentric beam*. This technique is described in detail in the subsequent sections.

The iterative system-level procedure outlined above is similar to what is described in Chapter F5 for the Commercial Design Software Study, except that this chapter focuses solely on the modeling techniques of cross-frames in 3D models only (i.e., shell elements, truss elements, eccentric beams). In the Commercial Design Software Study, several iterations of the same bridge model are conducted, but for purposes of evaluating simplified 2D modeling procedures (i.e., plate and eccentric beam, grillage models).

Following this introductory section, the member-level, panel-level, and system-level studies are detailed in Sections F4.1, F4.2, and 0, respectively. Computational results are presented, as well as commentary on the observed trends. Section F4.4 summarizes the findings of the R-Factory Study, which serves as the basis for the proposed modifications outlined in the main body of the report and Appendix A.

F4.1 Member-Level Studies

Prior to studying the behavior of cross-frame panels and systems, member-level studies focus on the

fundamental behavior of eccentrically loaded single angles. The RT evaluated simplified analytical methods to quantify the effects of bending on the stiffness of a single-angle cross-frame member. In this section, those simplified methods are outlined, and the results are compared to and validated against experimental test results performed by past UT Austin research. The knowledge gained from evaluating isolated single-angle members is then extrapolated to evaluating full cross-frame panels in Section F4.2.

F4.1.1 Simplified Model

As stated above, the RT sought to develop a simplified analytical tool that quantifies the effects of eccentric loading on the axial stiffness of single-angle sections. Given that the pin-ended truss modeling approach is widely used in practice, the primary goal was to utilize this analytical tool to then derive appropriate stiffness modification factors, *R*, to conform to the traditional approach.

To start, the RT reviewed past research. Wang (2013) developed a simple analytical model to quantify eccentric effects on the stiffness of a cross-frame member. The model, however, was limited to just the single angle and gusset plate components of the cross-frame system (i.e., there was no consideration for the eccentricity introduced by the connection plates). Despite those limitations, a stiffness modification factor was derived on a member-by-member basis that would be uniformly assigned to all members in a panel. This modification factor was also independent of any assumed deformation pattern (Figure F4-1), which is different than expressions derived by Battistini et al.

The model was shown to produce approximate stiffness modification factors with errors on the order of ±25% when compared to laboratory experimental measurements and FEA data. Wang hypothesized that the discrepancy in the results was due to the connection plates not being explicitly considered in the analytical model. Despite those observed errors, the simplified method was promising given its inherent independence of the cross-frame deformed shape. The stiffness reduction is simply a function of the cross-frame member (single angle) and its connection details. With that in mind, the RT elected to expand on this previous work by explicitly considering the connection plates and the overlapped portions of the cross-frame system (i.e., single-angle-to-gusset and gusset-to-connection overlaps). Before introducing the proposed analytical model, a brief discussion on the sources of eccentricity is provided.

At the most fundamental level, the eccentric load path in a cross-frame member is introduced by the presence of one-sided connections, which are typically welded. This is demonstrated schematically in Figure F4-2, where the assumed load path for each orthogonal axis of the cross-frame member is depicted along with the simplified modeling approach for which cross-frames are treated as pin-ended truss elements. Note that diagonals and top strut are hidden for clarity; the discussion for these members is identical to that of the bottom strut.

In the cross-sectional view (or the in-plane axis of the cross-frame), there could be a slight eccentricity as the load is distributed through the single-angle section and into the gusset plate. This eccentricity can be mitigated or eliminated altogether by specifying a balanced weld detail (i.e., the centroid of the weld group coincides with the centroid of the single-angle member). It should be noted that, in the development of the 3D shell-element models in the system-level studies (Section F4.3), the overlapping elements are constrained around the entire intersecting perimeter, which assumes an unbalanced weld detail. Still, these effects are small and are therefore neglected in the proposed analytical model developed herein. As such, no recommendations are made to AASHTO LRFD related to balanced and unbalanced welds.

Instead, the eccentric load paths in the out-of-plane direction are of more importance to the stiffness modification factor, which is depicted in the right figures in Figure F4-2. In the out-of-plane direction, the internal axial force must transition twice at each end of the cross-frame due to the connection-to-gusset connection and the gusset-to-angle connection. These eccentric “jumps” have a considerable impact on the stiffness response of cross-frame members and systems.

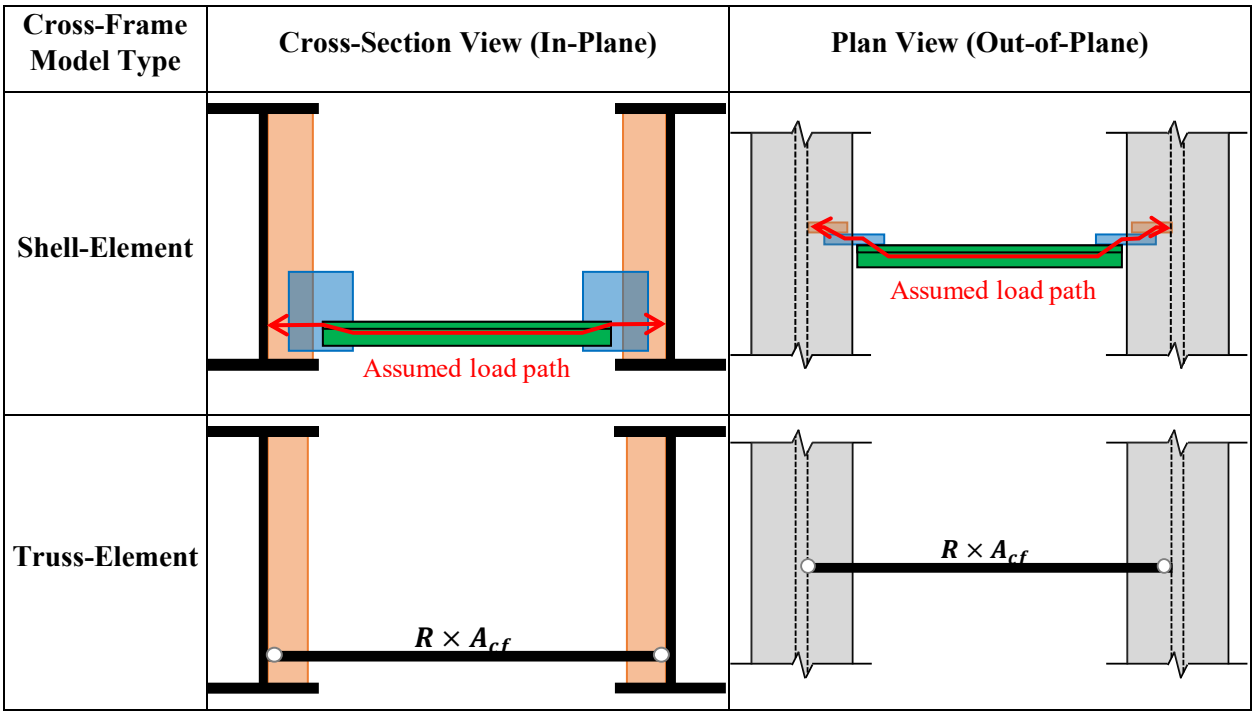

Figure F4-2: Assumed eccentric load path through a cross-frame member along both orthogonal axes (left) and the corresponding, typical 3D modeling simplification (right)

Again, an analytical model was developed that explicitly considers these eccentric "jumps" in the load path, which in turn is used to derive stiffness modification factors to be implemented in traditional truss-element models. The proposed model, in conjunction with the traditional modeling approach, is illustrated schematically in Figure F4-3. Given that the out-of-plane eccentricities are more critical than the in-plane eccentricities, the proposed analytical model focuses only on out-of-plane bending effects (i.e., the in-plane load path, which is not pictured in Figure F4-3, is assumed concentric in both cases).

On the left, the proposed analytical model is shown, which is more representative of realistic conditions. The connection plate, gusset plate, and single-angle member (as well as the overlapped portions) are transformed into equivalent beam elements with their own respective axial and flexural stiffness (area, moment of inertia, and length). That is to say, these components are treated as beam elements with flexural degrees of freedom. A discussion on this process is provided below. Additionally, the eccentric load path is explicitly considered.

On the right, the traditional approach to modeling cross-frames in a 3D analytical model is shown. A pin-ended truss element is considered whose properties are associated with the angle member only (i.e., a cross-sectional area of RA_a and a moment of inertia that is irrelevant) and whose length is equal to the girder spacing (S_g). Ultimately, stiffness modification factors, R, are derived by equating the axial stiffness of both sets of models in Figure F4-3.

In terms of the analytical model, the RT examined several different iterations but ultimately settled on the more refined model presented in Figure F4-3. The critical moment of inertia of each element in the analytical model, shown in the figure, is taken about the out-of-plane bending axis. The "jumps" in the neutral axis, or the eccentricities, are represented by rigid offsets, whose lengths are based on the distances between the neutral axes of the connected components. For example, the "jump" between the connection plate and gusset plate elements is equal to the summation of half the connection plate thickness and half the gusset plate thickness. The overlapped sections and their associated composite section properties are also

considered as a unique cross-section (e.g. gusset-to-angle overlap designated as "O2" in the figure for "overlap #2"). Additional assumptions for the refined model are outlined below:

- The vertical offsets shown in Figure F4-3 are considered rigid, which implies that the welded connections between plates and angles perfectly constrains these elements together.
- The length of each individual beam component (e.g. angle length L_a in Figure F4-3) is taken assuming there are no shear lag effects. In other words, the length of the angle member starts precisely at the termination of the gusset plate and ends at the gusset plate edge on the opposite side of the angle; the length of overlap #2 (angle-to-gusset overlap) is taken as the distance between the edge of the angle section and the termination of the gusset plate.
- Section properties (i.e., A, out-of-plane I, in-plane I, and length L) of the connection and gusset plates are based on a Whitmore approach. An example for a bottom strut member is presented in Figure F4-4, where the assumed distribution of an internal axial force is highlighted in red. The force is transmitted through the single-angle section, and the stress disperses at a 30-degree angle to maintain consistency with the Whitmore approach. A similar assumption is made for the force transmitted through the connection plate. Thus, the effective height of the connection and gusset plates engaged in distributing the force is taken as $b_{eff,c}$ and $b_{eff,g}$, respectively. These dimensions are then used to compute the equivalent area and moment of inertia values. Although not demonstrated in Figure F4-4 for a level bottom strut, the mid-section length approach adopted by AASHTO Article 6.14.2.8.4 can be used to determine the effective length of a gusset and/or connection plate when transmitting force from a diagonal member.
- Section properties of the equivalent overlapped portions are taken from an assumed composite section. As an example for overlap #2, the equivalent area is taken as the summation of the single angle and the effective gusset plate (from previous bulleted item), and the equivalent out-of-plane moment of inertia is taken as the summation of the individual $1/12bh^3$ terms and Ad^2 terms (about the centroid of the composite section).
- The out-of-plane stiffness of the connection plate is amplified by a factor of two (i.e., $2I_c$). Figure F4-5 illustrates the difference between the out-of-plane eccentric effects on the "real" conditions and the idealized conditions. In the real conditions, the connection plate is supported about the web and flanges of the girder, such that restraint against out-of-plane rotation is increased. In the idealized conditions for the assumed analytical model, the extra restraint provided by the flange welds and the portion of the web outside of the effective height is removed. Thus, in order to better represent the stiffness of the connection plate as an equivalent beam element, the RT conducted some additional finite-element analyses. It was determined that, for the most common connection plate conditions, the "real" system is approximately twice as stiff as the idealized system; hence, a factor of two is uniformly assigned.
- Unlike the pin-ended truss models, rotations are not released at both ends of the analytical model. The distortional stiffness of the girder web is assumed substantial enough to warrant in-plane and out-of-plane rotational restraint of the cross-frame system. This is also demonstrated graphically in Figure F4-5.
- Although shown one way in Figure F4-4, the face on which the angle member is connected to the gusset plate could be reversed. In fact, the RT mimicked standard details across the country in the development of its shell-element and eccentric-beam models to avoid intersection of diagonal members (i.e., one diagonal is represented as shown in Figure F4-4; the other diagonal is modeled with the angle on the opposite face of the gusset).
- Refer to Section F4.3.2 below for an example on how the effective section properties of this analytical model were computed.

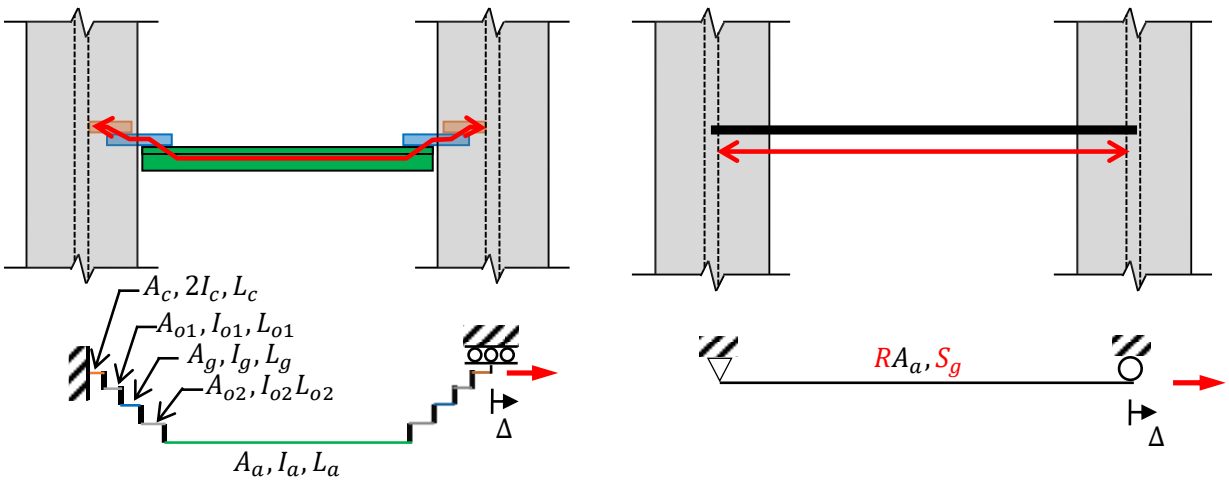

Figure F4-3: Assumed analytical model to represent the eccentric end connections (left) versus the modeling approach commonly used to represent cross-frame members (right)

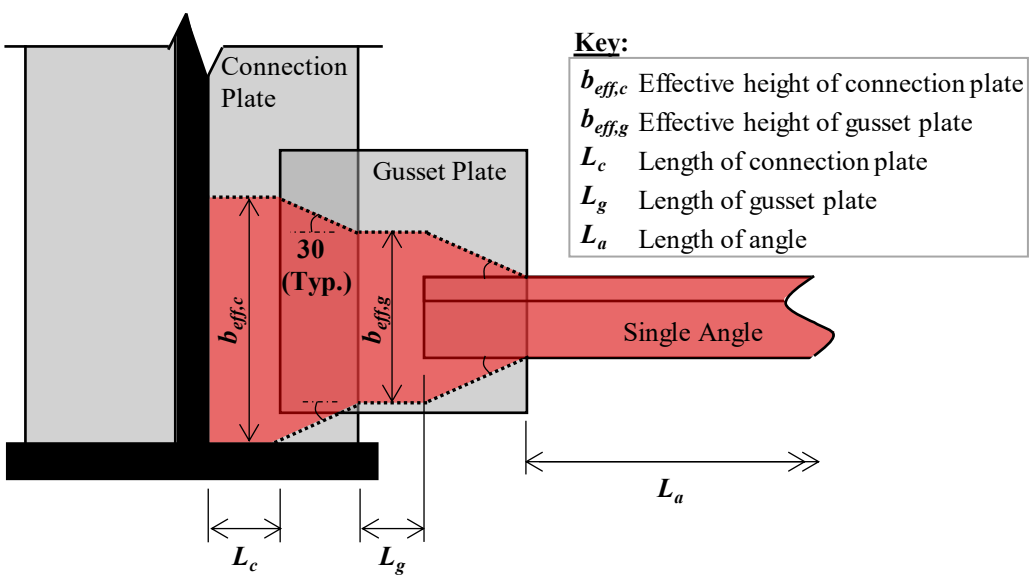

Figure F4-4: Assumed Whitmore section to determine effective height and length connection and gusset plates

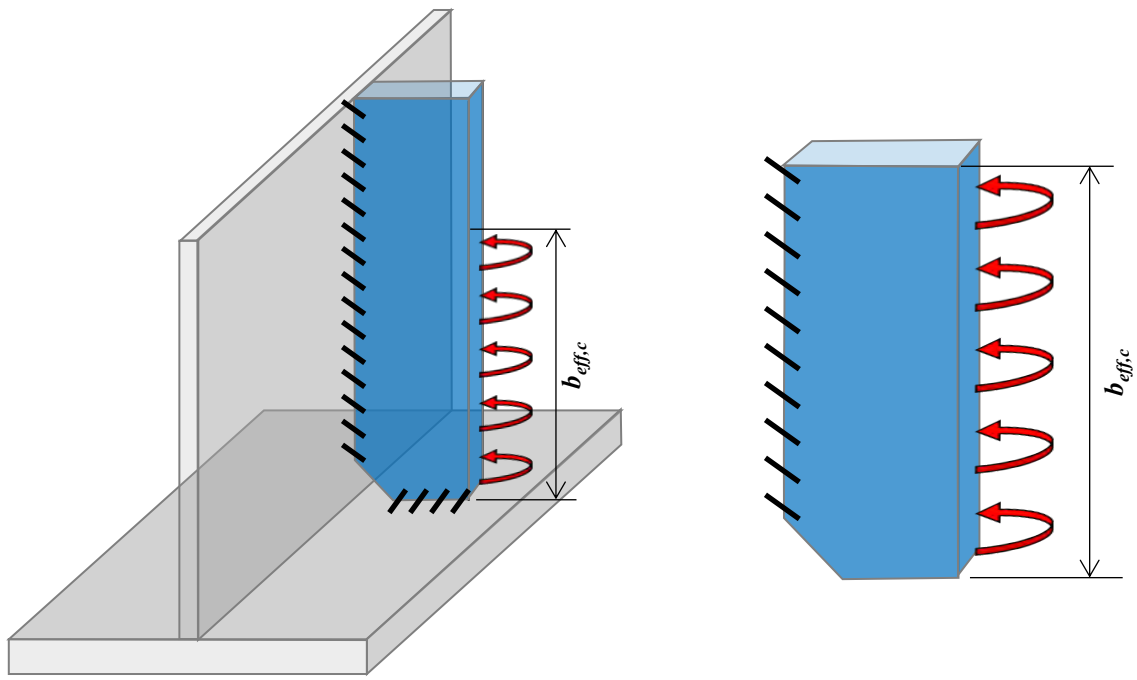

Figure F4-5: Out-of-plane stiffness of connection plate for (left) real conditions and (right) idealized conditions

From the analytical model outlined above, the appropriate R-factor for a given cross-frame member is the ratio of $\Delta_{truss}/\Delta_{ana}$, where Δ_{truss} is the axial displacement of the right model without consideration of an R-factor and Δ_{ana} is the axial displacement of the refined left model. In comparing the refined model (left) and the pin-ended truss method used prevalently in commercial software (right), it is apparent that the computed axial displacements Δ will vary for most cross-frame geometries and conditions. The distinct differences in the models and how they affect the estimated stiffness of the cross-frame are described by the following:

- Consideration of the eccentric load path will amplify the axial displacements in the refined model (left). In computing the axial displacement, only axial deformations need to be considered in the right model; on the left, however, both axial and bending contributions to the axial displacement must be considered. This fundamental difference was the impetus of developing simplified R-factors. By virtue of the additional bending components, this behavior will increase Δ_{ana} with respect to Δ_{truss} and thus ***reduces the R-factor***.
- The simple, truss model replaces the stiffer connection and gusset plates with additional length of an often, more flexible single-angle member. This is demonstrated in Figure F4-3 by reporting the length of the truss-element model as the center-to-center spacing of the girders, S_g. This behavior often has the opposite effect on the R-factor as the previous bulleted item; it tends to increase Δ_{truss} with respect to Δ_{ana} and thus ***increases the R-factor***.
- Although not explicitly captured in the refined, analytical model, the RT observed in its FEA studies the effects of in-plane rotational restraint provided by the connection and gusset plates. This is best illustrated by Figure F4-6, which compares the in-plane deformed shape of a pin-ended truss element to the deformed shape considering end rotational restraint (not to scale). From this sketch, it is evident that the in-plane benefits of the connection and gusset plates are neglected when representing the cross-frame as a pin-ended truss member. Similar to the second item, this behavior decreases Δ_{ana} with respect to Δ_{truss} and thus ***increases the R-factor***.

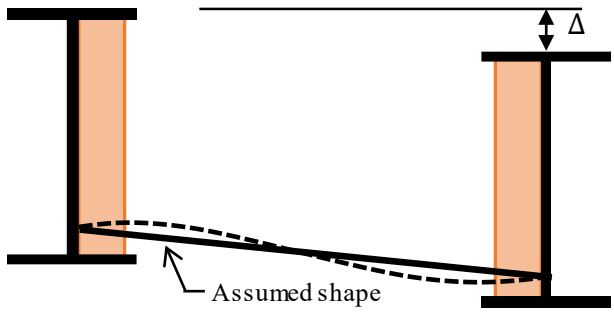

Figure F4-6: Scaled view demonstrating the in-plane restraint provided by the connection (and/or gusset plate)

Traditionally, stiffness modification factors have only explicitly addressed the effect of eccentricities that decrease the R-factor. The analytical model previously developed by Wang, for example, did not consider the effects that increase the R-factor. It should be noted that, in rare occasions, the net effect of these three factors could potentially result in an R-factor above unity depending on the relative stiffness parameters of the connection plate, gusset plate, and cross-frame member. A series of calculations were performed to verify this assertion and investigate these three effects in greater detail.

F4.1.2 Analytical Results

Through the principle of virtual work (PVW), the RT developed a spreadsheet that computes the appropriate R-factor of an isolated single angle member based on a series of geometric inputs including connection plate, gusset plate, and single angle dimensions. The RT then conducted a parametric study using the PVW. Various single angle sections were considered, ranging from 3-inch legs up to 6-inch legs and 1/4-inch thickness up to 7/8-inch thickness. Both equal-leg and unequal-leg angles were considered, as well as various gusset plate dimensions that are commonly used in practice. For the unequal-leg angles, both legs were evaluated as the leg connected to the gusset plate to study its effect on the R-factor. Additionally, the face on which the angle was connected to the gusset plate (relative to the face on which the connection plate is connected to the gusset) was studied.

Table F4-1 summarizes the range of parameters considered; parameters not listed in the table were taken as constants based on typical dimensions found in practice (e.g. connection plate thickness taken as a constant 0.5 inches). An R-factor was derived for every combination to evaluate the relative impact of each parameter on the stiffness modification factor. In total, over 42,000 cases were evaluated as part of this analytical study.

Table F4-1: Parameters considered in the analytical-model parametric study

Parameter	Range of Values
Angle section	{ L3x3x1/4, L3x3x1/2, L3-1/2x2-1/2x5/16, L3-1/2x3x1/2, L3-1/2x3-1/2x5/16, L3-1/2x3-1/2x1/2, L4x3x3/8, L4x3-1/2x3/8, L4x4x3/8, L4x4x5/8, L5x3x1/2, L5x3-1/2x3/4, L5x5x1/2, L5x5x3/4, L6x3-1/2x1/2, L6x4x7/8, L6x6x5/8, L6x6x7/8}
Angle length [ft]	{6, 7, 8, 9, 10, 11, 12, 13, 14}
Connected leg[a]	{Short, long}
Connection face[b]	{Same side, opposite side}
Gusset height [in]	{12, 15, 18, 21, 24}
Gusset length [in][c]	{1, 2, 3, 4}
Gusset thickness [1/16th in]	{6, 7, 8, 9, 10, 11, 12, 13, 14}
Connection plate dimensions	See list of assumptions below

Notes:
[a]Only applies to unequal leg angle sections; refers to which leg is connected to gusset
[b]Refers to which face of the gusset the angle is connected (i.e., either same side of connection plate or opposite side)
[c]Gusset length based on the assumptions outlined in Figure F4-4; represents the clear length between edge of connection plate and edge of angle section

Given the number of cases and parameters considered, many figures were generated from the data set. Rather than present every one, Figure F4-7 and Figure F4-8 are representative of the full data set and highlight key aspects. Figure F4-7 presents the R-factor derived from the analytical model as a function of the gusset plate out-of-plane flexural stiffness (i.e., EI_g/L_g). Refer to Figure F4-4 and the associated commentary on the definition of these variables. In this figure, the full data set is plotted as well as a filtered data set for clarity. The filters include 8-foot long, L4x4x3/8 angles with 2-inch long gusset dimensions. Figure F4-8 presents the R-factor as a function of the angle length; again, the full data set is presented as well as a filtered data set (L5x5x1/2 angle sections and ½-inch thick, 2-inch long gussets).

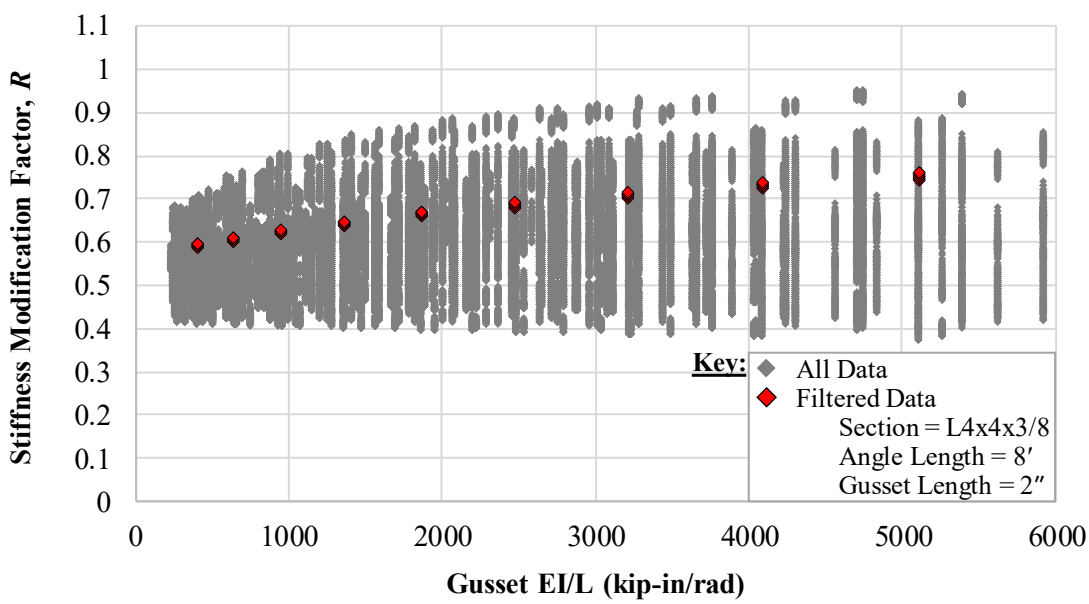

Figure F4-7: Stiffness modification factor derived as a function of the gusset plate flexural stiffness

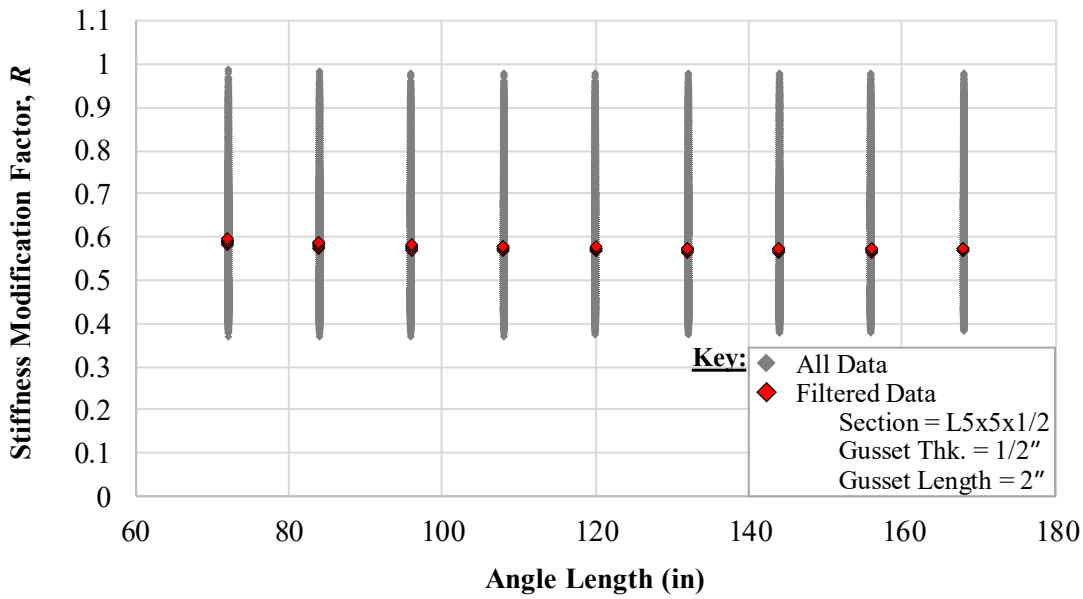

Figure F4-8: Stiffness modification factor derived as a function of the angle length

There a few important trends observed from Figure F4-7 and Figure F4-8:

- The stiffness modification factor, derived from the analytical model, varies between 0.40 and approximately unity depending on the geometry of connection plate, gusset plate, and angle. A large scatter is observed for the entire data set. This range of values is generally consistent with previous R-factor studies.
- The gusset plate flexural stiffness and the derived R-factor are positively correlated based on the filtered data in Figure F4-7. Although not explicitly shown in the filtered results, the trends are similar for all other subsets of data. Note that, as the gusset plate *EI/L* value increases, two counteracting events occur: (i) the eccentricity increases in the connection which amplifies bending in the angle member and (ii) the rotational stiffness of the model increases, which reduces displacements. Based on the results of this study, it is evident that the latter condition outweighs the former, which results in an increased R-factor. This observation is verified with the panel- and system-level studies.
- There is little correlation observed between angle length and the R-factor based on the results of Figure F4-8. This trend is consistent with the full data set not explicitly shown in this appendix. This trend has significant design implications. For a typical cross-frame, the strut and diagonal members have different lengths. Thus for a member-level approach to R-factors, a designer would assign separate reduction factors for struts and diagonals, which would be cumbersome. Instead, the same R-factor can be assigned for all members in the cross-frame panel with minimal effect.

F4.1.3 Comparison to Experimental Results

To verify its accuracy, the RT compared the analytical model with the results of a laboratory experiment. McDonald and Frank (2009) conducted a series of static and fatigue tests on single-angle members eccentrically fastened to gusset plates. The static tensile tests, in particular, were performed to failure; however, for the purposes of NCHRP Project 12-113 and the analytical model, the elastic stiffness of the eccentrically loaded angle is the focus.

Using the axial load-displacement curves measured from the static tests, McDonald and Frank obtained the elastic stiffness of several test specimens. The elastic stiffness of the test specimen considers not only deformations due to axial stress but also deformations due to bending of the section, which is influenced by the eccentric connections and the in-plane and out-of-plane restraint provided by the test machine clamps. An example of a test specimen and a static test is provided in Figure F4-9 and Figure F4-10, respectively. Note that the specimens were comprised of only a single-angle member and a gusset plate. Therefore, the analytical model and PVW calculations outlined above were modified to neglect any contributions for a connection plate. It was assumed that the ends of the specimens were fully fixed about both axes of rotation by the clamps.

Figure F4-9: Eccentrically loaded single-angle specimen (McDonald and Frank 2009)

Figure F4-10: Sample static test conducted on single-angle specimen (McDonald and Frank 2009)

In total, three different test specimens were tested and compared with the analytical solution. The relevant parameters of the test specimens are presented in Table F4-2. Refer to Figure F4-4 for definitions of the angle, overlap, and gusset plate lengths. Only the test specimens with unbalanced weld details (i.e., welded around the full perimeter of the gusset-angle overlap) are considered in this comparison to maintain

consistency with the 3D shell-element modeling approach discussed in subsequent sections.

The comparative results of the lab experiments and the analytical solutions are provided in Table F4-3. The applied load represents a load stage for which linear, elastic behavior was still observed. The measured displacements and corresponding elastic stiffness at that load stage are then compared to the total displacement (axial and bending) and stiffness estimated by the analytical, PVW approach. The R-factor is then determined by comparing the estimated axial displacements assuming the full length of the specimen was comprised of a pin-ended angle section (i.e., *PL*/*AE* displacement) and the total displacement computed from the analytical model. It can be observed that the predicted and measured elastic stiffnesses agree well, indicating the simplified analytical model accurately represents the behavior of an eccentrically loaded single-angle member.

Table F4-2: Parameters of test specimens studied (McDonald and Frank 2009)

Test ID	Angle Section			Overlap	Gusset Plate		
	Section	Connected Leg	Length, L_a (in)	Length, L_{o2} (in)	Thickness, t (in)	Width, b (in)	Length, L_g (in)
44E	L4x4x3/8	4	25	7.25	1.5	7.125	16.75
53SE	L5x3x3/8	5	26	7.25	1.5	7.125	16.75
53LE	L5x3x3/8	3	23.75	7.25	1.5	7.125	16.75

Table F4-3: Comparison of experimental results and analytical solution

Test ID	Applied Load (kips)	Experimental Data		Analytical Model				
		Total Disp. (in)	Elastic Stiffness (kip/in)	Displacement (in)			Elastic Stiffness (kip/in)	R-Factor
				Axial	Flexural	Total		
44E	100	0.097	*1030*	0.045	0.054	0.099	*1010*	0.89
53SE	50	0.057	*880*	0.023	0.031	0.054	*920*	0.82
53LE	50	0.047	*1070*	0.022	0.025	0.047	*1060*	0.92

As noted previously though, the RT developed an analytical model for two reasons: (i) to provide a simple, general solution for quantifying the effects of eccentric end connections that is easy to use and (ii) to gain a better understanding of the fundamental behavior of these eccentrically-loaded axial members. The results of this validated, member-level analytical study are used to supplement the panel- and system- level FEA studies outlined herein. Ultimately, the RT believes that FEA results that are supported by simple, analytical tools with a strong fundamental basis offers the best solution to the problem.

F4.2 Panel-Level Studies

The goal of the panel-level studies is to expand on the member-level studies and examine the load-induced behavior of full cross-frame panels when subjected to various deformation patterns. In this section, the 3D modeling approach and parametric study of this study are outlined (Section F4.2.1). The results of the parametric study, which highlights the variability in the R-factor response, are then presented in Section

F4.2.2 with commentary. Lastly, additional spot checks investigating connection plate dimensions and K-frames are presented in Section F4.2.3.

F4.2.1 Panel-Level Modeling Approach

Prior to conducting any new analytical studies, the RT reviewed past research related to cross-frame panel stiffness. Wang (2013) conducted extensive studies on cross-frame panel stiffness and ultimately: (i) developed 3D FEA models to match the measured response of laboratory experiments and (ii) conducted parametric studies.

Similar to Battistini et al., this previous work was focused on cross-frame stiffness response during the construction of bridge girders where lateral-torsional buckling is the primary concern, not fatigue. Therefore, equal rotation of adjacent girders was the assumed deformation pattern (Figure F4-1). Figure F4-11 depicts the laboratory experiments conducted by Wang along with the associated FEA model. The FEA model in the figure demonstrates uniform rotation loading and explicitly considers the eccentric end connections caused by the one-sided connection of the angles.

For the R-Factor Study of NCHRP Project 12-113, the RT aimed to extend the analytical component of the previous work performed by Wang by investigating the other two deformation patterns commonly observed in cross-frames in a composite bridge system: differential vertical deflection and differential rotation. As such, finite-element models similar to the one illustrated in Figure F4-11 were replicated for the various loading patterns. Given the scope of the project, additional experimental tests were not performed.

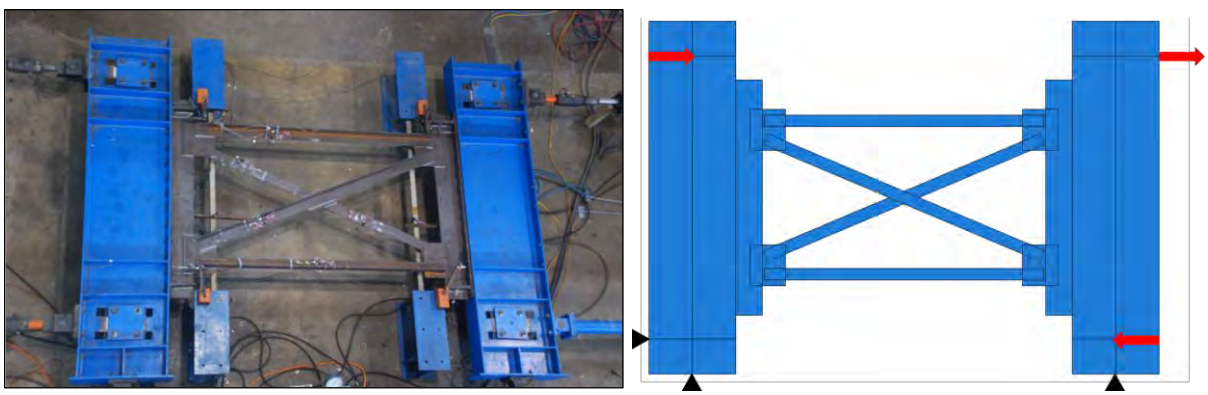

Figure F4-11: Laboratory cross-frame stiffness test from Wang (2013) and associated FEA model developed by the RT

Unlike the member-level studies in the previous subsection, the overall torsional stiffness of the cross-frame panel is of interest in the panel-level studies (i.e., the global stiffness response to an applied external moment). To analytically compute the stiffness of the panel under an applied moment, the RT adopted an approach that was consistent with the experimental measuring technique used by Wang (2013). Lateral and vertical displacements were taken at specific locations on the frame from the FEA models, which is illustrated schematically in Figure F4-12. The calculation procedure is summarized by Eq. F4.5 through F4.8:

$$\theta_x = \frac{(\delta_1 - \delta_2) + (\delta_3 - \delta_4)}{2h_b} \qquad F4.5$$

$$\theta_y = \frac{(\delta_5 - \delta_6)}{S'} \qquad F4.6$$

$$\theta_T = \theta_x + \theta_y \qquad F4.7$$

$$\beta = \frac{M}{\theta_T} \qquad F4.8$$

where: h_b = distance from δ_1 to δ_2, S' is the distance from δ_5 to δ_6; M = applied moment in the cross-frame as computed by a force couple; and β = torsional stiffness of the noncomposite cross-frame panel. Note that this procedure is consistent for various loading conditions (i.e., the three deformation patterns outlined in Figure F4-1).

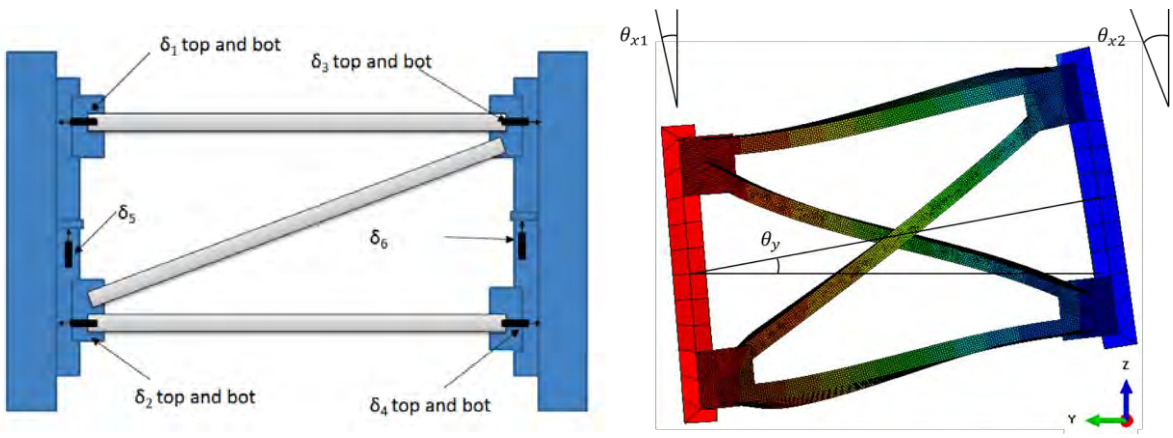

Figure F4-12: Computation of cross-frame stiffness from laboratory test and FEA analysis

Next, the RT investigated the basic modeling assumptions to ensure accurate results of its FEA studies relative to the experimental tests. More specifically, the RT studied the method by which angle sections are attached and constrained to the gusset plate (i.e., the welded connection) in the finite-element model. In total, four different connections were investigated, including the portions of the connection that were constrained (surface-to-surface and edge-to-edge) and how the rotational degree-of-freedom (released or constrained) was handled. The four conditions considered were as follows:

- Surface-to-surface connection and rotational degree-of-freedom (RDOF) constrained,
- Surface-to-surface connection and RDOF released,
- Edge-to-edge connection and RDOF constrained, and
- Edge-to-edge connection and RDOF released.

Figure F4-13 demonstrates the difference between surface-to-surface connections and edge-to-edge connections. Surface-to-surface connections constrain all overlapping components of the connected angle leg and the gusset plate (i.e., the entire overlapping surface is tied together). In contrast, edge-to-edge connections only constrain overlapping edges of the same elements, which simulates welds more precisely. The RDOF is simply related to the rotational fixities provided by the assumed constraints. A released condition implies that the connection is more flexible than the constrained condition. In all cases though, an unbalanced weld detail is represented, where the centroid of the angle member does not coincide with the centroid of the weld constraints. Refer to Section F4.1 for a detailed discussion on balanced and

unbalanced welds.

As noted in the Phase I summary (Appendix D), most state DOTs specify a slip-critical (SC) bolted connection between the cross-frame member and the gusset plate with TxDOT being a key exception. Given that the present study is focused on the cross-frame response within the elastic range, it is assumed that SC bolted connections do not slip at these service-level loads. In terms of stiffness, the response of a bolted connection and a welded connection should be nearly identical. Therefore, the RT is of the opinion that the elastic stiffness of a cross-frame does not depend on bolted versus welded connections and is relatively unaffected by the connection method. The cross-frame stiffness, however, is a function of the member sizes and geometry. With that in mind, the RT elected to examine various cross-frame geometries and dimensions in this study but not different connection methods.

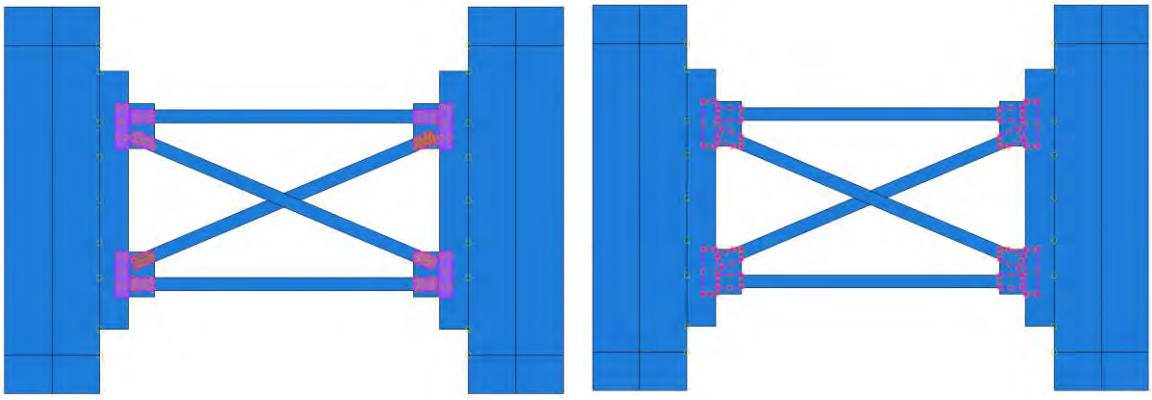

Figure F4-13: Surface-to-surface (left) and edge-to-edge (right) connections in cross-frame members

To ensure reliable analytical results, the RT studied the impact of each connection condition on the cross-frame stiffness. The RT replicated the specific cross-frame panel studied analytically and experimentally by Wang and compared the stiffness results between the different modeling approaches. From the laboratory test, the torsional stiffness of cross-frame was measured as 872,000 kip-in/rad under equal rotation loading. Table F4-4 compares the measured data with the various analytical results.

Table F4-4: Cross-frame stiffness from laboratory test and Abaqus analysis

Connection Details	Stiffness [10^3 x kip-in/rad]
Surface-to-surface, RDOF constrain	905
Surface-to-surface, RDOF release	891
Edge-to-edge, RDOF constrain	905
Edge-to-edge, RDOF release	869
Laboratory results	872

From Table F4-4, it is apparent that the connection details have a small influence on the panel stiffness when compared to the laboratory measurements. As expected, releasing the RDOF softens the connection and results in a more flexible system. Additionally, when the RDOF is constrained, the surface-to-surface and edge-to-edge connection effects are negligible as the entire overlapped section is rigidly tied together along all four faces. Considering the computational benefits of the surface-to-surface connection and the good agreement with the measured results, the RT elected to use surface-to-surface connections with the

RDOF released for its panel-level and system-level studies.

F4.2.2 Parametric Study Results

With a reliable modeling approach developed, the next step was to carry out a parametric FEA study and investigate a variety of cross-frame geometries subjected to the various deformation patterns. In general, the stiffness of a shell-element model (all cross-frame components modeled as shell elements) is compared to the equivalent truss-element model, which is consistent with the approach adopted by many 3D commercial software programs. The ratio of the shell-element stiffness, which explicitly considers the detrimental effects of an eccentric end connection as well as the effects of additional in-plane rotational restraint, and the truss-element model stiffness is represented as the R-factor. This procedure is similar to that described for the member-level study, except that the measured stiffness now applies to the full cross-frame panel, and not just an isolated member. The stiffness modification factor, R, is expressed mathematically as the following:

$$R = \frac{\beta_{shell}}{\beta_{truss}} \qquad F4.9$$

where: β = torsional stiffness of the entire cross-frame panel for either the shell-element model or the truss-element model.

Figure F4-14 depicts the general modeling approach for the truss-element model and the shell-element models built for this study. The large plate elements to the left and right of the cross-frame panel represent the girder, which is effectively treated as a rigid element. Thus, the focus is the cross-frame members and not any local distortional effects in the girders.

The inclination angles of the diagonals in both sets of models were held constant to ensure similar geometries, which is also illustrated in Figure F4-14. This is an important distinction as different inclination angles would invalidate the direct comparison between the shell-element and truss-element models.

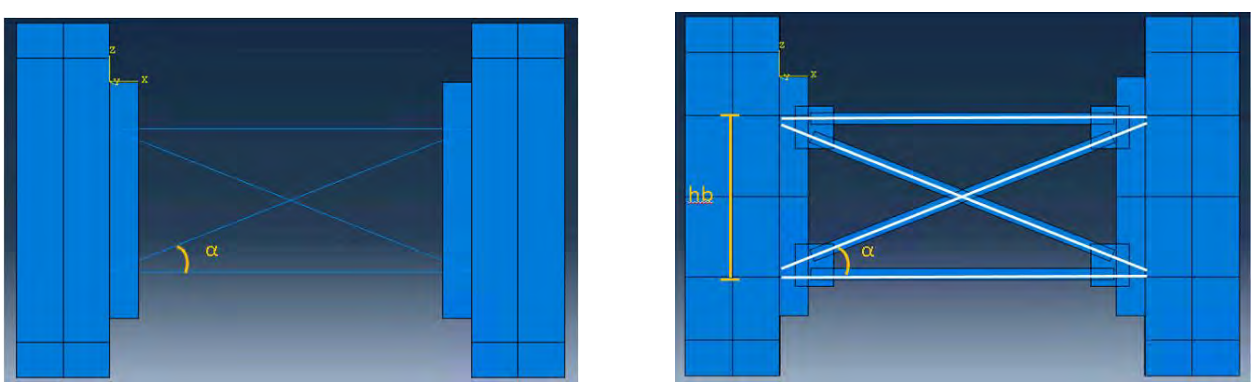

Figure F4-14: Truss-element (left) and shell-element (right) panel models used in panel-level studies

The variables considered in the panel-level parametric study included girder spacing, cross-frame height, gusset plate thickness, and angle sizes. Table F4-5 presents the range of values considered for each parameter, which are representative values in practical bridge applications.

For this study, the girder spacing was assumed to be always larger than the girder depth, which implies that more flexible cross-frames are evaluated. Gusset plate thickness values range from 1/4 inch to 3/4 inch; note that the height and width dimensions of the plate were held constant to achieve adequate weld lengths

and proportioning of the connection. The connection plate dimensions were maintained at a constant 9-inch width and a ½-inch thickness. Note that additional dimensions were examined via several spot-check models in Section F4.2.3.

Only equal-leg angles were considered, ranging from 3-inch to 6-inch leg lengths and 1/4-inch to 5/8-inch thicknesses. The study was also limited to X-type cross-frames only; K-type cross-frames are examined in Section F4.2.3 for several spot-check models. Even with these limitations imposed, about 2,000 unique cross-frame geometries were developed as part of this parametric study. Note that the number of shell-element models exceeds that of the truss-element models because truss-element models do not explicitly model the gusset plate; thus, that variable is eliminated in truss-element models.

Table F4-5: Parameters considered in the panel-level parametric study

Parameter	Range of Values [in]
Cross-frame height	{48, 60, 72, 84, 96}
Girder spacing	{96, 108, 120, 132, 144}
Angle leg width (equal leg only)	{3, 4, 5}
Angle leg thickness	{1/4, 3/8, 1/2, 5/8}
Gusset plate thickness	{1/2, 3/4}

These parameters were evaluated for their relative impact on the panel stiffness and the associated R-factor. Each unique cross-frame was loaded to simulate the various loading deformation patterns: (i) equal rotation, (ii) differential vertical displacement, and (ii) differential rotation. To capture the effective stiffness under these loading conditions, stiffness modification factors under each loading case were evaluated independently. Figure F4-15 shows the applied loading mechanisms and boundary conditions used to simulate each load case in the FEA model, where supports are represented as black arrows demonstrating the direction of the applied reaction. Although not shown, loading and boundary conditions are identically applied to the simplified truss-element models.

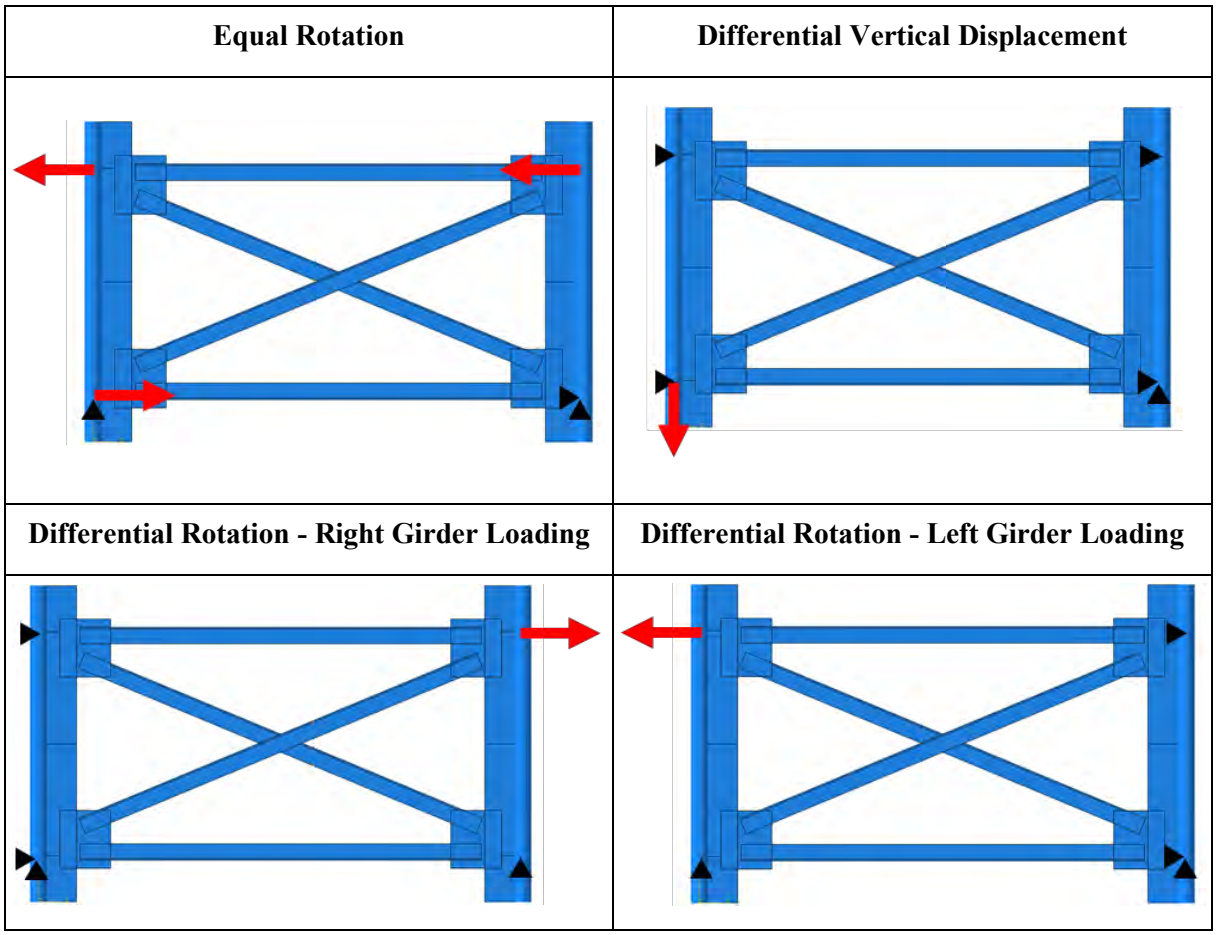

Figure F4-15: Three loading cases considered in the panel-level FEA parametric study

For reference, sample output is provided in Figure F4-16 that demonstrates the resulting deflected shapes for each of these loading conditions. Note that the color contours in this figure correspond to total displacement, largely highlighting the out-of-plane displacements cause by the eccentric load path. Additionally, the in-plane rotational restraint of the connection and gusset plate is also evident. A first-order analysis was conducted to maintain consistency with previous panel-level parametric studies (W. Wang 2013).

Equal Rotation	Differential Vertical Displacement
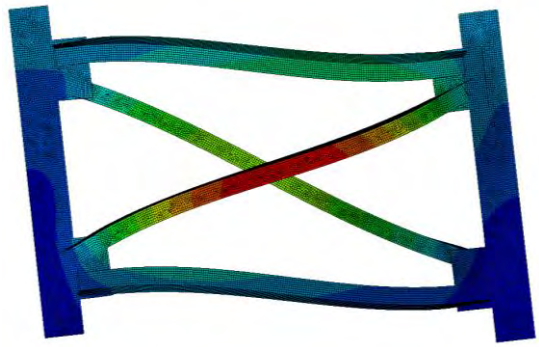	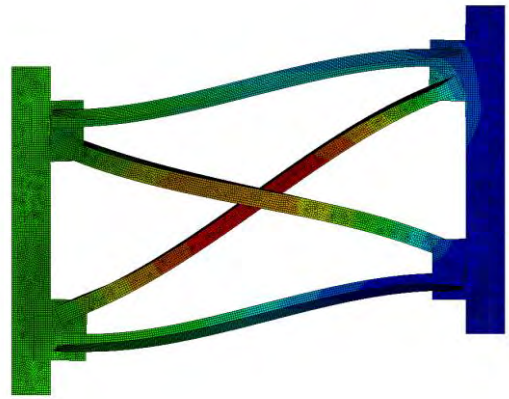
Differential Rotation - Right Girder Loading	**Differential Rotation - Left Girder Loading**
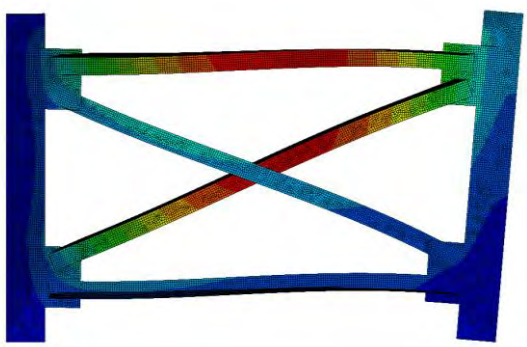	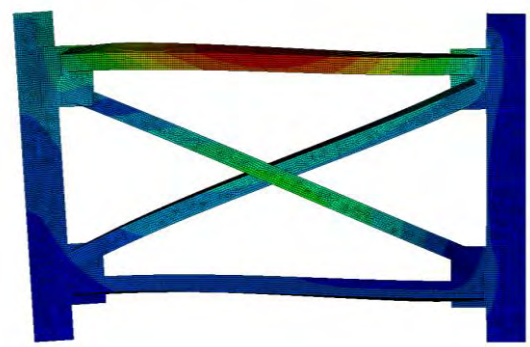

Figure F4-16: Sample deflected shapes corresponding to the various loading conditions considered

As illustrated in Figure F4-15 and Figure F4-16, the differential rotation case is evaluated with two separate loading conditions, "Right Girder Loading" and "Left Girder Loading," whereas the equal rotation and differential vertical displacement cases are considered with only one condition. After conducting preliminary analyses, the RT observed a considerable discrepancy in computed cross-frame stiffness when applying differential-rotation loads of identical magnitudes to the left and right girders. It was discovered the orientation of the cross-frame diagonal member connection had substantial impact on the response of the cross-frame system. This is depicted schematically in Figure F4-17, which presents a detailed close-up of the top strut and diagonal connection for both "left" and "right" loading conditions.

In the "right" loading condition, only the top strut and the grey diagonal member are engaged. These two members are connected to the same face of the gusset plate. In this case, the corresponding eccentricity of this connection is additive with respect to the gusset-to-connection plate connection. Conversely in the "left" loading condition, only the top strut and the yellow diagonal member are engaged. The diagonal in this scenario is fastened to the opposite face of the gusset plate as the top strut. This, in turn, often has a beneficial effect on the stiffness response by reducing the eccentricity. For X-type cross-frames, the

diagonal members must be connected to opposite faces of the gusset plates to avoid interference at the cross-over point. The position of the struts can vary and depend on the standard DOT details and fabricator preference. Note that the orientation presented in Figure F4-17 is based on the standard detail provided by many DOTs.

Despite sharing the same geometry and eccentric load path, a similar discrepancy in load direction effects is not observed for the equal rotation and differential vertical displacement cases. For these two deformation patterns, both diagonals are engaged. Therefore, the computed cross-frame stiffness inherently considers the effects of both diagonal connections and is effectively "averaged out."

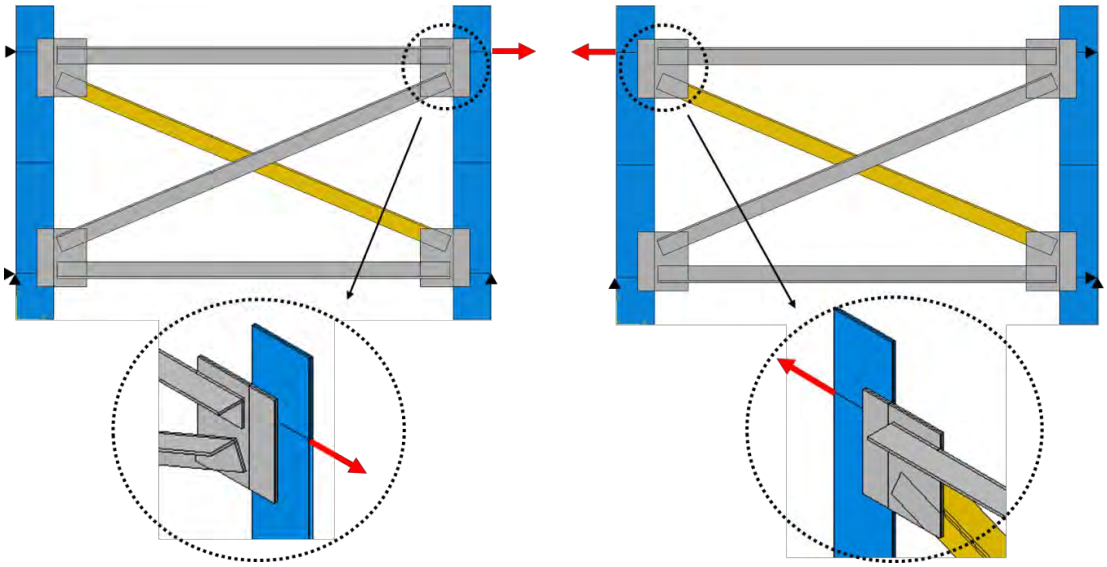

Figure F4-17: Assumed orientation of cross-frame members for differential-rotation loading

To demonstrate the effects on the eccentric load path, take the cross-frame presented in Figure F4-17 as an example. In this case, L4x4x3/8 angles are used with ½-inch gusset and connection plates. For the "right" loading case, the total eccentricity of strut and diagonal are both +1.88 inches. For the "left" loading case, the eccentricity of the strut is still +1.88 inches; however, the eccentricity of the diagonal is -0.88 inches in the opposite direction, which has a counteracting effect. The RT found that the orientation of the connection can make a significant difference on the stiffness response of the cross-frame, as is demonstrated herein.

Before showing the full results of the parametric study, an example is provided for context. The cross-frame presented in Figure F4-17, which is identical to the cross-frame experimentally tested by Wang (2013), is selected. Recall that the single angle members are taken as L4x4x3/8 sections and the gusset and connection plates are a ½-inch thick.

Table F4-6 summarizes the results of this sample data set. Both the computed panel stiffness for the shell-element model, β_{shell}, and the corresponding modification factor, R, are tabulated for the various loading cases considered. In review of the reported values, it is apparent that the equal rotation and differential vertical displacement cases result in nearly identical stiffness responses. A major discrepancy, however, is noted with the differential rotation case.

The stiffness response of the cross-frame panel is considerably smaller for "right" loading, a case in which the eccentric load path of the angle members is additive to the connection-to-gusset connection. Thus, a more flexible response is expected given a more flexible connection. The opposite is true for the "left" loading case, where the strut and diagonal have counteracting eccentricities. The difference in the response ranges from a computed modification factor of 0.42 and 0.71, which is significant. Notice, however, that

the "average" of those two loading conditions, a case in which both diagonals would be engaged, would be approximately the same as the equal rotation and differential vertical displacement cases.

Table F4-6: Sample computed cross-frame stiffnesses and modification factors for various loading cases

Loading Case	Computed Shell-Element Stiffness [1000 kip-in/rad]	Computed R-Factor
Equal Rotation	868	0.55
Differential Vertical Displacement	888	0.56
Differential Rotation - Right Girder Loading	663	0.42
Differential Rotation - Left Girder Loading	1,126	0.71

A similar procedure was conducted for every unique cross-frame panel considered in the parametric study. Figure F4-18 summarizes those results. The computed R-factor derived from Eq. F4.9 is plotted separately for the given loading condition. Each data point is grouped by angle leg thickness to highlight the relative impact of the parameters on the results. Within each grouping, various angle leg lengths and girder spacing-to-panel height ratios are grouped and presented. Figure F4-18 provides specific callouts to demonstrate how the various parameters are presented. Additionally, the results presented correspond to a constant gusset plate thickness of 0.5 inches only; note that an increase in gusset plate thickness has been shown to generally produce higher modification factors.

Figure F4-18 presents the results of the four loading conditions previously outlined and depicted in Figure F4-15, as well as one additional case. The additional load case considers the combined effect of the "left" and "right" girder loading scenarios, such that both diagonals are engaged. This load case is effectively the "average" condition discussed above for the differentia rotation condition. This is designated as the "average" condition in Figure F4-18.

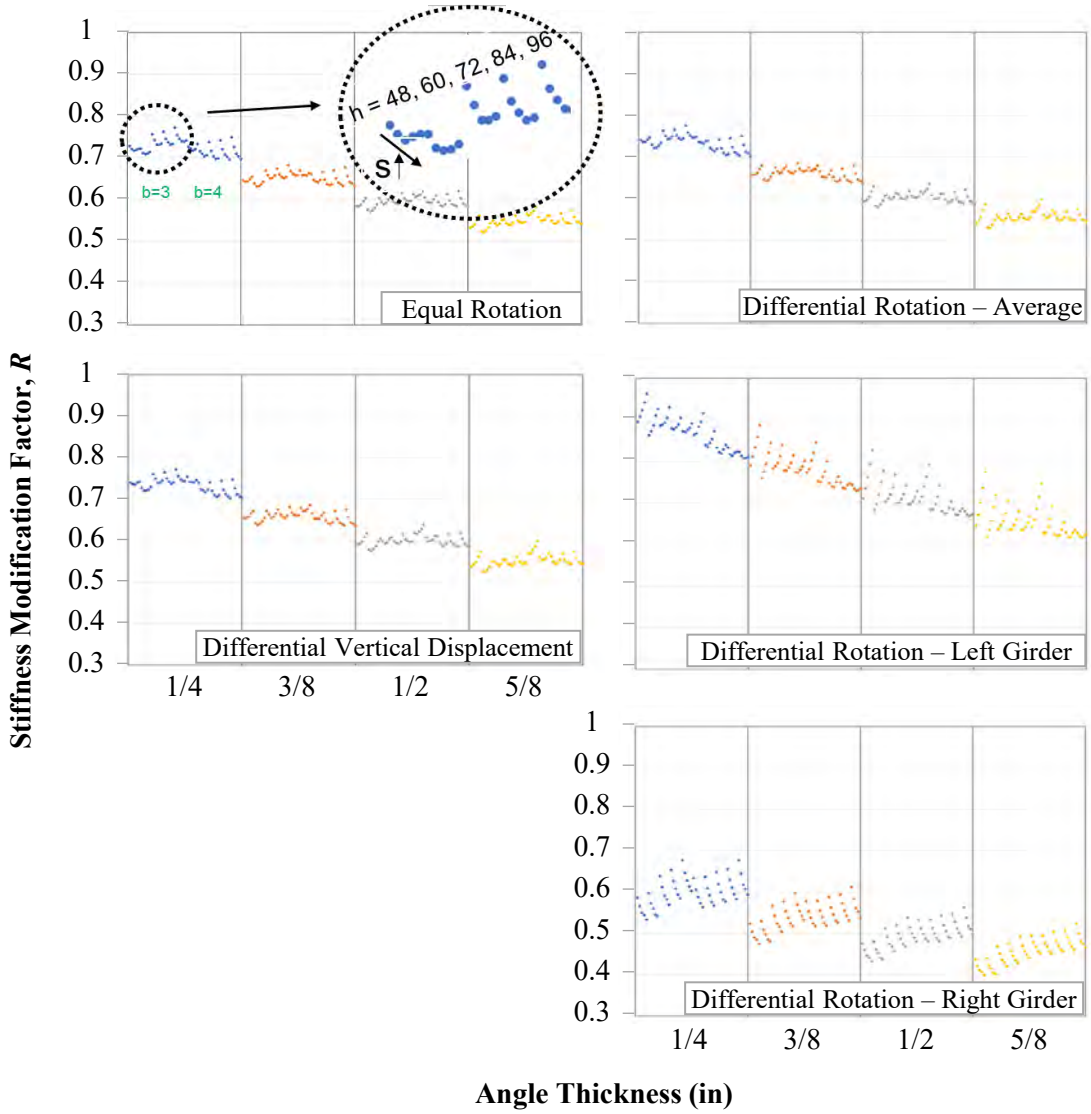

Figure F4-18: Computed stiffness modification factors for various loading conditions and angle thicknesses

From Figure F4-18, the following observations can be made:

- In general, the parameters of the single angle section (thickness, leg width) and the aspect ratio of the panel (girder spacing, panel height) affect the computed modification factor, *R*. The Battistini R-factor equation (2016) showed that increasing the S/h_b ratio (girder spacing-to-panel height), $\bar{y}$ (distance between the face of the connected leg and the neutral axis of the angle section), and *t* (angle leg thickness) results in a decreased R-factor for the equal rotation condition. Similar trends are generally observed from the results of this present study.
- The "average" differential rotation case typically results in similar R-factors as the uniform rotation and differential vertical displacement cases. However, the scatter in the results can be significant depending on which girder rotates relative to the adjacent one (i.e., which cross-frame diagonal is engaged). R-factors between 0.4 and 1.0 were observed for the "left" and "right" loading cases for differential rotation.

The cross-frame parameters (angle thickness, angle leg width, girder spacing, panel height, gusset thickness) are typically controlled by the designer. Even for these well-established parameters, there is substantial variability in the R-factor response, as observed from the member-level study. The assumed deformation pattern and the force distribution through the diagonal members, on the other hand, are largely dependent on the position of the truck. Truck position, which can be highly variable, also has a significant effect on the appropriate modification factor.

Given the variability and uncertainty in the response due to different geometries and loading conditions, developing a closed-form, general-use solution similar to Battistini et al. (2016) would be challenging and impractical for design. For a simplicity standpoint, assigning a single modification factor for each cross-frame member, similar to the current approach in AASHTO LRFD, is desirable. This is particularly true since the orientation of the cross-frame connections (increasing or decreasing eccentricities) may not be known during the design process. With that in mind, the system-level studies in the next subsection evaluate the most appropriate modification factor to assign for the majority of bridge superstructures in service. An independent parametric study that quantifies the impact of an assumed R-factor on the cross-frame force prediction in composite bridge systems is outlined.

F4.2.3 Spot-Check Results

As noted in the preceding subsection, the RT maintained constant connection plate dimensions in the parametric study to set a reasonable limit on the number of cases examined. As such, a ½-inch thick, 9-inch wide connection plate was used in the analytical study to be consistent with the experimental tests conducted by Wang (2013). It should be noted, however, that this connection plate violates the stiffener slenderness ratios established by AASHTO LRFD Eq. 6.10.11.1.2-2, which states that the width of a stiffener shall not exceed 16 times its thickness (i.e., $b/t = 9 / 0.5 = 18 > 16$). Despite this violation, the RT was confident that this slight increase in connection plate slenderness had minimal impact on the R-factor results produced by the panel-level R-Factor Study. Additionally, the parametric study was limited to only X-type cross-frames. Given that they are also prevent used across the US, it is prudent to computationally study the stiffness of K-frames as well.

To verify this assertion and expand the scope of the study, additional spot-check models were developed. Section F4.2.3.1 addresses the connection plate studies, and Section F4.2.3.2 addresses the K-frame studies.

F4.2.3.1 Connection Plate Dimensions

Given that the width of a ½-inch thick connection plate shall not exceed 8 inches in width per AASHTO LRFD Specifications, the RT elected to conduct additional analyses with 7-inch and 8-inch wide plates. Figure F4-19 presents the typical connection-to-gusset plate connections used in this spot-check study for various connection plate widths. Note that it was decided (i) to maintain at least a 4-inch overlap between the two plates to represent more realistic, practical conditions and (ii) to maintain consistent inclination angles in the diagonals for consistency. As such, the gusset plate width was widened accordingly to satisfy the restrictions set.

For reference, the left figure represents the connection used in the panel-level parametric study (i.e., 9-inch wide connection plate and a 12-inch wide gusset plate). The middle figure represents the connection detail for an 8-inch wide connection plate with the corresponding 13-inch wide gusset, and the right figure represents the connection detail for a 7-inch wide connection plate with the corresponding 14-inch wide gusset. Each of these connection details were subsequently applied to three different X-type cross-frame geometries, which is illustrated in Table F4-7.

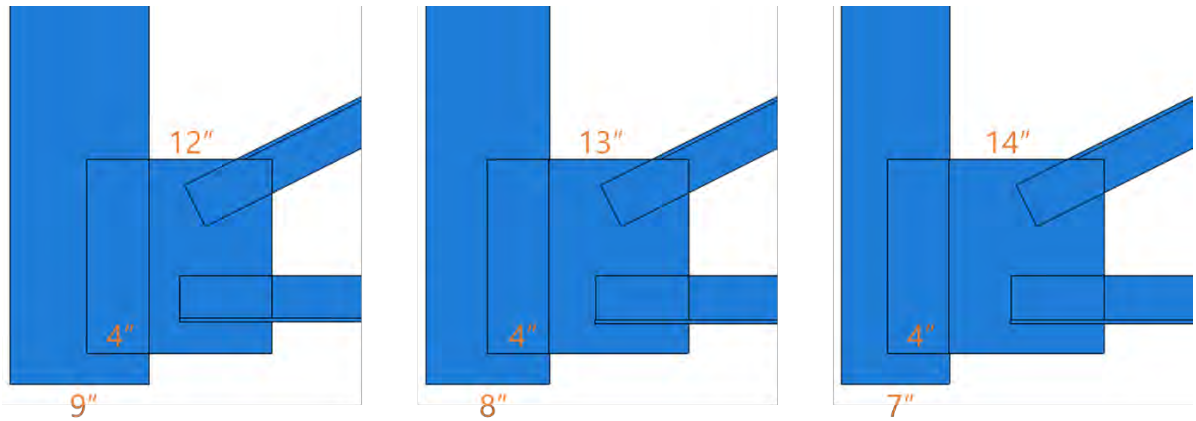

Figure F4-19: Connection details for 9-, 8-, and 7-inch wide connection plates

Table F4-7: Cross-frame geometries considered in connection-plate spot-check studies

Parameters	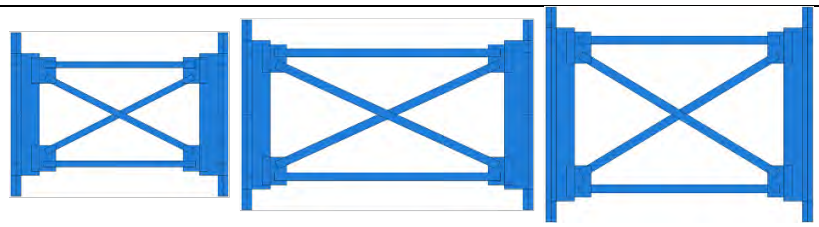		
	Case 1	**Case 2**	**Case 3**
Girder spacing [in]	96	132	120
Cross-frame height [in]	48	60	72

For each one of these cross-frame configurations and connection details, the panels were loaded under the same five loading conditions are those identified in the preceding section: equal rotation, differential vertical displacement, differential rotation, differential rotation (right girder loading), and differential rotation (left girder loading). The loading conditions are shown schematically in Figure F4-23.

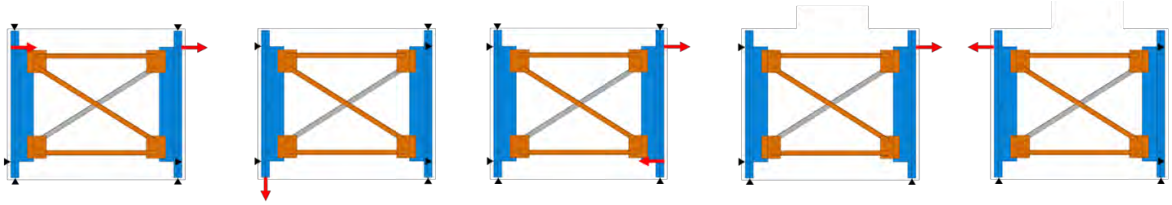

(a) Equal Rotation | (b) Differential Vertical Disp. | (c) Differential Rotation | (d) Differential Rotation (Right) | (e) Differential Rotation (Left)

Figure F4-20: Loading cases considered in the X-frame spot check

Table F4-8 through Table F4-10 summarize the computed stiffness modification factors from these various analytical studies. Recall that the computed R-factor represents the relative difference in stiffness between a shell-element model and a truss-element model. Table F4-8 specifically addresses Case 1 cross-frame

configuration from Table F4-7 (i.e., 8-foot girder spacing and 4-foot cross-frame height). Table F4-9 addresses Case 2, and Table F4-10 addresses Case 3.

Table F4-8: Computed modification factors for different connection plate lengths (configuration Case 1 in Table F4-7)

Connection Plate Width [in]	Computed R-Factor				
	Equal Rotation	Differential Vertical Disp.	Differential Rotation	Differential Rotation (Right)	Differential Rotation (Left)
9	0.73	0.74	0.74	0.90	0.59
8	0.72	0.73	0.73	0.87	0.60
7	0.73	0.73	0.74	0.86	0.61

Table F4-9: Computed modification factors for different connection plate lengths (configuration Case 2 in Table F4-7)

Connection Plate Width [in]	Computed R-Factor				
	Equal Rotation	Differential Vertical Disp.	Differential Rotation	Differential Rotation (Right)	Differential Rotation (Left)
9	0.64	0.65	0.65	0.78	0.53
8	0.64	0.65	0.65	0.76	0.53
7	0.64	0.65	0.65	0.75	0.54

Table F4-10: Computed modification factors for different connection plate lengths (configuration Case 3 in Table F4-7)

Connection Plate Width [in]	Computed R-Factor				
	Equal Rotation	Differential Vertical Disp.	Differential Rotation	Differential Rotation (Right)	Differential Rotation (Left)
9	0.59	0.59	0.59	0.68	0.51
8	0.58	0.59	0.59	0.66	0.51
7	0.58	0.58	0.58	0.64	0.52

From the tables, it is evident that the connection plate width and subsequent changes in the connection detailing have minimal effect on the computed R-factor for all loading conditions. For instance, changing the connection plate width from 9 inches to 7 inches reduces the R-factor from 0.73 to 0.72 for the equal rotation deformation pattern of Case 1. From these spot-check results, the RT is confident that the parametric study results presented in Section F4.2.2 are applicable for a variety of loading conditions and cross-frame dimensions, despite the slender connection plate assumption.

F4.2.3.2 K-Type Cross-Frames

In terms of K-type cross-frames, the diagonals do not cross over at their mid-length, as they do in X-frames. Thus, the diagonal members in K-frames are typically fabricated and connected to the same side of their corresponding gusset plates. Thus, the issue outlined in Figure F4-17 (i.e., significantly different stiffness response of "left" girder loading versus "right" girder loading) should theoretically not be an issue for K-frames. In the spot-check models, this assertion was verified for a sample cross-frame configuration.

The cross-frame panel and loading conditions summarized in Table F4-6 are replicated for a K-type configuration. For reference, the applied loads and deformed shapes for each loading condition are graphically presented in Figure F4-21. Note that an additional equal rotation case is evaluated: translating the top strut and translating the bottom strut, where the diagonals intersect at mid-length. There are represented as "Equal Rotation – Top" and "Equal Rotation – Bottom" in the figure.

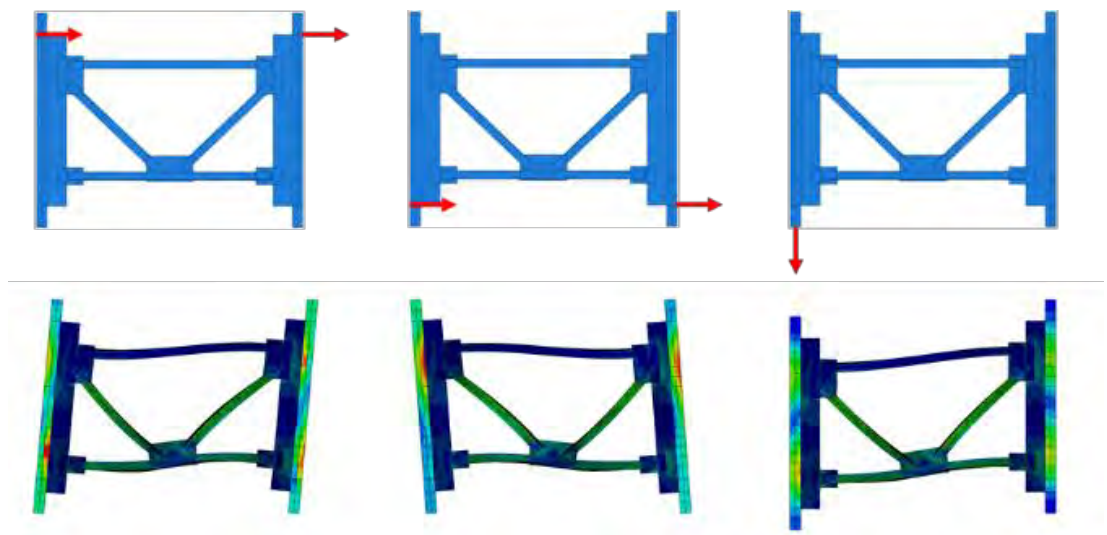

(a) Equal Rotation (Top) (b) Equal Rotation (Bottom) (c) Differential Vertical Disp.

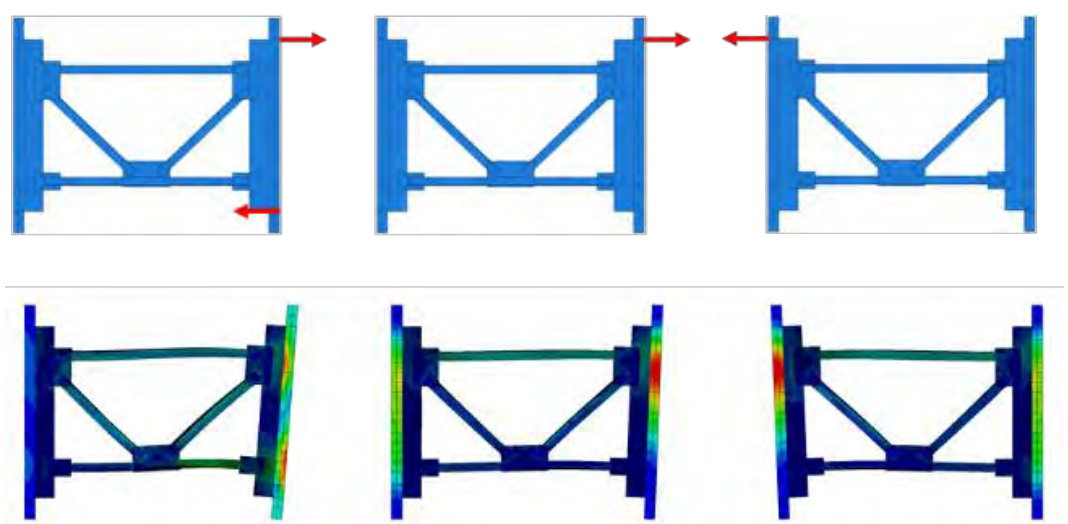

(d) Differential Rotation (e) Differential Rotation (Right) (f) Differential Rotation (Left)

Figure F4-21: Loading cases and deflected shapes considered in K-frame spot check

Table F4-11, similar to Table F4-6, compares the computed torsional stiffness of the cross-frame panel for the various loading conditions. Recall from Table F4-6 that the differential-rotation deformation patterns resulted in substantially different responses due to the connections details of the two diagonal members. Given that the diagonals in a K-frame are identically connected at both ends, it is evident in Table F4-11 that a similar trend is not observed. For all loading cases, the reported stiffness values are approximately the same (i.e., within 1%). Thus, it can be concluded that K-frames are not as sensitive to load pattern given the symmetry of the end connections, thereby verifying the assertion above.

Table F4-11: Sample computed cross-frame stiffness for K-frame subjected to various load cases

Loading Case	Computed Shell-Element Stiffness [1000 kip-in/rad]
Equal Rotation Top	810
Equal Rotation Bottom	810
Differential Vertical Displacement	814
Differential Rotation	800
Differential Rotation - Right Girder Loading	815
Differential Rotation - Left Girder Loading	815

F4.3 System-Level Studies

The system-level study builds on the member-level and panel-level studies outlined previously. Member-level studies evaluated the stiffness of isolated cross-frame members; panel-level studies evaluated the global stiffness of an isolated, noncomposite panel. The system-level study is now used to assess the accuracy of the R-factor approach to modeling cross-frames in 3D composite bridge structures with various connection and gusset plate thicknesses. More specifically, the appropriate R-factor is sought for a variety of bridge and cross-frame geometries, as well as the sensitivity of the cross-frame response due to the assigned R-factor.

To make those assessments, a variety of analytical studies was conducted as part of the system-level study. The subsections herein address each one of those studies independently. Section F4.3.1 outlines a preliminary analysis performed in the early stages of Phase III to evaluate the accuracy of the Battistini et al. formulation for use on composite bridges in service.

Section F4.3.2 performs a scaled parametric study to evaluate these effects on skewed and/or horizontally curved bridge systems. Section F4.3.3 expands on Section F4.3.2 and outlines a comprehensive parametric study used to evaluate the overall sensitivity of cross-frame forces to the assigned modification factor. This parametric study is limited to straight bridges with normal supports, as the relative impact of connection details (e.g. gusset plate thickness) is the primary focus.

For each individual study, the RT builds and compares multiple versions of the same 3D bridge model. Each iteration investigates a different approach to modeling the cross-frame elements, while the rest of the 3D model remains unchanged. In general, the rigorous shell-element model serves as the benchmark model, for which the rest of the iterations are compared. This serves as the most accurate representation of the bridge superstructure. Then, truss-element models are developed where the assigned R-factor is varied. Lastly, Section F4.3.2 investigates the use of a proposed eccentric-beam modeling approach, which is based on the member-level analytical model described in Section F4.1.1. Thus, for each individual study, the following model iterations are considered:

- Shell-element model (representing the most accurate solution),

- Truss-element model with different stiffness modification factors (range of values depends on study), and
- Eccentric-beam model (applies only to Section F4.3.2).

Figure F4-22 illustrates the general shell-element and truss-element modeling approaches consistently used in the system-level studies. Note that in the shell-element model, all individual plate and angle sections are explicitly considered as shell elements. In both cases though, the inclination angle was held constant to maintain consistency in the results. That is to say, truss elements in the truss-element models were positioned to coincide with the centroids and working points of the single-angle members in the shell-element models.

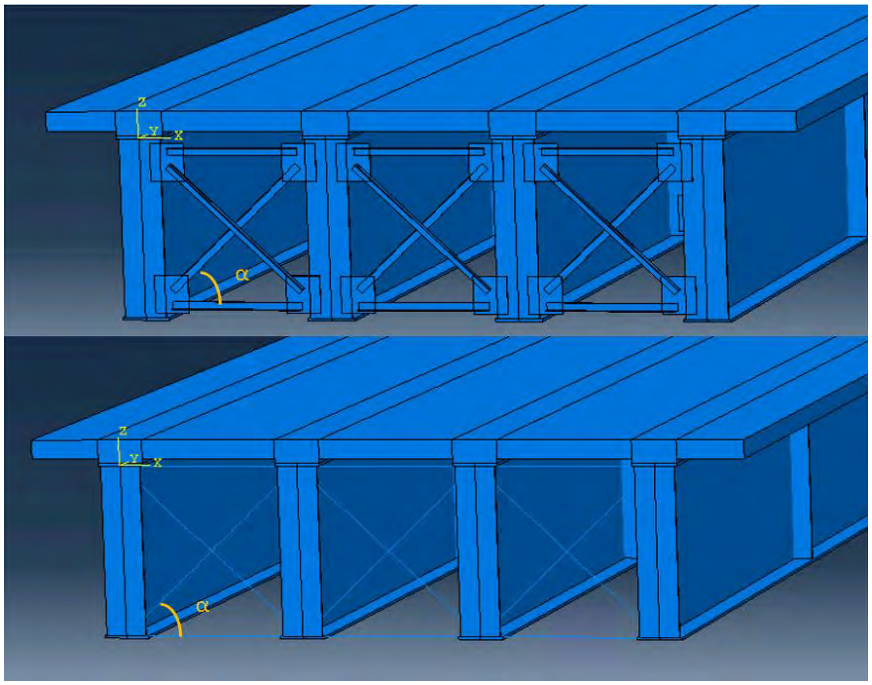

Figure F4-22: Shell- (top) and truss-element (bottom) models used in the system-level parametric study

F4.3.1 Preliminary Study

As documented in Section F3.1.1, shell- and truss-element cross-frame modeling of the three instrumented bridges was completed in the early stages of Phase III. From this exercise, the RT observed that the cross-frame forces obtained from the truss-element approach, which were based on R-factors derived from Battistini et al., agreed well with the shell-element model and the measured data for Bridge 1 (straight and normal) and Bridge 3 (curved and normal). The truss-element model generally produced cross-frame force predictions within 5% of the shell-element model. However, more significant discrepancies were observed from Bridge 2 (straight and skewed).

The RT recognized that the errors in the Bridge 2 model were related to the assigned stiffness modification factor. Based on the geometry and relevant section properties, typical intermediate cross-frames were assigned a respective R-factor of 0.59, 0.46, and 0.54 for Bridges 1, 2, and 3 based on the Battistini regression equation. Note that the stiffness modification of Bridge 2 is noticeably lower than the other two bridges, largely due to the S/h_b term in the equation. The respective girder spacing to cross-frame depth ratios are approximately 1.55, 1.8, and 1.0 for Bridges 1, 2, and 3. With this as motivation, the RT elected to conduct a preliminary analytical study to further evaluate cross-frames of different proportions with low

R-factor values, similar to Bridge 2. The RT primarily sought an explanation for the errors observed in the Bridge 2 truss-element models.

The RT conducted a preliminary parametric study, which included the following parameters: support skew angle, girder spacing, girder depth, and gusset plate thickness. Girder spacing and girder depth are variables explicitly considered in the regression equations, whereas support skew and gusset plate thickness are not. The parametric study consisted of a straight 125-foot, five-girder span with composite girders. Regardless of support skew, cross-frames were spaced at 12.5-feet on center and were positioned normal to the girders. Two separate models were built (cross-frames modeled as shell elements and cross-frames modeled as truss elements with a variable stiffness modification factor), and the results were compared.

For each individual parameter, the RT varied the magnitude while holding the remaining parameters constant. The range of values considered for each parameter of interest is summarized in Table F4-12. The RT considered exaggerated ranges for some variables to better illustrate their respective impacts on the results; for instance, 15-foot girder spacings were considered despite being an impractical value in practice. Using the regression equations, the R-factors ranging from 0.30 to 0.58 were considered by varying the S/h_b term; thus, the focus of the preliminary analysis was on relatively flexible cross-frame systems with R-factors less than 0.50.

Table F4-12: Range of values considered for preliminary system-level study

Parameters	Range of Values
Support skew angle [degrees]	{0, 45, 60}
Girder spacing [ft]	{5, 10, 15}
Girder depth [ft]	{5, 8, 11}
Gusset plate thickness [in]	{3/8, 1/2, 3/4}

Table F4-13 and Table F4-14 present a sample of the results obtained during this study. In both tables, the results correspond to the same straight, 125-foot span bridge with normal supports. Estimated cross-frame forces of the critical bottom strut and diagonal members are shown; an identical static load similar to the controlled live load tests (four, 50-kip sand trucks) was applied in both cases. Table F4-13 presents results for a bridge with 5-foot girder spacing, and Table F4-14 presents results for a bridge with 15-foot girder spacing. Using the Battistini regression formula, the stiffness reduction factor should be 0.58 and 0.30 for the models corresponding to Table F4-13 and Table F4-14, respectively. Additional R-factors were also considered to demonstrate the sensitivity of the cross-frame response. The Battistini results, however, are italicized in the tables to emphasize the differences in the results. It should also be noted that support skew angle had negligible effect on the comparative results, such that the variability observed in Table F4-13 and Table F4-14 for normal bridges was similar to that of skewed bridges.

From Table F4-13, it is evident that the truss-element model implementing stiffness modification factors from the regression equation produce accurate results when compared to the rigorous shell-element model. However in Table F4-14, for the bridge with 15-foot girder spacing and an R-factor of 0.30 according to the regression equation, more than 30% error is observed for both the critical bottom strut and diagonal member. In these cases, the predicted cross-frame forces were substantially underestimated by the truss-element approach. Instead, the truss-element model produces the best results when a larger stiffness modification of 0.60 is assigned.

Table F4-13: Predicted cross-frame forces for critical bottom strut and diagonal in straight bridge with 5-foot girder spacing using various stiffness reduction factors

Assigned Stiffness Reduction	Diagonal Axial Force			Bottom Strut Axial Force		
	Shell Element Model	Truss-Element Model	% Error	Shell Element Model	Truss-Element Model	% Error
0.5	5.28	4.58	-13.3	3.31	3.14	-5.1
0.58	*5.28*	*4.79*	*-9.2*	*3.31*	*3.32*	*0.2*
0.6	5.28	4.97	-5.9	3.31	3.46	4.5
0.8	5.28	5.26	-0.4	3.31	3.70	11.7
1.0	5.28	5.55	5.1	3.31	3.94	19.1

Table F4-14: Predicted cross-frame forces for critical bottom strut and diagonal in straight bridge with 15-foot girder spacing using various stiffness reduction factors

Assigned Stiffness Reduction	Diagonal Axial Force			Bottom Strut Axial Force		
	Shell Element Model	Truss-Element Model	% Error	Shell Element Model	Truss-Element Model	% Error
0.3	*9.47*	*6.04*	*-36.2*	*6.66*	*4.41*	*-33.8*
0.5	9.47	8.03	-15.2	6.66	5.78	-13.1
0.6	9.47	9.24	-2.5	6.66	6.52	-2.0
0.8	9.47	10.27	8.5	6.66	7.10	6.6
1.0	9.47	11.48	21.2	6.66	7.68	15.4

Based on the findings of this initial system-level study, the accuracy of the Battistini et al. formulation was questioned for composite bridge conditions, particularly for flexible cross-frames with higher S/h_b ratios. Recall that the formulation is based on an assumed deformed shape in the construction state in which adjacent noncomposite girders rotate due to lateral-torsional buckling. The behavior of a cross-frame has been shown to be very different for a composite bridge system in service, where truck position and bridge geometry induce complex load demands on a cross-frame.

F4.3.2 Spot-Check Models

The parametric study documented in Section F4.3.3 hereafter focuses primarily on the correlation between connection details and the stiffness of cross-frames in composite systems. R-factors are determined for a variety of cross-frames in straight and normal bridges only. However, in order to make general-use recommendations to AASHTO LRFD that apply to all steel I-girder bridges, these R-factors must be evaluated for skewed and/or curved bridge systems as well. Thus, this section serves as a prelude to Section F4.3.3 and evaluates the stiffness modification approach for skewed and/curved bridges.

Rather than conduct a full-scale parametric study similar to the Fatigue Loading Study or the system-level R-Factor Study in subsequent Section F4.3.3, the RT elected to instead perform spot checks. Given the schedule constraints of the project, conducting a full-scale study was not feasible. However, evaluating stiffness modification factors for a representative set of skewed and curved bridges was deemed suitable.

As such, the RT built and compared several iterations of the same 3D bridge model, including shell- and truss-element models with variable R-factors, similar to the procedures outlined in previous subsections. However, for these spot-check models, an additional modeling approach was investigated: modeling cross-frames as eccentric-beam elements. This concept originated from the member-level studies documented in Section F4.1.1 and is further explained in Section F4.3.2.1 herein. The three unique approaches are depicted schematically in Figure F4-23 for reference. Note that this figure is similar to Figure F3-1, except that the eccentric-beam model is now included.

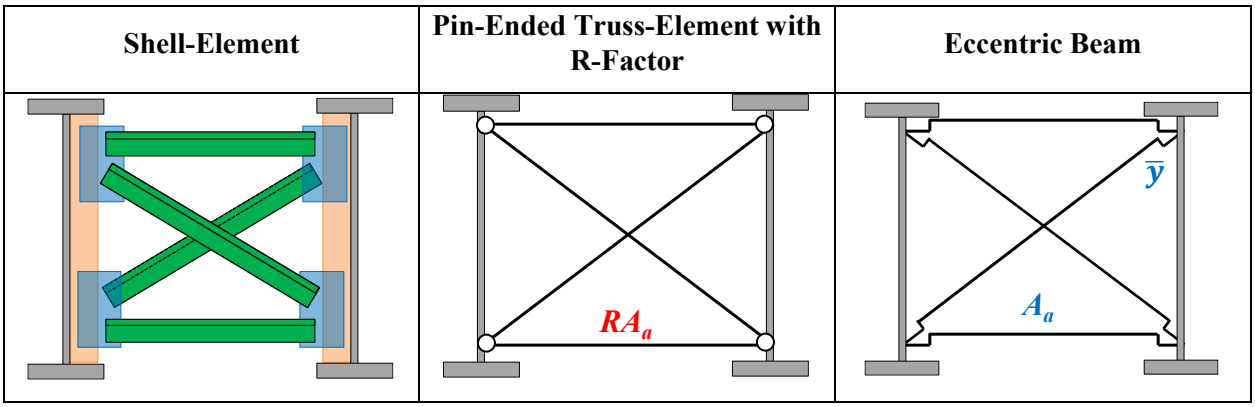

Figure F4-23: Various cross-frame modeling approaches considered in system-level studies

As a means to compare the analysis methods, the RT selected representative bridges from the 4,104-model matrix used in the Fatigue Loading Study (Section F3.1.2). Given the computational efforts required to produce multiple iterations of the same model, 20 bridges with different geometries were chosen for use in the spot-check analysis. These 20 bridges sample key parameters from the full 4,104-model matrix that typically affect cross-frame force predictions, namely support skew and bridge curvature. Of the 20 selected models, straight and horizontally curved bridges were included, as well as those with normal and skewed supports. A variety of single-span and continuous, two-span systems were also studied.

To study the impacts of gusset plate thickness, two different conditions were studied for each set of these models: ½-inch thick and 1-inch thick gusset plates. The length and width dimensions of the gussets were selected to achieve adequate detailing proportions in accordance with Battisinti et al. (2013), similar to Section F4.3.3. Note that the gusset thickness is explicitly considered in the shell-element and eccentric-beam approaches, but not in the truss-element approach. In total, 200 unique models were developed as part of this study as is shown with the following:

- Shell-element model: (20 bridges) x {1/2″, 1″} gusset plate = 40 models
- Truss-element model: (20 bridges) x {R = 1.0, 0.9, 0.8, 0.7, 0.6, 0.5} = 120 models
- Eccentric-beam model: (20 bridges) x {1/2″, 1″} gusset plate = 40 models
- Total models: 40 + 120 + 40 = 200 models (10 models per bridge)

The RT believes that the findings from this sample set are also applicable to a wider range of bridge geometries. For reference, the pertinent variables that describe the overall geometry and cross-frame layout of these sample bridges are summarized in Table F4-10 and Table F4-11. Table F4-10 presents ten straight bridges, and Table F4-11 presents ten curved bridges. Note that the 20 bridges selected for this study are identical to those considered in the Commercial Design Software Study documented in Chapter F5, for which simplified 2-D techniques are evaluated.

Ultimately, the effectiveness of the simplified model (i.e., truss-element model with assigned R-factor or eccentric-beam model) is evaluated as a ratio between the predicted axial force in select cross-frames from the simplified models to the predicted force in the same members from the shell-element model. This is

described algebraically as F_{truss}/F_{shell}. Rather than compare the stiffness of the models indirectly, it is more appropriate to evaluate the ability of the simplified model to accurately obtain design forces, which is of most importance to designers.

A ratio of unity represents perfect agreement between the shell-element model and the simplified truss-element model. This implies that the correct stiffness modification factor is assigned to the truss element representing the cross-frame member. Values below unity indicate that the assigned R-factor is likely too low (i.e., the cross-frame attracts less force). In other words, the truss-element model underpredicts the cross-frame force when compared to the more accurate shell-element model (i.e., unconservative estimate), and an increase in the modification factor is needed. The opposite is true for force ratios above unity.

Following this introduction, the motivation and assumptions behind the eccentric-beam approach are summarized. Then, results from the scaled parametric study are presented to highlight the performance of these modeling techniques for skewed and/or curved bridges.

Table F4-15: Independent variables describing 20 representative bridges in system-level R-Factor Study (straight bridges)

Parameter	Model ID									
	233-2	**253-3**	**277-2**	**1179-2**	**1181-2**	**1181-4**	**1183-2**	**1187-2**	**1213-3**	**1249-2**
Governing CF Location[a]	M-I	M-I	M-I	IS	IS	IS	IS	ES	M-I	M-I
Governing CF Member[b]	BS	BS	BS	BS	BS	BS	BS	BS	BS	BS
No. spans	1	1	1	2	2	2	2	2	2	2
L/d ratio	30	30	30	35	35	35	35	35	35	35
Girder spacing [ft]	8	10	6	8	8	8	8	8	10	6
No. girders	5	5	5	5	5	5	5	5	5	5
Support skew [deg.][c]	60	0	0	30	60	60	60	60,0,-60	0	0
Radius of curvature [ft]	Infinite	Infinite	Infinite	Infinite	Infinite	Infinite	Infinite	Infinite	Infinite	Infinite
Cross-frame spacing [ft]	20	20	20	20	20	20	20	20	20	20
Cross-frame layout[d]	Cont.	Cont.	Cont.	Cont.	Cont.	Cont.	Stag.	Stag.	Cont.	Cont.
Web depth [in]	72	72	96	72	72	72	72	72	72	96
Deck thickness [in]	8	10	8	8	8	8	8	8	10	8
Cross-frame type	X	X	X	X	X	K	X	X	X	X
Cross-frame area [in^2]	2.86	2.86	2.86	2.86	2.86	2.86	2.86	2.86	2.86	2.86
Concrete modulus [ksi]	5000	5000	5000	5000	5000	5000	5000	5000	5000	5000

Notes:
[a]M-I = interior bay near maximum positive dead load moment region; IS = interior support; ES = end support
[b]BS = bottom strut
[c] Model 1187-2 has trapezoidal support skew layout, rest of models have parallel skew
[d] Cont. = contiguous line of cross-frames, Stag. = staggered line of cross-frames

Table F4-16: Independent variables describing 20 representative bridges in system-level R-Factor Study (curved bridges)

Parameter	Model ID									
	59-2	**83-3**	**115-2**	**747-2**	**753-2**	**755-2**	**755-4**	**761-2**	**909-2**	**925-3**
Governing CF Location[a]	IS	M-I	M-E	ES	ES	ES	ES	ES	M-I	M-I
Governing CF Member[b]	BS	D2	D2	BS	D1	D1	BS	D1	BS	D2
No. spans	1	1	1	2	2	2	2	2	2	2
L/d ratio	25	25	25	30	30	30	30	30	30	30
Girder spacing [ft]	8	10	6	8	8	8	8	8	6	10
No. girders	5	5	5	5	5	5	5	5	5	5
Support skew [deg.][c]	60	0	0	30	60	60	60	60,0,-60	0	0
Radius of curvature [ft]	750	750	750	750	1500	750	750	1500	750	750
Cross-frame spacing [ft]	20	20	20	20	20	20	20	20	20	20
Cross-frame layout[d]	Cont.	Cont.	Cont.	Cont.	Cont.	Cont.	Cont.	Cont.	Cont.	Cont.
Web depth [in]	72	72	96	72	72	72	72	72	96	72
Deck thickness [in]	8	10	8	8	8	8	8	8	8	10
Cross-frame type	X	X	X	X	X	X	K	X	X	X
Cross-frame area [in^2]	2.86	2.86	2.86	2.86	2.86	2.86	2.86	2.86	2.86	2.86
Concrete modulus [ksi]	5000	5000	5000	5000	5000	5000	5000	5000	5000	5000

Notes:
[a]M-E = exterior bay near maximum positive dead load moment region; M-I = interior bay near maximum positive dead load moment region; IS = interior support; ES = end support
[b]D1 = diagonal 1; D2 = diagonal 2; BS = bottom strut
[c] Model 761-2 has trapezoidal support skew layout, rest of models have parallel skew
[d] Cont. = contiguous line of cross-frames

F4.3.2.1 Eccentric-Beam Modeling Approach

Given the scatter observed in the panel-level study documented in Section F4.2, the RT elected to explore an alternative approach to modeling cross-frames in 3D bridge models. The RT sought a methodology more refined than the pin-ended truss elements, yet simpler to employ than the shell-element approach. Rather than model the cross-frames as a pin-ended truss element and modify by an R-factor as is traditionally done, the RT investigated a technique in which cross-frames and plates are represented as eccentric beam elements. The eccentric-beam approach does not necessarily correspond to one specific technique but rather encompasses a wide range of modeling assumptions with varying levels of accuracy and modeling simplicity.

The eccentric-beam approach was initially adapted from the simple analytical model documented in Section F4.1.1. In this approach, cross-frames are modeled as beam elements with flexural degrees of freedom. The eccentric load path and resulting effects of bending on the axial stiffness of single-angle cross-frame members are explicitly considered. The axial and flexural rigidity of the connection and gusset plates are also represented by beam elements with effective section properties.

In total, three different variations of the eccentric-beam modeling approach were explored, ranging from more refined to very simplistic. Each variation is presented schematically in Figure F4-24. It should be noted that these three methodologies represent just a few of the many possible sets of modeling assumptions. Thus, this study is not intended to be comprehensive in nature, but rather it makes generalized observations about explicitly modeling the eccentric load path as opposed to the R-factor approach.

The three eccentric-beam modeling variations considered are outlined in Figure F4-25. To demonstrate how the effective section properties are computed for each variation, sample calculations are also presented in Figure F4-25, which are based on the sample cross-frame panel shown in Figure F4-24.

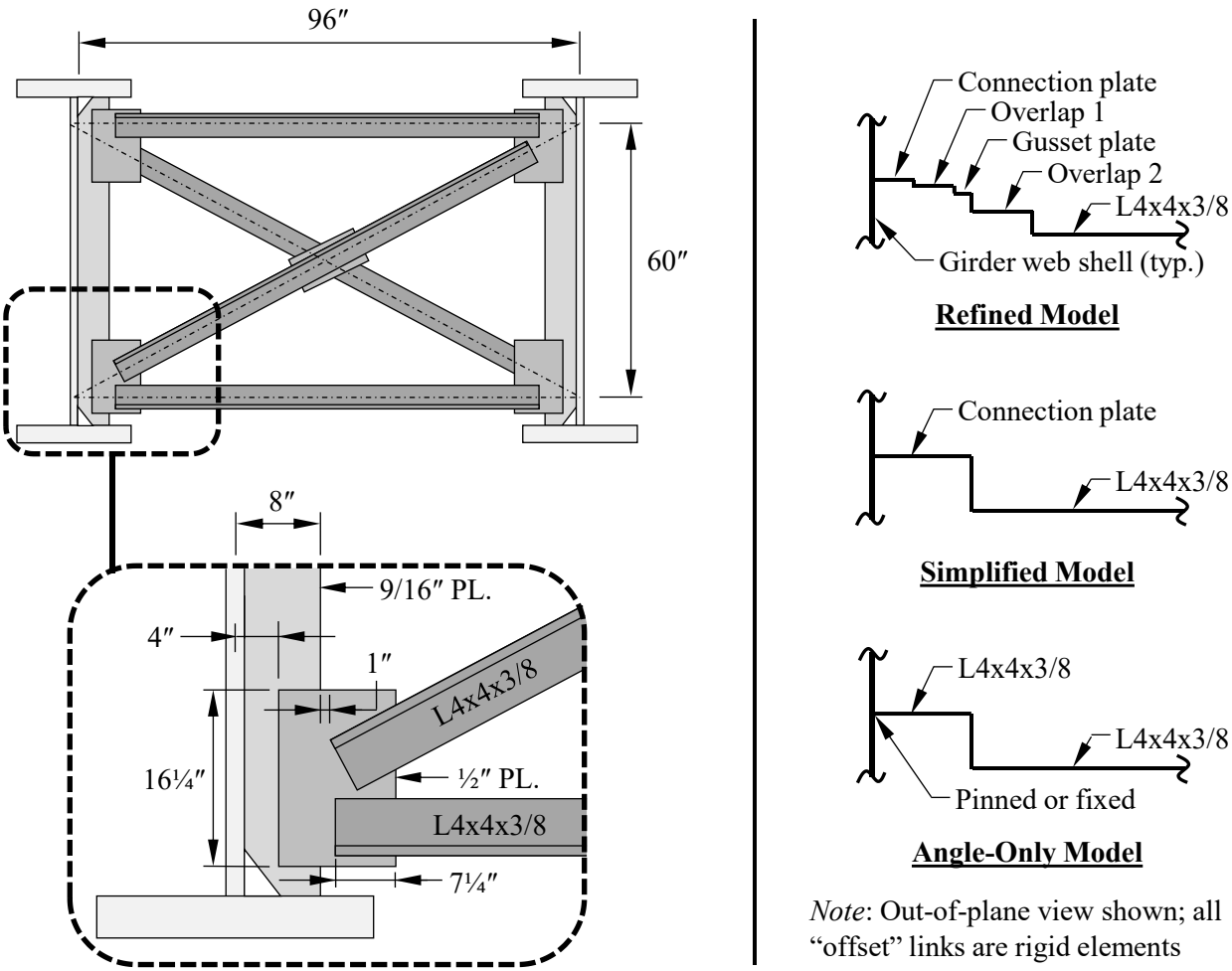

Figure F4-24: Sample cross-frame panel and the corresponding eccentric-beam models

The following calculations demonstrate how the effective section properties were computed (i.e., length L, area A, in-plane moment of inertia I_x, out-of-plane moment of inertia I_y, and eccentric offset $\bar{y}$) for the various eccentric-beam models. Figure F4-24 schematically shows the differences between the different modeling techniques, ranging from the refined model (explicitly considering all individual components and overlapped portions) to an angle-only model (only considering the angle section with an eccentric "jump"). The refined model, simplified model, and angle-only model are addressed separately herein.

Refined Model

The refined eccentric-beam model (referred to as the "refined model" herein) is generally identical to that illustrated in Figure F4-3 for the member-level studies. The connection plate, gusset plate, and overlap portions are represented as beam elements with equivalent section properties based on the dimensional procedures outlined in Figure F4-4. The out-of-plane eccentricities are directly considered in the model, and the in-plane rotational restraint of the connection is considered by not releasing rotation at cross-frame ends like is traditionally done with the pin-ended truss modeling approach.

For simplicity, the individual components are examined in the following order: connection plate, gusset plate, angle section, overlap 1, and overlap 2 (refer to Figure F4-24 for the naming convention). Note that the calculations presented below (especially in terms of member length) are based on the bottom strut member, but similar calculations can be made for the diagonal members.

⟶ *Connection plate*

As presented in Figure F4-4, the assumed length of each individual component neglects shear lag effects. Thus, the length of the beam element representing the connection plate is taken as the centerline of the girder web to the edge of the gusset plate. This length is computed based on the dimensions presented in Figure F4-24.

In determining the area and moment of inertia values for the connection plate, the biggest challenge and assumption is related to the height of the plate effective in transferring the force. Employing the Whitmore approach illustrated schematically in Figure F4-4, the effective height of the connection plate can be geometrically approximated. Note that the effective height calculation can vary from member-to-member depending on how the cross-frame member and gusset plates are positioned relative to the girder and connection plate. Theoretically, a unique effective height can be computed for every equivalent "connection plate" beam element; however, to simplify the approach and to avoid confusion, the calculation for all corresponding "connection plate" beam elements is based on the bottom strut member shown below. Also recall that the flexural stiffness of the connection plate, both in-plane and out-of-plane is amplified by a factor of two based on the discussion related to Figure F4-5.

The beam element representing the connection plate is modeled about the mid-section of the plate, such that there is no eccentric offset associated with these elements. This is summarized below.

Length: $L_c = 4in$ (per Figure F4-24)

Effective height: $b_{eff,c} = 13.625in$

Area: $A_c = b_{eff,c} t_{cp} = (13.625in)(0.5625in) = 7.7in^2$

In-plane moment of inertia: $I_{x,c} = 2\left[{}^{1}/_{12}\, t_{cp} {b_{eff,c}}^3\right] = {}^{2}/_{12}\,(0.5625in)(13.625in)^3 = 237in^4$

Figure F4-25: Sample calculation of effective section properties for the various eccentric-beam modeling approaches

Out-of-plane moment of inertia $I_{y,c} = 2\left[{}^{1}/_{12}\, b_{eff,c} t_{cp}{}^{3}\right] = {}^{2}/_{12}\,(13.625in)(0.5625in)^3 = 0.40in^4$

Eccentric offset: $\bar{y}_c = 0in$

Note that the in-plane flexural rigidity of the connection plate greatly exceeds the out-of-plane flexural rigidity. This distinction plays a significant role in the simplified procedures outlined below.

⟶ *Gusset plate*

Before determining the overlapped sections, the equivalent section properties of the gusset plate segment must first be computed. The length of this element is taken as the edge of the connection plate to the edge of the angle member (Figure F4-24).

Similar to the connection plate, the effective height of the gusset plate is determined via the Whitmore approach on the bottom strut member. Dissimilar to the connection plate, the in-plane and out-of-plane flexural stiffness is not modified to account for an attachment to the girder flanges.

Additionally, an eccentric offset is considered based on the centerline offset distances between the connection plate and the gusset plate. Note that the eccentric load paths of the diagonal members differ; each diagonal is connected to a different face of the gusset plates to avoid interference at the cross-over point. As such, the offset dimensions can and will vary in this refined procedure. For clarity, only the eccentric offset related to the sketch in Figure F4-24 is presented herein.

Length: $L_g = 1in$ (per Figure F4-24)

Effective height: $b_{eff,g} = 9.32in$

Area: $A_g = b_{eff,g} t_{gp} = (9.32in)(0.5in) = 4.7in^2$

In-plane moment of inertia: $I_{x,g} = {}^{1}/_{12}\, t_{gp} b_{eff,g}{}^{3} = {}^{1}/_{12}\,(0.5in)(9.32in)^3 = 34in^4$

Out-of-plane moment of inertia $I_{y,g} = {}^{1}/_{12}\, b_{eff,g} t_{gp}{}^{3} = {}^{1}/_{12}\,(9.32in)(0.5in)^3 = 0.10in^4$

Eccentric offset: $\bar{y}_g = {}^{t_{cp}}/_{2} + {}^{t_{gp}}/_{2} = {}^{1}/_{2}\,(0.5625in + 0.5in) = 0.53in$

⟶ *Angle section*

The length of the angle section is taken as the edge of the gusset plate to edge of opposite gusset plate. The area, moment of inertia properties, and centroidal distances are based on the values tabulated in the AISC Manual.

Length: $L_a = 63.5in$ (per Figure F4-24)

Area: $A_a = 2.86in^2$ (per AISC Manual)

In-plane moment of inertia: $I_{x,a} = 4.32in^4$ (per AISC Manual)

Out-of-plane moment of inertia $I_{y,a} = 4.32in^4$ (per AISC Manual)

Figure F4-25 (con't): Sample calculation of effective section properties for the various eccentric-beam modeling approaches

Eccentric offset: $\bar{y}_a = {}^{t_{cp}}/_2 + t_{gp} + \bar{y} = {}^1/_2\,(0.5625in) + 0.5in + 1.13in = 1.91in$

⟶ *Overlap 1 & 2 Sections*

Overlap 1 corresponds to the overlapped portion of the connection and gusset plates, whereas overlap 2 corresponds to the overlapped portion of the gusset plate and cross-frame angle. The equivalent beam element that represents these overlapped segments treats the connected parts as a composite section. In other words, the area, moment of inertia values, and eccentric offsets are computed as a composite section. This procedure is outlined below. Additionally, the lengths of the overlapped segments are based on Figure F4-4 and as shown in Figure F4-24.

For overlap segment 1:

Length: $L_a = 4in$ (per Figure F4-24)

Area: $A_{o1} = A_c + A_g = (7.7in^2) + (4.7in^2) = 12.4in^2$

Eccentric offset: $\bar{y}_{o1} = \frac{\bar{y}_c A_c + \bar{y}_g A_g}{A_{o1}} = \frac{(0in)(7.7in^2)+(0.53in)(4.7in^2)}{12.4in^2} = 0.20in$

In-plane moment of inertia: $I_{x,o1} = I_{x,c} + I_{x,g} = (237in^4) + (34in^4) = 271in^4$

Out-of-plane moment of inertia $I_{y,o1} = I_{y,c} + I_{y,g} + A_c(\bar{y}_c - \bar{y}_{o1})^2 + A_g(\bar{y}_g - \bar{y}_{o1})^2 = (0.40in^4) + (0.10in^4) + (7.7in^2)(0 - 0.20in)^2 + (4.7in^2)(0.53 - 0.20in)^2 = 1.3in^4$

For overlap segment 2:

Length: $L_a = 7.25in$ (per Figure F4-24)

Area: $A_{o2} = A_g + A_a = (4.7in^2) + (2.86in^2) = 7.6in^2$

Eccentric offset: $\bar{y}_{o2} = {}^{t_{cp}}/_2 + \frac{\bar{y}_g A_g + \bar{y}_a A_a}{A_{o1}} = {}^{(0.5625in)}/_2 + \frac{(0.53in)(4.7in^2)+(1.19in)(2.86in^2)}{7.6in^2} = 1.06in$

In-plane moment of inertia: $I_{x,o2} = I_{x,g} + I_{x,a} = (34in^4) + (4.32in^4) = 38in^4$

Out-of-plane moment of inertia $I_{y,o2} = I_{y,g} + I_{y,a} + A_g(\bar{y}_g - \bar{y}_{o2})^2 + A_a(\bar{y}_a - \bar{y}_{o2})^2 = (0.10in^4) + (4.32in^4) + (4.7in^2)(0.53 - 1.06in)^2 + (2.86in^2)(1.91 - 1.06in)^2 = 7.8in^4$

<u>Simplified Model</u>

The simplified model does not explicitly consider the gusset plate and the overlapped portions; however, it does account for the out-of-plane flexibility introduced by the connection plate and the primary eccentric offset of the cross-frame angle member. In terms of practicality, this approach simplifies the design process by eliminating the need to have cross-frame connection details and dimensions established at the time of structural analysis. As illustrated in Figure F4-24, this method is described by the connection plate and angle

Figure F4-25 (con't): Sample calculation of effective section properties for the various eccentric-beam modeling approaches

member only with one eccentric jump. The following sections outline the procedures used to compute the effective section properties of these equivalent beam segments.

⟶ *Connection plate*

In this simplified approach, the assumed length of the connection plate is taken as the distance from the centerline of the web to the edge of the angle member, or 9 inches per Figure F4-24. Thus, this singular beam segment effectively accounts for both the connection and gusset plates. In the development of the area and moment of inertia, the effective height is taken as the full height of the gusset plate. It has been demonstrated that the analysis results are not significantly influenced by this dimension, such that the designer can base this dimension on a "reasonable guess" such as an estimated gusset plate size if the connection dimensions are not known at the time of modeling.

Similar to the refined approach, the in-plane and out-of-plane flexural rigidity of the connection plate is amplified to account for the restraint provided by the girder flange connection.

Length: $L_c = 9in$

Effective height: $b_{eff,c} = 16.25in$ (Approximated as the full gusset height)

Area: $A_c = b_{eff,c}t_{cp} = (16.25in)(0.5625in) = 9.1in^2$

In-plane moment of inertia: $I_{x,c} = 2[{}^1/_{12}\, t_{cp}{b_{eff,c}}^3] = {}^2/_{12}\,(0.5625in)(16.25in)^3 = 402in^4$

Out-of-plane moment of inertia $I_{y,c} = 2[{}^1/_{12}\, b_{eff,c}{t_{cp}}^3] = {}^2/_{12}\,(16.25in)(0.5625in)^3 = 0.5in^4$

Eccentric offset: $\bar{y}_c = 0in$

⟶ *Angle section*

The length of the angle section in the simplified method is taken as the full length of the member neglecting shear lag effects or connections. The area and moment of inertia properties are taken from the AISC Manual. The eccentric offset is simply taken as the "full" eccentricity measured from the centroid of the connection plate to the centroid of the single angle. Unlike the refined methods which explicitly considers the unique "jumps" in the out-of-plane load path, this simplified method only considers the primary "jump" to the angle section. This is demonstrated below.

Length: $L_a = 78in$

Area: $A_a = 2.86in^2$ (per AISC Manual)

In-plane moment of inertia: $I_{x,a} = 4.32in^4$ (per AISC Manual)

Out-of-plane moment of inertia $I_{y,a} = 4.32in^4$ (per AISC Manual)

Eccentric offset: $\bar{y}_a = {}^{t_{cp}}/_2 + t_{gp} + \bar{y} = {}^1/_2\,(0.5625in) + 0.5in + 1.13in = 1.91in$

<u>Angle-Only Model</u>

The angle-only model is similar to the simplified model above, except that an additional simplifying

Figure F4-25 (con't): Sample calculation of effective section properties for the various eccentric-beam modeling approaches

assumption is made with regards to the equivalent section properties. This approach attempts to mimic the R-factor approach (i.e., cross-frames modeled as truss-elements with modified axial rigidity) but replaces the modification factor with explicitly representing the eccentric offset.

The advantage of the R-factor approach is that the designer does not need any information about the connection details; that is to say, the designer only models the cross-frame using the angle section properties. As demonstrated throughout this appendix, the slight disadvantage of the R-factor approach is that the appropriate modification factor is highly variable and depends on a number of parameters including the loading conditions. Thus, this angle-only approach outlined herein implements the advantageous aspects of the R-factor approach but eliminates the potential source of variability associated with the assigned R-factor.

The calculations below summarize the pertinent section properties associated with this approach. Note that the beam element representing the connection plate in the previous method is replaced with the angle section properties. Thus, angle section 1 refers to the beam element connecting to the girder web, and angle section 2 refers to the primary cross-frame member.

In making this simplifying assumption, it should be noted that the out-of-plane flexural stiffness in angle section 1 is now significantly higher than the previous methods (i.e., $I_{y,a} >> I_{y,c}$). The results presented in the appendix demonstrate that this assumption tends to overestimate the total stiffness of the cross-frame panel, despite the eccentric offset being explicitly modeled. As such, the RT considered two variations of the angle-only approach: (i) not releasing the flexural degrees of freedom at the ends of the eccentric beam elements (as outlined above) and (ii) releasing the flexural degrees of freedom at the ends. Case ii attempts to capture the out-of-plane flexibility associated with the connection and gusset plates in an approximate fashion. Figure F4-24 depicts these different methods schematically.

⟶ *Angle section 1*

As outlined above, angle section 1 represents the connection and gusset plates using the L4x4x3/8 section properties, similar to the R-factor approach. Similar to the simplified method above, the assumed length of this beam segment is taken as the distance from the centerline of the web to the edge of the angle member, or 9 inches. The effective area and moment of inertia values are taken directly from the AISC Manual, which highlights the benefits and ease-of-use of this approximate approach.

Length:	$L_{a1} = 9in$
Area:	$A_{a1} = 2.86in^2$ (per AISC Manual)
In-plane moment of inertia:	$I_{x,a1} = 4.32in^4$ (per AISC Manual)
Out-of-plane moment of inertia	$I_{y,a1} = 4.32in^4$ (per AISC Manual)
Eccentric offset:	$\bar{y}_{a1} = 0in$

⟶ *Angle section 2*

As outlined above, angle section 2 is equivalent beam segment that represents the cross-frame member. The properties are identical to angle section 1, except for the length and the eccentric offset (which was previously computed).

Length:	$L_{a2} = 78in$

Figure F4-25 (con't): Sample calculation of effective section properties for the various eccentric-beam modeling approaches

Area:	$A_{a2} = 2.86in^2$ (per AISC Manual)
In-plane moment of inertia:	$I_{x,a2} = 4.32in^4$ (per AISC Manual)
Out-of-plane moment of inertia	$I_{y,a}2 = 4.32in^4$ (per AISC Manual)
Eccentric offset:	$\bar{y}_{a2} = {}^{t_{cp}}/_{2} + t_{gp} + \bar{y} = {}^{1}/_{2}\,(0.5625in) + 0.5in + 1.13in = 1.91in$

Figure F4-25 (con't): Sample calculation of effective section properties for the various eccentric-beam modeling approaches

A screenshot of the refined eccentric-beam approach is provided in Figure F4-26; although its appearance is not dramatically different than the truss-element approach, the eccentric "jumps" are evident at the ends of the beams to represent the connection details. Although not shown in Figure F4-25, a similar procedure was also used to develop equivalent beam properties for K-type cross-frames.

It is important to note that an offset dimension of 6 inches (i.e., measured from the centroid of the strut members to the inside face of the corresponding girder flange) was assumed in the development of all three model types (shell, truss, and eccentric beam). As discussed in Chapter F5, many 3D commercial software programs do not model this offset, but instead connect the cross-frame members directly into the share node along the web-to-flange juncture. The traditional approach is conservative on two different fronts: (i) the inclination angle of diagonal is steeper without the offset and (ii) the total depth and stiffness of cross-frame panel increases, which in turn generally increases cross-frame force effects. In the traditional approach, web stiffeners are not required as cross-section distortional effects become negligible.

The RT elected to model the vertical offset and the web stiffeners to maintain consistency with the other 3D modeling approaches in this chapter. The implications of including this offset or not are explored in Chapter F5.

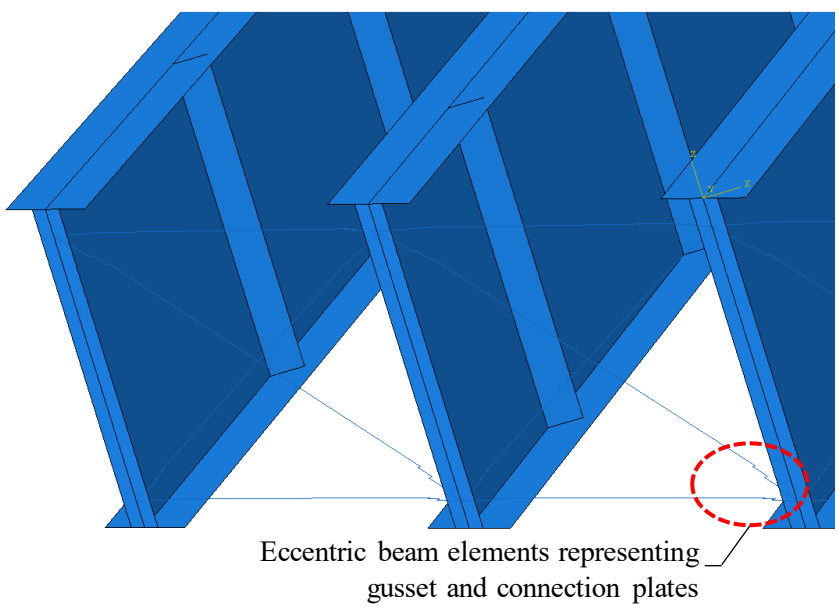

Figure F4-26: Close-up view of eccentric-beam approach for cross-frames in 3D FEA models

Given that the eccentric-beam approaches outlined above, especially the refined model, better represents the stiffness of the cross-frame panel, it is anticipated that these models accurately predict cross-frame forces when compared to the shell-element models. Computational results are presented in the next subsection to demonstrate the accuracy of the proposed modeling approaches.

F4.3.2.2 Analytical Results

As outlined above, 20 bridges were evaluated with a series of finite element models. In total, 10 model iterations per bridge were performed. Of the 10 model iterations, two included a shell-element approach to modeling cross-frames, six included the R-factor approach, and two included the proposed eccentric-beam approaches. For each iteration, an identical influence-surface analysis was conducted similar to those presented in Chapter F3.

In terms of loading, a single AASHTO fatigue truck was moved along the length of the respective influence surface at various transverse lane positions (i.e., one-foot increments) in both the forward and backward directions. For each simulated truck passage, an influence-line plot is provided that shows the full stress or force cycle that a particular cross-frame element would experience during this moving load case. Ultimately, the lane position that maximizes the stress or force cycle in that particular element is of most interest; thus, the RT reports only the critical load case in the results herein, unless noted otherwise. The critical force (or stress) range is then considered the unfactored, design force (or stress) for the Fatigue I or II limit states. The procedure described above is identical to that used in the Fatigue Loading Study in Chapter F3.

Before discussing the implications of employing the proposed eccentric-beam approach to modeling cross-frames, Figure F4-27 summarizes a sample set of results for the truss-element, R-factor approach. In this figure, the design force range for each model iteration of a sample bridge is reported (based on the critical loading case). Along the x-axis, the results for the various truss-element models are considered as a function of the applied modification factor, R = {0.5, 0.6, 0.7, 0.8, 0.9, and 1.0}. Along the y-axis, the F_{truss}/F_{shell} ratio is plotted.

Again, a value of unity indicates that the assigned R-factor resulted in perfect agreement with the shell-element model. Values above unity imply that the truss-element model is too stiff (i.e. the member attracts too much force) and that the R-factor should be reduced; however, this case represents a conservative design assumption with respect to the fatigue limit state (i.e., analysis model produces excessive design forces). The opposite is true for values below unity. In the call-outs on Figure F4-27, note that the "exact" R-factor, where the line intersects F_{truss}/F_{shell} = 1.0, is included for each member presented. For example, the "exact" R for the bottom strut in the 1/2-inch gusset case is 0.73.

Figure F4-27 presents this data for three select cross-frame members in the sample bridge model. The select cross-frames are as follows: (i) a bottom strut near the maximum positive dead load moment region (i.e., approximately 0.35L from the end support where L is the span length), (ii) a top strut from the same cross-frame panel, and (iii) a diagonal near the intermediate skewed support.

The figure also differentiates the models by gusset plate thickness (1/2-inch or 1-inch thick). Note that the gusset plate thickness only affects the shell-element model directly, as the truss-element models do not explicitly represent gusset plates. Thus, only the denominator in the F_{truss}/F_{shell} ratio is impacted between the top (1/2-inch thick) and the bottom (1-inch thick) plots in Figure F4-27.

The bridge of interest is 277-2, which is a two-span, straight bridge with skewed supports. For more information regarding the pertinent parameters of the superstructure, refer to Table F4-10. For reference, a sketch of the framing plan and typical cross-section are provided (not to scale); the skewed diaphragms at end and intermediate supports are included in the model but neglected in the figures for clarity.

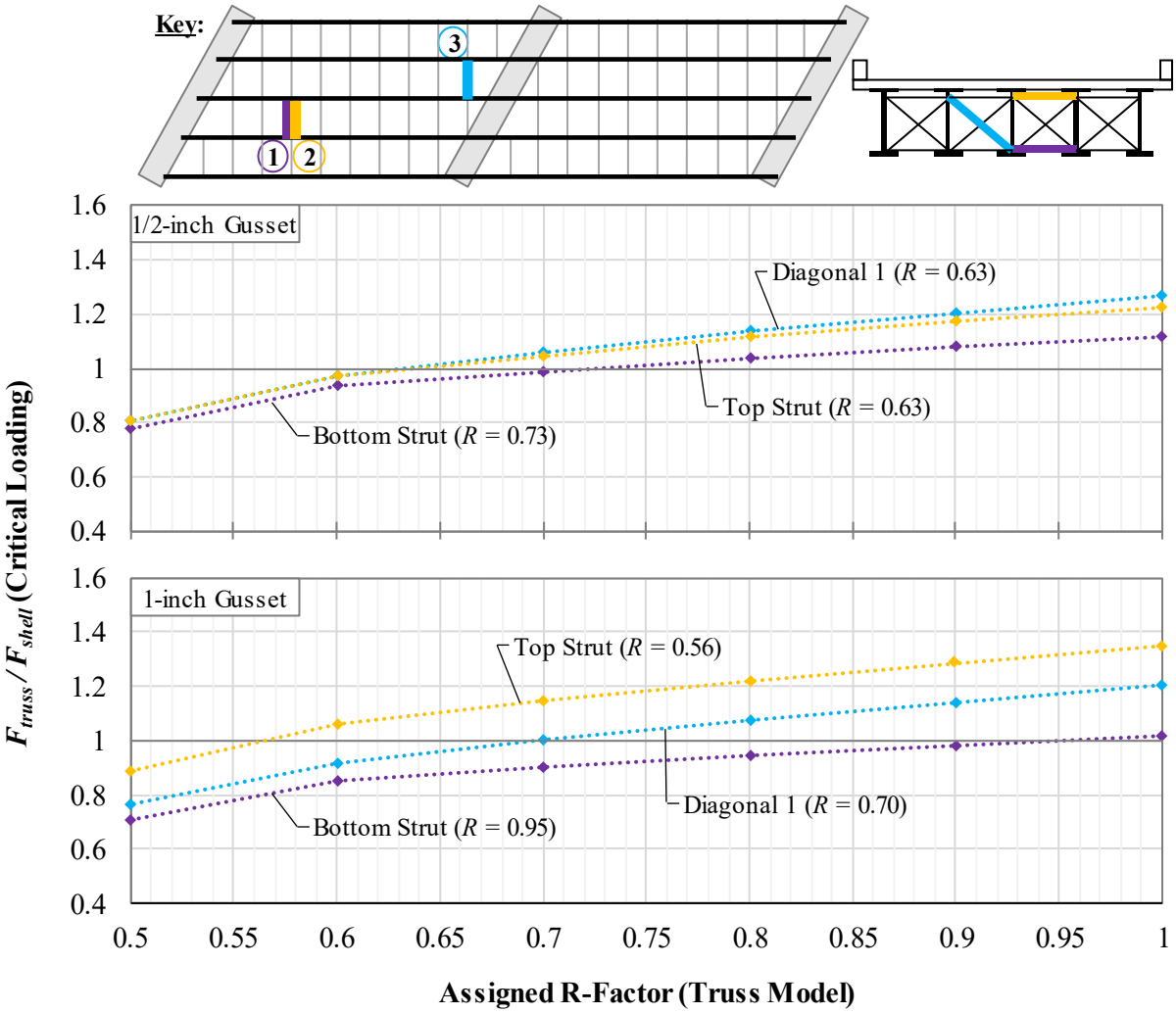

Figure F4-27: Example data from two-span, continuous skewed bridge demonstrating the predicted cross-frame design force range from the truss-element approach (using various R-factors) and the shell-element approach

The following observations can be made from Figure F4-27:

- As expected, the reduction assigned to the cross-frame stiffness is not directly correlated to the force reduction in the predicted response (i.e., the cross-frame force is not 1:1 dependent on the stiffness modification due to the high degree of indeterminacy in the bridge system). In other words, a 10% reduction in the R-factor does not result in a 10% reduction in the estimated cross-frame force.
- Rather, a 10% reduction in the R-factor generally results in a 5% reduction on average in the estimated cross-frame force. That relationship typically holds true for modification factors above 0.6. Below R = 0.6, the rate at which the F_{truss}/F_{shell} approaches zero increases. Ultimately, a modification factor of zero would result in F_{truss}/F_{shell} = 0, despite not being shown in the figure. This assumed 2:1 relationship (x% reduction in $R \approx x/2$% reduction in force) has significant design implications. For example, if the acceptable level of error in the predicted cross-frame force is

established as 10%, the R-factor likely needs to be within 20% of the exact value (recall that it is conservative from a fatigue perspective to assign higher R-factors).

- Even for cross-frame members of similar geometries and eccentricities, the "exact" R-factor for these critical loading conditions can vary. For example, the "exact" R-factor for the bottom strut is 0.73 compared to 0.63 for the top strut in the same cross-frame panel. This variability highlights the impact of load position and deformation patterns on the assumed stiffness of the cross-frame panel.
- The gusset plate thickness impacts the response of the cross-frame in the shell-element model. As the gusset plate thickness increases, the stiffness of the cross-frame tends to also increase; this observed behavior is consistent with the results presented in Sections F4.1 and F4.2. As such, the exact R-factor for the bridge with 1-inch thick gusset plates tends to exceed the exact R-factor for the bridge with 1/2-inch thick gussets. For example, the exact R-factor for the diagonal member evaluated was 0.63 for 1/2-inch gussets and 0.77 for 1-inch gussets.
- In general, the results presented in Figure F4-27 are representative of the full data set in terms of the observed variability.

Figure F4-27 represents the results of just one bridge in the 20-bridge sample set. Rather than evaluate the effectiveness of the R-factor approach for every cross-frame member and every transverse lane passage, it is more important to just focus on the governing cross-frame member in every bridge (i.e., cross-frame with the maximum force range). That way, more generalized observations about the stiffness modification factors can be made. Note that a similar approach was taken when compiling the data obtained from the Fatigue Loading Study (Sections F3.2.1 and F3.2.2).

Thus, for each iteration of a given bridge model (truss-element models with different R-factors), the governing design force range, which corresponds to one critical cross-frame member, is determined. The design forces produced from the truss-element models are then compared to the design forces produced from the shell-element model (in the same way as Figure F4-27, F_{truss}/F_{shell}) and compiled in the form of box-and-whiskers plots, Figure F4-29 and Figure F4-30.

As outlined in Section F3.2.2, box-and-whiskers provide a graphical means to present scatter in a data set (i.e., a discrete probability density function). For Figure F4-29 and Figure F4-30, the box-and-whiskers components are organized by the assigned R-factor in the truss-element model. Therefore, each box-and-whiskers represents a data set of twenty F_{truss}/F_{shell} ratios corresponding to the truss-element models with R = {0.5, 0.6, 0.7, 0.8, 0.9, and 1.0}. The transformation from a probability density function to a box-and-whiskers plot is demonstrated graphically in Figure F4-28 for the models assigned a stiffness modification factor of 0.5; a similar procedure is performed for the other R-factors. Figure F4-28 illustrates how the minimum, 25th percentile, median, 75th percentile, maximum, and mean values of the data set are computed. For the R = 0.5 example, the respective mean and maximum F_{truss}/F_{shell} ratio were 0.82 and 0.98 based on the 20 representative bridges, which indicates that assigned R = 0.5 always underpredicted the design force when compared to the benchmark shell-element model.

As stated above, Figure F4-29 and Figure F4-30 present the combined results of all model iterations performed as part of this system-level spot-check study. Figure F4-29 presents the results for bridges with 1/2-inch thick gusset plates, and Figure F4-30 for bridges with 1-inch thick gusset plates. By presenting the box-and-whiskers of the results for various R-factors side-by-side, the RT can evaluate which R-factor generally produces the most accurate representations of the "true" cross-frames stiffness (i.e., the shell-element model). In addition to the box-and-whiskers, a line graph representing the 25th-percentile of each data set is provided, whose meaning is outlined below.

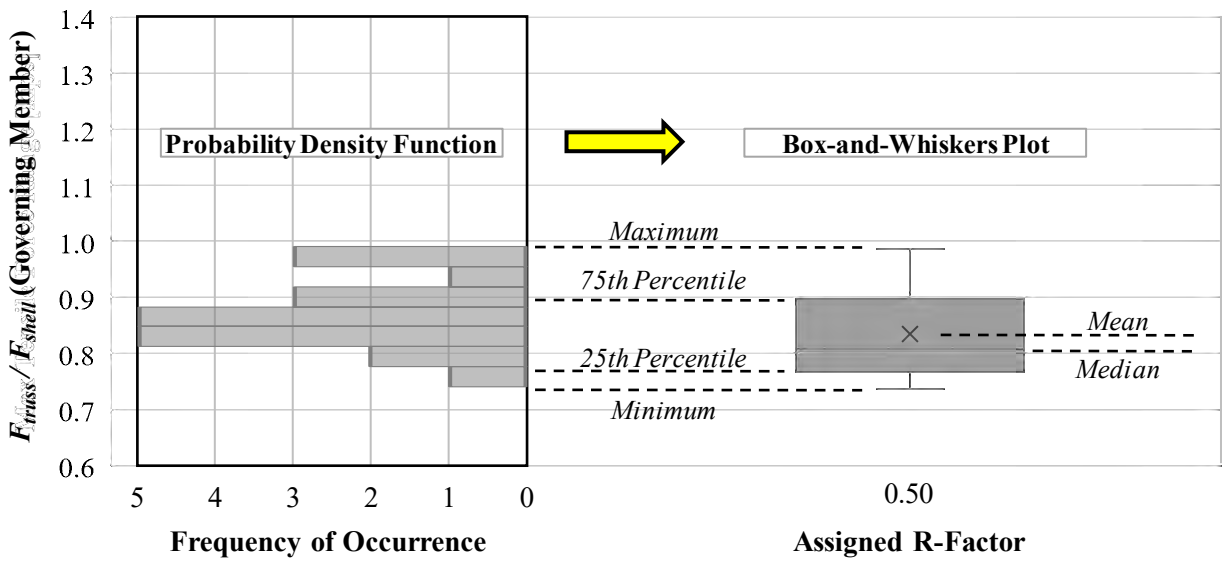

Figure F4-28: Sample data set (truss-element models with R = 0.5) demonstrating the development of the box-and-whiskers plot in Figure F4-29

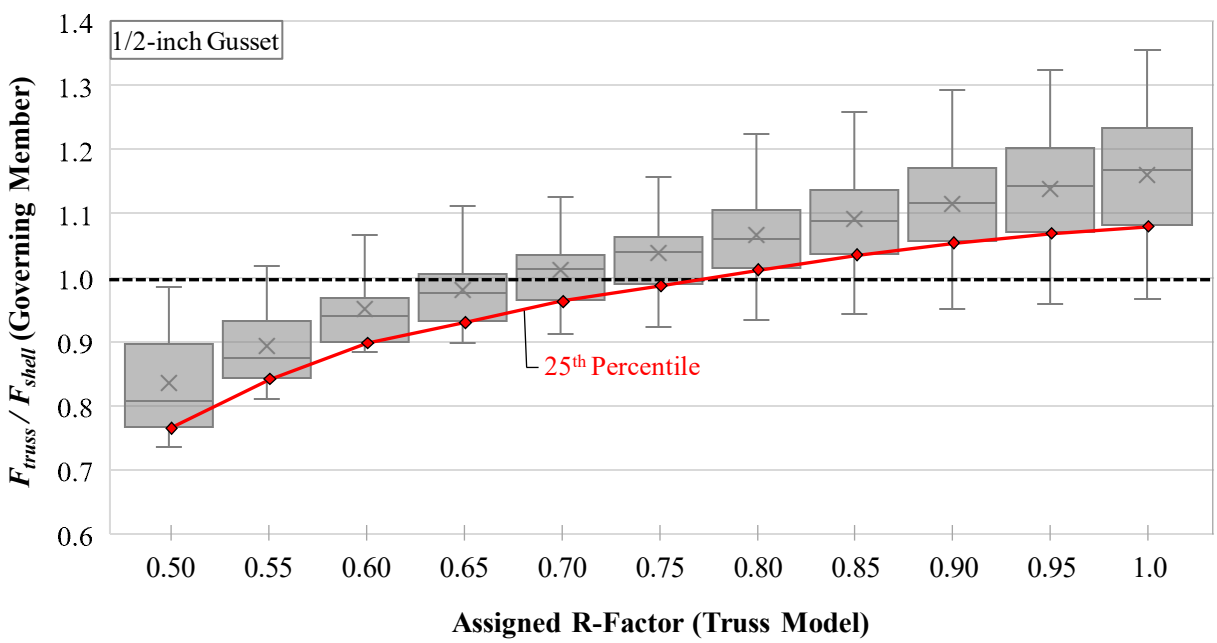

Figure F4-29: Box-and-whiskers plot indicating the overall level of accuracy for a given R-factor (1/2-inch gusset plate)

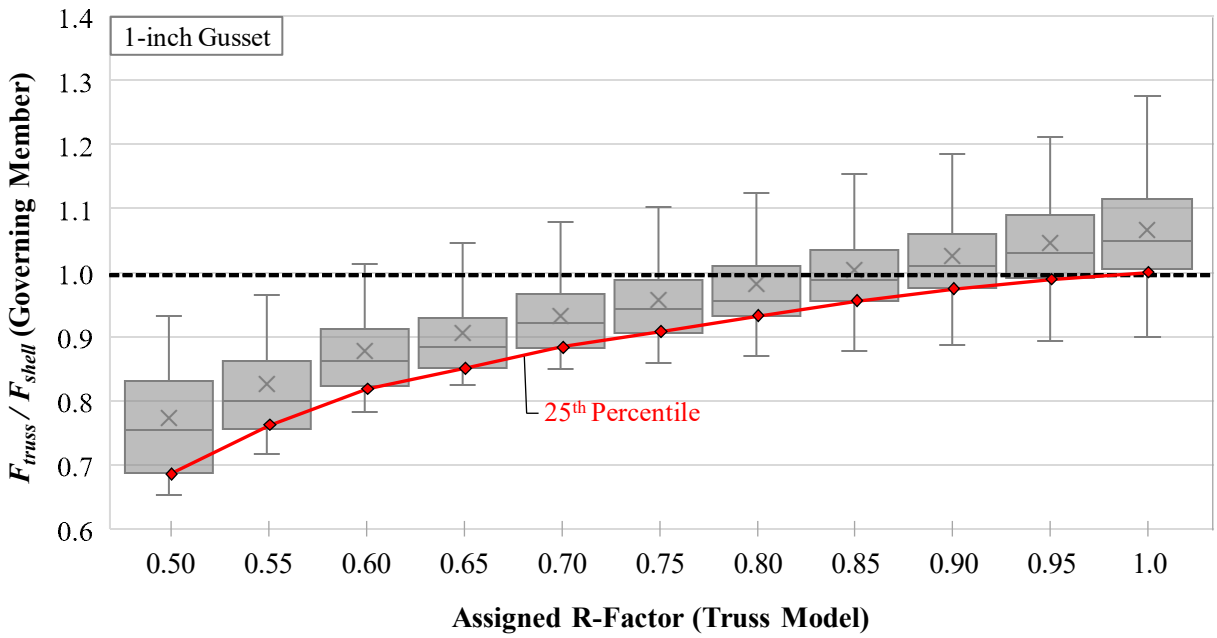

Figure F4-30: Box-and-whiskers plot indicating the overall level of accuracy for a given R-factor (1-inch gusset plate)

Similar to the one sample bridge in Figure F4-27, the following observations can be made about the full data set from Figure F4-29 and Figure F4-30:

- As the assigned R-factor increases, the design force in the truss-element model increases which in turn increases the F_{truss}/F_{shell} ratio. In other words, the R-factor and F_{truss}/F_{shell} ratio are positively correlated. Thus, it is conservative from a fatigue design perspective to assign higher stiffness modification factors.
- Despite the positive correlation, there is still significant variability in the observed response even for this scaled parametric study. The accuracy of the truss-element model in terms of predicted cross-frame forces is not only a function of the assigned modification factor but also the bridge geometry and loading conditions. For example, the respective max and min F_{truss}/F_{shell} ratios for the $R = 0.5$ case are 0.98 and 0.73.
- In general, the F_{truss}/F_{shell} ratio decreases as the gusset plate thickness increases. This is attributed to the fact that an increased gusset thickness results in a stiffer cross-frame, which then attracts more force to the shell-element model. With a larger value in the denominator, the corresponding F_{truss}/F_{shell} ratio decreases. Therefore, in order to achieve good agreement between truss- and shell-element models, it is more appropriate to assign larger R-factors for bridges with thicker gusset plates.
- From the observations above, it is apparent that developing an expression that precisely predicts the "exact" R-factor for any general bridge model (i.e., the R-factor for which F_{truss}/F_{shell} always achieves unity) is not practical or feasible. The "exact" R-factor is a function of many parameters including bridge geometry, loading conditions, cross-frame details (e.g. gusset plate thickness), and member type (e.g. bottom strut vs. diagonal). Thus, it is more appropriate to assign a uniform R-factor to all cross-frame members that statistically represents the majority of bridge conditions, similar to the $R = 0.65$ approach currently adopted in AASHTO LRFD.
- With that in mind, it is not appropriate to ensure every bridge model results in conservative

estimates of cross-frame fatigue forces ($F_{truss}/F_{shell} \geq 1$). Instead, the RT elected to base its proposed modification factor on the 25th-percentile value of the data sets. In other words, the intersection of the 25th-percentile line and unity represents the assigned R-factor that provides a conservative estimate of cross-frame design forces for 75% of the bridges. For the 25% of the bridges that result in unconservative estimates, it has been shown that the truss-element model is still within 10% of the rigorous shell-element model, which is deemed reasonable.

- Using that metric, the most appropriate R-factor to assign for the bridges with 1/2-inch and 1-inch gussets is 0.75 and 0.95, respectively. These values are later compared to the full-scale parametric study in Section F4.3.3.

Considering the variability observed in Figure F4-29 and Figure F4-30, the results of the eccentric-beam approach ("refined model" only; refer to Figure F4-25) are now introduced to examine its potential benefits. Figure F4-31, like Figure F4-27, presents the results of the same two-span continuous, skewed bridge loaded by a single AASHTO fatigue truck; the same cross-frame members are also examined. However, in this case, only 1/2-inch thick gussets are considered and only the cross-frame response due to a single lane position is shown. Here, a single, unfactored AASHTO fatigue truck is moved along the length of the bridge, centered about the centerline of the bridge deck. The resulting influence-line plots are depicted for each model iteration, which now includes the refined eccentric-beam approach. Note that only the axial-force component of the beam element is reported and compared to the axial-force output from the shell-element and truss-element approaches. The "envelope" of the R-factor approach is also given (i.e., $R = 1.0$ and $R = 0.5$), as well as $R = 0.6$ for reference.

While Figure F4-31 focuses on the refined eccentric-beam model only, an examination of the simplified versions are presented later in this section.

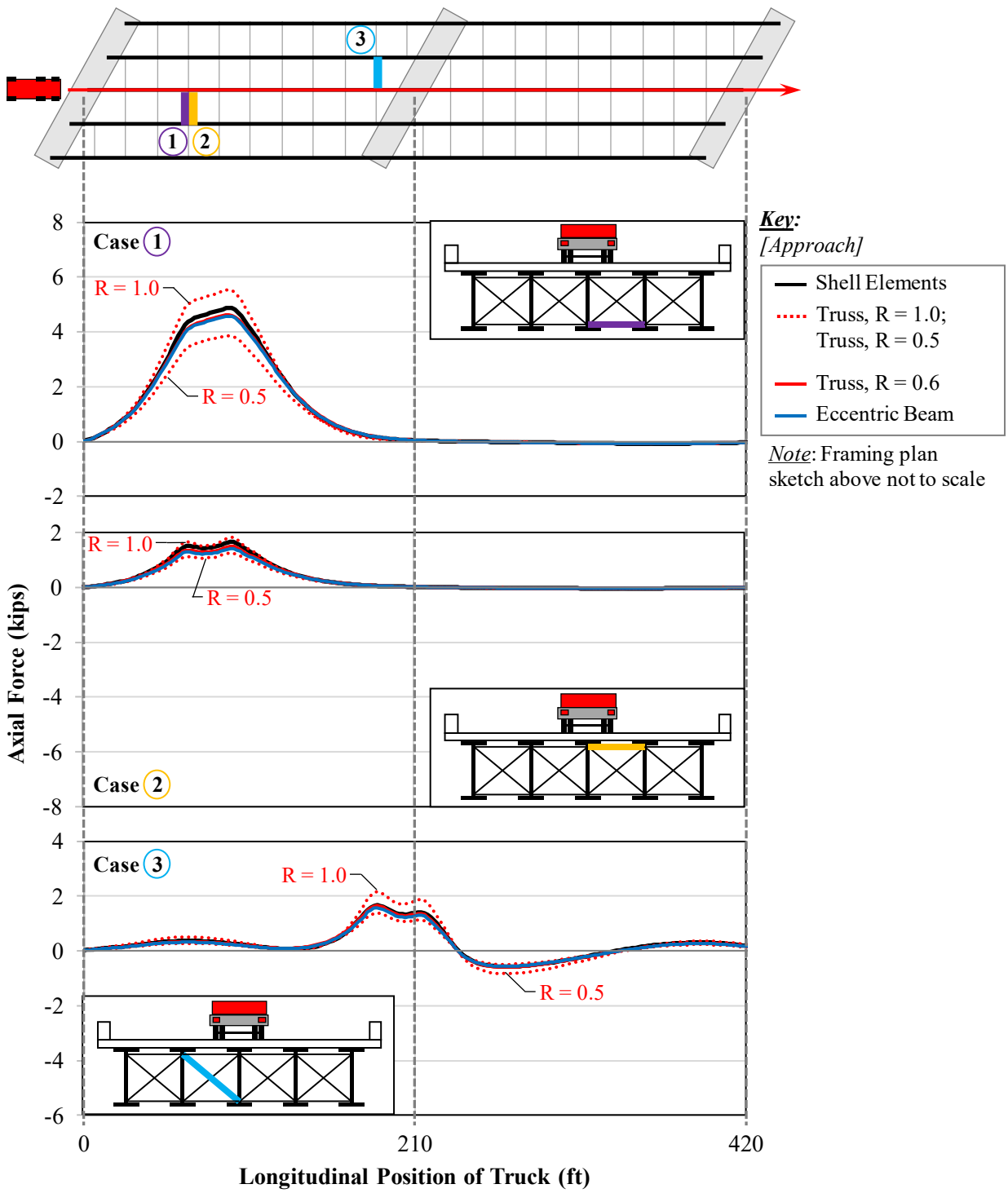

Figure F4-31: Example data from two-span, continuous skewed bridge demonstrating the predicted cross-frame design force range from the truss-element approach (using various R-factors), the shell-element approach, and the refined eccentric-beam element

It is apparent in review of the example data set in Figure F4-31 that the refined eccentric-beam approach accurately represents the stiffness of the cross-frame panel when compared to the refined shell-element

model. The force predictions are consistently within 5% of the shell-element model for this sample case. In contrast, there is a significant range of accuracy associated with the truss-element approach when comparing $R = 1.0$ and $R = 0.5$ cases. Although not presented, the same conclusion is made when the gusset plate is taken as one inch. In that scenario, the "exact" R-factors would be closer to 0.8 than what is shown on Figure F4-27 when 1/2-inch gusset plates were considered.

Similar to the truss-element models previously, the performance of the refined eccentric-beam approach is now evaluated for the entire data set. In other words, Figure F4-32 and Figure F4-33 expand on Figure F4-31, which represents one specific example, via box-and-whiskers plots. Figure F4-32 (1/2-inch gussets) and Figure F4-33 (1-inch gussets) are identical to Figure F4-29 and Figure F4-30, except that the scatter in the eccentric-beam approach is now included. Additionally, the F_{truss}/F_{shell} ratio along the y-axis is generalized and replaced with $F_{simplified}/F_{shell}$ given the fact that the refined eccentric-beam model is not a truss-element model but is a simplified model.

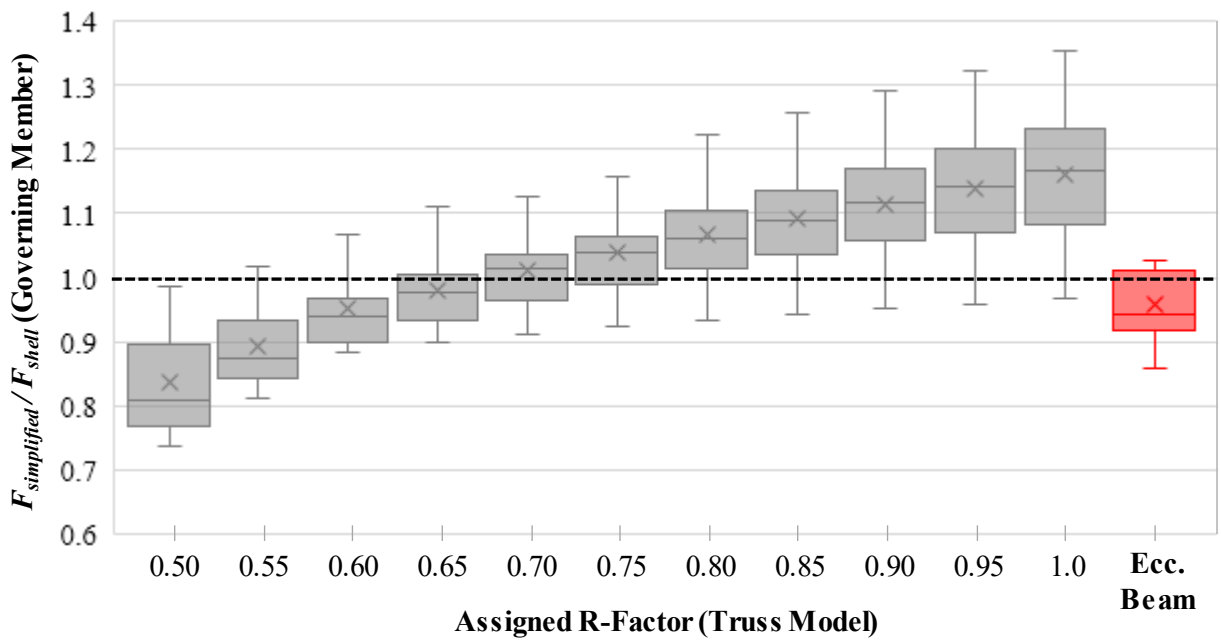

Figure F4-32: Box-and-whiskers plot indicating the overall level of accuracy for the eccentric-beam modeling approach compared to the truss-element approach (1/2-inch gusset plate)

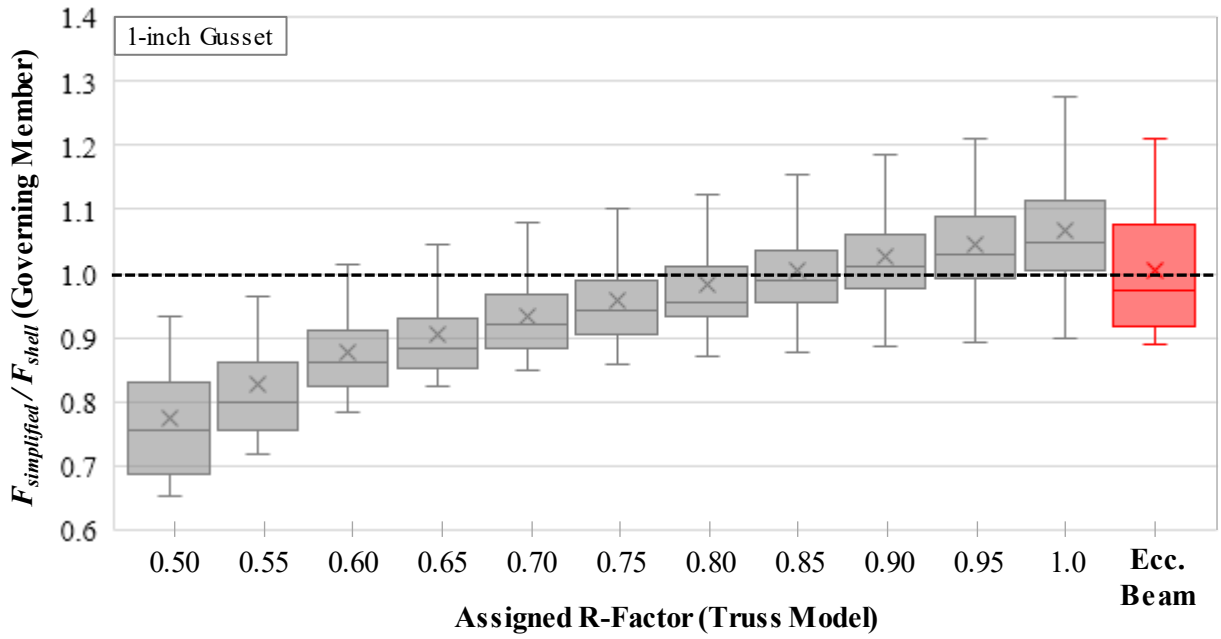

Figure F4-33: Box-and-whiskers plot indicating the overall level of accuracy for the eccentric-beam modeling approach compared to the truss-element approach (1-inch gusset plate)

The following observations can be made about the full data set from Figure F4-32 and Figure F4-33:

- For the bridges with 1/2-inch and 1-inch gusset plates, the refined eccentric-beam models predict the cross-frame fatigue design forces with reasonable levels of accuracy. For the 1/2-inch gusset case, the $F_{simplified}/F_{shell}$ ratio is 0.96 on average with a maximum of 1.03 and a minimum of 0.86. In other words, the eccentric-beam produces results within 4% of the shell-element model on average, which is good agreement but on the slightly unconservative side.
- For the 1-inch gusset case, the observed variability is slightly larger, but average response is accurate. The mean, max, and min values are 1.01, 1.21, and 0.89, respectively.

As outlined above, the results presented in Figure F4-31 through Figure F4-33 were based on the "refined" eccentric-beam model only. To illustrate the impacts of the more simplified eccentric-beam models, Figure F4-34 presents sample influence-line results from the same skewed, two-span continuous bridge from Figure F4-31. In this figure, two different responses are examined: (i) the axial force in the bottom strut member near the skewed intermediate support when the AASHTO fatigue truck traverses the bridge along the barrier and (ii) the axial force in the bottom strut member (interior bay) near the maximum positive dead load moment region when the AASHTO fatigue truck traverses the bridge along its centerline.

For each cross-frame response, several different results are presented including the shell-element model (which serves as the control), the truss-element model range (i.e., $R = 0.5$ and $R = 1.0$), the refined eccentric-beam model, the simplified eccentric-beam model, and the truss-only eccentric-beam models (both fixed-end and pinned-end). The various responses are superimposed on the same graph. Additionally, the total force ranges and the percent error relative to the control model are tabulated for reference.

Refer to Figure F4-25 for a detailed description of each eccentric-beam modeling approach. Note that the calculations in that figure correspond to the cross-frame panel dimensions and connections used in the development of these bridge models. For instance, the shell-element model represented the cross-frame panels precisely as shown in the left sketches of Figure F4-24. Also note the scale along the vertical axis is

different for the top and bottom plots in Figure F4-34.

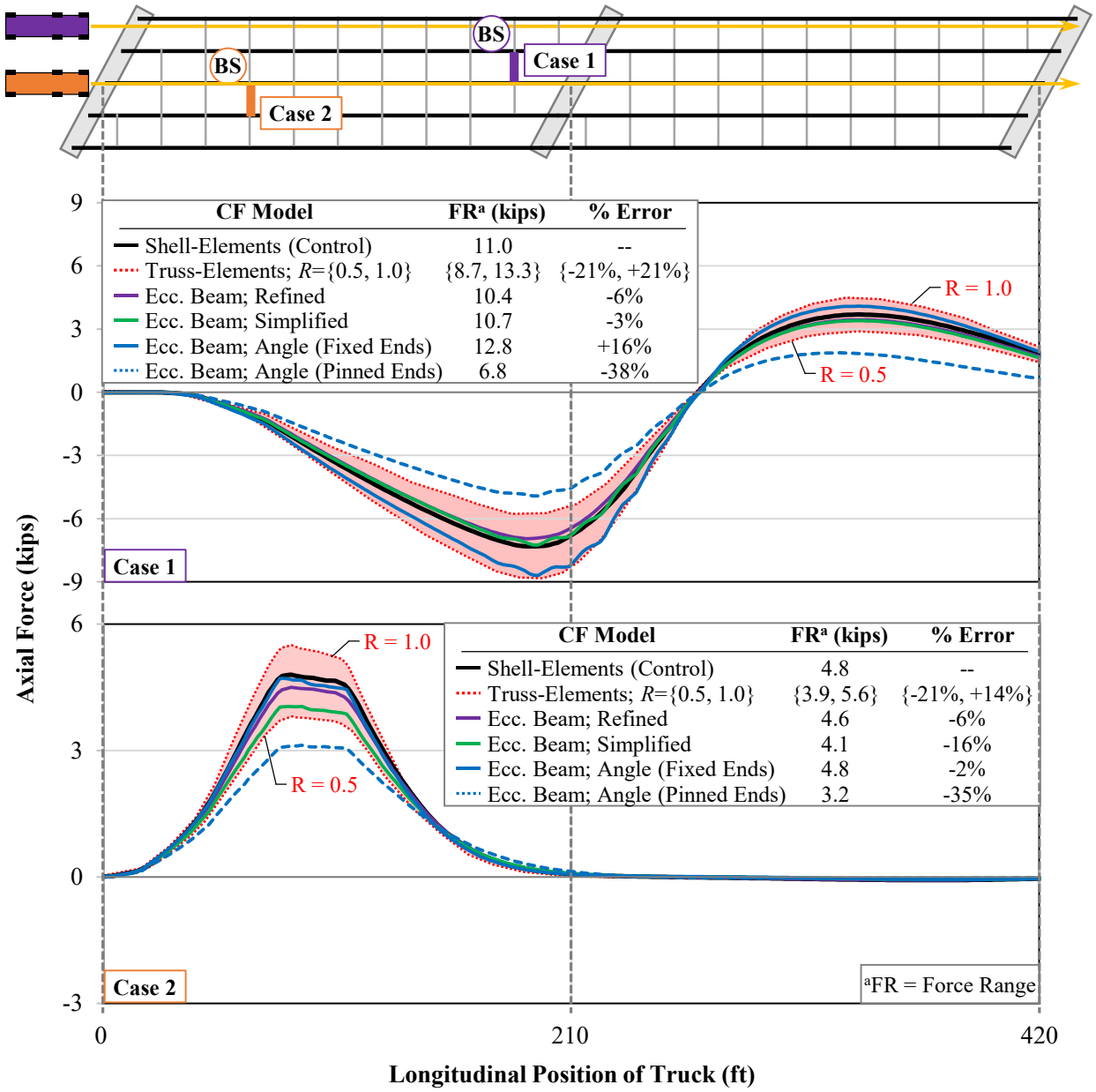

Figure F4-34: Example data demonstrating the predicted cross-frame force range for the various the eccentric-beam models (same bridges as Figure F4-31)

The following observations can be made about the full data set from Figure F4-34:

- Similar to the results presented above, the truss-element model approach has significant variability depending on which R-factor is assigned. Note that a modification factor of approximately 0.75 would produce the most accurate results in both cases shown in Figure F4-34, which is consistent with the conclusions of the R-Factor Study presented in F4.4 below.
- In both loading scenarios, the refined eccentric-beam model produces relatively accurate results when compared to the shell-element model (6% conservative). This is a similar observation to the

results of parametric study presented above. For instance, these two data points are close to the mean of the eccentric-beam data set (box-and-whiskers) shown in Figure F4-29 (i.e., a $F_{simplified}/F_{shell}$ ratio of 0.94).

- The simplified eccentric-beam model, which neglects the individual eccentric offsets caused by the connection and gusset plates, has more variability but generally produces reasonably accurate and conservative results. Recall from Figure F4-25 that this approach is much simpler to employ in practice and requires much less information about the cross-frame connection details.
- The angle-only models are largely dependent on the assumed end restraints. When the beam ends are fixed rotationally to the girder web, the stiffness of the cross-frame panel tends to be overestimated, which results in slightly over-conservative force effects (but still less conservative than the truss-element model assuming R = 1.0). Despite the eccentric offset being explicitly modeled, the out-of-plane flexural rigidity is greatly overestimated at the end connections by using the angle section properties for the full length of the modeled element.
- When the beam ends are pinned (to account for the rotational flexibility of the connection plates), the overall cross-frame stiffness tends to be vastly underestimated (even more underestimated than the truss-element model with R = 0.5). Thus, the cross-frame force effects are significantly unconservative with respect to the shell-element model. It can be observed from this sample data that an eccentric-beam approach, for which rotation is released at its ends, is not an appropriate 3D modeling technique for cross-frames.
- In review of the angle-only models, the "real" rotational restraint at the ends of the beam elements is somewhere between the idealized fixed and pinned scenario. Although not studied here, a rotational spring with finite stiffness could be explored as an alternative as well.

The biggest takeaway from the sample results in Figure F4-34 is that accurately representing the out-of-plane flexibility associated with the connection and gusset plates is vital for eccentric-beam models. The angle-only models generally do a poor job of representing that end flexibility (assuming idealized fixed or pinned end conditions), whereas the simplified and refined models showed much more promise.

In general, the eccentric-beam approaches eliminate several sources of uncertainty associated with the R-factor approach (e.g. eccentric distances, relative stiffness of gusset and connection plates, effect of load position on the deformed shape). However, modeling a cross-frame based on the refined methodology requires knowledge of the gusset and connection plate thicknesses prior to designing those elements. This potentially lends itself to an iterative process where the engineer starts with an assumed geometry (likely based on standard DOT details) and updates the model based on project-specific design decisions. This iterative process, though, affects the shell-element and refined eccentric-beam approaches equally. In contrast, the simplified methodology, although less precise and accurate, reasonably approximates the flexibility of the connection plate without having full detailed dimensions of the cross-frame connections.

Based on these perceived advantages, the RT believes this modeling technique has potential to serve as an alternative for bridge designers and commercial software packages. As a reference, the commentary language in AASHTO LRFD (C4.6.3.3.4) that discusses the use of the R-factor is provided herein:

"In addition, the axial rigidity of single-angle members and flange-connected tee-section cross-frame members is reduced due to end connection eccentricities (Wang et al., 2012). <u>In lieu of a more accurate analysis</u>, $(AE)_{eq}$ of equal leg single angles, unequal leg single angles connected to the long leg, and flange-connected tee-section members may be taken as 0.65AE."

As underlined in the provision above, the eccentric-beam approaches (namely the refined and simplified approaches) likely qualify as a "more accurate analysis," but do not require bridge designers to assemble labor-intensive, 3D FEA models with cross-frames modeled as shell elements. The overall conclusions with regards to this proposed analysis procedure are provided in Section F4.4 below.

F4.3.3 Parametric Study

To expand on the preliminary work outlined in Section F4.3.1 and the scaled study in Section F4.3.2, the RT conducted a larger scale parametric study. The same general approach was taken as before, except that a more comprehensive set of parameters was evaluated. Multiple iterations of the same 3D bridge model were assessed, including the benchmark shell-element model and truss-element models with various modification factors assigned (1.0, 0.9, 0.8, 0.7, 0.6, and 0.5). The otherwise identical truss-element models were analyzed for each assigned modification factor, and the predicted cross-frame forces are compared to the results from the shell-element models. Ultimately, the accuracy of the R-factor approach is evaluated by the F_{truss}/F_{shell} ratio, which was defined in the previous section. Note that eccentric-beam models were not evaluated as part of this study.

Table F4-17 summarizes the parameters evaluated. The parameters are largely the same as those used in the panel-level study (Table F4-5), except that a concrete deck with thickness values ranging from 8 inches to 12 inches was also considered as an independent variable. In total, the RT analyzed 324 shell model bridges and 108 truss model bridges. Note that the variable gusset thickness only impacts the shell-element models; hence, the number of shell-element models exceeded the number of truss-element models. For simplicity, all bridges considered were straight, 200-foot single-span units supported by four girders and normal supports. Additional studies on skewed and/or curved bridges are provided in the subsequent section. Thus, respective span-to-depth ratios of 33, 25, and 20 were studied.

In each bridge model, two cross-frame panels at midspan (edge bay and interior bay) were investigated, as these represent the most critical in a single-span system. The panels of interest are highlighted in Figure F4-35 for reference. Each X-type cross-frame has four members (top strut, bottom strut, and two diagonals). However, as demonstrated in previous studies, top strut forces in composite systems tend to be insignificant compared to the other members. Therefore, the RT excluded the results of top strut members herein and only evaluated the bottom strut and diagonals.

To simplify the loading conditions for this robust study and limit computation time, the RT did not run an influence-surface analysis and instead applied 12 static load cases using the AASHTO fatigue truck. For the six cross-frame members of interest, two different loads were assigned: one that maximizes tension and one that maximizes compression. The position of the truck corresponding to these critical cases was predetermined from preliminary analysis. Given that the bridge is supported by normally oriented piers, the load influence is highly localized and predictable, which simplified this process.

In summary, the total number of static analyses performed for the shell models was 3,888 (324 models × 12 load cases), and the total number of analyses for the truss models was 7,776 (108 models × 6 R-factors × 12 load cases). The figures presented hereafter summarize the results of these analytical studies.

Table F4-17: Parameters considered in the preliminary system-level parametric study

Parameter	Range of Values
Girder depth, *d* [ft]	{6, 8, 10}
Girder spacing [ft]	{*d*, *d* + 4′, *d* + 8′}
Gusset thickness [in]	{1/4, 1/2, 3/4}
Angle section	{L3x3x1/4, L4x4x3/8, L5x5x1/2, L6x6x5/8}
Deck thickness [in]	{8, 10, 12}

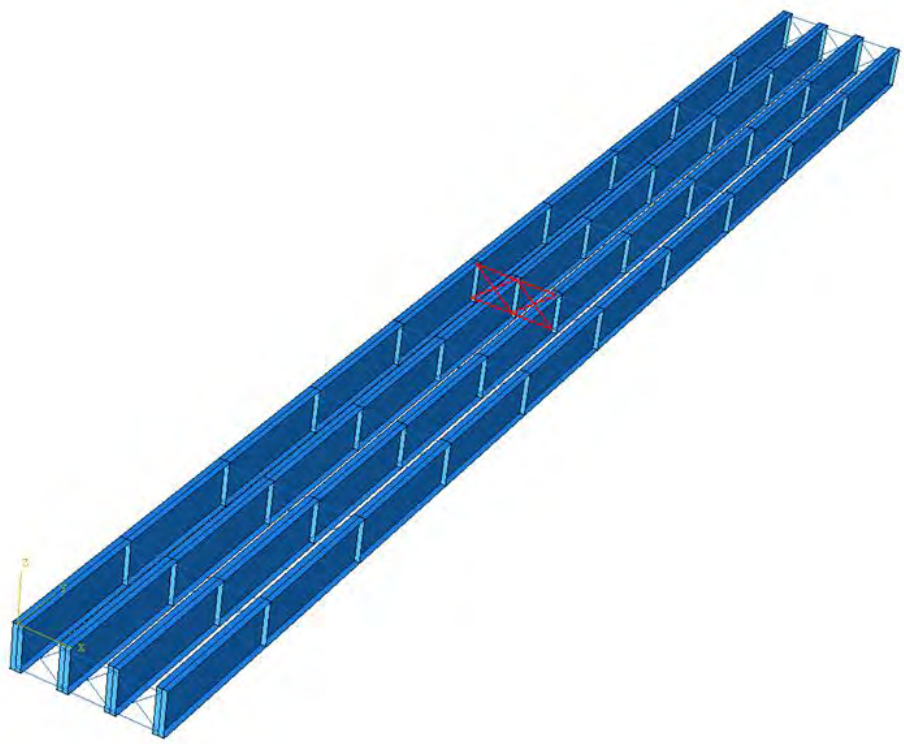

Figure F4-35: Cross-frame panels investigated as part of the system-level study

Much like Figure F4-29 and Figure F4-30 previously, the results of this parametric study are presented in the form of a box-and-whiskers plot (Figure F4-36 through Figure F4-38). In each box-and-whiskers component, the corresponding F_{truss}/F_{shell} ratios for all six cross-frame members (with respect to the two governing load cases) in every bridge model is considered. The figures illustrate the impact of the assigned R-factor and the gusset plate thickness by plotting those results independently. Figure F4-36 presents the results of all bridges with 1/4-inch gusset plates, Figure F4-37 for 1/2-inch gusset plates, and Figure F4-38 for 3/4-inch gusset plates. Similar to the discussion in Section F4.3.2.2, a line representing the 25th-percentile value of each data set is overlaid on the box-and-whiskers plots, as well as a line represent the mean values. For more information regarding the development of these plots, refer to the previous section.

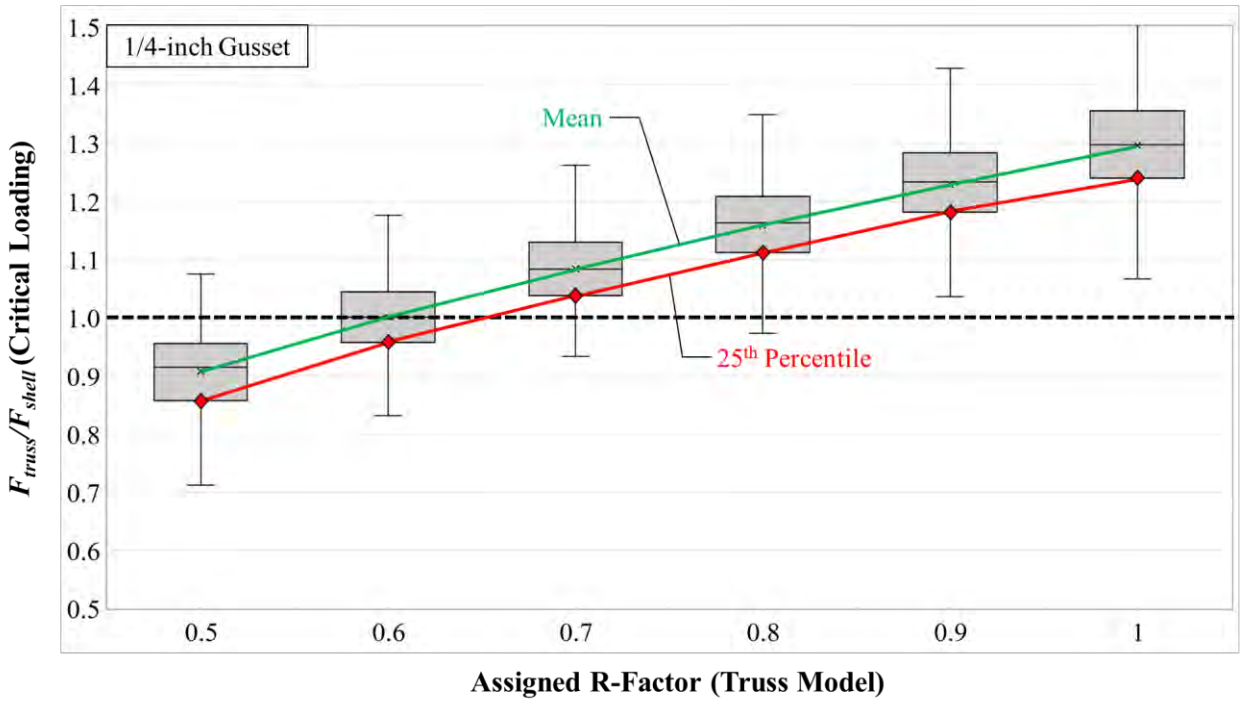

Figure F4-36: Box-and-whiskers plot indicating the overall level of accuracy for a given R-factor (1/4-inch gusset plate)

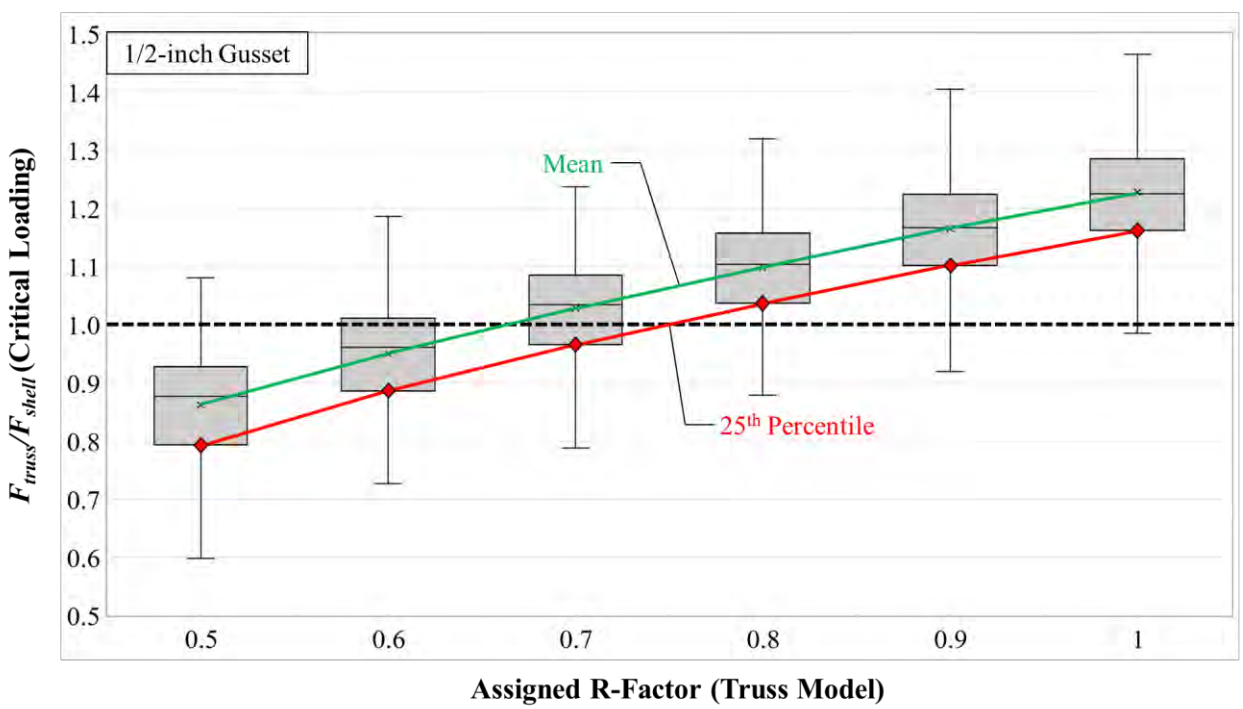

Figure F4-37: Box-and-whiskers plot indicating the overall level of accuracy for a given R-factor (1/2-inch gusset plate)

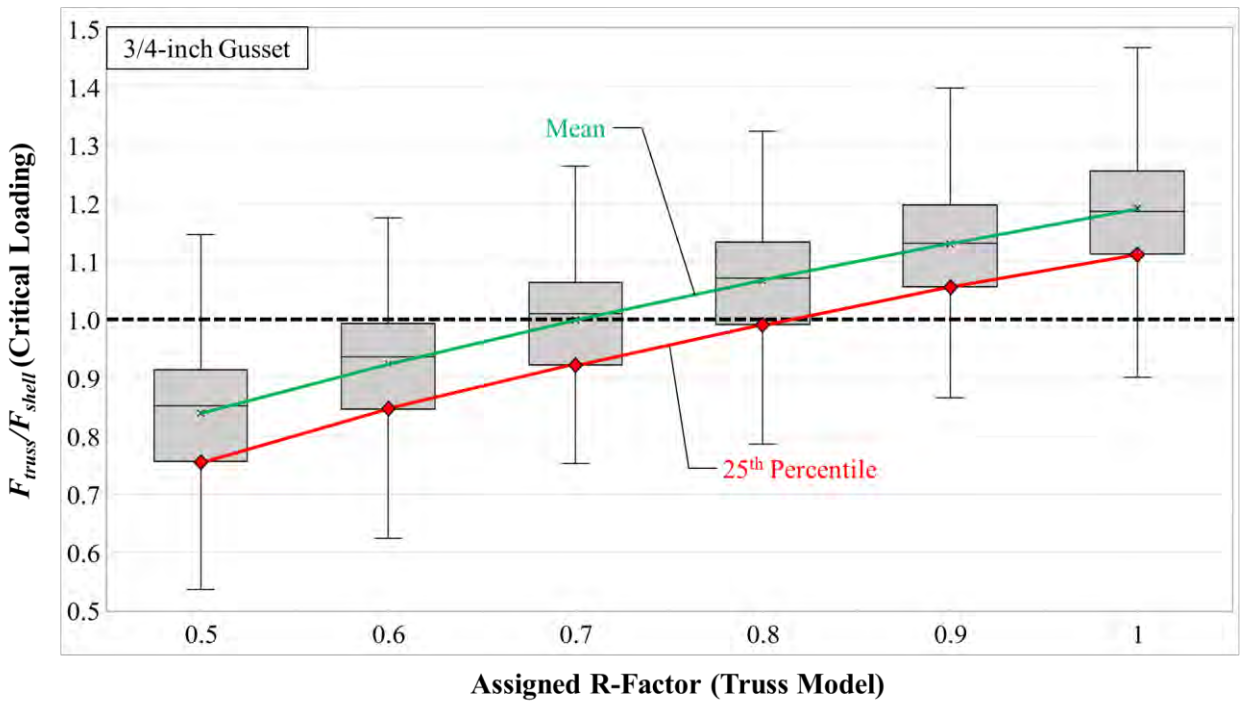

Figure F4-38: Box-and-whiskers plot indicating the overall level of accuracy for a given R-factor (3/4-inch gusset plate)

The trends observed from Figure F4-36 through Figure F4-38 (straight bridge with normal supports) are nearly identical to that of Figure F4-29 and Figure F4-30 (skewed and/or curved bridges). These are summarized briefly below:

- The force demands predicted by the R-factor approach can be highly variable and are a function of the member type and truck position, which is a highly uncertain variable.
- The F_{truss}/F_{shell} ratio decreases as the gusset plate thickness increases, which is consistent with all previous member-, panel-, and system-level study results shown previously.
- Using the 25th-percentile line as the metric, the most appropriate R-factor to assign for the normal, straight bridges with 1/4-inch, 1/2-inch, and 1-inch gussets is 0.65, 0.75 and 0.81, respectively. This behavior is summarized in Table F4-18, which presents these results as well as the R-factors using the mean value as the metric. Recall from Figure F4-29 and Figure F4-30 that the most appropriate R-factor for skewed and/or curved bridges with 1/2-inch and 1-inch gussets was 0.75 and 0.95, respectively.

Table F4-18: R-factor results from system-level parametric study

Gusset thickness [in]	Appropriate R-factor	
	Mean	25th Percentile
1/4	0.60	**0.65**
1/2	0.66	**0.75**
3/4	0.70	**0.81**

Based on the results of Section F4.3.2 and F4.3.3, there are three potential approaches for handling the variable response of the R-factor approach in terms of AASHTO LRFD. These are listed below from most sophisticated to most simplistic, as well as potential pros and cons to each approach:

- *Develop a member-specific and bridge-specific expression that provides a precise R-factor*. Given the variability in the response and the uncertain nature of live loads on bridge structures, this approach is neither feasible nor practical for implementation in AASHTO. The expression would inevitability be extremely complex and would still likely produce scattered results.
- *Develop an R-factor that is a direct function of the gusset plate thickness*. Rather than develop an expression that explicitly considers all pertinent bridge and cross-frame parameters (e.g. girder spacing, angle thickness), this approach simply focuses on gusset plate thickness which has been shown to substantially impact the "exact" R-factor (e.g. Table F4-18). This procedure could be easily implemented as an equation or a table. However, given that the gusset plate thickness may vary during the design process, this approach potentially lends itself to an iterative analysis procedure. Even with this extra level of refinement, the results could still be variable.
- *Develop a single R-factor that generally represents the behavior of all cross-frame members in a conservative manner (similar to the current 0.65 approach in 9th Edition AASHTO LRFD)*. As demonstrated with all previous results, pinpointing an "exact" R-factor is very difficult given its inherent dependence on the loading conditions and the associated deformation patterns. Regardless of how the cross-frames are modeled and R-factors are assigned, some error in cross-frame force predictions is to be expected when compared to the shell-element modeling approach. With that said, assigning a single R-factor for all cross-frame members, regardless of connection details, bridge geometry, and loading conditions, is a viable option.

After weighing the options, the RT elected to recommend the use of a single R-factor (option 3) similar to the current approach taken in AASHTO Article C4.6.3.3.4. Rather than assign a stiffness modification factor of 0.65, which was derived for a noncomposite system, a more appropriate factor is 0.75 for the composite condition. This is based on the system-level results presented above for 1/2-inch gussets, which are the most common size found on bridge structures in the US. Obviously, a bridge utilizing thicker gussets would warrant a slightly larger R-factor. But given the variability observed in the parametric study, applying R = 0.75 still produces fairly accurate results.

F4.4 Major Outcomes

Based on the results of the R-Factor Study presented in the preceding subsections, there are two major conclusions that can be drawn with respect to simplified 3D analysis methods for cross-frame design:

- The appropriate R-factor to be assigned in truss-element models is largely a function of bridge geometry, cross-frame details, and uncertain loading conditions. Consequently, considerable scatter was observed in all three phases of analytical studies: member-level, panel-level, and system-level. Still, the R-factor approach is a simple solution to a complex problem that produces reasonably accurate approximations of the true cross-frame stiffness. Considering that many designers often prefer simple alternatives over sophisticated refined analyses, it serves an important role in AASHTO LRFD guidance moving forward.
- In terms of implementation into AASHTO LRFD, the most logical approach to handling the uncertainty to the approach is to recommend the use of a single R-factor, similar to the current approach adopted into the specifications. Rather than use R = 0.65, R = 0.75 has been shown to produce more accurate results in composite systems when compared to benchmark solutions. As such, it is recommended to propose two separate factors, R_{con} for construction stages (0.65) and R_{ser} for in-service conditions (0.75).

- The proposed eccentric-beam model represents an approach that is slightly more refined than the conventional use of pin-ended truss elements, but less complex than modeling cross-frames with shell elements. As long as the out-of-plane connection plate flexibility is properly considered, the results demonstrated that the proposed method improves repeatability and reliability of 3D models by eliminating several sources of uncertainty associated with the R-factor approach. Although the R-factor approach serves a vital purpose in practice due to its ease-of-use and familiarity, the proposed eccentric-beam method offers another approach to engineers seeking a more refined solution.

The RT drafted proposed modifications to AASHTO LRFD with regards to 3D cross-frame modeling techniques based on the findings listed above. Refer to the main body of the report and Appendix A for the proposed language and commentary.

CHAPTER F5

Commercial Design Software Study

As introduced in Chapters F1 and F2, the Commercial Design Software Study investigates commercial software programs and their ability to accurately predict cross-frame forces for various bridge geometries and cross-frame configurations. A scaled parametric study was conducted to evaluate several modeling techniques commonly used in design practice for a variety of straight and curved bridges with normal and skewed supports. More specifically, the RT examined and compared different 2D and 3D modeling procedures with respect to cross-frame behavior. Chapter F5 herein outlines the computational work conducted for the Commercial Design Software Study and also provides results to substantiate the AASHTO LRFD design recommendations summarized in the main body of the report and Appendix A.

Following this introductory section, a brief description of the 2D and 3D modeling techniques evaluated are outlined in Section F5.1 as well as the scope of the scaled parametric study. Section F5.2 addresses the equivalent beam approach often utilized for cross-frames in 2D bridge models, and Section F5.3 offers several improvement techniques for these 2D methods. Section F5.4 compares the predicted cross-frame response for various modeling techniques. Commentary on the generalized observations and trends is then provided in Section F5.5, from which the design recommendations in the main body of the report and Appendix A are based.

F5.1 Overall Process

As with most structural analysis applications, a critical question that engineers often face is whether to adopt a 2D or 3D refined analysis model. One-dimensional (1D) line girder analyses can be useful tools for girder analysis and design of simple structures but generally provide no information related to cross-frame behavior. As such, 1D analyses are not examined in this study. 2D analysis methods, on the other hand, have been shown to produce accurate results for girder forces, but that performance is historically less understood and quantified for cross-frame forces.

To improve understanding in these areas, extensive research has been conducted on the limitations and benefits of the various modeling techniques commonly used, ranging from simplified 2D methods to high-fidelity 3D finite element solutions. NCHRP Report 725 (White, et al. 2012) investigated a variety of analysis techniques with respect to noncomposite bridge systems; AASHTO G13.1 Guidelines (2014) summarize many of these past findings, and AASHTO Article 4.6.3 and its commentary highlight key recommendations related to that work. Still, little guidance has been provided on how these analysis techniques affect the predicted response of cross-frame elements and systems in composite systems. As part of NCHRP Project 12-113 and specifically Task 11, the Commercial Design Software Study evaluated various 2D and 3D modeling techniques with respect to determining live-load force effects in cross-frame elements of composite girder systems.

Based on the results of the industry survey documented in Appendix D, the RT initially selected a 2D program (Software B) and a 3D program (Software A) to evaluate given their popularity among the bridge design community.

Software B incorporates two different 2D modeling approaches, which are widely used by the design industry and documented in AASHTO Article 4.6.6.3.2: (i) grillage/grid models and (ii) plate and eccentric beam (PEB) models. Software A, on the other hand, is a general-use program that specializes in 3D bridge analysis and design but is equally capable of conducting simplified 2D analyses (i.e., grid/grillage models and PEB models). Because the specific analysis techniques are of more importance to the project scope than the software brand itself, the RT elected to conduct all "commercial software" studies in the general-use Software A package. By making that decision, the RT was able to make more generalized observations about the modeling approaches, rather than only citing program-specific differences. Before fully adopting this approach, the RT developed similar 2D models of the three field-instrumented bridges using the built-in functions of Software B and manually in the general-use Software A. Cross-frame results from each program were compared, and good agreement was obtained. Thus, the 2D modeling approach in Software A and Software B are consistent.

By using Software A to conduct all 2D and 3D commercial software analyses, two major benefits are realized. First, rather than being restricted to the inherent "black-box" assumptions adopted by the Software B software, manually developing 2D models in a general-use program provides more flexibility especially in terms of implementing several modeling improvement methods (Section F5.3). Secondly, this general approach shifted the focus away from comparing specific commercial software programs and instead highlighted the modeling approach, which is of more general value to designers.

As previously suggested, the goal of the Commercial Design Software Study is to compare the predicted cross-frame response for various 2D and 3D modeling techniques with respect to the validated approach, which was detailed extensively in Section F3.1. In general terms, the following procedure was performed: build duplicate bridge models using various simplified techniques and compare the results to the solutions obtained from similar 3D FEA models in Abaqus, whose modeling procedures were validated by field-measured data (as documented in Appendix E). This general procedure is similar to the approach outlined in the R-Factor Study (Chapter F4).

Chapter F4 specifically examines how cross-frames, which are comprised of eccentrically-connected angle sections and gusset plates, are typically simplified as pin-ended truss elements in 3D models. Thus, Chapter F4 compares the results of 3D shell-element models (i.e., cross-frames modeled as shell elements), 3D truss-element models (i.e., cross-frames modeled as truss elements with the appropriate *R*-factor), and 3D eccentric-beam models (i.e., cross-frames modeled as beam elements explicitly representing the eccentric "jumps" in load path). In this case, the 3D shell-element models served as the basis for the comparisons given that this approach is the most accurate representation of the actual cross-frame.

Conversely, Chapter F5 focuses on the limitations of 2D modeling techniques. Thus, this chapter compares the results of 3D truss-element models (defined above) and various 2D models (e.g. grillage and PEB), where the 3D truss-element models serve as the basis for comparisons. More specifically, the RT compared the 3D truss-element models in Abaqus, which were used in the Fatigue Loading Study, with the following analysis methods in the general-use software package, Software A:

- 3D model (cross-frame modeled with truss elements; stiffness modification, *R*, taken as 0.6 to maintain consistency with Section F3.1.2 of this appendix),
- 2D PEB model (cross-frames idealized as equivalent beams; modifications outlined in Section F5.3 below and $R = 0.6$ inherently considered in equivalent beam properties), and
- 2D grillage or grid model (cross-frames idealized as equivalent beams; modifications outlined in Section F5.3 below and $R = 0.6$ inherently considered in equivalent beam properties).

As noted above, the stiffness modification factor ($R = 0.6$) was directly applied in the development of the equivalent beams in the 2D models, thereby reducing the equivalent beam section properties. Given that the 3D Abaqus model serves as the standard by which these other analysis methods are compared, it is

referred to as the "control" model hereafter. The general approach for these simplified methods, which are outlined sequentially below, are based on the guidelines documented in AASHTO G13.1 Guidelines for Steel Bridge Analysis (2014) and NCHRP Report 725 (2012).

3D modeling of bridge systems in commercial software can vary from package-to-package and engineer-to-engineer. The accuracy of the model as it pertains to cross-frame forces can be sensitive to the assumptions made by the designer. With this in mind, the RT adopted a common modeling approach and a set of assumptions when developing the models in the 3D commercial software package. The results presented in this chapter are intended to be representative of most 3D software packages and modeling assumptions likely utilized by bridge designers. However, it is important to note that some variability in the results should be anticipated for a different software package or a different set of assumptions.

The 3D commercial software models were developed similarly to the 3D Abaqus model (i.e., the control model). The concrete deck and girder webs were modeled with shell elements. However, girder flanges were modeled as beam elements rather than shells. The top flange of the girder and the deck were constrained together to simulate composite action. Cross-frames were treated as pin-ended truss elements that frame into a node at the girder web-to-flange junction, which is traditionally done in commercial software programs as introduced in Section F4.3.2.1. Eccentric end connections were considered by assigning an R-factor that was consistent with the control model (R = 0.6) to eliminate eccentric end connections as a source of uncertainty in this study.

Transverse stiffeners were provided to stiffen the web and preclude distortional effects that would reduce the effective stiffness of the cross-frame. Given that the cross-frame elements frame into the shared web-flange node, web distortion is not expected to be substantial. However, automating the modeling of web stiffeners is a built-in feature in Software A, so the RT elected to include them for completeness.

Bearings were modeled as bidirectional linear springs on the bottom flange with stiffness values consistent with common bearings used in practice. A mesh sensitivity study was conducted, similar to what was performed for the 3D Abaqus model, to converge on an optimal discretization size for efficiency and accuracy. Lastly, the built-in influence-surface feature of Software A was utilized to move a unit, 1-kip load along the length and width of the bridge deck.

The 2D PEB models were developed in accordance with AASHTO LRFD Article 4.6.3.3.1. The concrete deck was explicitly modeled as a shell element. However, the girders were modeled as beam elements offset from the deck shell to represent the height difference between the centroids of the respective components. The shells representing the concrete deck and the beam elements representing the girders were constrained together to simulate composite action. Given that the depth component of the girders is neglected in the PEB modeling approach, cross-frames cannot be explicitly modeled. Instead, they are represented as equivalent beams, as outlined in more detail in the subsequent section.

Similar to the 3D approach above, bearings were represented as linear springs, except that they acted at the centroid of the girder section. Additionally, at least one intermediate node was placed on the beam element representing the girder between two adjacent cross-frame intersections on that beam. This is particularly important for curved bridge systems, which generally model the girders as a series of chorded, straight-line segments. In these cases, at least one additional node was placed between the cross-frame-to-girder connections. The influence-surface loads were applied directly to the deck shell, in the same manner as the 3D model.

Similar to the 2D PEB approach, the 2D grillage models were developed based on the guidelines provided in AASHTO LRFD Article 4.6.3.3.1 and its commentary. For 2D grillage models, the deck shell is not explicitly modeled. Instead, live load force distribution is typically based on simplified distribution factors in AASHTO. There are, however, procedures to approximately consider the contributions of the concrete deck as a transverse load distribution mechanism, as is discussed later. Girders, much like the 2D PEB

approach, were modeled as beam elements. However, the section properties of the beam elements in grillage models consider the composite section. Thus, the grillage models inherently reflect the longitudinal stiffness of the deck but neglect its transverse stiffness. Similar to the PEB approach, at least one intermediate node was placed along the girder beam element between adjacent cross-frame intersections.

Cross-frames and bearings in grillage models were handled the same way as with the PEB models. Lastly, implementation of the influence-surface loads is more challenging in grillage models, considering the deck is no longer explicitly modeled. Instead, the lever rule was utilized to assign a percentage of the unit load to the neighboring girders. One of the major limitations of 2D grillage models is the inability to adequately perform an influence-surface analysis without the use of empirical or simplified methods.

Table F5-1 summarizes the general techniques for the various analysis methods considered in the study. The table serves to highlight the major differences in how the key load-distributing elements were represented, namely the deck, girders, and cross-frames. Note that Table F5-1 does not consider any modifications that potentially improve the predicted response of the bridge; however, these concepts are introduced in subsequent sections. A visual representation of each analysis method is shown in Figure F5-1 with screenshots from a sample bridge model.

Table F5-1: Parameters considered in the analytical-model parametric study

Element	Analysis Method			
	Control	**3D**	**2D PEB**	**2D Grillage**
Concrete deck	Shell	Shell	Shell	--
Girders	Shells	Shells/beams	Beam element[a]	Beam element[a]
Cross-frames	Truss element	Truss element	Equivalent beam[b]	Equivalent beam[b]

Notes:
[a]In PEB model, beam element represents steel section alone; in grillage model, beam element represents effective composite section
[b]There are multiple procedures by which the equivalent beam is computed, as is discussed in the subsequent section

Based on the descriptions of each analysis method, it is apparent that the 2D approaches rely heavily on simplifications and thus have a greater potential for error. This is particularly true for cross-frame force predictions in 2D models because cross-frames are modeled as equivalent beams. In context of Figure F5-1, it is expected that the performance of the analysis method moving left to right will worsen with respect to predicting cross-frame forces.

Control (3D Abaqus)	3D
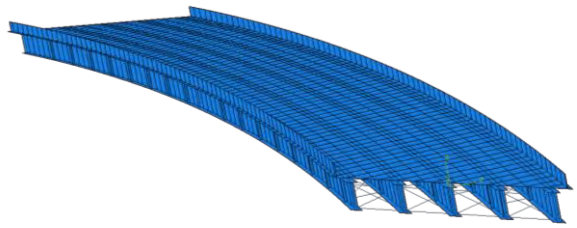	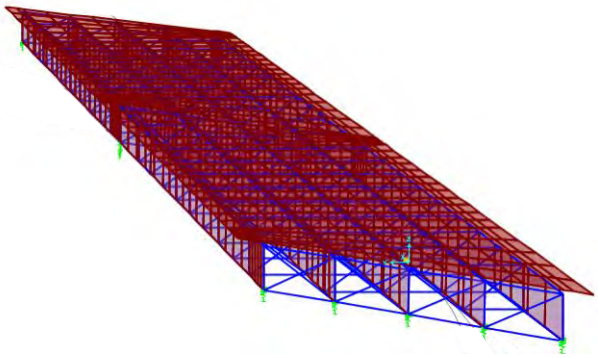
2D PEB	**2D Grillage**
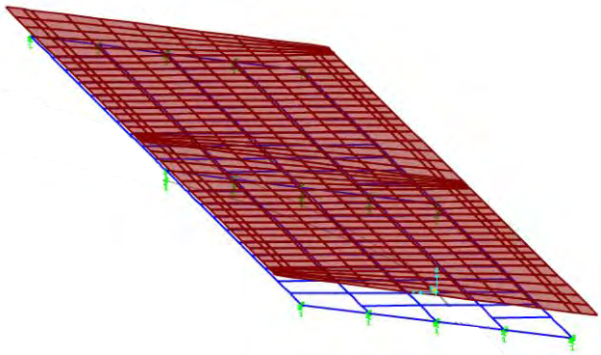	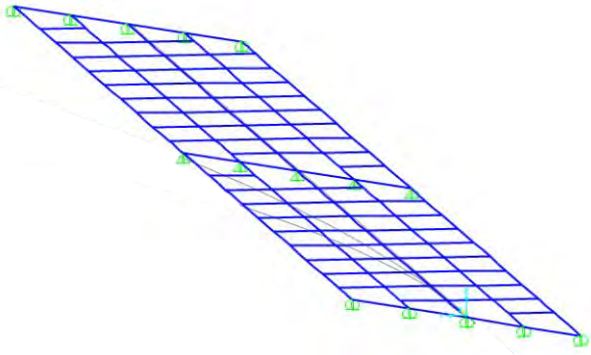

Figure F5-1: Screenshot of the various analysis methods considered in the study

The various models outlined above were developed for a scaled version of the 4,104-model matrix outlined in Section F3.1.2. The same 20 bridges that were evaluated for the system-level R-Factor Study (Section F4.3) are also studied for the Commercial Design Software Study. These 20 bridges sample key parameters from the full 4,104-model matrix that most often affect cross-frame force predictions in 2D simplified analyses, namely support skew and bridge curvature. Thus, information or knowledge gained from this abbreviated study is directly applicable to the broader range of bridges considered in the Fatigue Loading Study. For each of the 20 representative models, the RT conducted an influence-surface analysis (or equivalent) for the various iterations illustrated in Figure F5-1. For reference, the pertinent variables that describe the overall geometry and cross-frame layout of these sample bridges were previously summarized in Table F4-10 and Table F4-11.

As introduced above, 2D analysis models eliminate the depth component of the steel superstructure system. As such, cross-frames are simplified as equivalent beam elements in 2D analyses. This procedure is outlined in the next subsection.

F5.2 Equivalent Beam Approach for Cross-Frames

For both 2D grillage and PEB modeling approaches discussed in the preceding subsection, cross-frames are commonly converted into equivalent beams for analysis purposes and converted back into a truss system for obtaining internal member forces. This section briefly introduces this concept to provide context for discussions herein. Figure F5-2 illustrates this process graphically.

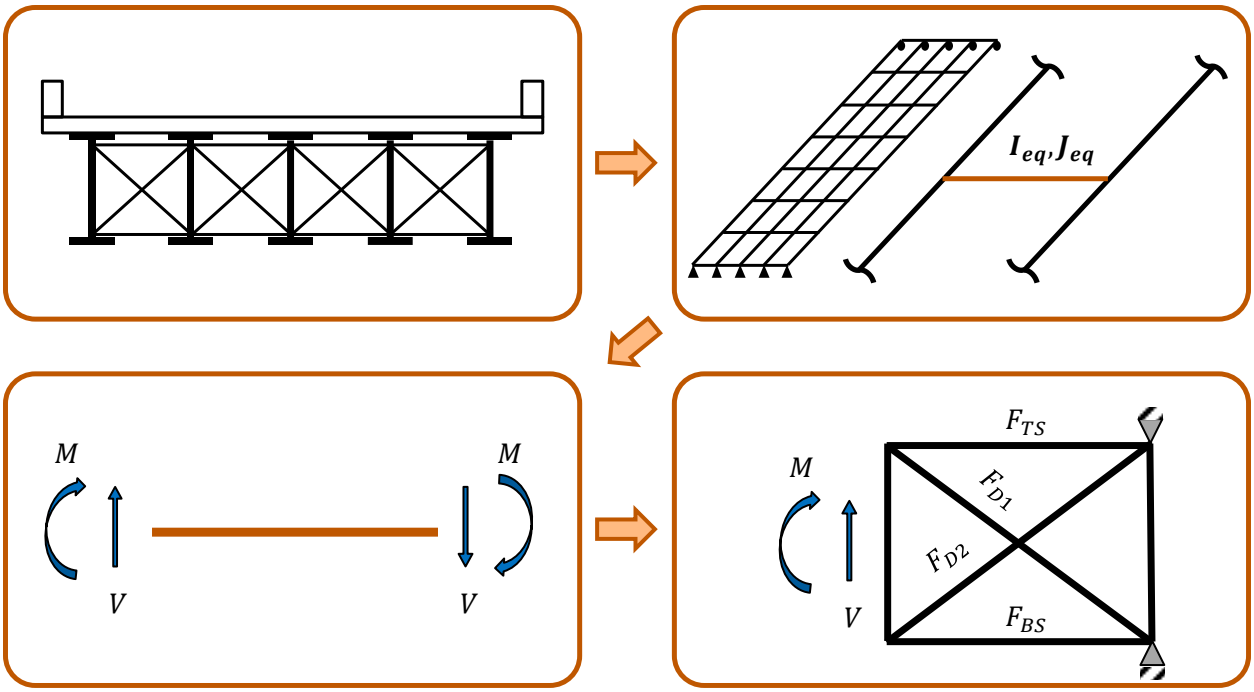

Figure F5-2: General process for equivalent beam approach to analyzing cross-frames

Because girders are modeled as beam elements in 2D analyses, the depth component of the steel superstructure is not reflected. Therefore, cross-frames are also modeled as beam elements at an elevation corresponding to the centroid of the cross-frame panel (i.e., mid-depth of the girder typically), which is illustrated in the top right quadrant of Figure F5-2. To represent the stiffness of the cross-frame when modeled as a beam, several different methods are commonly used to compute an equivalent moment of inertia, torsional constant, and shear area. These methods are outlined in Section F5.3. The 2D models are then analyzed, resulting in equivalent beam elements with distinct end moments and a constant shear. This is represented in the bottom left quadrant of Figure F5-2.

Lastly, these end moments and shears are applied as external loads on a single truss-panel model, where internal axial forces in struts and diagonals are computed. The end moments are often resolved as a force couple between the top and bottom nodes of the truss. Individual moment components at the top and bottom nodes are disregarded, which implies the in-plane bending effects associated with the connection and gusset plate connections are negligible. This assumption, although consistent with the 3D pin-ended truss modeling approach of cross-frames, deviates slightly from the true behavior of cross-frames (Figure F4-6).

For X-type cross-frames as depicted above, the end shears are equally distributed between top and bottom nodes resulting in equal and opposite diagonal member forces; for K-type cross-frames, the vertical shear component is resistant entirely by the diagonal member so no distribution assumption is required. These common assumptions are examined further in the subsequent sections.

Particularly for heavily skewed and/or curved bridges, this equivalent beam approach is thought to produce cross-frame force results with varying levels of accuracy. For example, it is clear from Figure F5-2 that top and bottom struts will always have equal and opposite force predictions with this method. In reality, this behavior is seldom observed. The data measured from the field experiments and the FEA studies described in this appendix have indicated that top struts typically develop very little force, due to the cross-frame panel being a part of a larger composite system. With the background information outlined, the next subsection offers and explores specific improvements on these simplified 2D methodologies.

F5.3 Approaches for Improving 2D Analyses

In conjunction with the 2D models outlined previously, several improvement techniques based on NCHRP Report 725 (2012) and past experience were explored for purposes in the Commercial Design Software Study. These improvement techniques range from analysis (upper right quadrant of Figure F5-2) to postprocessing (bottom right quadrant of Figure F5-2) assumptions. The RT evaluated these techniques on a variety of bridge models, and the results are presented in the subsequent section. These techniques, along with their designation as analysis or postprocessing modifications, are summarized as follows:

1. **Improve the equivalent cross-frame beam properties [Analysis]**. As outlined in NCHRP Report 725, there are three approaches by which cross-frames can be transformed into an equivalent beam for use in 2D models (upper right quadrant of Figure F5-2). These approaches are described as the flexural-analogy approach, the shear-analogy approach, and the Timoshenko beam element. For the sake of brevity, refer to Section 3.2.3 of NCHRP Report 725 for a detailed description of each method. By default, Software B utilizes only the flexural-analogy approach for both its grillage and PEB models. These restrictions further highlight the benefits of using a flexible, general-use commercial software program for this study. Per NCHRP Report 725, the Timoshenko beam provides the most realistic estimate of the cross-frame stiffness because it considers both flexural and shear deformations. To verify this assertion in the context of composite systems, the RT assessed each approach by implementing them into 20 representative bridge models. Note that this improvement technique is applicable to both 2D grid and PEB models.

2. **Use an equivalent torsion constant for the beam elements representing girders to account for the neglected warping stiffness [Analysis]**. As documented in NCHRP Report 725, many software programs neglect the warping stiffness term when idealizing 3D girders as beam elements in 2D analyses. This results in a significant underestimation of the torsional stiffness of the system. Significant errors in predicted bridge response (e.g. deflections and cross-frame forces) have been shown to occur on noncomposite systems, particularly in skewed and curved bridges.

   NCHRP Report 725 (2012) proposed an equivalent torsional constant (J_{eq}) that approximates the combined effects of the St. Venant and warping components of the girder torsional rigidity. When assigning J_{eq} to the beam elements representing the girders, significant improvements to the bridge response were observed by the NCHRP researchers when compared to a 3D FEA benchmark solution. This was demonstrated for a noncomposite system subjected to dead loads only.

   Given that the current study is focused on composite systems subjected to live loads, the RT explored J_{eq} properties for 2D grillage and PEB models and found that this modification is less impactful for composite systems. In a composite system, the torsional stiffness of the concrete deck is substantial compared to the added contribution of the warping stiffness in the girders. Therefore, implementing an equivalent torsional constant for girders was shown to have little effect on the cross-frame force predictions. Consequently, the results from 2D models presented later in Section F5.4 include J_{eq} torsional properties for completeness; however, it is important to note that the results without the modified term are nearly identical.

3. **Consider the transverse stiffness of the deck by modifying the stiffness properties of the equivalent cross-frame beams [Analysis]**. Given that 2D PEB models represent the deck as a shell element, this technique is only applicable to grillage models, which do not physically model the deck. In this modification, the transverse stiffness of the deck is simulated using (i) equivalent section properties or (ii) notional beams. This is demonstrated schematically in Figure F5-3, which is an improved adaptation of Figure F5-2 for grillage models.

In the top right quadrant of Figure F5-3, the section properties of the equivalent cross-frame beam are modified by simply summing the contributions from both the cross-frame (as previously determined by the Timoshenko beam approach) and the deck, whose effective width is taken as half the distance to the nearest cross-frame on each side. Thus, the additional moment of inertia, shear area, and torsional constant contributed by the applicable concrete deck strip (as modified by the appropriate modular ratio) is added to the equivalent cross-frame beam properties.

In addition to the effective property approach, consideration of the transverse deck stiffness can also be implemented with separate, notional transverse beam elements in the grillage model per AASHTO Article C4.6.6.3.4. This method is not explicitly presented in Figure F5-3 but was evaluated as part of this study.

4. **Reconsider the distribution of shear forces and moments when postprocessing results [Postprocessing]**. As introduced previously, the end moments obtained from 2D analyses are often resolved as equal and opposite force couples to the top and bottom nodes of the truss, and end shears are assumed equally distributed to top and bottom nodes for X-type cross-frames (as demonstrated by the bottom left quadrant of Figure F5-2). These assumptions, although simple to implement, can produce significant errors for composite bridge systems as is shown by the results herein. 3D FEA results and measured data has shown that top and bottom struts generally do not have equal and opposite forces; similarly, diagonal members generally do not have equal and opposite forces in X-frames. As such, the RT proposed a unique postprocessing tool for both 2D grillage and 2D PEB models. The grillage technique is presented schematically in the bottom right quadrant of Figure F5-3, and the PEB technique is presented schematically in the bottom right quadrant of Figure F5-4. Both figures are improved adaptations of Figure F5-2.

   The grillage improvement technique is related to the equivalent section properties approach outlined in item #3 above (i.e., considering the contributions of the transverse deck stiffness). By effectively increasing the stiffness of the equivalent beam to account for the contributions of the concrete deck, considerations for the deck must also be made when postprocessing results. Otherwise, the force demands on the cross-frame elements will be artificially amplified due to the increase in assigned stiffness. In contrast, the methodology below is not applicable to the notional beam approach introduced in item #3. For that case, the end moments and shears obtained for the equivalent cross-frame beam can be resolved directly to the cross-frame truss model given that the contributions of the concrete deck are explicitly and independently considered in analysis.

   Rather than applying the end moments and shear on just the cross-frame panel, the applied loads are resolved on a composite system including the cross-frame and deck. This is demonstrated in Figure F5-3. The end moment is resolved between the centroid of the deck and the centroid of the bottom strut, which results in a moment arm of H (or the distance between the respective centroids). This modification is intended to remedy the problem of having equal and opposite strut forces, which has been shown to be inaccurate based on field data and 3D FEA results. In reality, the top strut will contribute a small portion to the internal moment distribution in composite systems (i.e., not zero). However, given that the top strut is often near the neutral axis of this pseudo-composite beam (using elastic beam theory), the force resultant will be close to zero; therefore, the moment arm H assumption is reasonable. The beam analogy is also illustrated on Figure F5-3 with a schematic elastic, flexural stress distribution.

It should be noted that in noncomposite systems, equal and opposite force distribution in the struts is anticipated given that the cross-frame moments can only be resolved by a force couple in the struts (since there is no deck to absorb load). Thus, it is apparent from this simple discussion that the behavior of cross-frames in noncomposite and composite systems is different and should be treated as such in analysis. This discussion is advanced further in subsequent sections.

Additionally, in this proposed technique for 2D grillage models, the shear force acting on the equivalent beam must be distributed to the concrete deck and cross-frame panel. The RT utilized a rational approach in which the shear force is distributed based on the relative stiffness of the deck and cross-frame (i.e., Eqs. F3.8 and F3.9) to determine V_{deck} and V_{CF}. Although, other methodologies are possible. The distribution of V_{CF} to the top and bottom nodes of the cross-frame truss is discussed below.

The PEB postprocessing technique differs from the grillage technique in that the internal moments and shears obtained from the analysis (via equivalent beams) only consider the contributions from the cross-frame panel. Recall that the stiffness of the concrete deck is explicitly considered by shell elements in the PEB modeling approach. Thus, in the process of converting end moments and shears into cross-frame force effects, the added discussion about moment arm H above is not relevant.

With that in mind, the remaining discussion relates to how the vertical shear force (V_{CF}) acting on the cross-frame panel is distributed to the top and bottom nodes. This significantly impacts the assumed force effects in the cross-frame members, particularly for the diagonals which are directly related to the vertical component of the nodal forces. The RT explored solutions to this problem and compared the behavior of noncomposite and composite systems. Ultimately, the equal-distribution "50-50" assumption (i.e., $0.5V_{CF}$ to the top node and $0.5V_{CF}$ to the bottom nodes) is compared to a "100-0" assumption (i.e., conservatively and independently evaluate the cases in which 100% of V_{CF} is resisted by the top node and 100% of V_{CF} is resisted by the bottom node). This is demonstrated schematically in Figure F5-4, where the percentage of shear force distribution is represented by variable n.

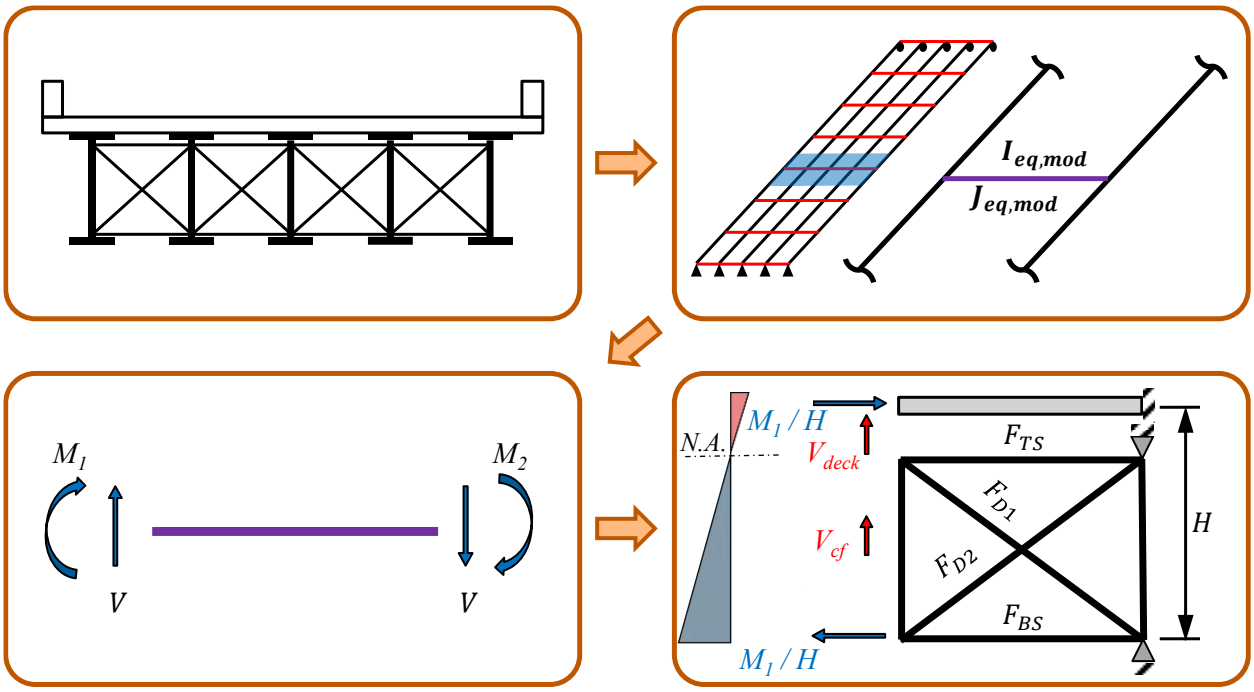

Figure F5-3: General process for improved 2D grillage analysis

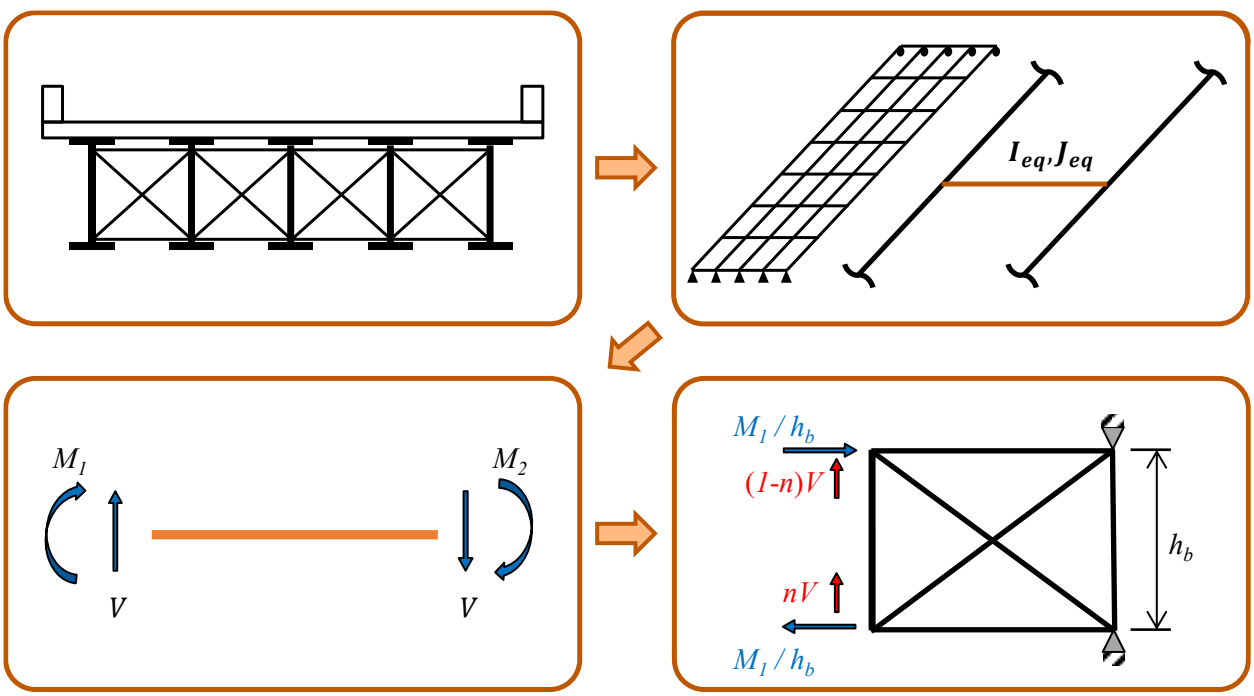

Figure F5-4: General process for improved 2D PEB analysis

Table F5-2 summarizes the analysis-related improvement techniques outlined above and the relative impact on deck, girder, and cross-frame elements. Blank table entries indicate that no modifications are made to

that particular element. As introduced above, a scaled parametric study was conducted to assess the performance of each technique; the results of this study are documented in Section F5.4. Recall that the equivalent torsional constant for girders was deemed ineffective for improving cross-frame forces. Therefore, it is not specifically addressed herein. Instead, the results in Section F5.4 focus on the other two improvement methods, improved equivalent beam properties for PEB and grillage models and composite considerations for grillage models only.

Table F5-2: Summary of improved analysis techniques for 2D models

Element	2D Analysis Improvement Techniques		
	Improve Equivalent Cross-Frame Beams[a]	Equivalent Torsional Constant for Girders[a]	Equivalent Cross-Frame Beams[b]
Concrete deck	--	--	Consider with equivalent cross-frame beam
Girders	--	Assign J_{eq} to girder properties	--
Cross-frames	Use Timoshenko beam approach	--	Adjust equivalent section properties to include deck

Notes:
[a]Applies to both grillage and PEB models
[b]Applies to grillage models only

F5.4 Comparative Results

To demonstrate the limitations of simplified 2D analysis methods, comparative results are presented herein. Similar to the Fatigue Loading Study, an abundance of cross-frame data was obtained from the Commercial Design Software Study. To simplify the results and discussion for the reader, a similar outline with respect to data presentation is followed in this section as was done for Section F3.1.8. Rather than present detailed results for the entire data set, representative sample sets are first shown in Sections F5.4.1 and F5.4.2. These sections address different aspects of the results. Section F5.4.1 presents sample influence-line results to introduce the general limitations of 2D analysis methods to the reader; Section F5.4.2 investigates the influence of composite action on the accuracy of the 2D models. Section F5.4.3 then compiles and summarizes the results for the full data set. Lastly, Section F5.4.4 proposes an alternative postprocessing procedure for 2D PEB analyses.

F5.4.1 Sample Influence-Line Results

As a starting point, Figure F5-5, Figure F5-6, and Figure F5-7 comprehensively compare the predicted cross-frame response for various analysis methods under a specified moving load. Replicating these types of plots, however, for every cross-frame member and various loading conditions is not feasible nor meaningful to the reader. Instead, these sample figures are used to highlight key trends and observations with respect to the various 2D analysis methods.

Figure F5-5, Figure F5-6, and Figure F5-7 present cross-frame results for a portion of the full data set. Each figure represents a unique bridge geometry. Figure F5-5, Figure F5-6, and Figure F5-7 show the respective cross-frame responses for Bridges 277-2, 1181-2, and 755-2. Bridge 277-2 represents a straight bridge with normal supports. Bridge 1181-2 represents a straight bridge with skewed supports, and Bridge 755-2

represents a curved bridge with skewed supports. Refer to Table F4-10 and Table F4-11 for more information regarding the overall geometry and cross-frame layout of these three bridges.

For each figure, the results of the three select cross-frame locations are shown: (i) a bottom strut near the maximum positive dead load moment region (i.e., approximately 0.35*L* from the end support where *L* is the span length) referred to as Case 1, (ii) a top strut from the same cross-frame panel referred to as Case 2, and (iii) a diagonal near the intermediate skewed support referred to as Case 3. The exact locations of these cross-frames are not identical between the three representative bridges shown; however, the general location with respect to the span of interest is similar. This is demonstrated schematically in the framing plan sketches in Figure F5-5, Figure F5-6, and Figure F5-7.

For each plot, the AASHTO fatigue truck was moved longitudinally along the centerline of the bridge as is depicted. Figure F5-5, Figure F5-6, and Figure F5-7 plot the axial-force response of the respective cross-frame members as a function of the truck position along the bridge length, measured from the front axle to the start of the bridge. These graphs are similar to the influence-line plots presented in Figure F3-27. This process was repeated for several variations of the same bridge model. In other words, several analysis models were executed including the 3D validated approach in Abaqus (control) and the following methods in the commercial software program Software A:

- 3D model,
- 2D PEB model with equivalent cross-frame beams based on shear-analogy approach,
- 2D PEB model with equivalent cross-frame beams based on flexural-analogy approach,
- Improved 2D PEB model with equivalent cross-frame beams based on Timoshenko approach,
- 2D grid/grillage model with equivalent cross-frame beams based on flexural-analogy approach,
- 2D grid/grillage model with equivalent cross-frame beams based on Timoshenko approach, and
- Improved 2D grid/grillage model with equivalent cross-frame beams considering transverse stiffness of concrete deck.

Recall that the specifics of these 2D modeling approaches (e.g. equivalent cross-frame beam analogies) were outlined in the preceding subsections of Chapter F5. Simplified 2D analyses have been generally perceived to produce erroneous cross-frame results in heavily curved bridges and near skewed supports, as it is generally unable to capture the torsional response and complex load path of the bridge at these critical locations. These sample results begin to address these perceptions and highlight key deficiencies of the simplified 2D analyses.

Note that, for the PEB and grillage models, equal distribution of cross-frame shear is assumed between top and bottom nodes when postprocessing analysis results. The implications of using a different distribution assumption are addressed in the subsequent section.

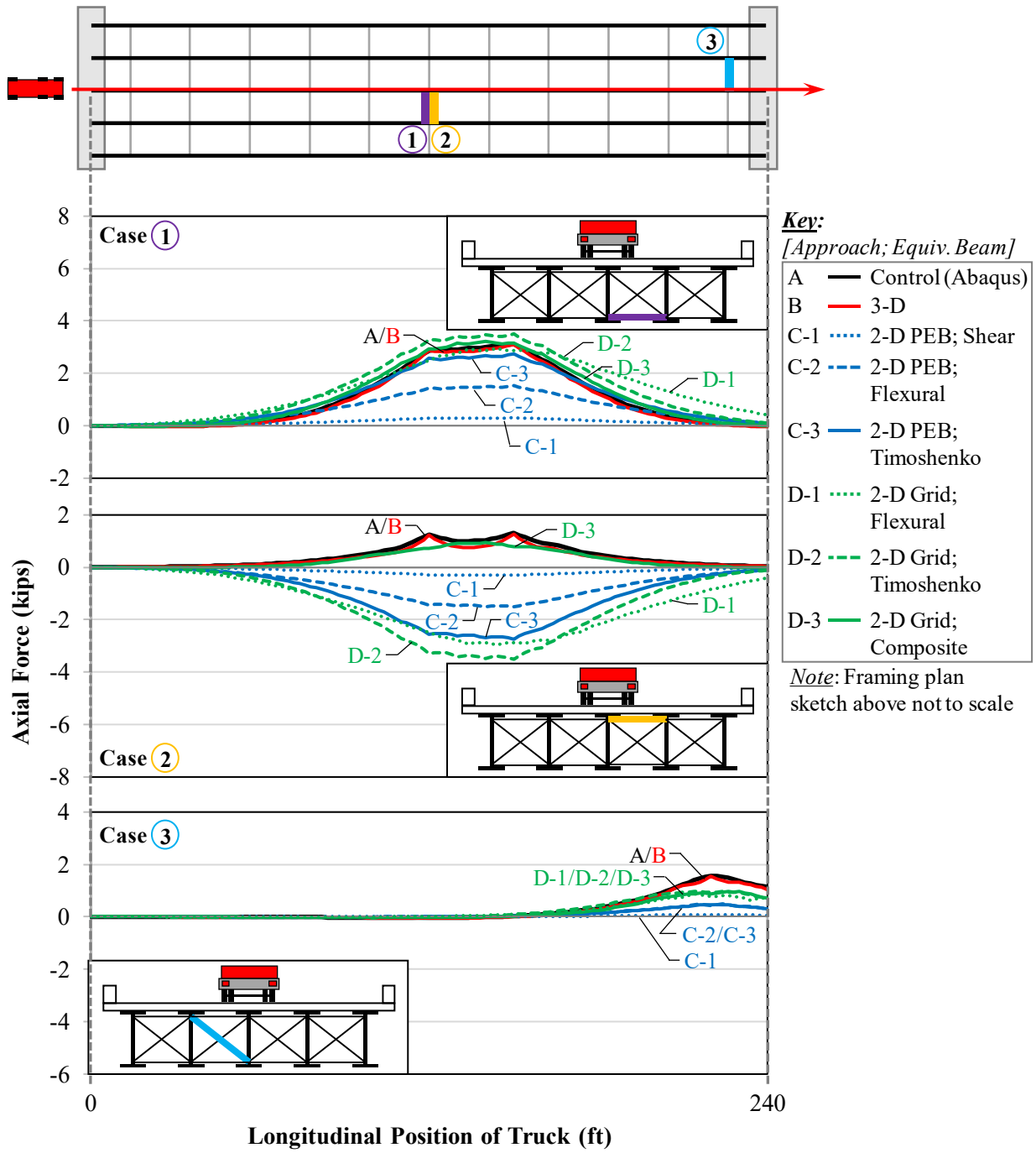

Figure F5-5: Comparison of analysis methods for three select cross-frame members in a straight bridge with normal supports

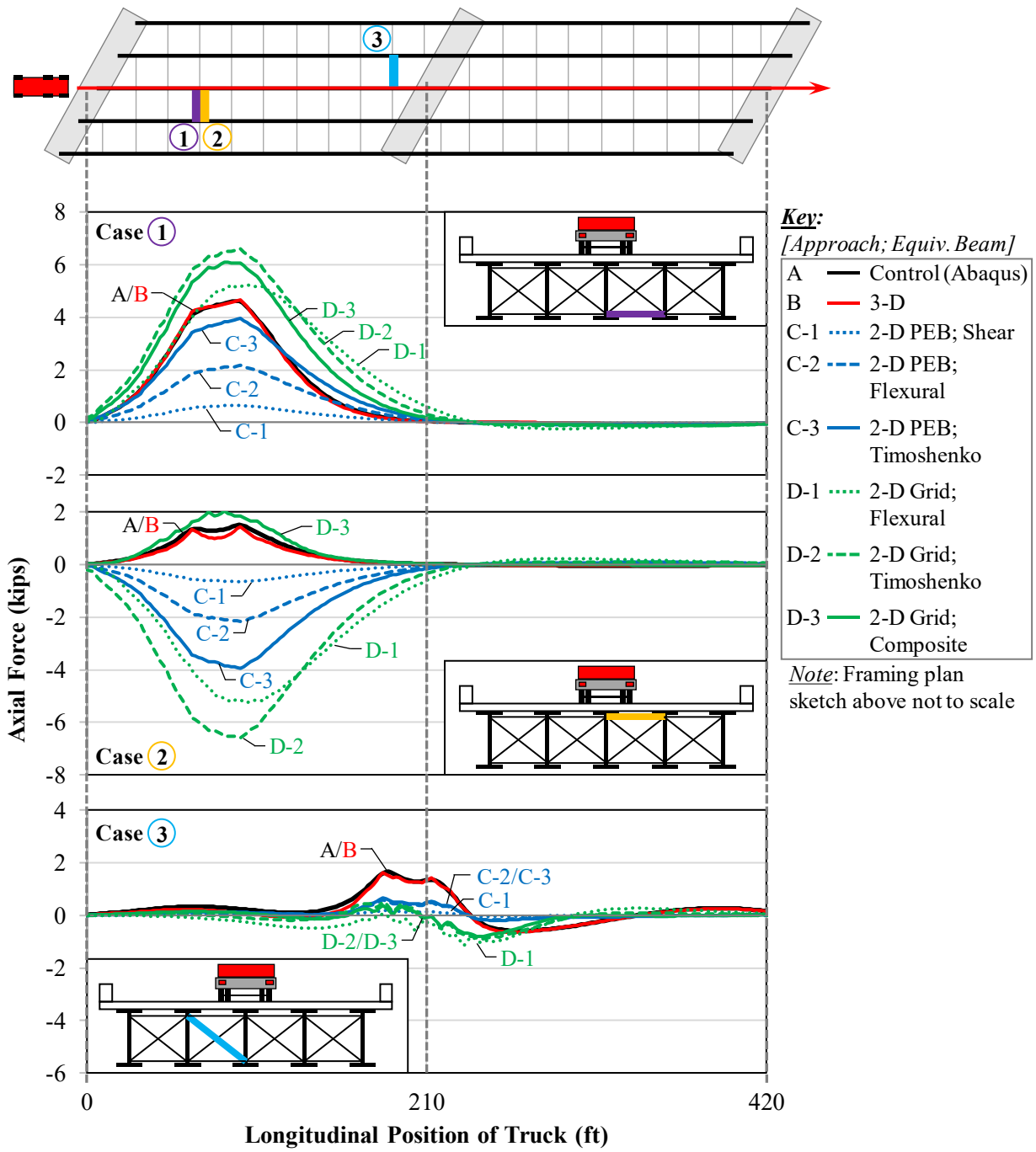

Figure F5-6: Comparison of analysis methods for three select cross-frame members in a straight bridge with skewed supports

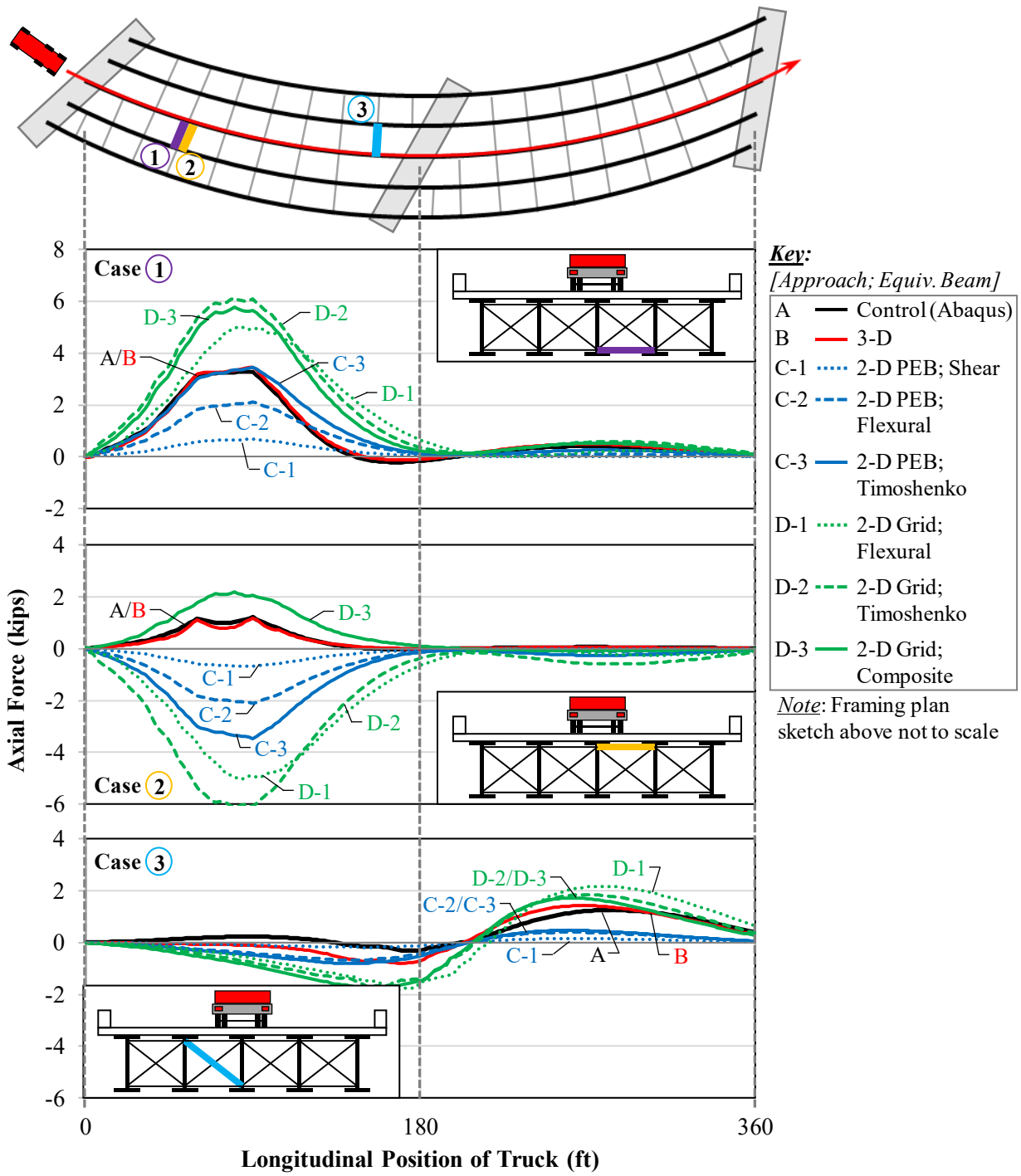

Figure F5-7: Comparison of analysis methods for three select cross-frame members in a curved bridge with skewed supports

From Figure F5-5, Figure F5-6, and Figure F5-7, the following observations can be made when comparing the results of a specific cross-frame location across each bridge model:

Case 1 (bottom strut near the maximum positive dead load moment region):

- The 3D commercial software model generally produces excellent results when compared to the validated 3D FEA model in Abaqus (within a few percent). Given that the commercial software modeling approach is nearly identical to that of the control model, this trend was anticipated. This also indicates that the connection point of the cross-frame members (i.e., into a shared node on the web-flange junction versus at an offset distance along the web) is less impactful for 3D models.
- The 2D PEB model using the Timoshenko analogy generally produces accurate results of bottom strut forces when compared to the refined 3D models. When using the flexural or shear analogies for the equivalent beam sections, though, the cross-frame stiffness can be poorly represented. As a result, the cross-frame forces are shown to have significant error in these sample results.
- The 2D grid models generally do a poor job at predicting the cross-frame forces, except for the straight bridge with normal supports. Simulating its transverse stiffness contributions without explicitly modeling the concrete deck is challenging; consequently, substantial variability in the predicted response is anticipated for more complex bridge systems.

Case 2 (top strut near the maximum positive dead load moment region):

- Similar to Case 1, the 3D commercial software model generally produces excellent results when compared to the validated 3D FEA model in Abaqus.
- For the 2D analyses that do not consider the contributions of the deck when postprocessing the analysis results (bottom right quadrant of Figure F5-3), the top strut results are equal magnitude and opposite sign to those of comparable cases presented for the bottom strut members (Case 1). This is a function of the simplified postprocessing used when converting the equivalent beam back into a truss. As illustrated in this example, this simplification generally results in erroneous results for top strut forces.
- This error is corrected in the 2D grillage model using cross-frame beams with equivalent section properties to account for the contributions of the deck. Albeit the correct sign, the magnitudes are still generally overestimated with this procedure.

Case 3 (diagonal near the intermediate/end support):

- In general, the axial-force response of the diagonal near a skewed support is more complex than the cross-frame members near the maximum positive dead load moment region or a normal support. This behavior is consistent with the field-measured data obtained from instrumented Bridge 2 and the results presented in Chapter F3.
- The simplified 2D modeling approaches (both PEB and grid) result in significant error for its prediction of cross-frame force ranges, especially for the bridges with skewed supports. This is largely attributed to the complex behavior near skewed supports that is not adequately captured by two-dimensional modeling approaches, as well as the postprocessing assumptions with regards to shear force distribution.

In reviewing data beyond the three sample results presented above (specifically bridges with X-type cross-frames), it was clearly evident that the predicted 2D-model response of bottom strut members was much more accurate than the predicted response of diagonal or top strut members. This behavior was apparent even for simple bridge geometries. In other words, the variability observed in the response was not only a function of the bridge geometry (i.e.,, straight versus curved, normal supports versus skewed supports) but also the cross-frame member type (i.e., bottom strut versus diagonals).

The variability associated with bridge geometry is attributed more to analysis error (i.e., how the analysis determines end shears and moments on the equivalent cross-frame beam), whereas variability associated with member type is attributed more to postprocessing error (i.e., how those end shears and moments are converted into cross-frame member forces). With that in mind, Section F5.4.2 examines this behavior in the context of noncomposite and composite systems to determine the root cause of these discrepancies.

F5.4.2 Postprocessing Error

With the general trends laid out in Section F5.4.1, this section explores the error associated with the postprocessing assumptions inherent to 2D modeling approaches. Analysis is performed for noncomposite and composite systems to better understand how a composite deck affects the distribution of forces in cross-frame systems. Recall that NCHRP Report 725 investigated these simplified 2D analysis methods in the context of noncomposite systems. Thus, the study presented herein examines the validity of these widely accepted 2D approaches for composite systems. Namely, the RT sought answers to the following questions: *are the assumptions inherent with noncomposite systems (e.g., equal shear distribution to top and bottom nodes) valid for composite systems; and, if not, how does an engineer make adjustments to correct these assumptions*?

Before examining more complex bridge systems, Figure F5-8 and Figure F5-9 first present the results of a single-span, straight bridge with normal supports (Bridge 253-3). The response of a midspan cross-frame panel is evaluated for two different static loading conditions: applying a 100-kip load just to the left of the cross-frame panel of interest and applying a 100-kip load just to the right. Figure F5-8 corresponds to "left" girder loading, and Figure F5-9 corresponds to "right" girder loading. By studying different loading conditions, the relative impact of load position can also be assessed.

By starting with a simple bridge geometry, the postprocessing procedures can be isolated from any complexities introduced with support skews and horizontal curvature. For reference, Table F4-10 presents the pertinent parameters that describe the geometry of the bridge in the figures (e.g., deck thickness and girder spacing). In both figures, four different analysis methods are compared:

- 3D Software A model of a composite system (top right quadrant of Figure F5-8 and Figure F5-9),
- 3D Software A model of a noncomposite system (bottom right quadrant),
- 2D PEB model of a composite system utilizing the Timoshenko beam approach for equivalent cross-frame beam properties and the equivalent torsion constant (J_{eq}) for girder beam properties (top left quadrant),
- 2D PEB model of a noncomposite system utilizing the Timoshenko beam approach for equivalent cross-frame beam properties and the equivalent torsion constant (J_{eq}) for girder beam properties (bottom left quadrant).

Given that the preliminary results presented in Figure F5-5, Figure F5-6, and Figure F5-7 demonstrated the benefits of PEB models over grillage models, the results in this section are focused on PEB methods. For the 3D analyses (right side of figures), the axial force output from the cross-frame members is presented, followed by the nodal forces required to equilibrate the panel. For the 2D PEB analyses (left side of figures), the shear and moments produced from the equivalent beam analysis are presented, followed by the cross-frame force effects computed based the common postprocessing assumptions previously outlined (i.e., moment resolved by a force couple to the top and bottom nodes; shear force equally distributed top and bottom).

For each figure, there are three metrics by which the results can be compared, as itemized below:

1. *The total shear force acting on the cross-frame panel relative to the shear force in the concrete deck*. This value provides an indication of how accurate the equivalent beam properties in the 2D model are compared to the corresponding 3D model. For instance, if the total shear force determined from the 3D model exceeds that of the 2D PEB model, then the stiffness of the equivalent cross-frame is potentially underestimated. The opposite would be true if the total shear force of the 2D PEB model exceeds the 3D model.

2. *The distribution of that total shear force to the top and bottom nodes*. Recall from the discussions in Chapter F4 that load-induced cross-frame forces are a result of differential displacements of

longitudinal girders, both vertical and rotational in nature. Thus, the axial force induced in any cross-frame member is a product of its deformation pattern, or the relative movement of its connections to the girders. Girder displacements in noncomposite systems, particularly rotations, are different than girder displacements in composite systems. To demonstrate this behavior in simple terms, an idealized deformation pattern is provided in Figure F5-10. Figure F5-10 schematically depicts a common displaced shape of a X-type cross-frame panel under applied vertical loads; a noncomposite system is compared to a composite system (which is similar to Figure F3-34). Note that the displacements are greatly exaggerated and that rigid-body motion has been removed for clarity.

In comparing the noncomposite and composite systems, it is evident that noncomposite girders generally rotate about their centroid under applied vertical loads. Consequently, the top and bottom struts tend to deform equal magnitudes but in opposite directions, which results in equal-and-opposite axial force effects in those members. This type of girder displacement does not induce significant force effects in diagonal members. Hence, any load-induced forces in cross-frame diagonals due to differential vertical girder displacement (which is not presented in Figure F5-10) are expected to be nearly equal in magnitude and opposite in sign, similar to the struts.

In contrast, composite girders tend to rotate out-of-plane about a point higher on the cross-section due to composite action with the concrete deck. The deformation demand on the top strut, as a result, is marginal as it is located near the point of girder rotation. In relative terms, the bottom strut deforms significantly more, which is illustrated in Figure F5-10. Under this idealized displaced shape, the top strut sees little to no force effects whereas the bottom strut sees substantial axial tension. To maintain compatibility with the girder displacements, both diagonal members in the X-frame must also deform under axial tension.

Thus, when this idealized deformation pattern is paired with differential vertical displacement (which often results in equal-and-opposite diagonal forces itself), the net effect is unbalanced diagonal forces. Cases in which the diagonals are both in tension or both in compression are not uncommon. This generally explains why the equal-and-opposite force distribution in X-type cross-frames is observed in noncomposite systems but not in composite systems, where realistic deformation patterns are highly complex. For K-type cross-frames, this discussion is less influential as the diagonal members share the same node along the bottom strut; in these cases, the equal-and-opposite force distribution in diagonal members is anticipated.

Based on the simplistic, idealized demonstration in Figure F5-10, it is apparent that equal-and-opposite force magnitudes in the diagonal members of X-frames is not common in composite bridges. Consequently, assuming equal shear force distribution in the postprocessing phase of 2D PEB models will generally lead to poor results of cross-frame diagonals. With that in mind, evaluating the "true" shear force distribution from the 3D models provides an indication of how significant the effects illustrated in Figure F5-10 are.

3. *The relative difference between top strut forces and bottom strut forces*. Similar to the discussion in item #2 above, it is anticipated that bottom strut force effects will greatly exceed top strut force effects in composite systems. By evaluating the relative difference between these two magnitudes, the effects of composite action can be quantified. The sign of the top strut force can also provide an indication as to where the point of girder rotation exists along the depth of the cross-section (e.g., if the top and bottom struts are both in tension, then the point of rotation is likely above the top strut).

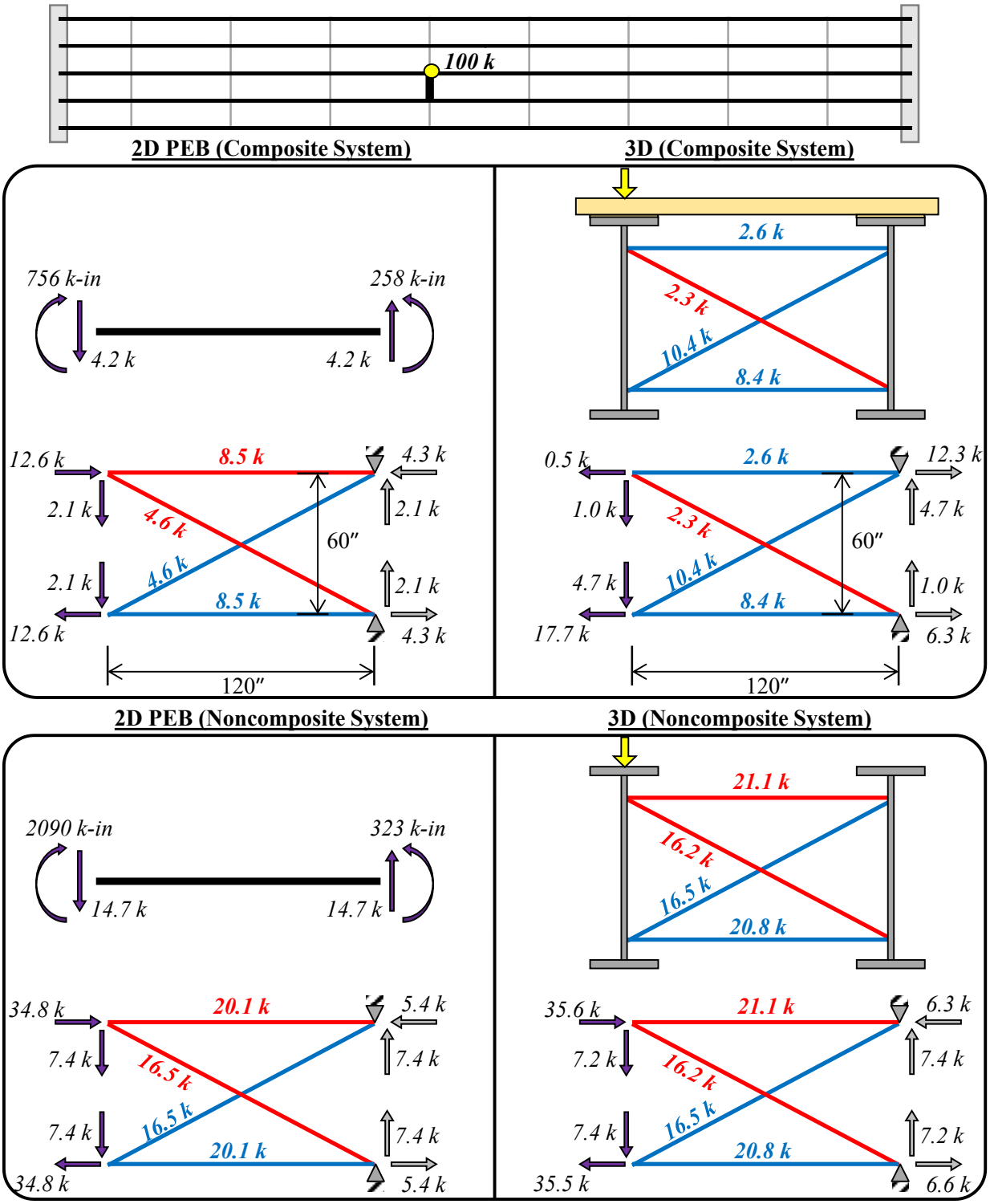

Figure F5-8: Sample 2D PEB and 3D cross-frame results for straight bridge with normal supports (noncomposite and composite) under static load

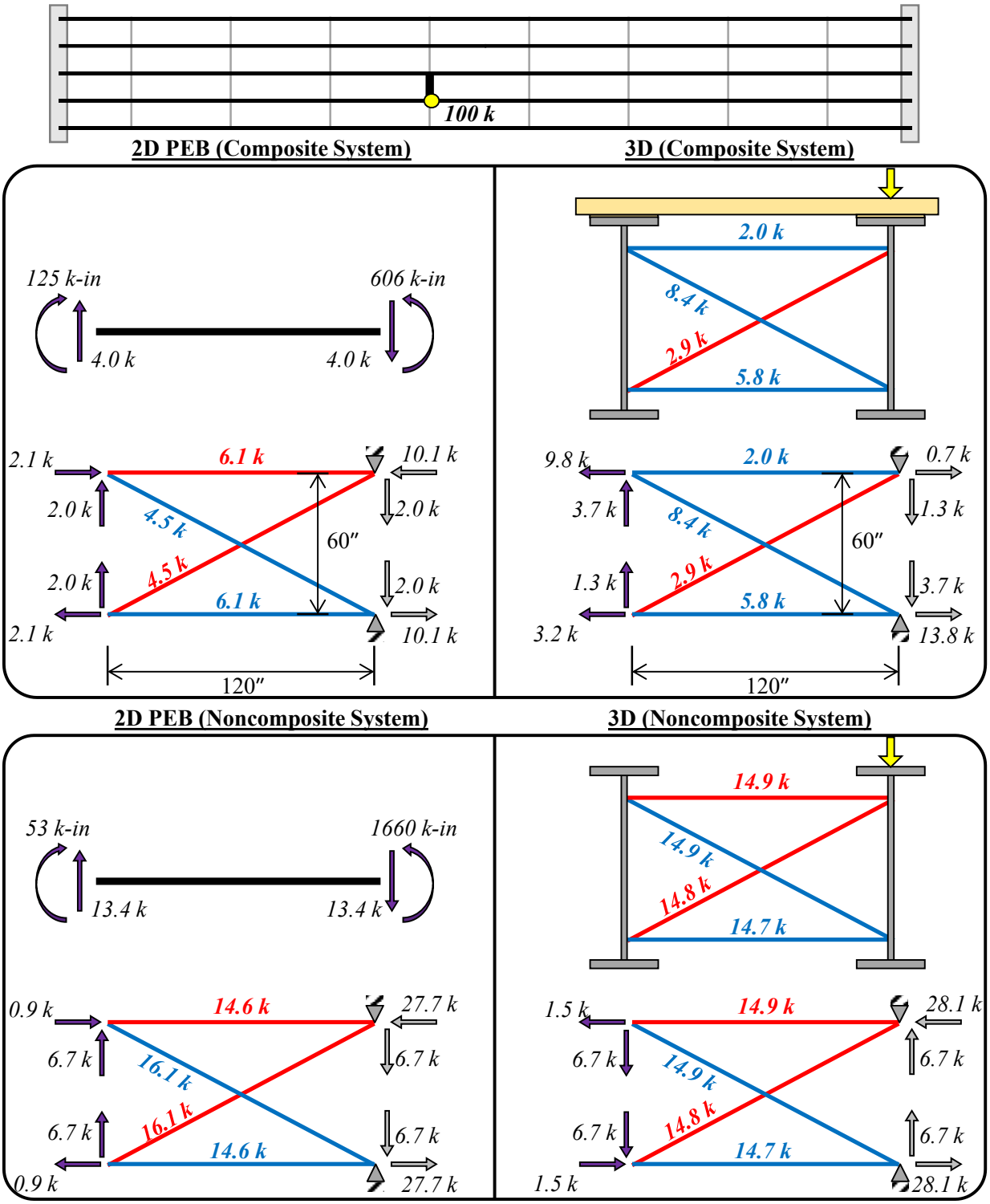

Figure F5-9: Sample 2D PEB and 3D cross-frame results for straight bridge with normal supports (noncomposite and composite) under static load

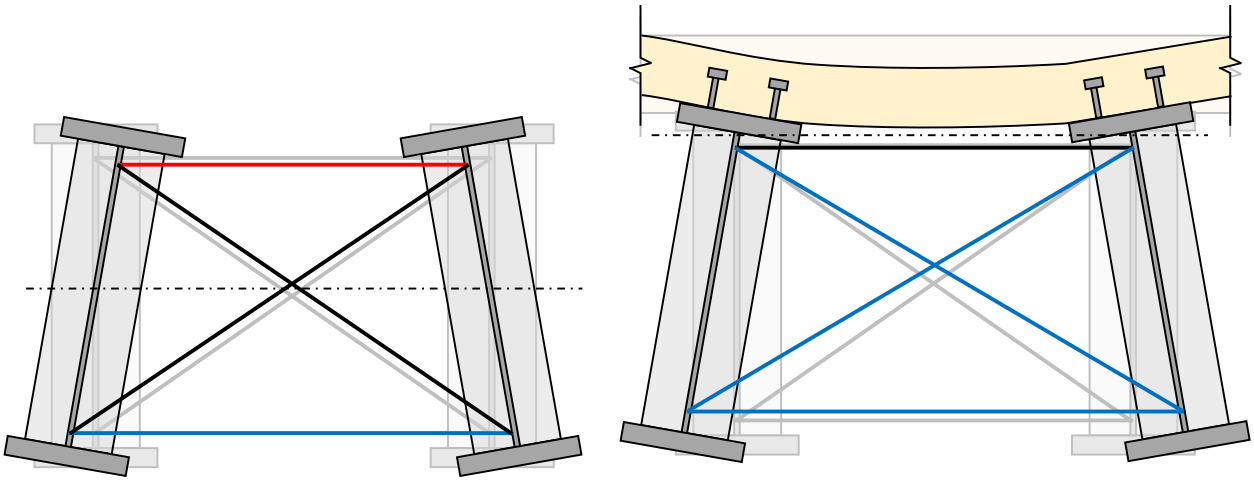

Figure F5-10: Idealized deformation pattern of noncomposite (left) and composite (right) systems

In the context of the three comparative metrics established above, the following observations can be made about Figure F5-8 and Figure F5-9:

- *Total shear force*: For both load conditions on the noncomposite system, the total cross-frame shear force estimated from the 2D PEB model is nearly identical to that of the 3D model. For instance, the 2D model estimated the total shear force from the first loading scenario (Figure F5-8) as 14.8 kips, whereas the 3D model estimated it as 14.6 kips. This indicates that the Timoshenko beam analogy is accurate for the noncomposite system. For reference, the shear-analogy approach produced a total cross-frame shear of 10.6 kips for this same example, despite not being shown in the figure. This indicates that the shear-analogy underestimates the cross-frame stiffness, which in turn underpredicts the force effects (similar to the results illustrated in Section F5.4.1).

  For the composite system, the total cross-frame shear force is underestimated in the 2D PEB models (e.g. 4.2 kips versus 5.7 kips in Figure F5-8). This relationship is explored further in this section.

- *Shear force distribution*: For the noncomposite system, the 3D models demonstrate that shear force is equally distributed top and bottom (and subsequently equal-and-opposite diagonal force effects). As a result, the "50-50" distribution assumption commonly utilized in 2D postprocessing is valid for noncomposite conditions. Thus, the 2D models accurately predict the force effects in the diagonal members for both loading conditions.

  For the composite system, the 3D analysis model demonstrates that load-induced forces in diagonal members are not equal-and-opposite. For example, Figure F5-8 shows 2.3 kips of compression in one diagonal and 10.4 kips of tension in the other, resulting in an "80-20" distribution of the total shear force. Thus, when comparing cross-frame forces results, it is evident that the 2D PEB postprocessing procedure produces inaccurate results (e.g. 4.6 kips of compression and 4.6 kips of tension, compared to 2.3 kips of compression and 10.4 kips of tension).

- *Moment force couple distribution*: As introduced above, the current postprocessing approach is to resolve the equivalent beam moment into a force couple about the top and bottom cross-frame nodes, disregarding the effects of composite action. For the noncomposite system, the 3D analysis results indicate that top and bottom struts are nearly equal-and-opposite, as expected (e.g. 21.1 kips of compression in the top strut and 20.8 kips of tension in the bottom strut of Figure F5-8).

Therefore, the 2D PEB model accurately predicts top and bottom strut forces when compared to the 3D counterpart model (e.g. 20.1 kips of compression in the top strut and 20.1 kips of tension in the bottom strut for the same load case).

For the composite system, this equal-and-opposite relationship does not hold true. The 3D model indicates that, for both loading scenarios, the top strut force effects share the same sign as the bottom strut, but the magnitude is significantly less. For example, the results in Figure F5-8 show 2.6 kips of tension in the top strut and 8.4 kips of tension in the bottom strut of Figure F5-8. In contrast, the 2D PEB model produces 8.5 kips of compression in the same top strut and 8.5 kips of tension in the bottom strut.

There is substantial error associated with the top strut member in the composite system. However, for both loading scenarios, the error in the bottom strut member is minimal (i.e., within 5% conservative in both cases). Despite the inconsistencies and oversimplifications in the 2D analysis and postprocessing, this same general trend related to bottom strut members is typically observed assuming the equivalent beam properties are accurate (i.e., the Timoshenko beam approach is utilized). The bottom strut results in Figure F5-5 through Figure F5-7 are additional examples of this trend.

Given that 2D PEB models generally produce reasonably accurate estimates for bottom strut force effects, especially for simple bridge geometries, it is important to note when these limitations and shortcomings become critical. If a bottom strut cross-frame member maximizes load-induced force effects and governs fatigue design, then this simplified analysis and postprocessing procedure likely produces reasonable estimates of the governing design forces. If diagonal members, however, govern the fatigue design (or much less likely top struts), then 2D PEB models under the commonly accepted approach may be grossly underestimating force effects. To expand on the findings from Figure F5-8 and Figure F5-9, which focus on a simple straight bridge with normal supports, the RT repeated these same studies for more complex bridge geometries and loading scenarios.

Three bridges were examined in addition to Bridge 253-3 presented above: Bridge 1181-2 (straight bridge with skewed supports and X-type cross-frames), Bridge 1181-4 (straight bridge with skewed supports and K-type cross-frames), and Bridge 909-2 (curved bridge with normal supports and X-type cross-frames). The parameters describing the overall bridge geometry and cross-frame layout were previously summarized in Table F4-10 and Table F4-11. For Bridges 1181-2 and 1181-4, an interior-bay cross-frame panel near the intermediate skewed support is examined, much like the midspan panel in Figure F5-8 and Figure F5-9. For Bridge 909-2, an interior-bay cross-frame panel near the maximum positive dead load moment region is examined. By studying different bridge geometries and cross-frame types (X or K), the RT can begin to formulate conclusions on the accuracy of 2D modeling approaches for a variety of common conditions.

Bridge 253-3 results above investigated two different extreme conditions: noncomposite and full in-service composite (concrete modulus, E_c, taken as 5,000 ksi). Rather than evaluate just the two extremes, the RT expanded its study by investigating different variations of E_c to better quantify how composite action affects cross-frame behavior. The RT elected to vary E_c as opposed to the deck thickness as to maintain a consistent centroid location for the concrete deck and to simplify discussions. The Software A analysis procedures previously described in this subsection are otherwise unchanged. As such, a total of 272 unique models were developed as part of this study as is shown with the following:

- 4 bridges {253-3, 1181-2, 1181-4, and 909-2}
- 4 model types {3D, 2D PEB using Timoshenko beam properties, 2D PEB using flexural-analogy properties, and 2D PEB using shear-analogy properties}

- 17 iterations of concrete modulus {0, 1, 5, 10, 50, 100, 250, 500, 1000, 1500, 2000, 2500, 3000, 3500, 4000, 4500, 5000 ksi}
- Total models: 4 × 4 × 17 = 272 models

Note that the E_c = 0 ksi case represents noncomposite conditions. Instead of completely removing the deck from the model, the deck was simulated with virtually no stiffness to expedite the repetitive calculations. Similar to the Bridge 253-3 results, the response of the specified cross-frame members in each bridge listed above is evaluated for two different static loading cases (100 kips in magnitude). The results corresponding to both load cases are presented below; they are arbitrarily indicated as Load Case 1 and 2. For reference, the location of load application relative to the framing plan is sketched in Figure F5-11 through Figure F5-14. The results presented herein follow the same organization as the three comparative metrics outlined above: total cross-frame shear, shear force distribution, and moment force couple distribution.

Figure F5-11 through Figure F5-14 show how the total shear force developed in the cross-frame panel of interest varies as a function of the concrete deck modulus (or the degree of composite action, in more general terms). Figure F5-11 specifically focuses on the straight bridge with normal supports (253-3). Figure F5-12 focuses on the straight bridge with skewed supports and X-type cross-frames (1181-2). Figure F5-13 focuses on the straight bridge with skewed supports and K-type cross-frames (1181-4), and Figure F5-14 focuses on the curved bridge (909-2). Figure F5-11 comprehensively compares 3D analysis results with all three equivalent beam iterations of 2D PEB models (Timoshenko, flexural-analogy, and shear-analogy). Figure F5-12 through Figure F5-14 focus just on the Timoshenko beam and flexural-analogy approaches, given the inherent inaccuracies with the shear-analogy approach.

Figure F5-15 demonstrates how the total shear force is distributed to the top and bottom nodes per the 3D analysis model. The results of the three bridges with X-type cross-frames are compiled. Recall that the discussion of shear force distribution is trivial for K-type cross-frames as the vertical force component is resisted entirely by the single diagonal on the respective side of the cross-frame; hence, results for Bridge 1181-4 are not included. Also note that, since the 2D models assume a "50-50" distribution, those results are also excluded as they do not add value to the graph.

In Figure F5-16, the ratio between the top strut force and the bottom strut force is plotted as a function of the assumed concrete deck modulus. The results of all four sample bridges are compiled and provided. Note that these results correspond to the 3D models only, as the 2D models assume an equal-and-opposite force couple in the postprocessing phase. Thus, the 2D analysis results do not add significant value to the graph.

The following additional notes provide important insight to the development and construction of Figure F5-11 through Figure F5-16:

- As previously mentioned, a framing plan sketch showing the location of the applied static load (i.e., Case 1 and Case 2) is provided in Figure F5-11 through Figure F5-14 for reference.
- A cross-frame diagram is provided in each plot to illustrate the nodal force or internal axial force that graph is specifically examining. For instance, Figure F5-11 through Figure F5-14 present the definition of total cross-frame shear force, V_{CF}.
- For all figures, the various results are evaluated for different concrete modulus values as indicated by the horizontal axis. As stated above, a modulus value of 0 ksi represents a noncomposite system, whereas values between 3,000 and 5,000 ksi are representative of most in-service, composite bridges in the US. The horizontal axis is presented on a log scale to clarify the noticeable change in behavior between 100 ksi and 1,000 ksi.
- In Figure F5-15, the shear force acting on the top node (V_{top}) and the bottom node (V_{bot}) are compared independently with the total cross-frame shear (V_{CF}). Thus, the sum of all V_{top} / V_{CF} and V_{top} / V_{CF} ratios equal one. Note that V_{top} and V_{bot} are arbitrarily taken relative to the left side of the cross-frame panel, as shown in the sketch. Had the shear forces been taken from the opposite side,

the values between V_{top} and V_{bot} would be flipped. However, the general behavior would remain the same given that the shear force is constant across the length of the cross-frame panel.

- In Figure F5-16, the ratio of the top strut force (P_{TS}) and the bottom strut force (P_{BS}) is compared to a similar ratio determined by elastic beam theory. In other words, the concrete deck, top strut, and bottom strut are treated as three force couples that develop the moment strength of a pseudo-composite transverse beam, similar to a reinforced concrete beam. The elastic neutral axis of this pseudo-composite beam is derived after transforming the effective concrete area with the corresponding modular ratio. Assuming an elastic stress distribution, the P_{TS} / P_{BS} ratio is related to beam curvature and is simplified as y_{TS} / y_{BS}, where y_{TS} *and* y_{BS} are the distances measured from the centroid of the respective strut to the computed neutral axis. Therefore, by comparing the analysis results to this idealized beam theory approach, the RT can evaluate the impact that composite action has on the distribution of bending moments through the deck and cross-frame panel.

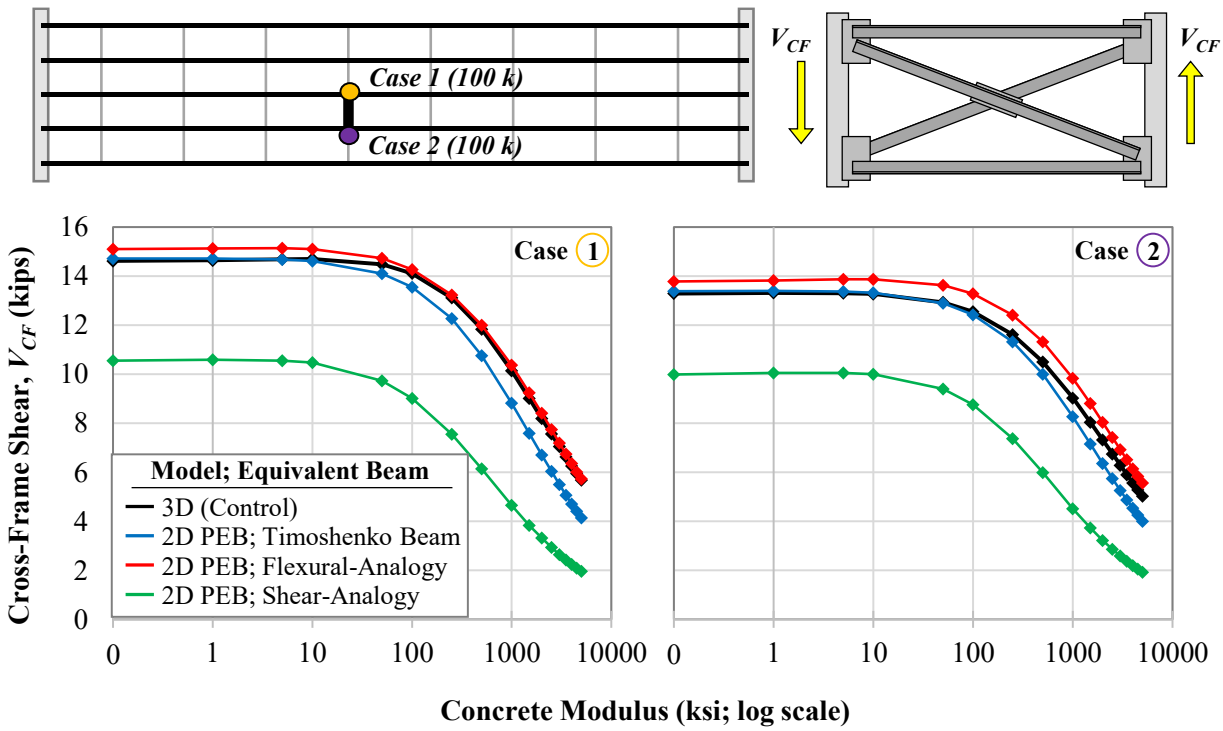

Figure F5-11: Total cross-frame shear force as a function of concrete deck modulus (Bridge 253-3)

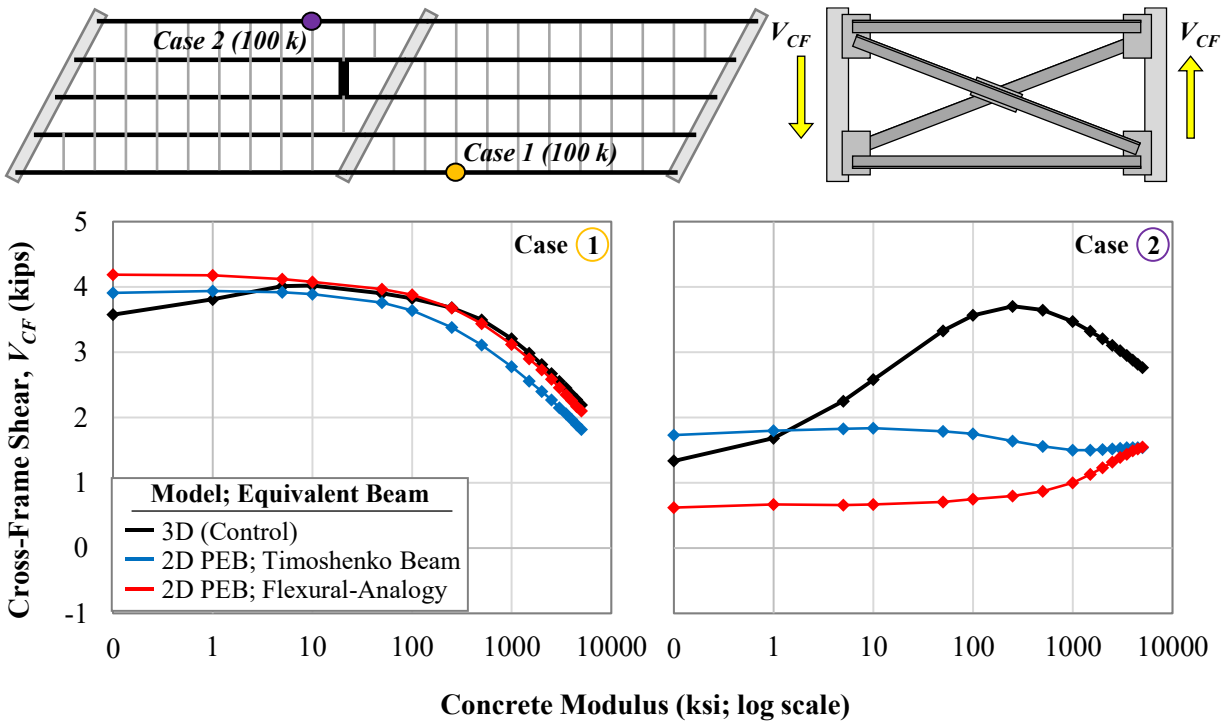

Figure F5-12: Total cross-frame shear force as a function of concrete deck modulus (Bridge 1181-2)

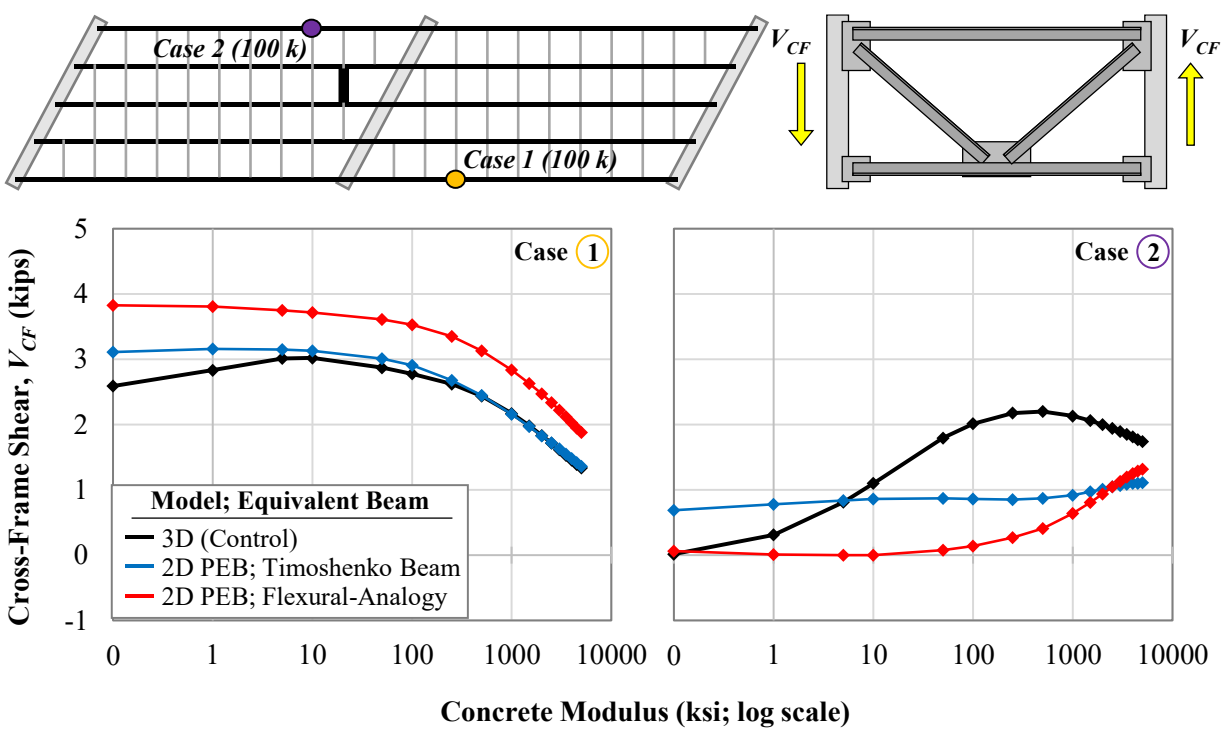

Figure F5-13: Total cross-frame shear force as a function of concrete deck modulus (Bridge 1181-4)

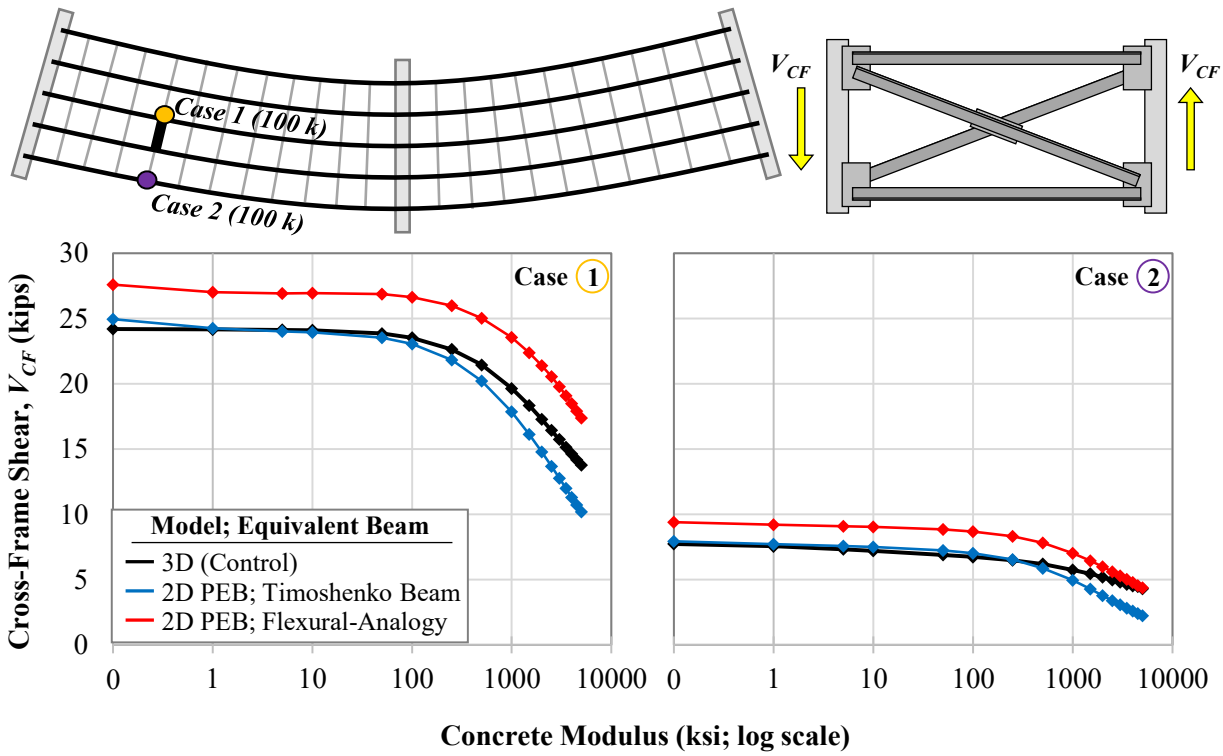

Figure F5-14: Total cross-frame shear force as a function of concrete deck modulus (Bridge 909-2)

The following observations can be made with regard to the total shear force estimated by the various analysis methods (Figure F5-11 through Figure F5-14):

- As the concrete modulus increases beyond zero (noncomposite), it intuitive that the cross-frame forces generally decrease. Not only does the relative stiffness of the concrete deck increase and thus attracts more force in the highly indeterminate system, but the girder displacements diminish as the global stiffness increases. However, as the concrete modulus approaches values exceeding 3,000 ksi or more, the relative change is less significant, which is consistent with the Fatigue Loading Study results presented in Figure F3-45.
- As demonstrated in Figure F5-11, the shear-analogy approach for equivalent beams produces significant underestimations of the cross-frame force demands for all variations of E_c.
- In general, the Timoshenko beam approach is accurate for noncomposite systems when compared to the 3D analysis, but the variability increases slightly for composite systems. Still, it is consistently the most accurate 2D equivalent-beam method in terms of cross-frame force predictions, as will be presented later in this subsection.
- The observed behavior for Load Case 2 in Figure F5-12 and Figure F5-13 is less predictable. Note that the vertical axis scale is much smaller than the other two figures due to the nature of the loading. In the other two cases, the applied load is in close proximity to the cross-frame panel of interest, such that the shear demands are more significant. In Figure F5-12 and Figure F5-13, though, the applied loads induce a torsional response to the superstructure, such that the net shear on the cross-frame of interest is generally small. Consequently, the discrepancy in the total cross-frame shear is less influential in terms of predicted cross-frame force effects, as is presented later.

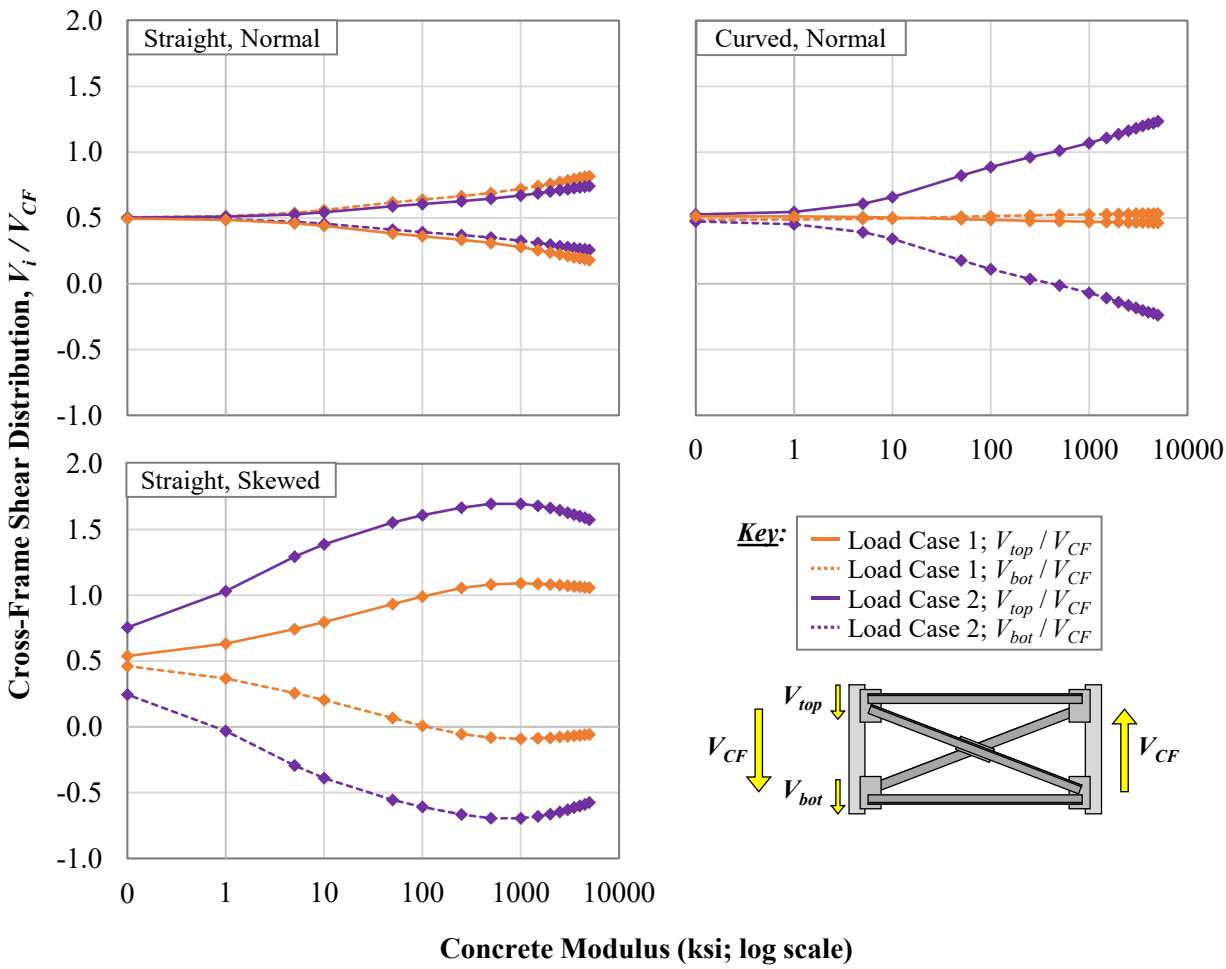

Figure F5-15: Shear force distribution as a function of concrete deck modulus for the three sample bridges with X-type cross-frames

The following observations can be made regarding the shear force distribution determined by 3D analyses (Figure F5-15):

- For noncomposite systems, especially the bridges with normal supports, the shear force is equally distributed top and bottom (same result as Figure F5-8 and Figure F5-9 before). The distribution for the straight bridge with skewed supports is slightly less balanced given the nature of the cross-frame deformation pattern.
- As the concrete deck becomes stiffer and composite action becomes more substantial, it is evident that the shear force distribution gradually diverges from the "50-50" assumption. For instance, the top shear reaction in the straight, skewed bridge for Load Case 2 is approximately 1.6 V_{CF} whereas the bottom shear reaction is over 0.6 V_{CF} in the opposite direction. In this particular instance, the observed behavior indicates that both diagonals were in significant compression.

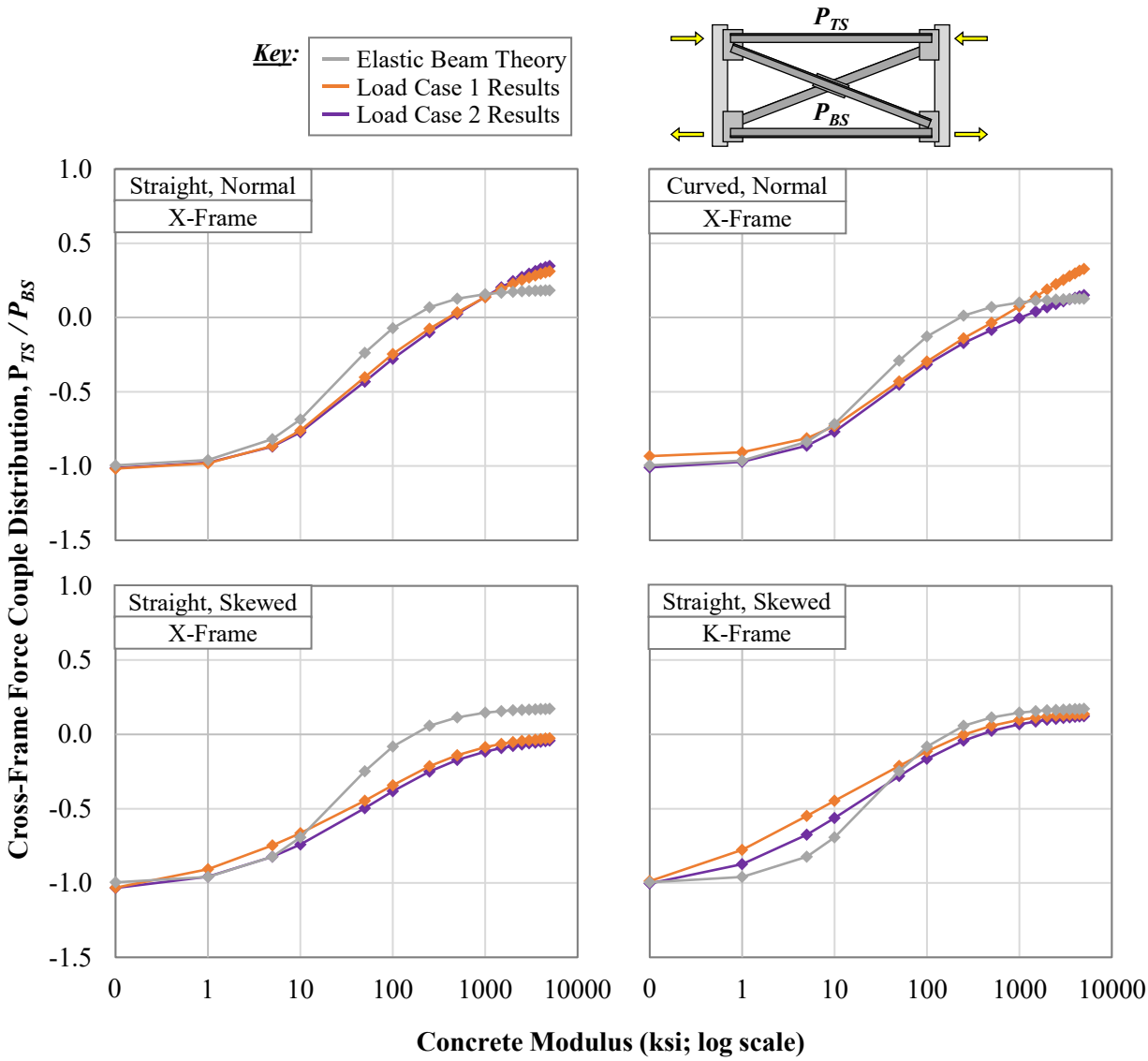

Figure F5-16: Force couple distribution as a function of concrete deck modulus for the four sample bridges

The following observations can be made regarding the force couple distribution determined by 3D analyses (Figure F5-16):

- For the noncomposite systems, the P_{TS} / P_{BS} ratio consistently converges to -1, which represents an equal-and-opposite force distribution in the struts. As the deck stiffens and composite action becomes more significant, the ratio tends to a small positive value. This indicates that the top strut shares the same sign as the bottom strut, but the magnitude is substantially smaller (i.e., a clear indication of composite behavior). In fact, the transition between a negative ratio and a positive ratio as E_c increases represents the condition in which the center of out-of-plane girder rotation moves above the top strut. At that point, the top and bottom strut forces would have the same sign.
- In general, the analysis results follow the same trends as the "elastic beam theory" benchmark solution, but not exactly. Thus, the flexural action assumed in the development of this idealized

curve is apparent in the realistic data, but the deviation from that curve is due to the fact that the "true" deformation patterns are not identical to the idealized one.

With general observations established about the validity of common analysis and postprocessing procedures, the next step is to compare the predicted force effects between 3D and 2D models. Utilizing those common assumptions (i.e., equivalent beam moment resolved as a force couple and equivalent beam shear equally distributed to top and bottom nodes of X-frames), 2D PEB results are compared to the 3D solutions. The results for each of the four sample bridges are compiled and presented in Figure F5-17. In total, eight different graphs are presented. The two "columns" represent the two distinct load cases examined for each bridge. The four "rows" represent the different bridges evaluated as part of this study.

The horizontal axis represents the elastic modulus of the concrete deck and is presented on log scale. The vertical axis represents the relative error of the 2D PEB model relative to the corresponding 3D model. Note that only the results using the Timoshenko beam analogy are shown. Relative error values of zero indicate perfect agreement between the 3D model and the simplified 2D model. Relative error values exceeding 1.0 indicate the 2D models overestimate the force effects in excess of 100%; the opposite is true for relative errors below -1.0. For clarity, data points beyond -1.0 and 1.0 are eliminated from view.

The relative error associated with the diagonal members and the bottom strut member(s) are graphed separately. The lines are color-coordinated based on the cross-frame sketch provided in the corners of each graph. The results for top struts are excluded given that they are generally lightly loaded members.

The following observations can be made regarding the relative error associated with the simplified 2D modeling procedures (Figure F5-17):

- For noncomposite bridges, relative error approaches zero for all member types and all bridge types. This is especially true for straight and normal bridges, as the 2D PEB methods produce very accurate results, which is consistent with the findings of NCHRP Report 725. This is largely attributed to two ideas: (i) the Timoshenko beam approach accurately represents the cross-frame stiffness in the analysis and (ii) the common postprocessing procedures are valid for noncomposite systems. Note that the error increases slightly with more complex bridge systems (i.e., skewed or curved bridges). For example, the relative error associated with the "red" X-frame diagonal in the skewed bridge for E_c = 0 ksi is approximately 20% conservative under Load Case 1. Under Load Case 2, the relative error is not shown largely due to the fact the absolute magnitude of the force is small. In this case, any slight discrepancies typically result in large error values.
- For all typical composite systems evaluated (i.e., E_c exceeding 3,000 ksi), the error associated with bottom strut members is typically small (within 5-10%). Despite its limitations and oversimplifications, 2D methods produce accurate force estimates of bottoms strut members. This is consistent with the results presented previously in Chapter F5.
- For diagonal members in X-type cross-frames, the errors generally become excessive as E_c increases. One diagonal tends to a large positive value, and the other tends to a large negative value. For example, the relative error associated with the diagonal members of the curved bridge under Load Case 2 approach +100% and -100% error, respectively for E_c = 5,000 ksi. This is attributed mainly to the equal shear force distribution assumed with the postprocessing methods.
- For diagonals in K-type cross-frames, the errors are much more manageable than those with X-type cross-frames. For these cross-frame types, recall that the distribution of shear force distribution is not meaningful.
- Although not explicitly shown, relative error magnitudes associated with 2D PEB models using the flexural-analogy approach for equivalent beams are more substantial than those shown in Figure F5-17 for the Timoshenko beam approach. Thus, it can be concluded that the Timoshenko beam approach is more appropriate for noncomposite and composite systems.

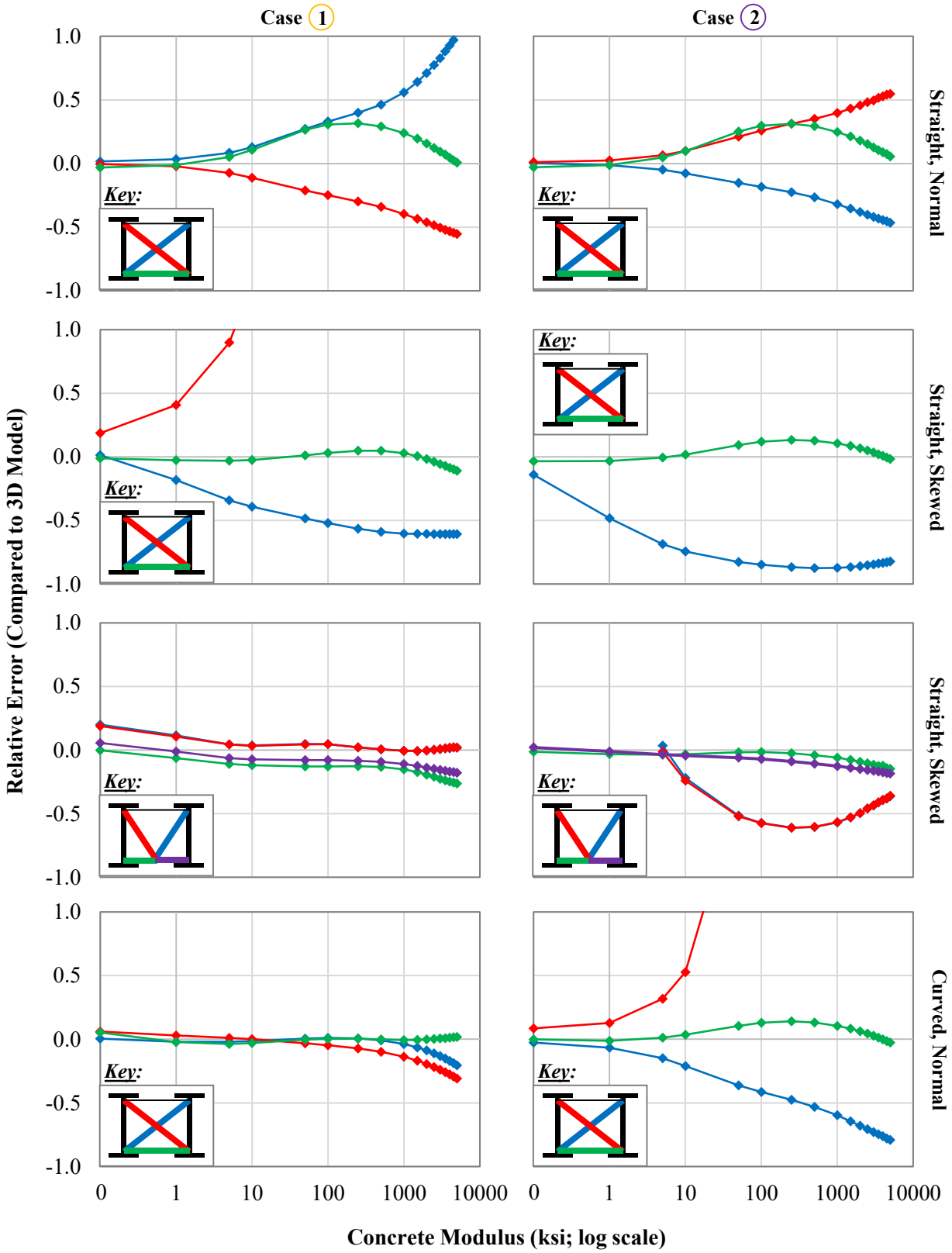

Figure F5-17: Analysis error as a function of concrete deck modulus for the four sample bridges

From Figure F5-16, it is apparent that 2D analysis methods produce poor cross-frame force estimates in two areas: (i) in top strut members and (ii) in X-frame diagonal members regardless of bridge type. Erroneous, overly conservative results in top struts are not generally impactful in terms of cross-frame fatigue design. These members typically do not govern fatigue design such that those results, accurate or not, can be disregarded. Erroneous diagonal member forces, on the other hand, can have significant impact on the cross-frame fatigue design of a bridge. As such, it is prudent to reevaluate how designers typically handle the postprocessing of 2D analysis models to ensure more reliable results (or avoid overly unconservative force estimates).

The major challenge in developing a simple postprocessing modification is that the degree in which the shear force distribution varies. In noncomposite systems, diagonal forces typically see nearly equal-and-opposite forces. In the composite systems evaluated as part of Figure F5-15, shear force distribution was shown to vary from nearly equal to 150% V_{CF} at one node and -50% at the other. The distribution is a function of bridge type, loading, and subsequently the induced deformation pattern, which is difficult to quantify without developing a 3D model. An alternative method is explored in Section F5.4.4.

F5.4.3 Parametric Study

To further assess the performance of 2D analysis methods, the remaining 16 bridges in the 20-bridge parametric study (detailed in Section F5.1) were analyzed. For each of the preselected cross-frame members, the maximum force range was computed based on the critical lane passage of the AASHTO fatigue truck. Thus, the results in this section differ slightly than the previous results in Section F5.4.2, which were based on static loads. This procedure was performed a variety of analysis methods, as documented in Section F5.1.

It should be noted that, in some cases, the governing lane conditions between the 3D and simplified 2D models differed. For example, a 3D model indicated that a specific cross-frame member under a specific transverse lane passage maximized force effects, whereas the corresponding 2D model indicated force in the same member was maximized by a different lane passage. To maintain consistency, the governing lane position was established based on the control model (i.e., the 3D validated model in Abaqus); the results of the simplified analysis models were then obtained from those established parameters.

Figure F5-18 and Figure F5-19 present this data in the form of a box-and-whiskers graph, similar to those previously shown in the appendix. Each box-and-whiskers plot represents a set of unfactored design force effects obtained from the various analysis models. Along the y-axis, the governing force effects derived for each iteration of the 20 representative bridges (Table F4-10 and Table F4-11) are compared to the control model. The percent error with respect to the results of the control model is reported. Zero percent error indicates perfect agreement between the simplified commercial software models and the control. Positive error indicates that the simplified analysis conservatively overestimates the predicted force effects, and negative error indicates the opposite.

In terms of accuracy, it is desirable that the simplified methods provide solutions within about 10% of the validated solution within marginal deviation in the box-and-whisker (i.e., vertical distance between whisker tails). In terms of a conservative design approach, it is preferred to positive error over negative error.

In Figure F5-18, the analysis error (2D versus 3D control results) associated with every preselected cross-frame member is plotted. In Figure F5-19, the results corresponding to bottom strut members are differentiate from diagonal members based on the lengthy discussion in Section F5.4.2. In both figures, the results are categorized by the modeling technique along the horizontal x-axis (3D, 2D grillage with flexural-analogy equivalent beams, and 2D PEB with shear-analogy, flexural-analogy and Timoshenko equivalent beams). Note that the equivalent cross-frame beam improvement technique is not included in this figure for clarity.

Figure F5-20 expands on Figure F5-18 and Figure F5-19 by breaking up the bottom strut results based on bridge geometry. For the 2D PEB results, only models utilizing the Timoshenko beam approach are included for clarity. Note that the skew index and connectivity index established in NCHRP Report 725 and defined in Eqs. F3.6 and F3.7 are used to differentiate straight and curved bridges with or without support skews.

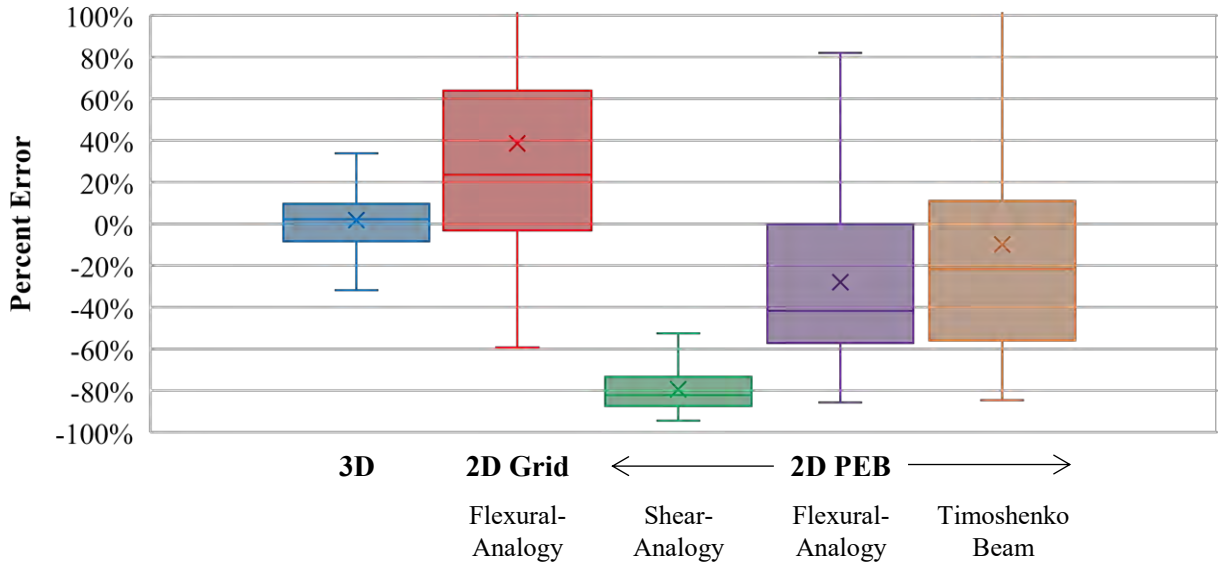

Figure F5-18: Box-and-whiskers plot demonstrating the range of analysis error obtained from the Commercial Design Software Study (all cross-frame member types)

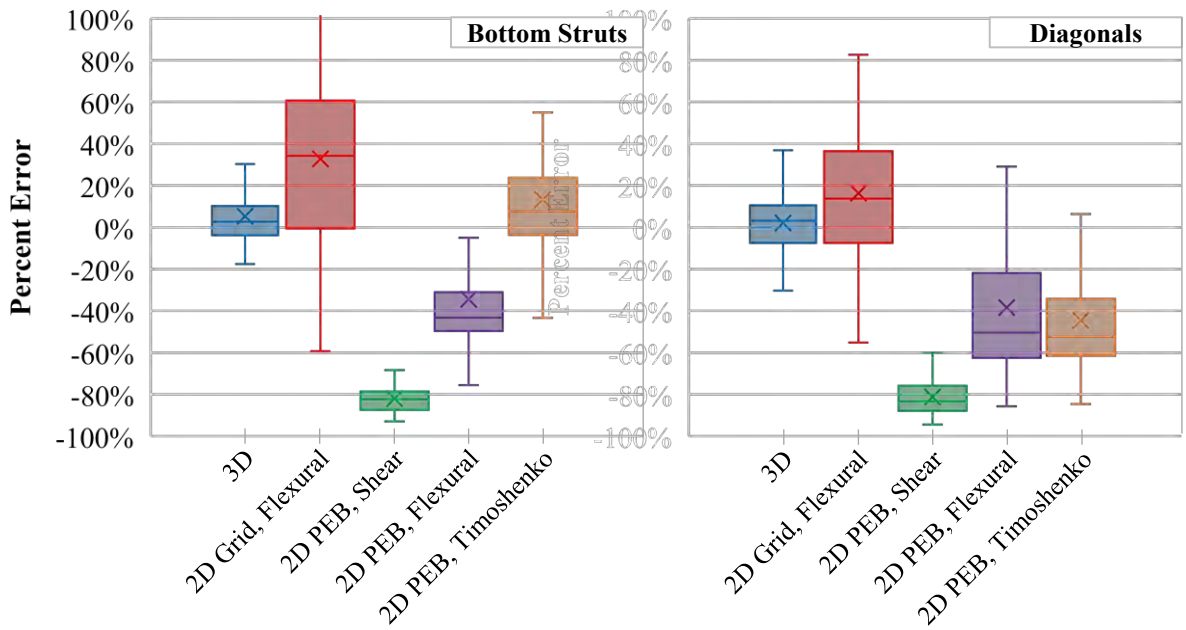

Figure F5-19: Box-and-whiskers plot demonstrating the range of analysis error obtained from the Commercial Design Software Study (bottom struts versus diagonals)

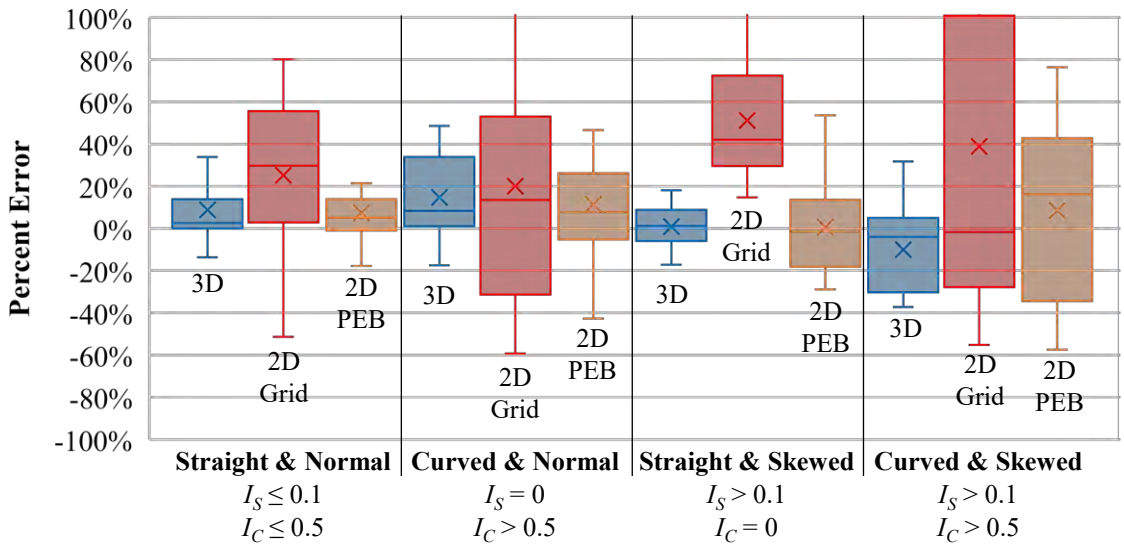

Figure F5-20: Box-and-whiskers plot demonstrating the range of analysis error obtained for different bridge geometries (bottom struts only)

From Figure F5-18, the following generalized observations can be made when comparing the analysis error reported across the full data set:

- The 3D commercial software analysis generally provides cross-frame results that agree well with the control model. On average, the predicted design force range was 2% conservative. The observed scatter in the results was also small.
- For the 2D analysis methods, significantly variability is observed. This behavior is attributed to: (i) the full data set including skewed and/or curved bridges and (ii) the postprocessing errors inherent with the 2D analysis methods outlined in Section F5.4.2.
- More specifically, the 2D grillage/grid model using the flexural-analogy for the development of equivalent cross-frame beams shows considerable scatter in the predicted cross-frame response. In some cases, the model predicted design forces above 100% conservative and below 60% unconservative. The upper tails of several box-and-whiskers are beyond the scale of the vertical axis, given the large discrepancies observed.
- The 2D PEB models (shear-analogy) consistently underpredict the governing design force range (-80% error on average). As discussed above, the stiffness of the cross-frame is severely underestimated with this approach, which in turn severely underestimates the load-induced force effects.
- The 2D PEB models (flexural-analogy) improve upon the shear-analogy approach but still underpredict the design force ranges. For straight and normal bridges, the average reported error was -25% (with more scatter).
- The 2D PEB (Timoshenko beams) provide the most accurate solutions with respect to 2D models but still result in significant errors. The average error was -10%, but with considerable scatter.

To explore the effects of cross-frame member type, Figure F5-19 compares the results from bottom struts versus diagonals (top struts are neglected). The following generalized observations can be made from that figure with a particular emphasis on PEB methods:

- Again, 3D commercial software models are generally within 10% regardless of member type.

- 2D PEB models are generally conservative (between 0% and 20% conservative) for bottom struts but are unconservative for diagonals (between 40 and 60%). This is attributed to the equal shear assumption used in the postprocessing procedure outlined above.

To explore the effects of bridge geometry, Figure F5-20 compares the results in terms of skew and connectivity indices. Recall that only bottom strut results are presented in this figure for clarity. The following generalized observations can be made from that figure with a particular emphasis on PEB methods:

- 3D models generally perform well for all cases. Thus, 3D models offer consistently reliable results in terms of cross-frame forces primarily because girder and cross-frame depth are accurately represented.
- There is more variability observed with grillage models than PEB models (Timoshenko beam) for all bridge types.
- In general, 2D PEB models are consistently conservative in terms of their bottom strut force estimates. However, scatter in the results is more evident as the bridges becomes more skewed and/or more curved. For instance, the percent errors range from 0 to 15% conservative for straight and normal bridges, whereas the percent error ranges from 70% conservative to -20% unconservative for curved and skewed bridges.
- Although not presented, the results for diagonal members are more variable than what is shown in Figure F5-20 for bottom struts.

It is evident from the results that 3D models offer increased repeatability and reliability in terms of cross-frame force effects. However, the biggest setback to simplified 2D analyses (particularly PEB models) is related to diagonal members and the postprocessing assumptions. This statement is independent of bridge type, although analysis error becomes more apparent for complex systems. Consequently, Section F5.4.4 explores a simplified method to enhance the postprocessing procedures for 2D analysis methods.

F5.4.4 Alternative 2D Postprocessing Procedure

There are potentially many ways to manipulate 2D grillage and PEB analysis results to produce more reasonable estimates of cross-frame design forces. As discussed previously, equivalent beam moments from grillage models (excluding those that use notional beams to represent the transverse stiffness of the deck) can be resolved based on the equivalent truss/deck model illustrated in Figure F5-3. Equivalent beam models from PEB models, despite providing equal-and-opposite strut force effects, have been shown to produce reasonable estimates of the more critical bottom strut members. In both grillage and PEB models, though, the distribution of shear force, which directly impacts diagonal member force effects, is highly variable.

The RT explored a simple procedure to resolve this issue. A simple alternative to the “50-50” distribution is to conservatively design each diagonal member for 100% of the total cross-frame shear. That is to say, the top and bottom struts are handled in the same manner as presented above (i.e., equal-and-opposite force distribution, but neglect the top struts in design), but the diagonals are handled differently. This procedure is schematically shown in Figure F5-21, which is a modified adaptation of Figure F5-8.

First, note that the 2D analysis output (i.e., end shear and moments on the equivalent cross-frame beam) is identical to that of Figure F5-8. Second, the top and bottom strut forces are computed (i) assuming the end moment of 756 kip-in is applied as a force couple to the top and bottom nodes and (ii) assuming the end shear of 4.2 kips is equally distributed top and bottom. This produces a top strut design force equal to 8.5 kips of compression and a bottom strut design force equal to 8.5 kips in tension, which is the same as Figure F5-8. In this instance, the top strut force can be disregarded, and the bottom strut force from the 2D analysis (8.5 kips) is in good agreement with the 3D analysis (8.4 kips).

Lastly, the diagonal forces are calculated independently assuming 100% of V_{CF} is applied to the node of interest. In Figure F5-21, the full 4.2 kips of shear is applied to the bottom node to maximize force in the tension diagonal (9.4 kips), which shows much better agreement to the 3D analysis (10.4 kips) than Figure F5-8 (4.6 kips) did. A similar procedure for the top node was performed, although not explicitly shown in the figure, which results in 9.4 kips of compression in the opposite diagonal. This simple method, despite producing equal-and-opposite diagonal forces, produces design magnitudes generally closer to the 3D analysis (at least for the critical diagonal member).

The RT acknowledges that there are obvious limitations to this simplified method. Given that the true governing member of this cross-frame panel would be the tension diagonal, designing for 9.4 kips of compression is overly conservative. It must also be recognized that this procedure could potentially be overly conservative in some cases, where the true shear distribution is closer to "50-50" (e.g. Load Case 1 of curved bridge or noncomposite systems in general). Similarly, this procedure could still be unconservative for cases in which the shear at one node exceeds 100% V_{CF} (e.g. Load Case 2 of straight, skewed bridge). As stated above, this simple procedure is one of many possible solutions to this problem. Yet, the only way to ensure reliably accurate results, regardless of bridge type, is to develop a 3D model.

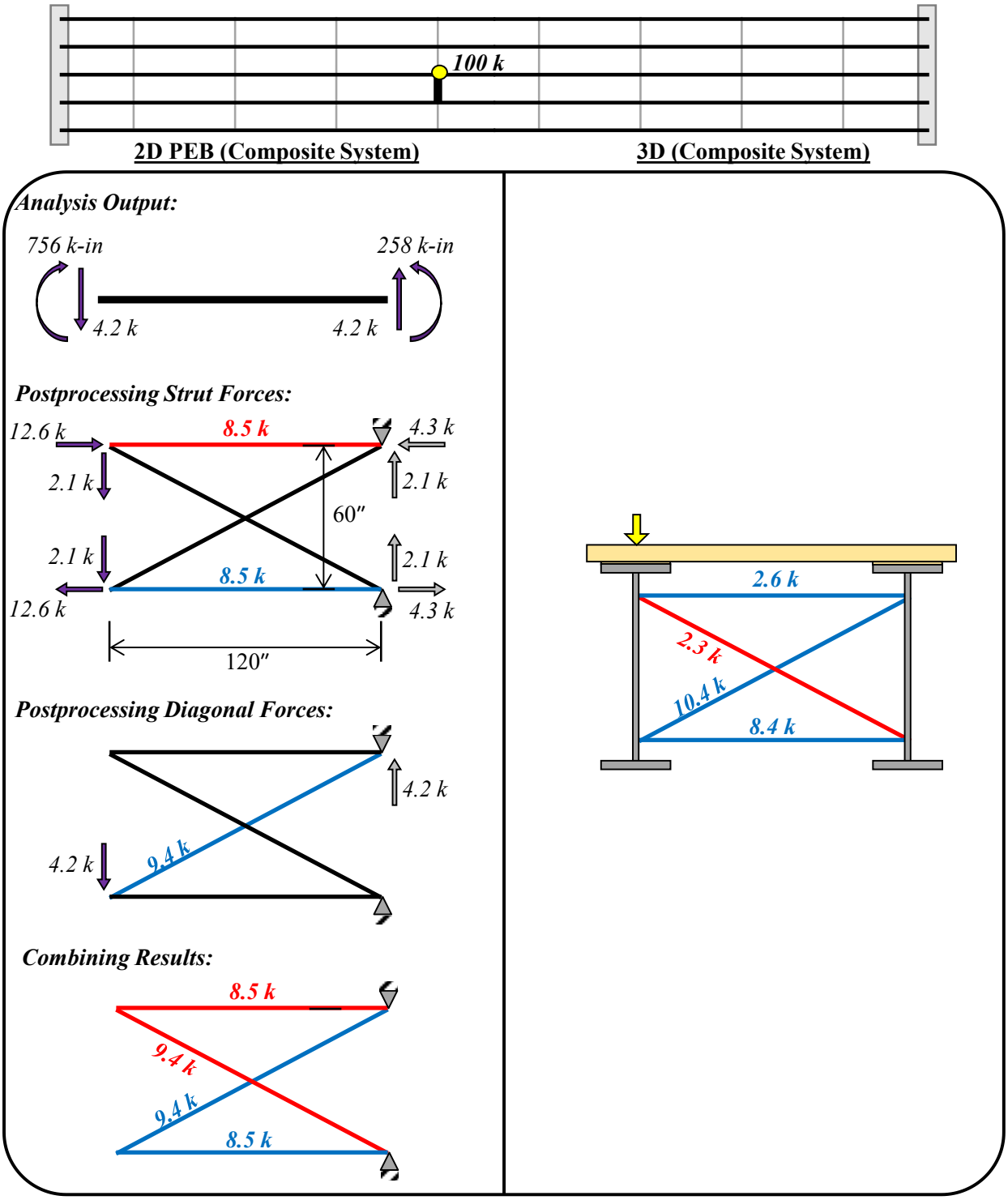

Figure F5-21: Alternative postprocessing procedure demonstrated through Load Case 1 on Bridge 253-3

F5.5 Major Outcomes

Based on the results of the Commercial Design Software Study presented in the preceding subsections, there are several conclusions that can be drawn with respect to simplified analysis methods for cross-frame design:

- In general terms, designers must be cognizant of the potential trade-offs between sophisticated and simplified analysis (in terms of accuracy and ease of use). A central theme explored throughout the appendix was related to the balance between increased computational complexity and improved reliability versus simplified modeling and improved ease-of-use. The results presented in this chapter clearly highlight this trade-off. The designer must make informed decisions in terms of the analysis performed. The conclusions below are intended to provide practicing engineers the technical and quantitative background to help inform those decisions, while not necessarily advocating one or the other for a specific project need.
- In all cases, 3D refined analysis produces improved accuracy for predicting cross-frame forces compared to 2D analytical approaches. Although 3D models are more time-consuming to develop than the 2D counterparts, these models offer solutions with improved accuracy, reliability, and repeatability. The traditional approach of connecting cross-frame members into a shared node along the web-to-flange juncture is also acceptable.
- 2D PEB models will generally produce more accurate results than 2D grillage models because the concrete deck is explicitly considered. Although there are methods to consider the effective transverse stiffness of the deck, it is more accurate to represent the deck as a thin shell element that is rigidly connected to the girder to simulate composite action.
- Common postprocessing practices for 2D methods tend to produce erroneous results for top strut members and inaccurate results for diagonal members in X-frames, regardless of bridge type. A simple, conservative approach has been presented, but alternative methods can be explored by the designer or programmers.
- The commonly used improvement methods for 2D analyses generally improve the predicted response of the cross-frames. Assuming the postprocessing procedures are accurate, these same approaches have been shown to provide more variable results for curved and/or skewed bridges, especially for bridges where the critical cross-frames are in close proximity to the skewed supports.
- If a designer elects to use a 2D modeling approach for these complex cases, the RT strongly recommends incorporating simple modifications to the model (e.g. Timoshenko approach for equivalent cross-frame beams and considering the transverse stiffness of concrete for grillage-type models) and postprocessing (e.g. conservatively applying full cross-frame shear force in the design of X-frame diagonals). Still, even after implementing these improvements to 2D analyses, substantial error is likely in cross-frame force predictions, especially in bridges with significant horizontal curvature and/or support skews.

The RT drafted proposed modifications to AASHTO LRFD with regards to 2D and 3D modeling techniques based on the findings listed above. Refer to the main body of the report and Appendix A for the proposed language and commentary.

CHAPTER F6

Stability Study

As introduced in Chapters F1 and F2, the Stability Study is focused on investigating two major design issues for cross-frame systems with regards to structural stability: (i) development of stability bracing requirements for steel I-girders during construction and in-service extending available solutions to include regions with bottom flanges in compression in multi-span continuous bridges with nonprismatic girders and (ii) combination of stability bracing strength requirements with consideration of force effects generated during construction and throughout the service life of the bridge. Although the major stability force effects likely come from gravity loading during deck casting, the impact of forces induced from other sources such as wind, overhang construction loads, etc. need to be considered. This chapter addresses item (i), whereas item (ii) is largely addressed in the design examples (Appendix B and C).

As outlined previously, cross-frames have a number of functions in steel bridge systems. In addition to helping distribute gravity and lateral loads in the finished bridge, their primary function is to serve as stability braces during erection and improve the LTB resistance of the noncomposite steel I-girders. In multi-span, composite systems for which the top flange is continuously braced along the length, cross-frames can also provide additional stability in the negative moment regions where the bottom flange is in compression.

Effective beam bracing can be achieved by either preventing out-of-plane lateral displacement of the compression flange (lateral braces) or restraining twist of the cross-section (torsional braces), as demonstrated by Yura (2001). Bracing systems for column, beam, and frame applications generally fit into one of the four categories depicted in Figure F6-1. Relative bracing, as the name suggests, controls the relative movement of two adjacent points at different lengths along the main members (e.g. bottom flange lateral bracing). Relative bracing is also referred to a panel bracing. Point braces (also known as nodal or discrete braces) control the deformation of a single point along the length of the member (e.g. cross-frames). Continuous bracing controls deformations along the entire length of the member (e.g. composite deck through welded shear studs), and lean-on braces come in a variety of applications such as relying on lightly loaded members to brace heavily loaded members through simple struts (e.g. lean-on braces).

Cross-frames, which restrain twist of the cross-section at discrete locations along the length of a bridge girder, are aptly categorized as torsional point braces. Cross-frames, like any stability brace, must satisfy both stiffness and strength requirements to adequately brace a beam from LTB and to prevent excessive deformations at critical buckling loads. As documented extensively in the main body of the report and Appendix D, the AISC Specifications commonly used for building design is the first major specification in the world to include guidance for stability bracing design. In the current AISC Specifications (2016), the bracing provisions are located in Appendix 6, and Appendix 6.3.2a provides specific strength and stiffness guidance for torsional point braces such as cross-frames.

In contrast, AASHTO LRFD has no guidance for stability bracing requirements. As such, the primary goal of the Stability Study and Chapter F6 herein was to develop design guidance in the context of steel I-girder bridge systems. The current provisions in AISC provide a good foundation for the development of provisions to be implemented into AASHTO LRFD. Consequently, these provisions were reviewed and modified based on a series of finite-element studies.

Following this introduction, Section F6.1 focuses on the stability strength requirements of cross-frames in bridge applications; Section F6.2 addresses the stiffness requirements. Section F6.3 investigates the effects of nonprismatic sections and moment gradients on the buckling capacity of bridge girders, and Section F6.4 summarizes the major outcomes of the individual studies. The major outcomes serve as the basis for the proposed modifications discussed i in the main body of the report and Appendix A.

Note that the analysis and results reported in this chapter are largely based on independent studies that were spawned by AISC T3 (Analysis, Stability, and Loads) and of the AASHTO T-14 (Steel Bridge Committee) subcommittees. Members of the RT have documented the findings of these studies in recent archival publications. Section F6.1 is based on the work conducted by Liu and Helwig (2020). Similarly, Section F6.2 and F6.3 respectively follow Liu and Helwig (2020) and Reichenbach et al. (2020). Thus, the subsections herein summarize the results and findings that are directly related to the scope of NCHRP Project 12-113. For additional information on each topic, refer to the journal articles.

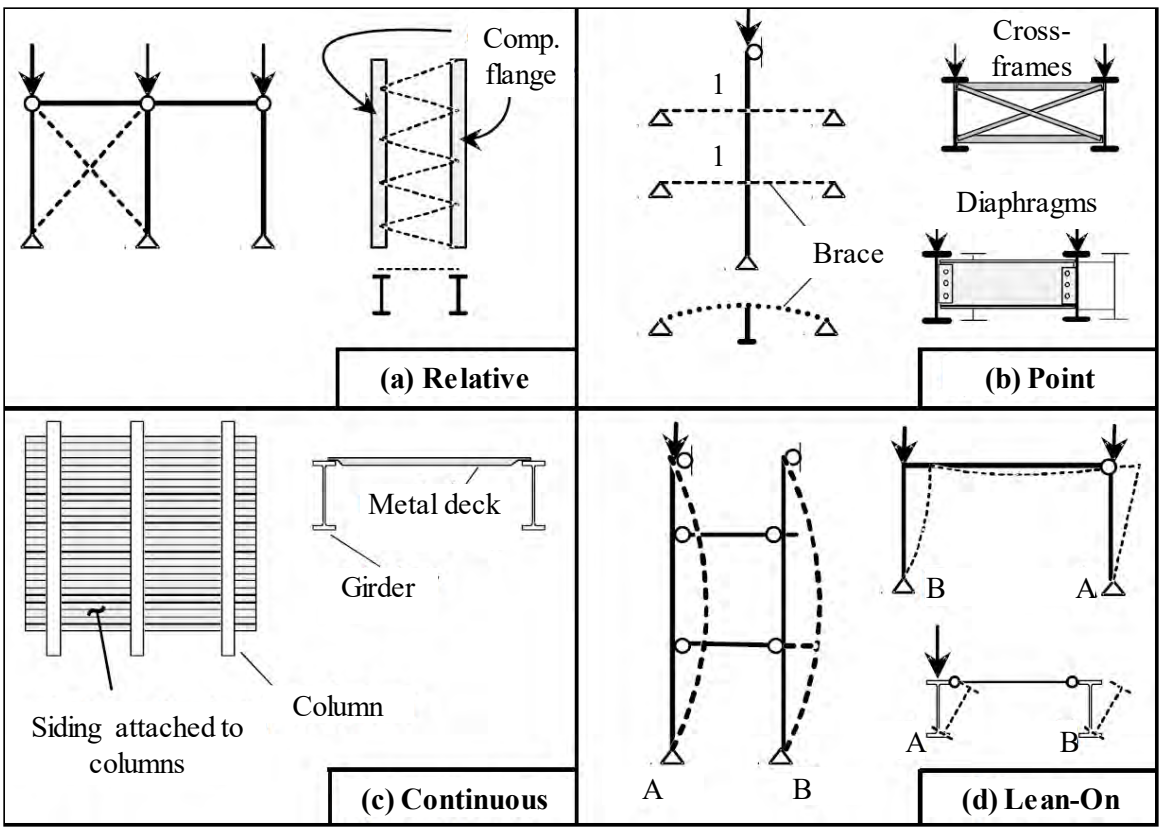

Figure F6-1: Types of stability bracing for columns, frames, and frames (Helwig and Yura 2015)

F6.1 Bracing Strength Requirements

As introduced above, cross-frames must possess adequate strength, among other characteristics, to limit the out-of-plane deformations at the corresponding design forces. The goal of the Stability Study is to assess applications of the established design provisions in AISC Specifications and archival literature for implementation into AASHTO LRFD. With that in mind, it is important to note that the torsional brace strength requirement in the latest edition of AISC (2016) was significantly changed from previous editions of the specification (2010). In general, Section F6.1 herein examines both versions of the AISC design

recommendations. The RT conducted a computational parametric study that evaluates the accuracy of each approach with respect to cross-frame design in steel I-girder bridges.

Following this introduction, Section F6.1.1 identifies the differences in the methodologies by providing relevant background information. Section F6.1.2 outlines the parametric study and FEA procedures used to evaluate these design provisions, and Section F6.1.3 presents the results with commentary.

F6.1.1 Background

Before outlining the bracing strength requirements established in AISC, it is important to define the concept of "ideal" brace stiffness. The ideal stiffness is the brace stiffness required for a perfectly straight member to reach a specified capacity or load level. The upper limit of that capacity is the bifurcation load corresponding to buckling between brace points. The concept of ideal stiffness was originally established by Winter (1960) for columns. Winter observed that, in the context of column buckling, providing the ideal stiffness at an intermediate brace allowed "real" imperfect columns to achieve enhanced buckling capacities (i.e., buckling between brace points); however, the out-of-plane deformations can become excessive at elevated loads. Instead, providing increments of the ideal stiffness limits those deformations.

Based upon previous research studies (Yura 2001), the provisions in AISC generally require designers to provide at least twice the ideal stiffness to control brace forces and deformations. Providing twice the ideal stiffness will generally limit the maximum deformation to a magnitude equal to the initial imperfection for columns. Twice the ideal stiffness is also typically applied to beam bracing problems; however, the deformation is often larger than the initial imperfection at the maximum load levels.

The brace force is often taken as the brace stiffness multiplied by the magnitude of the initial imperfection. For torsional bracing systems, simplifications covered in the commentary of AISC (2016) were applied to the stiffness formation outlined in Yura (2001) to produce the following required stiffness, which is given as Eq. A-6-11a in the current AISC Specifications (2016):

$$\beta_{T,req} = \frac{2.4LM_r{}^2}{\phi nEI_{yeff}C_b{}^2} \qquad F6.1$$

where: β_{Tbr} = required system torsional brace stiffness; L = span length; M_r = maximum factored moment within the critical unbraced segment; n = number of intermediate braces within the span; I_{yeff} = effective moment of inertia; ϕ is the resistance factor (taken as 0.75); and C_b = moment gradient factor assuming the beam buckles between the brace points. The total stiffness of the torsional bracing system must exceed the required stiffness in Eq. F6.1. The stiffness requirements are examined further in Section F6.2.

In addition to stiffness requirements, stability bracing must also satisfy strength requirements. As discussed in the introductory section of this chapter, a distinct change in bracing strength requirements occurred between the 14th Edition AISC Specifications (2010) and the current 15th Edition (2016). Applying some simplifications which are documented in the commentary, the original 2010 version of the torsional brace strength requirement, given as Eq. A-6-9 in the specifications, was as follows:

$$M_{br} = \beta_T\theta_o = \frac{0.024M_rL}{nC_bL_b} \qquad F6.2$$

where: β_T = required system torsional brace stiffness (based on twice the ideal stiffness); θ_o = initial imperfection in terms of a twist angle; and L_b = unbraced length of the critical segment.

Again, the equation is based upon the assumption that twice the ideal stiffness is provided and that the resulting deformation at the intermediate brace point is equal to the initial imperfection. The initial

imperfection is based on the critical imperfection shape, as defined by Wang and Helwig (2005). Wang and Helwig demonstrated that the critical shape imperfection for torsional bracing consists of a lateral sweep of the compression flange equal to $L_b/500$ (sweep tolerance) and the tension flange is straight, producing an initial twist equal to $L_b/500h_o$, where L_b and h_o are the respective unbraced length and distance between flange centroids. In addition, the expression in Eq. F6.2 was based primarily on the assumption of elastic buckling behavior.

In contrast, the latest AISC Specification (2016) introduced a change in the torsional brace moment equation based upon a study conducted by Prado and White (2015). The researchers carried out a detailed investigation on the stability bracing requirements with an emphasis on inelastic buckling of relatively short unbraced lengths. This research prompted the revision in the torsional brace moment equation, which is also given as Eq. A-6-9 in the current specifications:

$$M_{br} = 0.02M_r \qquad \textit{F6.3}$$

This expression is simply a function of the internal moment in the critical unbraced segment. Although the simplicity of Eq. F6.3 is attractive, the applicability of the expression for general design situations is questionable when compared to the longstanding strength equations predicted by Eq. F6.2.

To compare the two expressions directly, Eq. F6.2 can be reduced to provide a strength requirement that is a function of the beam design moment, M_r. Assuming a moment gradient factor C_b of 1.0 (which is reasonable considering moment gradient factors of the critical regions usually approach unity as more intermediate braces are introduced) and taking the unbraced length as a function of the number of intermediate (i.e., $L_b = L / (n + 1)$), Eq. F6.2 reduces to the following:

$$M_{br} = \frac{0.024M_r(n+1)}{n} \qquad \textit{F6.4}$$

To demonstrate the range of values of Eq. F6.4 in comparison to Eq. F6.3, Table F6-1 presents the required brace strength for varying number of intermediate brace points. From the table, it is apparent that the 14th Edition AISC (2010) strength requirements produce torsional brace forces that are considerably larger than the 15th Edition (2016) requirements. As the number of intermediate braces increase, the 2010 provisions tend towards a minimum value of 2.6% of M_r compared to a constant value of 2% of M_r as predicted by the 2016 provisions. The noticeable difference clearly warranted additional studies, which are presented in the subsequent section.

Table F6-1: Variation of Eq. F6.2 as a function of the number of braces

	Number of braces						
	1	**2**	**3**	**4**	**5**	**…**	**10**
M_{br} / M_r	0.048	0.036	0.032	0.030	0.029	…	0.026

F6.1.2 Parametric Finite-Element Study

To investigate the torsional brace strength behavior, parametric finite element analyses were carried out on twin I-girder systems using Abaqus. The following subsections outline different components of the parametric study, ranging from the FEA assumptions to the loading conditions. The results from the full study are documented in Liu and Helwig (2020). As mentioned earlier, although members of the RT worked on this study, the effort was actually undertaken based upon inconsistencies in the AISC bracing provisions

and not specifically for this NCHRP study. However, the results are directly applicable for the NCHRP study and therefore warrant discussion.

F6.1.2.1 Finite-Element Approach

Girder cross-sections (web and flanges) were modeled using shell elements. Torsional braces (cross-frames), which were modeled as truss elements, framed into shared nodes on the web-flange junction in between adjacent girders (Figure F6-2). Because the braces were "full-depth," cross-sectional distortion was precluded, and web stiffeners were unnecessary. Cross-frames were taken as Z-type frames, for which only one diagonal exists in the panel. It is important to note that the specific type of cross-frame or torsional brace is not important with respect to the torsional strength requirements; consequently, a simple Z-type was selected.

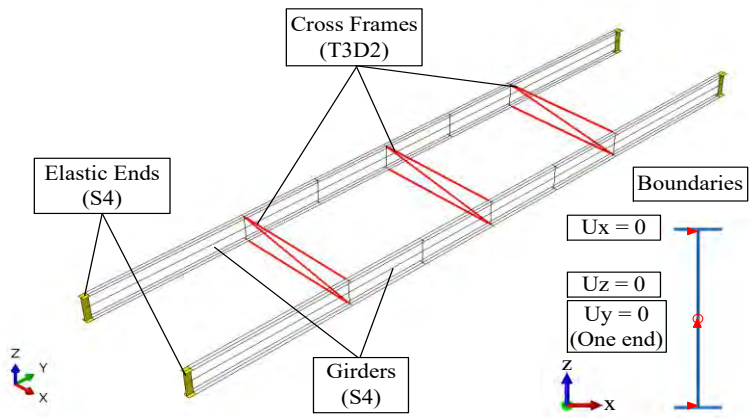

Figure F6-2: Geometry and boundary conditions of twin-girder systems

Both elastic and inelastic material analyses were carried out in the investigation. A square mesh of 2 inches was assigned to all shell elements to adequately capture inelastic effects. In terms of material inelasticity, a bilinear material model was assumed as depicted in Figure F6-3. The elastic slope of the stress-strain curve was taken as 29,000 ksi; in the inelastic region, the material was treated as elastic-perfectly plastic. The effects of strain hardening were not considered since the deformations associated with the buckling analysis were not significant enough to reach strain hardening levels. The effects of residual stresses were also not considered since preliminary results demonstrated that elastic materials produced more critical results.

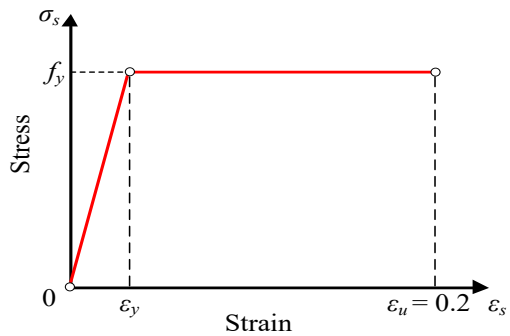

Figure F6-3: Elastic, perfectly plastic stress-strain relationship assumed in the FEA studies

F6.1.2.2 Range of Parameters and Loading Conditions

Three different cross sections were considered in the study, which primarily investigate different flange dimensions, as illustrated in Figure F6-4. These cross-sections are referred to as Cross-section 1, 2, and 3 herein. The span and web depth of the girders were held constant at 100 feet and 48 inches, respectively. Consequently, a constant span-to-depth ratio (L/d) of 25 was evaluated, which is representative of common bridge girders used in practice. To maintain a relatively stocky web and avoid web local buckling, the web thickness was maintained at 0.75 inches (i.e., web slenderness of 64). Similarly, for each different flange width, the flange thickness was selected to provide a slenderness ratio of 8, which is compact for grade 50 steel. Note that only prismatic girders were considered in this parametric study.

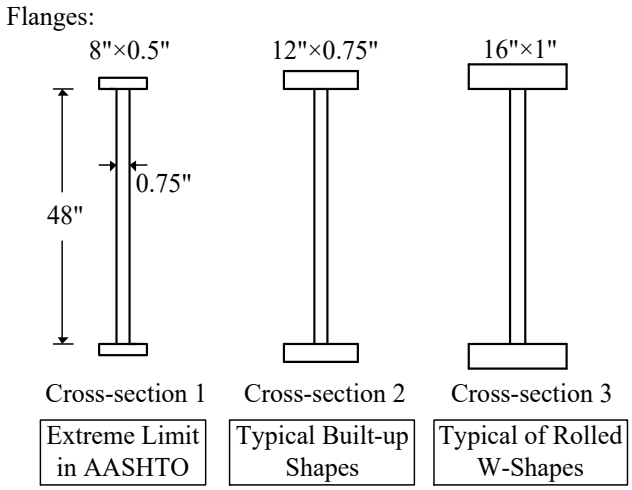

Figure F6-4: Cross-sections considered in the parametric study

The slenderness of the girders was reflected in the flange-width-to-web-depth ratio (b_f/d). Given the various flange widths considered, three different ratios were considered: 1/6, 1/4, and 1/3. The value of 1/6 is the extreme limit for built-up sections allowed in AASHTO LRFD (2020), while the value of 1/3 is more consistent with rolled sections.

The number of intermediate braces provided on the beams also varied from one to five, resulting in unbraced lengths ranging from 50 feet to 16.67 feet, which is consistent with bridge construction practices in the US.

To avoid issues with global system buckling (Yura, Helwig, et al. 2008), the girder spacing ranged from 20 feet to 30 feet. The spacing of 30 feet was required for cases with a larger number of intermediate braces. In those cases, a wider "base" was necessary to ensure LTB of the individual beams between brace points governed over a system buckling mode.

Note that the previous study by Prado and White (2015), which resulted in the revised brace strength requirements in AISC 15th Edition, made use of a single beam where torsional braces were represented as springs. In practice, torsional braces consist of flexural members or trusses (cross-frames) framing between adjacent girders.

As is discussed subsequently, the interaction between the adjacent girders and the intermediate braces is extremely important with regards to the distribution and magnitudes of the brace forces. As outlined previously, a twin-girder system was utilized as it is the minimum number of girders in a bridge superstructure. The results, however, are representative of systems with several girders. Figure F6-2 presents the general layout and boundary conditions of the twin-girder systems.

In some cases, the simulation for the inelastic cases did not converge largely in part due to the stress concentration at the end of girders. Therefore, a 12-inch long segment at the ends of the girders was modeled with elastic material to prevent localized yielding effects at point boundary supports. The in-plane boundary conditions of the twin-girders consisted of simple supports applied at the mid-height points of cross sections. Twist was restrained at the ends of the girders by restraining lateral movement at the top and bottom of the webs; however, the sections were free to warp at the supports.

In addition to various girder cross-sections, the RT also examined different loading conditions. Figure F6-5 shows the loading conditions considered in this study, including uniform moment and uniformly distributed loading. The distributed loads were either applied at the top flange or at mid-height of the sections to study the impacts of load height. Note that torsional braces are schematically shown as "X" symbols along the mid-height of the web; however, twist restraint was provided as noted above.

An additional spot check was performed to examine bracing demands in beams subjected to reverse-curvature bending, particularly in the negative moment region. That loading scenario is also demonstrated in Figure F6-5. The moment gradient shown is analogous to a fixed-fixed beam with uniformly distributed loads along the entire length (i.e., $wL^2/12$ at the ends and $wL^2/24$ at midspan), which is representative of an interior span of a continuous unit. Fixed supports, however, are not provided in the analysis model.

Note that the noncomposite condition is represented in this reverse-curvature spot check. Thus, additional lateral and torsional restraint provided by a composite concrete deck and shear studs are not considered. As noted in the introduction of this chapter and Section F6.3, LTB and cross-frame bracing requirements are typically not a concern in composite bridge systems. Hence, no additional bracing studies are conducted for the composite condition.

Only mid-height loads are examined for this spot check condition. Additionally, only a case with five intermediate braces are considered in an attempt to maximize the negative bending moment the first cross-frame would experience. For example, a three-brace scheme would result in the first cross-frame line near the inflection point; a five-brace scheme, on the other hand, places a brace in the negative moment region with significant moment gradient. As such, the five-brace scheme was deemed more critical and was therefore evaluated as a spot check.

Loading Type	Sketch
Uniform moment	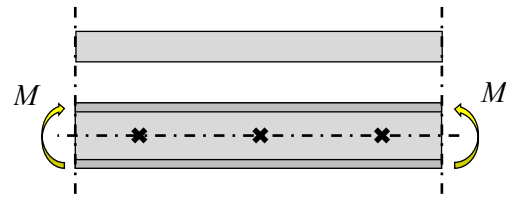
Distributed load at top flange	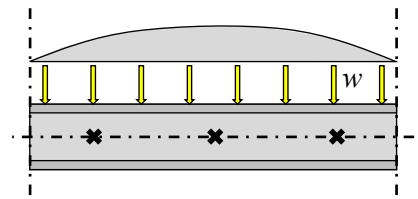
Distributed load at mid-height	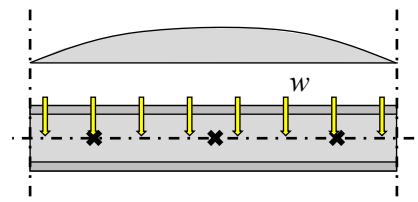
Reverse-curvature bending (mid-height loading)[a]	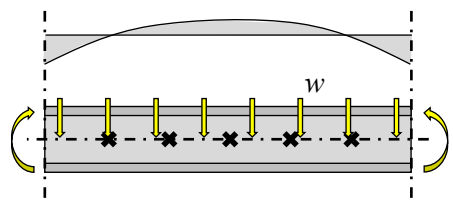
Note: [a]Represents a spot check model only; only n = 5 was evaluated	

Figure F6-5: Various loading conditions (n = 3 intermediate brace locations illustrated)

For the single-curvature bending cases, it was observed that the critical segment for buckling that resulted in the largest brace forces was always the section near midspan, where positive moment was maximized. As such, the critical imperfection was assumed in these critical areas, as outlined in the subsequent section. For reverse-curvature bending, it is not always as clear which segment is critical for buckling. Negative moment regions, although generally having larger moment magnitudes, are aided by steeper moment gradients (i.e., larger C_b factors). In contrast, positive moment regions have smaller moment magnitudes but typically have C_b values close to unity, especially as additional intermediate braces are added.

Thus, it was observed that the critical brace (i.e., maximum bracing forces) depended on the location of the critical imperfection. For instance, the midspan brace forces were maximized when the imperfection was assumed along the compression top flange at that same location. In contrast, the brace forces at the first intermediate brace line were maximized when the imperfection was assumed along the compression bottom flange at that location. This is explained further in Section F6.1.2.4.

F6.1.2.3 Critical Imperfection

Figure F6-6 presents the assumed initial imperfection shape of the girder, an asymmetric shape whereby the critical compression flange is displaced laterally. This assumed asymmetrical shape is consistent with the approach taken by Prado and White. To achieve this shape analytically, the compression flange was displaced at selected nodes prior to load application and buckling analysis; element birth-and-death was then utilized for the brace members such that bracing forces were not induced in the stage where the imperfections were specified.

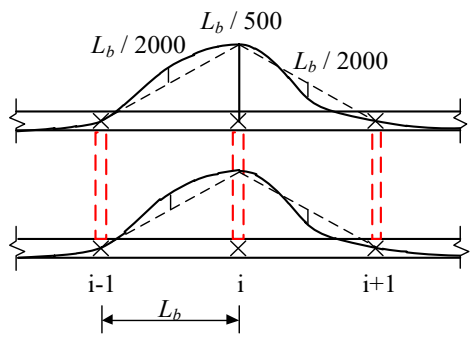

Figure F6-6: Assumed initial imperfection shape used in the brace strength study

For the single-curvature bending cases, the imperfection illustrated in Figure F6-6 was implemented along the top flange at midspan of the beams, where positive moment is maximized. For the reverse-curvature bending spot check, the imperfection was implemented at two distinct locations: along the top flange at midspan (where positive moment is maximized) and along the bottom flange near the first intermediate cross-frame line (where negative moment at a brace point is maximized). Note that the imperfection was not implemented at the support condition, where negative moment is actually largest. At these locations, lateral deformation at the support is often prevented by the bearings, which tends to benefit the torsional bracing requirements. Consequently, it is assumed that the first intermediate cross-frame is more critical than the support cross-frame despite the differences in girder moment magnitudes.

F6.1.2.4 Steps in Parametric Study

Once the RT settled on the modeling parameters outlined above, the next step was to develop an analytical testing procedure to determine cross-frame brace moments. The process involved three distinct analyses in Abaqus, which are summarized below. Note that these three steps were performed for every unique cross-section and bracing scheme considered in the parametric study.

1. **Conduct an eigenvalue buckling analysis on the twin-girder system**. In this analysis, the girders are assumed perfectly straight. The primary objectives of the eigenvalue study are twofold: (i) to obtain the ideal stiffness of the cross-frame required to force the girders to buckle between the braced points and (ii) establish the moment level corresponding to buckling between the braced points.

   The analytical solution for the critical buckling moment was then validated against theoretical solutions. In cases with more than one intermediate brace, however, the critical buckling segment often received warping restraint from the adjacent beam segments with lower moment levels. Since

warping restraints are not generally relied upon in design specifications, the Timoshenko (1961) buckling solution for a doubly-symmetric section and uniform-moment loading, which is readily adopted in design specifications, was used to identify the critical buckling moment between the brace points:

$$M_{cr} = \frac{C_b \pi}{L_b} \sqrt{EI_y GJ + I_y C_w \left(\frac{\pi E}{L_b}\right)^2} \qquad F6.5$$

where: L_b = spacing between cross-frames or the unbraced length; J = torsional constant; C_w = warping constant; G = elastic shear modulus; and C_b = moment gradient factor that accounts for the beneficial effects of variable moment along an unbraced length (based on AISC Specifications). The remainder of the variables have been previously defined.

2. **Obtain the initial imperfect shape of the twin-girder system by statically displacing the top flange in accordance with Figure F6-6**. As previously noted, the RT ensured that the cross-frame elements did not pick up any locked-in forces in this stage of the analysis.
3. **Run incremental analyses on the imperfect system for various loading conditions and material properties (elastic or inelastic)**. In this final stage, the cross-frames were assigned twice the ideal stiffness to match the current assumption in the AISC bracing provisions. Recall that this parameter was determined in the first step. As external loads were incrementally applied, the girder deformations and brace forces were recorded. These incremental analyses serve as the basis for the figures presented herein.

From this procedure, data was obtained to characterize the behavior of cross-frames as torsional braces. These results are presented in subsequent sections.

F6.1.2.5 Evaluation of Brace Moments

Prior to discussing the strength behavior of torsional braces, an overview of how the brace moments were calculated is warranted. As an example, Table F6-2 presents the brace forces as a function of M/M_{cr} (where M is the applied uniform moment and M_{cr} is the critical moment corresponding to buckling between brace points) for an analysis including: (i) cross-section 2 and (ii) n = 1, a single cross-frame at midspan. These brace moments were obtained from step 3 outlined in the previous subsection. In Figure F6-7, the brace moments are sketched for the case M/M_{cr} = 0.75 for reference.

The externally applied moments are identical for both girders in the twin-girder system, which implies the internal movements should also be identical. As the applied moment increases and the system deforms, however, shears develop at the interface between the girder and the brace. One girder has an upward shear, while the other has a downward shear, which results in unbalanced internal moments in the twin-girder system (i.e., right girder has more moment than left girder). Wang and Helwig (2005) showed that the cross-frame forces are a function of the girder moment at the location of the brace. In this case, because the right girder has a higher internal moment at the brace point, the force couple applied to the brace is higher on the right than the left. The larger moment is also evident in the deformed shape shown in Figure F6-7, where the right girder deforms more severely and its top flange buckles in a reverse-curvature mode, whereas the top flange of the left girder deforms in a half-sign curve due to the lower moment level.

An idealized maximum and minimum force couple can be obtained from the strut forces. For example, the maximum value would be the top strut force multiplied by the depth of the brace (1.49 kip × 48 inches = 71.5 kip-inch). The minimum is 1.37 kips × 48 inches = 65.8 kip-inch, and the average is 68.7 kip-inch. In design, an engineer would normally have "equal" girder design moments from a first-order analysis; therefore, the average force is used in all graphs herein to maintain consistency. However, in reality, one

girder will impart a higher brace moment than the adjacent girder due to the internal shears developed at increasing deformations.

The relative difference in the brace moments will generally be significant for twin-girder systems and become smaller for wider systems with more girders across the width. As reported in the results section herein, some analyses did not reach convergence above 90-95% of M_{cr}. Due to the internal shears, the brace moment corresponding to the heavier loaded girder was often larger than M_{cr}, but the average ratio of M/M_{cr} was less than unity.

Table F6-2: Computed brace forces for various girder moments

M_{br} / M_r	Brace force (kips)			Brace moment (kip-in)		
	Top strut, $F_{b,top}$	Bottom strut, $F_{b,bot}$	Diagonal, $F_{b,diag}$	Maximum, $M_{b,max}$	Minimum, $M_{b,min}$	Average, $M_{b,min}$
0.25	0.15	0.15	0.31	7.2	7.0	7.1
0.50	0.55	0.52	1.08	26.3	25.0	25.6
0.75	1.49	1.37	2.91	71.5	65.8	68.6
1.00	5.31	4.65	10.09	254.9	223.1	239.0

Notes: Brace moment, $M_b = F_b * d$, where d is the depth of the bracing and girders

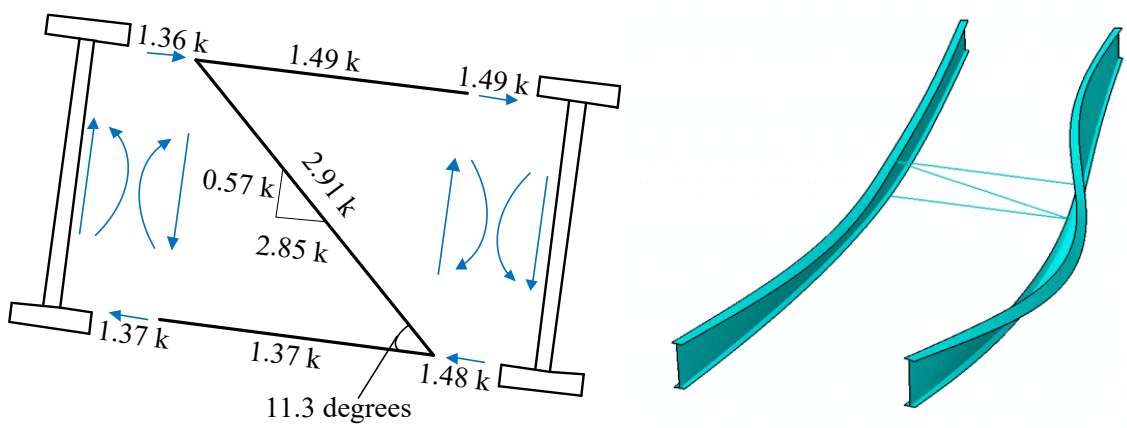

Figure F6-7: An example demonstrating how brace moments were distributed to the struts and diagonal members (left) and the corresponding buckled shape (right)

F6.1.3 Pertinent Results

Before general results of the full data set are shown, a brief discussion of the elastic and inelastic behavior of bridge girders is warranted through an example. Figure F6-8 shows a graph of applied moment versus the corresponding brace moment for the following parameters: Cross-section 2 with five intermediate braces (n = 5) and uniform moment loading. As the applied load increased sequentially, the out-of-plane girder deformations and corresponding brace moments resulting from second-order effects on the initial imperfection were recorded. Along the x-axis, the brace moment, M_b (the average value as determined by Section F6.1.2.5), is normalized by the externally applied uniform moment, M. Along the y-axis, the applied moment is normalized by the critical buckling capacity between braces points, M_{cr}, as determined by Eq. F6.5.

Four curves are presented which correspond to cases with an elastic material and three cases of inelastic material limits (i.e., a yield strength of 36, 50, and 70 ksi). As noted earlier, no residual stresses were considered. The response of all four curves is essentially coincident up until the cases with inelastic material exhibit yielding, at which point the curves flatten. The inelastic curves diverge from the cases that are still elastic and ultimately reach a maximum brace strength requirement corresponding to plastification of the cross-section rather than buckling.

Although the maximum brace moments for the cases with inelastic materials are smaller than the case with elastic materials, the comparison is not significant since the analyses were controlled by different limit states. The cases with higher material yield strengths experienced more significant torsional deformations and therefore larger brace moments than the cases with a lower yield strength. In fact, the RT observed that elastic materials (which were controlled by stability limit states) always resulted in the largest buckling-related deformations and consequently the largest brace moments. In comparison, many of the cases considered by Prado and White had a relatively short unbraced length and were controlled by plastification of the cross section assuming grade 50 steel.

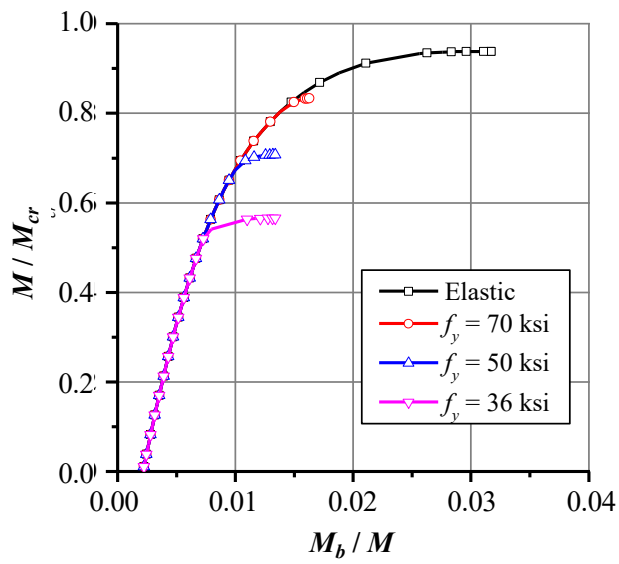

Figure F6-8: Brace moments under varying material yield limits (Cross-section 2 with uniform moment loading and 5 intermediate braces)

In general, tailoring brace strength requirements around a specific material yield strength is not advisable. It can potentially lead to unconservative estimates of the stability brace moments, as demonstrated by the example in Figure F6-8. Instead, provisions for brace strength should be applicable for a variety of material yield strengths and also consider the number of intermediate brace points. The expression should also be applicable for more general cases with larger and smaller unbraced lengths. As such, subsequent results present solutions with both elastic and inelastic materials considering the yield strengths of 36, 50, and 70 ksi.

To expand on the sample data presented in Figure F6-8, Figure F6-9 shows brace moments as a function of applied uniform-moment loading for all three cross-sections considered. Cases are shown for n = {1, 3, and 5}. Cases with an even number of intermediate braces between the supports (n = 2 and n = 4) are not shown; in these instances, a brace location does not coincide with the location of maximum internal moment in the girder, which typically results in smaller brace strength demands. Although the girders were subjected to uniform moment, the maximum moment still occurs near mid-span due to buckling deformations and the

internal shears from the braces. The observation of smaller maximum brace moments for cases with $n = 2$ and $n = 4$ is also consistent with the study presented in Wang and Helwig (2005), which found that brace force is a function of the internal girder moment at the brace location.

In Figure F6-9, both elastic and inelastic analyses are considered. Elastic analysis results are presented for $n = \{1, 3, \text{and } 5\}$; inelastic analysis results are presented for $n = 5$ only. Although inelastic materials were also considered for $n = 1$, and $n = 3$, the curves were not significantly different than the elastic cases, except at very large deformations when P-delta effects led to yielding of the section and relatively large deformations. Thus, only one representative plot is shown for inelastic response. Because each curve represents a different unbraced length and girder cross-section that impacts the buckling capacity, the applied and bracing moments are normalized in the same manner as Figure F6-8.

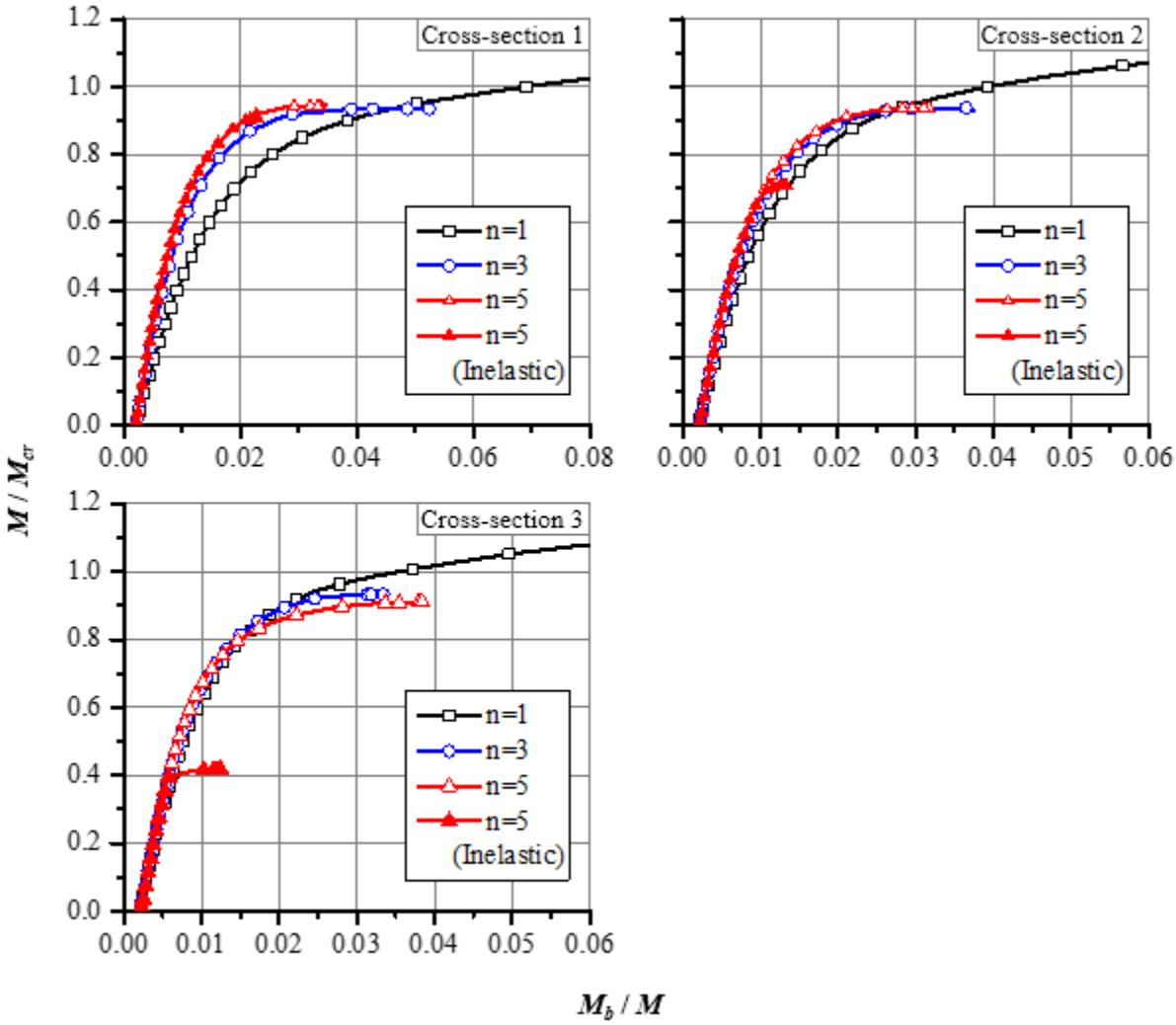

Figure F6-9: Brace moments as a function of applied bending moment (under uniform-moment loading)

From Figure F6-9, the following observations can be made with regards to brace strength requirements and girders subjected to uniform moment loading and various intermediate bracing schemes:

- For elastic materials on all three sections, the relative magnitude of the brace forces at the maximum girder moments decrease with an increased number of intermediate braces. In addition, the relative change in brace force tends to decrease as more braces are added (i.e., there is a large reduction going from $n = 1$ to $n = 3$, but the reduction is less going from $n = 3$ to $n = 5$).
- Some of the analyses did not reach convergence beyond 90~98% of M_{cr} for the cases with $n = 3$ and $n = 5$ due to excessive girder deflections. However, this level of convergence is reasonable since it is within the resistance factor ($\phi = 0.9$) and provides a representative level for the bracing moment.
- The curve for inelastic materials with $n = 5$ had smaller brace moments than the cases with elastic materials, which is consistent with the observations outlined for Figure F6-8. As noted in the earlier discussion, the sections with inelastic effects were controlled by cross-sectional yielding and not instability. Therefore, all subsequent results presented in this section focus on elastic materials since such conditions are more critical than cases with inelastic materials.
- Lastly, comparing the responses of the three different cross-sections shows that the magnitude of the brace moments increases for more flexible sections. In other words, sections with smaller b_f/d ratios tend to have larger brace moments (i.e., brace moments associated with cross-section 1 exceed brace moments associated with Cross-section 3).

In addition to uniform-moment loading, cases with a uniformly distributed load were also considered. Figure F6-10 presents graphs of the required brace moments for cases with distributed loads applied at two different locations along the height of a girder cross sections. The graphs on the left represent top flange loading, while the graphs on the right represent mid-height loading. Similar to the previous figures, Figure F6-10 normalizes applied and brace moments, as well as includes only odd number of intermediate braces between the end supports.

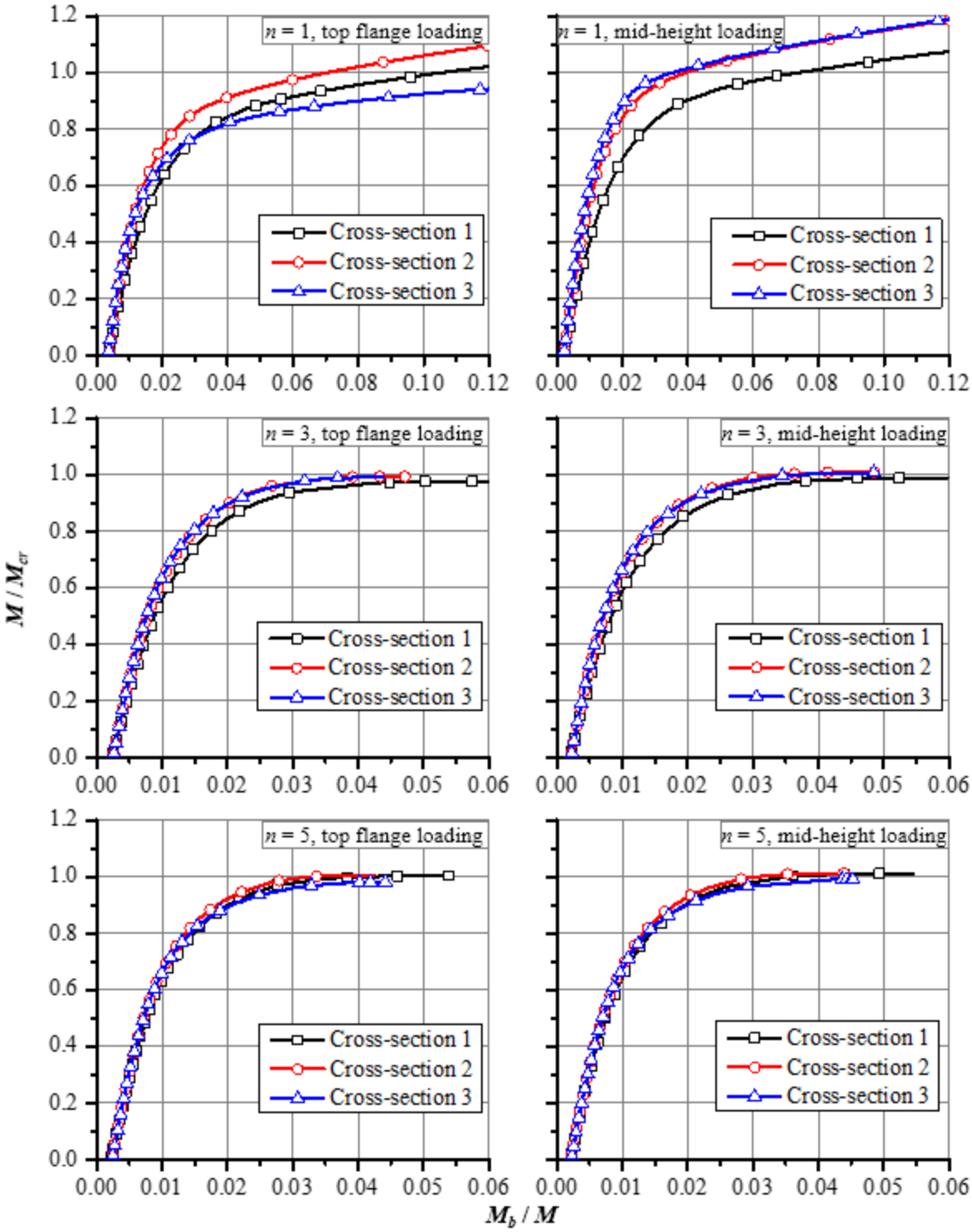

Figure F6-10: Brace moments as a function of applied bending moment (under transverse loading)

From Figure F6-10, the following observations can be made with regards to brace strength requirements and uniformly distributed loading:

- In comparing Figure F6-9 (uniform moment) and Figure F6-10 (uniformly distributed loading), it is evident that moment gradient generally results in considerably larger brace forces. For uniform-moment loading, typical brace moments ranged from approximately 3% to 6% of the maximum applied moment. For the cases with moment gradient, the brace moments ranged from 3% to 10% depending on load height effects and the specific cross section. Note that the current 15th Edition AISC brace strength equation (Eq. F6.3) produces estimates of the brace moment on the order of 100 to 200% unconservative.
- Top flange loading is generally more critical than mid-height loading, and girders with fewer intermediate braces result in the larger normalized brace moments.
- For most analyses, slender sections resulted in larger brace forces; however, in some cases the stockiest section (cross-section 3) resulted in the largest brace force as a percentage of the applied moment. The much wider flange for cross-section 3 leads to a larger critical brace moment compared to cross-sections 1 and 2, such that applied moment M was relatively large.

Table F6-3 summarizes the torsional bracing strength requirements for the twin-girder system. As noted above, different cross sections, numbers of intermediate braces, and loading conditions were evaluated. The previous figures demonstrated the curves tend to flatten as M/M_{cr} approaches 1.0, and in some instances convergence was not reached above 90-98% of M_{cr}. In Table F6-3, the brace moments are presented for either $M/M_{cr} = 1$ or the largest load that convergence was achieved, which was typically capped at $M/M_{cr} = 0.9$.

Although some of the brace moments tabulated are approximately 2% at $M/M_{cr} = 0.9$ (for analyses that did not converge), it should be emphasized that brace moments tend to increase dramatically as the applied moment increases from $M/M_{cr} = 0.9$ to $M/M_{cr} = 1$. The brace moment has been shown to grow between 50 and 100% beyond an applied moment of 90% of M_{cr}. As such, these cases which may not appear critical can be rather significant.

Table F6-3: Summary of strength requirements of torsional bracing for different cross sections and load conditions

Loading Conditions	n	1			3			5		
	b_f / d	1/6	1/4	1/3	1/6	1/4	1/3	1/6	1/4	1/3
Uniform Moment	M_b / M	6.9%	3.9%	3.7%	2.7%	2.2%	2.2%	2.0%	2.0%	3.0%
	M / M_{cr}	100%	100%	100%	90%	90%	90%	90%	90%	90%
Top Flange Loading	M_b / M	10.4%	7.3%	7.7%	2.5%	2.0%	2.0%	4.0%	3.4%	2.0%
	M / M_{cr}	100%	100%	90%	90%	90%	90%	100%	100%	90%
Mid-Height Loading	M_b / M	7.3%	4.0%	3.3%	2.5%	2.0%	2.0%	4.0%	3.4%	2.0%
	M / M_{cr}	100%	100%	100%	90%	90%	90%	100%	100%	90%

In general, the brace moments reported are significantly larger than the $0.02M$ requirement given by the current AISC expression (Eq. F6.3). In many cases, the FEA results were more than 100% larger. Rather, the RT recommends that designers use the brace strength equation from the 14th Edition Specification given in Eq. F6.2.

Even with implementing this equation in AASHTO LRFD, it is evident from Table F6-3 that the required brace moments can still exceed Eq. F6.2 (i.e., a minimum brace moment of 2.6% of M_{cr}). However, there are mitigating factors that lessen the demands reported in the table. As previously noted, stability brace moments are extremely sensitive to the shape and distribution of the initial imperfection in girders. In most

situations, though, the actual imperfection will not match the critical shape, resulting in smaller brace forces than predicted by the analyses in this study (and shown in Table F6-3). Also, in many situations, the brace sizes often utilized in design will exceed the stiffness required by Eq. F6.1, which will typically result in smaller stability-induced forces. With that in mind, the RT believes that Eq. F6.2 is suitable for implementation into AASHTO LRFD.

Given that Table F6-3 focuses entirely on single-curvature bending cases, it is prudent to verify these conclusions with a reverse-curvature bending spot check. To demonstrate bracing demands in beams subjected to significant moment gradient, sample results are presented in Figure F6-11. Beams with Cross-section 1 properties were subjected to the applied loads and moment gradients illustrated at the bottom of Figure F6-5. As previously noted, five intermediate braces were implemented to maximize the negative moments at the first intermediate cross-frame line. For the sake of comparison, Figure F6-11 presents the results of four different loading and critical imperfection scenarios:

- Uniform moment with the critical imperfection along the top flange at midspan;
- Single-curvature, uniformly distributed mid-height loading with the critical imperfection along the top flange at midspan;
- Reverse-curvature, uniformly distributed mid-height loading with the critical imperfection along the top flange at midspan;
- Reverse-curvature, uniformly distributed mid-height loading with the critical imperfection along the bottom flange at the first intermediate cross-frame line.

Note that in the third and fourth scenarios listed, the loading conditions were identical. Only the location of the critical imperfection was varied to study its impact on the results.

In previous figures shown in this section, only the midspan cross-frame results were provided, as bracing demands were maximized at this location for single-curvature bending (due to girder moment magnitudes and girder displacements). For reverse-curvature bending, however, that behavior is intuitively less clear. As such, Figure F6-11 presents the bracing force demands of three different cross-frames in the five-brace scheme. It should be noted that the results are not symmetric (e.g. cross-frame lines 2 and 4 produce different results) due to the asymmetric nature of the initial imperfection. Thus, only the results related to the more critical half of the beam are presented.

Figure F6-11 is otherwise constructed similarly to Figure F6-10 with one key exception. Along the horizontal and vertical axes, the maximum applied moment, M, is taken as the maximum negative moment at the support for consistency. M_{cr} is then based on the end segment, which was shown to buckle before the segments in the positive moment region. This is clearly denoted at the top of the figure. Sketches are also provided for each loading and imperfection condition, for reference.

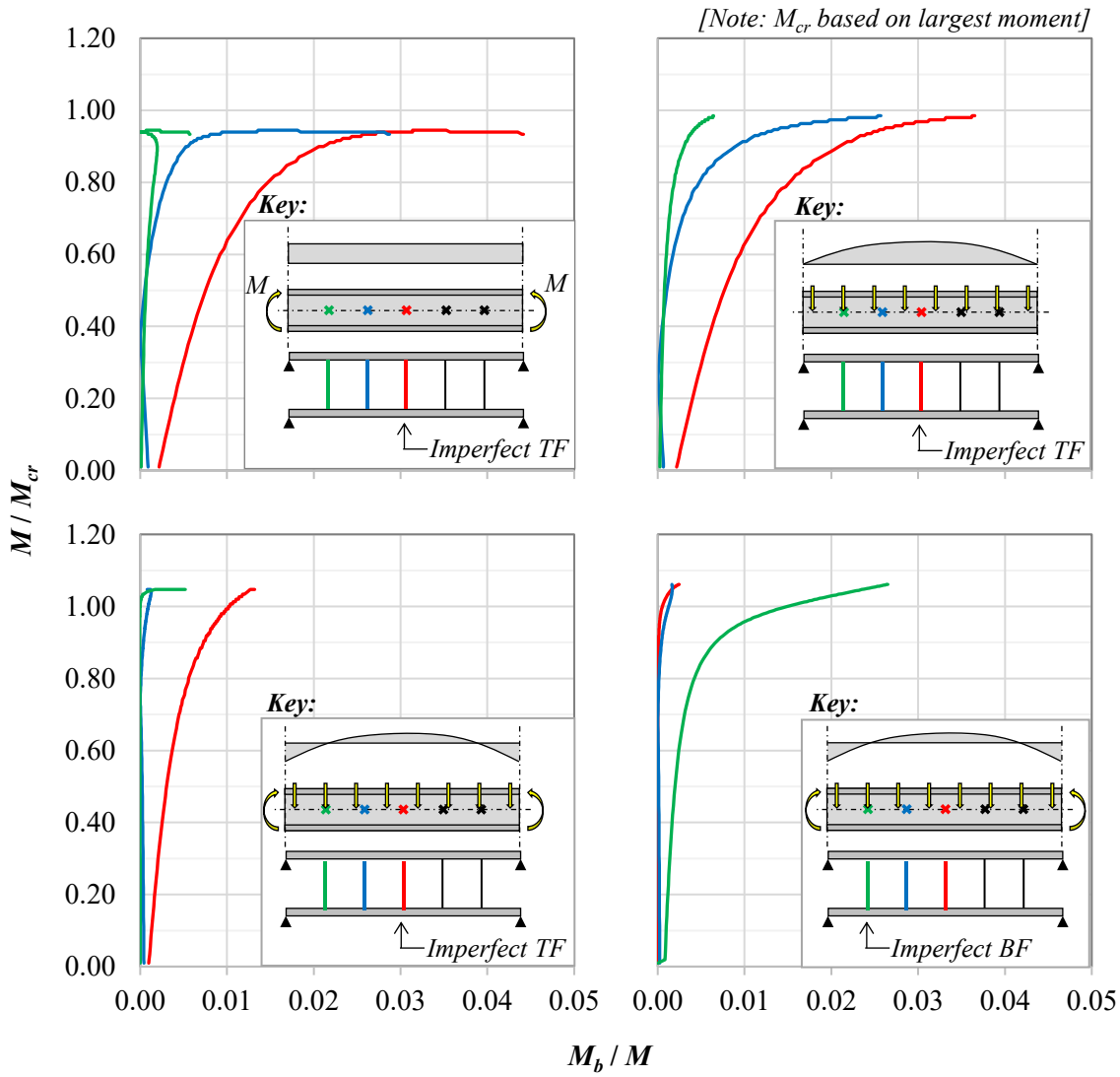

Figure F6-11: Brace moments as a function of reverse-curvature bending (Cross-section 1; n = 5; mid-height loading)

- In the uniform-moment case, it is evident that the midspan brace experiences the largest bracing demands. This validates the assumption used throughout the development of the previous figures. Additionally, the midspan brace moment approaches 2% of the maximum applied moment at M/M_{cr} = 0.9 (i.e., analysis did not converge at 100% of M_{cr}). This result is consistent with Table F6-3.
- In the single-curvature uniformly distributed load case, it also evident that the midspan brace experiences the largest bracing demands. Note that the critical values are consistent with what is reported in Table F6-3.
- For the reverse-curvature bending cases, the critical cross-frame coincides with the location of the critical imperfection, as expected. In the bottom left plot (imperfection along the top flange at midspan), the bracing moment approaches 1% of the maximum applied moment (taken as the negative moment value at the support) as M_{cr} is reached. The other two braces presented pick up nearly no bracing forces, even at the elevated load magnitudes. In the bottom right plot (imperfection along the bottom flange at the first brace line), the bracing moment approaches 1.5%

of the maximum applied moment. The "negative moment" brace is likely more critical than the "midspan" brace for this case, given that the end segment was more susceptible to buckling based on finite-element results. These cases still produce less force demands than the comparable single-curvature conditions.

- For these spot check conditions, it is generally observed that bracing demands are more critical in single-curvature bending conditions with less moment gradient (i.e., smaller C_b factor) than reverse-curvature conditions with significant moment gradient. This is reflected in Eq. F6.2, for which the C_b factor of the unbraced segment of interest is in the denominator.

Based on these results, it can be concluded that Eq. F6.2 is conservatively valid for reverse-curvature bending conditions in noncomposite systems. For cases with variable unbraced segment lengths and moment gradient factors, the bracing moment shall be based on the segment that maximizes the M_r/C_bL_b component of the equation regardless of which flange is in compression. In doing so, this ensures the critical condition is covered. All cross-frame braces in the span would be subsequently designed for the worst-case condition. These three variables are segment-specific, whereas the other variables and constants are consistent for the given span (e.g., span length L is taken as the full length under consideration).

Members of the RT have been working on another study unrelated to this NCHRP investigation that focuses on the increment of the ideal stiffness that will control the amount of deformation at the brace to a value equal to the initial imperfection such that Eq. F6.2 provides better estimates of the brace strength. The more appropriate increment of the ideal stiffness appears to be approximately three, as is discussed subsequently in this chapter. Section F6.2 herein outlines the parametric FEA study and results evaluating the appropriate stiffness of cross-frames serving as torsional braces.

F6.2 Bracing Stiffness Requirements

As covered in the Chapter F6 introduction and Section F6.1.1, cross-frames must possess adequate strength and stiffness to brace a bridge girder against LTB particularly during the erection process. Section F6.1 was dedicated to the strength requirements, and Section F6.2 herein is dedicated to the stiffness requirements. Before presenting the results of a FEA parametric study, a brief literature review is provided, and the current AISC design procedures are addressed in Section F6.2.1. Section F6.2.2 outlines the parametric study and FEA procedures used to evaluate these design provisions, and Section F6.2.3 presents the results with commentary.

F6.2.1 Background

As defined previously, the "ideal" stiffness of a beam or column brace (β_i) relates to the stiffness required for a perfectly straight element to reach a specified buckling capacity between said brace points. Since "real" structural members are not perfectly straight (i.e., they possess some initial imperfection, or out-of-straightness over the length), the current design assumption is to provide twice the ideal stiffness. Based on the work conducted by Winter (1960), it was found that providing twice the ideal stiffness ($2\beta_i$) for columns limits the out-of-plane deformations to a value equal to the initial imperfection as the applied load reaches the critical buckling load.

Winter showed that this assumption works quite well for columns. As a result, it serves as the basis for column bracing requirements in AISC Specifications. However, this assumption has not been formally validated for beam stability applications. Despite the lack of research, the "twice the ideal stiffness" still serves as the basis for beam bracing requirements, as was documented with Eq. F6.1 above. In response, the RT conducted a parametric study that investigates the effects of girder cross-section, loading conditions, intermediate bracing schemes, girder spacing, and number of girders on the required stiffness of a torsional beam brace (i.e., a cross-frame). As is presented in subsequent sections, the RT investigates the use of three

times the ideal stiffness ($3\beta_i$) for steel I-girder applications for AASHTO LRFD.

Although not documented extensively in this appendix, it should be noted that the actual brace stiffness must exceed the required stiffness, as determined by Eq. F6.1 and modified herein (i.e., $\beta_T \geq \beta_{T,req}$). Traditionally, the torsional stiffness of a cross-frame is determined from analytical solutions developed by Yura (2001), which were presented previously with Eqs. F4.3 and F4.4. In reality, though, the torsional stiffness of a brace is a combination of several different factors including: (i) brace stiffness, β_b, (ii) cross-sectional distortion, β_{sec}, and (iii) in-plane girder stiffness of the beams, β_g. These individual stiffness components tend to follow the expression for springs in series, as demonstrated mathematically with the following expression:

$$\frac{1}{\beta_T} = \frac{1}{\beta_b} + \frac{1}{\beta_{sec}} + \frac{1}{\beta_g} \qquad F6.6$$

A mathematical review of Eq. F6.6 shows that the total stiffness of the system, β_T, is always less than the smallest of the three individual terms on the right of the equation. For example, a stiff cross-frame with poor, flexible details will severely limit the stiffness response of the system; or a flexible in-plane girder stiffness, which effectively equates to a narrow, slender superstructure, will diminish the adequacy of a cross-frame. For the sake of clarity, a detailed discussion on these individual terms is not provided in this appendix, as it is beyond the scope of NCHRP Project 12-113. Rather, refer to Appendix D, which outlined these stiffness components in great detail based on previous research conducted at UT Austin.

F6.2.2 Parametric Finite-Element Study

To investigate the torsional brace stiffness behavior, parametric finite element analyses were carried out on multi- I-girder systems using Abaqus. As previously documented, the work in this study was actually carried out as an investigation of the AISC bracing provisions and not specifically for this NCHRP study; however, the results are directly pertinent and therefore warrant discussion. The following subsections outline different components of the parametric study, ranging from the FEA assumptions to the loading conditions. Note that many of the modeling parameters outlined previously in Section F6.1.2.1 were also used for the present study with a few notable exceptions. Thus, the focus of the subsequent sections is on highlighting those subtle differences rather than repeating the same information.

F6.2.2.1 Finite-Element Approach

The parametric FEA models developed in this study consisted of multiple I-girders and intermediate cross-frame braces in noncomposite systems (i.e., to represent the most critical stage for beam buckling during steel erection or deck construction). The multiple-girder systems and cross-frame elements are representative of steel bridge applications in the US. Similar to the brace strength models in Section F6.1.2.1, the brace stiffness models employed "full-depth" Z-type cross-frame elements to brace girder elements, and girders were built from shell elements meshed in 2-inch squares. Figure F6-12 depicts the layout and boundary conditions of the multi-girder systems. As an example, a two- and four-girder system are depicted, but different variations were considered in the study.

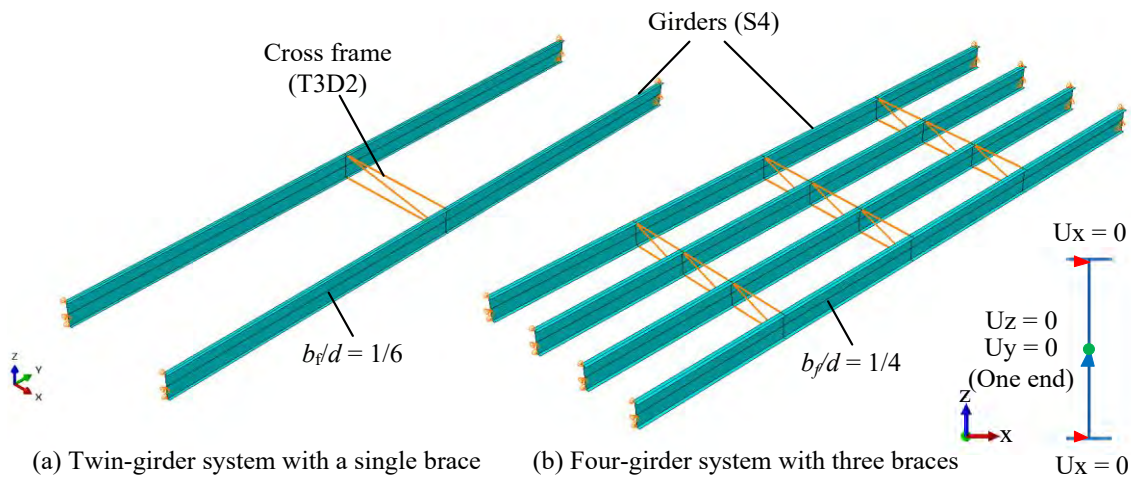

(a) Twin-girder system with a single brace (b) Four-girder system with three braces

Figure F6-12: Geometry and boundary conditions used for bracing stiffness model

The primary difference between the brace strength model and the brace stiffness model was the effect of material inelasticity. From Section F6.1, it was demonstrated that elastic materials generally produce more critical demands for cross-frame stiffness and strength. As such, only elastic materials with no residual stresses were considered in the present FEA study.

F6.2.2.2 Range of Parameters and Loading Conditions

In general, the loading conditions and girder cross-sections considered in the present study are identical to that of the brace strength study previously documented. For instance, loading conditions included uniform-moment loading and distributed loading applied at either the top flange or mid-height of the girder; additionally, three different cross-sections were examined which primarily focused on flange-width-to-depth ratios (b_f /d): 1/6, 1/4, and 1/3. 100-foot long girders were considered with a variable number of intermediate braces (n = {1, 3, 5}), which corresponded to unbraced lengths ranging from 50 feet to 16.67 feet. To avoid issues with system buckling discussed in the previous sections, girder spacing ranged from 20 feet to 30 feet, which is especially critical for twin-girder systems. Refer to Figure F6-4 and Figure F6-5 for more information regarding the shared parameters between studies.

The primary difference, though, between the brace strength FEA study and the stiffness study herein is the consideration of multiple girders. In the present study, multi-girder systems including 2, 3, 4, and 6 girders across the width were studied. Again, Figure F6-12 illustrates a sample four-girder bridge examined. Regardless of the number of girders, applied loads and critical imperfections (presented in next subsection) were the same.

F6.2.2.3 Critical Imperfection

As previously demonstrated, the response of a girder and cross-frame braces is highly sensitive to the initial imperfection assumed. Similar to Section F6.1.2.3, an asymmetrical imperfection was assumed in this study based on work conducted by Wang and Helwig (2005) and Prado and White (2015). The magnitude and distribution of the initial imperfection was identical to that of the brace strength study. For reference, Figure F6-13 graphically depicts this assumed shape imperfection for a twin-girder system.

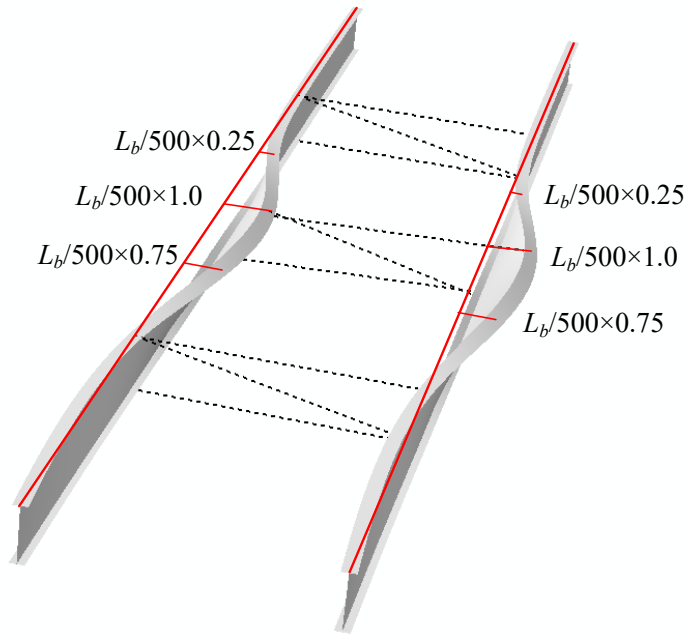

Figure F6-13: Assumed initial imperfection in the bracing stiffness model (similar to Figure F6-6)

F6.2.2.4 Preliminary Steps in Parametric Study

Similar to brace strength study and Section F6.1, the process of the present FEA study involved three distinct analyses in Abaqus, which are summarized below. Similarly, these three steps were performed for every unique cross-section and bracing scheme considered in the parametric study.

1. **Conduct an eigenvalue buckling analysis on the multi-girder system subjected to equal, uniform-moment loading**. Similar to Section F6.1.2.4, the two objectives of the eigenvalue study on perfectly straight girders are: (i) to obtain the cross-frame stiffness required to buckle the girders between the braced points and (ii) the moment level corresponding to buckling between the braced points. The critical buckling load obtained from the FEA model is then validated against the theoretical solution presented in Eq. F6.5.
2. **Obtain the initial imperfect shape of the multi-girder system by statically displacing the top flange in accordance with Figure F6-13**. As previously noted, the RT ensured that the cross-frame elements did not pick up any locked-in forces in this stage of the analysis.
3. **Run incremental analyses on the imperfect system for various loading conditions and cross-frame stiffness values (multipliers of the ideal stiffness)**. In this final stage, the stiffness of the cross-frames is examined for its effect on the out-of-plane twists of the girders (relative to the initial imperfection). Brace stiffness to ideal stiffness ratios, β_b / β_i, of {2, 2.5, 3, and 4} were studied. Recall that for column braces, providing twice the ideal stiffness has been shown to limit out-of-plane deformations equal to the initial imperfection at critical loads. This behavior is studied in girders for various levels of cross-frame stiffness. Similar to the brace strength study, girder deformations and brace forces are recorded as external load is incrementally applied.

From this procedure, the RT obtained data that characterized the stiffness behavior of cross-frames as torsional braces. These results are presented in subsequent sections.

F6.2.3 Pertinent Results

Before presenting general results of the full data, a sample set is shown to illustrate key aspects of the analytical results. Figure F6-14 presents the twist of the imperfect girder cross-section at midspan (i.e., the critical location) as a function of the applied moment magnitude (also taken at midspan) for the following select parameters: a twin-girder system ($n_g = 2$) comprised of Cross-section 2, one intermediate brace ($n = 1$), and uniformly distributed loading on the top flange. As the applied load increased sequentially, the out-of-plane girder deformations resulting from second-order effects on the initial imperfection were recorded.

Along the x-axis, the cross-sectional twist of the girder at midspan, θ, is normalized by the initial imperfection, θ_o, as defined in Eq. F6.2. The θ/θ_o ratio equals 1.0 at no applied load given the assumed initial imperfection. Along the y-axis, the applied moment, M, is normalized by the critical buckling capacity between braces points, M_{cr}. The applied moment for a single girder is taken as the average internal moment among the multi-girder system. In some cases, the applied moment does not reach M_{cr}, due to in-plane stiffness effects. Instead, it is limited to 97% to 99% M_{cr}. This response is plotted for twin-girder systems with various levels of cross-frame stiffness: 2, 2.5, 3, and 4 times the ideal stiffness, β_i. Recall that the values for β_i and M_{cr} are obtained from the eigenvalue analyses.

Many of these same plots were produced for different sets of parameters. The primary goal of the plots is to determine the cross-frame stiffness that limits the θ/θ_o ratio to 2.0 at the critical buckling load (i.e., $M/M_{cr} = 1.0$). A ratio of two represents the case in which the induced deformations at the buckling load is equal to the initial imperfection, which serves as the basis for AISC current design procedures and Eq. F6.2.

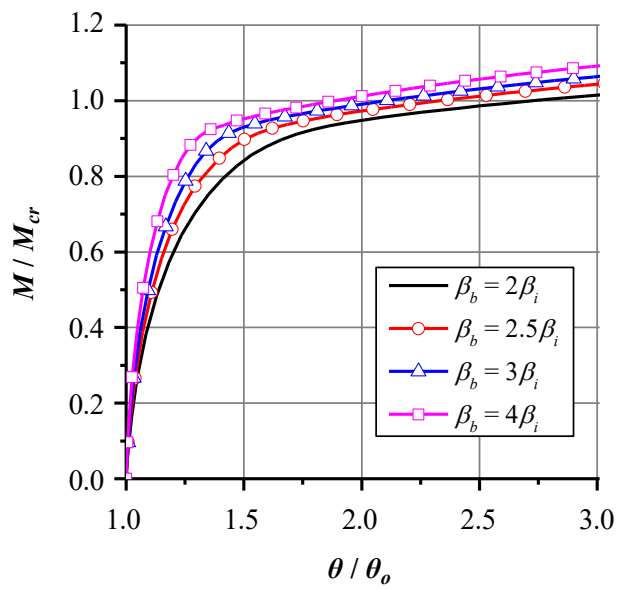

Figure F6-14: Girder cross-sectional twist as a function of applied uniform moment for various brace stiffness values (n = 1, cross-section 2, and top flange loading)

From Figure F6-14, it is apparent that providing twice the ideal stiffness results in $\theta/\theta_o = 2.7$ for this particular example. The desired θ/θ_o ratio of 2 is, however, achieved when supplying 3 to 4 times the ideal stiffness. Additionally, a stiffer brace not only reduces the relative deformations in the girders but also reduces the force demands in the brace members themselves, which impacts the brace strength requirements discussed in Section F6.1. Similar observations were also made for different sets of bracing and girder parameters.

Figure F6-15, Figure F6-16, and Figure F6-17 expand on Figure F6-14 by presenting larger portions of the data set. These figures now present the critical θ/θ_o ratio (i.e., the maximum twist at $M = M_{cr}$) as a function of different parameters. Thus, rather than presenting the incremental stages of the analysis, only the behavior at the critical load stage is presented. Figure F6-15 investigates the impact of girder spacing, Figure F6-16 investigates the number of girders in the system, and Figure F6-17 investigates the girder cross-sections. For each figure, the prominent parameter is presented along the x-axis, where the remainder of the parameters are held constant to limit and clarify the discussion. For example in Figure F6-15, only systems with two girders (Cross-section 2) and top flange loading are depicted.

Similar to Figure F6-14, the responses are plotted for girder systems with various levels of cross-frame stiffness: 2, 2.5, 3, and 4 times the ideal stiffness, β_i. Various intermediate bracing schemes are also examined: $n = \{1, 3, 5\}$.

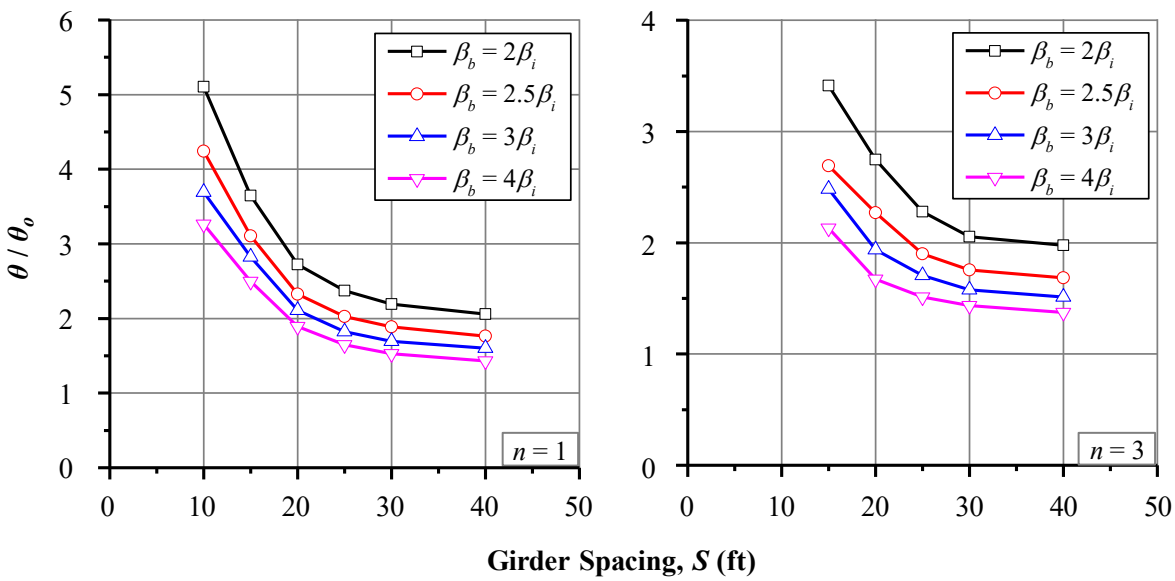

Figure F6-15: Girder cross-sectional twist as a function of girder spacing (twin-girder system, Cross-section 2, top flange loading)

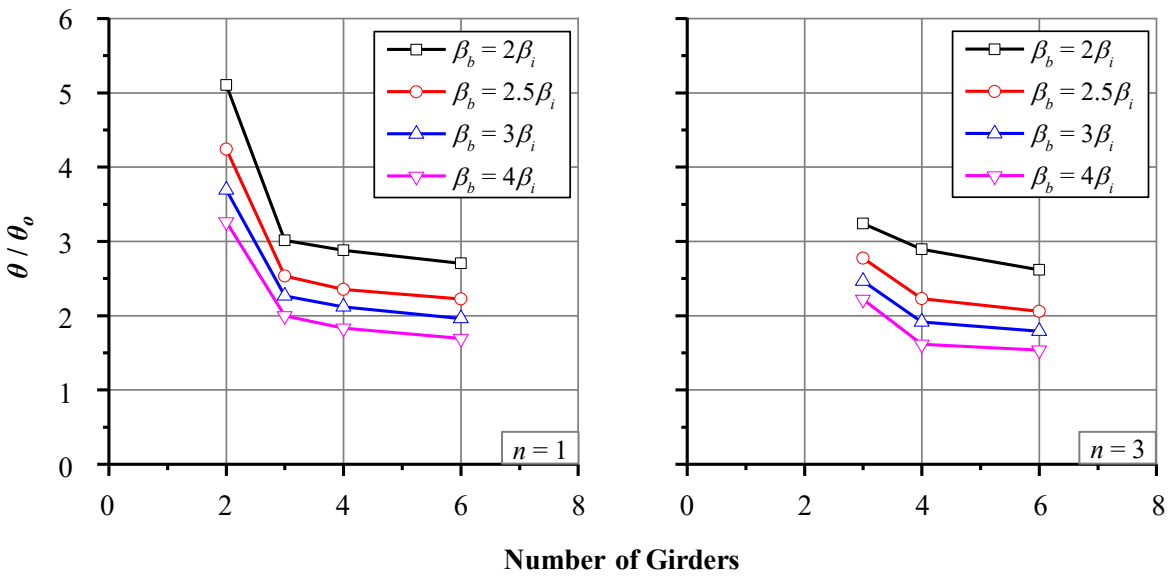

Figure F6-16: Girder cross-sectional twist as a function of number of girders (10-foot girder spacing, Cross-section 2, top flange loading)

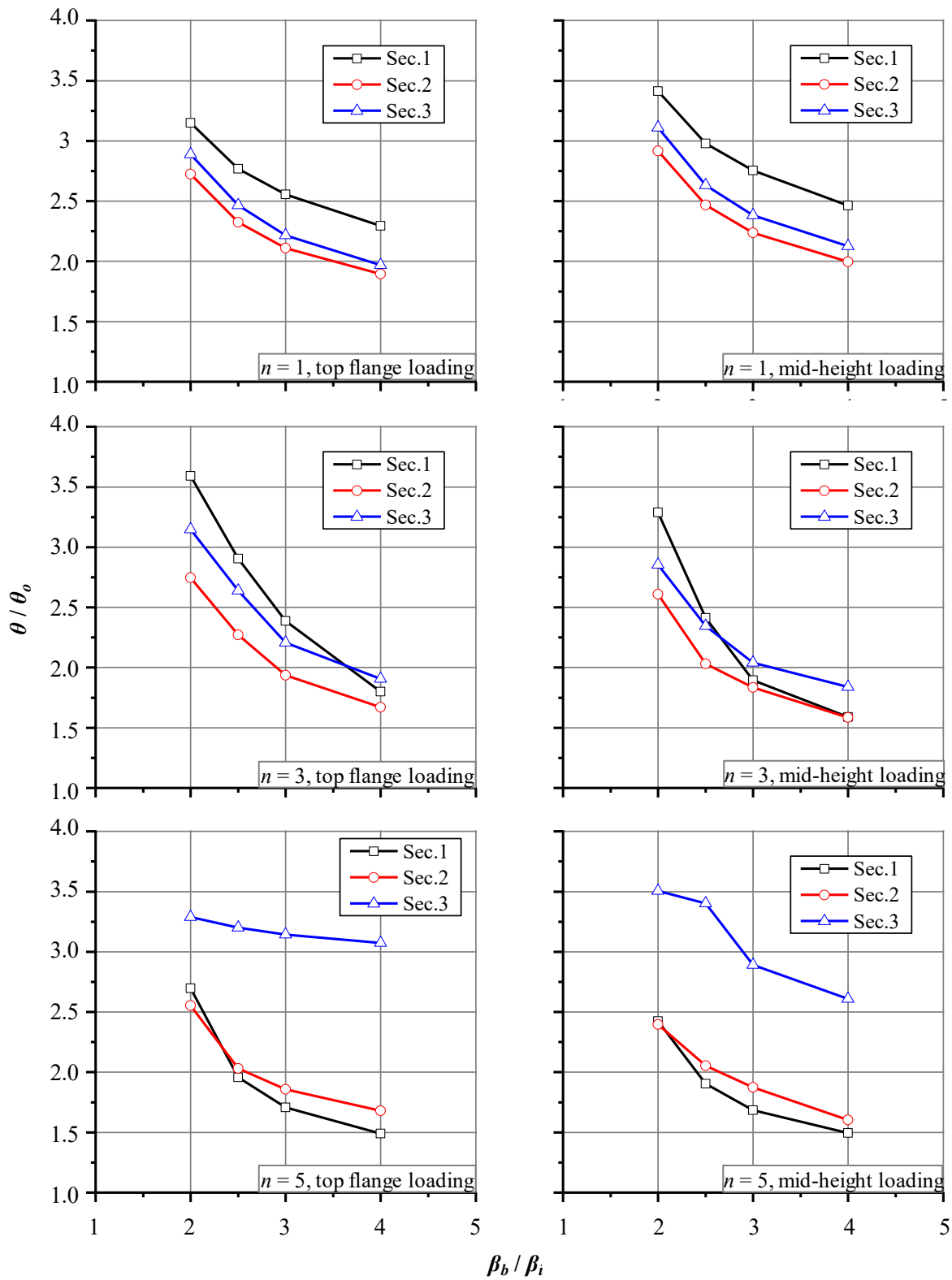

Figure F6-17: Girder cross-sectional twist as a function of applied uniform moment for various brace stiffness values (twin-girder system)

From Figure F6-15, Figure F6-16, and Figure F6-17, the following observations can be made with regards to brace stiffness requirements and various girder and brace parameters:

- The relative girder twist induced at critical buckling loads decreases as the brace stiffness increases. In all cases, assigning stiffer cross-frame elements mitigates girder deformations.
- In general, adding intermediate braces (regardless of the stiffness) decreases the relative cross-section twists with some exceptions.
- (Figure F6-15) Increasing the girder spacing, particularly in twin-girder systems, not only improves the system buckling capacity but also decreases the stiffness demands for the cross-frame braces. Take a system with one intermediate brace and a 20-foot girder spacing as an example (left plot of Figure F6-15). Assigning twice the ideal stiffness ($2\beta_i$) to the cross-frame results in girder twists equal to 2.8 times θ_o, the initial imperfection. In constant, assigning three times the ideal stiffness ($3\beta_i$) results in a reduced final twist equal to $2.1\theta_o$.
- (Figure F6-16) For the twin-girder cases, the cross-sectional twists are heavily influenced by the force couple induced by the brace forces. As such, a dramatic increase in cross-frame stiffness demands are observed for $n_g = 2$. This observed behavior is similar to the girder spacing discussion above. An increase in girder redundancy increases the in-plane stiffness of the bridge system, which in turn leads to smaller girder deformations at critical buckling loads. Take the case with one intermediate brace ($n = 1$) and three times the ideal stiffness ($3\beta_i$) as an example (left plot of Figure F6-16). For a twin-girder system, the final girder twist is equal to $3.6\theta_o$; for a four-girder system, the final twist is significantly reduced to $2.2\theta_o$.
- (Figure F6-17) For a given brace stiffness (β_b / β_i), the induced twist associated with Cross-section 2 girders are generally smaller than girders with Cross-section 1 (slender flange section) and Cross-section 3 (stocky flange section), which is perhaps counterintuitive. However, slender sections (e.g. $b_f / d = 1/6$) typically have a smaller lateral bending moment of inertia (I_y) and torsional inertia (J), which consequently produces more substantial lateral and torsional deformation at critical buckling loads. For stockier flange sections (e.g. $b_f / d = 1/6$), the critical buckling moment, M_{cr}, is typically large, which in turn increases the ideal stiffness of the cross-frame brace. For these conditions, the brace stiffness, β_b, tends to outweigh the in-plane girder stiffness, β_b, which was introduced in Eq. F6.6; consequently, the effect of in-plane girder stiffness is more critical for girders with stocky flange sections, particularly in narrow twin-girder systems. This leads to larger twist deformations in the girders. Thus, the intermediate flange section (Cross-section 2) tends to limit twist deformations more than the two extreme sections for two independent reasons.
- (Figure F6-17) Top flange loading and the mid-height loading result in similar deformation behavior. The effect of the transverse loading locations on the stiffness requirement for torsional bracing is marginal
- In general, assigning three times the ideal stiffness tends to result in girder cross-sectional twists closer to 2 times θ_o than assigning twice the ideal stiffness.

Table F6-4 summarizes the torsional bracing stiffness requirements based on the results of the parametric study. The final girder twist (as a ratio of the initial imperfection) is tabulated for various cross-frame stiffness values, loading conditions, and girder cross-sections. Note that these results correspond to twin girders only, as this system has been shown to be most critical. For each θ/θ_o ratio reported, the corresponding M / M_{cr} value is also shown. In most cases, the applied moment reached the critical buckling moment (i.e., $M / M_{cr} = 100\%$). However, there were a few instances in which the critical buckling moment was not achieved; in those cases, the girder twist at the maximum girder moment recorded is presented instead.

Table F6-4: Summary of stiffness requirements of torsional bracing for different cross sections and load conditions

Loading Type	Cross-Frame Stiff., β_b	n^a	1 (C_b = 1.30)			3 (C_b = 1.06)			5 (C_b = 1.03)		
		b_f / d	1/6	1/4	1/3	1/6	1/4	1/3	1/6	1/4	1/3
Top Flange Loading	$2\beta_i$	θ / θ_o	3.15	2.72	2.89	3.59	2.74	3.15	2.7	2.55	3.29
		M / M_{cr}	100%	100%	100%	98%	99%	99%	100%	100%	98%
	$2.5\beta_i$	θ / θ_o	2.77	2.32	2.46	2.9	2.27	2.64	1.96	2.03	3.2
		M / M_{cr}	100%	100%	100%	99%	100%	100%	100%	100%	99%
	$3\beta_i$	θ / θ_o	2.56	2.11	2.22	2.39	1.94	2.21	1.71	1.86	3.14
		M / M_{cr}	100%	100%	100%	100%	100%	100%	100%	100%	99%
	$4\beta_i$	θ / θ_o	2.3	1.89	1.97	1.8	1.67	1.91	1.49	1.68	3.07
		M / M_{cr}	100%	100%	100%	100%	100%	100%	100%	100%	99%
Mid-Height Loading	$2\beta_i$	θ / θ_o	3.41	2.92	3.11	3.29	2.61	2.85	2.42	2.4	3.51
		M / M_{cr}	100%	100%	100%	99%	100%	100%	100%	94%	99%
	$2.5\beta_i$	θ / θ_o	2.98	2.47	2.63	2.41	2.03	2.35	1.9	2.05	3.4
		M / M_{cr}	100%	100%	100%	100%	100%	100%	100%	100%	99%
	$3\beta_i$	θ / θ_o	2.76	2.24	2.38	1.89	1.83	2.04	1.68	1.87	2.89
		M / M_{cr}	100%	100%	100%	100%	100%	100%	100%	100%	100%
	$4\beta_i$	θ / θ_o	2.46	2	2.13	1.59	1.59	1.84	1.49	1.6	2.61
		M / M_{cr}	100%	100%	100%	100%	100%	100%	100%	100%	100%

Notes:
[a]Given the uniformly distributed loading ($wL^2/8$ type loading) the moment gradient factor, C_b, is a function of the bracing scheme

In general, the table shows that providing twice the ideal stiffness ($2\beta_i$) typically results in load-induced girder twists exceeding the assumed twist in Eq. F6.2 (i.e., $\theta / \theta_o > 2$). This implies that the current assumption built into AISC Specifications and mainly Eqs. F6.1 and F6.2 are invalid. However, the cross-sectional twist can be reduced to magnitudes more consistent with the assumed values by requiring braces to possess three times the ideal stiffness ($3\beta_i$). Therefore, for implementation into AASHTO LRFD, it is advised that Eq. F6.1 be modified to inherently consider three times the ideal stiffness as a means to limit girder deformations. This is presented mathematically with the following expression:

$$\beta_{T,req} = \frac{3.6LM_r{}^2}{\phi nEI_{yeff}C_b{}^2} \qquad F6.7$$

Note that the constant in the equation has increased 50% (i.e., from 2.4 to 3.6) to account for these recommended changes. This modification not only impacts the brace stiffness requirements, but also the brace strength requirements. Recall from Section F6.1.1 that the brace strength equations are effectively the required brace stiffness multiplied by the assumed initial imperfection. With that in mind, it is also recommended to modify Eq. F6.2 to account for the $3\beta_i$ assumption outlined above. This is reflected with the revised expression below:

$$M_{br} = \beta_T\theta_o = \frac{0.036M_rL}{nC_bL_b} \qquad F6.8$$

F6.3 Negative Bending and Moment Gradient Factors

In addition to the bracing strength and stiffness requirements for steel bridge applications, the Stability Study was also tasked with investigating the stability of girders (prismatic and nonprismatic) in the negative moment region of continuous systems (primarily in the noncomposite condition during steel erection and deck construction). As discussed in the introduction to Chapter F6, several members of the RT were involved with an independent study in conjunction with an ad-hoc committee under the guidance of the AASHTO T-14 Committee. The work and recommendations are documented fully in Reichenbach et al. (2020).

The refereed journal article explores two different aspects of LTB and nonprismatic girders, as summarized by the following objectives: (i) to develop a simplified design procedure to evaluate the LTB capacity of generic double- and singly-symmetric, nonprismatic beams under uniform-moment loading and (ii) to investigate the appropriate C_b expressions to use for these same complex sections when subjected to a variety of moment gradients. In terms of the first objective, the RT developed a simplified weighted average approach that converts a nonprismatic beam section into an equivalent prismatic segment with effective section properties. In essence, the buckling capacity of the equivalent, prismatic segment (using theoretical LTB solutions such as Eq. F6.5) was calibrated to provide approximate, yet conservative estimates of the "true" buckling capacity of the nonprismatic beam (determined from finite element studies). This process was done analytically through an expansive FEA parametric study. The first objective, although important to AASHTO LRFD given the lack of guidance in this area, is not directly related to NCHRP Project 12-113.

The second objective of the AASHTO T-14 study, however, is tangentially related to the present study. The RT evaluated the buckling behavior of nonprismatic bridge girders, particularly in negative moment regions of continuous units, in the context of moment gradient factors, C_b. Given that this independent study has design implications that are relevant to the scope of NCHRP Project 12-113, abbreviated results and findings are summarized in this appendix. For further information and commentary not included in this appendix for clarity, refer to the journal article.

The goal of Section F6.3 is to summarize the AASHTO T-14 Study as it pertains to nonprismatic bridge girders. Following this introduction, Section F6.3.1 outlines pertinent background information to contextualize the material for the reader. Section F6.3.2 describes the parametric study and the FEA methodology used to evaluate moment gradient effects on nonprismatic girders, and Section F6.3.3 presents the results with commentary.

F6.3.1 Background

As introduced above, LTB in bridge applications is most critical during girder erection and slab construction. Although the bending moments during construction are smaller in magnitude than the live load moments in the completed structure, the girders are most susceptible to instability at this stage. During construction, the steel section alone generally supports the entire load and all permanent bracing may not be installed.

In the finished structure, the composite deck provides significant continuous lateral and torsional restraint to the top flange such that LTB is rarely a problem. For simple spans, for which only the top flange is in compression, girders are not prone to LTB. In continuous spans, the stability behavior of continuous girders in the negative moment region (i.e., the bottom flange is in compression) is often questioned by designers.

As discussed by Yura (2001), though, the composite deck not only continuously braces the top flange but also provides additional bracing benefits to the bottom compression flange in these regions, assuming web distortion is adequately considered. With that said, web distortional buckling is more of a concern than LTB

in negative moment regions. Web-distortional buckling, which is not sensitive to unbraced length like the classic LTB solutions, is caused by improperly detailing web stiffeners or neglecting them altogether. Figure F6-18 depicts this type of buckling schematically.

For sections with stocky webs such as rolled beams, web distortion is not a significant issue because the web slenderness ratio is low. In other words, the out-of-plane bending stiffness of the web plate is substantial which precludes any distortional effects from occurring. For plate girders with noncompact or slender webs, which is far more common in bridge applications, web stiffeners must be properly proportioned and detailed to control distortion. Assuming the stiffeners are adequately sized and fabricated to contact the top flange with friction or welds, LTB and/or web distortional buckling is prevented.

Yura (2001) outlines an equation to estimate the distortional capacity of an unstiffened web. However, given that stocky bearing stiffeners are almost always included at the region of maximum negative moment, these effects are typically not an issue. Additionally, the girder bearings themselves provide lateral restraint and some torsional restraint to the bottom compression flange, which further mitigates this problem.

Even with this discussion above, cross-frames are typically provided by designers in negative moment regions to control LTB. The restraint provided from the deck to the bottom flange is often neglected in design as well, as documented in AASHTO Article C6.10.8.2.3. With that in mind, the primary goal of this analytical study was to evaluate the LTB behavior of girders, prismatic and nonprismatic, under various moment gradients that include reverse-curvature bending (i.e., negative moment regions) without consideration of the composite deck.

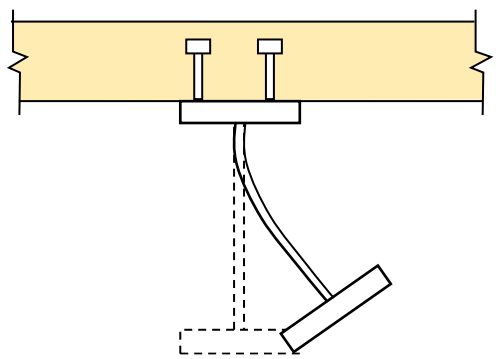

Figure F6-18: Web-distortional buckling of composite girder in negative moment regions (Yura 2001)

Given the complexities of the limit state, most design specifications have adopted simplified, approximate approaches for estimating the LTB resistance of a bridge girder. Classic LTB solutions such as Eq. F6.5 or similar, which are often utilized in design specifications, make use of solutions derived for uniform-moment loading and employ approximate correction factors (C_b) to account for the benefits of moment gradient. The moment gradient factor, C_b, amplifies the LTB resistance with respect to worst-case uniform moment loading to account for the non-uniform distribution of compressive stresses in the critical flange.

Before outlining moment gradient factors, a discussion on the LTB solution for uniform-moment loading is warranted. Many different forms of the classic LTB solution (Timoshenko 1961) are commonly found in design specifications. In AASHTO LRFD, Eq. A6.3.3-8 presents the exact theoretical solution for doubly-symmetric I-sections under uniform moment. Eq. 6.10.8.2.3-8 provides a conservative approximation of the exact theoretical solution by taking the St. Venant torsional constant equal to zero (i.e., take $J = 0$), which is especially reasonable as the web slenderness approaches the noncompact limits. By employing these simplifications, AASHTO Eq. 6.10.8.2.3 provides conservative estimates that inherently consider the following limitations of the classic LTB solution (Eq. F6.5):

1. As stated above, the classic LTB solution is derived for doubly-symmetric sections. In many cases, however, bridge girders are singly-symmetric due to composite construction. Exact, theoretical solutions do exist for singly-symmetric sections that are comparable to Eq. F6.5, but they increase in complexity as shown with the following expressions (Ziemian 2010):

$$M_{cr} = \frac{\pi^2 E I_y}{{L_b}^2}\left\{\frac{\beta_x}{2} + \sqrt{\left(\frac{\beta_x}{2}\right)^2 + \left[\frac{C_w}{I_y} + \frac{GJ}{EI_y}\frac{{L_b}^2}{\pi^2}\right]}\right\} \qquad F6.9$$

$$\beta_x = \frac{1}{I_x}\int_A y(x^2 + y^2)dA - 2y_o \qquad F6.10$$

   where: β_x = coefficient of monosymmetry; I_x = major-axis moment of inertia; x and y = centroidal coordinates; and y_o = distance between the shear center and the centroid. The integration in Eq. F6.10 is performed over the cross-sectional area, A. The remainder of the variables were previously defined with Eq. F6.5. Note that this expression reduces to Eq. F6.5 for doubly-symmetric shapes.

   Although these equations do not appear to be overly complex on the surface, the expression for the monosymmetry parameter is generally not practical for design. Consequently, design specifications typically employ simplified expressions such as AASHTO Eq. 6.10.8.2.3, which have been shown to produce reasonably conservative estimates for singly-symmetric sections when compared to the complex, exact solution presented above.

2. The classic LTB solution does not explicitly consider the limiting effects of web distortion. That is to say, Eq. F6.5 was derived assuming the web remains undistorted (i.e., straight) in the deformed, buckled shape. By employing simplified Eq. 6.10.8.2.3 in AASHTO LRFD, any reductions in buckling capacity due to web flexibility (especially for noncompact and slender webs) are inherently considered by providing conservative approximates.

3. The classic LTB solution was also based on the assumption of mid-height loading. In reality, bridge girders are often loaded along its top flange (e.g. wet concrete deck during construction). Top flange loading has been shown to significantly reduce the LTB capacity when compared to mid-height loading due to the overturning effect; in contrast, loads applied to the bottom flange provide a restoring force to the cross-section that generally increases the capacity.

   Despite its severity, there are several mitigating factors that greatly diminish the impact of top flange loading such that load height effects are often not considered in design (particularly in terms of the established C_b factors). For reference, Helwig et al. (1997) and Ziemian (2010) document these mitigating factors in depth.

4. For a girder with multiple intermediate braces along the length, the warping restraint provided to the critical unbraced segment from adjacent segments of less moment magnitude is typically neglected. Designers can apply refined analysis techniques to quantify the contributions from those adjacent segments, but this practice is not commonly done. Thus, Eq. 6.10.8.2.3 further provides a conservative estimate of the true buckling capacity.

Expressions for C_b factors are often developed computationally by comparing FEA solutions of the following: (i) for the eigenvalue buckling load of an unbraced beam segment when subjected to uniform moment loading ($M_{cr,FEA,UM}$) and (ii) the eigenvalue buckling load of the same beam segment when subjected to a specific moment gradient ($M_{cr,FEA,MG}$). This relationship is expressed mathematically with the following expression:

$$C_{b,FEA} = \frac{M_{cr,FEA,MG}}{M_{cr,FEA,UM}} \qquad F6.11$$

Note that the subscript "FEA" is added to emphasize that the moment gradient factors are based on finite element results. In addition to the moment gradient, these analytically derived solutions are sensitive to several girder and bracing parameters including as span-to-depth ratio, intermediate brace spacing, and monosymmetry.

Given that this procedure can be computationally intensive, most specifications have instead adopted approximate approaches for estimating the C_b factor to further simplify the design process. These approximate approaches, which are generally simplified as a function of only the moment diagram, are intended to produce reasonable estimates of the FEA solutions. Currently, AASHTO and AISC Specifications utilize different formulations to approximate these factors for design, which vary in accuracy and ease-of-use.

The C_b expression in AASHTO (2017) Article 6.10.8.2.3 (Eq. 6.10.8.2.3-7) is based upon a long-standing equation that was included in the AISC Specification up through the first edition of the Load and Resistance Factor Design Specification (1986). The original C_b expression was applicable to beams with no loading between the brace points, resulting in linear moment diagrams. In an effort to make the solution applicable for general conditions, AASHTO enforced several exceptions that can be confusing to interpret and can produce overly conservative estimates in many practical cases. For clarity, the current AASHTO expression is not presented in this appendix.

The current C_b expression in the AISC Specification (2016) first appeared in the second edition of LRFD (1994) and is primarily applicable to doubly-symmetric I-shaped sections and channels. An expression for singly-symmetric I-shaped sections developed by Helwig et al. (1997) is also provided in the AISC Chapter F Commentary. In contrast to AASHTO, the Chapter F Commentary expression is simpler to apply in design and is applicable for singly-symmetric beams with reverse-curvature bending. The equation in full is presented below:

$$C_b = \left[\frac{12.5M_{max}}{2.5M_{max} + 3M_A + 4M_B + 3M_C}\right] R_m \leq 3.0 \qquad F6.12$$

$$R_m = \begin{cases} 0.5 + 2\left(\frac{I_{y,top}}{I_y}\right)^2, & reverse - curvature\ bending \\ 1.0, & single - curvature\ bending \end{cases} \qquad F6.13$$

where: M_{max} = absolute value of the maximum moment in the unbraced segment; and M_A, M_B, M_C = respective absolute values of the quarter-point, midpoint, and three-quarter-point moment in the unbraced segment. $I_{y,top}/I_y$ (or ρ_{top}) = degree of monosymmetry with respect to the top flange; $I_{y,top}$ and I_y are the respective moments of inertia of the top flange and the entire section relative to the axis through the web (i.e., the moment about the minimum principle axis). The degree of monosymmetry describes the relative difference between top and bottom flange sizes in terms of its respective weak-axis moment of inertia.

The portion in the square brackets in Eq. F6.12 is the long-standing moment gradient expression for doubly-symmetric I-shapes and channels that has been included in the AISC Specification since 1994. The R_m term outside the square brackets adjusts the C_b value for singly-symmetric sections subjected to reverse-curvature bending within an unbraced length. The R_m term is binary in nature. It is taken as unity for single-curvature bending and is active for any case with reverse-curvature bending, regardless of the moment gradient shape.

Also note that the AISC C_b expression for singly-symmetric sections (Eq. F6.12) is capped at 3.0, which takes effect for the relatively rare case of high ρ_{top} values (i.e., a much larger top flange than bottom flange). For doubly-symmetric I-shaped girders, ρ_{top} is 0.5 (neglecting the small I_y contribution from the web), and R_m is equal to 1.0.

Past FEA studies have shown that the AISC C_b expression provides reasonable estimates of the LTB capacity of both doubly-symmetric and singly-symmetric sections subjected to a variety of moment gradients (Helwig et al. 1997). However, these previous studies on the accuracy and applicability of the AISC expression were limited to prismatic sections. Thus, Eqs. F6.12 and F6.13 have yet to be evaluated for nonprismatic sections. In fact, little guidance is available on the LTB behavior of nonprismatic sections.

With this in mind, the primary objective of this study was to examine the performance of the AISC C_b expression for nonprismatic beams under various moment gradients that commonly occur in steel bridge applications. Given the complexity of the current expression in AASHTO, the RT examined the AISC expression for possible implementation into AASHTO LRFD.

F6.3.2 Parametric Finite-Element Study

To investigate the LTB behavior of nonprismatic girders, parametric finite element analyses were carried using Abaqus. The following subsections outline different components of the parametric study, ranging from the FEA assumptions to the loading conditions.

F6.3.2.1 Finite-Element Approach

Abaqus was used to develop the 3D girder models and conduct the parametric studies. In general, elastic eigenvalue buckling analyses were performed to determine critical buckling loads for a variety of girders, both prismatic and nonprismatic, and a variety of moment gradients. Girders were modeled with a series of shell elements; for nonprismatic girders (namely girders with stepped flanges), the thickness of the flange shells varied along the length of the girder. In those nonprismatic cases, the flange shells were offset vertically relative to the web shell to maintain the clear height of the web between the inside faces of the top and bottom flanges as traditionally done in practice.

Additionally, web stiffeners were added at end supports and spaced at a distance equal to the girder web depth along the beam length to control local web buckling or web distortion that may affect the LTB response. As outlined in the background section, the focus of the present study was on traditional LTB solutions, for which web distortion is precluded.

Given that bracing was not the primary emphasis of this study, cross-frames were not explicitly modeled as was done in Sections F6.1 and F6.2. Instead, the RT assumed that braces with adequate stiffness and strength were provided such that out-of-plane girder deformations at brace points were negligible. As such, torsional braces were simulated at beam ends by restraining out-of-plane translation at the top and bottom flange-to-web junctions and by permitting the cross-sections to warp. In-plane supports were simulated by preventing vertical (gravity) displacement at one end of the unbraced beam segment and preventing both vertical and longitudinal displacement at the other end. These supports were assigned at mid-height of the section, as illustrated in Figure F6-19.

A mesh size of 2 inches, which resulted in 30 elements along the web depth, was selected based on a mesh sensitivity study. By achieving good agreement between the FEA solutions and the exact theoretical solution given in Eqs. F6.9 and F6.10 (exact solution of doubly- or singly-symmetric sections) for cases with prismatic sections, the selected mesh density and boundary conditions were verified and deemed suitable. An element aspect ratio as close to unity as practical was selected. Figure F6-19 shows an isometric

and cross-section view of the general layout and boundary conditions of the model. Note that the web stiffeners are hidden for clarity.

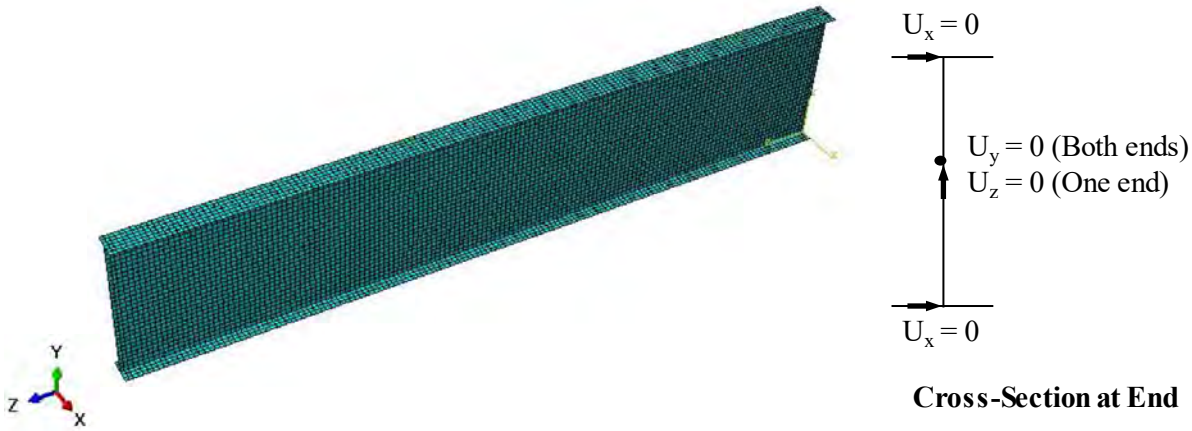

Figure F6-19: General layout and boundary conditions used in the parametric FEA model

Specific intermediate bracing schemes were achieved in Abaqus by modeling only the unbraced segment of interest, unlike the bracing strength and stiffness studies previously documented. This approach was consistent with most design specifications, which conservatively neglect the warping restraint provided by adjacent unbraced segments of lesser internal moment.

By only modeling the critical unbraced segment, uniform moment conditions were achieved with concentrated end moments, and the various moment gradients were achieved with a combination of a uniformly distributed transverse load and end moments. End moments were created by applying a force couple to the top and bottom flanges at each end of the unbraced segment. Rather than applying coupled point loads to the ends of the flanges, effective forces were instead distributed along the width of the respective flange and applied as a line load to minimize localized buckling effects at the application of load. For example, if the effective flange force on a 12-inch wide flange is 1 kip, then a 0.083 kips/inch line load was applied along the flange width.

F6.3.2.2 Ranges of Parameters and Loading Conditions

The variables evaluated as part of the parametric FEA study included: (i) span-to-depth ratio and intermediate bracing scheme, (ii) degree of monosymmetry, (iii) variation in flange transitions (degree of nonprismatic variation), and (iv) moment gradient and span configuration. These four categories of parameters are addressed independently in this subsection herein.

Considering all of the parameters, a total of 32,480 analyses (including uniform moment loading and various moment gradients) were conducted on 14,040 unique prismatic and nonprismatic beams. The intent was not to consider every possible geometry or condition that can possibly occur, but rather focus on practical systems that are most commonly encountered in design.

Span-to-Depth Ratio and Presence of Intermediate Bracing

Span-to-web depth ratios of 15, 20, 25, and 30 were considered, which are representative of values commonly found in steel I-girder bridge design. Within each of the span-to-depth ratios considered, different bracing schemes were also evaluated to study their effect on the LTB behavior. Braces only at the ends ($L_b = L$) were considered as well as cases with intermediate bracing. Intermediate bracing schemes of one-half ($L_b = L/2$) and one-third ($L_b = L/3$) of the span length were considered, which produced unbraced

length-to-depth ratios of {7.5, 10, 12.5, 15} and {5, 6.67, 8.33, 10}, respectively. The cases with larger unbraced lengths are representative of steel girders during the erection process before all permanent bracing is installed. Although less critical for LTB, cases with the smaller brace spacing represent girders during slab or deck casting and in the final constructed state.

Degree of Monosymmetry

As defined previously, the degree of monosymmetry, ρ, describes the weak-axis moment of inertia of the compression flange relative to that of the entire section. The parametric study was conducted with ρ values ranging from 0.1 to 0.9. This range is similar to the limits allowed in AASHTO Article 6.10.2.2 ($0.091 \leq \rho \leq 0.91$). Sections that do not satisfy these limits are essentially T-sections, for which the LTB behavior is difficult to predict computationally due to web distortion and local buckling effects. Consequently, most design specifications recommend a C_b of 1.0 for sections outside of the bounds listed above.

Given that both single- and reverse-curvature bending cases are evaluated and that the compression flange may vary between the top and bottom flanges along the unbraced length, the degree of monosymmetry with respect to the top flange is the adopted notation. As such, ρ_{top} is used, which is consistent with the notation in Helwig et al. (1997) and Eq. F6.13. For practical composite girder applications, ρ_{top} typically ranges from 0.2 to 0.5, for which the size of the top flange is smaller than or equal to the size of the bottom flange. Sections in negative moment regions are often doubly-symmetric (ρ_{top} = 0.5). Although results for ρ_{top} outside of the practical range are presented in this appendix for completeness, the primary focus is intended for sections that occur the most often in practice for which $0.2 \leq \rho_{top} \leq 0.5$.

While tapered web members are sometimes used in the negative moment region of bridge girders, only sections with constant web depth were considered. The distance between the flange centroids was thus maintained at a constant 60 inches, and the web thickness was fixed at 7/8 inch. For all cases, the web slenderness (68.6) satisfied the compact web slenderness limits assuming grade 50 steel as a means to prevent web distortional effects.

The various ρ_{top} values were achieved by adjusting the relative width and/or thickness of the top and bottom flanges. Flange width-to-thickness ratios were selected to satisfy compact slenderness limits in both AISC and AASHTO. Figure F6-20 depicts a typical cross-section used in the FEA studies for $\rho_{top} \leq 0.5$. Note that a section with $\rho_{top} > 0.5$ is similar to its counterpart for $\rho_{top} < 0.5$, except that the flange sizes are reversed.

For nonprismatic beams, the ρ_{top} value in the FEA analyses was often not uniform along the unbraced length. For the sake of clarity, the ρ_{top} values reported in the results subsequently presented correspond to the monosymmetry of the smallest cross-section, or the base section, which is identified as $\rho_{top,base}$. The flange sizes outside of the base section are indicated in the results as multipliers applied to the base section, as discussed next.

Nonprismatic Sections

Three parameters that describe a nonprismatic section (namely stepped flanges) are as follow: (i) variations in flange thickness or width, (ii) location of the transition with respect to the brace points of an unbraced beam, and (iii) number of transitions along an unbraced segment. The RT developed a systematic way to handle these parameters in the FEA study, as outlined hereafter.

For each nonprismatic case considered, the thickness and/or the width of the flanges was varied at discrete locations along the unbraced segment. Relative to the base (smaller) section, flange thicknesses were increased by the following multipliers: {1, 1.25, 1.5, 1.75, 2}. In a similar fashion, flange widths were increased relative to the base section by a different set of multipliers: {1, 1.15, 1.3, 1.5}. To simplify discussions, the increase in flange dimensions (thickness or width) is described as a multiplier to the weak-axis moment of inertia ($I_{y,top}$ or $I_{y,bot}$) of the base section. Thus, the case in which the $I_{y,top}$ multiplier = $I_{y,bot}$ multiplier = 1 represents a prismatic beam. I_y multipliers corresponding to an increased thickness included

1, 1.25, 1.5, 1.75, and 2, while I_y multipliers corresponding to an increased width included 1, 1.52, 2.20, and 3.375 (e.g. $1.5^3 = 3.375$). The largest flange transition considered in the study included an I_y multiplier of 6.75, in which the flange thickness was increased by 2 and the width by 1.5 ($2 * 1.5^3 = 6.75$).

For highly monosymmetric sections in the study for which $\rho_{top,base} \leq 0.2$, applying large I_y multipliers often resulted in flange dimensions that were deemed impractical for typical built-up girder designs. As such, flange and cross-section proportion limits were imposed to filter out these extreme cases. Nonprismatic beam with a resulting flange exceeding three inches in thickness or any unique cross-section for which $\rho_{top} < 0.091$ or $\rho_{top} > 0.91$ (i.e., to satisfy AASHTO Article 6.10.2.2) were filtered from the data presented herein. These limits ensure that the girders evaluated are efficiently designed and could be transported and lifted with conventional shipping and erection procedures during construction.

The location of the flange transitions was also varied to study its effect on the LTB behavior. For a span of length L, transitions at $0.1L$, $0.2L$, $0.3L$, and $0.4L$ (relative to the closest end of the beam) were evaluated. Additionally, cases in which the location of the top flange transition differed from the location of the bottom flange transition were also considered; in these cases, the transitions occurred at some combination of $0.1L$, $0.2L$, $0.3L$, and $0.4L$ of the full span. These cases are depicted schematically in Figure F6-21.

Increased flange sections are typically used in design at locations of maximum positive and negative moment, which are generally a function of the span configuration and boundary conditions. To ensure that the most common cases were considered, three different flange transition schemes were utilized in the study based on three span configurations found in bridge design: (i) simply-supported single spans (abbreviated as S herein), (ii) interior spans of a continuous unit (I), and (iii) end spans of a continuous unit (E). For the simple-span condition, flange transitions were taken as symmetric about the midspan of the beam; for the continuous span cases, transitions were considered in the negative moment regions at the ends of the beam, which is consistent with common design practice. Note that the assumed span arrangement does not impact the boundary conditions in the finite element model; rather, it simply characterizes the flange transition scheme with which it is typically associated.

Lastly, this study evaluated unbraced beam segments with up to four total flange transitions along the unbraced length, resulting in a maximum of three unique cross-sections. Cases with numerous transitions are representative of long-span girders with no intermediate bracing during erection. Cases with fewer transitions are more common, especially as intermediate bracing is added and unbraced lengths are shortened. These different flange transitions schemes are depicted in Figure F6-21.

As an example, a specific case is depicted in Figure F6-20, which illustrates the plate thicknesses used to develop the nonprismatic girder ($\rho_{top,base} = 0.3$) for the simple span case (S) with $I_{y,top}$ and $I_{y,bot}$ multipliers of 1 and 1.5, respectively. The two transitions for this specific example occur at $0.3L$ from each end, resulting in two unique cross-sections along the length: "small" (section A-A) and "large" (section B-B). The different combinations of these parameters are depicted schematically in Figure F6-21. Figure F6-20 and Figure F6-21 are presented to provide the reader with the scope of the parametric study and not to highlight any specific geometry.

Note that a case in which the top flange multiplier exceeds the bottom flange multiplier was not considered, as this is uncommon for composite girder design. The $I_{y,top}$ multiplier was therefore either equal to or less than the $I_{y,bot}$ multiplier for all cases. By varying the bottom flange dimensions relative to the top flange dimensions, it is also apparent that the value of ρ_{top} is no longer constant along an unbraced length, as was demonstrated in the Figure F6-20 example.

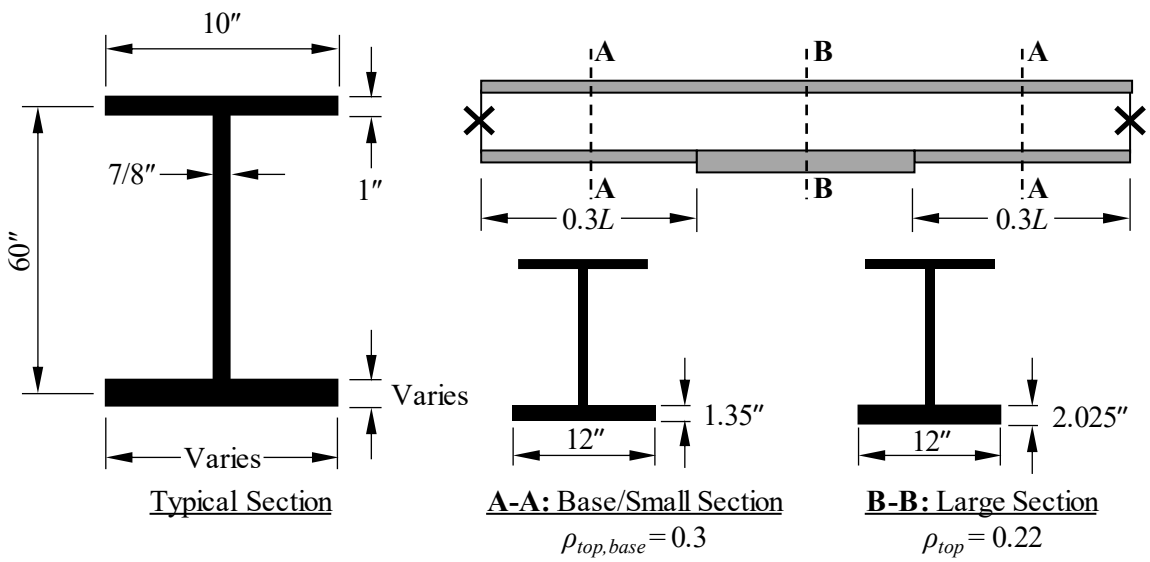

Figure F6-20: Typical cross-section used in the parametric study and an example showing how a simply-supported nonprismatic girder with flange transitions is developed

The flange transitions shown in Figure F6-21 were also maintained for the different intermediate bracing schemes. For purposes of clarification, an example is presented in Figure F6-22 for the simple span case, where the transitions occur at 0.3L from the beam ends (as noted earlier, transitions were also placed at 0.1L, 0.2L, and 0.4L from the ends). Figure F6-22 shows the same beam with zero, one, and two intermediate braces. Note that for the two-brace case, the transition at 0.3L occurs beyond the limits of the unbraced segment considered; therefore, a prismatic section would be evaluated for this specific case. Although not presented, a similar layout is considered for all transition locations and for all the continuous, interior span (I) and continuous, end span cases (E).

			Span Configuration		
			Simple Span	Continuous, Interior Span	Continuous, End Span
Flange Transition	1 C. Sect.[a]	Prismatic $I_{y,top}$ Mult. = 1 $I_{y,bot}$ Mult. = 1	Section 1 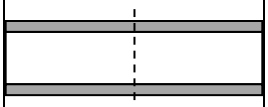	Section 1 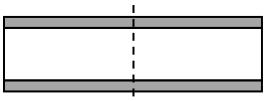	Section 1 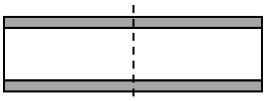
	Two Cross-Sections[a]	$I_{y,top,2}$ Mult. = 1 $I_{y,bot,2}$ Mult. = Varies[b]	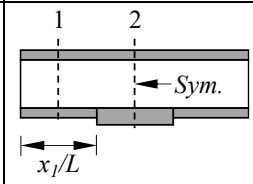	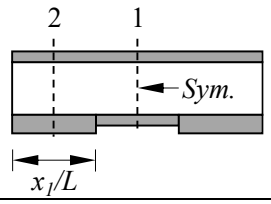	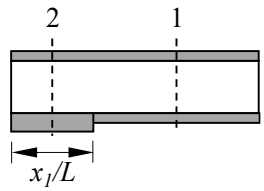
		$I_{y,top,2}$ Mult. = Varies[b] $I_{y,bot,2}$ Mult. = Varies[b]	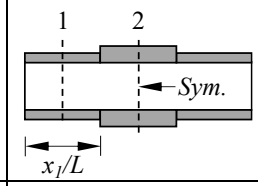	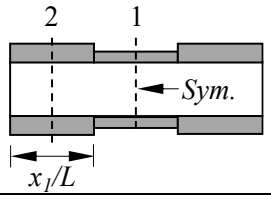	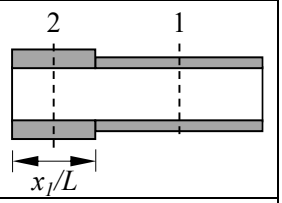
	Three Cross-Sections[a]	$I_{y,top,2}$ Mult. = 1 $I_{y,top,3}$ Mult. = Varies[b] $I_{y,bot,2}$ Mult. = Varies[b] $I_{y,bot,3}$ Mult. = $I_{y,bot,2}$ Mult.	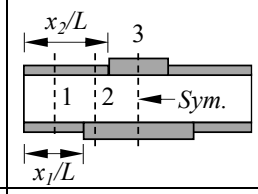	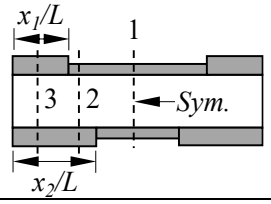	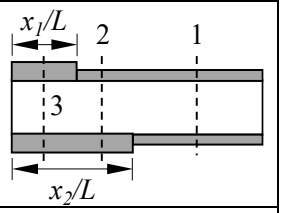
		$I_{y,top,2}$ Mult. = 1 $I_{y,top,3}$ Mult. = 1 $I_{y,bot,2}$ Mult. = Varies[c] $I_{y,bot,3}$ Mult. = Varies[c]	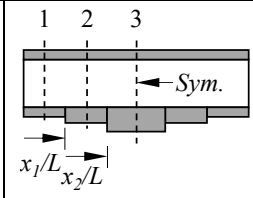	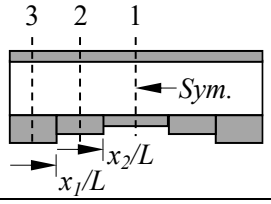	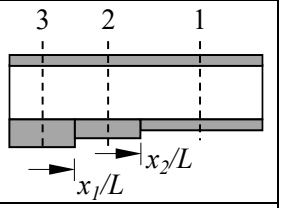
		$I_{y,top,2}$ Mult. = Varies[c] $I_{y,top,3}$ Mult. = Varies[c] $I_{y,bot,2}$ Mult. = Varies[c] $I_{y,bot,3}$ Mult. = Varies[c]	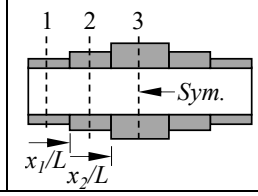	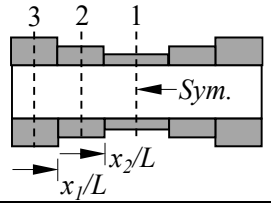	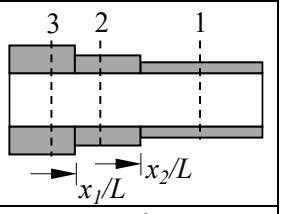

Note: Abbreviations: "Mult." = multiplier, "C. Sect." = cross-sections, and "Sym." = symmetric
[a] Represents the number of unique cross-sections along the unbraced length; x_i/L values vary and are either 0.1L, 0.2L, 0.3L, or 0.4L as previously outlined.
[b] For unbraced lengths with two cross-sections, "varies" indicates that the flange dimensions are increased within the transition region as previously outlined.
[c] For unbraced lengths with three cross-sections, "varies" indicates that the flange dimensions are increased at each new transition.

Figure F6-21: Flange transitions considered in the parametric study

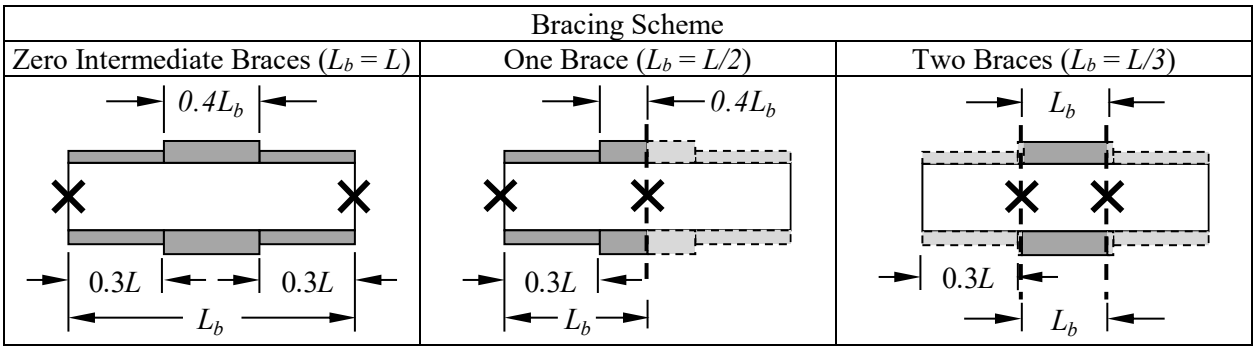

Figure F6-22: Flange transition cases for simply-supported condition with different intermediate bracing schemes

Moment Gradient and Span Configuration

Based upon the various bracing schemes introduced, nine different moment gradients along with the uniform moment case were evaluated. The nine cases were considered the most representative for bridges throughout the construction and service life that maximize the impact of moment gradient and nonprismatic section properties. Figure F6-23 presents these cases graphically.

The nine moment gradient cases categorize girder types into the same span configurations previously outlined: simply-supported single span (S), interior span of a continuous unit (I), and end span of a continuous unit (E). These three support conditions represent the most common span arrangements for steel girders used in bridges. The moment gradients of a typical interior span configuration are represented approximately by a fixed-fixed beam, while the corresponding moment gradients in end-span configurations are represented approximately by a propped cantilever. The fixed-fixed and propped cantilever conditions are extreme cases since the flexibility of a continuous beam will result in lower negative moment values and higher positive moment values; however, the resulting moment gradients for these cases are reasonable approximations of the corresponding conditions. Both single-curvature and reverse-curvature bending cases are included.

As indicated by the moment diagrams in Figure F6-23, only uniformly distributed loads at mid-height were considered. Major gravity loads on girders during construction are uniformly distributed (steel and wet concrete self-weight), and concentrated loads are much less significant. In the final constructed stage, girders are typically designed for a moment envelope (due to patterned loads for buildings or moving loads for bridges), which generally follow shapes similar to the diagrams in Figure F6-23. As such, moment gradients resulting from large concentrated forces were considered less important for most applications and were thus excluded from the parametric study.

Additionally, only cases with two or fewer intermediate braces were considered in the investigation. Although longer span systems generally have more than two intermediate braces, the resulting effects of moment gradient for these cases is greatly reduced. As intermediate braces are added and the unbraced length of beams decrease, the moment diagram approaches the case of uniform moment (i.e., C_b factor tends to unity), and the LTB stability limit state becomes less critical in lieu of the yielding limit state. The most critical bracing conditions for moment gradient on nonprismatic sections generally range from zero intermediate braces to two intermediate braces. Despite neglecting cases with three or more intermediate braces, the expressions for the C_b factors capture the trends as additional braces are added and are therefore directly applicable in these cases.

Moment gradients are abbreviated with an alphanumeric identifier, where the letter signifies the span configuration (as documented previously) and the integer signifies the number of intermediate braces (0 for

zero intermediate braces, 1 for one intermediate brace, 2 for two intermediate braces). This nomenclature is illustrated in Figure F6-23.

With these factors in mind, it is important to highlight where each of these simple moment gradients would occur during the construction and service life of a girder. Cases S-0, I-0, and E-0, in which no intermediate braces are used, represent worst-case conditions during steel erection where girder self-weight is the primary loading. These cases represent the first girder erected in a given span. Although temporary bracing can be added at the discretion of the erector, the stability of the first girder with no intermediate bracing will always be the first critical case to be evaluated. The impact of nonprismatic section properties on the behavior will also generally be the most pronounced for these cases.

The corresponding cases with one or two intermediate braces largely represent a girder during slab or deck casting or in its final constructed state, but only the more critical unbraced segments were considered. As mentioned previously, LTB is rarely a problem once the slab cures since the girders are continuously restrained laterally and torsionally by the concrete deck and other permanent bracing. The one condition in which questions are sometimes raised regarding LTB in the finished structure is the negative moment region around interior supports where compression is present in the bottom flange. Cases I-2 and E-2 specifically investigate this condition. For these special cases, the continuous lateral and torsional restraint provided by the deck to the top flange in these cases was conservatively neglected. In summary, the nine moment gradient cases considered are not exhaustive but encompass the most common loading conditions on unbraced girder segments that are likely critical for girder stability.

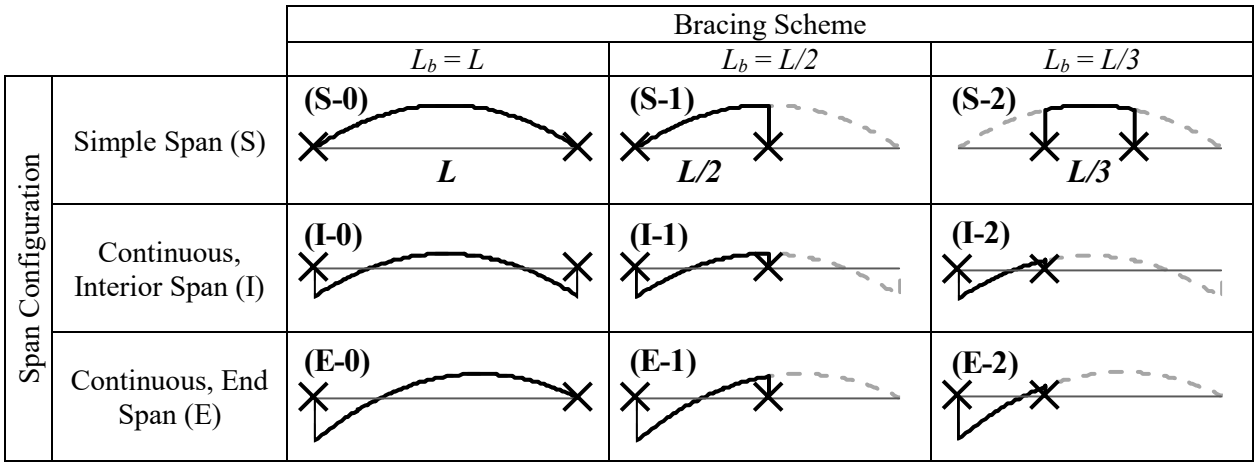

Figure F6-23: Moment gradients considered in the parametric study

As discussed in Section F6.3.2.1, various moment gradient conditions were achieved in the 3D model with a combination of a uniformly distributed transverse load and end moments, given that only the unbraced segment of interest is modeled. For reference, Figure F6-24 demonstrates how moment gradient effects are simulated on an unbraced segment of a larger bridge girder through an example. The applied loading for moment gradient cases S-0, S-1, and S-2 are presented.

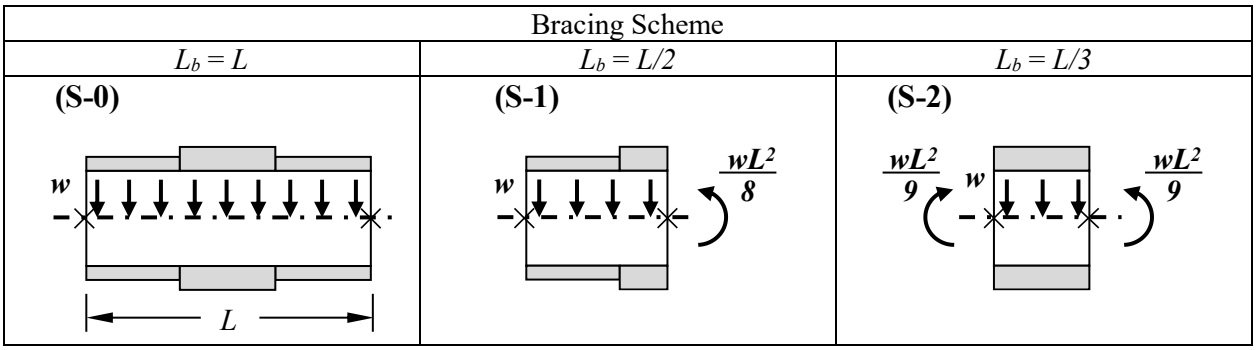

Figure F6-24: Applied loading scheme for simply-supported condition with different intermediate bracing schemes

F6.3.2.3 Steps in Parametric Study

Once the RT settled on the modeling parameters outlined above, the next step was to develop an analytical testing procedure to determine the effects of moment gradient on the LTB behavior of nonprismatic girders. The process involved two distinct analyses in Abaqus, which are summarized below. Note that these three steps were performed for every unique beam section (prismatic and nonprismatic) and bracing scheme considered in the parametric study.

1. **Conduct an eigenvalue buckling analysis on the beam of interest subjected to uniform-moment loading**. In this analysis, the baseline buckling behavior is established for the prismatic or nonprismatic beam at hand (i.e., $M_{cr,FEA,UM}$ in Eq. F6.11). Given that uniform-moment loading represents the worst-case scenario for LTB, the critical buckling load is smaller than that determined in the next step.
2. **Conduct an eigenvalue buckling analysis on the same beam subjected to a moment gradient**. Step 1 is effectively repeated, except that now a moment gradient is applied. The resulting buckling capacity ($M_{cr,FEA,MG}$) is derived. This process is then repeated for different variations of the moment gradients outlined previously.
3. **Compute the analytically derived $C_{b,FEA}$ factor (Eq. F6.11) and compare to the AISC C_b expression (Eqs. F6.12 and F6.13)**. In this final stage, the accuracy of the AISC moment gradient factor with respect to nonprismatic beams is evaluated. If good agreement is observed between the analytical and simplified hand solutions, then this approach is suitable for implementation into AASHTO LRFD.

   For prismatic sections in single-curvature bending, $C_{b,FEA}$ need only be checked at the location of maximum moment in the compression flange. For singly-symmetric, nonprismatic sections with reverse-curvature bending, the calculation of $C_{b,FEA}$ involves several checks depending on the region of the beam that controls the LTB. Because multiple regions of the beam might be subjected to compression and variations in the flange size, the moments corresponding to the critical buckling load in all unique compression flanges are checked against the uniform moment case ($M_{cr,FEA,UM}$), which must also be evaluated for two cases: the top flange in compression and the bottom flange in compression.

   In comparing the FEA solution using F6.11 and the C_b design solution using Eqs. F6.12 and F6.13, the ρ_{top} term in Eq. F6.13 was taken as $\rho_{top,base}$ for nonprismatic girders. As stated earlier, the smaller section is referred to as the "base section" and is used in the calculation of $\rho_{top,base}$. Unless noted otherwise, the degree of monosymmetry on the x-axis was established for $\rho_{top,base}$ for all subsequent graphs.

From this procedure, the RT obtained data that characterizes the LTB behavior of nonprismatic bridge girders. These results are presented in subsequent sections.

F6.3.3 Pertinent Results

For all combinations of variables in the parametric study, critical buckling loads under uniform moment loading and various moment gradients were determined using Abaqus output. Eq. F6.11 was used to compute $C_{b,FEA}$, and comparisons were made with Eqs. F6.12 and F6.13, the AISC C_b expression. This is the procedure that was previously outlined in Section F6.3.2.3. As a starting point, Figure F6-25 through Figure F6-27 show comparisons of AISC C_b expression with the FEA solutions for various degrees of monosymmetry, flange transitions, intermediate bracing schemes, and moment gradients.

Over 18,000 elastic buckling analyses were conducted as part of this moment gradient study. For clarity, only specific cases are graphed at first to demonstrate the basic behavior; however, each presented case is representative of the full set of results. The intent of the figures is to illustrate the relative impact of each variable on the moment gradient factor. This was accomplished by varying one parameter while holding the others constant for each figure.

Figure F6-25 varies the span-to-depth ratio and holds the I_y multiplier constant at {1,1} (i.e., the beams are prismatic); the transition location is not applicable since only prismatic beams are considered. In contrast, Figure F6-26 varies the I_y multiplier and holds the respective L/h ratio and transition location constant at 15 and $0.3L$. Note that the I_y multiplier cases plotted include a prismatic section {1,1}, a section in which both flange thicknesses are increased {1.75, 1.75}, and a section in which just the bottom flange width is increased {1, 2.2}. Figure F6-27 varies the transition location and holds the respective L/h ratio and I_y multiplier constant at 15 and {1, 2.2}. For Figure F6-25, only moment gradients I-0 and E-0 are presented. For Figure F6-26 and Figure F6-27, moment gradients S-0, S-1, I-0, I-1, E-0, and E-1 are presented.

In general, it is evident that the AISC C_b equation follows the trends well and provides reasonable and conservative approximations of the FEA results for the majority of the cases. The level of conservatism depends on the specific set of parameters, particularly for cases in which $\rho_{top,base} > 0.8$ and the AISC equation is capped at 3.0. However, even for large unbraced lengths, a C_b of 3.0 will often result in a capacity close to or larger than the yield moment of the section, M_y (or plastic moment M_p); thus, the level of conservatism for higher values of $\rho_{top,base}$ generally has no impact on practical problems since the limit state of yielding will almost always control over LTB. In addition, sections with a degree of monosymmetry greater than 0.5 are uncommon in composite girder design, as previously noted.

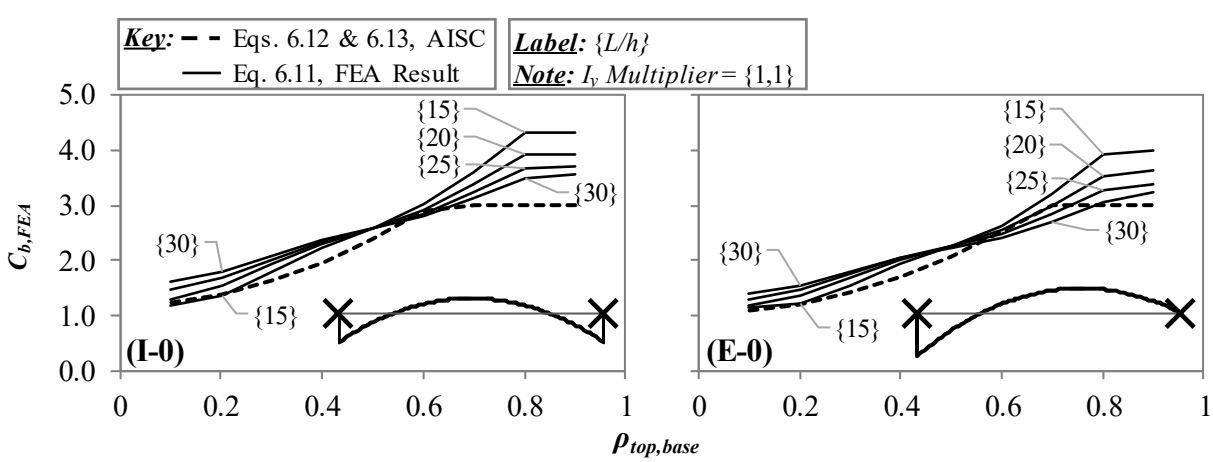

Figure F6-25: FEA results compared to the AISC approximate solution (Eqs. F6.12 and F6.13) for various span-to-depth ratios and moment gradient cases I-0 and E-0

Trends observed from Figure F6-25, in which the L/h ratios are varied, are as follows:

- $C_{b,FEA}$ varies slightly with the L/h ratio, especially for $\rho_{top,base} > 0.5$. In these rare cases, however, the limit state of yielding will often govern over the LTB resistance as modified by a high moment gradient factor.
- For $\rho_{top,base} < 0.5$, girders with $L/h = 15$ result in slightly lower moment gradient factors than girders with $L/h = 30$. Thus, a smaller span-to-depth ratio (i.e., deeper girder for a given span length) is generally more critical (i.e., lower $C_{b,FEA}$) for practical values of $\rho_{top,base}$. Despite the smaller moment gradient effects, it is worth noting that beams with lower L/h ratios will often have higher buckling capacities due to the shortened unbraced lengths than an equivalent beam with a higher L/h ratio. In any case, Eqs. F6.12 and F6.13 provide a reasonable approximation of the finite element solutions for $\rho_{top,base} < 0.5$.

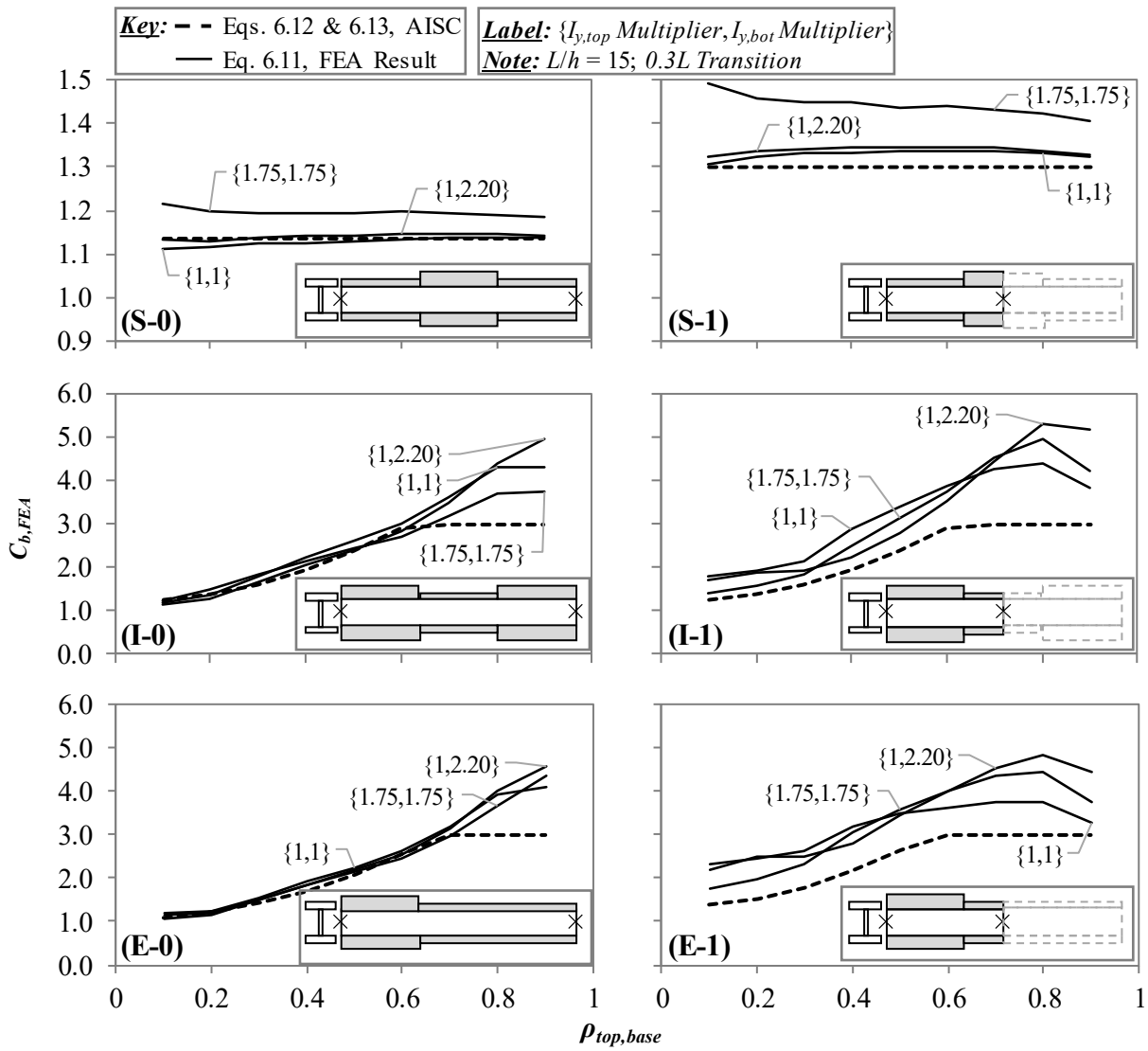

Figure F6-26: FEA results compared to the AISC approximate solution (Eqs. F6.12 and F6.13) for various I_y multipliers and moment gradient cases S-0, S-1, I-0, I-1, E-0, and E-1

Trends observed from Figure F6-26, in which the I_y multipliers are varied, are as follows:

- When compared to prismatic sections with I_y multipliers of {1,1}, highly nonprismatic sections (either increased flange widths or thicknesses) have an effect on $C_{b,FEA}$, but the trend is not consistent and depends largely on the moment gradient.
- For $\rho_{top,base}$ < 0.5, nonprismatic sections generally result in lower $C_{b,FEA}$ values. The AISC C_b expression generally has good agreement with the finite element solutions.

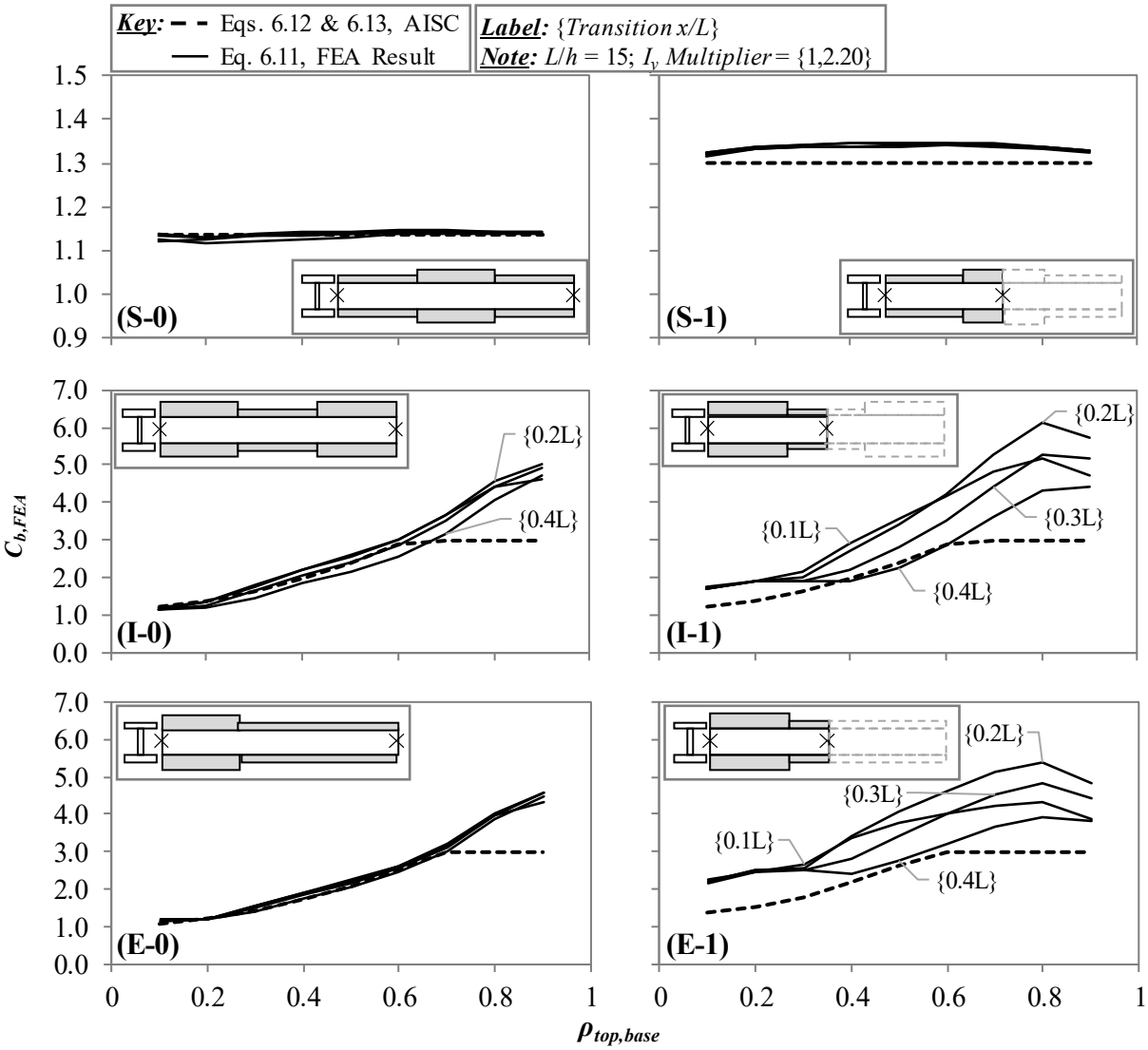

Figure F6-27: FEA results compared to the AISC approximate solution (Eqs. F6.12 and F6.13) for various transition locations and moment gradient cases S-0, S-1, I-0, I-1, E-0, and E-1

Trends observed from Figure F6-27, in which the transition locations are varied, are as follows:

- The location of the transition region either has little-to-no effect on the moment gradient factors (e.g. moment gradient case S-0) or has a substantial effect (e.g. moment gradient case E-1).
- There are a few instances in which the AISC expression is unconservative compared to the FEA solution by a small amount, specifically when the transition is very close to the brace point (e.g.

0.4L transition and moment gradient case I-1). In general though, Eqs. F6.12 and F6.13 provide a reasonable approximation for C_b for these complex geometries.

Figure F6-28 presents special cases in which the moment gradient is steep and includes a small portion of reverse-curvature bending, which is a common condition in the negative moment region of a composite, continuous girder. These special cases correspond to moment gradient cases I-2 and E-2, in which two intermediate braces are added to the full beam and $L_b = L/3$. The bottom flange is primarily in compression except for the portion of the unbraced length near the intermediate brace location. The ratio of the smaller end moment to the larger end moment (M_{small}/M_{large}) is -0.33 and -0.22, respectively, where M_{small} and M_{large} are determined independently of the sign (e.g. for end moments of -1000 kip-in and +500 kip-in, M_{small} is taken as +500 kip-in and M_{large} as -1000 kip-in). Additionally, the respective inflection point is within 0.33L_b and 0.25L_b of the brace point with end moment M_{small} for these cases (that distance is defined as x_{inf} herein). In contrast, the M_{small}/M_{large} ratios are -0.5 for cases I-1 and E-1, and the respective inflection points for the same cases are 0.56L_b and 0.5L_b from the brace point with M_{small}.

For Figure F6-28, the most important aspect in the AISC expression is the use of the R_m factor. The figure includes a comparison of the finite element solution with two forms of Eq. F6.12: with the R_m term and without the R_m term. The R_m factor (Eq. F6.13) is limited in that it becomes an active term for any and all reverse-curvature bending, even for cases in which the inflection point is close to the brace point and the moment is relatively small at the end closest to the inflection point. Because of this, Eq. F6.13 does not capture the behavior well for these special cases due to the inclusion of the R_m term. Instead, better correlation with the $C_{b,FEA}$ values are provided when the R_m term is neglected.

Rather than presenting all variables as in Figure F6-25 through Figure F6-27, Figure F6-28 varies the transition location and holds the respective L/h ratio and I_y multiplier constant at 15 and {1.75, 1.75}, which represent conditions in which the AISC expression was the least conservative from the cases graphed in Figure F6-25 through Figure F6-27.

It is evident from Figure F6-28 that, when the R_m term is included, Eq. F6.12 is relatively conservative for $\rho_{top,base} < 0.5$ and potentially unconservative for $\rho_{top,base} > 0.6$ as the inflection point becomes closer to the nearest brace point. Conversely, when the R_m term is neglected, Eq. F6.12 provides more accurate estimates for all practical values of $\rho_{top,base}$.

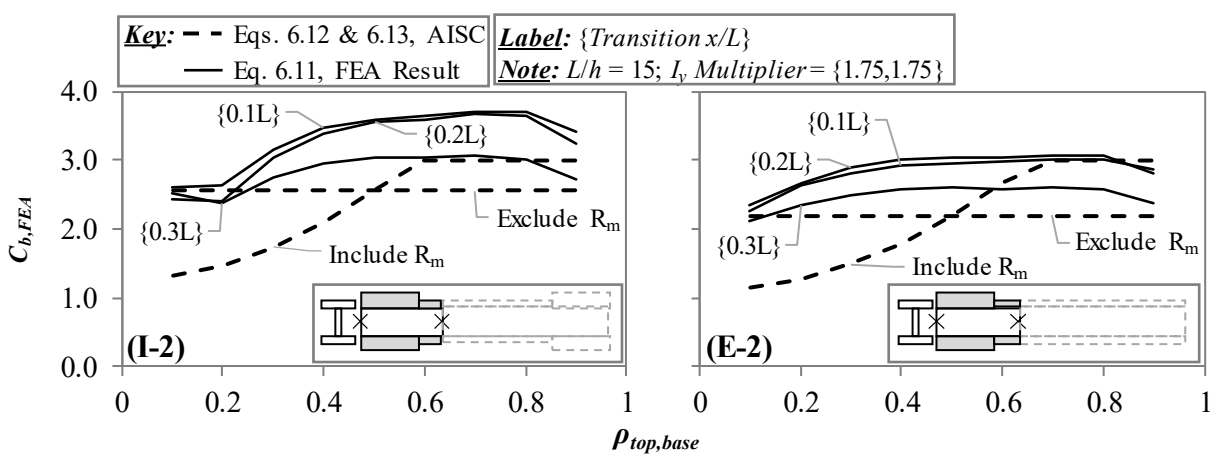

Figure F6-28: FEA results compared to the AISC approximate solution (Eqs. F6.12 and F6.13) for various transition locations and moment gradient cases I-2 and E-2

From Figure F6-26 through Figure F6-28, there is a noted transition in behavior as the inflection point moves closer to the brace point with the smaller end moment, M_{small}. For cases with significant reverse-

curvature bending (i.e., the inflection point is near the midpoint of the unbraced segment or there is more than one inflection point), a positive correlation between moment gradient effects and degree of monosymmetry (ρ_{top}) is observed, and R_m should be included (Figure F6-26 and Figure F6-27). For cases with slight reverse curvature (i.e., the inflection point is close to the brace point), ρ_{top} has less impact on the moment gradient effects, and R_m should be neglected (Figure F6-28).

The results presented thus far consisted of select results that are representative of the full data set. In total, over 18,000 cases of unique moment gradients and girder geometries were considered in the parametric study. Before presenting the full range of data related to nonprismatic geometries, it is worthwhile to focus on the behavior of prismatic beams subjected to different moment gradients, the case for which Eqs. F6.12 and F6.13 were originally developed. Figure F6-29 presents the FEA solutions normalized by the approximations determined from Eq. F6.12; these results are graphed as a function of ρ_{top}.

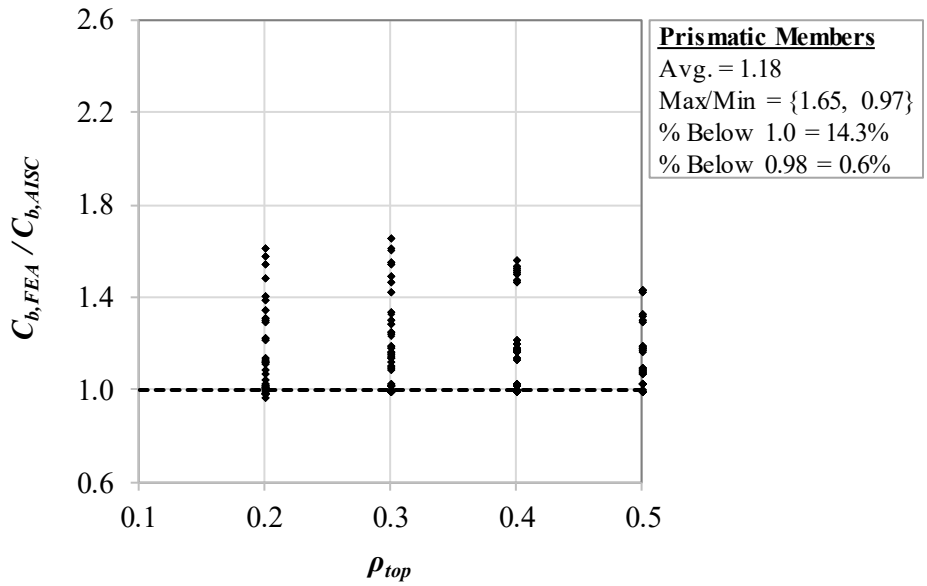

Figure F6-29: Evaluating the accuracy of Eqs. F6.12 and F6.13 for all prismatic beams in the parametric study

Recall that the cases with ρ_{top} = 0.5 correspond to doubly-symmetric sections, and Eq. F6.12 reduces to the long-standing C_b expression in the main body of AISC (2016). From Figure F6-29, the AISC C_b expression in this case varies from essentially exact to a value that is approximately 65% conservative. The cases that are over 40% conservative correspond to reverse-curvature bending where the AISC expression generally provides a value above 2.0, and the FEA solution is even larger. When the critical LTB resistance is amplified by larger C_b values, yielding generally governs over LTB.

Considering the range of moment gradients and bracing schemes evaluated on prismatic sections in this study, Eqs. F6.12 and F6.13 were within 18% of the FEA solution on average. Despite having 14% of the cases less than unity, the lowest ratio observed was 0.97. While the value of 1.0 is the perceived division between "conservative" and "unconservative" approximations produced by Eq. F6.12, it is not uncommon to obtain FEA solutions up to 2% lower than the theoretical buckling solution for uniform moment loading. Therefore, the percent below 1.0 and 0.98 (or the "percent unconservative") are both provided in the graph for reference. Considering the 0.98 limit, only 0.6% of the results for prismatic sections were deemed unconservative.

While the results in Figure F6-29 indicate the accuracy of Eq. F6.12 for prismatic sections, Figure F6-30 summarizes the results for the full data set covering the nine different moment gradient cases and the various nonprismatic beam parameters outlined previously. Again, the ratio of $C_{b,FEA}/C_{b,AISC}$ is graphed as a function of $\rho_{top,eff}$, which is the degree of monosymmetry of the length-weighted effective section. Similar to Figure F6-29, the level of conservatism provided by Eqs. F6.12 and F6.13 is evaluated relative to 1.0 and 0.98 in Figure F6-30. The results presented in Figure F6-30 reflect the removal of the R_m term for moment gradient cases I-2 and E-2 and consider only practical cases in which $0.2 \leq \rho_{top,base} \leq 0.5$.

Within this practical set of conditions, there were several outliers (less than 1% of all data points) observed in which the AISC expression produced significantly unconservative estimates of the FEA solution (i.e., $C_{b,FEA}/C_{b,AISC}$ ratio between 0.6 and 0.9). Those few cases correspond to highly-monosymmetric, nonprismatic beams subjected to reverse-curvature bending, where the "large" section comprised the majority of the unbraced length. These conditions represent an extreme limit of the parameters considered in the study. Given the increased unlikelihood of a beam meeting those exact geometric and loading specifications, these special cases were filtered from Figure F6-30. However, to maintain validity of the procedure and avoid potential unconservativism, limits are imposed to restrict use of the AISC C_b expression for these extreme conditions.

For unbraced beam segments under reverse-curvature bending for which $0.25 \leq \rho_{top,eff} \leq 0.35$ and $x_{small} \leq 0.20$, the designer shall limit I_y multipliers to 3.0 or less. For more extreme cases where $\rho_{top,eff} < 0.25$ and $x_{small} \leq 0.20$, the I_y multiplier shall be limited to a maximum of 2.0. In total, nearly 7,200 prismatic and nonprismatic beams (of the over 18,000 evaluated) satisfied the limits outlined above and are plotted herein.

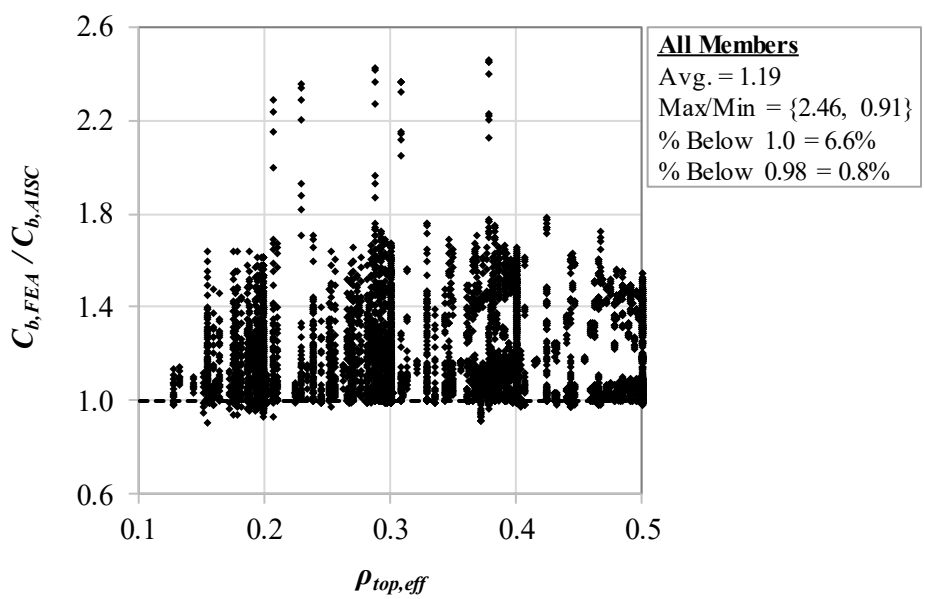

Figure F6-30: Evaluating the accuracy of Eqs. F6.12 and F6.13 for all nonprismatic beams in the parametric study

Although Figure F6-30 show outliers up to 146% conservative, it is clear that the AISC C_b expression provides reasonably conservative and reliable estimates of the FEA-based solutions, which include complex conditions such as moment gradient, monosymmetry, and nonprismatic sections. The range of accuracy between Eqs. F6.12 and F6.13 and the FEA solutions for nonprismatic sections is very similar to the results for prismatic sections. The conservative cases in which the $C_{b,FEA}$ /$C_{b,AISC}$ ratio exceeded 1.8 corresponded to highly monosymmetric, nonprismatic beams subjected to moment gradient cases E-2 and I-2. On

average, Eq. F6.12 provided an estimate that was 19% conservative compared to the FEA-based moment gradient factor. With the previously discussed limits imposed, Eq. F6.12 produced an unconservative estimate for only 0.8% of the nonprismatic beam conditions studied (using 0.98 as the threshold).

The few cases in Figure F6-30 in which an unconservative value was produced correspond to highly-monosymmetric, nonprismatic beams in which I_y multipliers in excess of 3 were considered and the "large" section generally comprised the majority of the unbraced length. The most severe unconservative estimates occurred for moment gradient case I-1. The cases in which the $C_{b,FEA}$ /$C_{b,AISC}$ ratio exceeded 1.8 corresponded to highly monosymmetric, nonprismatic beams subjected to moment gradient cases E-2 and I-2.

In general, the AISC C_b expression is simple to implement in practice and was shown to provide reasonable estimates of the buckling solution for complex singly-symmetric and nonprismatic girders subjected to single- or reverse-curvature bending. For girder sections within practical values of ρ_{top}, these approximate solutions produce estimates on the order of 0-30% conservative on average.

However, based upon the comparisons to FEA solutions, the RT recommends slight modifications to the R_m factor given in Eqs. F6.12 and F6.13. The current approach in AISC applies the R_m factor for any reverse-curvature bending and neglects the factor for single-curvature bending. The RT proposes that, in addition to single-curvature bending, the R_m factor should also be neglected for cases of reverse-curvature bending where x_{inf} (the distance between the inflection point and the braced end with the smallest end moment, M_{small}) is less than $0.375L_b$ and M_{small}/M_{large} ranges from 0 to -0.5. It is important to note that both criteria must be satisfied to neglect the term. By setting the upper limit on M_{small}/M_{large} equal to zero, it precludes the use of R_m on moment gradients with two inflection points. The moment gradients corresponding to these proposed changes are shown schematically in Figure F6-31.

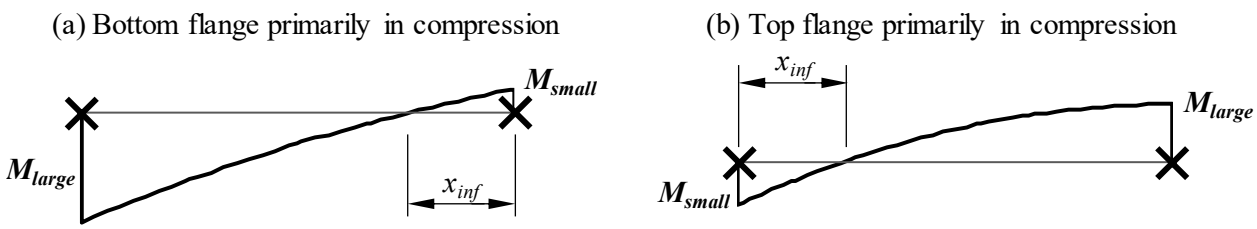

Figure F6-31: Schematic of special moment gradient cases in which R_m term requires modification

Therefore, the AISC C_b expression presented in Eq. F6.12 remains unchanged and is repeated in Eq. F6.14. The R_m term from Eq. F6.13, however, is modified to accommodate the aforementioned rules, as shown in Eq. F6.15.

$$C_b = \left[\frac{12.5M_{max}}{2.5M_{max} + 3M_A + 4M_B + 3M_C}\right] R_m \leq 3.0 \qquad F6.14$$

$$R_m = \begin{cases} 0.5 + 2\left(\rho_{top,base}\right)^2, & otherwise \\ 1.0, & if \begin{cases} single - curvature\ bending \\ -1/2 < M_{small}/M_{large} < 0;\ x_{inf} \leq 3L_b/8 \end{cases} \end{cases} \qquad F6.15$$

Note that the $I_{y,top}/I_y$ (or ρ_{top}) term in Eq. F6.13 has been modified to $\rho_{top,base}$ here, as was previously discussed. This slight adjustment makes the R_m factor applicable to all general prismatic or nonprismatic sections. It should be noted that Eq. F6.15 still exhibits a potential discontinuity in the predicted buckling response, particularly for singly-symmetric beams subjected to moment gradients with an inflection point at or near $0.375L_b$ from the brace point. In that respect, the current approach (Eq. F6.13) and the proposed approach (Eq. F6.15) are similar. However, the proposed expression improves upon and corrects the most obvious limitations of Eq. F6.13 to provide conservative estimates for the most common moment gradient cases. A solution that eliminates the discontinuity would undoubtedly increase in complexity compared to Eq. F6.15. Due to its simplicity, the RT believe Eqs. F6.14 and F6.15 represent the preferred methodology.

F6.4 Major Outcomes

Based on the results of the Stability Study presented in the preceding subsections, there a several conclusions that can be drawn with respect to the bracing requirements of cross-frames and the LTB behavior of nonprismatic girders:

- In terms of implementation into AASHTO LRFD, the RT determined that the torsional brace strength requirements from the 14th Edition of AISC (2010) are more appropriate than the current 15th Edition (2016). The 15th Edition, which requires a design brace moment of 2% of the maximum girder moment, was shown to significantly underpredict the required brace moment. In contrast, the 14th Edition version of the strength requirements is a function of the bracing layout and moment gradient factor. The proposed expression was provided in Eq. F6.8 above.
- Historically, design specifications have required engineers to provide torsional brace stiffness equivalent to twice the ideal stiffness. This rule of thumb was developed by Winter (1960) and was largely validated for columns rather than beams. Through FEA parametric studies, the RT concluded that providing three times the ideal stiffness better limits girder deformations and cross-frame forces at critical buckling loads. A proposed modification to the current AISC approach was therefore provided in Eq. F6.7.
- Given the complexities and limitations of the current C_b expression in AASHTO LRFD, the RT determined that the AISC C_b expression performs quite well for nonprismatic beams, particularly under reverse-curvature bending. The RT recommends that the AISC approach be adopted into AASHTO LRFD with one notable modification to the R_m term, which accounts for reverse-curvature bending cases. The proposed equations are provided in Eq. F6.14 and F6.15.

The RT drafted proposed modifications to AASHTO LRFD with regards to torsional stability bracing and LTB behavior based on the findings listed above. Refer to the main body of the report and Appendix A for the proposed language and commentary.

References

American Association of State Highway and Transportation Officials. 2014. *G13.1 Guidelines for Steel Girder Bridge Analysis.* 2nd.

—. 2017. *LRFD Bridge Design Specifications.* 8th Ed. Washington, D.C.

—. 2020. *LRFD Bridge Design Specifications.* 9th. Washington, D.C.

American Institute of Steel Construction. 1986. *Load and Resistance Factor Design Specification for Structural Steel Buildings.* Chicago, IL.

—. 2010. *Specification for Structural Steel Buildings - 14th Edition.* Chicago, IL.

—. 2016. *Specification for Structural Steel Buildings - 15th Edition.* Chicago, IL.

American Society of Testing and Materials. 2017. "Standard Practices for Cycle Counting in Fatigue Analysis." ASTM E1049-85.

Barth, K. 2015. *Steel Bridge Design Handbook Design Example 2A: Two-Span Continuous Straight Composite Steel I-Girder Bridge.* Washington, DC: Federal Highway Administration.

Battistini, A., W. Wang, S. Donahue, T. Helwig, M. Engelhardt, and K. Frank. 2013. *Improved Cross Frame Details.* TxDOT 0-6564 Final Report, Texas Department of Transportation.

Battistini, A., W. Wang, T. Helwig, M. Engelhardt, and K. Frank. 2016. "Stiffness Behavior of Cross Frame in Steel Bridge Systems." *Journal of Bridge Engineering* 21 (6).

Battistini, A., W. Wang, T. Helwig, M. Engelhardt, and K. Frank. 2016. "Stiffness Behavior of Cross Frame in Steel Bridge Systems." *Journal of Bridge Engineering* (American Society of Civil Engineers) 21 (6).

Connor, R., and J. Fisher. 2006. "Identifying Effective and Ineffective Retrofits for Distortion Fatigue Cracking in Steel Bridges Using Field Instrumentation." *Journal of Bridge Engineering* (American Society of Civil Engineers) 11 (6): 745-752.

Helwig, T., and J. Yura. 2015. *Steel Bridge Design Handbook: Bracing System Design.* Technical Report, Washington, D.C.: Federal Highway Administration.

Helwig, T., K. Frank, and J. Yura. 1997. "Lateral-Torsional Buckling of Singly Symmetric I-Beams." *Jounral of Structural Engineering* 123 (9): 1172-1179.

Liu, Y., and T. Helwig. 2020. "Torsional Brace Strength Requirements for Steel I-Girder Systems." *Journal of Bridge Engineering* (American Society of Civil Engineers) 146 (1): 1-11.

Liu, Y., and T. Helwig. 2020. "Torsional Bracing Stiffness Requirements for Steel I-Girder Systems." *Journal of Structural Engineering* (American Society of Civil Engineers).

McDonald, G., and K. Frank. 2009. *The Fatigue Performance of Angle Cross-Frame Members in Bridges.* MS Thesis, Austin, Texas: The University of Texas at Austin.

Miner, M. 1945. "Cumulative Damage in Fatigue." *Journal of Applied Mechanics* 12: 159-164.

Modjeski and Masters. 2015. *Bridges for Service Life Beyond 100 Years: Service Limit State Design.* SHRP 2 Report S2-R19B-RW-1, Washington, D.C.: Transportation Research Board.

Nowak, A. 1999. *Calibration of LRFD Bridge Design Code.* NCHRP Report 368, Washington, D.C.: Transportation Research Board.

Pelphrey, J., C Higgins, B. Sivakumar, and R. Groff. 2008. "State-Specific LRFR Live Load Factors Using Weigh-in-Motion Data." *Journal of Bridge Engineering* (American Society of Civil Engineers) 13 (4): 339-350.

Prado, E., and White. D. 2015. "Assessment of Basic Steel I-Section Beam Bracing Requirements by Test Simulation." Report to the Metal Building Manufacturers Association.

Reichenbach, M., Y. Liu, T. Helwig, and M. Engelhardt. 2020. "Lateral-Torsional Buckling of Singly-Symmetric I-Girders with Stepped Flanges." *Journal of Structural Engineering* (American Society of Civil Engineers).

Rivera, J., and B. Chavel. 2015. *Steel Bridge Design Handbook Design Example 3: Three-Span Continuous Horizontally Curved Composite Steel I-Girder Bridge.* Washington, DC: Federal Highway Administration.

Taylor, A., and M. Ojalvo. 1966. "Torsional Restraint of Lateral Buckling." *Journal of the Structural Division* (American Society of Civil Engineers) 92 (ST2): 115-129.

Texas Department of Transportation. 2020. *Transportation Planning Maps.* https://www.txdot.gov/inside-txdot/division/transportation-planning/maps.html.

Timoshenko, S., and Gere, J. 1961. *Theory of Elastic Stability.* New York: McGraw-Hill.

Wang, L., and T. Helwig. 2005. "Critical Imperfections for Beam Bracing Systems." *Journal of Structural Engineering* (American Society of Civil Engineers) 131 (6): 933-940.

Wang, W. 2013. *A Study of Stiffness of Steel Bridge Cross Frames.* PhD Dissertation, Austin, TX: The University of Texas at Austin.

White, D., D. Coletti, B. Chavel, A. Sanchez, C. Ozgur, J. Jimenez Chong, R. Leon, et al. 2012. *Guidelines for Analysis Methods and Construction Engineering of Curved and Skewed Steel Girder Bridges.* NCHRP Report 725, Washington, D.C.: Transportation Research Board.

Winter, G. 1960. "Lateral Bracing of Columns and Beams." *Journal of Structural Engineering* (American Society of Civil Engineers) 125: 809-825.

Yura, J. 2001. "Fundamentals of Beam Bracing." *Engineering Journal* (American Institute of Steel Construction) 11-26.

Yura, J., T. Helwig, R. Herman, and C. Zhou. 2008. "Global Lateral Buckling of I-Shaped Girder Systems." *Journal of Structural Engineering* (American Society of Civil Engineers) 134 (9): 1487-1494.

Ziemian, R., ed. 2010. *Stability Design Criteria for Metal Structures.* 6th. Hoboken, NJ: John Wiley & Sons, Inc.

CHAPTER F7

Analytical Testing Matrix

For reference, this chapter tabulates all 13 independent variables used to describe the 4,104 unique bridges analyzed as part of the Fatigue Loading Study. In the subsequent page, notes and abbreviation lists are provided to enhance understanding of the table.

Note: The following table summarizes all parameters used to describe and develop the 4,104 models in the Fatigue Loading Study. Note that only the 13 independent variables are shown. Independent constants and dependent variables are discussed in the body of the report. This table is intended to be a reference for the results shown in the report.

Model ID	Geometry									Cross-section		CF detail		Mat'l
	n_{span}	L/d ratio	s_g [ft]	n_{girder}	Support skew [deg]; Layout		R [ft]	s_{cf} [ft]	CF layout	d_w [in]	t_{deck} [in]	CF type	A_{cf} [in^2]	E_c [ksi]
1-1	1	25	6	3	0	Parallel	1500	20	Cont.	72	8	X	2.86	3600
1-2	1	25	6	3	0	Parallel	1500	20	Cont.	72	8	X	2.86	5000
1-3	1	25	6	3	0	Parallel	1500	20	Cont.	72	10	X	2.86	5000
1-4	1	25	6	3	0	Parallel	1500	20	Cont.	72	8	K	2.86	5000
1-5	1	25	6	3	0	Parallel	1500	20	Cont.	72	8	X	4.79	5000
2-1	1	25	6	3	0	Parallel	1500	30	Cont.	72	8	X	2.86	5000
3-1	1	25	6	3	0	Parallel	750	20	Cont.	72	8	X	2.86	3600
3-2	1	25	6	3	0	Parallel	750	20	Cont.	72	8	X	2.86	5000
3-3	1	25	6	3	0	Parallel	750	20	Cont.	72	10	X	2.86	5000
3-4	1	25	6	3	0	Parallel	750	20	Cont.	72	8	K	2.86	5000
3-5	1	25	6	3	0	Parallel	750	20	Cont.	72	8	X	4.79	5000
4-1	1	25	6	3	0	Parallel	750	30	Cont.	72	8	X	2.86	5000
5-1	1	25	6	3	30	Parallel	1500	20	Cont.	72	8	X	2.86	3600
5-2	1	25	6	3	30	Parallel	1500	20	Cont.	72	8	X	2.86	5000
5-3	1	25	6	3	30	Parallel	1500	20	Cont.	72	10	X	2.86	5000
5-4	1	25	6	3	30	Parallel	1500	20	Cont.	72	8	K	2.86	5000
5-5	1	25	6	3	30	Parallel	1500	20	Cont.	72	8	X	4.79	5000
6-1	1	25	6	3	30	Parallel	1500	30	Cont.	72	8	X	2.86	5000
7-1	1	25	6	3	30	Parallel	750	20	Cont.	72	8	X	2.86	3600
7-2	1	25	6	3	30	Parallel	750	20	Cont.	72	8	X	2.86	5000
7-3	1	25	6	3	30	Parallel	750	20	Cont.	72	10	X	2.86	5000
7-4	1	25	6	3	30	Parallel	750	20	Cont.	72	8	K	2.86	5000
7-5	1	25	6	3	30	Parallel	750	20	Cont.	72	8	X	4.79	5000
8-1	1	25	6	3	30	Parallel	750	30	Cont.	72	8	X	2.86	5000
9-1	1	25	6	3	60	Parallel	1500	20	Cont.	72	8	X	2.86	3600
9-2	1	25	6	3	60	Parallel	1500	20	Cont.	72	8	X	2.86	5000
9-3	1	25	6	3	60	Parallel	1500	20	Cont.	72	10	X	2.86	5000
9-4	1	25	6	3	60	Parallel	1500	20	Cont.	72	8	K	2.86	5000
9-5	1	25	6	3	60	Parallel	1500	20	Cont.	72	8	X	4.79	5000
10-1	1	25	6	3	60	Parallel	1500	30	Cont.	72	8	X	2.86	5000
11-1	1	25	6	3	60	Parallel	750	20	Cont.	72	8	X	2.86	3600
11-2	1	25	6	3	60	Parallel	750	20	Cont.	72	8	X	2.86	5000
11-3	1	25	6	3	60	Parallel	750	20	Cont.	72	10	X	2.86	5000
11-4	1	25	6	3	60	Parallel	750	20	Cont.	72	8	K	2.86	5000
11-5	1	25	6	3	60	Parallel	750	20	Cont.	72	8	X	4.79	5000
12-1	1	25	6	3	60	Parallel	750	30	Cont.	72	8	X	2.86	5000
13-1	1	25	6	3	60	Trap.	1500	20	Cont.	72	8	X	2.86	3600
13-2	1	25	6	3	60	Trap.	1500	20	Cont.	72	8	X	2.86	5000
13-3	1	25	6	3	60	Trap.	1500	20	Cont.	72	10	X	2.86	5000
13-4	1	25	6	3	60	Trap.	1500	20	Cont.	72	8	K	2.86	5000
13-5	1	25	6	3	60	Trap.	1500	20	Cont.	72	8	X	4.79	5000
14-1	1	25	6	3	60	Trap.	1500	30	Cont.	72	8	X	2.86	5000
15-1	1	25	6	3	60	Trap.	750	20	Cont.	72	8	X	2.86	3600
15-2	1	25	6	3	60	Trap.	750	20	Cont.	72	8	X	2.86	5000
15-3	1	25	6	3	60	Trap.	750	20	Cont.	72	10	X	2.86	5000
15-4	1	25	6	3	60	Trap.	750	20	Cont.	72	8	K	2.86	5000
15-5	1	25	6	3	60	Trap.	750	20	Cont.	72	8	X	4.79	5000
16-1	1	25	6	3	60	Trap.	750	30	Cont.	72	8	X	2.86	5000
17-1	1	25	6	5	0	Parallel	1500	20	Cont.	72	8	X	2.86	3600
17-2	1	25	6	5	0	Parallel	1500	20	Cont.	72	8	X	2.86	5000
17-3	1	25	6	5	0	Parallel	1500	20	Cont.	72	10	X	2.86	5000
17-4	1	25	6	5	0	Parallel	1500	20	Cont.	72	8	K	2.86	5000
17-5	1	25	6	5	0	Parallel	1500	20	Cont.	72	8	X	4.79	5000
18-1	1	25	6	5	0	Parallel	1500	30	Cont.	72	8	X	2.86	5000
19-1	1	25	6	5	0	Parallel	750	20	Cont.	72	8	X	2.86	3600
19-2	1	25	6	5	0	Parallel	750	20	Cont.	72	8	X	2.86	5000
19-3	1	25	6	5	0	Parallel	750	20	Cont.	72	10	X	2.86	5000
19-4	1	25	6	5	0	Parallel	750	20	Cont.	72	8	K	2.86	5000
19-5	1	25	6	5	0	Parallel	750	20	Cont.	72	8	X	4.79	5000
20-1	1	25	6	5	0	Parallel	750	30	Cont.	72	8	X	2.86	5000
21-1	1	25	6	5	30	Parallel	1500	20	Cont.	72	8	X	2.86	3600
21-2	1	25	6	5	30	Parallel	1500	20	Cont.	72	8	X	2.86	5000
21-3	1	25	6	5	30	Parallel	1500	20	Cont.	72	10	X	2.86	5000
21-4	1	25	6	5	30	Parallel	1500	20	Cont.	72	8	K	2.86	5000
21-5	1	25	6	5	30	Parallel	1500	20	Cont.	72	8	X	4.79	5000
22-1	1	25	6	5	30	Parallel	1500	30	Cont.	72	8	X	2.86	5000
23-1	1	25	6	5	30	Parallel	750	20	Cont.	72	8	X	2.86	3600
23-2	1	25	6	5	30	Parallel	750	20	Cont.	72	8	X	2.86	5000
23-3	1	25	6	5	30	Parallel	750	20	Cont.	72	10	X	2.86	5000
23-4	1	25	6	5	30	Parallel	750	20	Cont.	72	8	K	2.86	5000
23-5	1	25	6	5	30	Parallel	750	20	Cont.	72	8	X	4.79	5000

Model ID	Geometry									Cross-section		CF detail		Mat'l
	n_{span}	L/d ratio	s_g [ft]	n_{girder}	Support skew [deg];	Layout	R [ft]	s_{cf} [ft]	CF layout	d_w [in]	t_{deck} [in]	CF type	A_{cf} [in^2]	E_c [ksi]
24-1	1	25	6	5	30	Parallel	750	30	Cont.	72	8	X	2.86	5000
25-1	1	25	6	5	60	Parallel	1500	20	Cont.	72	8	X	2.86	3600
25-2	1	25	6	5	60	Parallel	1500	20	Cont.	72	8	X	2.86	5000
25-3	1	25	6	5	60	Parallel	1500	20	Cont.	72	10	X	2.86	5000
25-4	1	25	6	5	60	Parallel	1500	20	Cont.	72	8	K	2.86	5000
25-5	1	25	6	5	60	Parallel	1500	20	Cont.	72	8	X	4.79	5000
26-1	1	25	6	5	60	Parallel	1500	30	Cont.	72	8	X	2.86	5000
27-1	1	25	6	5	60	Parallel	750	20	Cont.	72	8	X	2.86	3600
27-2	1	25	6	5	60	Parallel	750	20	Cont.	72	8	X	2.86	5000
27-3	1	25	6	5	60	Parallel	750	20	Cont.	72	10	X	2.86	5000
27-4	1	25	6	5	60	Parallel	750	20	Cont.	72	8	K	2.86	5000
27-5	1	25	6	5	60	Parallel	750	20	Cont.	72	8	X	4.79	5000
28-1	1	25	6	5	60	Parallel	750	30	Cont.	72	8	X	2.86	5000
29-1	1	25	6	5	60	Trap.	1500	20	Cont.	72	8	X	2.86	3600
29-2	1	25	6	5	60	Trap.	1500	20	Cont.	72	8	X	2.86	5000
29-3	1	25	6	5	60	Trap.	1500	20	Cont.	72	10	X	2.86	5000
29-4	1	25	6	5	60	Trap.	1500	20	Cont.	72	8	K	2.86	5000
29-5	1	25	6	5	60	Trap.	1500	20	Cont.	72	8	X	4.79	5000
30-1	1	25	6	5	60	Trap.	1500	30	Cont.	72	8	X	2.86	5000
31-1	1	25	6	5	60	Trap.	750	20	Cont.	72	8	X	2.86	3600
31-2	1	25	6	5	60	Trap.	750	20	Cont.	72	8	X	2.86	5000
31-3	1	25	6	5	60	Trap.	750	20	Cont.	72	10	X	2.86	5000
31-4	1	25	6	5	60	Trap.	750	20	Cont.	72	8	K	2.86	5000
31-5	1	25	6	5	60	Trap.	750	20	Cont.	72	8	X	4.79	5000
32-1	1	25	6	5	60	Trap.	750	30	Cont.	72	8	X	2.86	5000
33-1	1	25	8	3	0	Parallel	1500	20	Cont.	72	8	X	2.86	3600
33-2	1	25	8	3	0	Parallel	1500	20	Cont.	72	8	X	2.86	5000
33-3	1	25	8	3	0	Parallel	1500	20	Cont.	72	10	X	2.86	5000
33-4	1	25	8	3	0	Parallel	1500	20	Cont.	72	8	K	2.86	5000
33-5	1	25	8	3	0	Parallel	1500	20	Cont.	72	8	X	4.79	5000
34-1	1	25	8	3	0	Parallel	1500	30	Cont.	72	8	X	2.86	5000
35-1	1	25	8	3	0	Parallel	750	20	Cont.	72	8	X	2.86	3600
35-2	1	25	8	3	0	Parallel	750	20	Cont.	72	8	X	2.86	5000
35-3	1	25	8	3	0	Parallel	750	20	Cont.	72	10	X	2.86	5000
35-4	1	25	8	3	0	Parallel	750	20	Cont.	72	8	K	2.86	5000
35-5	1	25	8	3	0	Parallel	750	20	Cont.	72	8	X	4.79	5000
36-1	1	25	8	3	0	Parallel	750	30	Cont.	72	8	X	2.86	5000
37-1	1	25	8	3	30	Parallel	1500	20	Cont.	72	8	X	2.86	3600
37-2	1	25	8	3	30	Parallel	1500	20	Cont.	72	8	X	2.86	5000
37-3	1	25	8	3	30	Parallel	1500	20	Cont.	72	10	X	2.86	5000
37-4	1	25	8	3	30	Parallel	1500	20	Cont.	72	8	K	2.86	5000
37-5	1	25	8	3	30	Parallel	1500	20	Cont.	72	8	X	4.79	5000
38-1	1	25	8	3	30	Parallel	1500	30	Cont.	72	8	X	2.86	5000
39-1	1	25	8	3	30	Parallel	750	20	Cont.	72	8	X	2.86	3600
39-2	1	25	8	3	30	Parallel	750	20	Cont.	72	8	X	2.86	5000
39-3	1	25	8	3	30	Parallel	750	20	Cont.	72	10	X	2.86	5000
39-4	1	25	8	3	30	Parallel	750	20	Cont.	72	8	K	2.86	5000
39-5	1	25	8	3	30	Parallel	750	20	Cont.	72	8	X	4.79	5000
40-1	1	25	8	3	30	Parallel	750	30	Cont.	72	8	X	2.86	5000
41-1	1	25	8	3	60	Parallel	1500	20	Cont.	72	8	X	2.86	3600
41-2	1	25	8	3	60	Parallel	1500	20	Cont.	72	8	X	2.86	5000
41-3	1	25	8	3	60	Parallel	1500	20	Cont.	72	10	X	2.86	5000
41-4	1	25	8	3	60	Parallel	1500	20	Cont.	72	8	K	2.86	5000
41-5	1	25	8	3	60	Parallel	1500	20	Cont.	72	8	X	4.79	5000
42-1	1	25	8	3	60	Parallel	1500	30	Cont.	72	8	X	2.86	5000
43-1	1	25	8	3	60	Parallel	750	20	Cont.	72	8	X	2.86	3600
43-2	1	25	8	3	60	Parallel	750	20	Cont.	72	8	X	2.86	5000
43-3	1	25	8	3	60	Parallel	750	20	Cont.	72	10	X	2.86	5000
43-4	1	25	8	3	60	Parallel	750	20	Cont.	72	8	K	2.86	5000
43-5	1	25	8	3	60	Parallel	750	20	Cont.	72	8	X	4.79	5000
44-1	1	25	8	3	60	Parallel	750	30	Cont.	72	8	X	2.86	5000
45-1	1	25	8	3	60	Trap.	1500	20	Cont.	72	8	X	2.86	3600
45-2	1	25	8	3	60	Trap.	1500	20	Cont.	72	8	X	2.86	5000
45-3	1	25	8	3	60	Trap.	1500	20	Cont.	72	10	X	2.86	5000
45-4	1	25	8	3	60	Trap.	1500	20	Cont.	72	8	K	2.86	5000
45-5	1	25	8	3	60	Trap.	1500	20	Cont.	72	8	X	4.79	5000
46-1	1	25	8	3	60	Trap.	1500	30	Cont.	72	8	X	2.86	5000
47-1	1	25	8	3	60	Trap.	750	20	Cont.	72	8	X	2.86	3600
47-2	1	25	8	3	60	Trap.	750	20	Cont.	72	8	X	2.86	5000
47-3	1	25	8	3	60	Trap.	750	20	Cont.	72	10	X	2.86	5000
47-4	1	25	8	3	60	Trap.	750	20	Cont.	72	8	K	2.86	5000
47-5	1	25	8	3	60	Trap.	750	20	Cont.	72	8	X	4.79	5000
48-1	1	25	8	3	60	Trap.	750	30	Cont.	72	8	X	2.86	5000
49-1	1	25	8	5	0	Parallel	1500	20	Cont.	72	8	X	2.86	3600
49-2	1	25	8	5	0	Parallel	1500	20	Cont.	72	8	X	2.86	5000
49-3	1	25	8	5	0	Parallel	1500	20	Cont.	72	10	X	2.86	5000
49-4	1	25	8	5	0	Parallel	1500	20	Cont.	72	8	K	2.86	5000
49-5	1	25	8	5	0	Parallel	1500	20	Cont.	72	8	X	4.79	5000
50-1	1	25	8	5	0	Parallel	1500	30	Cont.	72	8	X	2.86	5000

Model ID	Geometry									Cross-section		CF detail		Mat'l
	n_{span}	L/d ratio	s_g [ft]	n_{girder}	Support skew [deg];	Layout	R [ft]	s_{cf} [ft]	CF layout	d_w [in]	t_{deck} [in]	CF type	A_{cf} [in^2]	E_c [ksi]
51-1	1	25	8	5	0	Parallel	750	20	Cont.	72	8	X	2.86	3600
51-2	1	25	8	5	0	Parallel	750	20	Cont.	72	8	X	2.86	5000
51-3	1	25	8	5	0	Parallel	750	20	Cont.	72	10	X	2.86	5000
51-4	1	25	8	5	0	Parallel	750	20	Cont.	72	8	K	2.86	5000
51-5	1	25	8	5	0	Parallel	750	20	Cont.	72	8	X	4.79	5000
52-1	1	25	8	5	0	Parallel	750	30	Cont.	72	8	X	2.86	5000
53-1	1	25	8	5	30	Parallel	1500	20	Cont.	72	8	X	2.86	3600
53-2	1	25	8	5	30	Parallel	1500	20	Cont.	72	8	X	2.86	5000
53-3	1	25	8	5	30	Parallel	1500	20	Cont.	72	10	X	2.86	5000
53-4	1	25	8	5	30	Parallel	1500	20	Cont.	72	8	K	2.86	5000
53-5	1	25	8	5	30	Parallel	1500	20	Cont.	72	8	X	4.79	5000
54-1	1	25	8	5	30	Parallel	1500	30	Cont.	72	8	X	2.86	5000
55-1	1	25	8	5	30	Parallel	750	20	Cont.	72	8	X	2.86	3600
55-2	1	25	8	5	30	Parallel	750	20	Cont.	72	8	X	2.86	5000
55-3	1	25	8	5	30	Parallel	750	20	Cont.	72	10	X	2.86	5000
55-4	1	25	8	5	30	Parallel	750	20	Cont.	72	8	K	2.86	5000
55-5	1	25	8	5	30	Parallel	750	20	Cont.	72	8	X	4.79	5000
56-1	1	25	8	5	30	Parallel	750	30	Cont.	72	8	X	2.86	5000
57-1	1	25	8	5	60	Parallel	1500	20	Cont.	72	8	X	2.86	3600
57-2	1	25	8	5	60	Parallel	1500	20	Cont.	72	8	X	2.86	5000
57-3	1	25	8	5	60	Parallel	1500	20	Cont.	72	10	X	2.86	5000
57-4	1	25	8	5	60	Parallel	1500	20	Cont.	72	8	K	2.86	5000
57-5	1	25	8	5	60	Parallel	1500	20	Cont.	72	8	X	4.79	5000
58-1	1	25	8	5	60	Parallel	1500	30	Cont.	72	8	X	2.86	5000
59-1	1	25	8	5	60	Parallel	750	20	Cont.	72	8	X	2.86	3600
59-2	1	25	8	5	60	Parallel	750	20	Cont.	72	8	X	2.86	5000
59-3	1	25	8	5	60	Parallel	750	20	Cont.	72	10	X	2.86	5000
59-4	1	25	8	5	60	Parallel	750	20	Cont.	72	8	K	2.86	5000
59-5	1	25	8	5	60	Parallel	750	20	Cont.	72	8	X	4.79	5000
60-1	1	25	8	5	60	Parallel	750	30	Cont.	72	8	X	2.86	5000
61-1	1	25	8	5	60	Trap.	1500	20	Cont.	72	8	X	2.86	3600
61-2	1	25	8	5	60	Trap.	1500	20	Cont.	72	8	X	2.86	5000
61-3	1	25	8	5	60	Trap.	1500	20	Cont.	72	10	X	2.86	5000
61-4	1	25	8	5	60	Trap.	1500	20	Cont.	72	8	K	2.86	5000
61-5	1	25	8	5	60	Trap.	1500	20	Cont.	72	8	X	4.79	5000
62-1	1	25	8	5	60	Trap.	1500	30	Cont.	72	8	X	2.86	5000
63-1	1	25	8	5	60	Trap.	750	20	Cont.	72	8	X	2.86	3600
63-2	1	25	8	5	60	Trap.	750	20	Cont.	72	8	X	2.86	5000
63-3	1	25	8	5	60	Trap.	750	20	Cont.	72	10	X	2.86	5000
63-4	1	25	8	5	60	Trap.	750	20	Cont.	72	8	K	2.86	5000
63-5	1	25	8	5	60	Trap.	750	20	Cont.	72	8	X	4.79	5000
64-1	1	25	8	5	60	Trap.	750	30	Cont.	72	8	X	2.86	5000
65-1	1	25	10	3	0	Parallel	1500	20	Cont.	72	8	X	2.86	3600
65-2	1	25	10	3	0	Parallel	1500	20	Cont.	72	8	X	2.86	5000
65-3	1	25	10	3	0	Parallel	1500	20	Cont.	72	10	X	2.86	5000
65-4	1	25	10	3	0	Parallel	1500	20	Cont.	72	8	K	2.86	5000
65-5	1	25	10	3	0	Parallel	1500	20	Cont.	72	8	X	4.79	5000
66-1	1	25	10	3	0	Parallel	1500	30	Cont.	72	8	X	2.86	5000
67-1	1	25	10	3	0	Parallel	750	20	Cont.	72	8	X	2.86	3600
67-2	1	25	10	3	0	Parallel	750	20	Cont.	72	8	X	2.86	5000
67-3	1	25	10	3	0	Parallel	750	20	Cont.	72	10	X	2.86	5000
67-4	1	25	10	3	0	Parallel	750	20	Cont.	72	8	K	2.86	5000
67-5	1	25	10	3	0	Parallel	750	20	Cont.	72	8	X	4.79	5000
68-1	1	25	10	3	0	Parallel	750	30	Cont.	72	8	X	2.86	5000
69-1	1	25	10	3	30	Parallel	1500	20	Cont.	72	8	X	2.86	3600
69-2	1	25	10	3	30	Parallel	1500	20	Cont.	72	8	X	2.86	5000
69-3	1	25	10	3	30	Parallel	1500	20	Cont.	72	10	X	2.86	5000
69-4	1	25	10	3	30	Parallel	1500	20	Cont.	72	8	K	2.86	5000
69-5	1	25	10	3	30	Parallel	1500	20	Cont.	72	8	X	4.79	5000
70-1	1	25	10	3	30	Parallel	1500	30	Cont.	72	8	X	2.86	5000
71-1	1	25	10	3	30	Parallel	750	20	Cont.	72	8	X	2.86	3600
71-2	1	25	10	3	30	Parallel	750	20	Cont.	72	8	X	2.86	5000
71-3	1	25	10	3	30	Parallel	750	20	Cont.	72	10	X	2.86	5000
71-4	1	25	10	3	30	Parallel	750	20	Cont.	72	8	K	2.86	5000
71-5	1	25	10	3	30	Parallel	750	20	Cont.	72	8	X	4.79	5000
72-1	1	25	10	3	30	Parallel	750	30	Cont.	72	8	X	2.86	5000
73-1	1	25	10	3	60	Parallel	1500	20	Cont.	72	8	X	2.86	3600
73-2	1	25	10	3	60	Parallel	1500	20	Cont.	72	8	X	2.86	5000
73-3	1	25	10	3	60	Parallel	1500	20	Cont.	72	10	X	2.86	5000
73-4	1	25	10	3	60	Parallel	1500	20	Cont.	72	8	K	2.86	5000
73-5	1	25	10	3	60	Parallel	1500	20	Cont.	72	8	X	4.79	5000
74-1	1	25	10	3	60	Parallel	1500	30	Cont.	72	8	X	2.86	5000
75-1	1	25	10	3	60	Parallel	750	20	Cont.	72	8	X	2.86	3600
75-2	1	25	10	3	60	Parallel	750	20	Cont.	72	8	X	2.86	5000
75-3	1	25	10	3	60	Parallel	750	20	Cont.	72	10	X	2.86	5000
75-4	1	25	10	3	60	Parallel	750	20	Cont.	72	8	K	2.86	5000
75-5	1	25	10	3	60	Parallel	750	20	Cont.	72	8	X	4.79	5000
76-1	1	25	10	3	60	Parallel	750	30	Cont.	72	8	X	2.86	5000
77-1	1	25	10	3	60	Trap.	1500	20	Cont.	72	8	X	2.86	3600

Model ID	Geometry									Cross-section		CF detail		Mat'l
	n_{span}	L/d ratio	s_g [ft]	n_{girder}	Support skew [deg]; Layout		R [ft]	s_{cf} [ft]	CF layout	d_w [in]	t_{deck} [in]	CF type	A_{cf} [in^2]	E_c [ksi]
77-2	1	25	10	3	60	Trap.	1500	20	Cont.	72	8	X	2.86	5000
77-3	1	25	10	3	60	Trap.	1500	20	Cont.	72	10	X	2.86	5000
77-4	1	25	10	3	60	Trap.	1500	20	Cont.	72	8	K	2.86	5000
77-5	1	25	10	3	60	Trap.	1500	20	Cont.	72	8	X	4.79	5000
78-1	1	25	10	3	60	Trap.	1500	30	Cont.	72	8	X	2.86	5000
79-1	1	25	10	3	60	Trap.	750	20	Cont.	72	8	X	2.86	3600
79-2	1	25	10	3	60	Trap.	750	20	Cont.	72	8	X	2.86	5000
79-3	1	25	10	3	60	Trap.	750	20	Cont.	72	10	X	2.86	5000
79-4	1	25	10	3	60	Trap.	750	20	Cont.	72	8	K	2.86	5000
79-5	1	25	10	3	60	Trap.	750	20	Cont.	72	8	X	4.79	5000
80-1	1	25	10	3	60	Trap.	750	30	Cont.	72	8	X	2.86	5000
81-1	1	25	10	5	0	Parallel	1500	20	Cont.	72	8	X	2.86	3600
81-2	1	25	10	5	0	Parallel	1500	20	Cont.	72	8	X	2.86	5000
81-3	1	25	10	5	0	Parallel	1500	20	Cont.	72	10	X	2.86	5000
81-4	1	25	10	5	0	Parallel	1500	20	Cont.	72	8	K	2.86	5000
81-5	1	25	10	5	0	Parallel	1500	20	Cont.	72	8	X	4.79	5000
82-1	1	25	10	5	0	Parallel	1500	30	Cont.	72	8	X	2.86	5000
83-1	1	25	10	5	0	Parallel	750	20	Cont.	72	8	X	2.86	3600
83-2	1	25	10	5	0	Parallel	750	20	Cont.	72	8	X	2.86	5000
83-3	1	25	10	5	0	Parallel	750	20	Cont.	72	10	X	2.86	5000
83-4	1	25	10	5	0	Parallel	750	20	Cont.	72	8	K	2.86	5000
83-5	1	25	10	5	0	Parallel	750	20	Cont.	72	8	X	4.79	5000
84-1	1	25	10	5	0	Parallel	750	30	Cont.	72	8	X	2.86	5000
85-1	1	25	10	5	30	Parallel	1500	20	Cont.	72	8	X	2.86	3600
85-2	1	25	10	5	30	Parallel	1500	20	Cont.	72	8	X	2.86	5000
85-3	1	25	10	5	30	Parallel	1500	20	Cont.	72	10	X	2.86	5000
85-4	1	25	10	5	30	Parallel	1500	20	Cont.	72	8	K	2.86	5000
85-5	1	25	10	5	30	Parallel	1500	20	Cont.	72	8	X	4.79	5000
86-1	1	25	10	5	30	Parallel	1500	30	Cont.	72	8	X	2.86	5000
87-1	1	25	10	5	30	Parallel	750	20	Cont.	72	8	X	2.86	3600
87-2	1	25	10	5	30	Parallel	750	20	Cont.	72	8	X	2.86	5000
87-3	1	25	10	5	30	Parallel	750	20	Cont.	72	10	X	2.86	5000
87-4	1	25	10	5	30	Parallel	750	20	Cont.	72	8	K	2.86	5000
87-5	1	25	10	5	30	Parallel	750	20	Cont.	72	8	X	4.79	5000
88-1	1	25	10	5	30	Parallel	750	30	Cont.	72	8	X	2.86	5000
89-1	1	25	10	5	60	Parallel	1500	20	Cont.	72	8	X	2.86	3600
89-2	1	25	10	5	60	Parallel	1500	20	Cont.	72	8	X	2.86	5000
89-3	1	25	10	5	60	Parallel	1500	20	Cont.	72	10	X	2.86	5000
89-4	1	25	10	5	60	Parallel	1500	20	Cont.	72	8	K	2.86	5000
89-5	1	25	10	5	60	Parallel	1500	20	Cont.	72	8	X	4.79	5000
90-1	1	25	10	5	60	Parallel	1500	30	Cont.	72	8	X	2.86	5000
91-1	1	25	10	5	60	Parallel	750	20	Cont.	72	8	X	2.86	3600
91-2	1	25	10	5	60	Parallel	750	20	Cont.	72	8	X	2.86	5000
91-3	1	25	10	5	60	Parallel	750	20	Cont.	72	10	X	2.86	5000
91-4	1	25	10	5	60	Parallel	750	20	Cont.	72	8	K	2.86	5000
91-5	1	25	10	5	60	Parallel	750	20	Cont.	72	8	X	4.79	5000
92-1	1	25	10	5	60	Parallel	750	30	Cont.	72	8	X	2.86	5000
93-1	1	25	10	5	60	Trap.	1500	20	Cont.	72	8	X	2.86	3600
93-2	1	25	10	5	60	Trap.	1500	20	Cont.	72	8	X	2.86	5000
93-3	1	25	10	5	60	Trap.	1500	20	Cont.	72	10	X	2.86	5000
93-4	1	25	10	5	60	Trap.	1500	20	Cont.	72	8	K	2.86	5000
93-5	1	25	10	5	60	Trap.	1500	20	Cont.	72	8	X	4.79	5000
94-1	1	25	10	5	60	Trap.	1500	30	Cont.	72	8	X	2.86	5000
95-1	1	25	10	5	60	Trap.	750	20	Cont.	72	8	X	2.86	3600
95-2	1	25	10	5	60	Trap.	750	20	Cont.	72	8	X	2.86	5000
95-3	1	25	10	5	60	Trap.	750	20	Cont.	72	10	X	2.86	5000
95-4	1	25	10	5	60	Trap.	750	20	Cont.	72	8	K	2.86	5000
95-5	1	25	10	5	60	Trap.	750	20	Cont.	72	8	X	4.79	5000
96-1	1	25	10	5	60	Trap.	750	30	Cont.	72	8	X	2.86	5000
97-1	1	25	6	3	0	Parallel	1500	20	Cont.	96	8	X	2.86	3600
97-2	1	25	6	3	0	Parallel	1500	20	Cont.	96	8	X	2.86	5000
97-3	1	25	6	3	0	Parallel	1500	20	Cont.	96	10	X	2.86	5000
97-4	1	25	6	3	0	Parallel	1500	20	Cont.	96	8	K	2.86	5000
97-5	1	25	6	3	0	Parallel	1500	20	Cont.	96	8	X	4.79	5000
98-1	1	25	6	3	0	Parallel	1500	30	Cont.	96	8	X	2.86	5000
99-1	1	25	6	3	0	Parallel	750	20	Cont.	96	8	X	2.86	3600
99-2	1	25	6	3	0	Parallel	750	20	Cont.	96	8	X	2.86	5000
99-3	1	25	6	3	0	Parallel	750	20	Cont.	96	10	X	2.86	5000
99-4	1	25	6	3	0	Parallel	750	20	Cont.	96	8	K	2.86	5000
99-5	1	25	6	3	0	Parallel	750	20	Cont.	96	8	X	4.79	5000
100-1	1	25	6	3	0	Parallel	750	30	Cont.	96	8	X	2.86	5000
101-1	1	25	6	3	30	Parallel	1500	20	Cont.	96	8	X	2.86	3600
101-2	1	25	6	3	30	Parallel	1500	20	Cont.	96	8	X	2.86	5000
101-3	1	25	6	3	30	Parallel	1500	20	Cont.	96	10	X	2.86	5000
101-4	1	25	6	3	30	Parallel	1500	20	Cont.	96	8	K	2.86	5000
101-5	1	25	6	3	30	Parallel	1500	20	Cont.	96	8	X	4.79	5000
102-1	1	25	6	3	30	Parallel	1500	30	Cont.	96	8	X	2.86	5000
103-1	1	25	6	3	30	Parallel	750	20	Cont.	96	8	X	2.86	3600
103-2	1	25	6	3	30	Parallel	750	20	Cont.	96	8	X	2.86	5000

Model ID	Geometry									Cross-section		CF detail		Mat'l
	n_{span}	L/d ratio	s_g [ft]	n_{girder}	Support skew [deg];	Layout	R [ft]	s_{cf} [ft]	CF layout	d_w [in]	t_{deck} [in]	CF type	A_{cf} [in^2]	E_c [ksi]
103-3	1	25	6	3	30	Parallel	750	20	Cont.	96	10	X	2.86	5000
103-4	1	25	6	3	30	Parallel	750	20	Cont.	96	8	K	2.86	5000
103-5	1	25	6	3	30	Parallel	750	20	Cont.	96	8	X	4.79	5000
104-1	1	25	6	3	30	Parallel	750	30	Cont.	96	8	X	2.86	5000
105-1	1	25	6	3	60	Parallel	1500	20	Cont.	96	8	X	2.86	3600
105-2	1	25	6	3	60	Parallel	1500	20	Cont.	96	8	X	2.86	5000
105-3	1	25	6	3	60	Parallel	1500	20	Cont.	96	10	X	2.86	5000
105-4	1	25	6	3	60	Parallel	1500	20	Cont.	96	8	K	2.86	5000
105-5	1	25	6	3	60	Parallel	1500	20	Cont.	96	8	X	4.79	5000
106-1	1	25	6	3	60	Parallel	1500	30	Cont.	96	8	X	2.86	5000
107-1	1	25	6	3	60	Parallel	750	20	Cont.	96	8	X	2.86	3600
107-2	1	25	6	3	60	Parallel	750	20	Cont.	96	8	X	2.86	5000
107-3	1	25	6	3	60	Parallel	750	20	Cont.	96	10	X	2.86	5000
107-4	1	25	6	3	60	Parallel	750	20	Cont.	96	8	K	2.86	5000
107-5	1	25	6	3	60	Parallel	750	20	Cont.	96	8	X	4.79	5000
108-1	1	25	6	3	60	Parallel	750	30	Cont.	96	8	X	2.86	5000
109-1	1	25	6	3	60	Trap.	1500	20	Cont.	96	8	X	2.86	3600
109-2	1	25	6	3	60	Trap.	1500	20	Cont.	96	8	X	2.86	5000
109-3	1	25	6	3	60	Trap.	1500	20	Cont.	96	10	X	2.86	5000
109-4	1	25	6	3	60	Trap.	1500	20	Cont.	96	8	K	2.86	5000
109-5	1	25	6	3	60	Trap.	1500	20	Cont.	96	8	X	4.79	5000
110-1	1	25	6	3	60	Trap.	1500	30	Cont.	96	8	X	2.86	5000
111-1	1	25	6	3	60	Trap.	750	20	Cont.	96	8	X	2.86	3600
111-2	1	25	6	3	60	Trap.	750	20	Cont.	96	8	X	2.86	5000
111-3	1	25	6	3	60	Trap.	750	20	Cont.	96	10	X	2.86	5000
111-4	1	25	6	3	60	Trap.	750	20	Cont.	96	8	K	2.86	5000
111-5	1	25	6	3	60	Trap.	750	20	Cont.	96	8	X	4.79	5000
112-1	1	25	6	3	60	Trap.	750	30	Cont.	96	8	X	2.86	5000
113-1	1	25	6	5	0	Parallel	1500	20	Cont.	96	8	X	2.86	3600
113-2	1	25	6	5	0	Parallel	1500	20	Cont.	96	8	X	2.86	5000
113-3	1	25	6	5	0	Parallel	1500	20	Cont.	96	10	X	2.86	5000
113-4	1	25	6	5	0	Parallel	1500	20	Cont.	96	8	K	2.86	5000
113-5	1	25	6	5	0	Parallel	1500	20	Cont.	96	8	X	4.79	5000
114-1	1	25	6	5	0	Parallel	1500	30	Cont.	96	8	X	2.86	5000
115-1	1	25	6	5	0	Parallel	750	20	Cont.	96	8	X	2.86	3600
115-2	1	25	6	5	0	Parallel	750	20	Cont.	96	8	X	2.86	5000
115-3	1	25	6	5	0	Parallel	750	20	Cont.	96	10	X	2.86	5000
115-4	1	25	6	5	0	Parallel	750	20	Cont.	96	8	K	2.86	5000
115-5	1	25	6	5	0	Parallel	750	20	Cont.	96	8	X	4.79	5000
116-1	1	25	6	5	0	Parallel	750	30	Cont.	96	8	X	2.86	5000
117-1	1	25	6	5	30	Parallel	1500	20	Cont.	96	8	X	2.86	3600
117-2	1	25	6	5	30	Parallel	1500	20	Cont.	96	8	X	2.86	5000
117-3	1	25	6	5	30	Parallel	1500	20	Cont.	96	10	X	2.86	5000
117-4	1	25	6	5	30	Parallel	1500	20	Cont.	96	8	K	2.86	5000
117-5	1	25	6	5	30	Parallel	1500	20	Cont.	96	8	X	4.79	5000
118-1	1	25	6	5	30	Parallel	1500	30	Cont.	96	8	X	2.86	5000
119-1	1	25	6	5	30	Parallel	750	20	Cont.	96	8	X	2.86	3600
119-2	1	25	6	5	30	Parallel	750	20	Cont.	96	8	X	2.86	5000
119-3	1	25	6	5	30	Parallel	750	20	Cont.	96	10	X	2.86	5000
119-4	1	25	6	5	30	Parallel	750	20	Cont.	96	8	K	2.86	5000
119-5	1	25	6	5	30	Parallel	750	20	Cont.	96	8	X	4.79	5000
120-1	1	25	6	5	30	Parallel	750	30	Cont.	96	8	X	2.86	5000
121-1	1	25	6	5	60	Parallel	1500	20	Cont.	96	8	X	2.86	3600
121-2	1	25	6	5	60	Parallel	1500	20	Cont.	96	8	X	2.86	5000
121-3	1	25	6	5	60	Parallel	1500	20	Cont.	96	10	X	2.86	5000
121-4	1	25	6	5	60	Parallel	1500	20	Cont.	96	8	K	2.86	5000
121-5	1	25	6	5	60	Parallel	1500	20	Cont.	96	8	X	4.79	5000
122-1	1	25	6	5	60	Parallel	1500	30	Cont.	96	8	X	2.86	5000
123-1	1	25	6	5	60	Parallel	750	20	Cont.	96	8	X	2.86	3600
123-2	1	25	6	5	60	Parallel	750	20	Cont.	96	8	X	2.86	5000
123-3	1	25	6	5	60	Parallel	750	20	Cont.	96	10	X	2.86	5000
123-4	1	25	6	5	60	Parallel	750	20	Cont.	96	8	K	2.86	5000
123-5	1	25	6	5	60	Parallel	750	20	Cont.	96	8	X	4.79	5000
124-1	1	25	6	5	60	Parallel	750	30	Cont.	96	8	X	2.86	5000
125-1	1	25	6	5	60	Trap.	1500	20	Cont.	96	8	X	2.86	3600
125-2	1	25	6	5	60	Trap.	1500	20	Cont.	96	8	X	2.86	5000
125-3	1	25	6	5	60	Trap.	1500	20	Cont.	96	10	X	2.86	5000
125-4	1	25	6	5	60	Trap.	1500	20	Cont.	96	8	K	2.86	5000
125-5	1	25	6	5	60	Trap.	1500	20	Cont.	96	8	X	4.79	5000
126-1	1	25	6	5	60	Trap.	1500	30	Cont.	96	8	X	2.86	5000
127-1	1	25	6	5	60	Trap.	750	20	Cont.	96	8	X	2.86	3600
127-2	1	25	6	5	60	Trap.	750	20	Cont.	96	8	X	2.86	5000
127-3	1	25	6	5	60	Trap.	750	20	Cont.	96	10	X	2.86	5000
127-4	1	25	6	5	60	Trap.	750	20	Cont.	96	8	K	2.86	5000
127-5	1	25	6	5	60	Trap.	750	20	Cont.	96	8	X	4.79	5000
128-1	1	25	6	5	60	Trap.	750	30	Cont.	96	8	X	2.86	5000
129-1	1	25	8	3	0	Parallel	1500	20	Cont.	96	8	X	2.86	3600
129-2	1	25	8	3	0	Parallel	1500	20	Cont.	96	8	X	2.86	5000
129-3	1	25	8	3	0	Parallel	1500	20	Cont.	96	10	X	2.86	5000

Model ID	Geometry									Cross-section		CF detail		Mat'l
	n_{span}	L/d ratio	s_g [ft]	n_{girder}	Support skew [deg]; Layout		R [ft]	s_{cf} [ft]	CF layout	d_w [in]	t_{deck} [in]	CF type	A_{cf} [in^2]	E_c [ksi]
129-4	1	25	8	3	0	Parallel	1500	20	Cont.	96	8	K	2.86	5000
129-5	1	25	8	3	0	Parallel	1500	20	Cont.	96	8	X	4.79	5000
130-1	1	25	8	3	0	Parallel	1500	30	Cont.	96	8	X	2.86	5000
131-1	1	25	8	3	0	Parallel	750	20	Cont.	96	8	X	2.86	3600
131-2	1	25	8	3	0	Parallel	750	20	Cont.	96	8	X	2.86	5000
131-3	1	25	8	3	0	Parallel	750	20	Cont.	96	10	X	2.86	5000
131-4	1	25	8	3	0	Parallel	750	20	Cont.	96	8	K	2.86	5000
131-5	1	25	8	3	0	Parallel	750	20	Cont.	96	8	X	4.79	5000
132-1	1	25	8	3	0	Parallel	750	30	Cont.	96	8	X	2.86	5000
133-1	1	25	8	3	30	Parallel	1500	20	Cont.	96	8	X	2.86	3600
133-2	1	25	8	3	30	Parallel	1500	20	Cont.	96	8	X	2.86	5000
133-3	1	25	8	3	30	Parallel	1500	20	Cont.	96	10	X	2.86	5000
133-4	1	25	8	3	30	Parallel	1500	20	Cont.	96	8	K	2.86	5000
133-5	1	25	8	3	30	Parallel	1500	20	Cont.	96	8	X	4.79	5000
134-1	1	25	8	3	30	Parallel	1500	30	Cont.	96	8	X	2.86	5000
135-1	1	25	8	3	30	Parallel	750	20	Cont.	96	8	X	2.86	3600
135-2	1	25	8	3	30	Parallel	750	20	Cont.	96	8	X	2.86	5000
135-3	1	25	8	3	30	Parallel	750	20	Cont.	96	10	X	2.86	5000
135-4	1	25	8	3	30	Parallel	750	20	Cont.	96	8	K	2.86	5000
135-5	1	25	8	3	30	Parallel	750	20	Cont.	96	8	X	4.79	5000
136-1	1	25	8	3	30	Parallel	750	30	Cont.	96	8	X	2.86	5000
137-1	1	25	8	3	60	Parallel	1500	20	Cont.	96	8	X	2.86	3600
137-2	1	25	8	3	60	Parallel	1500	20	Cont.	96	8	X	2.86	5000
137-3	1	25	8	3	60	Parallel	1500	20	Cont.	96	10	X	2.86	5000
137-4	1	25	8	3	60	Parallel	1500	20	Cont.	96	8	K	2.86	5000
137-5	1	25	8	3	60	Parallel	1500	20	Cont.	96	8	X	4.79	5000
138-1	1	25	8	3	60	Parallel	1500	30	Cont.	96	8	X	2.86	5000
139-1	1	25	8	3	60	Parallel	750	20	Cont.	96	8	X	2.86	3600
139-2	1	25	8	3	60	Parallel	750	20	Cont.	96	8	X	2.86	5000
139-3	1	25	8	3	60	Parallel	750	20	Cont.	96	10	X	2.86	5000
139-4	1	25	8	3	60	Parallel	750	20	Cont.	96	8	K	2.86	5000
139-5	1	25	8	3	60	Parallel	750	20	Cont.	96	8	X	4.79	5000
140-1	1	25	8	3	60	Parallel	750	30	Cont.	96	8	X	2.86	5000
141-1	1	25	8	3	60	Trap.	1500	20	Cont.	96	8	X	2.86	3600
141-2	1	25	8	3	60	Trap.	1500	20	Cont.	96	8	X	2.86	5000
141-3	1	25	8	3	60	Trap.	1500	20	Cont.	96	10	X	2.86	5000
141-4	1	25	8	3	60	Trap.	1500	20	Cont.	96	8	K	2.86	5000
141-5	1	25	8	3	60	Trap.	1500	20	Cont.	96	8	X	4.79	5000
142-1	1	25	8	3	60	Trap.	1500	30	Cont.	96	8	X	2.86	5000
143-1	1	25	8	3	60	Trap.	750	20	Cont.	96	8	X	2.86	3600
143-2	1	25	8	3	60	Trap.	750	20	Cont.	96	8	X	2.86	5000
143-3	1	25	8	3	60	Trap.	750	20	Cont.	96	10	X	2.86	5000
143-4	1	25	8	3	60	Trap.	750	20	Cont.	96	8	K	2.86	5000
143-5	1	25	8	3	60	Trap.	750	20	Cont.	96	8	X	4.79	5000
144-1	1	25	8	3	60	Trap.	750	30	Cont.	96	8	X	2.86	5000
145-1	1	25	8	5	0	Parallel	1500	20	Cont.	96	8	X	2.86	3600
145-2	1	25	8	5	0	Parallel	1500	20	Cont.	96	8	X	2.86	5000
145-3	1	25	8	5	0	Parallel	1500	20	Cont.	96	10	X	2.86	5000
145-4	1	25	8	5	0	Parallel	1500	20	Cont.	96	8	K	2.86	5000
145-5	1	25	8	5	0	Parallel	1500	20	Cont.	96	8	X	4.79	5000
146-1	1	25	8	5	0	Parallel	1500	30	Cont.	96	8	X	2.86	5000
147-1	1	25	8	5	0	Parallel	750	20	Cont.	96	8	X	2.86	3600
147-2	1	25	8	5	0	Parallel	750	20	Cont.	96	8	X	2.86	5000
147-3	1	25	8	5	0	Parallel	750	20	Cont.	96	10	X	2.86	5000
147-4	1	25	8	5	0	Parallel	750	20	Cont.	96	8	K	2.86	5000
147-5	1	25	8	5	0	Parallel	750	20	Cont.	96	8	X	4.79	5000
148-1	1	25	8	5	0	Parallel	750	30	Cont.	96	8	X	2.86	5000
149-1	1	25	8	5	30	Parallel	1500	20	Cont.	96	8	X	2.86	3600
149-2	1	25	8	5	30	Parallel	1500	20	Cont.	96	8	X	2.86	5000
149-3	1	25	8	5	30	Parallel	1500	20	Cont.	96	10	X	2.86	5000
149-4	1	25	8	5	30	Parallel	1500	20	Cont.	96	8	K	2.86	5000
149-5	1	25	8	5	30	Parallel	1500	20	Cont.	96	8	X	4.79	5000
150-1	1	25	8	5	30	Parallel	1500	30	Cont.	96	8	X	2.86	5000
151-1	1	25	8	5	30	Parallel	750	20	Cont.	96	8	X	2.86	3600
151-2	1	25	8	5	30	Parallel	750	20	Cont.	96	8	X	2.86	5000
151-3	1	25	8	5	30	Parallel	750	20	Cont.	96	10	X	2.86	5000
151-4	1	25	8	5	30	Parallel	750	20	Cont.	96	8	K	2.86	5000
151-5	1	25	8	5	30	Parallel	750	20	Cont.	96	8	X	4.79	5000
152-1	1	25	8	5	30	Parallel	750	30	Cont.	96	8	X	2.86	5000
153-1	1	25	8	5	60	Parallel	1500	20	Cont.	96	8	X	2.86	3600
153-2	1	25	8	5	60	Parallel	1500	20	Cont.	96	8	X	2.86	5000
153-3	1	25	8	5	60	Parallel	1500	20	Cont.	96	10	X	2.86	5000
153-4	1	25	8	5	60	Parallel	1500	20	Cont.	96	8	K	2.86	5000
153-5	1	25	8	5	60	Parallel	1500	20	Cont.	96	8	X	4.79	5000
154-1	1	25	8	5	60	Parallel	1500	30	Cont.	96	8	X	2.86	5000
155-1	1	25	8	5	60	Parallel	750	20	Cont.	96	8	X	2.86	3600
155-2	1	25	8	5	60	Parallel	750	20	Cont.	96	8	X	2.86	5000
155-3	1	25	8	5	60	Parallel	750	20	Cont.	96	10	X	2.86	5000
155-4	1	25	8	5	60	Parallel	750	20	Cont.	96	8	K	2.86	5000

Model ID	Geometry									Cross-section		CF detail		Mat'l
	n_{span}	L/d ratio	s_g [ft]	n_{girder}	Support skew [deg];	Layout	R [ft]	s_{cf} [ft]	CF layout	d_w [in]	t_{deck} [in]	CF type	A_{cf} [in^2]	E_c [ksi]
155-5	1	25	8	5	60	Parallel	750	20	Cont.	96	8	X	4.79	5000
156-1	1	25	8	5	60	Parallel	750	30	Cont.	96	8	X	2.86	5000
157-1	1	25	8	5	60	Trap.	1500	20	Cont.	96	8	X	2.86	3600
157-2	1	25	8	5	60	Trap.	1500	20	Cont.	96	8	X	2.86	5000
157-3	1	25	8	5	60	Trap.	1500	20	Cont.	96	10	X	2.86	5000
157-4	1	25	8	5	60	Trap.	1500	20	Cont.	96	8	K	2.86	5000
157-5	1	25	8	5	60	Trap.	1500	20	Cont.	96	8	X	4.79	5000
158-1	1	25	8	5	60	Trap.	1500	30	Cont.	96	8	X	2.86	5000
159-1	1	25	8	5	60	Trap.	750	20	Cont.	96	8	X	2.86	3600
159-2	1	25	8	5	60	Trap.	750	20	Cont.	96	8	X	2.86	5000
159-3	1	25	8	5	60	Trap.	750	20	Cont.	96	10	X	2.86	5000
159-4	1	25	8	5	60	Trap.	750	20	Cont.	96	8	K	2.86	5000
159-5	1	25	8	5	60	Trap.	750	20	Cont.	96	8	X	4.79	5000
160-1	1	25	8	5	60	Trap.	750	30	Cont.	96	8	X	2.86	5000
161-1	1	25	10	3	0	Parallel	1500	20	Cont.	96	8	X	2.86	3600
161-2	1	25	10	3	0	Parallel	1500	20	Cont.	96	8	X	2.86	5000
161-3	1	25	10	3	0	Parallel	1500	20	Cont.	96	10	X	2.86	5000
161-4	1	25	10	3	0	Parallel	1500	20	Cont.	96	8	K	2.86	5000
161-5	1	25	10	3	0	Parallel	1500	20	Cont.	96	8	X	4.79	5000
162-1	1	25	10	3	0	Parallel	1500	30	Cont.	96	8	X	2.86	5000
163-1	1	25	10	3	0	Parallel	750	20	Cont.	96	8	X	2.86	3600
163-2	1	25	10	3	0	Parallel	750	20	Cont.	96	8	X	2.86	5000
163-3	1	25	10	3	0	Parallel	750	20	Cont.	96	10	X	2.86	5000
163-4	1	25	10	3	0	Parallel	750	20	Cont.	96	8	K	2.86	5000
163-5	1	25	10	3	0	Parallel	750	20	Cont.	96	8	X	4.79	5000
164-1	1	25	10	3	0	Parallel	750	30	Cont.	96	8	X	2.86	5000
165-1	1	25	10	3	30	Parallel	1500	20	Cont.	96	8	X	2.86	3600
165-2	1	25	10	3	30	Parallel	1500	20	Cont.	96	8	X	2.86	5000
165-3	1	25	10	3	30	Parallel	1500	20	Cont.	96	10	X	2.86	5000
165-4	1	25	10	3	30	Parallel	1500	20	Cont.	96	8	K	2.86	5000
165-5	1	25	10	3	30	Parallel	1500	20	Cont.	96	8	X	4.79	5000
166-1	1	25	10	3	30	Parallel	1500	30	Cont.	96	8	X	2.86	5000
167-1	1	25	10	3	30	Parallel	750	20	Cont.	96	8	X	2.86	3600
167-2	1	25	10	3	30	Parallel	750	20	Cont.	96	8	X	2.86	5000
167-3	1	25	10	3	30	Parallel	750	20	Cont.	96	10	X	2.86	5000
167-4	1	25	10	3	30	Parallel	750	20	Cont.	96	8	K	2.86	5000
167-5	1	25	10	3	30	Parallel	750	20	Cont.	96	8	X	4.79	5000
168-1	1	25	10	3	30	Parallel	750	30	Cont.	96	8	X	2.86	5000
169-1	1	25	10	3	60	Parallel	1500	20	Cont.	96	8	X	2.86	3600
169-2	1	25	10	3	60	Parallel	1500	20	Cont.	96	8	X	2.86	5000
169-3	1	25	10	3	60	Parallel	1500	20	Cont.	96	10	X	2.86	5000
169-4	1	25	10	3	60	Parallel	1500	20	Cont.	96	8	K	2.86	5000
169-5	1	25	10	3	60	Parallel	1500	20	Cont.	96	8	X	4.79	5000
170-1	1	25	10	3	60	Parallel	1500	30	Cont.	96	8	X	2.86	5000
171-1	1	25	10	3	60	Parallel	750	20	Cont.	96	8	X	2.86	3600
171-2	1	25	10	3	60	Parallel	750	20	Cont.	96	8	X	2.86	5000
171-3	1	25	10	3	60	Parallel	750	20	Cont.	96	10	X	2.86	5000
171-4	1	25	10	3	60	Parallel	750	20	Cont.	96	8	K	2.86	5000
171-5	1	25	10	3	60	Parallel	750	20	Cont.	96	8	X	4.79	5000
172-1	1	25	10	3	60	Parallel	750	30	Cont.	96	8	X	2.86	5000
173-1	1	25	10	3	60	Trap.	1500	20	Cont.	96	8	X	2.86	3600
173-2	1	25	10	3	60	Trap.	1500	20	Cont.	96	8	X	2.86	5000
173-3	1	25	10	3	60	Trap.	1500	20	Cont.	96	10	X	2.86	5000
173-4	1	25	10	3	60	Trap.	1500	20	Cont.	96	8	K	2.86	5000
173-5	1	25	10	3	60	Trap.	1500	20	Cont.	96	8	X	4.79	5000
174-1	1	25	10	3	60	Trap.	1500	30	Cont.	96	8	X	2.86	5000
175-1	1	25	10	3	60	Trap.	750	20	Cont.	96	8	X	2.86	3600
175-2	1	25	10	3	60	Trap.	750	20	Cont.	96	8	X	2.86	5000
175-3	1	25	10	3	60	Trap.	750	20	Cont.	96	10	X	2.86	5000
175-4	1	25	10	3	60	Trap.	750	20	Cont.	96	8	K	2.86	5000
175-5	1	25	10	3	60	Trap.	750	20	Cont.	96	8	X	4.79	5000
176-1	1	25	10	3	60	Trap.	750	30	Cont.	96	8	X	2.86	5000
177-1	1	25	10	5	0	Parallel	1500	20	Cont.	96	8	X	2.86	3600
177-2	1	25	10	5	0	Parallel	1500	20	Cont.	96	8	X	2.86	5000
177-3	1	25	10	5	0	Parallel	1500	20	Cont.	96	10	X	2.86	5000
177-4	1	25	10	5	0	Parallel	1500	20	Cont.	96	8	K	2.86	5000
177-5	1	25	10	5	0	Parallel	1500	20	Cont.	96	8	X	4.79	5000
178-1	1	25	10	5	0	Parallel	1500	30	Cont.	96	8	X	2.86	5000
179-1	1	25	10	5	0	Parallel	750	20	Cont.	96	8	X	2.86	3600
179-2	1	25	10	5	0	Parallel	750	20	Cont.	96	8	X	2.86	5000
179-3	1	25	10	5	0	Parallel	750	20	Cont.	96	10	X	2.86	5000
179-4	1	25	10	5	0	Parallel	750	20	Cont.	96	8	K	2.86	5000
179-5	1	25	10	5	0	Parallel	750	20	Cont.	96	8	X	4.79	5000
180-1	1	25	10	5	0	Parallel	750	30	Cont.	96	8	X	2.86	5000
181-1	1	25	10	5	30	Parallel	1500	20	Cont.	96	8	X	2.86	3600
181-2	1	25	10	5	30	Parallel	1500	20	Cont.	96	8	X	2.86	5000
181-3	1	25	10	5	30	Parallel	1500	20	Cont.	96	10	X	2.86	5000
181-4	1	25	10	5	30	Parallel	1500	20	Cont.	96	8	K	2.86	5000
181-5	1	25	10	5	30	Parallel	1500	20	Cont.	96	8	X	4.79	5000

Model ID	Geometry									Cross-section		CF detail		Mat'l
	n_{span}	L/d ratio	s_g [ft]	n_{girder}	Support skew [deg];	Layout	R [ft]	s_{cf} [ft]	CF layout	d_w [in]	t_{deck} [in]	CF type	A_{cf} [in^2]	E_c [ksi]
182-1	1	25	10	5	30	Parallel	1500	30	Cont.	96	8	X	2.86	5000
183-1	1	25	10	5	30	Parallel	750	20	Cont.	96	8	X	2.86	3600
183-2	1	25	10	5	30	Parallel	750	20	Cont.	96	8	X	2.86	5000
183-3	1	25	10	5	30	Parallel	750	20	Cont.	96	10	X	2.86	5000
183-4	1	25	10	5	30	Parallel	750	20	Cont.	96	8	K	2.86	5000
183-5	1	25	10	5	30	Parallel	750	20	Cont.	96	8	X	4.79	5000
184-1	1	25	10	5	30	Parallel	750	30	Cont.	96	8	X	2.86	5000
185-1	1	25	10	5	60	Parallel	1500	20	Cont.	96	8	X	2.86	3600
185-2	1	25	10	5	60	Parallel	1500	20	Cont.	96	8	X	2.86	5000
185-3	1	25	10	5	60	Parallel	1500	20	Cont.	96	10	X	2.86	5000
185-4	1	25	10	5	60	Parallel	1500	20	Cont.	96	8	K	2.86	5000
185-5	1	25	10	5	60	Parallel	1500	20	Cont.	96	8	X	4.79	5000
186-1	1	25	10	5	60	Parallel	1500	30	Cont.	96	8	X	2.86	5000
187-1	1	25	10	5	60	Parallel	750	20	Cont.	96	8	X	2.86	3600
187-2	1	25	10	5	60	Parallel	750	20	Cont.	96	8	X	2.86	5000
187-3	1	25	10	5	60	Parallel	750	20	Cont.	96	10	X	2.86	5000
187-4	1	25	10	5	60	Parallel	750	20	Cont.	96	8	K	2.86	5000
187-5	1	25	10	5	60	Parallel	750	20	Cont.	96	8	X	4.79	5000
188-1	1	25	10	5	60	Parallel	750	30	Cont.	96	8	X	2.86	5000
189-1	1	25	10	5	60	Trap.	1500	20	Cont.	96	8	X	2.86	3600
189-2	1	25	10	5	60	Trap.	1500	20	Cont.	96	8	X	2.86	5000
189-3	1	25	10	5	60	Trap.	1500	20	Cont.	96	10	X	2.86	5000
189-4	1	25	10	5	60	Trap.	1500	20	Cont.	96	8	K	2.86	5000
189-5	1	25	10	5	60	Trap.	1500	20	Cont.	96	8	X	4.79	5000
190-1	1	25	10	5	60	Trap.	1500	30	Cont.	96	8	X	2.86	5000
191-1	1	25	10	5	60	Trap.	750	20	Cont.	96	8	X	2.86	3600
191-2	1	25	10	5	60	Trap.	750	20	Cont.	96	8	X	2.86	5000
191-3	1	25	10	5	60	Trap.	750	20	Cont.	96	10	X	2.86	5000
191-4	1	25	10	5	60	Trap.	750	20	Cont.	96	8	K	2.86	5000
191-5	1	25	10	5	60	Trap.	750	20	Cont.	96	8	X	4.79	5000
192-1	1	25	10	5	60	Trap.	750	30	Cont.	96	8	X	2.86	5000
193-1	1	30	6	3	0	Parallel	Infinite	20	Cont.	72	8	X	2.86	3600
193-2	1	30	6	3	0	Parallel	Infinite	20	Cont.	72	8	X	2.86	5000
193-3	1	30	6	3	0	Parallel	Infinite	20	Cont.	72	10	X	2.86	5000
193-4	1	30	6	3	0	Parallel	Infinite	20	Cont.	72	8	K	2.86	5000
193-5	1	30	6	3	0	Parallel	Infinite	20	Cont.	72	8	X	4.79	5000
194-1	1	30	6	3	0	Parallel	Infinite	30	Cont.	72	8	X	2.86	5000
195-1	1	30	6	3	30	Parallel	Infinite	20	Cont.	72	8	X	2.86	3600
195-2	1	30	6	3	30	Parallel	Infinite	20	Cont.	72	8	X	2.86	5000
195-3	1	30	6	3	30	Parallel	Infinite	20	Cont.	72	10	X	2.86	5000
195-4	1	30	6	3	30	Parallel	Infinite	20	Cont.	72	8	K	2.86	5000
195-5	1	30	6	3	30	Parallel	Infinite	20	Cont.	72	8	X	4.79	5000
196-1	1	30	6	3	30	Parallel	Infinite	30	Cont.	72	8	X	2.86	5000
197-1	1	30	6	3	60	Parallel	Infinite	20	Cont.	72	8	X	2.86	3600
197-2	1	30	6	3	60	Parallel	Infinite	20	Cont.	72	8	X	2.86	5000
197-3	1	30	6	3	60	Parallel	Infinite	20	Cont.	72	10	X	2.86	5000
197-4	1	30	6	3	60	Parallel	Infinite	20	Cont.	72	8	K	2.86	5000
197-5	1	30	6	3	60	Parallel	Infinite	20	Cont.	72	8	X	4.79	5000
198-1	1	30	6	3	60	Parallel	Infinite	30	Cont.	72	8	X	2.86	5000
199-1	1	30	6	3	60	Parallel	Infinite	20	Stag.	72	8	X	2.86	3600
199-2	1	30	6	3	60	Parallel	Infinite	20	Stag.	72	8	X	2.86	5000
199-3	1	30	6	3	60	Parallel	Infinite	20	Stag.	72	10	X	2.86	5000
199-4	1	30	6	3	60	Parallel	Infinite	20	Stag.	72	8	K	2.86	5000
199-5	1	30	6	3	60	Parallel	Infinite	20	Stag.	72	8	X	4.79	5000
200-1	1	30	6	3	60	Parallel	Infinite	30	Stag.	72	8	X	2.86	5000
201-1	1	30	6	3	60	Trap.	Infinite	20	Cont.	72	8	X	2.86	3600
201-2	1	30	6	3	60	Trap.	Infinite	20	Cont.	72	8	X	2.86	5000
201-3	1	30	6	3	60	Trap.	Infinite	20	Cont.	72	10	X	2.86	5000
201-4	1	30	6	3	60	Trap.	Infinite	20	Cont.	72	8	K	2.86	5000
201-5	1	30	6	3	60	Trap.	Infinite	20	Cont.	72	8	X	4.79	5000
202-1	1	30	6	3	60	Trap.	Infinite	30	Cont.	72	8	X	2.86	5000
203-1	1	30	6	3	60	Trap.	Infinite	20	Stag.	72	8	X	2.86	3600
203-2	1	30	6	3	60	Trap.	Infinite	20	Stag.	72	8	X	2.86	5000
203-3	1	30	6	3	60	Trap.	Infinite	20	Stag.	72	10	X	2.86	5000
203-4	1	30	6	3	60	Trap.	Infinite	20	Stag.	72	8	K	2.86	5000
203-5	1	30	6	3	60	Trap.	Infinite	20	Stag.	72	8	X	4.79	5000
204-1	1	30	6	3	60	Trap.	Infinite	30	Stag.	72	8	X	2.86	5000
205-1	1	30	6	5	0	Parallel	Infinite	20	Cont.	72	8	X	2.86	3600
205-2	1	30	6	5	0	Parallel	Infinite	20	Cont.	72	8	X	2.86	5000
205-3	1	30	6	5	0	Parallel	Infinite	20	Cont.	72	10	X	2.86	5000
205-4	1	30	6	5	0	Parallel	Infinite	20	Cont.	72	8	K	2.86	5000
205-5	1	30	6	5	0	Parallel	Infinite	20	Cont.	72	8	X	4.79	5000
206-1	1	30	6	5	0	Parallel	Infinite	30	Cont.	72	8	X	2.86	5000
207-1	1	30	6	5	30	Parallel	Infinite	20	Cont.	72	8	X	2.86	3600
207-2	1	30	6	5	30	Parallel	Infinite	20	Cont.	72	8	X	2.86	5000
207-3	1	30	6	5	30	Parallel	Infinite	20	Cont.	72	10	X	2.86	5000
207-4	1	30	6	5	30	Parallel	Infinite	20	Cont.	72	8	K	2.86	5000
207-5	1	30	6	5	30	Parallel	Infinite	20	Cont.	72	8	X	4.79	5000
208-1	1	30	6	5	30	Parallel	Infinite	30	Cont.	72	8	X	2.86	5000

Model ID	Geometry									Cross-section		CF detail		Mat'l
	n_{span}	L/d ratio	s_g [ft]	n_{girder}	Support skew [deg]; Layout		R [ft]	s_{cf} [ft]	CF layout	d_w [in]	t_{deck} [in]	CF type	A_{cf} [in^2]	E_c [ksi]
209-1	1	30	6	5	60	Parallel	Infinite	20	Cont.	72	8	X	2.86	3600
209-2	1	30	6	5	60	Parallel	Infinite	20	Cont.	72	8	X	2.86	5000
209-3	1	30	6	5	60	Parallel	Infinite	20	Cont.	72	10	X	2.86	5000
209-4	1	30	6	5	60	Parallel	Infinite	20	Cont.	72	8	K	2.86	5000
209-5	1	30	6	5	60	Parallel	Infinite	20	Cont.	72	8	X	4.79	5000
210-1	1	30	6	5	60	Parallel	Infinite	30	Cont.	72	8	X	2.86	5000
211-1	1	30	6	5	60	Parallel	Infinite	20	Stag.	72	8	X	2.86	3600
211-2	1	30	6	5	60	Parallel	Infinite	20	Stag.	72	8	X	2.86	5000
211-3	1	30	6	5	60	Parallel	Infinite	20	Stag.	72	10	X	2.86	5000
211-4	1	30	6	5	60	Parallel	Infinite	20	Stag.	72	8	K	2.86	5000
211-5	1	30	6	5	60	Parallel	Infinite	20	Stag.	72	8	X	4.79	5000
212-1	1	30	6	5	60	Parallel	Infinite	30	Stag.	72	8	X	2.86	5000
213-1	1	30	6	5	60	Trap.	Infinite	20	Cont.	72	8	X	2.86	3600
213-2	1	30	6	5	60	Trap.	Infinite	20	Cont.	72	8	X	2.86	5000
213-3	1	30	6	5	60	Trap.	Infinite	20	Cont.	72	10	X	2.86	5000
213-4	1	30	6	5	60	Trap.	Infinite	20	Cont.	72	8	K	2.86	5000
213-5	1	30	6	5	60	Trap.	Infinite	20	Cont.	72	8	X	4.79	5000
214-1	1	30	6	5	60	Trap.	Infinite	30	Cont.	72	8	X	2.86	5000
215-1	1	30	6	5	60	Trap.	Infinite	20	Stag.	72	8	X	2.86	3600
215-2	1	30	6	5	60	Trap.	Infinite	20	Stag.	72	8	X	2.86	5000
215-3	1	30	6	5	60	Trap.	Infinite	20	Stag.	72	10	X	2.86	5000
215-4	1	30	6	5	60	Trap.	Infinite	20	Stag.	72	8	K	2.86	5000
215-5	1	30	6	5	60	Trap.	Infinite	20	Stag.	72	8	X	4.79	5000
216-1	1	30	6	5	60	Trap.	Infinite	30	Stag.	72	8	X	2.86	5000
217-1	1	30	8	3	0	Parallel	Infinite	20	Cont.	72	8	X	2.86	3600
217-2	1	30	8	3	0	Parallel	Infinite	20	Cont.	72	8	X	2.86	5000
217-3	1	30	8	3	0	Parallel	Infinite	20	Cont.	72	10	X	2.86	5000
217-4	1	30	8	3	0	Parallel	Infinite	20	Cont.	72	8	K	2.86	5000
217-5	1	30	8	3	0	Parallel	Infinite	20	Cont.	72	8	X	4.79	5000
218-1	1	30	8	3	0	Parallel	Infinite	30	Cont.	72	8	X	2.86	5000
219-1	1	30	8	3	30	Parallel	Infinite	20	Cont.	72	8	X	2.86	3600
219-2	1	30	8	3	30	Parallel	Infinite	20	Cont.	72	8	X	2.86	5000
219-3	1	30	8	3	30	Parallel	Infinite	20	Cont.	72	10	X	2.86	5000
219-4	1	30	8	3	30	Parallel	Infinite	20	Cont.	72	8	K	2.86	5000
219-5	1	30	8	3	30	Parallel	Infinite	20	Cont.	72	8	X	4.79	5000
220-1	1	30	8	3	30	Parallel	Infinite	30	Cont.	72	8	X	2.86	5000
221-1	1	30	8	3	60	Parallel	Infinite	20	Cont.	72	8	X	2.86	3600
221-2	1	30	8	3	60	Parallel	Infinite	20	Cont.	72	8	X	2.86	5000
221-3	1	30	8	3	60	Parallel	Infinite	20	Cont.	72	10	X	2.86	5000
221-4	1	30	8	3	60	Parallel	Infinite	20	Cont.	72	8	K	2.86	5000
221-5	1	30	8	3	60	Parallel	Infinite	20	Cont.	72	8	X	4.79	5000
222-1	1	30	8	3	60	Parallel	Infinite	30	Cont.	72	8	X	2.86	5000
223-1	1	30	8	3	60	Parallel	Infinite	20	Stag.	72	8	X	2.86	3600
223-2	1	30	8	3	60	Parallel	Infinite	20	Stag.	72	8	X	2.86	5000
223-3	1	30	8	3	60	Parallel	Infinite	20	Stag.	72	10	X	2.86	5000
223-4	1	30	8	3	60	Parallel	Infinite	20	Stag.	72	8	K	2.86	5000
223-5	1	30	8	3	60	Parallel	Infinite	20	Stag.	72	8	X	4.79	5000
224-1	1	30	8	3	60	Parallel	Infinite	30	Stag.	72	8	X	2.86	5000
225-1	1	30	8	3	60	Trap.	Infinite	20	Cont.	72	8	X	2.86	3600
225-2	1	30	8	3	60	Trap.	Infinite	20	Cont.	72	8	X	2.86	5000
225-3	1	30	8	3	60	Trap.	Infinite	20	Cont.	72	10	X	2.86	5000
225-4	1	30	8	3	60	Trap.	Infinite	20	Cont.	72	8	K	2.86	5000
225-5	1	30	8	3	60	Trap.	Infinite	20	Cont.	72	8	X	4.79	5000
226-1	1	30	8	3	60	Trap.	Infinite	30	Cont.	72	8	X	2.86	5000
227-1	1	30	8	3	60	Trap.	Infinite	20	Stag.	72	8	X	2.86	3600
227-2	1	30	8	3	60	Trap.	Infinite	20	Stag.	72	8	X	2.86	5000
227-3	1	30	8	3	60	Trap.	Infinite	20	Stag.	72	10	X	2.86	5000
227-4	1	30	8	3	60	Trap.	Infinite	20	Stag.	72	8	K	2.86	5000
227-5	1	30	8	3	60	Trap.	Infinite	20	Stag.	72	8	X	4.79	5000
228-1	1	30	8	3	60	Trap.	Infinite	30	Stag.	72	8	X	2.86	5000
229-1	1	30	8	5	0	Parallel	Infinite	20	Cont.	72	8	X	2.86	3600
229-2	1	30	8	5	0	Parallel	Infinite	20	Cont.	72	8	X	2.86	5000
229-3	1	30	8	5	0	Parallel	Infinite	20	Cont.	72	10	X	2.86	5000
229-4	1	30	8	5	0	Parallel	Infinite	20	Cont.	72	8	K	2.86	5000
229-5	1	30	8	5	0	Parallel	Infinite	20	Cont.	72	8	X	4.79	5000
230-1	1	30	8	5	0	Parallel	Infinite	30	Cont.	72	8	X	2.86	5000
231-1	1	30	8	5	30	Parallel	Infinite	20	Cont.	72	8	X	2.86	3600
231-2	1	30	8	5	30	Parallel	Infinite	20	Cont.	72	8	X	2.86	5000
231-3	1	30	8	5	30	Parallel	Infinite	20	Cont.	72	10	X	2.86	5000
231-4	1	30	8	5	30	Parallel	Infinite	20	Cont.	72	8	K	2.86	5000
231-5	1	30	8	5	30	Parallel	Infinite	20	Cont.	72	8	X	4.79	5000
232-1	1	30	8	5	30	Parallel	Infinite	30	Cont.	72	8	X	2.86	5000
233-1	1	30	8	5	60	Parallel	Infinite	20	Cont.	72	8	X	2.86	3600
233-2	1	30	8	5	60	Parallel	Infinite	20	Cont.	72	8	X	2.86	5000
233-3	1	30	8	5	60	Parallel	Infinite	20	Cont.	72	10	X	2.86	5000
233-4	1	30	8	5	60	Parallel	Infinite	20	Cont.	72	8	K	2.86	5000
233-5	1	30	8	5	60	Parallel	Infinite	20	Cont.	72	8	X	4.79	5000
234-1	1	30	8	5	60	Parallel	Infinite	30	Cont.	72	8	X	2.86	5000
235-1	1	30	8	5	60	Parallel	Infinite	20	Stag.	72	8	X	2.86	3600

Model ID	Geometry									Cross-section		CF detail		Mat'l
	n_{span}	L/d ratio	s_g [ft]	n_{girder}	Support skew [deg]; Layout		R [ft]	s_{cf} [ft]	CF layout	d_w [in]	t_{deck} [in]	CF type	A_{cf} [in^2]	E_c [ksi]
235-2	1	30	8	5	60	Parallel	Infinite	20	Stag.	72	8	X	2.86	5000
235-3	1	30	8	5	60	Parallel	Infinite	20	Stag.	72	10	X	2.86	5000
235-4	1	30	8	5	60	Parallel	Infinite	20	Stag.	72	8	K	2.86	5000
235-5	1	30	8	5	60	Parallel	Infinite	20	Stag.	72	8	X	4.79	5000
236-1	1	30	8	5	60	Parallel	Infinite	30	Stag.	72	8	X	2.86	5000
237-1	1	30	8	5	60	Trap.	Infinite	20	Cont.	72	8	X	2.86	3600
237-2	1	30	8	5	60	Trap.	Infinite	20	Cont.	72	8	X	2.86	5000
237-3	1	30	8	5	60	Trap.	Infinite	20	Cont.	72	10	X	2.86	5000
237-4	1	30	8	5	60	Trap.	Infinite	20	Cont.	72	8	K	2.86	5000
237-5	1	30	8	5	60	Trap.	Infinite	20	Cont.	72	8	X	4.79	5000
238-1	1	30	8	5	60	Trap.	Infinite	30	Cont.	72	8	X	2.86	5000
239-1	1	30	8	5	60	Trap.	Infinite	20	Stag.	72	8	X	2.86	3600
239-2	1	30	8	5	60	Trap.	Infinite	20	Stag.	72	8	X	2.86	5000
239-3	1	30	8	5	60	Trap.	Infinite	20	Stag.	72	10	X	2.86	5000
239-4	1	30	8	5	60	Trap.	Infinite	20	Stag.	72	8	K	2.86	5000
239-5	1	30	8	5	60	Trap.	Infinite	20	Stag.	72	8	X	4.79	5000
240-1	1	30	8	5	60	Trap.	Infinite	30	Stag.	72	8	X	2.86	5000
241-1	1	30	10	3	0	Parallel	Infinite	20	Cont.	72	8	X	2.86	3600
241-2	1	30	10	3	0	Parallel	Infinite	20	Cont.	72	8	X	2.86	5000
241-3	1	30	10	3	0	Parallel	Infinite	20	Cont.	72	10	X	2.86	5000
241-4	1	30	10	3	0	Parallel	Infinite	20	Cont.	72	8	K	2.86	5000
241-5	1	30	10	3	0	Parallel	Infinite	20	Cont.	72	8	X	4.79	5000
242-1	1	30	10	3	0	Parallel	Infinite	30	Cont.	72	8	X	2.86	5000
243-1	1	30	10	3	30	Parallel	Infinite	20	Cont.	72	8	X	2.86	3600
243-2	1	30	10	3	30	Parallel	Infinite	20	Cont.	72	8	X	2.86	5000
243-3	1	30	10	3	30	Parallel	Infinite	20	Cont.	72	10	X	2.86	5000
243-4	1	30	10	3	30	Parallel	Infinite	20	Cont.	72	8	K	2.86	5000
243-5	1	30	10	3	30	Parallel	Infinite	20	Cont.	72	8	X	4.79	5000
244-1	1	30	10	3	30	Parallel	Infinite	30	Cont.	72	8	X	2.86	5000
245-1	1	30	10	3	60	Parallel	Infinite	20	Cont.	72	8	X	2.86	3600
245-2	1	30	10	3	60	Parallel	Infinite	20	Cont.	72	8	X	2.86	5000
245-3	1	30	10	3	60	Parallel	Infinite	20	Cont.	72	10	X	2.86	5000
245-4	1	30	10	3	60	Parallel	Infinite	20	Cont.	72	8	K	2.86	5000
245-5	1	30	10	3	60	Parallel	Infinite	20	Cont.	72	8	X	4.79	5000
246-1	1	30	10	3	60	Parallel	Infinite	30	Cont.	72	8	X	2.86	5000
247-1	1	30	10	3	60	Parallel	Infinite	20	Stag.	72	8	X	2.86	3600
247-2	1	30	10	3	60	Parallel	Infinite	20	Stag.	72	8	X	2.86	5000
247-3	1	30	10	3	60	Parallel	Infinite	20	Stag.	72	10	X	2.86	5000
247-4	1	30	10	3	60	Parallel	Infinite	20	Stag.	72	8	K	2.86	5000
247-5	1	30	10	3	60	Parallel	Infinite	20	Stag.	72	8	X	4.79	5000
248-1	1	30	10	3	60	Parallel	Infinite	30	Stag.	72	8	X	2.86	5000
249-1	1	30	10	3	60	Trap.	Infinite	20	Cont.	72	8	X	2.86	3600
249-2	1	30	10	3	60	Trap.	Infinite	20	Cont.	72	8	X	2.86	5000
249-3	1	30	10	3	60	Trap.	Infinite	20	Cont.	72	10	X	2.86	5000
249-4	1	30	10	3	60	Trap.	Infinite	20	Cont.	72	8	K	2.86	5000
249-5	1	30	10	3	60	Trap.	Infinite	20	Cont.	72	8	X	4.79	5000
250-1	1	30	10	3	60	Trap.	Infinite	30	Cont.	72	8	X	2.86	5000
251-1	1	30	10	3	60	Trap.	Infinite	20	Stag.	72	8	X	2.86	3600
251-2	1	30	10	3	60	Trap.	Infinite	20	Stag.	72	8	X	2.86	5000
251-3	1	30	10	3	60	Trap.	Infinite	20	Stag.	72	10	X	2.86	5000
251-4	1	30	10	3	60	Trap.	Infinite	20	Stag.	72	8	K	2.86	5000
251-5	1	30	10	3	60	Trap.	Infinite	20	Stag.	72	8	X	4.79	5000
252-1	1	30	10	3	60	Trap.	Infinite	30	Stag.	72	8	X	2.86	5000
253-1	1	30	10	5	0	Parallel	Infinite	20	Cont.	72	8	X	2.86	3600
253-2	1	30	10	5	0	Parallel	Infinite	20	Cont.	72	8	X	2.86	5000
253-3	1	30	10	5	0	Parallel	Infinite	20	Cont.	72	10	X	2.86	5000
253-4	1	30	10	5	0	Parallel	Infinite	20	Cont.	72	8	K	2.86	5000
253-5	1	30	10	5	0	Parallel	Infinite	20	Cont.	72	8	X	4.79	5000
254-1	1	30	10	5	0	Parallel	Infinite	30	Cont.	72	8	X	2.86	5000
255-1	1	30	10	5	30	Parallel	Infinite	20	Cont.	72	8	X	2.86	3600
255-2	1	30	10	5	30	Parallel	Infinite	20	Cont.	72	8	X	2.86	5000
255-3	1	30	10	5	30	Parallel	Infinite	20	Cont.	72	10	X	2.86	5000
255-4	1	30	10	5	30	Parallel	Infinite	20	Cont.	72	8	K	2.86	5000
255-5	1	30	10	5	30	Parallel	Infinite	20	Cont.	72	8	X	4.79	5000
256-1	1	30	10	5	30	Parallel	Infinite	30	Cont.	72	8	X	2.86	5000
257-1	1	30	10	5	60	Parallel	Infinite	20	Cont.	72	8	X	2.86	3600
257-2	1	30	10	5	60	Parallel	Infinite	20	Cont.	72	8	X	2.86	5000
257-3	1	30	10	5	60	Parallel	Infinite	20	Cont.	72	10	X	2.86	5000
257-4	1	30	10	5	60	Parallel	Infinite	20	Cont.	72	8	K	2.86	5000
257-5	1	30	10	5	60	Parallel	Infinite	20	Cont.	72	8	X	4.79	5000
258-1	1	30	10	5	60	Parallel	Infinite	30	Cont.	72	8	X	2.86	5000
259-1	1	30	10	5	60	Parallel	Infinite	20	Stag.	72	8	X	2.86	3600
259-2	1	30	10	5	60	Parallel	Infinite	20	Stag.	72	8	X	2.86	5000
259-3	1	30	10	5	60	Parallel	Infinite	20	Stag.	72	10	X	2.86	5000
259-4	1	30	10	5	60	Parallel	Infinite	20	Stag.	72	8	K	2.86	5000
259-5	1	30	10	5	60	Parallel	Infinite	20	Stag.	72	8	X	4.79	5000
260-1	1	30	10	5	60	Parallel	Infinite	30	Stag.	72	8	X	2.86	5000
261-1	1	30	10	5	60	Trap.	Infinite	20	Cont.	72	8	X	2.86	3600
261-2	1	30	10	5	60	Trap.	Infinite	20	Cont.	72	8	X	2.86	5000

Model ID	Geometry									Cross-section		CF detail		Mat'l
	n_{span}	L/d ratio	s_g [ft]	n_{girder}	Support skew [deg]; Layout		R [ft]	s_{cf} [ft]	CF layout	d_w [in]	t_{deck} [in]	CF type	A_{cf} [in^2]	E_c [ksi]
261-3	1	30	10	5	60	Trap.	Infinite	20	Cont.	72	10	X	2.86	5000
261-4	1	30	10	5	60	Trap.	Infinite	20	Cont.	72	8	K	2.86	5000
261-5	1	30	10	5	60	Trap.	Infinite	20	Cont.	72	8	X	4.79	5000
262-1	1	30	10	5	60	Trap.	Infinite	30	Cont.	72	8	X	2.86	5000
263-1	1	30	10	5	60	Trap.	Infinite	20	Stag.	72	8	X	2.86	3600
263-2	1	30	10	5	60	Trap.	Infinite	20	Stag.	72	8	X	2.86	5000
263-3	1	30	10	5	60	Trap.	Infinite	20	Stag.	72	10	X	2.86	5000
263-4	1	30	10	5	60	Trap.	Infinite	20	Stag.	72	8	K	2.86	5000
263-5	1	30	10	5	60	Trap.	Infinite	20	Stag.	72	8	X	4.79	5000
264-1	1	30	10	5	60	Trap.	Infinite	30	Stag.	72	8	X	2.86	5000
265-1	1	30	6	3	0	Parallel	Infinite	20	Cont.	96	8	X	2.86	3600
265-2	1	30	6	3	0	Parallel	Infinite	20	Cont.	96	8	X	2.86	5000
265-3	1	30	6	3	0	Parallel	Infinite	20	Cont.	96	10	X	2.86	5000
265-4	1	30	6	3	0	Parallel	Infinite	20	Cont.	96	8	K	2.86	5000
265-5	1	30	6	3	0	Parallel	Infinite	20	Cont.	96	8	X	4.79	5000
266-1	1	30	6	3	0	Parallel	Infinite	30	Cont.	96	8	X	2.86	5000
267-1	1	30	6	3	30	Parallel	Infinite	20	Cont.	96	8	X	2.86	3600
267-2	1	30	6	3	30	Parallel	Infinite	20	Cont.	96	8	X	2.86	5000
267-3	1	30	6	3	30	Parallel	Infinite	20	Cont.	96	10	X	2.86	5000
267-4	1	30	6	3	30	Parallel	Infinite	20	Cont.	96	8	K	2.86	5000
267-5	1	30	6	3	30	Parallel	Infinite	20	Cont.	96	8	X	4.79	5000
268-1	1	30	6	3	30	Parallel	Infinite	30	Cont.	96	8	X	2.86	5000
269-1	1	30	6	3	60	Parallel	Infinite	20	Cont.	96	8	X	2.86	3600
269-2	1	30	6	3	60	Parallel	Infinite	20	Cont.	96	8	X	2.86	5000
269-3	1	30	6	3	60	Parallel	Infinite	20	Cont.	96	10	X	2.86	5000
269-4	1	30	6	3	60	Parallel	Infinite	20	Cont.	96	8	K	2.86	5000
269-5	1	30	6	3	60	Parallel	Infinite	20	Cont.	96	8	X	4.79	5000
270-1	1	30	6	3	60	Parallel	Infinite	30	Cont.	96	8	X	2.86	5000
271-1	1	30	6	3	60	Parallel	Infinite	20	Stag.	96	8	X	2.86	3600
271-2	1	30	6	3	60	Parallel	Infinite	20	Stag.	96	8	X	2.86	5000
271-3	1	30	6	3	60	Parallel	Infinite	20	Stag.	96	10	X	2.86	5000
271-4	1	30	6	3	60	Parallel	Infinite	20	Stag.	96	8	K	2.86	5000
271-5	1	30	6	3	60	Parallel	Infinite	20	Stag.	96	8	X	4.79	5000
272-1	1	30	6	3	60	Parallel	Infinite	30	Stag.	96	8	X	2.86	5000
273-1	1	30	6	3	60	Trap.	Infinite	20	Cont.	96	8	X	2.86	3600
273-2	1	30	6	3	60	Trap.	Infinite	20	Cont.	96	8	X	2.86	5000
273-3	1	30	6	3	60	Trap.	Infinite	20	Cont.	96	10	X	2.86	5000
273-4	1	30	6	3	60	Trap.	Infinite	20	Cont.	96	8	K	2.86	5000
273-5	1	30	6	3	60	Trap.	Infinite	20	Cont.	96	8	X	4.79	5000
274-1	1	30	6	3	60	Trap.	Infinite	30	Cont.	96	8	X	2.86	5000
275-1	1	30	6	3	60	Trap.	Infinite	20	Stag.	96	8	X	2.86	3600
275-2	1	30	6	3	60	Trap.	Infinite	20	Stag.	96	8	X	2.86	5000
275-3	1	30	6	3	60	Trap.	Infinite	20	Stag.	96	10	X	2.86	5000
275-4	1	30	6	3	60	Trap.	Infinite	20	Stag.	96	8	K	2.86	5000
275-5	1	30	6	3	60	Trap.	Infinite	20	Stag.	96	8	X	4.79	5000
276-1	1	30	6	3	60	Trap.	Infinite	30	Stag.	96	8	X	2.86	5000
277-1	1	30	6	5	0	Parallel	Infinite	20	Cont.	96	8	X	2.86	3600
277-2	1	30	6	5	0	Parallel	Infinite	20	Cont.	96	8	X	2.86	5000
277-3	1	30	6	5	0	Parallel	Infinite	20	Cont.	96	10	X	2.86	5000
277-4	1	30	6	5	0	Parallel	Infinite	20	Cont.	96	8	K	2.86	5000
277-5	1	30	6	5	0	Parallel	Infinite	20	Cont.	96	8	X	4.79	5000
278-1	1	30	6	5	0	Parallel	Infinite	30	Cont.	96	8	X	2.86	5000
279-1	1	30	6	5	30	Parallel	Infinite	20	Cont.	96	8	X	2.86	3600
279-2	1	30	6	5	30	Parallel	Infinite	20	Cont.	96	8	X	2.86	5000
279-3	1	30	6	5	30	Parallel	Infinite	20	Cont.	96	10	X	2.86	5000
279-4	1	30	6	5	30	Parallel	Infinite	20	Cont.	96	8	K	2.86	5000
279-5	1	30	6	5	30	Parallel	Infinite	20	Cont.	96	8	X	4.79	5000
280-1	1	30	6	5	30	Parallel	Infinite	30	Cont.	96	8	X	2.86	5000
281-1	1	30	6	5	60	Parallel	Infinite	20	Cont.	96	8	X	2.86	3600
281-2	1	30	6	5	60	Parallel	Infinite	20	Cont.	96	8	X	2.86	5000
281-3	1	30	6	5	60	Parallel	Infinite	20	Cont.	96	10	X	2.86	5000
281-4	1	30	6	5	60	Parallel	Infinite	20	Cont.	96	8	K	2.86	5000
281-5	1	30	6	5	60	Parallel	Infinite	20	Cont.	96	8	X	4.79	5000
282-1	1	30	6	5	60	Parallel	Infinite	30	Cont.	96	8	X	2.86	5000
283-1	1	30	6	5	60	Parallel	Infinite	20	Stag.	96	8	X	2.86	3600
283-2	1	30	6	5	60	Parallel	Infinite	20	Stag.	96	8	X	2.86	5000
283-3	1	30	6	5	60	Parallel	Infinite	20	Stag.	96	10	X	2.86	5000
283-4	1	30	6	5	60	Parallel	Infinite	20	Stag.	96	8	K	2.86	5000
283-5	1	30	6	5	60	Parallel	Infinite	20	Stag.	96	8	X	4.79	5000
284-1	1	30	6	5	60	Parallel	Infinite	30	Stag.	96	8	X	2.86	5000
285-1	1	30	6	5	60	Trap.	Infinite	20	Cont.	96	8	X	2.86	3600
285-2	1	30	6	5	60	Trap.	Infinite	20	Cont.	96	8	X	2.86	5000
285-3	1	30	6	5	60	Trap.	Infinite	20	Cont.	96	10	X	2.86	5000
285-4	1	30	6	5	60	Trap.	Infinite	20	Cont.	96	8	K	2.86	5000
285-5	1	30	6	5	60	Trap.	Infinite	20	Cont.	96	8	X	4.79	5000
286-1	1	30	6	5	60	Trap.	Infinite	30	Cont.	96	8	X	2.86	5000
287-1	1	30	6	5	60	Trap.	Infinite	20	Stag.	96	8	X	2.86	3600
287-2	1	30	6	5	60	Trap.	Infinite	20	Stag.	96	8	X	2.86	5000
287-3	1	30	6	5	60	Trap.	Infinite	20	Stag.	96	10	X	2.86	5000

Model ID	Geometry									Cross-section		CF detail		Mat'l
	n_{span}	L/d ratio	s_g [ft]	n_{girder}	Support skew [deg]; Layout		R [ft]	s_{cf} [ft]	CF layout	d_w [in]	t_{deck} [in]	CF type	A_{cf} [in^2]	E_c [ksi]
287-4	1	30	6	5	60	Trap.	Infinite	20	Stag.	96	8	K	2.86	5000
287-5	1	30	6	5	60	Trap.	Infinite	20	Stag.	96	8	X	4.79	5000
288-1	1	30	6	5	60	Trap.	Infinite	30	Stag.	96	8	X	2.86	5000
289-1	1	30	8	3	0	Parallel	Infinite	20	Cont.	96	8	X	2.86	3600
289-2	1	30	8	3	0	Parallel	Infinite	20	Cont.	96	8	X	2.86	5000
289-3	1	30	8	3	0	Parallel	Infinite	20	Cont.	96	10	X	2.86	5000
289-4	1	30	8	3	0	Parallel	Infinite	20	Cont.	96	8	K	2.86	5000
289-5	1	30	8	3	0	Parallel	Infinite	20	Cont.	96	8	X	4.79	5000
290-1	1	30	8	3	0	Parallel	Infinite	30	Cont.	96	8	X	2.86	5000
291-1	1	30	8	3	30	Parallel	Infinite	20	Cont.	96	8	X	2.86	3600
291-2	1	30	8	3	30	Parallel	Infinite	20	Cont.	96	8	X	2.86	5000
291-3	1	30	8	3	30	Parallel	Infinite	20	Cont.	96	10	X	2.86	5000
291-4	1	30	8	3	30	Parallel	Infinite	20	Cont.	96	8	K	2.86	5000
291-5	1	30	8	3	30	Parallel	Infinite	20	Cont.	96	8	X	4.79	5000
292-1	1	30	8	3	30	Parallel	Infinite	30	Cont.	96	8	X	2.86	5000
293-1	1	30	8	3	60	Parallel	Infinite	20	Cont.	96	8	X	2.86	3600
293-2	1	30	8	3	60	Parallel	Infinite	20	Cont.	96	8	X	2.86	5000
293-3	1	30	8	3	60	Parallel	Infinite	20	Cont.	96	10	X	2.86	5000
293-4	1	30	8	3	60	Parallel	Infinite	20	Cont.	96	8	K	2.86	5000
293-5	1	30	8	3	60	Parallel	Infinite	20	Cont.	96	8	X	4.79	5000
294-1	1	30	8	3	60	Parallel	Infinite	30	Cont.	96	8	X	2.86	5000
295-1	1	30	8	3	60	Parallel	Infinite	20	Stag.	96	8	X	2.86	3600
295-2	1	30	8	3	60	Parallel	Infinite	20	Stag.	96	8	X	2.86	5000
295-3	1	30	8	3	60	Parallel	Infinite	20	Stag.	96	10	X	2.86	5000
295-4	1	30	8	3	60	Parallel	Infinite	20	Stag.	96	8	K	2.86	5000
295-5	1	30	8	3	60	Parallel	Infinite	20	Stag.	96	8	X	4.79	5000
296-1	1	30	8	3	60	Parallel	Infinite	30	Stag.	96	8	X	2.86	5000
297-1	1	30	8	3	60	Trap.	Infinite	20	Cont.	96	8	X	2.86	3600
297-2	1	30	8	3	60	Trap.	Infinite	20	Cont.	96	8	X	2.86	5000
297-3	1	30	8	3	60	Trap.	Infinite	20	Cont.	96	10	X	2.86	5000
297-4	1	30	8	3	60	Trap.	Infinite	20	Cont.	96	8	K	2.86	5000
297-5	1	30	8	3	60	Trap.	Infinite	20	Cont.	96	8	X	4.79	5000
298-1	1	30	8	3	60	Trap.	Infinite	30	Cont.	96	8	X	2.86	5000
299-1	1	30	8	3	60	Trap.	Infinite	20	Stag.	96	8	X	2.86	3600
299-2	1	30	8	3	60	Trap.	Infinite	20	Stag.	96	8	X	2.86	5000
299-3	1	30	8	3	60	Trap.	Infinite	20	Stag.	96	10	X	2.86	5000
299-4	1	30	8	3	60	Trap.	Infinite	20	Stag.	96	8	K	2.86	5000
299-5	1	30	8	3	60	Trap.	Infinite	20	Stag.	96	8	X	4.79	5000
300-1	1	30	8	3	60	Trap.	Infinite	30	Stag.	96	8	X	2.86	5000
301-1	1	30	8	5	0	Parallel	Infinite	20	Cont.	96	8	X	2.86	3600
301-2	1	30	8	5	0	Parallel	Infinite	20	Cont.	96	8	X	2.86	5000
301-3	1	30	8	5	0	Parallel	Infinite	20	Cont.	96	10	X	2.86	5000
301-4	1	30	8	5	0	Parallel	Infinite	20	Cont.	96	8	K	2.86	5000
301-5	1	30	8	5	0	Parallel	Infinite	20	Cont.	96	8	X	4.79	5000
302-1	1	30	8	5	0	Parallel	Infinite	30	Cont.	96	8	X	2.86	5000
303-1	1	30	8	5	30	Parallel	Infinite	20	Cont.	96	8	X	2.86	3600
303-2	1	30	8	5	30	Parallel	Infinite	20	Cont.	96	8	X	2.86	5000
303-3	1	30	8	5	30	Parallel	Infinite	20	Cont.	96	10	X	2.86	5000
303-4	1	30	8	5	30	Parallel	Infinite	20	Cont.	96	8	K	2.86	5000
303-5	1	30	8	5	30	Parallel	Infinite	20	Cont.	96	8	X	4.79	5000
304-1	1	30	8	5	30	Parallel	Infinite	30	Cont.	96	8	X	2.86	5000
305-1	1	30	8	5	60	Parallel	Infinite	20	Cont.	96	8	X	2.86	3600
305-2	1	30	8	5	60	Parallel	Infinite	20	Cont.	96	8	X	2.86	5000
305-3	1	30	8	5	60	Parallel	Infinite	20	Cont.	96	10	X	2.86	5000
305-4	1	30	8	5	60	Parallel	Infinite	20	Cont.	96	8	K	2.86	5000
305-5	1	30	8	5	60	Parallel	Infinite	20	Cont.	96	8	X	4.79	5000
306-1	1	30	8	5	60	Parallel	Infinite	30	Cont.	96	8	X	2.86	5000
307-1	1	30	8	5	60	Parallel	Infinite	20	Stag.	96	8	X	2.86	3600
307-2	1	30	8	5	60	Parallel	Infinite	20	Stag.	96	8	X	2.86	5000
307-3	1	30	8	5	60	Parallel	Infinite	20	Stag.	96	10	X	2.86	5000
307-4	1	30	8	5	60	Parallel	Infinite	20	Stag.	96	8	K	2.86	5000
307-5	1	30	8	5	60	Parallel	Infinite	20	Stag.	96	8	X	4.79	5000
308-1	1	30	8	5	60	Parallel	Infinite	30	Stag.	96	8	X	2.86	5000
309-1	1	30	8	5	60	Trap.	Infinite	20	Cont.	96	8	X	2.86	3600
309-2	1	30	8	5	60	Trap.	Infinite	20	Cont.	96	8	X	2.86	5000
309-3	1	30	8	5	60	Trap.	Infinite	20	Cont.	96	10	X	2.86	5000
309-4	1	30	8	5	60	Trap.	Infinite	20	Cont.	96	8	K	2.86	5000
309-5	1	30	8	5	60	Trap.	Infinite	20	Cont.	96	8	X	4.79	5000
310-1	1	30	8	5	60	Trap.	Infinite	30	Cont.	96	8	X	2.86	5000
311-1	1	30	8	5	60	Trap.	Infinite	20	Stag.	96	8	X	2.86	3600
311-2	1	30	8	5	60	Trap.	Infinite	20	Stag.	96	8	X	2.86	5000
311-3	1	30	8	5	60	Trap.	Infinite	20	Stag.	96	10	X	2.86	5000
311-4	1	30	8	5	60	Trap.	Infinite	20	Stag.	96	8	K	2.86	5000
311-5	1	30	8	5	60	Trap.	Infinite	20	Stag.	96	8	X	4.79	5000
312-1	1	30	8	5	60	Trap.	Infinite	30	Stag.	96	8	X	2.86	5000
313-1	1	30	10	3	0	Parallel	Infinite	20	Cont.	96	8	X	2.86	3600
313-2	1	30	10	3	0	Parallel	Infinite	20	Cont.	96	8	X	2.86	5000
313-3	1	30	10	3	0	Parallel	Infinite	20	Cont.	96	10	X	2.86	5000
313-4	1	30	10	3	0	Parallel	Infinite	20	Cont.	96	8	K	2.86	5000

Model ID	Geometry									Cross-section		CF detail		Mat'l
	n_{span}	L/d ratio	s_g [ft]	n_{girder}	Support skew [deg]; Layout		R [ft]	s_{cf} [ft]	CF layout	d_w [in]	t_{deck} [in]	CF type	A_{cf} [in^2]	E_c [ksi]
313-5	1	30	10	3	0	Parallel	Infinite	20	Cont.	96	8	X	4.79	5000
314-1	1	30	10	3	0	Parallel	Infinite	30	Cont.	96	8	X	2.86	5000
315-1	1	30	10	3	30	Parallel	Infinite	20	Cont.	96	8	X	2.86	3600
315-2	1	30	10	3	30	Parallel	Infinite	20	Cont.	96	8	X	2.86	5000
315-3	1	30	10	3	30	Parallel	Infinite	20	Cont.	96	10	X	2.86	5000
315-4	1	30	10	3	30	Parallel	Infinite	20	Cont.	96	8	K	2.86	5000
315-5	1	30	10	3	30	Parallel	Infinite	20	Cont.	96	8	X	4.79	5000
316-1	1	30	10	3	30	Parallel	Infinite	30	Cont.	96	8	X	2.86	5000
317-1	1	30	10	3	60	Parallel	Infinite	20	Cont.	96	8	X	2.86	3600
317-2	1	30	10	3	60	Parallel	Infinite	20	Cont.	96	8	X	2.86	5000
317-3	1	30	10	3	60	Parallel	Infinite	20	Cont.	96	10	X	2.86	5000
317-4	1	30	10	3	60	Parallel	Infinite	20	Cont.	96	8	K	2.86	5000
317-5	1	30	10	3	60	Parallel	Infinite	20	Cont.	96	8	X	4.79	5000
318-1	1	30	10	3	60	Parallel	Infinite	30	Cont.	96	8	X	2.86	5000
319-1	1	30	10	3	60	Parallel	Infinite	20	Stag.	96	8	X	2.86	3600
319-2	1	30	10	3	60	Parallel	Infinite	20	Stag.	96	8	X	2.86	5000
319-3	1	30	10	3	60	Parallel	Infinite	20	Stag.	96	10	X	2.86	5000
319-4	1	30	10	3	60	Parallel	Infinite	20	Stag.	96	8	K	2.86	5000
319-5	1	30	10	3	60	Parallel	Infinite	20	Stag.	96	8	X	4.79	5000
320-1	1	30	10	3	60	Parallel	Infinite	30	Stag.	96	8	X	2.86	5000
321-1	1	30	10	3	60	Trap.	Infinite	20	Cont.	96	8	X	2.86	3600
321-2	1	30	10	3	60	Trap.	Infinite	20	Cont.	96	8	X	2.86	5000
321-3	1	30	10	3	60	Trap.	Infinite	20	Cont.	96	10	X	2.86	5000
321-4	1	30	10	3	60	Trap.	Infinite	20	Cont.	96	8	K	2.86	5000
321-5	1	30	10	3	60	Trap.	Infinite	20	Cont.	96	8	X	4.79	5000
322-1	1	30	10	3	60	Trap.	Infinite	30	Cont.	96	8	X	2.86	5000
323-1	1	30	10	3	60	Trap.	Infinite	20	Stag.	96	8	X	2.86	3600
323-2	1	30	10	3	60	Trap.	Infinite	20	Stag.	96	8	X	2.86	5000
323-3	1	30	10	3	60	Trap.	Infinite	20	Stag.	96	10	X	2.86	5000
323-4	1	30	10	3	60	Trap.	Infinite	20	Stag.	96	8	K	2.86	5000
323-5	1	30	10	3	60	Trap.	Infinite	20	Stag.	96	8	X	4.79	5000
324-1	1	30	10	3	60	Trap.	Infinite	30	Stag.	96	8	X	2.86	5000
325-1	1	30	10	5	0	Parallel	Infinite	20	Cont.	96	8	X	2.86	3600
325-2	1	30	10	5	0	Parallel	Infinite	20	Cont.	96	8	X	2.86	5000
325-3	1	30	10	5	0	Parallel	Infinite	20	Cont.	96	10	X	2.86	5000
325-4	1	30	10	5	0	Parallel	Infinite	20	Cont.	96	8	K	2.86	5000
325-5	1	30	10	5	0	Parallel	Infinite	20	Cont.	96	8	X	4.79	5000
326-1	1	30	10	5	0	Parallel	Infinite	30	Cont.	96	8	X	2.86	5000
327-1	1	30	10	5	30	Parallel	Infinite	20	Cont.	96	8	X	2.86	3600
327-2	1	30	10	5	30	Parallel	Infinite	20	Cont.	96	8	X	2.86	5000
327-3	1	30	10	5	30	Parallel	Infinite	20	Cont.	96	10	X	2.86	5000
327-4	1	30	10	5	30	Parallel	Infinite	20	Cont.	96	8	K	2.86	5000
327-5	1	30	10	5	30	Parallel	Infinite	20	Cont.	96	8	X	4.79	5000
328-1	1	30	10	5	30	Parallel	Infinite	30	Cont.	96	8	X	2.86	5000
329-1	1	30	10	5	60	Parallel	Infinite	20	Cont.	96	8	X	2.86	3600
329-2	1	30	10	5	60	Parallel	Infinite	20	Cont.	96	8	X	2.86	5000
329-3	1	30	10	5	60	Parallel	Infinite	20	Cont.	96	10	X	2.86	5000
329-4	1	30	10	5	60	Parallel	Infinite	20	Cont.	96	8	K	2.86	5000
329-5	1	30	10	5	60	Parallel	Infinite	20	Cont.	96	8	X	4.79	5000
330-1	1	30	10	5	60	Parallel	Infinite	30	Cont.	96	8	X	2.86	5000
331-1	1	30	10	5	60	Parallel	Infinite	20	Stag.	96	8	X	2.86	3600
331-2	1	30	10	5	60	Parallel	Infinite	20	Stag.	96	8	X	2.86	5000
331-3	1	30	10	5	60	Parallel	Infinite	20	Stag.	96	10	X	2.86	5000
331-4	1	30	10	5	60	Parallel	Infinite	20	Stag.	96	8	K	2.86	5000
331-5	1	30	10	5	60	Parallel	Infinite	20	Stag.	96	8	X	4.79	5000
332-1	1	30	10	5	60	Parallel	Infinite	30	Stag.	96	8	X	2.86	5000
333-1	1	30	10	5	60	Trap.	Infinite	20	Cont.	96	8	X	2.86	3600
333-2	1	30	10	5	60	Trap.	Infinite	20	Cont.	96	8	X	2.86	5000
333-3	1	30	10	5	60	Trap.	Infinite	20	Cont.	96	10	X	2.86	5000
333-4	1	30	10	5	60	Trap.	Infinite	20	Cont.	96	8	K	2.86	5000
333-5	1	30	10	5	60	Trap.	Infinite	20	Cont.	96	8	X	4.79	5000
334-1	1	30	10	5	60	Trap.	Infinite	30	Cont.	96	8	X	2.86	5000
335-1	1	30	10	5	60	Trap.	Infinite	20	Stag.	96	8	X	2.86	3600
335-2	1	30	10	5	60	Trap.	Infinite	20	Stag.	96	8	X	2.86	5000
335-3	1	30	10	5	60	Trap.	Infinite	20	Stag.	96	10	X	2.86	5000
335-4	1	30	10	5	60	Trap.	Infinite	20	Stag.	96	8	K	2.86	5000
335-5	1	30	10	5	60	Trap.	Infinite	20	Stag.	96	8	X	4.79	5000
336-1	1	30	10	5	60	Trap.	Infinite	30	Stag.	96	8	X	2.86	5000
337-1	2	25	6	3	0	Parallel	1500	20	Cont.	72	8	X	2.86	3600
337-2	2	25	6	3	0	Parallel	1500	20	Cont.	72	8	X	2.86	5000
337-3	2	25	6	3	0	Parallel	1500	20	Cont.	72	10	X	2.86	5000
337-4	2	25	6	3	0	Parallel	1500	20	Cont.	72	8	K	2.86	5000
337-5	2	25	6	3	0	Parallel	1500	20	Cont.	72	8	X	4.79	5000
338-1	2	25	6	3	0	Parallel	1500	30	Cont.	72	8	X	2.86	5000
339-1	2	25	6	3	0	Parallel	750	20	Cont.	72	8	X	2.86	3600
339-2	2	25	6	3	0	Parallel	750	20	Cont.	72	8	X	2.86	5000
339-3	2	25	6	3	0	Parallel	750	20	Cont.	72	10	X	2.86	5000
339-4	2	25	6	3	0	Parallel	750	20	Cont.	72	8	K	2.86	5000
339-5	2	25	6	3	0	Parallel	750	20	Cont.	72	8	X	4.79	5000

Model ID	Geometry									Cross-section		CF detail		Mat'l
	n_{span}	L/d ratio	s_g [ft]	n_{girder}	Support skew [deg];	Layout	R [ft]	s_{cf} [ft]	CF layout	d_w [in]	t_{deck} [in]	CF type	A_{cf} [in^2]	E_c [ksi]
340-1	2	25	6	3	0	Parallel	750	30	Cont.	72	8	X	2.86	5000
341-1	2	25	6	3	30	Parallel	1500	20	Cont.	72	8	X	2.86	3600
341-2	2	25	6	3	30	Parallel	1500	20	Cont.	72	8	X	2.86	5000
341-3	2	25	6	3	30	Parallel	1500	20	Cont.	72	10	X	2.86	5000
341-4	2	25	6	3	30	Parallel	1500	20	Cont.	72	8	K	2.86	5000
341-5	2	25	6	3	30	Parallel	1500	20	Cont.	72	8	X	4.79	5000
342-1	2	25	6	3	30	Parallel	1500	30	Cont.	72	8	X	2.86	5000
343-1	2	25	6	3	30	Parallel	750	20	Cont.	72	8	X	2.86	3600
343-2	2	25	6	3	30	Parallel	750	20	Cont.	72	8	X	2.86	5000
343-3	2	25	6	3	30	Parallel	750	20	Cont.	72	10	X	2.86	5000
343-4	2	25	6	3	30	Parallel	750	20	Cont.	72	8	K	2.86	5000
343-5	2	25	6	3	30	Parallel	750	20	Cont.	72	8	X	4.79	5000
344-1	2	25	6	3	30	Parallel	750	30	Cont.	72	8	X	2.86	5000
345-1	2	25	6	3	60	Parallel	1500	20	Cont.	72	8	X	2.86	3600
345-2	2	25	6	3	60	Parallel	1500	20	Cont.	72	8	X	2.86	5000
345-3	2	25	6	3	60	Parallel	1500	20	Cont.	72	10	X	2.86	5000
345-4	2	25	6	3	60	Parallel	1500	20	Cont.	72	8	K	2.86	5000
345-5	2	25	6	3	60	Parallel	1500	20	Cont.	72	8	X	4.79	5000
346-1	2	25	6	3	60	Parallel	1500	30	Cont.	72	8	X	2.86	5000
347-1	2	25	6	3	60	Parallel	750	20	Cont.	72	8	X	2.86	3600
347-2	2	25	6	3	60	Parallel	750	20	Cont.	72	8	X	2.86	5000
347-3	2	25	6	3	60	Parallel	750	20	Cont.	72	10	X	2.86	5000
347-4	2	25	6	3	60	Parallel	750	20	Cont.	72	8	K	2.86	5000
347-5	2	25	6	3	60	Parallel	750	20	Cont.	72	8	X	4.79	5000
348-1	2	25	6	3	60	Parallel	750	30	Cont.	72	8	X	2.86	5000
349-1	2	25	6	3	60	Trap.	1500	20	Cont.	72	8	X	2.86	3600
349-2	2	25	6	3	60	Trap.	1500	20	Cont.	72	8	X	2.86	5000
349-3	2	25	6	3	60	Trap.	1500	20	Cont.	72	10	X	2.86	5000
349-4	2	25	6	3	60	Trap.	1500	20	Cont.	72	8	K	2.86	5000
349-5	2	25	6	3	60	Trap.	1500	20	Cont.	72	8	X	4.79	5000
350-1	2	25	6	3	60	Trap.	1500	30	Cont.	72	8	X	2.86	5000
351-1	2	25	6	3	60	Trap.	750	20	Cont.	72	8	X	2.86	3600
351-2	2	25	6	3	60	Trap.	750	20	Cont.	72	8	X	2.86	5000
351-3	2	25	6	3	60	Trap.	750	20	Cont.	72	10	X	2.86	5000
351-4	2	25	6	3	60	Trap.	750	20	Cont.	72	8	K	2.86	5000
351-5	2	25	6	3	60	Trap.	750	20	Cont.	72	8	X	4.79	5000
352-1	2	25	6	3	60	Trap.	750	30	Cont.	72	8	X	2.86	5000
353-1	2	25	6	5	0	Parallel	1500	20	Cont.	72	8	X	2.86	3600
353-2	2	25	6	5	0	Parallel	1500	20	Cont.	72	8	X	2.86	5000
353-3	2	25	6	5	0	Parallel	1500	20	Cont.	72	10	X	2.86	5000
353-4	2	25	6	5	0	Parallel	1500	20	Cont.	72	8	K	2.86	5000
353-5	2	25	6	5	0	Parallel	1500	20	Cont.	72	8	X	4.79	5000
354-1	2	25	6	5	0	Parallel	1500	30	Cont.	72	8	X	2.86	5000
355-1	2	25	6	5	0	Parallel	750	20	Cont.	72	8	X	2.86	3600
355-2	2	25	6	5	0	Parallel	750	20	Cont.	72	8	X	2.86	5000
355-3	2	25	6	5	0	Parallel	750	20	Cont.	72	10	X	2.86	5000
355-4	2	25	6	5	0	Parallel	750	20	Cont.	72	8	K	2.86	5000
355-5	2	25	6	5	0	Parallel	750	20	Cont.	72	8	X	4.79	5000
356-1	2	25	6	5	0	Parallel	750	30	Cont.	72	8	X	2.86	5000
357-1	2	25	6	5	30	Parallel	1500	20	Cont.	72	8	X	2.86	3600
357-2	2	25	6	5	30	Parallel	1500	20	Cont.	72	8	X	2.86	5000
357-3	2	25	6	5	30	Parallel	1500	20	Cont.	72	10	X	2.86	5000
357-4	2	25	6	5	30	Parallel	1500	20	Cont.	72	8	K	2.86	5000
357-5	2	25	6	5	30	Parallel	1500	20	Cont.	72	8	X	4.79	5000
358-1	2	25	6	5	30	Parallel	1500	30	Cont.	72	8	X	2.86	5000
359-1	2	25	6	5	30	Parallel	750	20	Cont.	72	8	X	2.86	3600
359-2	2	25	6	5	30	Parallel	750	20	Cont.	72	8	X	2.86	5000
359-3	2	25	6	5	30	Parallel	750	20	Cont.	72	10	X	2.86	5000
359-4	2	25	6	5	30	Parallel	750	20	Cont.	72	8	K	2.86	5000
359-5	2	25	6	5	30	Parallel	750	20	Cont.	72	8	X	4.79	5000
360-1	2	25	6	5	30	Parallel	750	30	Cont.	72	8	X	2.86	5000
361-1	2	25	6	5	60	Parallel	1500	20	Cont.	72	8	X	2.86	3600
361-2	2	25	6	5	60	Parallel	1500	20	Cont.	72	8	X	2.86	5000
361-3	2	25	6	5	60	Parallel	1500	20	Cont.	72	10	X	2.86	5000
361-4	2	25	6	5	60	Parallel	1500	20	Cont.	72	8	K	2.86	5000
361-5	2	25	6	5	60	Parallel	1500	20	Cont.	72	8	X	4.79	5000
362-1	2	25	6	5	60	Parallel	1500	30	Cont.	72	8	X	2.86	5000
363-1	2	25	6	5	60	Parallel	750	20	Cont.	72	8	X	2.86	3600
363-2	2	25	6	5	60	Parallel	750	20	Cont.	72	8	X	2.86	5000
363-3	2	25	6	5	60	Parallel	750	20	Cont.	72	10	X	2.86	5000
363-4	2	25	6	5	60	Parallel	750	20	Cont.	72	8	K	2.86	5000
363-5	2	25	6	5	60	Parallel	750	20	Cont.	72	8	X	4.79	5000
364-1	2	25	6	5	60	Parallel	750	30	Cont.	72	8	X	2.86	5000
365-1	2	25	6	5	60	Trap.	1500	20	Cont.	72	8	X	2.86	3600
365-2	2	25	6	5	60	Trap.	1500	20	Cont.	72	8	X	2.86	5000
365-3	2	25	6	5	60	Trap.	1500	20	Cont.	72	10	X	2.86	5000
365-4	2	25	6	5	60	Trap.	1500	20	Cont.	72	8	K	2.86	5000
365-5	2	25	6	5	60	Trap.	1500	20	Cont.	72	8	X	4.79	5000
366-1	2	25	6	5	60	Trap.	1500	30	Cont.	72	8	X	2.86	5000

Model ID	Geometry									Cross-section		CF detail		Mat'l
	n_{span}	L/d ratio	s_g [ft]	n_{girder}	Support skew [deg]; Layout		R [ft]	s_{cf} [ft]	CF layout	d_w [in]	t_{deck} [in]	CF type	A_{cf} [in^2]	E_c [ksi]
367-1	2	25	6	5	60	Trap.	750	20	Cont.	72	8	X	2.86	3600
367-2	2	25	6	5	60	Trap.	750	20	Cont.	72	8	X	2.86	5000
367-3	2	25	6	5	60	Trap.	750	20	Cont.	72	10	X	2.86	5000
367-4	2	25	6	5	60	Trap.	750	20	Cont.	72	8	K	2.86	5000
367-5	2	25	6	5	60	Trap.	750	20	Cont.	72	8	X	4.79	5000
368-1	2	25	6	5	60	Trap.	750	30	Cont.	72	8	X	2.86	5000
369-1	2	25	6	7	0	Parallel	1500	20	Cont.	72	8	X	2.86	3600
369-2	2	25	6	7	0	Parallel	1500	20	Cont.	72	8	X	2.86	5000
369-3	2	25	6	7	0	Parallel	1500	20	Cont.	72	10	X	2.86	5000
369-4	2	25	6	7	0	Parallel	1500	20	Cont.	72	8	K	2.86	5000
369-5	2	25	6	7	0	Parallel	1500	20	Cont.	72	8	X	4.79	5000
370-1	2	25	6	7	0	Parallel	1500	30	Cont.	72	8	X	2.86	5000
371-1	2	25	6	7	0	Parallel	750	20	Cont.	72	8	X	2.86	3600
371-2	2	25	6	7	0	Parallel	750	20	Cont.	72	8	X	2.86	5000
371-3	2	25	6	7	0	Parallel	750	20	Cont.	72	10	X	2.86	5000
371-4	2	25	6	7	0	Parallel	750	20	Cont.	72	8	K	2.86	5000
371-5	2	25	6	7	0	Parallel	750	20	Cont.	72	8	X	4.79	5000
372-1	2	25	6	7	0	Parallel	750	30	Cont.	72	8	X	2.86	5000
373-1	2	25	6	7	30	Parallel	1500	20	Cont.	72	8	X	2.86	3600
373-2	2	25	6	7	30	Parallel	1500	20	Cont.	72	8	X	2.86	5000
373-3	2	25	6	7	30	Parallel	1500	20	Cont.	72	10	X	2.86	5000
373-4	2	25	6	7	30	Parallel	1500	20	Cont.	72	8	K	2.86	5000
373-5	2	25	6	7	30	Parallel	1500	20	Cont.	72	8	X	4.79	5000
374-1	2	25	6	7	30	Parallel	1500	30	Cont.	72	8	X	2.86	5000
375-1	2	25	6	7	30	Parallel	750	20	Cont.	72	8	X	2.86	3600
375-2	2	25	6	7	30	Parallel	750	20	Cont.	72	8	X	2.86	5000
375-3	2	25	6	7	30	Parallel	750	20	Cont.	72	10	X	2.86	5000
375-4	2	25	6	7	30	Parallel	750	20	Cont.	72	8	K	2.86	5000
375-5	2	25	6	7	30	Parallel	750	20	Cont.	72	8	X	4.79	5000
376-1	2	25	6	7	30	Parallel	750	30	Cont.	72	8	X	2.86	5000
377-1	2	25	6	7	60	Parallel	1500	20	Cont.	72	8	X	2.86	3600
377-2	2	25	6	7	60	Parallel	1500	20	Cont.	72	8	X	2.86	5000
377-3	2	25	6	7	60	Parallel	1500	20	Cont.	72	10	X	2.86	5000
377-4	2	25	6	7	60	Parallel	1500	20	Cont.	72	8	K	2.86	5000
377-5	2	25	6	7	60	Parallel	1500	20	Cont.	72	8	X	4.79	5000
378-1	2	25	6	7	60	Parallel	1500	30	Cont.	72	8	X	2.86	5000
379-1	2	25	6	7	60	Parallel	750	20	Cont.	72	8	X	2.86	3600
379-2	2	25	6	7	60	Parallel	750	20	Cont.	72	8	X	2.86	5000
379-3	2	25	6	7	60	Parallel	750	20	Cont.	72	10	X	2.86	5000
379-4	2	25	6	7	60	Parallel	750	20	Cont.	72	8	K	2.86	5000
379-5	2	25	6	7	60	Parallel	750	20	Cont.	72	8	X	4.79	5000
380-1	2	25	6	7	60	Parallel	750	30	Cont.	72	8	X	2.86	5000
381-1	2	25	6	7	60	Trap.	1500	20	Cont.	72	8	X	2.86	3600
381-2	2	25	6	7	60	Trap.	1500	20	Cont.	72	8	X	2.86	5000
381-3	2	25	6	7	60	Trap.	1500	20	Cont.	72	10	X	2.86	5000
381-4	2	25	6	7	60	Trap.	1500	20	Cont.	72	8	K	2.86	5000
381-5	2	25	6	7	60	Trap.	1500	20	Cont.	72	8	X	4.79	5000
382-1	2	25	6	7	60	Trap.	1500	30	Cont.	72	8	X	2.86	5000
383-1	2	25	6	7	60	Trap.	750	20	Cont.	72	8	X	2.86	3600
383-2	2	25	6	7	60	Trap.	750	20	Cont.	72	8	X	2.86	5000
383-3	2	25	6	7	60	Trap.	750	20	Cont.	72	10	X	2.86	5000
383-4	2	25	6	7	60	Trap.	750	20	Cont.	72	8	K	2.86	5000
383-5	2	25	6	7	60	Trap.	750	20	Cont.	72	8	X	4.79	5000
384-1	2	25	6	7	60	Trap.	750	30	Cont.	72	8	X	2.86	5000
385-1	2	25	8	3	0	Parallel	1500	20	Cont.	72	8	X	2.86	3600
385-2	2	25	8	3	0	Parallel	1500	20	Cont.	72	8	X	2.86	5000
385-3	2	25	8	3	0	Parallel	1500	20	Cont.	72	10	X	2.86	5000
385-4	2	25	8	3	0	Parallel	1500	20	Cont.	72	8	K	2.86	5000
385-5	2	25	8	3	0	Parallel	1500	20	Cont.	72	8	X	4.79	5000
386-1	2	25	8	3	0	Parallel	1500	30	Cont.	72	8	X	2.86	5000
387-1	2	25	8	3	0	Parallel	750	20	Cont.	72	8	X	2.86	3600
387-2	2	25	8	3	0	Parallel	750	20	Cont.	72	8	X	2.86	5000
387-3	2	25	8	3	0	Parallel	750	20	Cont.	72	10	X	2.86	5000
387-4	2	25	8	3	0	Parallel	750	20	Cont.	72	8	K	2.86	5000
387-5	2	25	8	3	0	Parallel	750	20	Cont.	72	8	X	4.79	5000
388-1	2	25	8	3	0	Parallel	750	30	Cont.	72	8	X	2.86	5000
389-1	2	25	8	3	30	Parallel	1500	20	Cont.	72	8	X	2.86	3600
389-2	2	25	8	3	30	Parallel	1500	20	Cont.	72	8	X	2.86	5000
389-3	2	25	8	3	30	Parallel	1500	20	Cont.	72	10	X	2.86	5000
389-4	2	25	8	3	30	Parallel	1500	20	Cont.	72	8	K	2.86	5000
389-5	2	25	8	3	30	Parallel	1500	20	Cont.	72	8	X	4.79	5000
390-1	2	25	8	3	30	Parallel	1500	30	Cont.	72	8	X	2.86	5000
391-1	2	25	8	3	30	Parallel	750	20	Cont.	72	8	X	2.86	3600
391-2	2	25	8	3	30	Parallel	750	20	Cont.	72	8	X	2.86	5000
391-3	2	25	8	3	30	Parallel	750	20	Cont.	72	10	X	2.86	5000
391-4	2	25	8	3	30	Parallel	750	20	Cont.	72	8	K	2.86	5000
391-5	2	25	8	3	30	Parallel	750	20	Cont.	72	8	X	4.79	5000
392-1	2	25	8	3	30	Parallel	750	30	Cont.	72	8	X	2.86	5000
393-1	2	25	8	3	60	Parallel	1500	20	Cont.	72	8	X	2.86	3600

Model ID	Geometry									Cross-section		CF detail		Mat'l
	n_{span}	L/d ratio	s_g [ft]	n_{girder}	Support skew [deg]; Layout		R [ft]	s_{cf} [ft]	CF layout	d_w [in]	t_{deck} [in]	CF type	A_{cf} [in^2]	E_c [ksi]
393-2	2	25	8	3	60	Parallel	1500	20	Cont.	72	8	X	2.86	5000
393-3	2	25	8	3	60	Parallel	1500	20	Cont.	72	10	X	2.86	5000
393-4	2	25	8	3	60	Parallel	1500	20	Cont.	72	8	K	2.86	5000
393-5	2	25	8	3	60	Parallel	1500	20	Cont.	72	8	X	4.79	5000
394-1	2	25	8	3	60	Parallel	1500	30	Cont.	72	8	X	2.86	5000
395-1	2	25	8	3	60	Parallel	750	20	Cont.	72	8	X	2.86	3600
395-2	2	25	8	3	60	Parallel	750	20	Cont.	72	8	X	2.86	5000
395-3	2	25	8	3	60	Parallel	750	20	Cont.	72	10	X	2.86	5000
395-4	2	25	8	3	60	Parallel	750	20	Cont.	72	8	K	2.86	5000
395-5	2	25	8	3	60	Parallel	750	20	Cont.	72	8	X	4.79	5000
396-1	2	25	8	3	60	Parallel	750	30	Cont.	72	8	X	2.86	5000
397-1	2	25	8	3	60	Trap.	1500	20	Cont.	72	8	X	2.86	3600
397-2	2	25	8	3	60	Trap.	1500	20	Cont.	72	8	X	2.86	5000
397-3	2	25	8	3	60	Trap.	1500	20	Cont.	72	10	X	2.86	5000
397-4	2	25	8	3	60	Trap.	1500	20	Cont.	72	8	K	2.86	5000
397-5	2	25	8	3	60	Trap.	1500	20	Cont.	72	8	X	4.79	5000
398-1	2	25	8	3	60	Trap.	1500	30	Cont.	72	8	X	2.86	5000
399-1	2	25	8	3	60	Trap.	750	20	Cont.	72	8	X	2.86	3600
399-2	2	25	8	3	60	Trap.	750	20	Cont.	72	8	X	2.86	5000
399-3	2	25	8	3	60	Trap.	750	20	Cont.	72	10	X	2.86	5000
399-4	2	25	8	3	60	Trap.	750	20	Cont.	72	8	K	2.86	5000
399-5	2	25	8	3	60	Trap.	750	20	Cont.	72	8	X	4.79	5000
400-1	2	25	8	3	60	Trap.	750	30	Cont.	72	8	X	2.86	5000
401-1	2	25	8	5	0	Parallel	1500	20	Cont.	72	8	X	2.86	3600
401-2	2	25	8	5	0	Parallel	1500	20	Cont.	72	8	X	2.86	5000
401-3	2	25	8	5	0	Parallel	1500	20	Cont.	72	10	X	2.86	5000
401-4	2	25	8	5	0	Parallel	1500	20	Cont.	72	8	K	2.86	5000
401-5	2	25	8	5	0	Parallel	1500	20	Cont.	72	8	X	4.79	5000
402-1	2	25	8	5	0	Parallel	1500	30	Cont.	72	8	X	2.86	5000
403-1	2	25	8	5	0	Parallel	750	20	Cont.	72	8	X	2.86	3600
403-2	2	25	8	5	0	Parallel	750	20	Cont.	72	8	X	2.86	5000
403-3	2	25	8	5	0	Parallel	750	20	Cont.	72	10	X	2.86	5000
403-4	2	25	8	5	0	Parallel	750	20	Cont.	72	8	K	2.86	5000
403-5	2	25	8	5	0	Parallel	750	20	Cont.	72	8	X	4.79	5000
404-1	2	25	8	5	0	Parallel	750	30	Cont.	72	8	X	2.86	5000
405-1	2	25	8	5	30	Parallel	1500	20	Cont.	72	8	X	2.86	3600
405-2	2	25	8	5	30	Parallel	1500	20	Cont.	72	8	X	2.86	5000
405-3	2	25	8	5	30	Parallel	1500	20	Cont.	72	10	X	2.86	5000
405-4	2	25	8	5	30	Parallel	1500	20	Cont.	72	8	K	2.86	5000
405-5	2	25	8	5	30	Parallel	1500	20	Cont.	72	8	X	4.79	5000
406-1	2	25	8	5	30	Parallel	1500	30	Cont.	72	8	X	2.86	5000
407-1	2	25	8	5	30	Parallel	750	20	Cont.	72	8	X	2.86	3600
407-2	2	25	8	5	30	Parallel	750	20	Cont.	72	8	X	2.86	5000
407-3	2	25	8	5	30	Parallel	750	20	Cont.	72	10	X	2.86	5000
407-4	2	25	8	5	30	Parallel	750	20	Cont.	72	8	K	2.86	5000
407-5	2	25	8	5	30	Parallel	750	20	Cont.	72	8	X	4.79	5000
408-1	2	25	8	5	30	Parallel	750	30	Cont.	72	8	X	2.86	5000
409-1	2	25	8	5	60	Parallel	1500	20	Cont.	72	8	X	2.86	3600
409-2	2	25	8	5	60	Parallel	1500	20	Cont.	72	8	X	2.86	5000
409-3	2	25	8	5	60	Parallel	1500	20	Cont.	72	10	X	2.86	5000
409-4	2	25	8	5	60	Parallel	1500	20	Cont.	72	8	K	2.86	5000
409-5	2	25	8	5	60	Parallel	1500	20	Cont.	72	8	X	4.79	5000
410-1	2	25	8	5	60	Parallel	1500	30	Cont.	72	8	X	2.86	5000
411-1	2	25	8	5	60	Parallel	750	20	Cont.	72	8	X	2.86	3600
411-2	2	25	8	5	60	Parallel	750	20	Cont.	72	8	X	2.86	5000
411-3	2	25	8	5	60	Parallel	750	20	Cont.	72	10	X	2.86	5000
411-4	2	25	8	5	60	Parallel	750	20	Cont.	72	8	K	2.86	5000
411-5	2	25	8	5	60	Parallel	750	20	Cont.	72	8	X	4.79	5000
412-1	2	25	8	5	60	Parallel	750	30	Cont.	72	8	X	2.86	5000
413-1	2	25	8	5	60	Trap.	1500	20	Cont.	72	8	X	2.86	3600
413-2	2	25	8	5	60	Trap.	1500	20	Cont.	72	8	X	2.86	5000
413-3	2	25	8	5	60	Trap.	1500	20	Cont.	72	10	X	2.86	5000
413-4	2	25	8	5	60	Trap.	1500	20	Cont.	72	8	K	2.86	5000
413-5	2	25	8	5	60	Trap.	1500	20	Cont.	72	8	X	4.79	5000
414-1	2	25	8	5	60	Trap.	1500	30	Cont.	72	8	X	2.86	5000
415-1	2	25	8	5	60	Trap.	750	20	Cont.	72	8	X	2.86	3600
415-2	2	25	8	5	60	Trap.	750	20	Cont.	72	8	X	2.86	5000
415-3	2	25	8	5	60	Trap.	750	20	Cont.	72	10	X	2.86	5000
415-4	2	25	8	5	60	Trap.	750	20	Cont.	72	8	K	2.86	5000
415-5	2	25	8	5	60	Trap.	750	20	Cont.	72	8	X	4.79	5000
416-1	2	25	8	5	60	Trap.	750	30	Cont.	72	8	X	2.86	5000
417-1	2	25	8	7	0	Parallel	1500	20	Cont.	72	8	X	2.86	3600
417-2	2	25	8	7	0	Parallel	1500	20	Cont.	72	8	X	2.86	5000
417-3	2	25	8	7	0	Parallel	1500	20	Cont.	72	10	X	2.86	5000
417-4	2	25	8	7	0	Parallel	1500	20	Cont.	72	8	K	2.86	5000
417-5	2	25	8	7	0	Parallel	1500	20	Cont.	72	8	X	4.79	5000
418-1	2	25	8	7	0	Parallel	1500	30	Cont.	72	8	X	2.86	5000
419-1	2	25	8	7	0	Parallel	750	20	Cont.	72	8	X	2.86	3600
419-2	2	25	8	7	0	Parallel	750	20	Cont.	72	8	X	2.86	5000

Model ID	Geometry									Cross-section		CF detail		Mat'l
	n_{span}	L/d ratio	s_g [ft]	n_{girder}	Support skew [deg];	Layout	R [ft]	s_{cf} [ft]	CF layout	d_w [in]	t_{deck} [in]	CF type	A_{cf} [in^2]	E_c [ksi]
419-3	2	25	8	7	0	Parallel	750	20	Cont.	72	10	X	2.86	5000
419-4	2	25	8	7	0	Parallel	750	20	Cont.	72	8	K	2.86	5000
419-5	2	25	8	7	0	Parallel	750	20	Cont.	72	8	X	4.79	5000
420-1	2	25	8	7	0	Parallel	750	30	Cont.	72	8	X	2.86	5000
421-1	2	25	8	7	30	Parallel	1500	20	Cont.	72	8	X	2.86	3600
421-2	2	25	8	7	30	Parallel	1500	20	Cont.	72	8	X	2.86	5000
421-3	2	25	8	7	30	Parallel	1500	20	Cont.	72	10	X	2.86	5000
421-4	2	25	8	7	30	Parallel	1500	20	Cont.	72	8	K	2.86	5000
421-5	2	25	8	7	30	Parallel	1500	20	Cont.	72	8	X	4.79	5000
422-1	2	25	8	7	30	Parallel	1500	30	Cont.	72	8	X	2.86	5000
423-1	2	25	8	7	30	Parallel	750	20	Cont.	72	8	X	2.86	3600
423-2	2	25	8	7	30	Parallel	750	20	Cont.	72	8	X	2.86	5000
423-3	2	25	8	7	30	Parallel	750	20	Cont.	72	10	X	2.86	5000
423-4	2	25	8	7	30	Parallel	750	20	Cont.	72	8	K	2.86	5000
423-5	2	25	8	7	30	Parallel	750	20	Cont.	72	8	X	4.79	5000
424-1	2	25	8	7	30	Parallel	750	30	Cont.	72	8	X	2.86	5000
425-1	2	25	8	7	60	Parallel	1500	20	Cont.	72	8	X	2.86	3600
425-2	2	25	8	7	60	Parallel	1500	20	Cont.	72	8	X	2.86	5000
425-3	2	25	8	7	60	Parallel	1500	20	Cont.	72	10	X	2.86	5000
425-4	2	25	8	7	60	Parallel	1500	20	Cont.	72	8	K	2.86	5000
425-5	2	25	8	7	60	Parallel	1500	20	Cont.	72	8	X	4.79	5000
426-1	2	25	8	7	60	Parallel	1500	30	Cont.	72	8	X	2.86	5000
427-1	2	25	8	7	60	Parallel	750	20	Cont.	72	8	X	2.86	3600
427-2	2	25	8	7	60	Parallel	750	20	Cont.	72	8	X	2.86	5000
427-3	2	25	8	7	60	Parallel	750	20	Cont.	72	10	X	2.86	5000
427-4	2	25	8	7	60	Parallel	750	20	Cont.	72	8	K	2.86	5000
427-5	2	25	8	7	60	Parallel	750	20	Cont.	72	8	X	4.79	5000
428-1	2	25	8	7	60	Parallel	750	30	Cont.	72	8	X	2.86	5000
429-1	2	25	8	7	60	Trap.	1500	20	Cont.	72	8	X	2.86	3600
429-2	2	25	8	7	60	Trap.	1500	20	Cont.	72	8	X	2.86	5000
429-3	2	25	8	7	60	Trap.	1500	20	Cont.	72	10	X	2.86	5000
429-4	2	25	8	7	60	Trap.	1500	20	Cont.	72	8	K	2.86	5000
429-5	2	25	8	7	60	Trap.	1500	20	Cont.	72	8	X	4.79	5000
430-1	2	25	8	7	60	Trap.	1500	30	Cont.	72	8	X	2.86	5000
431-1	2	25	8	7	60	Trap.	750	20	Cont.	72	8	X	2.86	3600
431-2	2	25	8	7	60	Trap.	750	20	Cont.	72	8	X	2.86	5000
431-3	2	25	8	7	60	Trap.	750	20	Cont.	72	10	X	2.86	5000
431-4	2	25	8	7	60	Trap.	750	20	Cont.	72	8	K	2.86	5000
431-5	2	25	8	7	60	Trap.	750	20	Cont.	72	8	X	4.79	5000
432-1	2	25	8	7	60	Trap.	750	30	Cont.	72	8	X	2.86	5000
433-1	2	25	10	3	0	Parallel	1500	20	Cont.	72	8	X	2.86	3600
433-2	2	25	10	3	0	Parallel	1500	20	Cont.	72	8	X	2.86	5000
433-3	2	25	10	3	0	Parallel	1500	20	Cont.	72	10	X	2.86	5000
433-4	2	25	10	3	0	Parallel	1500	20	Cont.	72	8	K	2.86	5000
433-5	2	25	10	3	0	Parallel	1500	20	Cont.	72	8	X	4.79	5000
434-1	2	25	10	3	0	Parallel	1500	30	Cont.	72	8	X	2.86	5000
435-1	2	25	10	3	0	Parallel	750	20	Cont.	72	8	X	2.86	3600
435-2	2	25	10	3	0	Parallel	750	20	Cont.	72	8	X	2.86	5000
435-3	2	25	10	3	0	Parallel	750	20	Cont.	72	10	X	2.86	5000
435-4	2	25	10	3	0	Parallel	750	20	Cont.	72	8	K	2.86	5000
435-5	2	25	10	3	0	Parallel	750	20	Cont.	72	8	X	4.79	5000
436-1	2	25	10	3	0	Parallel	750	30	Cont.	72	8	X	2.86	5000
437-1	2	25	10	3	30	Parallel	1500	20	Cont.	72	8	X	2.86	3600
437-2	2	25	10	3	30	Parallel	1500	20	Cont.	72	8	X	2.86	5000
437-3	2	25	10	3	30	Parallel	1500	20	Cont.	72	10	X	2.86	5000
437-4	2	25	10	3	30	Parallel	1500	20	Cont.	72	8	K	2.86	5000
437-5	2	25	10	3	30	Parallel	1500	20	Cont.	72	8	X	4.79	5000
438-1	2	25	10	3	30	Parallel	1500	30	Cont.	72	8	X	2.86	5000
439-1	2	25	10	3	30	Parallel	750	20	Cont.	72	8	X	2.86	3600
439-2	2	25	10	3	30	Parallel	750	20	Cont.	72	8	X	2.86	5000
439-3	2	25	10	3	30	Parallel	750	20	Cont.	72	10	X	2.86	5000
439-4	2	25	10	3	30	Parallel	750	20	Cont.	72	8	K	2.86	5000
439-5	2	25	10	3	30	Parallel	750	20	Cont.	72	8	X	4.79	5000
440-1	2	25	10	3	30	Parallel	750	30	Cont.	72	8	X	2.86	5000
441-1	2	25	10	3	60	Parallel	1500	20	Cont.	72	8	X	2.86	3600
441-2	2	25	10	3	60	Parallel	1500	20	Cont.	72	8	X	2.86	5000
441-3	2	25	10	3	60	Parallel	1500	20	Cont.	72	10	X	2.86	5000
441-4	2	25	10	3	60	Parallel	1500	20	Cont.	72	8	K	2.86	5000
441-5	2	25	10	3	60	Parallel	1500	20	Cont.	72	8	X	4.79	5000
442-1	2	25	10	3	60	Parallel	1500	30	Cont.	72	8	X	2.86	5000
443-1	2	25	10	3	60	Parallel	750	20	Cont.	72	8	X	2.86	3600
443-2	2	25	10	3	60	Parallel	750	20	Cont.	72	8	X	2.86	5000
443-3	2	25	10	3	60	Parallel	750	20	Cont.	72	10	X	2.86	5000
443-4	2	25	10	3	60	Parallel	750	20	Cont.	72	8	K	2.86	5000
443-5	2	25	10	3	60	Parallel	750	20	Cont.	72	8	X	4.79	5000
444-1	2	25	10	3	60	Parallel	750	30	Cont.	72	8	X	2.86	5000
445-1	2	25	10	3	60	Trap.	1500	20	Cont.	72	8	X	2.86	3600
445-2	2	25	10	3	60	Trap.	1500	20	Cont.	72	8	X	2.86	5000
445-3	2	25	10	3	60	Trap.	1500	20	Cont.	72	10	X	2.86	5000

Model ID	Geometry									Cross-section		CF detail		Mat'l
	n_{span}	L/d ratio	s_g [ft]	n_{girder}	Support skew [deg]; Layout		R [ft]	s_{cf} [ft]	CF layout	d_w [in]	t_{deck} [in]	CF type	A_{cf} [in^2]	E_c [ksi]
445-4	2	25	10	3	60	Trap.	1500	20	Cont.	72	8	K	2.86	5000
445-5	2	25	10	3	60	Trap.	1500	20	Cont.	72	8	X	4.79	5000
446-1	2	25	10	3	60	Trap.	1500	30	Cont.	72	8	X	2.86	5000
447-1	2	25	10	3	60	Trap.	750	20	Cont.	72	8	X	2.86	3600
447-2	2	25	10	3	60	Trap.	750	20	Cont.	72	8	X	2.86	5000
447-3	2	25	10	3	60	Trap.	750	20	Cont.	72	10	X	2.86	5000
447-4	2	25	10	3	60	Trap.	750	20	Cont.	72	8	K	2.86	5000
447-5	2	25	10	3	60	Trap.	750	20	Cont.	72	8	X	4.79	5000
448-1	2	25	10	3	60	Trap.	750	30	Cont.	72	8	X	2.86	5000
449-1	2	25	10	5	0	Parallel	1500	20	Cont.	72	8	X	2.86	3600
449-2	2	25	10	5	0	Parallel	1500	20	Cont.	72	8	X	2.86	5000
449-3	2	25	10	5	0	Parallel	1500	20	Cont.	72	10	X	2.86	5000
449-4	2	25	10	5	0	Parallel	1500	20	Cont.	72	8	K	2.86	5000
449-5	2	25	10	5	0	Parallel	1500	20	Cont.	72	8	X	4.79	5000
450-1	2	25	10	5	0	Parallel	1500	30	Cont.	72	8	X	2.86	5000
451-1	2	25	10	5	0	Parallel	750	20	Cont.	72	8	X	2.86	3600
451-2	2	25	10	5	0	Parallel	750	20	Cont.	72	8	X	2.86	5000
451-3	2	25	10	5	0	Parallel	750	20	Cont.	72	10	X	2.86	5000
451-4	2	25	10	5	0	Parallel	750	20	Cont.	72	8	K	2.86	5000
451-5	2	25	10	5	0	Parallel	750	20	Cont.	72	8	X	4.79	5000
452-1	2	25	10	5	0	Parallel	750	30	Cont.	72	8	X	2.86	5000
453-1	2	25	10	5	30	Parallel	1500	20	Cont.	72	8	X	2.86	3600
453-2	2	25	10	5	30	Parallel	1500	20	Cont.	72	8	X	2.86	5000
453-3	2	25	10	5	30	Parallel	1500	20	Cont.	72	10	X	2.86	5000
453-4	2	25	10	5	30	Parallel	1500	20	Cont.	72	8	K	2.86	5000
453-5	2	25	10	5	30	Parallel	1500	20	Cont.	72	8	X	4.79	5000
454-1	2	25	10	5	30	Parallel	1500	30	Cont.	72	8	X	2.86	5000
455-1	2	25	10	5	30	Parallel	750	20	Cont.	72	8	X	2.86	3600
455-2	2	25	10	5	30	Parallel	750	20	Cont.	72	8	X	2.86	5000
455-3	2	25	10	5	30	Parallel	750	20	Cont.	72	10	X	2.86	5000
455-4	2	25	10	5	30	Parallel	750	20	Cont.	72	8	K	2.86	5000
455-5	2	25	10	5	30	Parallel	750	20	Cont.	72	8	X	4.79	5000
456-1	2	25	10	5	30	Parallel	750	30	Cont.	72	8	X	2.86	5000
457-1	2	25	10	5	60	Parallel	1500	20	Cont.	72	8	X	2.86	3600
457-2	2	25	10	5	60	Parallel	1500	20	Cont.	72	8	X	2.86	5000
457-3	2	25	10	5	60	Parallel	1500	20	Cont.	72	10	X	2.86	5000
457-4	2	25	10	5	60	Parallel	1500	20	Cont.	72	8	K	2.86	5000
457-5	2	25	10	5	60	Parallel	1500	20	Cont.	72	8	X	4.79	5000
458-1	2	25	10	5	60	Parallel	1500	30	Cont.	72	8	X	2.86	5000
459-1	2	25	10	5	60	Parallel	750	20	Cont.	72	8	X	2.86	3600
459-2	2	25	10	5	60	Parallel	750	20	Cont.	72	8	X	2.86	5000
459-3	2	25	10	5	60	Parallel	750	20	Cont.	72	10	X	2.86	5000
459-4	2	25	10	5	60	Parallel	750	20	Cont.	72	8	K	2.86	5000
459-5	2	25	10	5	60	Parallel	750	20	Cont.	72	8	X	4.79	5000
460-1	2	25	10	5	60	Parallel	750	30	Cont.	72	8	X	2.86	5000
461-1	2	25	10	5	60	Trap.	1500	20	Cont.	72	8	X	2.86	3600
461-2	2	25	10	5	60	Trap.	1500	20	Cont.	72	8	X	2.86	5000
461-3	2	25	10	5	60	Trap.	1500	20	Cont.	72	10	X	2.86	5000
461-4	2	25	10	5	60	Trap.	1500	20	Cont.	72	8	K	2.86	5000
461-5	2	25	10	5	60	Trap.	1500	20	Cont.	72	8	X	4.79	5000
462-1	2	25	10	5	60	Trap.	1500	30	Cont.	72	8	X	2.86	5000
463-1	2	25	10	5	60	Trap.	750	20	Cont.	72	8	X	2.86	3600
463-2	2	25	10	5	60	Trap.	750	20	Cont.	72	8	X	2.86	5000
463-3	2	25	10	5	60	Trap.	750	20	Cont.	72	10	X	2.86	5000
463-4	2	25	10	5	60	Trap.	750	20	Cont.	72	8	K	2.86	5000
463-5	2	25	10	5	60	Trap.	750	20	Cont.	72	8	X	4.79	5000
464-1	2	25	10	5	60	Trap.	750	30	Cont.	72	8	X	2.86	5000
465-1	2	25	10	7	0	Parallel	1500	20	Cont.	72	8	X	2.86	3600
465-2	2	25	10	7	0	Parallel	1500	20	Cont.	72	8	X	2.86	5000
465-3	2	25	10	7	0	Parallel	1500	20	Cont.	72	10	X	2.86	5000
465-4	2	25	10	7	0	Parallel	1500	20	Cont.	72	8	K	2.86	5000
465-5	2	25	10	7	0	Parallel	1500	20	Cont.	72	8	X	4.79	5000
466-1	2	25	10	7	0	Parallel	1500	30	Cont.	72	8	X	2.86	5000
467-1	2	25	10	7	0	Parallel	750	20	Cont.	72	8	X	2.86	3600
467-2	2	25	10	7	0	Parallel	750	20	Cont.	72	8	X	2.86	5000
467-3	2	25	10	7	0	Parallel	750	20	Cont.	72	10	X	2.86	5000
467-4	2	25	10	7	0	Parallel	750	20	Cont.	72	8	K	2.86	5000
467-5	2	25	10	7	0	Parallel	750	20	Cont.	72	8	X	4.79	5000
468-1	2	25	10	7	0	Parallel	750	30	Cont.	72	8	X	2.86	5000
469-1	2	25	10	7	30	Parallel	1500	20	Cont.	72	8	X	2.86	3600
469-2	2	25	10	7	30	Parallel	1500	20	Cont.	72	8	X	2.86	5000
469-3	2	25	10	7	30	Parallel	1500	20	Cont.	72	10	X	2.86	5000
469-4	2	25	10	7	30	Parallel	1500	20	Cont.	72	8	K	2.86	5000
469-5	2	25	10	7	30	Parallel	1500	20	Cont.	72	8	X	4.79	5000
470-1	2	25	10	7	30	Parallel	1500	30	Cont.	72	8	X	2.86	5000
471-1	2	25	10	7	30	Parallel	750	20	Cont.	72	8	X	2.86	3600
471-2	2	25	10	7	30	Parallel	750	20	Cont.	72	8	X	2.86	5000
471-3	2	25	10	7	30	Parallel	750	20	Cont.	72	10	X	2.86	5000
471-4	2	25	10	7	30	Parallel	750	20	Cont.	72	8	K	2.86	5000

Model ID	Geometry									Cross-section		CF detail		Mat'l
	n_{span}	L/d ratio	s_g [ft]	n_{girder}	Support skew [deg];	Layout	R [ft]	s_{cf} [ft]	CF layout	d_w [in]	t_{deck} [in]	CF type	A_{cf} [in^2]	E_c [ksi]
471-5	2	25	10	7	30	Parallel	750	20	Cont.	72	8	X	4.79	5000
472-1	2	25	10	7	30	Parallel	750	30	Cont.	72	8	X	2.86	5000
473-1	2	25	10	7	60	Parallel	1500	20	Cont.	72	8	X	2.86	3600
473-2	2	25	10	7	60	Parallel	1500	20	Cont.	72	8	X	2.86	5000
473-3	2	25	10	7	60	Parallel	1500	20	Cont.	72	10	X	2.86	5000
473-4	2	25	10	7	60	Parallel	1500	20	Cont.	72	8	K	2.86	5000
473-5	2	25	10	7	60	Parallel	1500	20	Cont.	72	8	X	4.79	5000
474-1	2	25	10	7	60	Parallel	1500	30	Cont.	72	8	X	2.86	5000
475-1	2	25	10	7	60	Parallel	750	20	Cont.	72	8	X	2.86	3600
475-2	2	25	10	7	60	Parallel	750	20	Cont.	72	8	X	2.86	5000
475-3	2	25	10	7	60	Parallel	750	20	Cont.	72	10	X	2.86	5000
475-4	2	25	10	7	60	Parallel	750	20	Cont.	72	8	K	2.86	5000
475-5	2	25	10	7	60	Parallel	750	20	Cont.	72	8	X	4.79	5000
476-1	2	25	10	7	60	Parallel	750	30	Cont.	72	8	X	2.86	5000
477-1	2	25	10	7	60	Trap.	1500	20	Cont.	72	8	X	2.86	3600
477-2	2	25	10	7	60	Trap.	1500	20	Cont.	72	8	X	2.86	5000
477-3	2	25	10	7	60	Trap.	1500	20	Cont.	72	10	X	2.86	5000
477-4	2	25	10	7	60	Trap.	1500	20	Cont.	72	8	K	2.86	5000
477-5	2	25	10	7	60	Trap.	1500	20	Cont.	72	8	X	4.79	5000
478-1	2	25	10	7	60	Trap.	1500	30	Cont.	72	8	X	2.86	5000
479-1	2	25	10	7	60	Trap.	750	20	Cont.	72	8	X	2.86	3600
479-2	2	25	10	7	60	Trap.	750	20	Cont.	72	8	X	2.86	5000
479-3	2	25	10	7	60	Trap.	750	20	Cont.	72	10	X	2.86	5000
479-4	2	25	10	7	60	Trap.	750	20	Cont.	72	8	K	2.86	5000
479-5	2	25	10	7	60	Trap.	750	20	Cont.	72	8	X	4.79	5000
480-1	2	25	10	7	60	Trap.	750	30	Cont.	72	8	X	2.86	5000
481-1	2	25	6	3	0	Parallel	1500	20	Cont.	96	8	X	2.86	3600
481-2	2	25	6	3	0	Parallel	1500	20	Cont.	96	8	X	2.86	5000
481-3	2	25	6	3	0	Parallel	1500	20	Cont.	96	10	X	2.86	5000
481-4	2	25	6	3	0	Parallel	1500	20	Cont.	96	8	K	2.86	5000
481-5	2	25	6	3	0	Parallel	1500	20	Cont.	96	8	X	4.79	5000
482-1	2	25	6	3	0	Parallel	1500	30	Cont.	96	8	X	2.86	5000
483-1	2	25	6	3	0	Parallel	750	20	Cont.	96	8	X	2.86	3600
483-2	2	25	6	3	0	Parallel	750	20	Cont.	96	8	X	2.86	5000
483-3	2	25	6	3	0	Parallel	750	20	Cont.	96	10	X	2.86	5000
483-4	2	25	6	3	0	Parallel	750	20	Cont.	96	8	K	2.86	5000
483-5	2	25	6	3	0	Parallel	750	20	Cont.	96	8	X	4.79	5000
484-1	2	25	6	3	0	Parallel	750	30	Cont.	96	8	X	2.86	5000
485-1	2	25	6	3	30	Parallel	1500	20	Cont.	96	8	X	2.86	3600
485-2	2	25	6	3	30	Parallel	1500	20	Cont.	96	8	X	2.86	5000
485-3	2	25	6	3	30	Parallel	1500	20	Cont.	96	10	X	2.86	5000
485-4	2	25	6	3	30	Parallel	1500	20	Cont.	96	8	K	2.86	5000
485-5	2	25	6	3	30	Parallel	1500	20	Cont.	96	8	X	4.79	5000
486-1	2	25	6	3	30	Parallel	1500	30	Cont.	96	8	X	2.86	5000
487-1	2	25	6	3	30	Parallel	750	20	Cont.	96	8	X	2.86	3600
487-2	2	25	6	3	30	Parallel	750	20	Cont.	96	8	X	2.86	5000
487-3	2	25	6	3	30	Parallel	750	20	Cont.	96	10	X	2.86	5000
487-4	2	25	6	3	30	Parallel	750	20	Cont.	96	8	K	2.86	5000
487-5	2	25	6	3	30	Parallel	750	20	Cont.	96	8	X	4.79	5000
488-1	2	25	6	3	30	Parallel	750	30	Cont.	96	8	X	2.86	5000
489-1	2	25	6	3	60	Parallel	1500	20	Cont.	96	8	X	2.86	3600
489-2	2	25	6	3	60	Parallel	1500	20	Cont.	96	8	X	2.86	5000
489-3	2	25	6	3	60	Parallel	1500	20	Cont.	96	10	X	2.86	5000
489-4	2	25	6	3	60	Parallel	1500	20	Cont.	96	8	K	2.86	5000
489-5	2	25	6	3	60	Parallel	1500	20	Cont.	96	8	X	4.79	5000
490-1	2	25	6	3	60	Parallel	1500	30	Cont.	96	8	X	2.86	5000
491-1	2	25	6	3	60	Parallel	750	20	Cont.	96	8	X	2.86	3600
491-2	2	25	6	3	60	Parallel	750	20	Cont.	96	8	X	2.86	5000
491-3	2	25	6	3	60	Parallel	750	20	Cont.	96	10	X	2.86	5000
491-4	2	25	6	3	60	Parallel	750	20	Cont.	96	8	K	2.86	5000
491-5	2	25	6	3	60	Parallel	750	20	Cont.	96	8	X	4.79	5000
492-1	2	25	6	3	60	Parallel	750	30	Cont.	96	8	X	2.86	5000
493-1	2	25	6	3	60	Trap.	1500	20	Cont.	96	8	X	2.86	3600
493-2	2	25	6	3	60	Trap.	1500	20	Cont.	96	8	X	2.86	5000
493-3	2	25	6	3	60	Trap.	1500	20	Cont.	96	10	X	2.86	5000
493-4	2	25	6	3	60	Trap.	1500	20	Cont.	96	8	K	2.86	5000
493-5	2	25	6	3	60	Trap.	1500	20	Cont.	96	8	X	4.79	5000
494-1	2	25	6	3	60	Trap.	1500	30	Cont.	96	8	X	2.86	5000
495-1	2	25	6	3	60	Trap.	750	20	Cont.	96	8	X	2.86	3600
495-2	2	25	6	3	60	Trap.	750	20	Cont.	96	8	X	2.86	5000
495-3	2	25	6	3	60	Trap.	750	20	Cont.	96	10	X	2.86	5000
495-4	2	25	6	3	60	Trap.	750	20	Cont.	96	8	K	2.86	5000
495-5	2	25	6	3	60	Trap.	750	20	Cont.	96	8	X	4.79	5000
496-1	2	25	6	3	60	Trap.	750	30	Cont.	96	8	X	2.86	5000
497-1	2	25	6	5	0	Parallel	1500	20	Cont.	96	8	X	2.86	3600
497-2	2	25	6	5	0	Parallel	1500	20	Cont.	96	8	X	2.86	5000
497-3	2	25	6	5	0	Parallel	1500	20	Cont.	96	10	X	2.86	5000
497-4	2	25	6	5	0	Parallel	1500	20	Cont.	96	8	K	2.86	5000
497-5	2	25	6	5	0	Parallel	1500	20	Cont.	96	8	X	4.79	5000

Model ID	Geometry									Cross-section		CF detail		Mat'l
	n_{span}	L/d ratio	s_g [ft]	n_{girder}	Support skew [deg];	Layout	R [ft]	s_{cf} [ft]	CF layout	d_w [in]	t_{deck} [in]	CF type	A_{cf} [in^2]	E_c [ksi]
498-1	2	25	6	5	0	Parallel	1500	30	Cont.	96	8	X	2.86	5000
499-1	2	25	6	5	0	Parallel	750	20	Cont.	96	8	X	2.86	3600
499-2	2	25	6	5	0	Parallel	750	20	Cont.	96	8	X	2.86	5000
499-3	2	25	6	5	0	Parallel	750	20	Cont.	96	10	X	2.86	5000
499-4	2	25	6	5	0	Parallel	750	20	Cont.	96	8	K	2.86	5000
499-5	2	25	6	5	0	Parallel	750	20	Cont.	96	8	X	4.79	5000
500-1	2	25	6	5	0	Parallel	750	30	Cont.	96	8	X	2.86	5000
501-1	2	25	6	5	30	Parallel	1500	20	Cont.	96	8	X	2.86	3600
501-2	2	25	6	5	30	Parallel	1500	20	Cont.	96	8	X	2.86	5000
501-3	2	25	6	5	30	Parallel	1500	20	Cont.	96	10	X	2.86	5000
501-4	2	25	6	5	30	Parallel	1500	20	Cont.	96	8	K	2.86	5000
501-5	2	25	6	5	30	Parallel	1500	20	Cont.	96	8	X	4.79	5000
502-1	2	25	6	5	30	Parallel	1500	30	Cont.	96	8	X	2.86	5000
503-1	2	25	6	5	30	Parallel	750	20	Cont.	96	8	X	2.86	3600
503-2	2	25	6	5	30	Parallel	750	20	Cont.	96	8	X	2.86	5000
503-3	2	25	6	5	30	Parallel	750	20	Cont.	96	10	X	2.86	5000
503-4	2	25	6	5	30	Parallel	750	20	Cont.	96	8	K	2.86	5000
503-5	2	25	6	5	30	Parallel	750	20	Cont.	96	8	X	4.79	5000
504-1	2	25	6	5	30	Parallel	750	30	Cont.	96	8	X	2.86	5000
505-1	2	25	6	5	60	Parallel	1500	20	Cont.	96	8	X	2.86	3600
505-2	2	25	6	5	60	Parallel	1500	20	Cont.	96	8	X	2.86	5000
505-3	2	25	6	5	60	Parallel	1500	20	Cont.	96	10	X	2.86	5000
505-4	2	25	6	5	60	Parallel	1500	20	Cont.	96	8	K	2.86	5000
505-5	2	25	6	5	60	Parallel	1500	20	Cont.	96	8	X	4.79	5000
506-1	2	25	6	5	60	Parallel	1500	30	Cont.	96	8	X	2.86	5000
507-1	2	25	6	5	60	Parallel	750	20	Cont.	96	8	X	2.86	3600
507-2	2	25	6	5	60	Parallel	750	20	Cont.	96	8	X	2.86	5000
507-3	2	25	6	5	60	Parallel	750	20	Cont.	96	10	X	2.86	5000
507-4	2	25	6	5	60	Parallel	750	20	Cont.	96	8	K	2.86	5000
507-5	2	25	6	5	60	Parallel	750	20	Cont.	96	8	X	4.79	5000
508-1	2	25	6	5	60	Parallel	750	30	Cont.	96	8	X	2.86	5000
509-1	2	25	6	5	60	Trap.	1500	20	Cont.	96	8	X	2.86	3600
509-2	2	25	6	5	60	Trap.	1500	20	Cont.	96	8	X	2.86	5000
509-3	2	25	6	5	60	Trap.	1500	20	Cont.	96	10	X	2.86	5000
509-4	2	25	6	5	60	Trap.	1500	20	Cont.	96	8	K	2.86	5000
509-5	2	25	6	5	60	Trap.	1500	20	Cont.	96	8	X	4.79	5000
510-1	2	25	6	5	60	Trap.	1500	30	Cont.	96	8	X	2.86	5000
511-1	2	25	6	5	60	Trap.	750	20	Cont.	96	8	X	2.86	3600
511-2	2	25	6	5	60	Trap.	750	20	Cont.	96	8	X	2.86	5000
511-3	2	25	6	5	60	Trap.	750	20	Cont.	96	10	X	2.86	5000
511-4	2	25	6	5	60	Trap.	750	20	Cont.	96	8	K	2.86	5000
511-5	2	25	6	5	60	Trap.	750	20	Cont.	96	8	X	4.79	5000
512-1	2	25	6	5	60	Trap.	750	30	Cont.	96	8	X	2.86	5000
513-1	2	25	6	7	0	Parallel	1500	20	Cont.	96	8	X	2.86	3600
513-2	2	25	6	7	0	Parallel	1500	20	Cont.	96	8	X	2.86	5000
513-3	2	25	6	7	0	Parallel	1500	20	Cont.	96	10	X	2.86	5000
513-4	2	25	6	7	0	Parallel	1500	20	Cont.	96	8	K	2.86	5000
513-5	2	25	6	7	0	Parallel	1500	20	Cont.	96	8	X	4.79	5000
514-1	2	25	6	7	0	Parallel	1500	30	Cont.	96	8	X	2.86	5000
515-1	2	25	6	7	0	Parallel	750	20	Cont.	96	8	X	2.86	3600
515-2	2	25	6	7	0	Parallel	750	20	Cont.	96	8	X	2.86	5000
515-3	2	25	6	7	0	Parallel	750	20	Cont.	96	10	X	2.86	5000
515-4	2	25	6	7	0	Parallel	750	20	Cont.	96	8	K	2.86	5000
515-5	2	25	6	7	0	Parallel	750	20	Cont.	96	8	X	4.79	5000
516-1	2	25	6	7	0	Parallel	750	30	Cont.	96	8	X	2.86	5000
517-1	2	25	6	7	30	Parallel	1500	20	Cont.	96	8	X	2.86	3600
517-2	2	25	6	7	30	Parallel	1500	20	Cont.	96	8	X	2.86	5000
517-3	2	25	6	7	30	Parallel	1500	20	Cont.	96	10	X	2.86	5000
517-4	2	25	6	7	30	Parallel	1500	20	Cont.	96	8	K	2.86	5000
517-5	2	25	6	7	30	Parallel	1500	20	Cont.	96	8	X	4.79	5000
518-1	2	25	6	7	30	Parallel	1500	30	Cont.	96	8	X	2.86	5000
519-1	2	25	6	7	30	Parallel	750	20	Cont.	96	8	X	2.86	3600
519-2	2	25	6	7	30	Parallel	750	20	Cont.	96	8	X	2.86	5000
519-3	2	25	6	7	30	Parallel	750	20	Cont.	96	10	X	2.86	5000
519-4	2	25	6	7	30	Parallel	750	20	Cont.	96	8	K	2.86	5000
519-5	2	25	6	7	30	Parallel	750	20	Cont.	96	8	X	4.79	5000
520-1	2	25	6	7	30	Parallel	750	30	Cont.	96	8	X	2.86	5000
521-1	2	25	6	7	60	Parallel	1500	20	Cont.	96	8	X	2.86	3600
521-2	2	25	6	7	60	Parallel	1500	20	Cont.	96	8	X	2.86	5000
521-3	2	25	6	7	60	Parallel	1500	20	Cont.	96	10	X	2.86	5000
521-4	2	25	6	7	60	Parallel	1500	20	Cont.	96	8	K	2.86	5000
521-5	2	25	6	7	60	Parallel	1500	20	Cont.	96	8	X	4.79	5000
522-1	2	25	6	7	60	Parallel	1500	30	Cont.	96	8	X	2.86	5000
523-1	2	25	6	7	60	Parallel	750	20	Cont.	96	8	X	2.86	3600
523-2	2	25	6	7	60	Parallel	750	20	Cont.	96	8	X	2.86	5000
523-3	2	25	6	7	60	Parallel	750	20	Cont.	96	10	X	2.86	5000
523-4	2	25	6	7	60	Parallel	750	20	Cont.	96	8	K	2.86	5000
523-5	2	25	6	7	60	Parallel	750	20	Cont.	96	8	X	4.79	5000
524-1	2	25	6	7	60	Parallel	750	30	Cont.	96	8	X	2.86	5000

Model ID	Geometry									Cross-section		CF detail		Mat'l
	n_{span}	L/d ratio	s_g [ft]	n_{girder}	Support skew [deg]; Layout		R [ft]	s_{cf} [ft]	CF layout	d_w [in]	t_{deck} [in]	CF type	A_{cf} [in^2]	E_c [ksi]
525-1	2	25	6	7	60	Trap.	1500	20	Cont.	96	8	X	2.86	3600
525-2	2	25	6	7	60	Trap.	1500	20	Cont.	96	8	X	2.86	5000
525-3	2	25	6	7	60	Trap.	1500	20	Cont.	96	10	X	2.86	5000
525-4	2	25	6	7	60	Trap.	1500	20	Cont.	96	8	K	2.86	5000
525-5	2	25	6	7	60	Trap.	1500	20	Cont.	96	8	X	4.79	5000
526-1	2	25	6	7	60	Trap.	1500	30	Cont.	96	8	X	2.86	5000
527-1	2	25	6	7	60	Trap.	750	20	Cont.	96	8	X	2.86	3600
527-2	2	25	6	7	60	Trap.	750	20	Cont.	96	8	X	2.86	5000
527-3	2	25	6	7	60	Trap.	750	20	Cont.	96	10	X	2.86	5000
527-4	2	25	6	7	60	Trap.	750	20	Cont.	96	8	K	2.86	5000
527-5	2	25	6	7	60	Trap.	750	20	Cont.	96	8	X	4.79	5000
528-1	2	25	6	7	60	Trap.	750	30	Cont.	96	8	X	2.86	5000
529-1	2	25	8	3	0	Parallel	1500	20	Cont.	96	8	X	2.86	3600
529-2	2	25	8	3	0	Parallel	1500	20	Cont.	96	8	X	2.86	5000
529-3	2	25	8	3	0	Parallel	1500	20	Cont.	96	10	X	2.86	5000
529-4	2	25	8	3	0	Parallel	1500	20	Cont.	96	8	K	2.86	5000
529-5	2	25	8	3	0	Parallel	1500	20	Cont.	96	8	X	4.79	5000
530-1	2	25	8	3	0	Parallel	1500	30	Cont.	96	8	X	2.86	5000
531-1	2	25	8	3	0	Parallel	750	20	Cont.	96	8	X	2.86	3600
531-2	2	25	8	3	0	Parallel	750	20	Cont.	96	8	X	2.86	5000
531-3	2	25	8	3	0	Parallel	750	20	Cont.	96	10	X	2.86	5000
531-4	2	25	8	3	0	Parallel	750	20	Cont.	96	8	K	2.86	5000
531-5	2	25	8	3	0	Parallel	750	20	Cont.	96	8	X	4.79	5000
532-1	2	25	8	3	0	Parallel	750	30	Cont.	96	8	X	2.86	5000
533-1	2	25	8	3	30	Parallel	1500	20	Cont.	96	8	X	2.86	3600
533-2	2	25	8	3	30	Parallel	1500	20	Cont.	96	8	X	2.86	5000
533-3	2	25	8	3	30	Parallel	1500	20	Cont.	96	10	X	2.86	5000
533-4	2	25	8	3	30	Parallel	1500	20	Cont.	96	8	K	2.86	5000
533-5	2	25	8	3	30	Parallel	1500	20	Cont.	96	8	X	4.79	5000
534-1	2	25	8	3	30	Parallel	1500	30	Cont.	96	8	X	2.86	5000
535-1	2	25	8	3	30	Parallel	750	20	Cont.	96	8	X	2.86	3600
535-2	2	25	8	3	30	Parallel	750	20	Cont.	96	8	X	2.86	5000
535-3	2	25	8	3	30	Parallel	750	20	Cont.	96	10	X	2.86	5000
535-4	2	25	8	3	30	Parallel	750	20	Cont.	96	8	K	2.86	5000
535-5	2	25	8	3	30	Parallel	750	20	Cont.	96	8	X	4.79	5000
536-1	2	25	8	3	30	Parallel	750	30	Cont.	96	8	X	2.86	5000
537-1	2	25	8	3	60	Parallel	1500	20	Cont.	96	8	X	2.86	3600
537-2	2	25	8	3	60	Parallel	1500	20	Cont.	96	8	X	2.86	5000
537-3	2	25	8	3	60	Parallel	1500	20	Cont.	96	10	X	2.86	5000
537-4	2	25	8	3	60	Parallel	1500	20	Cont.	96	8	K	2.86	5000
537-5	2	25	8	3	60	Parallel	1500	20	Cont.	96	8	X	4.79	5000
538-1	2	25	8	3	60	Parallel	1500	30	Cont.	96	8	X	2.86	5000
539-1	2	25	8	3	60	Parallel	750	20	Cont.	96	8	X	2.86	3600
539-2	2	25	8	3	60	Parallel	750	20	Cont.	96	8	X	2.86	5000
539-3	2	25	8	3	60	Parallel	750	20	Cont.	96	10	X	2.86	5000
539-4	2	25	8	3	60	Parallel	750	20	Cont.	96	8	K	2.86	5000
539-5	2	25	8	3	60	Parallel	750	20	Cont.	96	8	X	4.79	5000
540-1	2	25	8	3	60	Parallel	750	30	Cont.	96	8	X	2.86	5000
541-1	2	25	8	3	60	Trap.	1500	20	Cont.	96	8	X	2.86	3600
541-2	2	25	8	3	60	Trap.	1500	20	Cont.	96	8	X	2.86	5000
541-3	2	25	8	3	60	Trap.	1500	20	Cont.	96	10	X	2.86	5000
541-4	2	25	8	3	60	Trap.	1500	20	Cont.	96	8	K	2.86	5000
541-5	2	25	8	3	60	Trap.	1500	20	Cont.	96	8	X	4.79	5000
542-1	2	25	8	3	60	Trap.	1500	30	Cont.	96	8	X	2.86	5000
543-1	2	25	8	3	60	Trap.	750	20	Cont.	96	8	X	2.86	3600
543-2	2	25	8	3	60	Trap.	750	20	Cont.	96	8	X	2.86	5000
543-3	2	25	8	3	60	Trap.	750	20	Cont.	96	10	X	2.86	5000
543-4	2	25	8	3	60	Trap.	750	20	Cont.	96	8	K	2.86	5000
543-5	2	25	8	3	60	Trap.	750	20	Cont.	96	8	X	4.79	5000
544-1	2	25	8	3	60	Trap.	750	30	Cont.	96	8	X	2.86	5000
545-1	2	25	8	5	0	Parallel	1500	20	Cont.	96	8	X	2.86	3600
545-2	2	25	8	5	0	Parallel	1500	20	Cont.	96	8	X	2.86	5000
545-3	2	25	8	5	0	Parallel	1500	20	Cont.	96	10	X	2.86	5000
545-4	2	25	8	5	0	Parallel	1500	20	Cont.	96	8	K	2.86	5000
545-5	2	25	8	5	0	Parallel	1500	20	Cont.	96	8	X	4.79	5000
546-1	2	25	8	5	0	Parallel	1500	30	Cont.	96	8	X	2.86	5000
547-1	2	25	8	5	0	Parallel	750	20	Cont.	96	8	X	2.86	3600
547-2	2	25	8	5	0	Parallel	750	20	Cont.	96	8	X	2.86	5000
547-3	2	25	8	5	0	Parallel	750	20	Cont.	96	10	X	2.86	5000
547-4	2	25	8	5	0	Parallel	750	20	Cont.	96	8	K	2.86	5000
547-5	2	25	8	5	0	Parallel	750	20	Cont.	96	8	X	4.79	5000
548-1	2	25	8	5	0	Parallel	750	30	Cont.	96	8	X	2.86	5000
549-1	2	25	8	5	30	Parallel	1500	20	Cont.	96	8	X	2.86	3600
549-2	2	25	8	5	30	Parallel	1500	20	Cont.	96	8	X	2.86	5000
549-3	2	25	8	5	30	Parallel	1500	20	Cont.	96	10	X	2.86	5000
549-4	2	25	8	5	30	Parallel	1500	20	Cont.	96	8	K	2.86	5000
549-5	2	25	8	5	30	Parallel	1500	20	Cont.	96	8	X	4.79	5000
550-1	2	25	8	5	30	Parallel	1500	30	Cont.	96	8	X	2.86	5000
551-1	2	25	8	5	30	Parallel	750	20	Cont.	96	8	X	2.86	3600

Model ID	Geometry									Cross-section		CF detail		Mat'l
	n_{span}	L/d ratio	s_g [ft]	n_{girder}	Support skew [deg]; Layout		R [ft]	s_{cf} [ft]	CF layout	d_w [in]	t_{deck} [in]	CF type	A_{cf} [in^2]	E_c [ksi]
551-2	2	25	8	5	30	Parallel	750	20	Cont.	96	8	X	2.86	5000
551-3	2	25	8	5	30	Parallel	750	20	Cont.	96	10	X	2.86	5000
551-4	2	25	8	5	30	Parallel	750	20	Cont.	96	8	K	2.86	5000
551-5	2	25	8	5	30	Parallel	750	20	Cont.	96	8	X	4.79	5000
552-1	2	25	8	5	30	Parallel	750	30	Cont.	96	8	X	2.86	5000
553-1	2	25	8	5	60	Parallel	1500	20	Cont.	96	8	X	2.86	3600
553-2	2	25	8	5	60	Parallel	1500	20	Cont.	96	8	X	2.86	5000
553-3	2	25	8	5	60	Parallel	1500	20	Cont.	96	10	X	2.86	5000
553-4	2	25	8	5	60	Parallel	1500	20	Cont.	96	8	K	2.86	5000
553-5	2	25	8	5	60	Parallel	1500	20	Cont.	96	8	X	4.79	5000
554-1	2	25	8	5	60	Parallel	1500	30	Cont.	96	8	X	2.86	5000
555-1	2	25	8	5	60	Parallel	750	20	Cont.	96	8	X	2.86	3600
555-2	2	25	8	5	60	Parallel	750	20	Cont.	96	8	X	2.86	5000
555-3	2	25	8	5	60	Parallel	750	20	Cont.	96	10	X	2.86	5000
555-4	2	25	8	5	60	Parallel	750	20	Cont.	96	8	K	2.86	5000
555-5	2	25	8	5	60	Parallel	750	20	Cont.	96	8	X	4.79	5000
556-1	2	25	8	5	60	Parallel	750	30	Cont.	96	8	X	2.86	5000
557-1	2	25	8	5	60	Trap.	1500	20	Cont.	96	8	X	2.86	3600
557-2	2	25	8	5	60	Trap.	1500	20	Cont.	96	8	X	2.86	5000
557-3	2	25	8	5	60	Trap.	1500	20	Cont.	96	10	X	2.86	5000
557-4	2	25	8	5	60	Trap.	1500	20	Cont.	96	8	K	2.86	5000
557-5	2	25	8	5	60	Trap.	1500	20	Cont.	96	8	X	4.79	5000
558-1	2	25	8	5	60	Trap.	1500	30	Cont.	96	8	X	2.86	5000
559-1	2	25	8	5	60	Trap.	750	20	Cont.	96	8	X	2.86	3600
559-2	2	25	8	5	60	Trap.	750	20	Cont.	96	8	X	2.86	5000
559-3	2	25	8	5	60	Trap.	750	20	Cont.	96	10	X	2.86	5000
559-4	2	25	8	5	60	Trap.	750	20	Cont.	96	8	K	2.86	5000
559-5	2	25	8	5	60	Trap.	750	20	Cont.	96	8	X	4.79	5000
560-1	2	25	8	5	60	Trap.	750	30	Cont.	96	8	X	2.86	5000
561-1	2	25	8	7	0	Parallel	1500	20	Cont.	96	8	X	2.86	3600
561-2	2	25	8	7	0	Parallel	1500	20	Cont.	96	8	X	2.86	5000
561-3	2	25	8	7	0	Parallel	1500	20	Cont.	96	10	X	2.86	5000
561-4	2	25	8	7	0	Parallel	1500	20	Cont.	96	8	K	2.86	5000
561-5	2	25	8	7	0	Parallel	1500	20	Cont.	96	8	X	4.79	5000
562-1	2	25	8	7	0	Parallel	1500	30	Cont.	96	8	X	2.86	5000
563-1	2	25	8	7	0	Parallel	750	20	Cont.	96	8	X	2.86	3600
563-2	2	25	8	7	0	Parallel	750	20	Cont.	96	8	X	2.86	5000
563-3	2	25	8	7	0	Parallel	750	20	Cont.	96	10	X	2.86	5000
563-4	2	25	8	7	0	Parallel	750	20	Cont.	96	8	K	2.86	5000
563-5	2	25	8	7	0	Parallel	750	20	Cont.	96	8	X	4.79	5000
564-1	2	25	8	7	0	Parallel	750	30	Cont.	96	8	X	2.86	5000
565-1	2	25	8	7	30	Parallel	1500	20	Cont.	96	8	X	2.86	3600
565-2	2	25	8	7	30	Parallel	1500	20	Cont.	96	8	X	2.86	5000
565-3	2	25	8	7	30	Parallel	1500	20	Cont.	96	10	X	2.86	5000
565-4	2	25	8	7	30	Parallel	1500	20	Cont.	96	8	K	2.86	5000
565-5	2	25	8	7	30	Parallel	1500	20	Cont.	96	8	X	4.79	5000
566-1	2	25	8	7	30	Parallel	1500	30	Cont.	96	8	X	2.86	5000
567-1	2	25	8	7	30	Parallel	750	20	Cont.	96	8	X	2.86	3600
567-2	2	25	8	7	30	Parallel	750	20	Cont.	96	8	X	2.86	5000
567-3	2	25	8	7	30	Parallel	750	20	Cont.	96	10	X	2.86	5000
567-4	2	25	8	7	30	Parallel	750	20	Cont.	96	8	K	2.86	5000
567-5	2	25	8	7	30	Parallel	750	20	Cont.	96	8	X	4.79	5000
568-1	2	25	8	7	30	Parallel	750	30	Cont.	96	8	X	2.86	5000
569-1	2	25	8	7	60	Parallel	1500	20	Cont.	96	8	X	2.86	3600
569-2	2	25	8	7	60	Parallel	1500	20	Cont.	96	8	X	2.86	5000
569-3	2	25	8	7	60	Parallel	1500	20	Cont.	96	10	X	2.86	5000
569-4	2	25	8	7	60	Parallel	1500	20	Cont.	96	8	K	2.86	5000
569-5	2	25	8	7	60	Parallel	1500	20	Cont.	96	8	X	4.79	5000
570-1	2	25	8	7	60	Parallel	1500	30	Cont.	96	8	X	2.86	5000
571-1	2	25	8	7	60	Parallel	750	20	Cont.	96	8	X	2.86	3600
571-2	2	25	8	7	60	Parallel	750	20	Cont.	96	8	X	2.86	5000
571-3	2	25	8	7	60	Parallel	750	20	Cont.	96	10	X	2.86	5000
571-4	2	25	8	7	60	Parallel	750	20	Cont.	96	8	K	2.86	5000
571-5	2	25	8	7	60	Parallel	750	20	Cont.	96	8	X	4.79	5000
572-1	2	25	8	7	60	Parallel	750	30	Cont.	96	8	X	2.86	5000
573-1	2	25	8	7	60	Trap.	1500	20	Cont.	96	8	X	2.86	3600
573-2	2	25	8	7	60	Trap.	1500	20	Cont.	96	8	X	2.86	5000
573-3	2	25	8	7	60	Trap.	1500	20	Cont.	96	10	X	2.86	5000
573-4	2	25	8	7	60	Trap.	1500	20	Cont.	96	8	K	2.86	5000
573-5	2	25	8	7	60	Trap.	1500	20	Cont.	96	8	X	4.79	5000
574-1	2	25	8	7	60	Trap.	1500	30	Cont.	96	8	X	2.86	5000
575-1	2	25	8	7	60	Trap.	750	20	Cont.	96	8	X	2.86	3600
575-2	2	25	8	7	60	Trap.	750	20	Cont.	96	8	X	2.86	5000
575-3	2	25	8	7	60	Trap.	750	20	Cont.	96	10	X	2.86	5000
575-4	2	25	8	7	60	Trap.	750	20	Cont.	96	8	K	2.86	5000
575-5	2	25	8	7	60	Trap.	750	20	Cont.	96	8	X	4.79	5000
576-1	2	25	8	7	60	Trap.	750	30	Cont.	96	8	X	2.86	5000
577-1	2	25	10	3	0	Parallel	1500	20	Cont.	96	8	X	2.86	3600
577-2	2	25	10	3	0	Parallel	1500	20	Cont.	96	8	X	2.86	5000

Model ID	Geometry									Cross-section		CF detail		Mat'l
	n_{span}	L/d ratio	s_g [ft]	n_{girder}	Support skew [deg];	Layout	R [ft]	s_{cf} [ft]	CF layout	d_w [in]	t_{deck} [in]	CF type	A_{cf} [in^2]	E_c [ksi]
577-3	2	25	10	3	0	Parallel	1500	20	Cont.	96	10	X	2.86	5000
577-4	2	25	10	3	0	Parallel	1500	20	Cont.	96	8	K	2.86	5000
577-5	2	25	10	3	0	Parallel	1500	20	Cont.	96	8	X	4.79	5000
578-1	2	25	10	3	0	Parallel	1500	30	Cont.	96	8	X	2.86	5000
579-1	2	25	10	3	0	Parallel	750	20	Cont.	96	8	X	2.86	3600
579-2	2	25	10	3	0	Parallel	750	20	Cont.	96	8	X	2.86	5000
579-3	2	25	10	3	0	Parallel	750	20	Cont.	96	10	X	2.86	5000
579-4	2	25	10	3	0	Parallel	750	20	Cont.	96	8	K	2.86	5000
579-5	2	25	10	3	0	Parallel	750	20	Cont.	96	8	X	4.79	5000
580-1	2	25	10	3	0	Parallel	750	30	Cont.	96	8	X	2.86	5000
581-1	2	25	10	3	30	Parallel	1500	20	Cont.	96	8	X	2.86	3600
581-2	2	25	10	3	30	Parallel	1500	20	Cont.	96	8	X	2.86	5000
581-3	2	25	10	3	30	Parallel	1500	20	Cont.	96	10	X	2.86	5000
581-4	2	25	10	3	30	Parallel	1500	20	Cont.	96	8	K	2.86	5000
581-5	2	25	10	3	30	Parallel	1500	20	Cont.	96	8	X	4.79	5000
582-1	2	25	10	3	30	Parallel	1500	30	Cont.	96	8	X	2.86	5000
583-1	2	25	10	3	30	Parallel	750	20	Cont.	96	8	X	2.86	3600
583-2	2	25	10	3	30	Parallel	750	20	Cont.	96	8	X	2.86	5000
583-3	2	25	10	3	30	Parallel	750	20	Cont.	96	10	X	2.86	5000
583-4	2	25	10	3	30	Parallel	750	20	Cont.	96	8	K	2.86	5000
583-5	2	25	10	3	30	Parallel	750	20	Cont.	96	8	X	4.79	5000
584-1	2	25	10	3	30	Parallel	750	30	Cont.	96	8	X	2.86	5000
585-1	2	25	10	3	60	Parallel	1500	20	Cont.	96	8	X	2.86	3600
585-2	2	25	10	3	60	Parallel	1500	20	Cont.	96	8	X	2.86	5000
585-3	2	25	10	3	60	Parallel	1500	20	Cont.	96	10	X	2.86	5000
585-4	2	25	10	3	60	Parallel	1500	20	Cont.	96	8	K	2.86	5000
585-5	2	25	10	3	60	Parallel	1500	20	Cont.	96	8	X	4.79	5000
586-1	2	25	10	3	60	Parallel	1500	30	Cont.	96	8	X	2.86	5000
587-1	2	25	10	3	60	Parallel	750	20	Cont.	96	8	X	2.86	3600
587-2	2	25	10	3	60	Parallel	750	20	Cont.	96	8	X	2.86	5000
587-3	2	25	10	3	60	Parallel	750	20	Cont.	96	10	X	2.86	5000
587-4	2	25	10	3	60	Parallel	750	20	Cont.	96	8	K	2.86	5000
587-5	2	25	10	3	60	Parallel	750	20	Cont.	96	8	X	4.79	5000
588-1	2	25	10	3	60	Parallel	750	30	Cont.	96	8	X	2.86	5000
589-1	2	25	10	3	60	Trap.	1500	20	Cont.	96	8	X	2.86	3600
589-2	2	25	10	3	60	Trap.	1500	20	Cont.	96	8	X	2.86	5000
589-3	2	25	10	3	60	Trap.	1500	20	Cont.	96	10	X	2.86	5000
589-4	2	25	10	3	60	Trap.	1500	20	Cont.	96	8	K	2.86	5000
589-5	2	25	10	3	60	Trap.	1500	20	Cont.	96	8	X	4.79	5000
590-1	2	25	10	3	60	Trap.	1500	30	Cont.	96	8	X	2.86	5000
591-1	2	25	10	3	60	Trap.	750	20	Cont.	96	8	X	2.86	3600
591-2	2	25	10	3	60	Trap.	750	20	Cont.	96	8	X	2.86	5000
591-3	2	25	10	3	60	Trap.	750	20	Cont.	96	10	X	2.86	5000
591-4	2	25	10	3	60	Trap.	750	20	Cont.	96	8	K	2.86	5000
591-5	2	25	10	3	60	Trap.	750	20	Cont.	96	8	X	4.79	5000
592-1	2	25	10	3	60	Trap.	750	30	Cont.	96	8	X	2.86	5000
593-1	2	25	10	5	0	Parallel	1500	20	Cont.	96	8	X	2.86	3600
593-2	2	25	10	5	0	Parallel	1500	20	Cont.	96	8	X	2.86	5000
593-3	2	25	10	5	0	Parallel	1500	20	Cont.	96	10	X	2.86	5000
593-4	2	25	10	5	0	Parallel	1500	20	Cont.	96	8	K	2.86	5000
593-5	2	25	10	5	0	Parallel	1500	20	Cont.	96	8	X	4.79	5000
594-1	2	25	10	5	0	Parallel	1500	30	Cont.	96	8	X	2.86	5000
595-1	2	25	10	5	0	Parallel	750	20	Cont.	96	8	X	2.86	3600
595-2	2	25	10	5	0	Parallel	750	20	Cont.	96	8	X	2.86	5000
595-3	2	25	10	5	0	Parallel	750	20	Cont.	96	10	X	2.86	5000
595-4	2	25	10	5	0	Parallel	750	20	Cont.	96	8	K	2.86	5000
595-5	2	25	10	5	0	Parallel	750	20	Cont.	96	8	X	4.79	5000
596-1	2	25	10	5	0	Parallel	750	30	Cont.	96	8	X	2.86	5000
597-1	2	25	10	5	30	Parallel	1500	20	Cont.	96	8	X	2.86	3600
597-2	2	25	10	5	30	Parallel	1500	20	Cont.	96	8	X	2.86	5000
597-3	2	25	10	5	30	Parallel	1500	20	Cont.	96	10	X	2.86	5000
597-4	2	25	10	5	30	Parallel	1500	20	Cont.	96	8	K	2.86	5000
597-5	2	25	10	5	30	Parallel	1500	20	Cont.	96	8	X	4.79	5000
598-1	2	25	10	5	30	Parallel	1500	30	Cont.	96	8	X	2.86	5000
599-1	2	25	10	5	30	Parallel	750	20	Cont.	96	8	X	2.86	3600
599-2	2	25	10	5	30	Parallel	750	20	Cont.	96	8	X	2.86	5000
599-3	2	25	10	5	30	Parallel	750	20	Cont.	96	10	X	2.86	5000
599-4	2	25	10	5	30	Parallel	750	20	Cont.	96	8	K	2.86	5000
599-5	2	25	10	5	30	Parallel	750	20	Cont.	96	8	X	4.79	5000
600-1	2	25	10	5	30	Parallel	750	30	Cont.	96	8	X	2.86	5000
601-1	2	25	10	5	60	Parallel	1500	20	Cont.	96	8	X	2.86	3600
601-2	2	25	10	5	60	Parallel	1500	20	Cont.	96	8	X	2.86	5000
601-3	2	25	10	5	60	Parallel	1500	20	Cont.	96	10	X	2.86	5000
601-4	2	25	10	5	60	Parallel	1500	20	Cont.	96	8	K	2.86	5000
601-5	2	25	10	5	60	Parallel	1500	20	Cont.	96	8	X	4.79	5000
602-1	2	25	10	5	60	Parallel	1500	30	Cont.	96	8	X	2.86	5000
603-1	2	25	10	5	60	Parallel	750	20	Cont.	96	8	X	2.86	3600
603-2	2	25	10	5	60	Parallel	750	20	Cont.	96	8	X	2.86	5000
603-3	2	25	10	5	60	Parallel	750	20	Cont.	96	10	X	2.86	5000

Model ID	Geometry									Cross-section		CF detail		Mat'l
	n_{span}	L/d ratio	s_g [ft]	n_{girder}	Support skew [deg]; Layout		R [ft]	s_{cf} [ft]	CF layout	d_w [in]	t_{deck} [in]	CF type	A_{cf} [in^2]	E_c [ksi]
603-4	2	25	10	5	60	Parallel	750	20	Cont.	96	8	K	2.86	5000
603-5	2	25	10	5	60	Parallel	750	20	Cont.	96	8	X	4.79	5000
604-1	2	25	10	5	60	Parallel	750	30	Cont.	96	8	X	2.86	5000
605-1	2	25	10	5	60	Trap.	1500	20	Cont.	96	8	X	2.86	3600
605-2	2	25	10	5	60	Trap.	1500	20	Cont.	96	8	X	2.86	5000
605-3	2	25	10	5	60	Trap.	1500	20	Cont.	96	10	X	2.86	5000
605-4	2	25	10	5	60	Trap.	1500	20	Cont.	96	8	K	2.86	5000
605-5	2	25	10	5	60	Trap.	1500	20	Cont.	96	8	X	4.79	5000
606-1	2	25	10	5	60	Trap.	1500	30	Cont.	96	8	X	2.86	5000
607-1	2	25	10	5	60	Trap.	750	20	Cont.	96	8	X	2.86	3600
607-2	2	25	10	5	60	Trap.	750	20	Cont.	96	8	X	2.86	5000
607-3	2	25	10	5	60	Trap.	750	20	Cont.	96	10	X	2.86	5000
607-4	2	25	10	5	60	Trap.	750	20	Cont.	96	8	K	2.86	5000
607-5	2	25	10	5	60	Trap.	750	20	Cont.	96	8	X	4.79	5000
608-1	2	25	10	5	60	Trap.	750	30	Cont.	96	8	X	2.86	5000
609-1	2	25	10	7	0	Parallel	1500	20	Cont.	96	8	X	2.86	3600
609-2	2	25	10	7	0	Parallel	1500	20	Cont.	96	8	X	2.86	5000
609-3	2	25	10	7	0	Parallel	1500	20	Cont.	96	10	X	2.86	5000
609-4	2	25	10	7	0	Parallel	1500	20	Cont.	96	8	K	2.86	5000
609-5	2	25	10	7	0	Parallel	1500	20	Cont.	96	8	X	4.79	5000
610-1	2	25	10	7	0	Parallel	1500	30	Cont.	96	8	X	2.86	5000
611-1	2	25	10	7	0	Parallel	750	20	Cont.	96	8	X	2.86	3600
611-2	2	25	10	7	0	Parallel	750	20	Cont.	96	8	X	2.86	5000
611-3	2	25	10	7	0	Parallel	750	20	Cont.	96	10	X	2.86	5000
611-4	2	25	10	7	0	Parallel	750	20	Cont.	96	8	K	2.86	5000
611-5	2	25	10	7	0	Parallel	750	20	Cont.	96	8	X	4.79	5000
612-1	2	25	10	7	0	Parallel	750	30	Cont.	96	8	X	2.86	5000
613-1	2	25	10	7	30	Parallel	1500	20	Cont.	96	8	X	2.86	3600
613-2	2	25	10	7	30	Parallel	1500	20	Cont.	96	8	X	2.86	5000
613-3	2	25	10	7	30	Parallel	1500	20	Cont.	96	10	X	2.86	5000
613-4	2	25	10	7	30	Parallel	1500	20	Cont.	96	8	K	2.86	5000
613-5	2	25	10	7	30	Parallel	1500	20	Cont.	96	8	X	4.79	5000
614-1	2	25	10	7	30	Parallel	1500	30	Cont.	96	8	X	2.86	5000
615-1	2	25	10	7	30	Parallel	750	20	Cont.	96	8	X	2.86	3600
615-2	2	25	10	7	30	Parallel	750	20	Cont.	96	8	X	2.86	5000
615-3	2	25	10	7	30	Parallel	750	20	Cont.	96	10	X	2.86	5000
615-4	2	25	10	7	30	Parallel	750	20	Cont.	96	8	K	2.86	5000
615-5	2	25	10	7	30	Parallel	750	20	Cont.	96	8	X	4.79	5000
616-1	2	25	10	7	30	Parallel	750	30	Cont.	96	8	X	2.86	5000
617-1	2	25	10	7	60	Parallel	1500	20	Cont.	96	8	X	2.86	3600
617-2	2	25	10	7	60	Parallel	1500	20	Cont.	96	8	X	2.86	5000
617-3	2	25	10	7	60	Parallel	1500	20	Cont.	96	10	X	2.86	5000
617-4	2	25	10	7	60	Parallel	1500	20	Cont.	96	8	K	2.86	5000
617-5	2	25	10	7	60	Parallel	1500	20	Cont.	96	8	X	4.79	5000
618-1	2	25	10	7	60	Parallel	1500	30	Cont.	96	8	X	2.86	5000
619-1	2	25	10	7	60	Parallel	750	20	Cont.	96	8	X	2.86	3600
619-2	2	25	10	7	60	Parallel	750	20	Cont.	96	8	X	2.86	5000
619-3	2	25	10	7	60	Parallel	750	20	Cont.	96	10	X	2.86	5000
619-4	2	25	10	7	60	Parallel	750	20	Cont.	96	8	K	2.86	5000
619-5	2	25	10	7	60	Parallel	750	20	Cont.	96	8	X	4.79	5000
620-1	2	25	10	7	60	Parallel	750	30	Cont.	96	8	X	2.86	5000
621-1	2	25	10	7	60	Trap.	1500	20	Cont.	96	8	X	2.86	3600
621-2	2	25	10	7	60	Trap.	1500	20	Cont.	96	8	X	2.86	5000
621-3	2	25	10	7	60	Trap.	1500	20	Cont.	96	10	X	2.86	5000
621-4	2	25	10	7	60	Trap.	1500	20	Cont.	96	8	K	2.86	5000
621-5	2	25	10	7	60	Trap.	1500	20	Cont.	96	8	X	4.79	5000
622-1	2	25	10	7	60	Trap.	1500	30	Cont.	96	8	X	2.86	5000
623-1	2	25	10	7	60	Trap.	750	20	Cont.	96	8	X	2.86	3600
623-2	2	25	10	7	60	Trap.	750	20	Cont.	96	8	X	2.86	5000
623-3	2	25	10	7	60	Trap.	750	20	Cont.	96	10	X	2.86	5000
623-4	2	25	10	7	60	Trap.	750	20	Cont.	96	8	K	2.86	5000
623-5	2	25	10	7	60	Trap.	750	20	Cont.	96	8	X	4.79	5000
624-1	2	25	10	7	60	Trap.	750	30	Cont.	96	8	X	2.86	5000
625-1	2	30	6	3	0	Parallel	Infinite	20	Cont.	72	8	X	2.86	3600
625-2	2	30	6	3	0	Parallel	Infinite	20	Cont.	72	8	X	2.86	5000
625-3	2	30	6	3	0	Parallel	Infinite	20	Cont.	72	10	X	2.86	5000
625-4	2	30	6	3	0	Parallel	Infinite	20	Cont.	72	8	K	2.86	5000
625-5	2	30	6	3	0	Parallel	Infinite	20	Cont.	72	8	X	4.79	5000
626-1	2	30	6	3	0	Parallel	Infinite	30	Cont.	72	8	X	2.86	5000
627-1	2	30	6	3	0	Parallel	1500	20	Cont.	72	8	X	2.86	3600
627-2	2	30	6	3	0	Parallel	1500	20	Cont.	72	8	X	2.86	5000
627-3	2	30	6	3	0	Parallel	1500	20	Cont.	72	10	X	2.86	5000
627-4	2	30	6	3	0	Parallel	1500	20	Cont.	72	8	K	2.86	5000
627-5	2	30	6	3	0	Parallel	1500	20	Cont.	72	8	X	4.79	5000
628-1	2	30	6	3	0	Parallel	1500	30	Cont.	72	8	X	2.86	5000
629-1	2	30	6	3	0	Parallel	750	20	Cont.	72	8	X	2.86	3600
629-2	2	30	6	3	0	Parallel	750	20	Cont.	72	8	X	2.86	5000
629-3	2	30	6	3	0	Parallel	750	20	Cont.	72	10	X	2.86	5000
629-4	2	30	6	3	0	Parallel	750	20	Cont.	72	8	K	2.86	5000

Model ID	Geometry									Cross-section		CF detail		Mat'l
	n_{span}	L/d ratio	s_g [ft]	n_{girder}	Support skew [deg]; Layout		R [ft]	s_{cf} [ft]	CF layout	d_w [in]	t_{deck} [in]	CF type	A_{cf} [in^2]	E_c [ksi]
629-5	2	30	6	3	0	Parallel	750	20	Cont.	72	8	X	4.79	5000
630-1	2	30	6	3	0	Parallel	750	30	Cont.	72	8	X	2.86	5000
631-1	2	30	6	3	30	Parallel	Infinite	20	Cont.	72	8	X	2.86	3600
631-2	2	30	6	3	30	Parallel	Infinite	20	Cont.	72	8	X	2.86	5000
631-3	2	30	6	3	30	Parallel	Infinite	20	Cont.	72	10	X	2.86	5000
631-4	2	30	6	3	30	Parallel	Infinite	20	Cont.	72	8	K	2.86	5000
631-5	2	30	6	3	30	Parallel	Infinite	20	Cont.	72	8	X	4.79	5000
632-1	2	30	6	3	30	Parallel	Infinite	30	Cont.	72	8	X	2.86	5000
633-1	2	30	6	3	30	Parallel	1500	20	Cont.	72	8	X	2.86	3600
633-2	2	30	6	3	30	Parallel	1500	20	Cont.	72	8	X	2.86	5000
633-3	2	30	6	3	30	Parallel	1500	20	Cont.	72	10	X	2.86	5000
633-4	2	30	6	3	30	Parallel	1500	20	Cont.	72	8	K	2.86	5000
633-5	2	30	6	3	30	Parallel	1500	20	Cont.	72	8	X	4.79	5000
634-1	2	30	6	3	30	Parallel	1500	30	Cont.	72	8	X	2.86	5000
635-1	2	30	6	3	30	Parallel	750	20	Cont.	72	8	X	2.86	3600
635-2	2	30	6	3	30	Parallel	750	20	Cont.	72	8	X	2.86	5000
635-3	2	30	6	3	30	Parallel	750	20	Cont.	72	10	X	2.86	5000
635-4	2	30	6	3	30	Parallel	750	20	Cont.	72	8	K	2.86	5000
635-5	2	30	6	3	30	Parallel	750	20	Cont.	72	8	X	4.79	5000
636-1	2	30	6	3	30	Parallel	750	30	Cont.	72	8	X	2.86	5000
637-1	2	30	6	3	60	Parallel	Infinite	20	Cont.	72	8	X	2.86	3600
637-2	2	30	6	3	60	Parallel	Infinite	20	Cont.	72	8	X	2.86	5000
637-3	2	30	6	3	60	Parallel	Infinite	20	Cont.	72	10	X	2.86	5000
637-4	2	30	6	3	60	Parallel	Infinite	20	Cont.	72	8	K	2.86	5000
637-5	2	30	6	3	60	Parallel	Infinite	20	Cont.	72	8	X	4.79	5000
638-1	2	30	6	3	60	Parallel	Infinite	30	Cont.	72	8	X	2.86	5000
639-1	2	30	6	3	60	Parallel	Infinite	20	Stag.	72	8	X	2.86	3600
639-2	2	30	6	3	60	Parallel	Infinite	20	Stag.	72	8	X	2.86	5000
639-3	2	30	6	3	60	Parallel	Infinite	20	Stag.	72	10	X	2.86	5000
639-4	2	30	6	3	60	Parallel	Infinite	20	Stag.	72	8	K	2.86	5000
639-5	2	30	6	3	60	Parallel	Infinite	20	Stag.	72	8	X	4.79	5000
640-1	2	30	6	3	60	Parallel	Infinite	30	Stag.	72	8	X	2.86	5000
641-1	2	30	6	3	60	Parallel	1500	20	Cont.	72	8	X	2.86	3600
641-2	2	30	6	3	60	Parallel	1500	20	Cont.	72	8	X	2.86	5000
641-3	2	30	6	3	60	Parallel	1500	20	Cont.	72	10	X	2.86	5000
641-4	2	30	6	3	60	Parallel	1500	20	Cont.	72	8	K	2.86	5000
641-5	2	30	6	3	60	Parallel	1500	20	Cont.	72	8	X	4.79	5000
642-1	2	30	6	3	60	Parallel	1500	30	Cont.	72	8	X	2.86	5000
643-1	2	30	6	3	60	Parallel	750	20	Cont.	72	8	X	2.86	3600
643-2	2	30	6	3	60	Parallel	750	20	Cont.	72	8	X	2.86	5000
643-3	2	30	6	3	60	Parallel	750	20	Cont.	72	10	X	2.86	5000
643-4	2	30	6	3	60	Parallel	750	20	Cont.	72	8	K	2.86	5000
643-5	2	30	6	3	60	Parallel	750	20	Cont.	72	8	X	4.79	5000
644-1	2	30	6	3	60	Parallel	750	30	Cont.	72	8	X	2.86	5000
645-1	2	30	6	3	60	Trap.	Infinite	20	Cont.	72	8	X	2.86	3600
645-2	2	30	6	3	60	Trap.	Infinite	20	Cont.	72	8	X	2.86	5000
645-3	2	30	6	3	60	Trap.	Infinite	20	Cont.	72	10	X	2.86	5000
645-4	2	30	6	3	60	Trap.	Infinite	20	Cont.	72	8	K	2.86	5000
645-5	2	30	6	3	60	Trap.	Infinite	20	Cont.	72	8	X	4.79	5000
646-1	2	30	6	3	60	Trap.	Infinite	30	Cont.	72	8	X	2.86	5000
647-1	2	30	6	3	60	Trap.	Infinite	20	Stag.	72	8	X	2.86	3600
647-2	2	30	6	3	60	Trap.	Infinite	20	Stag.	72	8	X	2.86	5000
647-3	2	30	6	3	60	Trap.	Infinite	20	Stag.	72	10	X	2.86	5000
647-4	2	30	6	3	60	Trap.	Infinite	20	Stag.	72	8	K	2.86	5000
647-5	2	30	6	3	60	Trap.	Infinite	20	Stag.	72	8	X	4.79	5000
648-1	2	30	6	3	60	Trap.	Infinite	30	Stag.	72	8	X	2.86	5000
649-1	2	30	6	3	60	Trap.	1500	20	Cont.	72	8	X	2.86	3600
649-2	2	30	6	3	60	Trap.	1500	20	Cont.	72	8	X	2.86	5000
649-3	2	30	6	3	60	Trap.	1500	20	Cont.	72	10	X	2.86	5000
649-4	2	30	6	3	60	Trap.	1500	20	Cont.	72	8	K	2.86	5000
649-5	2	30	6	3	60	Trap.	1500	20	Cont.	72	8	X	4.79	5000
650-1	2	30	6	3	60	Trap.	1500	30	Cont.	72	8	X	2.86	5000
651-1	2	30	6	3	60	Trap.	750	20	Cont.	72	8	X	2.86	3600
651-2	2	30	6	3	60	Trap.	750	20	Cont.	72	8	X	2.86	5000
651-3	2	30	6	3	60	Trap.	750	20	Cont.	72	10	X	2.86	5000
651-4	2	30	6	3	60	Trap.	750	20	Cont.	72	8	K	2.86	5000
651-5	2	30	6	3	60	Trap.	750	20	Cont.	72	8	X	4.79	5000
652-1	2	30	6	3	60	Trap.	750	30	Cont.	72	8	X	2.86	5000
653-1	2	30	6	5	0	Parallel	Infinite	20	Cont.	72	8	X	2.86	3600
653-2	2	30	6	5	0	Parallel	Infinite	20	Cont.	72	8	X	2.86	5000
653-3	2	30	6	5	0	Parallel	Infinite	20	Cont.	72	10	X	2.86	5000
653-4	2	30	6	5	0	Parallel	Infinite	20	Cont.	72	8	K	2.86	5000
653-5	2	30	6	5	0	Parallel	Infinite	20	Cont.	72	8	X	4.79	5000
654-1	2	30	6	5	0	Parallel	Infinite	30	Cont.	72	8	X	2.86	5000
655-1	2	30	6	5	0	Parallel	1500	20	Cont.	72	8	X	2.86	3600
655-2	2	30	6	5	0	Parallel	1500	20	Cont.	72	8	X	2.86	5000
655-3	2	30	6	5	0	Parallel	1500	20	Cont.	72	10	X	2.86	5000
655-4	2	30	6	5	0	Parallel	1500	20	Cont.	72	8	K	2.86	5000
655-5	2	30	6	5	0	Parallel	1500	20	Cont.	72	8	X	4.79	5000

Model ID	Geometry									Cross-section		CF detail		Mat'l
	n_{span}	L/d ratio	s_g [ft]	n_{girder}	Support skew [deg];	Layout	R [ft]	s_{cf} [ft]	CF layout	d_w [in]	t_{deck} [in]	CF type	A_{cf} [in^2]	E_c [ksi]
656-1	2	30	6	5	0	Parallel	1500	30	Cont.	72	8	X	2.86	5000
657-1	2	30	6	5	0	Parallel	750	20	Cont.	72	8	X	2.86	3600
657-2	2	30	6	5	0	Parallel	750	20	Cont.	72	8	X	2.86	5000
657-3	2	30	6	5	0	Parallel	750	20	Cont.	72	10	X	2.86	5000
657-4	2	30	6	5	0	Parallel	750	20	Cont.	72	8	K	2.86	5000
657-5	2	30	6	5	0	Parallel	750	20	Cont.	72	8	X	4.79	5000
658-1	2	30	6	5	0	Parallel	750	30	Cont.	72	8	X	2.86	5000
659-1	2	30	6	5	30	Parallel	Infinite	20	Cont.	72	8	X	2.86	3600
659-2	2	30	6	5	30	Parallel	Infinite	20	Cont.	72	8	X	2.86	5000
659-3	2	30	6	5	30	Parallel	Infinite	20	Cont.	72	10	X	2.86	5000
659-4	2	30	6	5	30	Parallel	Infinite	20	Cont.	72	8	K	2.86	5000
659-5	2	30	6	5	30	Parallel	Infinite	20	Cont.	72	8	X	4.79	5000
660-1	2	30	6	5	30	Parallel	Infinite	30	Cont.	72	8	X	2.86	5000
661-1	2	30	6	5	30	Parallel	1500	20	Cont.	72	8	X	2.86	3600
661-2	2	30	6	5	30	Parallel	1500	20	Cont.	72	8	X	2.86	5000
661-3	2	30	6	5	30	Parallel	1500	20	Cont.	72	10	X	2.86	5000
661-4	2	30	6	5	30	Parallel	1500	20	Cont.	72	8	K	2.86	5000
661-5	2	30	6	5	30	Parallel	1500	20	Cont.	72	8	X	4.79	5000
662-1	2	30	6	5	30	Parallel	1500	30	Cont.	72	8	X	2.86	5000
663-1	2	30	6	5	30	Parallel	750	20	Cont.	72	8	X	2.86	3600
663-2	2	30	6	5	30	Parallel	750	20	Cont.	72	8	X	2.86	5000
663-3	2	30	6	5	30	Parallel	750	20	Cont.	72	10	X	2.86	5000
663-4	2	30	6	5	30	Parallel	750	20	Cont.	72	8	K	2.86	5000
663-5	2	30	6	5	30	Parallel	750	20	Cont.	72	8	X	4.79	5000
664-1	2	30	6	5	30	Parallel	750	30	Cont.	72	8	X	2.86	5000
665-1	2	30	6	5	60	Parallel	Infinite	20	Cont.	72	8	X	2.86	3600
665-2	2	30	6	5	60	Parallel	Infinite	20	Cont.	72	8	X	2.86	5000
665-3	2	30	6	5	60	Parallel	Infinite	20	Cont.	72	10	X	2.86	5000
665-4	2	30	6	5	60	Parallel	Infinite	20	Cont.	72	8	K	2.86	5000
665-5	2	30	6	5	60	Parallel	Infinite	20	Cont.	72	8	X	4.79	5000
666-1	2	30	6	5	60	Parallel	Infinite	30	Cont.	72	8	X	2.86	5000
667-1	2	30	6	5	60	Parallel	Infinite	20	Stag.	72	8	X	2.86	3600
667-2	2	30	6	5	60	Parallel	Infinite	20	Stag.	72	8	X	2.86	5000
667-3	2	30	6	5	60	Parallel	Infinite	20	Stag.	72	10	X	2.86	5000
667-4	2	30	6	5	60	Parallel	Infinite	20	Stag.	72	8	K	2.86	5000
667-5	2	30	6	5	60	Parallel	Infinite	20	Stag.	72	8	X	4.79	5000
668-1	2	30	6	5	60	Parallel	Infinite	30	Stag.	72	8	X	2.86	5000
669-1	2	30	6	5	60	Parallel	1500	20	Cont.	72	8	X	2.86	3600
669-2	2	30	6	5	60	Parallel	1500	20	Cont.	72	8	X	2.86	5000
669-3	2	30	6	5	60	Parallel	1500	20	Cont.	72	10	X	2.86	5000
669-4	2	30	6	5	60	Parallel	1500	20	Cont.	72	8	K	2.86	5000
669-5	2	30	6	5	60	Parallel	1500	20	Cont.	72	8	X	4.79	5000
670-1	2	30	6	5	60	Parallel	1500	30	Cont.	72	8	X	2.86	5000
671-1	2	30	6	5	60	Parallel	750	20	Cont.	72	8	X	2.86	3600
671-2	2	30	6	5	60	Parallel	750	20	Cont.	72	8	X	2.86	5000
671-3	2	30	6	5	60	Parallel	750	20	Cont.	72	10	X	2.86	5000
671-4	2	30	6	5	60	Parallel	750	20	Cont.	72	8	K	2.86	5000
671-5	2	30	6	5	60	Parallel	750	20	Cont.	72	8	X	4.79	5000
672-1	2	30	6	5	60	Parallel	750	30	Cont.	72	8	X	2.86	5000
673-1	2	30	6	5	60	Trap.	Infinite	20	Cont.	72	8	X	2.86	3600
673-2	2	30	6	5	60	Trap.	Infinite	20	Cont.	72	8	X	2.86	5000
673-3	2	30	6	5	60	Trap.	Infinite	20	Cont.	72	10	X	2.86	5000
673-4	2	30	6	5	60	Trap.	Infinite	20	Cont.	72	8	K	2.86	5000
673-5	2	30	6	5	60	Trap.	Infinite	20	Cont.	72	8	X	4.79	5000
674-1	2	30	6	5	60	Trap.	Infinite	30	Cont.	72	8	X	2.86	5000
675-1	2	30	6	5	60	Trap.	Infinite	20	Stag.	72	8	X	2.86	3600
675-2	2	30	6	5	60	Trap.	Infinite	20	Stag.	72	8	X	2.86	5000
675-3	2	30	6	5	60	Trap.	Infinite	20	Stag.	72	10	X	2.86	5000
675-4	2	30	6	5	60	Trap.	Infinite	20	Stag.	72	8	K	2.86	5000
675-5	2	30	6	5	60	Trap.	Infinite	20	Stag.	72	8	X	4.79	5000
676-1	2	30	6	5	60	Trap.	Infinite	30	Stag.	72	8	X	2.86	5000
677-1	2	30	6	5	60	Trap.	1500	20	Cont.	72	8	X	2.86	3600
677-2	2	30	6	5	60	Trap.	1500	20	Cont.	72	8	X	2.86	5000
677-3	2	30	6	5	60	Trap.	1500	20	Cont.	72	10	X	2.86	5000
677-4	2	30	6	5	60	Trap.	1500	20	Cont.	72	8	K	2.86	5000
677-5	2	30	6	5	60	Trap.	1500	20	Cont.	72	8	X	4.79	5000
678-1	2	30	6	5	60	Trap.	1500	30	Cont.	72	8	X	2.86	5000
679-1	2	30	6	5	60	Trap.	750	20	Cont.	72	8	X	2.86	3600
679-2	2	30	6	5	60	Trap.	750	20	Cont.	72	8	X	2.86	5000
679-3	2	30	6	5	60	Trap.	750	20	Cont.	72	10	X	2.86	5000
679-4	2	30	6	5	60	Trap.	750	20	Cont.	72	8	K	2.86	5000
679-5	2	30	6	5	60	Trap.	750	20	Cont.	72	8	X	4.79	5000
680-1	2	30	6	5	60	Trap.	750	30	Cont.	72	8	X	2.86	5000
681-1	2	30	6	7	0	Parallel	Infinite	20	Cont.	72	8	X	2.86	3600
681-2	2	30	6	7	0	Parallel	Infinite	20	Cont.	72	8	X	2.86	5000
681-3	2	30	6	7	0	Parallel	Infinite	20	Cont.	72	10	X	2.86	5000
681-4	2	30	6	7	0	Parallel	Infinite	20	Cont.	72	8	K	2.86	5000
681-5	2	30	6	7	0	Parallel	Infinite	20	Cont.	72	8	X	4.79	5000
682-1	2	30	6	7	0	Parallel	Infinite	30	Cont.	72	8	X	2.86	5000

Model ID	Geometry									Cross-section		CF detail		Mat'l
	n_{span}	L/d ratio	s_g [ft]	n_{girder}	Support skew [deg]; Layout		R [ft]	s_{cf} [ft]	CF layout	d_w [in]	t_{deck} [in]	CF type	A_{cf} [in^2]	E_c [ksi]
683-1	2	30	6	7	0	Parallel	1500	20	Cont.	72	8	X	2.86	3600
683-2	2	30	6	7	0	Parallel	1500	20	Cont.	72	8	X	2.86	5000
683-3	2	30	6	7	0	Parallel	1500	20	Cont.	72	10	X	2.86	5000
683-4	2	30	6	7	0	Parallel	1500	20	Cont.	72	8	K	2.86	5000
683-5	2	30	6	7	0	Parallel	1500	20	Cont.	72	8	X	4.79	5000
684-1	2	30	6	7	0	Parallel	1500	30	Cont.	72	8	X	2.86	5000
685-1	2	30	6	7	0	Parallel	750	20	Cont.	72	8	X	2.86	3600
685-2	2	30	6	7	0	Parallel	750	20	Cont.	72	8	X	2.86	5000
685-3	2	30	6	7	0	Parallel	750	20	Cont.	72	10	X	2.86	5000
685-4	2	30	6	7	0	Parallel	750	20	Cont.	72	8	K	2.86	5000
685-5	2	30	6	7	0	Parallel	750	20	Cont.	72	8	X	4.79	5000
686-1	2	30	6	7	0	Parallel	750	30	Cont.	72	8	X	2.86	5000
687-1	2	30	6	7	30	Parallel	Infinite	20	Cont.	72	8	X	2.86	3600
687-2	2	30	6	7	30	Parallel	Infinite	20	Cont.	72	8	X	2.86	5000
687-3	2	30	6	7	30	Parallel	Infinite	20	Cont.	72	10	X	2.86	5000
687-4	2	30	6	7	30	Parallel	Infinite	20	Cont.	72	8	K	2.86	5000
687-5	2	30	6	7	30	Parallel	Infinite	20	Cont.	72	8	X	4.79	5000
688-1	2	30	6	7	30	Parallel	Infinite	30	Cont.	72	8	X	2.86	5000
689-1	2	30	6	7	30	Parallel	1500	20	Cont.	72	8	X	2.86	3600
689-2	2	30	6	7	30	Parallel	1500	20	Cont.	72	8	X	2.86	5000
689-3	2	30	6	7	30	Parallel	1500	20	Cont.	72	10	X	2.86	5000
689-4	2	30	6	7	30	Parallel	1500	20	Cont.	72	8	K	2.86	5000
689-5	2	30	6	7	30	Parallel	1500	20	Cont.	72	8	X	4.79	5000
690-1	2	30	6	7	30	Parallel	1500	30	Cont.	72	8	X	2.86	5000
691-1	2	30	6	7	30	Parallel	750	20	Cont.	72	8	X	2.86	3600
691-2	2	30	6	7	30	Parallel	750	20	Cont.	72	8	X	2.86	5000
691-3	2	30	6	7	30	Parallel	750	20	Cont.	72	10	X	2.86	5000
691-4	2	30	6	7	30	Parallel	750	20	Cont.	72	8	K	2.86	5000
691-5	2	30	6	7	30	Parallel	750	20	Cont.	72	8	X	4.79	5000
692-1	2	30	6	7	30	Parallel	750	30	Cont.	72	8	X	2.86	5000
693-1	2	30	6	7	60	Parallel	Infinite	20	Cont.	72	8	X	2.86	3600
693-2	2	30	6	7	60	Parallel	Infinite	20	Cont.	72	8	X	2.86	5000
693-3	2	30	6	7	60	Parallel	Infinite	20	Cont.	72	10	X	2.86	5000
693-4	2	30	6	7	60	Parallel	Infinite	20	Cont.	72	8	K	2.86	5000
693-5	2	30	6	7	60	Parallel	Infinite	20	Cont.	72	8	X	4.79	5000
694-1	2	30	6	7	60	Parallel	Infinite	30	Cont.	72	8	X	2.86	5000
695-1	2	30	6	7	60	Parallel	Infinite	20	Stag.	72	8	X	2.86	3600
695-2	2	30	6	7	60	Parallel	Infinite	20	Stag.	72	8	X	2.86	5000
695-3	2	30	6	7	60	Parallel	Infinite	20	Stag.	72	10	X	2.86	5000
695-4	2	30	6	7	60	Parallel	Infinite	20	Stag.	72	8	K	2.86	5000
695-5	2	30	6	7	60	Parallel	Infinite	20	Stag.	72	8	X	4.79	5000
696-1	2	30	6	7	60	Parallel	Infinite	30	Stag.	72	8	X	2.86	5000
697-1	2	30	6	7	60	Parallel	1500	20	Cont.	72	8	X	2.86	3600
697-2	2	30	6	7	60	Parallel	1500	20	Cont.	72	8	X	2.86	5000
697-3	2	30	6	7	60	Parallel	1500	20	Cont.	72	10	X	2.86	5000
697-4	2	30	6	7	60	Parallel	1500	20	Cont.	72	8	K	2.86	5000
697-5	2	30	6	7	60	Parallel	1500	20	Cont.	72	8	X	4.79	5000
698-1	2	30	6	7	60	Parallel	1500	30	Cont.	72	8	X	2.86	5000
699-1	2	30	6	7	60	Parallel	750	20	Cont.	72	8	X	2.86	3600
699-2	2	30	6	7	60	Parallel	750	20	Cont.	72	8	X	2.86	5000
699-3	2	30	6	7	60	Parallel	750	20	Cont.	72	10	X	2.86	5000
699-4	2	30	6	7	60	Parallel	750	20	Cont.	72	8	K	2.86	5000
699-5	2	30	6	7	60	Parallel	750	20	Cont.	72	8	X	4.79	5000
700-1	2	30	6	7	60	Parallel	750	30	Cont.	72	8	X	2.86	5000
701-1	2	30	6	7	60	Trap.	Infinite	20	Cont.	72	8	X	2.86	3600
701-2	2	30	6	7	60	Trap.	Infinite	20	Cont.	72	8	X	2.86	5000
701-3	2	30	6	7	60	Trap.	Infinite	20	Cont.	72	10	X	2.86	5000
701-4	2	30	6	7	60	Trap.	Infinite	20	Cont.	72	8	K	2.86	5000
701-5	2	30	6	7	60	Trap.	Infinite	20	Cont.	72	8	X	4.79	5000
702-1	2	30	6	7	60	Trap.	Infinite	30	Cont.	72	8	X	2.86	5000
703-1	2	30	6	7	60	Trap.	Infinite	20	Stag.	72	8	X	2.86	3600
703-2	2	30	6	7	60	Trap.	Infinite	20	Stag.	72	8	X	2.86	5000
703-3	2	30	6	7	60	Trap.	Infinite	20	Stag.	72	10	X	2.86	5000
703-4	2	30	6	7	60	Trap.	Infinite	20	Stag.	72	8	K	2.86	5000
703-5	2	30	6	7	60	Trap.	Infinite	20	Stag.	72	8	X	4.79	5000
704-1	2	30	6	7	60	Trap.	Infinite	30	Stag.	72	8	X	2.86	5000
705-1	2	30	6	7	60	Trap.	1500	20	Cont.	72	8	X	2.86	3600
705-2	2	30	6	7	60	Trap.	1500	20	Cont.	72	8	X	2.86	5000
705-3	2	30	6	7	60	Trap.	1500	20	Cont.	72	10	X	2.86	5000
705-4	2	30	6	7	60	Trap.	1500	20	Cont.	72	8	K	2.86	5000
705-5	2	30	6	7	60	Trap.	1500	20	Cont.	72	8	X	4.79	5000
706-1	2	30	6	7	60	Trap.	1500	30	Cont.	72	8	X	2.86	5000
707-1	2	30	6	7	60	Trap.	750	20	Cont.	72	8	X	2.86	3600
707-2	2	30	6	7	60	Trap.	750	20	Cont.	72	8	X	2.86	5000
707-3	2	30	6	7	60	Trap.	750	20	Cont.	72	10	X	2.86	5000
707-4	2	30	6	7	60	Trap.	750	20	Cont.	72	8	K	2.86	5000
707-5	2	30	6	7	60	Trap.	750	20	Cont.	72	8	X	4.79	5000
708-1	2	30	6	7	60	Trap.	750	30	Cont.	72	8	X	2.86	5000
709-1	2	30	8	3	0	Parallel	Infinite	20	Cont.	72	8	X	2.86	3600

Model ID	Geometry									Cross-section		CF detail		Mat'l
	n_{span}	L/d ratio	s_g [ft]	n_{girder}	Support skew [deg];	Layout	R [ft]	s_{cf} [ft]	CF layout	d_w [in]	t_{deck} [in]	CF type	A_{cf} [in^2]	E_c [ksi]
709-2	2	30	8	3	0	Parallel	Infinite	20	Cont.	72	8	X	2.86	5000
709-3	2	30	8	3	0	Parallel	Infinite	20	Cont.	72	10	X	2.86	5000
709-4	2	30	8	3	0	Parallel	Infinite	20	Cont.	72	8	K	2.86	5000
709-5	2	30	8	3	0	Parallel	Infinite	20	Cont.	72	8	X	4.79	5000
710-1	2	30	8	3	0	Parallel	Infinite	30	Cont.	72	8	X	2.86	5000
711-1	2	30	8	3	0	Parallel	1500	20	Cont.	72	8	X	2.86	3600
711-2	2	30	8	3	0	Parallel	1500	20	Cont.	72	8	X	2.86	5000
711-3	2	30	8	3	0	Parallel	1500	20	Cont.	72	10	X	2.86	5000
711-4	2	30	8	3	0	Parallel	1500	20	Cont.	72	8	K	2.86	5000
711-5	2	30	8	3	0	Parallel	1500	20	Cont.	72	8	X	4.79	5000
712-1	2	30	8	3	0	Parallel	1500	30	Cont.	72	8	X	2.86	5000
713-1	2	30	8	3	0	Parallel	750	20	Cont.	72	8	X	2.86	3600
713-2	2	30	8	3	0	Parallel	750	20	Cont.	72	8	X	2.86	5000
713-3	2	30	8	3	0	Parallel	750	20	Cont.	72	10	X	2.86	5000
713-4	2	30	8	3	0	Parallel	750	20	Cont.	72	8	K	2.86	5000
713-5	2	30	8	3	0	Parallel	750	20	Cont.	72	8	X	4.79	5000
714-1	2	30	8	3	0	Parallel	750	30	Cont.	72	8	X	2.86	5000
715-1	2	30	8	3	30	Parallel	Infinite	20	Cont.	72	8	X	2.86	3600
715-2	2	30	8	3	30	Parallel	Infinite	20	Cont.	72	8	X	2.86	5000
715-3	2	30	8	3	30	Parallel	Infinite	20	Cont.	72	10	X	2.86	5000
715-4	2	30	8	3	30	Parallel	Infinite	20	Cont.	72	8	K	2.86	5000
715-5	2	30	8	3	30	Parallel	Infinite	20	Cont.	72	8	X	4.79	5000
716-1	2	30	8	3	30	Parallel	Infinite	30	Cont.	72	8	X	2.86	5000
717-1	2	30	8	3	30	Parallel	1500	20	Cont.	72	8	X	2.86	3600
717-2	2	30	8	3	30	Parallel	1500	20	Cont.	72	8	X	2.86	5000
717-3	2	30	8	3	30	Parallel	1500	20	Cont.	72	10	X	2.86	5000
717-4	2	30	8	3	30	Parallel	1500	20	Cont.	72	8	K	2.86	5000
717-5	2	30	8	3	30	Parallel	1500	20	Cont.	72	8	X	4.79	5000
718-1	2	30	8	3	30	Parallel	1500	30	Cont.	72	8	X	2.86	5000
719-1	2	30	8	3	30	Parallel	750	20	Cont.	72	8	X	2.86	3600
719-2	2	30	8	3	30	Parallel	750	20	Cont.	72	8	X	2.86	5000
719-3	2	30	8	3	30	Parallel	750	20	Cont.	72	10	X	2.86	5000
719-4	2	30	8	3	30	Parallel	750	20	Cont.	72	8	K	2.86	5000
719-5	2	30	8	3	30	Parallel	750	20	Cont.	72	8	X	4.79	5000
720-1	2	30	8	3	30	Parallel	750	30	Cont.	72	8	X	2.86	5000
721-1	2	30	8	3	60	Parallel	Infinite	20	Cont.	72	8	X	2.86	3600
721-2	2	30	8	3	60	Parallel	Infinite	20	Cont.	72	8	X	2.86	5000
721-3	2	30	8	3	60	Parallel	Infinite	20	Cont.	72	10	X	2.86	5000
721-4	2	30	8	3	60	Parallel	Infinite	20	Cont.	72	8	K	2.86	5000
721-5	2	30	8	3	60	Parallel	Infinite	20	Cont.	72	8	X	4.79	5000
722-1	2	30	8	3	60	Parallel	Infinite	30	Cont.	72	8	X	2.86	5000
723-1	2	30	8	3	60	Parallel	Infinite	20	Stag.	72	8	X	2.86	3600
723-2	2	30	8	3	60	Parallel	Infinite	20	Stag.	72	8	X	2.86	5000
723-3	2	30	8	3	60	Parallel	Infinite	20	Stag.	72	10	X	2.86	5000
723-4	2	30	8	3	60	Parallel	Infinite	20	Stag.	72	8	K	2.86	5000
723-5	2	30	8	3	60	Parallel	Infinite	20	Stag.	72	8	X	4.79	5000
724-1	2	30	8	3	60	Parallel	Infinite	30	Stag.	72	8	X	2.86	5000
725-1	2	30	8	3	60	Parallel	1500	20	Cont.	72	8	X	2.86	3600
725-2	2	30	8	3	60	Parallel	1500	20	Cont.	72	8	X	2.86	5000
725-3	2	30	8	3	60	Parallel	1500	20	Cont.	72	10	X	2.86	5000
725-4	2	30	8	3	60	Parallel	1500	20	Cont.	72	8	K	2.86	5000
725-5	2	30	8	3	60	Parallel	1500	20	Cont.	72	8	X	4.79	5000
726-1	2	30	8	3	60	Parallel	1500	30	Cont.	72	8	X	2.86	5000
727-1	2	30	8	3	60	Parallel	750	20	Cont.	72	8	X	2.86	3600
727-2	2	30	8	3	60	Parallel	750	20	Cont.	72	8	X	2.86	5000
727-3	2	30	8	3	60	Parallel	750	20	Cont.	72	10	X	2.86	5000
727-4	2	30	8	3	60	Parallel	750	20	Cont.	72	8	K	2.86	5000
727-5	2	30	8	3	60	Parallel	750	20	Cont.	72	8	X	4.79	5000
728-1	2	30	8	3	60	Parallel	750	30	Cont.	72	8	X	2.86	5000
729-1	2	30	8	3	60	Trap.	Infinite	20	Cont.	72	8	X	2.86	3600
729-2	2	30	8	3	60	Trap.	Infinite	20	Cont.	72	8	X	2.86	5000
729-3	2	30	8	3	60	Trap.	Infinite	20	Cont.	72	10	X	2.86	5000
729-4	2	30	8	3	60	Trap.	Infinite	20	Cont.	72	8	K	2.86	5000
729-5	2	30	8	3	60	Trap.	Infinite	20	Cont.	72	8	X	4.79	5000
730-1	2	30	8	3	60	Trap.	Infinite	30	Cont.	72	8	X	2.86	5000
731-1	2	30	8	3	60	Trap.	Infinite	20	Stag.	72	8	X	2.86	3600
731-2	2	30	8	3	60	Trap.	Infinite	20	Stag.	72	8	X	2.86	5000
731-3	2	30	8	3	60	Trap.	Infinite	20	Stag.	72	10	X	2.86	5000
731-4	2	30	8	3	60	Trap.	Infinite	20	Stag.	72	8	K	2.86	5000
731-5	2	30	8	3	60	Trap.	Infinite	20	Stag.	72	8	X	4.79	5000
732-1	2	30	8	3	60	Trap.	Infinite	30	Stag.	72	8	X	2.86	5000
733-1	2	30	8	3	60	Trap.	1500	20	Cont.	72	8	X	2.86	3600
733-2	2	30	8	3	60	Trap.	1500	20	Cont.	72	8	X	2.86	5000
733-3	2	30	8	3	60	Trap.	1500	20	Cont.	72	10	X	2.86	5000
733-4	2	30	8	3	60	Trap.	1500	20	Cont.	72	8	K	2.86	5000
733-5	2	30	8	3	60	Trap.	1500	20	Cont.	72	8	X	4.79	5000
734-1	2	30	8	3	60	Trap.	1500	30	Cont.	72	8	X	2.86	5000
735-1	2	30	8	3	60	Trap.	750	20	Cont.	72	8	X	2.86	3600
735-2	2	30	8	3	60	Trap.	750	20	Cont.	72	8	X	2.86	5000

Model ID	Geometry									Cross-section		CF detail		Mat'l
	n_{span}	L/d ratio	s_g [ft]	n_{girder}	Support skew [deg]; Layout		R [ft]	s_{cf} [ft]	CF layout	d_w [in]	t_{deck} [in]	CF type	A_{cf} [in^2]	E_c [ksi]
735-3	2	30	8	3	60	Trap.	750	20	Cont.	72	10	X	2.86	5000
735-4	2	30	8	3	60	Trap.	750	20	Cont.	72	8	K	2.86	5000
735-5	2	30	8	3	60	Trap.	750	20	Cont.	72	8	X	4.79	5000
736-1	2	30	8	3	60	Trap.	750	30	Cont.	72	8	X	2.86	5000
737-1	2	30	8	5	0	Parallel	Infinite	20	Cont.	72	8	X	2.86	3600
737-2	2	30	8	5	0	Parallel	Infinite	20	Cont.	72	8	X	2.86	5000
737-3	2	30	8	5	0	Parallel	Infinite	20	Cont.	72	10	X	2.86	5000
737-4	2	30	8	5	0	Parallel	Infinite	20	Cont.	72	8	K	2.86	5000
737-5	2	30	8	5	0	Parallel	Infinite	20	Cont.	72	8	X	4.79	5000
738-1	2	30	8	5	0	Parallel	Infinite	30	Cont.	72	8	X	2.86	5000
739-1	2	30	8	5	0	Parallel	1500	20	Cont.	72	8	X	2.86	3600
739-2	2	30	8	5	0	Parallel	1500	20	Cont.	72	8	X	2.86	5000
739-3	2	30	8	5	0	Parallel	1500	20	Cont.	72	10	X	2.86	5000
739-4	2	30	8	5	0	Parallel	1500	20	Cont.	72	8	K	2.86	5000
739-5	2	30	8	5	0	Parallel	1500	20	Cont.	72	8	X	4.79	5000
740-1	2	30	8	5	0	Parallel	1500	30	Cont.	72	8	X	2.86	5000
741-1	2	30	8	5	0	Parallel	750	20	Cont.	72	8	X	2.86	3600
741-2	2	30	8	5	0	Parallel	750	20	Cont.	72	8	X	2.86	5000
741-3	2	30	8	5	0	Parallel	750	20	Cont.	72	10	X	2.86	5000
741-4	2	30	8	5	0	Parallel	750	20	Cont.	72	8	K	2.86	5000
741-5	2	30	8	5	0	Parallel	750	20	Cont.	72	8	X	4.79	5000
742-1	2	30	8	5	0	Parallel	750	30	Cont.	72	8	X	2.86	5000
743-1	2	30	8	5	30	Parallel	Infinite	20	Cont.	72	8	X	2.86	3600
743-2	2	30	8	5	30	Parallel	Infinite	20	Cont.	72	8	X	2.86	5000
743-3	2	30	8	5	30	Parallel	Infinite	20	Cont.	72	10	X	2.86	5000
743-4	2	30	8	5	30	Parallel	Infinite	20	Cont.	72	8	K	2.86	5000
743-5	2	30	8	5	30	Parallel	Infinite	20	Cont.	72	8	X	4.79	5000
744-1	2	30	8	5	30	Parallel	Infinite	30	Cont.	72	8	X	2.86	5000
745-1	2	30	8	5	30	Parallel	1500	20	Cont.	72	8	X	2.86	3600
745-2	2	30	8	5	30	Parallel	1500	20	Cont.	72	8	X	2.86	5000
745-3	2	30	8	5	30	Parallel	1500	20	Cont.	72	10	X	2.86	5000
745-4	2	30	8	5	30	Parallel	1500	20	Cont.	72	8	K	2.86	5000
745-5	2	30	8	5	30	Parallel	1500	20	Cont.	72	8	X	4.79	5000
746-1	2	30	8	5	30	Parallel	1500	30	Cont.	72	8	X	2.86	5000
747-1	2	30	8	5	30	Parallel	750	20	Cont.	72	8	X	2.86	3600
747-2	2	30	8	5	30	Parallel	750	20	Cont.	72	8	X	2.86	5000
747-3	2	30	8	5	30	Parallel	750	20	Cont.	72	10	X	2.86	5000
747-4	2	30	8	5	30	Parallel	750	20	Cont.	72	8	K	2.86	5000
747-5	2	30	8	5	30	Parallel	750	20	Cont.	72	8	X	4.79	5000
748-1	2	30	8	5	30	Parallel	750	30	Cont.	72	8	X	2.86	5000
749-1	2	30	8	5	60	Parallel	Infinite	20	Cont.	72	8	X	2.86	3600
749-2	2	30	8	5	60	Parallel	Infinite	20	Cont.	72	8	X	2.86	5000
749-3	2	30	8	5	60	Parallel	Infinite	20	Cont.	72	10	X	2.86	5000
749-4	2	30	8	5	60	Parallel	Infinite	20	Cont.	72	8	K	2.86	5000
749-5	2	30	8	5	60	Parallel	Infinite	20	Cont.	72	8	X	4.79	5000
750-1	2	30	8	5	60	Parallel	Infinite	30	Cont.	72	8	X	2.86	5000
751-1	2	30	8	5	60	Parallel	Infinite	20	Stag.	72	8	X	2.86	3600
751-2	2	30	8	5	60	Parallel	Infinite	20	Stag.	72	8	X	2.86	5000
751-3	2	30	8	5	60	Parallel	Infinite	20	Stag.	72	10	X	2.86	5000
751-4	2	30	8	5	60	Parallel	Infinite	20	Stag.	72	8	K	2.86	5000
751-5	2	30	8	5	60	Parallel	Infinite	20	Stag.	72	8	X	4.79	5000
752-1	2	30	8	5	60	Parallel	Infinite	30	Stag.	72	8	X	2.86	5000
753-1	2	30	8	5	60	Parallel	1500	20	Cont.	72	8	X	2.86	3600
753-2	2	30	8	5	60	Parallel	1500	20	Cont.	72	8	X	2.86	5000
753-3	2	30	8	5	60	Parallel	1500	20	Cont.	72	10	X	2.86	5000
753-4	2	30	8	5	60	Parallel	1500	20	Cont.	72	8	K	2.86	5000
753-5	2	30	8	5	60	Parallel	1500	20	Cont.	72	8	X	4.79	5000
754-1	2	30	8	5	60	Parallel	1500	30	Cont.	72	8	X	2.86	5000
755-1	2	30	8	5	60	Parallel	750	20	Cont.	72	8	X	2.86	3600
755-2	2	30	8	5	60	Parallel	750	20	Cont.	72	8	X	2.86	5000
755-3	2	30	8	5	60	Parallel	750	20	Cont.	72	10	X	2.86	5000
755-4	2	30	8	5	60	Parallel	750	20	Cont.	72	8	K	2.86	5000
755-5	2	30	8	5	60	Parallel	750	20	Cont.	72	8	X	4.79	5000
756-1	2	30	8	5	60	Parallel	750	30	Cont.	72	8	X	2.86	5000
757-1	2	30	8	5	60	Trap.	Infinite	20	Cont.	72	8	X	2.86	3600
757-2	2	30	8	5	60	Trap.	Infinite	20	Cont.	72	8	X	2.86	5000
757-3	2	30	8	5	60	Trap.	Infinite	20	Cont.	72	10	X	2.86	5000
757-4	2	30	8	5	60	Trap.	Infinite	20	Cont.	72	8	K	2.86	5000
757-5	2	30	8	5	60	Trap.	Infinite	20	Cont.	72	8	X	4.79	5000
758-1	2	30	8	5	60	Trap.	Infinite	30	Cont.	72	8	X	2.86	5000
759-1	2	30	8	5	60	Trap.	Infinite	20	Stag.	72	8	X	2.86	3600
759-2	2	30	8	5	60	Trap.	Infinite	20	Stag.	72	8	X	2.86	5000
759-3	2	30	8	5	60	Trap.	Infinite	20	Stag.	72	10	X	2.86	5000
759-4	2	30	8	5	60	Trap.	Infinite	20	Stag.	72	8	K	2.86	5000
759-5	2	30	8	5	60	Trap.	Infinite	20	Stag.	72	8	X	4.79	5000
760-1	2	30	8	5	60	Trap.	Infinite	30	Stag.	72	8	X	2.86	5000
761-1	2	30	8	5	60	Trap.	1500	20	Cont.	72	8	X	2.86	3600
761-2	2	30	8	5	60	Trap.	1500	20	Cont.	72	8	X	2.86	5000
761-3	2	30	8	5	60	Trap.	1500	20	Cont.	72	10	X	2.86	5000

Model ID	Geometry									Cross-section		CF detail		Mat'l
	n_{span}	L/d ratio	s_g [ft]	n_{girder}	Support skew [deg]; Layout		R [ft]	s_{cf} [ft]	CF layout	d_w [in]	t_{deck} [in]	CF type	A_{cf} [in^2]	E_c [ksi]
761-4	2	30	8	5	60	Trap.	1500	20	Cont.	72	8	K	2.86	5000
761-5	2	30	8	5	60	Trap.	1500	20	Cont.	72	8	X	4.79	5000
762-1	2	30	8	5	60	Trap.	1500	30	Cont.	72	8	X	2.86	5000
763-1	2	30	8	5	60	Trap.	750	20	Cont.	72	8	X	2.86	3600
763-2	2	30	8	5	60	Trap.	750	20	Cont.	72	8	X	2.86	5000
763-3	2	30	8	5	60	Trap.	750	20	Cont.	72	10	X	2.86	5000
763-4	2	30	8	5	60	Trap.	750	20	Cont.	72	8	K	2.86	5000
763-5	2	30	8	5	60	Trap.	750	20	Cont.	72	8	X	4.79	5000
764-1	2	30	8	5	60	Trap.	750	30	Cont.	72	8	X	2.86	5000
765-1	2	30	8	7	0	Parallel	Infinite	20	Cont.	72	8	X	2.86	3600
765-2	2	30	8	7	0	Parallel	Infinite	20	Cont.	72	8	X	2.86	5000
765-3	2	30	8	7	0	Parallel	Infinite	20	Cont.	72	10	X	2.86	5000
765-4	2	30	8	7	0	Parallel	Infinite	20	Cont.	72	8	K	2.86	5000
765-5	2	30	8	7	0	Parallel	Infinite	20	Cont.	72	8	X	4.79	5000
766-1	2	30	8	7	0	Parallel	Infinite	30	Cont.	72	8	X	2.86	5000
767-1	2	30	8	7	0	Parallel	1500	20	Cont.	72	8	X	2.86	3600
767-2	2	30	8	7	0	Parallel	1500	20	Cont.	72	8	X	2.86	5000
767-3	2	30	8	7	0	Parallel	1500	20	Cont.	72	10	X	2.86	5000
767-4	2	30	8	7	0	Parallel	1500	20	Cont.	72	8	K	2.86	5000
767-5	2	30	8	7	0	Parallel	1500	20	Cont.	72	8	X	4.79	5000
768-1	2	30	8	7	0	Parallel	1500	30	Cont.	72	8	X	2.86	5000
769-1	2	30	8	7	0	Parallel	750	20	Cont.	72	8	X	2.86	3600
769-2	2	30	8	7	0	Parallel	750	20	Cont.	72	8	X	2.86	5000
769-3	2	30	8	7	0	Parallel	750	20	Cont.	72	10	X	2.86	5000
769-4	2	30	8	7	0	Parallel	750	20	Cont.	72	8	K	2.86	5000
769-5	2	30	8	7	0	Parallel	750	20	Cont.	72	8	X	4.79	5000
770-1	2	30	8	7	0	Parallel	750	30	Cont.	72	8	X	2.86	5000
771-1	2	30	8	7	30	Parallel	Infinite	20	Cont.	72	8	X	2.86	3600
771-2	2	30	8	7	30	Parallel	Infinite	20	Cont.	72	8	X	2.86	5000
771-3	2	30	8	7	30	Parallel	Infinite	20	Cont.	72	10	X	2.86	5000
771-4	2	30	8	7	30	Parallel	Infinite	20	Cont.	72	8	K	2.86	5000
771-5	2	30	8	7	30	Parallel	Infinite	20	Cont.	72	8	X	4.79	5000
772-1	2	30	8	7	30	Parallel	Infinite	30	Cont.	72	8	X	2.86	5000
773-1	2	30	8	7	30	Parallel	1500	20	Cont.	72	8	X	2.86	3600
773-2	2	30	8	7	30	Parallel	1500	20	Cont.	72	8	X	2.86	5000
773-3	2	30	8	7	30	Parallel	1500	20	Cont.	72	10	X	2.86	5000
773-4	2	30	8	7	30	Parallel	1500	20	Cont.	72	8	K	2.86	5000
773-5	2	30	8	7	30	Parallel	1500	20	Cont.	72	8	X	4.79	5000
774-1	2	30	8	7	30	Parallel	1500	30	Cont.	72	8	X	2.86	5000
775-1	2	30	8	7	30	Parallel	750	20	Cont.	72	8	X	2.86	3600
775-2	2	30	8	7	30	Parallel	750	20	Cont.	72	8	X	2.86	5000
775-3	2	30	8	7	30	Parallel	750	20	Cont.	72	10	X	2.86	5000
775-4	2	30	8	7	30	Parallel	750	20	Cont.	72	8	K	2.86	5000
775-5	2	30	8	7	30	Parallel	750	20	Cont.	72	8	X	4.79	5000
776-1	2	30	8	7	30	Parallel	750	30	Cont.	72	8	X	2.86	5000
777-1	2	30	8	7	60	Parallel	Infinite	20	Cont.	72	8	X	2.86	3600
777-2	2	30	8	7	60	Parallel	Infinite	20	Cont.	72	8	X	2.86	5000
777-3	2	30	8	7	60	Parallel	Infinite	20	Cont.	72	10	X	2.86	5000
777-4	2	30	8	7	60	Parallel	Infinite	20	Cont.	72	8	K	2.86	5000
777-5	2	30	8	7	60	Parallel	Infinite	20	Cont.	72	8	X	4.79	5000
778-1	2	30	8	7	60	Parallel	Infinite	30	Cont.	72	8	X	2.86	5000
779-1	2	30	8	7	60	Parallel	Infinite	20	Stag.	72	8	X	2.86	3600
779-2	2	30	8	7	60	Parallel	Infinite	20	Stag.	72	8	X	2.86	5000
779-3	2	30	8	7	60	Parallel	Infinite	20	Stag.	72	10	X	2.86	5000
779-4	2	30	8	7	60	Parallel	Infinite	20	Stag.	72	8	K	2.86	5000
779-5	2	30	8	7	60	Parallel	Infinite	20	Stag.	72	8	X	4.79	5000
780-1	2	30	8	7	60	Parallel	Infinite	30	Stag.	72	8	X	2.86	5000
781-1	2	30	8	7	60	Parallel	1500	20	Cont.	72	8	X	2.86	3600
781-2	2	30	8	7	60	Parallel	1500	20	Cont.	72	8	X	2.86	5000
781-3	2	30	8	7	60	Parallel	1500	20	Cont.	72	10	X	2.86	5000
781-4	2	30	8	7	60	Parallel	1500	20	Cont.	72	8	K	2.86	5000
781-5	2	30	8	7	60	Parallel	1500	20	Cont.	72	8	X	4.79	5000
782-1	2	30	8	7	60	Parallel	1500	30	Cont.	72	8	X	2.86	5000
783-1	2	30	8	7	60	Parallel	750	20	Cont.	72	8	X	2.86	3600
783-2	2	30	8	7	60	Parallel	750	20	Cont.	72	8	X	2.86	5000
783-3	2	30	8	7	60	Parallel	750	20	Cont.	72	10	X	2.86	5000
783-4	2	30	8	7	60	Parallel	750	20	Cont.	72	8	K	2.86	5000
783-5	2	30	8	7	60	Parallel	750	20	Cont.	72	8	X	4.79	5000
784-1	2	30	8	7	60	Parallel	750	30	Cont.	72	8	X	2.86	5000
785-1	2	30	8	7	60	Trap.	Infinite	20	Cont.	72	8	X	2.86	3600
785-2	2	30	8	7	60	Trap.	Infinite	20	Cont.	72	8	X	2.86	5000
785-3	2	30	8	7	60	Trap.	Infinite	20	Cont.	72	10	X	2.86	5000
785-4	2	30	8	7	60	Trap.	Infinite	20	Cont.	72	8	K	2.86	5000
785-5	2	30	8	7	60	Trap.	Infinite	20	Cont.	72	8	X	4.79	5000
786-1	2	30	8	7	60	Trap.	Infinite	30	Cont.	72	8	X	2.86	5000
787-1	2	30	8	7	60	Trap.	Infinite	20	Stag.	72	8	X	2.86	3600
787-2	2	30	8	7	60	Trap.	Infinite	20	Stag.	72	8	X	2.86	5000
787-3	2	30	8	7	60	Trap.	Infinite	20	Stag.	72	10	X	2.86	5000
787-4	2	30	8	7	60	Trap.	Infinite	20	Stag.	72	8	K	2.86	5000

Model ID	Geometry									Cross-section		CF detail		Mat'l
	n_{span}	L/d ratio	s_g [ft]	n_{girder}	Support skew [deg]; Layout		R [ft]	s_{cf} [ft]	CF layout	d_w [in]	t_{deck} [in]	CF type	A_{cf} [in^2]	E_c [ksi]
787-5	2	30	8	7	60	Trap.	Infinite	20	Stag.	72	8	X	4.79	5000
788-1	2	30	8	7	60	Trap.	Infinite	30	Stag.	72	8	X	2.86	5000
789-1	2	30	8	7	60	Trap.	1500	20	Cont.	72	8	X	2.86	3600
789-2	2	30	8	7	60	Trap.	1500	20	Cont.	72	8	X	2.86	5000
789-3	2	30	8	7	60	Trap.	1500	20	Cont.	72	10	X	2.86	5000
789-4	2	30	8	7	60	Trap.	1500	20	Cont.	72	8	K	2.86	5000
789-5	2	30	8	7	60	Trap.	1500	20	Cont.	72	8	X	4.79	5000
790-1	2	30	8	7	60	Trap.	1500	30	Cont.	72	8	X	2.86	5000
791-1	2	30	8	7	60	Trap.	750	20	Cont.	72	8	X	2.86	3600
791-2	2	30	8	7	60	Trap.	750	20	Cont.	72	8	X	2.86	5000
791-3	2	30	8	7	60	Trap.	750	20	Cont.	72	10	X	2.86	5000
791-4	2	30	8	7	60	Trap.	750	20	Cont.	72	8	K	2.86	5000
791-5	2	30	8	7	60	Trap.	750	20	Cont.	72	8	X	4.79	5000
792-1	2	30	8	7	60	Trap.	750	30	Cont.	72	8	X	2.86	5000
793-1	2	30	10	3	0	Parallel	Infinite	20	Cont.	72	8	X	2.86	3600
793-2	2	30	10	3	0	Parallel	Infinite	20	Cont.	72	8	X	2.86	5000
793-3	2	30	10	3	0	Parallel	Infinite	20	Cont.	72	10	X	2.86	5000
793-4	2	30	10	3	0	Parallel	Infinite	20	Cont.	72	8	K	2.86	5000
793-5	2	30	10	3	0	Parallel	Infinite	20	Cont.	72	8	X	4.79	5000
794-1	2	30	10	3	0	Parallel	Infinite	30	Cont.	72	8	X	2.86	5000
795-1	2	30	10	3	0	Parallel	1500	20	Cont.	72	8	X	2.86	3600
795-2	2	30	10	3	0	Parallel	1500	20	Cont.	72	8	X	2.86	5000
795-3	2	30	10	3	0	Parallel	1500	20	Cont.	72	10	X	2.86	5000
795-4	2	30	10	3	0	Parallel	1500	20	Cont.	72	8	K	2.86	5000
795-5	2	30	10	3	0	Parallel	1500	20	Cont.	72	8	X	4.79	5000
796-1	2	30	10	3	0	Parallel	1500	30	Cont.	72	8	X	2.86	5000
797-1	2	30	10	3	0	Parallel	750	20	Cont.	72	8	X	2.86	3600
797-2	2	30	10	3	0	Parallel	750	20	Cont.	72	8	X	2.86	5000
797-3	2	30	10	3	0	Parallel	750	20	Cont.	72	10	X	2.86	5000
797-4	2	30	10	3	0	Parallel	750	20	Cont.	72	8	K	2.86	5000
797-5	2	30	10	3	0	Parallel	750	20	Cont.	72	8	X	4.79	5000
798-1	2	30	10	3	0	Parallel	750	30	Cont.	72	8	X	2.86	5000
799-1	2	30	10	3	30	Parallel	Infinite	20	Cont.	72	8	X	2.86	3600
799-2	2	30	10	3	30	Parallel	Infinite	20	Cont.	72	8	X	2.86	5000
799-3	2	30	10	3	30	Parallel	Infinite	20	Cont.	72	10	X	2.86	5000
799-4	2	30	10	3	30	Parallel	Infinite	20	Cont.	72	8	K	2.86	5000
799-5	2	30	10	3	30	Parallel	Infinite	20	Cont.	72	8	X	4.79	5000
800-1	2	30	10	3	30	Parallel	Infinite	30	Cont.	72	8	X	2.86	5000
801-1	2	30	10	3	30	Parallel	1500	20	Cont.	72	8	X	2.86	3600
801-2	2	30	10	3	30	Parallel	1500	20	Cont.	72	8	X	2.86	5000
801-3	2	30	10	3	30	Parallel	1500	20	Cont.	72	10	X	2.86	5000
801-4	2	30	10	3	30	Parallel	1500	20	Cont.	72	8	K	2.86	5000
801-5	2	30	10	3	30	Parallel	1500	20	Cont.	72	8	X	4.79	5000
802-1	2	30	10	3	30	Parallel	1500	30	Cont.	72	8	X	2.86	5000
803-1	2	30	10	3	30	Parallel	750	20	Cont.	72	8	X	2.86	3600
803-2	2	30	10	3	30	Parallel	750	20	Cont.	72	8	X	2.86	5000
803-3	2	30	10	3	30	Parallel	750	20	Cont.	72	10	X	2.86	5000
803-4	2	30	10	3	30	Parallel	750	20	Cont.	72	8	K	2.86	5000
803-5	2	30	10	3	30	Parallel	750	20	Cont.	72	8	X	4.79	5000
804-1	2	30	10	3	30	Parallel	750	30	Cont.	72	8	X	2.86	5000
805-1	2	30	10	3	60	Parallel	Infinite	20	Cont.	72	8	X	2.86	3600
805-2	2	30	10	3	60	Parallel	Infinite	20	Cont.	72	8	X	2.86	5000
805-3	2	30	10	3	60	Parallel	Infinite	20	Cont.	72	10	X	2.86	5000
805-4	2	30	10	3	60	Parallel	Infinite	20	Cont.	72	8	K	2.86	5000
805-5	2	30	10	3	60	Parallel	Infinite	20	Cont.	72	8	X	4.79	5000
806-1	2	30	10	3	60	Parallel	Infinite	30	Cont.	72	8	X	2.86	5000
807-1	2	30	10	3	60	Parallel	Infinite	20	Stag.	72	8	X	2.86	3600
807-2	2	30	10	3	60	Parallel	Infinite	20	Stag.	72	8	X	2.86	5000
807-3	2	30	10	3	60	Parallel	Infinite	20	Stag.	72	10	X	2.86	5000
807-4	2	30	10	3	60	Parallel	Infinite	20	Stag.	72	8	K	2.86	5000
807-5	2	30	10	3	60	Parallel	Infinite	20	Stag.	72	8	X	4.79	5000
808-1	2	30	10	3	60	Parallel	Infinite	30	Stag.	72	8	X	2.86	5000
809-1	2	30	10	3	60	Parallel	1500	20	Cont.	72	8	X	2.86	3600
809-2	2	30	10	3	60	Parallel	1500	20	Cont.	72	8	X	2.86	5000
809-3	2	30	10	3	60	Parallel	1500	20	Cont.	72	10	X	2.86	5000
809-4	2	30	10	3	60	Parallel	1500	20	Cont.	72	8	K	2.86	5000
809-5	2	30	10	3	60	Parallel	1500	20	Cont.	72	8	X	4.79	5000
810-1	2	30	10	3	60	Parallel	1500	30	Cont.	72	8	X	2.86	5000
811-1	2	30	10	3	60	Parallel	750	20	Cont.	72	8	X	2.86	3600
811-2	2	30	10	3	60	Parallel	750	20	Cont.	72	8	X	2.86	5000
811-3	2	30	10	3	60	Parallel	750	20	Cont.	72	10	X	2.86	5000
811-4	2	30	10	3	60	Parallel	750	20	Cont.	72	8	K	2.86	5000
811-5	2	30	10	3	60	Parallel	750	20	Cont.	72	8	X	4.79	5000
812-1	2	30	10	3	60	Parallel	750	30	Cont.	72	8	X	2.86	5000
813-1	2	30	10	3	60	Trap.	Infinite	20	Cont.	72	8	X	2.86	3600
813-2	2	30	10	3	60	Trap.	Infinite	20	Cont.	72	8	X	2.86	5000
813-3	2	30	10	3	60	Trap.	Infinite	20	Cont.	72	10	X	2.86	5000
813-4	2	30	10	3	60	Trap.	Infinite	20	Cont.	72	8	K	2.86	5000
813-5	2	30	10	3	60	Trap.	Infinite	20	Cont.	72	8	X	4.79	5000

Model ID	Geometry									Cross-section		CF detail		Mat'l
	n_{span}	L/d ratio	s_g [ft]	n_{girder}	Support skew [deg]; Layout		R [ft]	s_{cf} [ft]	CF layout	d_w [in]	t_{deck} [in]	CF type	A_{cf} [in^2]	E_c [ksi]
814-1	2	30	10	3	60	Trap.	Infinite	30	Cont.	72	8	X	2.86	5000
815-1	2	30	10	3	60	Trap.	Infinite	20	Stag.	72	8	X	2.86	3600
815-2	2	30	10	3	60	Trap.	Infinite	20	Stag.	72	8	X	2.86	5000
815-3	2	30	10	3	60	Trap.	Infinite	20	Stag.	72	10	X	2.86	5000
815-4	2	30	10	3	60	Trap.	Infinite	20	Stag.	72	8	K	2.86	5000
815-5	2	30	10	3	60	Trap.	Infinite	20	Stag.	72	8	X	4.79	5000
816-1	2	30	10	3	60	Trap.	Infinite	30	Stag.	72	8	X	2.86	5000
817-1	2	30	10	3	60	Trap.	1500	20	Cont.	72	8	X	2.86	3600
817-2	2	30	10	3	60	Trap.	1500	20	Cont.	72	8	X	2.86	5000
817-3	2	30	10	3	60	Trap.	1500	20	Cont.	72	10	X	2.86	5000
817-4	2	30	10	3	60	Trap.	1500	20	Cont.	72	8	K	2.86	5000
817-5	2	30	10	3	60	Trap.	1500	20	Cont.	72	8	X	4.79	5000
818-1	2	30	10	3	60	Trap.	1500	30	Cont.	72	8	X	2.86	5000
819-1	2	30	10	3	60	Trap.	750	20	Cont.	72	8	X	2.86	3600
819-2	2	30	10	3	60	Trap.	750	20	Cont.	72	8	X	2.86	5000
819-3	2	30	10	3	60	Trap.	750	20	Cont.	72	10	X	2.86	5000
819-4	2	30	10	3	60	Trap.	750	20	Cont.	72	8	K	2.86	5000
819-5	2	30	10	3	60	Trap.	750	20	Cont.	72	8	X	4.79	5000
820-1	2	30	10	3	60	Trap.	750	30	Cont.	72	8	X	2.86	5000
821-1	2	30	10	5	0	Parallel	Infinite	20	Cont.	72	8	X	2.86	3600
821-2	2	30	10	5	0	Parallel	Infinite	20	Cont.	72	8	X	2.86	5000
821-3	2	30	10	5	0	Parallel	Infinite	20	Cont.	72	10	X	2.86	5000
821-4	2	30	10	5	0	Parallel	Infinite	20	Cont.	72	8	K	2.86	5000
821-5	2	30	10	5	0	Parallel	Infinite	20	Cont.	72	8	X	4.79	5000
822-1	2	30	10	5	0	Parallel	Infinite	30	Cont.	72	8	X	2.86	5000
823-1	2	30	10	5	0	Parallel	1500	20	Cont.	72	8	X	2.86	3600
823-2	2	30	10	5	0	Parallel	1500	20	Cont.	72	8	X	2.86	5000
823-3	2	30	10	5	0	Parallel	1500	20	Cont.	72	10	X	2.86	5000
823-4	2	30	10	5	0	Parallel	1500	20	Cont.	72	8	K	2.86	5000
823-5	2	30	10	5	0	Parallel	1500	20	Cont.	72	8	X	4.79	5000
824-1	2	30	10	5	0	Parallel	1500	30	Cont.	72	8	X	2.86	5000
825-1	2	30	10	5	0	Parallel	750	20	Cont.	72	8	X	2.86	3600
825-2	2	30	10	5	0	Parallel	750	20	Cont.	72	8	X	2.86	5000
825-3	2	30	10	5	0	Parallel	750	20	Cont.	72	10	X	2.86	5000
825-4	2	30	10	5	0	Parallel	750	20	Cont.	72	8	K	2.86	5000
825-5	2	30	10	5	0	Parallel	750	20	Cont.	72	8	X	4.79	5000
826-1	2	30	10	5	0	Parallel	750	30	Cont.	72	8	X	2.86	5000
827-1	2	30	10	5	30	Parallel	Infinite	20	Cont.	72	8	X	2.86	3600
827-2	2	30	10	5	30	Parallel	Infinite	20	Cont.	72	8	X	2.86	5000
827-3	2	30	10	5	30	Parallel	Infinite	20	Cont.	72	10	X	2.86	5000
827-4	2	30	10	5	30	Parallel	Infinite	20	Cont.	72	8	K	2.86	5000
827-5	2	30	10	5	30	Parallel	Infinite	20	Cont.	72	8	X	4.79	5000
828-1	2	30	10	5	30	Parallel	Infinite	30	Cont.	72	8	X	2.86	5000
829-1	2	30	10	5	30	Parallel	1500	20	Cont.	72	8	X	2.86	3600
829-2	2	30	10	5	30	Parallel	1500	20	Cont.	72	8	X	2.86	5000
829-3	2	30	10	5	30	Parallel	1500	20	Cont.	72	10	X	2.86	5000
829-4	2	30	10	5	30	Parallel	1500	20	Cont.	72	8	K	2.86	5000
829-5	2	30	10	5	30	Parallel	1500	20	Cont.	72	8	X	4.79	5000
830-1	2	30	10	5	30	Parallel	1500	30	Cont.	72	8	X	2.86	5000
831-1	2	30	10	5	30	Parallel	750	20	Cont.	72	8	X	2.86	3600
831-2	2	30	10	5	30	Parallel	750	20	Cont.	72	8	X	2.86	5000
831-3	2	30	10	5	30	Parallel	750	20	Cont.	72	10	X	2.86	5000
831-4	2	30	10	5	30	Parallel	750	20	Cont.	72	8	K	2.86	5000
831-5	2	30	10	5	30	Parallel	750	20	Cont.	72	8	X	4.79	5000
832-1	2	30	10	5	30	Parallel	750	30	Cont.	72	8	X	2.86	5000
833-1	2	30	10	5	60	Parallel	Infinite	20	Cont.	72	8	X	2.86	3600
833-2	2	30	10	5	60	Parallel	Infinite	20	Cont.	72	8	X	2.86	5000
833-3	2	30	10	5	60	Parallel	Infinite	20	Cont.	72	10	X	2.86	5000
833-4	2	30	10	5	60	Parallel	Infinite	20	Cont.	72	8	K	2.86	5000
833-5	2	30	10	5	60	Parallel	Infinite	20	Cont.	72	8	X	4.79	5000
834-1	2	30	10	5	60	Parallel	Infinite	30	Cont.	72	8	X	2.86	5000
835-1	2	30	10	5	60	Parallel	Infinite	20	Stag.	72	8	X	2.86	3600
835-2	2	30	10	5	60	Parallel	Infinite	20	Stag.	72	8	X	2.86	5000
835-3	2	30	10	5	60	Parallel	Infinite	20	Stag.	72	10	X	2.86	5000
835-4	2	30	10	5	60	Parallel	Infinite	20	Stag.	72	8	K	2.86	5000
835-5	2	30	10	5	60	Parallel	Infinite	20	Stag.	72	8	X	4.79	5000
836-1	2	30	10	5	60	Parallel	Infinite	30	Stag.	72	8	X	2.86	5000
837-1	2	30	10	5	60	Parallel	1500	20	Cont.	72	8	X	2.86	3600
837-2	2	30	10	5	60	Parallel	1500	20	Cont.	72	8	X	2.86	5000
837-3	2	30	10	5	60	Parallel	1500	20	Cont.	72	10	X	2.86	5000
837-4	2	30	10	5	60	Parallel	1500	20	Cont.	72	8	K	2.86	5000
837-5	2	30	10	5	60	Parallel	1500	20	Cont.	72	8	X	4.79	5000
838-1	2	30	10	5	60	Parallel	1500	30	Cont.	72	8	X	2.86	5000
839-1	2	30	10	5	60	Parallel	750	20	Cont.	72	8	X	2.86	3600
839-2	2	30	10	5	60	Parallel	750	20	Cont.	72	8	X	2.86	5000
839-3	2	30	10	5	60	Parallel	750	20	Cont.	72	10	X	2.86	5000
839-4	2	30	10	5	60	Parallel	750	20	Cont.	72	8	K	2.86	5000
839-5	2	30	10	5	60	Parallel	750	20	Cont.	72	8	X	4.79	5000
840-1	2	30	10	5	60	Parallel	750	30	Cont.	72	8	X	2.86	5000

Model ID	Geometry									Cross-section		CF detail		Mat'l
	n_{span}	L/d ratio	s_g [ft]	n_{girder}	Support skew [deg]; Layout		R [ft]	s_{cf} [ft]	CF layout	d_w [in]	t_{deck} [in]	CF type	A_{cf} [in^2]	E_c [ksi]
841-1	2	30	10	5	60	Trap.	Infinite	20	Cont.	72	8	X	2.86	3600
841-2	2	30	10	5	60	Trap.	Infinite	20	Cont.	72	8	X	2.86	5000
841-3	2	30	10	5	60	Trap.	Infinite	20	Cont.	72	10	X	2.86	5000
841-4	2	30	10	5	60	Trap.	Infinite	20	Cont.	72	8	K	2.86	5000
841-5	2	30	10	5	60	Trap.	Infinite	20	Cont.	72	8	X	4.79	5000
842-1	2	30	10	5	60	Trap.	Infinite	30	Cont.	72	8	X	2.86	5000
843-1	2	30	10	5	60	Trap.	Infinite	20	Stag.	72	8	X	2.86	3600
843-2	2	30	10	5	60	Trap.	Infinite	20	Stag.	72	8	X	2.86	5000
843-3	2	30	10	5	60	Trap.	Infinite	20	Stag.	72	10	X	2.86	5000
843-4	2	30	10	5	60	Trap.	Infinite	20	Stag.	72	8	K	2.86	5000
843-5	2	30	10	5	60	Trap.	Infinite	20	Stag.	72	8	X	4.79	5000
844-1	2	30	10	5	60	Trap.	Infinite	30	Stag.	72	8	X	2.86	5000
845-1	2	30	10	5	60	Trap.	1500	20	Cont.	72	8	X	2.86	3600
845-2	2	30	10	5	60	Trap.	1500	20	Cont.	72	8	X	2.86	5000
845-3	2	30	10	5	60	Trap.	1500	20	Cont.	72	10	X	2.86	5000
845-4	2	30	10	5	60	Trap.	1500	20	Cont.	72	8	K	2.86	5000
845-5	2	30	10	5	60	Trap.	1500	20	Cont.	72	8	X	4.79	5000
846-1	2	30	10	5	60	Trap.	1500	30	Cont.	72	8	X	2.86	5000
847-1	2	30	10	5	60	Trap.	750	20	Cont.	72	8	X	2.86	3600
847-2	2	30	10	5	60	Trap.	750	20	Cont.	72	8	X	2.86	5000
847-3	2	30	10	5	60	Trap.	750	20	Cont.	72	10	X	2.86	5000
847-4	2	30	10	5	60	Trap.	750	20	Cont.	72	8	K	2.86	5000
847-5	2	30	10	5	60	Trap.	750	20	Cont.	72	8	X	4.79	5000
848-1	2	30	10	5	60	Trap.	750	30	Cont.	72	8	X	2.86	5000
849-1	2	30	10	7	0	Parallel	Infinite	20	Cont.	72	8	X	2.86	3600
849-2	2	30	10	7	0	Parallel	Infinite	20	Cont.	72	8	X	2.86	5000
849-3	2	30	10	7	0	Parallel	Infinite	20	Cont.	72	10	X	2.86	5000
849-4	2	30	10	7	0	Parallel	Infinite	20	Cont.	72	8	K	2.86	5000
849-5	2	30	10	7	0	Parallel	Infinite	20	Cont.	72	8	X	4.79	5000
850-1	2	30	10	7	0	Parallel	Infinite	30	Cont.	72	8	X	2.86	5000
851-1	2	30	10	7	0	Parallel	1500	20	Cont.	72	8	X	2.86	3600
851-2	2	30	10	7	0	Parallel	1500	20	Cont.	72	8	X	2.86	5000
851-3	2	30	10	7	0	Parallel	1500	20	Cont.	72	10	X	2.86	5000
851-4	2	30	10	7	0	Parallel	1500	20	Cont.	72	8	K	2.86	5000
851-5	2	30	10	7	0	Parallel	1500	20	Cont.	72	8	X	4.79	5000
852-1	2	30	10	7	0	Parallel	1500	30	Cont.	72	8	X	2.86	5000
853-1	2	30	10	7	0	Parallel	750	20	Cont.	72	8	X	2.86	3600
853-2	2	30	10	7	0	Parallel	750	20	Cont.	72	8	X	2.86	5000
853-3	2	30	10	7	0	Parallel	750	20	Cont.	72	10	X	2.86	5000
853-4	2	30	10	7	0	Parallel	750	20	Cont.	72	8	K	2.86	5000
853-5	2	30	10	7	0	Parallel	750	20	Cont.	72	8	X	4.79	5000
854-1	2	30	10	7	0	Parallel	750	30	Cont.	72	8	X	2.86	5000
855-1	2	30	10	7	30	Parallel	Infinite	20	Cont.	72	8	X	2.86	3600
855-2	2	30	10	7	30	Parallel	Infinite	20	Cont.	72	8	X	2.86	5000
855-3	2	30	10	7	30	Parallel	Infinite	20	Cont.	72	10	X	2.86	5000
855-4	2	30	10	7	30	Parallel	Infinite	20	Cont.	72	8	K	2.86	5000
855-5	2	30	10	7	30	Parallel	Infinite	20	Cont.	72	8	X	4.79	5000
856-1	2	30	10	7	30	Parallel	Infinite	30	Cont.	72	8	X	2.86	5000
857-1	2	30	10	7	30	Parallel	1500	20	Cont.	72	8	X	2.86	3600
857-2	2	30	10	7	30	Parallel	1500	20	Cont.	72	8	X	2.86	5000
857-3	2	30	10	7	30	Parallel	1500	20	Cont.	72	10	X	2.86	5000
857-4	2	30	10	7	30	Parallel	1500	20	Cont.	72	8	K	2.86	5000
857-5	2	30	10	7	30	Parallel	1500	20	Cont.	72	8	X	4.79	5000
858-1	2	30	10	7	30	Parallel	1500	30	Cont.	72	8	X	2.86	5000
859-1	2	30	10	7	30	Parallel	750	20	Cont.	72	8	X	2.86	3600
859-2	2	30	10	7	30	Parallel	750	20	Cont.	72	8	X	2.86	5000
859-3	2	30	10	7	30	Parallel	750	20	Cont.	72	10	X	2.86	5000
859-4	2	30	10	7	30	Parallel	750	20	Cont.	72	8	K	2.86	5000
859-5	2	30	10	7	30	Parallel	750	20	Cont.	72	8	X	4.79	5000
860-1	2	30	10	7	30	Parallel	750	30	Cont.	72	8	X	2.86	5000
861-1	2	30	10	7	60	Parallel	Infinite	20	Cont.	72	8	X	2.86	3600
861-2	2	30	10	7	60	Parallel	Infinite	20	Cont.	72	8	X	2.86	5000
861-3	2	30	10	7	60	Parallel	Infinite	20	Cont.	72	10	X	2.86	5000
861-4	2	30	10	7	60	Parallel	Infinite	20	Cont.	72	8	K	2.86	5000
861-5	2	30	10	7	60	Parallel	Infinite	20	Cont.	72	8	X	4.79	5000
862-1	2	30	10	7	60	Parallel	Infinite	30	Cont.	72	8	X	2.86	5000
863-1	2	30	10	7	60	Parallel	Infinite	20	Stag.	72	8	X	2.86	3600
863-2	2	30	10	7	60	Parallel	Infinite	20	Stag.	72	8	X	2.86	5000
863-3	2	30	10	7	60	Parallel	Infinite	20	Stag.	72	10	X	2.86	5000
863-4	2	30	10	7	60	Parallel	Infinite	20	Stag.	72	8	K	2.86	5000
863-5	2	30	10	7	60	Parallel	Infinite	20	Stag.	72	8	X	4.79	5000
864-1	2	30	10	7	60	Parallel	Infinite	30	Stag.	72	8	X	2.86	5000
865-1	2	30	10	7	60	Parallel	1500	20	Cont.	72	8	X	2.86	3600
865-2	2	30	10	7	60	Parallel	1500	20	Cont.	72	8	X	2.86	5000
865-3	2	30	10	7	60	Parallel	1500	20	Cont.	72	10	X	2.86	5000
865-4	2	30	10	7	60	Parallel	1500	20	Cont.	72	8	K	2.86	5000
865-5	2	30	10	7	60	Parallel	1500	20	Cont.	72	8	X	4.79	5000
866-1	2	30	10	7	60	Parallel	1500	30	Cont.	72	8	X	2.86	5000
867-1	2	30	10	7	60	Parallel	750	20	Cont.	72	8	X	2.86	3600

Model ID	Geometry									Cross-section		CF detail		Mat'l
	n_{span}	L/d ratio	s_g [ft]	n_{girder}	Support skew [deg]; Layout		R [ft]	s_{cf} [ft]	CF layout	d_w [in]	t_{deck} [in]	CF type	A_{cf} [in^2]	E_c [ksi]
867-2	2	30	10	7	60	Parallel	750	20	Cont.	72	8	X	2.86	5000
867-3	2	30	10	7	60	Parallel	750	20	Cont.	72	10	X	2.86	5000
867-4	2	30	10	7	60	Parallel	750	20	Cont.	72	8	K	2.86	5000
867-5	2	30	10	7	60	Parallel	750	20	Cont.	72	8	X	4.79	5000
868-1	2	30	10	7	60	Parallel	750	30	Cont.	72	8	X	2.86	5000
869-1	2	30	10	7	60	Trap.	Infinite	20	Cont.	72	8	X	2.86	3600
869-2	2	30	10	7	60	Trap.	Infinite	20	Cont.	72	8	X	2.86	5000
869-3	2	30	10	7	60	Trap.	Infinite	20	Cont.	72	10	X	2.86	5000
869-4	2	30	10	7	60	Trap.	Infinite	20	Cont.	72	8	K	2.86	5000
869-5	2	30	10	7	60	Trap.	Infinite	20	Cont.	72	8	X	4.79	5000
870-1	2	30	10	7	60	Trap.	Infinite	30	Cont.	72	8	X	2.86	5000
871-1	2	30	10	7	60	Trap.	Infinite	20	Stag.	72	8	X	2.86	3600
871-2	2	30	10	7	60	Trap.	Infinite	20	Stag.	72	8	X	2.86	5000
871-3	2	30	10	7	60	Trap.	Infinite	20	Stag.	72	10	X	2.86	5000
871-4	2	30	10	7	60	Trap.	Infinite	20	Stag.	72	8	K	2.86	5000
871-5	2	30	10	7	60	Trap.	Infinite	20	Stag.	72	8	X	4.79	5000
872-1	2	30	10	7	60	Trap.	Infinite	30	Stag.	72	8	X	2.86	5000
873-1	2	30	10	7	60	Trap.	1500	20	Cont.	72	8	X	2.86	3600
873-2	2	30	10	7	60	Trap.	1500	20	Cont.	72	8	X	2.86	5000
873-3	2	30	10	7	60	Trap.	1500	20	Cont.	72	10	X	2.86	5000
873-4	2	30	10	7	60	Trap.	1500	20	Cont.	72	8	K	2.86	5000
873-5	2	30	10	7	60	Trap.	1500	20	Cont.	72	8	X	4.79	5000
874-1	2	30	10	7	60	Trap.	1500	30	Cont.	72	8	X	2.86	5000
875-1	2	30	10	7	60	Trap.	750	20	Cont.	72	8	X	2.86	3600
875-2	2	30	10	7	60	Trap.	750	20	Cont.	72	8	X	2.86	5000
875-3	2	30	10	7	60	Trap.	750	20	Cont.	72	10	X	2.86	5000
875-4	2	30	10	7	60	Trap.	750	20	Cont.	72	8	K	2.86	5000
875-5	2	30	10	7	60	Trap.	750	20	Cont.	72	8	X	4.79	5000
876-1	2	30	10	7	60	Trap.	750	30	Cont.	72	8	X	2.86	5000
877-1	2	30	6	3	0	Parallel	Infinite	20	Cont.	96	8	X	2.86	3600
877-2	2	30	6	3	0	Parallel	Infinite	20	Cont.	96	8	X	2.86	5000
877-3	2	30	6	3	0	Parallel	Infinite	20	Cont.	96	10	X	2.86	5000
877-4	2	30	6	3	0	Parallel	Infinite	20	Cont.	96	8	K	2.86	5000
877-5	2	30	6	3	0	Parallel	Infinite	20	Cont.	96	8	X	4.79	5000
878-1	2	30	6	3	0	Parallel	Infinite	30	Cont.	96	8	X	2.86	5000
879-1	2	30	6	3	0	Parallel	1500	20	Cont.	96	8	X	2.86	3600
879-2	2	30	6	3	0	Parallel	1500	20	Cont.	96	8	X	2.86	5000
879-3	2	30	6	3	0	Parallel	1500	20	Cont.	96	10	X	2.86	5000
879-4	2	30	6	3	0	Parallel	1500	20	Cont.	96	8	K	2.86	5000
879-5	2	30	6	3	0	Parallel	1500	20	Cont.	96	8	X	4.79	5000
880-1	2	30	6	3	0	Parallel	1500	30	Cont.	96	8	X	2.86	5000
881-1	2	30	6	3	0	Parallel	750	20	Cont.	96	8	X	2.86	3600
881-2	2	30	6	3	0	Parallel	750	20	Cont.	96	8	X	2.86	5000
881-3	2	30	6	3	0	Parallel	750	20	Cont.	96	10	X	2.86	5000
881-4	2	30	6	3	0	Parallel	750	20	Cont.	96	8	K	2.86	5000
881-5	2	30	6	3	0	Parallel	750	20	Cont.	96	8	X	4.79	5000
882-1	2	30	6	3	0	Parallel	750	30	Cont.	96	8	X	2.86	5000
883-1	2	30	6	3	30	Parallel	Infinite	20	Cont.	96	8	X	2.86	3600
883-2	2	30	6	3	30	Parallel	Infinite	20	Cont.	96	8	X	2.86	5000
883-3	2	30	6	3	30	Parallel	Infinite	20	Cont.	96	10	X	2.86	5000
883-4	2	30	6	3	30	Parallel	Infinite	20	Cont.	96	8	K	2.86	5000
883-5	2	30	6	3	30	Parallel	Infinite	20	Cont.	96	8	X	4.79	5000
884-1	2	30	6	3	30	Parallel	Infinite	30	Cont.	96	8	X	2.86	5000
885-1	2	30	6	3	30	Parallel	1500	20	Cont.	96	8	X	2.86	3600
885-2	2	30	6	3	30	Parallel	1500	20	Cont.	96	8	X	2.86	5000
885-3	2	30	6	3	30	Parallel	1500	20	Cont.	96	10	X	2.86	5000
885-4	2	30	6	3	30	Parallel	1500	20	Cont.	96	8	K	2.86	5000
885-5	2	30	6	3	30	Parallel	1500	20	Cont.	96	8	X	4.79	5000
886-1	2	30	6	3	30	Parallel	1500	30	Cont.	96	8	X	2.86	5000
887-1	2	30	6	3	30	Parallel	750	20	Cont.	96	8	X	2.86	3600
887-2	2	30	6	3	30	Parallel	750	20	Cont.	96	8	X	2.86	5000
887-3	2	30	6	3	30	Parallel	750	20	Cont.	96	10	X	2.86	5000
887-4	2	30	6	3	30	Parallel	750	20	Cont.	96	8	K	2.86	5000
887-5	2	30	6	3	30	Parallel	750	20	Cont.	96	8	X	4.79	5000
888-1	2	30	6	3	30	Parallel	750	30	Cont.	96	8	X	2.86	5000
889-1	2	30	6	3	60	Parallel	Infinite	20	Cont.	96	8	X	2.86	3600
889-2	2	30	6	3	60	Parallel	Infinite	20	Cont.	96	8	X	2.86	5000
889-3	2	30	6	3	60	Parallel	Infinite	20	Cont.	96	10	X	2.86	5000
889-4	2	30	6	3	60	Parallel	Infinite	20	Cont.	96	8	K	2.86	5000
889-5	2	30	6	3	60	Parallel	Infinite	20	Cont.	96	8	X	4.79	5000
890-1	2	30	6	3	60	Parallel	Infinite	30	Cont.	96	8	X	2.86	5000
891-1	2	30	6	3	60	Parallel	Infinite	20	Stag.	96	8	X	2.86	3600
891-2	2	30	6	3	60	Parallel	Infinite	20	Stag.	96	8	X	2.86	5000
891-3	2	30	6	3	60	Parallel	Infinite	20	Stag.	96	10	X	2.86	5000
891-4	2	30	6	3	60	Parallel	Infinite	20	Stag.	96	8	K	2.86	5000
891-5	2	30	6	3	60	Parallel	Infinite	20	Stag.	96	8	X	4.79	5000
892-1	2	30	6	3	60	Parallel	Infinite	30	Stag.	96	8	X	2.86	5000
893-1	2	30	6	3	60	Parallel	1500	20	Cont.	96	8	X	2.86	3600
893-2	2	30	6	3	60	Parallel	1500	20	Cont.	96	8	X	2.86	5000

Model ID	Geometry									Cross-section		CF detail		Mat'l
	n_{span}	L/d ratio	s_g [ft]	n_{girder}	Support skew [deg]; Layout		R [ft]	s_{cf} [ft]	CF layout	d_w [in]	t_{deck} [in]	CF type	A_{cf} [in^2]	E_c [ksi]
893-3	2	30	6	3	60	Parallel	1500	20	Cont.	96	10	X	2.86	5000
893-4	2	30	6	3	60	Parallel	1500	20	Cont.	96	8	K	2.86	5000
893-5	2	30	6	3	60	Parallel	1500	20	Cont.	96	8	X	4.79	5000
894-1	2	30	6	3	60	Parallel	1500	30	Cont.	96	8	X	2.86	5000
895-1	2	30	6	3	60	Parallel	750	20	Cont.	96	8	X	2.86	3600
895-2	2	30	6	3	60	Parallel	750	20	Cont.	96	8	X	2.86	5000
895-3	2	30	6	3	60	Parallel	750	20	Cont.	96	10	X	2.86	5000
895-4	2	30	6	3	60	Parallel	750	20	Cont.	96	8	K	2.86	5000
895-5	2	30	6	3	60	Parallel	750	20	Cont.	96	8	X	4.79	5000
896-1	2	30	6	3	60	Parallel	750	30	Cont.	96	8	X	2.86	5000
897-1	2	30	6	3	60	Trap.	Infinite	20	Cont.	96	8	X	2.86	3600
897-2	2	30	6	3	60	Trap.	Infinite	20	Cont.	96	8	X	2.86	5000
897-3	2	30	6	3	60	Trap.	Infinite	20	Cont.	96	10	X	2.86	5000
897-4	2	30	6	3	60	Trap.	Infinite	20	Cont.	96	8	K	2.86	5000
897-5	2	30	6	3	60	Trap.	Infinite	20	Cont.	96	8	X	4.79	5000
898-1	2	30	6	3	60	Trap.	Infinite	30	Cont.	96	8	X	2.86	5000
899-1	2	30	6	3	60	Trap.	Infinite	20	Stag.	96	8	X	2.86	3600
899-2	2	30	6	3	60	Trap.	Infinite	20	Stag.	96	8	X	2.86	5000
899-3	2	30	6	3	60	Trap.	Infinite	20	Stag.	96	10	X	2.86	5000
899-4	2	30	6	3	60	Trap.	Infinite	20	Stag.	96	8	K	2.86	5000
899-5	2	30	6	3	60	Trap.	Infinite	20	Stag.	96	8	X	4.79	5000
900-1	2	30	6	3	60	Trap.	Infinite	30	Stag.	96	8	X	2.86	5000
901-1	2	30	6	3	60	Trap.	1500	20	Cont.	96	8	X	2.86	3600
901-2	2	30	6	3	60	Trap.	1500	20	Cont.	96	8	X	2.86	5000
901-3	2	30	6	3	60	Trap.	1500	20	Cont.	96	10	X	2.86	5000
901-4	2	30	6	3	60	Trap.	1500	20	Cont.	96	8	K	2.86	5000
901-5	2	30	6	3	60	Trap.	1500	20	Cont.	96	8	X	4.79	5000
902-1	2	30	6	3	60	Trap.	1500	30	Cont.	96	8	X	2.86	5000
903-1	2	30	6	3	60	Trap.	750	20	Cont.	96	8	X	2.86	3600
903-2	2	30	6	3	60	Trap.	750	20	Cont.	96	8	X	2.86	5000
903-3	2	30	6	3	60	Trap.	750	20	Cont.	96	10	X	2.86	5000
903-4	2	30	6	3	60	Trap.	750	20	Cont.	96	8	K	2.86	5000
903-5	2	30	6	3	60	Trap.	750	20	Cont.	96	8	X	4.79	5000
904-1	2	30	6	3	60	Trap.	750	30	Cont.	96	8	X	2.86	5000
905-1	2	30	6	5	0	Parallel	Infinite	20	Cont.	96	8	X	2.86	3600
905-2	2	30	6	5	0	Parallel	Infinite	20	Cont.	96	8	X	2.86	5000
905-3	2	30	6	5	0	Parallel	Infinite	20	Cont.	96	10	X	2.86	5000
905-4	2	30	6	5	0	Parallel	Infinite	20	Cont.	96	8	K	2.86	5000
905-5	2	30	6	5	0	Parallel	Infinite	20	Cont.	96	8	X	4.79	5000
906-1	2	30	6	5	0	Parallel	Infinite	30	Cont.	96	8	X	2.86	5000
907-1	2	30	6	5	0	Parallel	1500	20	Cont.	96	8	X	2.86	3600
907-2	2	30	6	5	0	Parallel	1500	20	Cont.	96	8	X	2.86	5000
907-3	2	30	6	5	0	Parallel	1500	20	Cont.	96	10	X	2.86	5000
907-4	2	30	6	5	0	Parallel	1500	20	Cont.	96	8	K	2.86	5000
907-5	2	30	6	5	0	Parallel	1500	20	Cont.	96	8	X	4.79	5000
908-1	2	30	6	5	0	Parallel	1500	30	Cont.	96	8	X	2.86	5000
909-1	2	30	6	5	0	Parallel	750	20	Cont.	96	8	X	2.86	3600
909-2	2	30	6	5	0	Parallel	750	20	Cont.	96	8	X	2.86	5000
909-3	2	30	6	5	0	Parallel	750	20	Cont.	96	10	X	2.86	5000
909-4	2	30	6	5	0	Parallel	750	20	Cont.	96	8	K	2.86	5000
909-5	2	30	6	5	0	Parallel	750	20	Cont.	96	8	X	4.79	5000
910-1	2	30	6	5	0	Parallel	750	30	Cont.	96	8	X	2.86	5000
911-1	2	30	6	5	30	Parallel	Infinite	20	Cont.	96	8	X	2.86	3600
911-2	2	30	6	5	30	Parallel	Infinite	20	Cont.	96	8	X	2.86	5000
911-3	2	30	6	5	30	Parallel	Infinite	20	Cont.	96	10	X	2.86	5000
911-4	2	30	6	5	30	Parallel	Infinite	20	Cont.	96	8	K	2.86	5000
911-5	2	30	6	5	30	Parallel	Infinite	20	Cont.	96	8	X	4.79	5000
912-1	2	30	6	5	30	Parallel	Infinite	30	Cont.	96	8	X	2.86	5000
913-1	2	30	6	5	30	Parallel	1500	20	Cont.	96	8	X	2.86	3600
913-2	2	30	6	5	30	Parallel	1500	20	Cont.	96	8	X	2.86	5000
913-3	2	30	6	5	30	Parallel	1500	20	Cont.	96	10	X	2.86	5000
913-4	2	30	6	5	30	Parallel	1500	20	Cont.	96	8	K	2.86	5000
913-5	2	30	6	5	30	Parallel	1500	20	Cont.	96	8	X	4.79	5000
914-1	2	30	6	5	30	Parallel	1500	30	Cont.	96	8	X	2.86	5000
915-1	2	30	6	5	30	Parallel	750	20	Cont.	96	8	X	2.86	3600
915-2	2	30	6	5	30	Parallel	750	20	Cont.	96	8	X	2.86	5000
915-3	2	30	6	5	30	Parallel	750	20	Cont.	96	10	X	2.86	5000
915-4	2	30	6	5	30	Parallel	750	20	Cont.	96	8	K	2.86	5000
915-5	2	30	6	5	30	Parallel	750	20	Cont.	96	8	X	4.79	5000
916-1	2	30	6	5	30	Parallel	750	30	Cont.	96	8	X	2.86	5000
917-1	2	30	6	5	60	Parallel	Infinite	20	Cont.	96	8	X	2.86	3600
917-2	2	30	6	5	60	Parallel	Infinite	20	Cont.	96	8	X	2.86	5000
917-3	2	30	6	5	60	Parallel	Infinite	20	Cont.	96	10	X	2.86	5000
917-4	2	30	6	5	60	Parallel	Infinite	20	Cont.	96	8	K	2.86	5000
917-5	2	30	6	5	60	Parallel	Infinite	20	Cont.	96	8	X	4.79	5000
918-1	2	30	6	5	60	Parallel	Infinite	30	Cont.	96	8	X	2.86	5000
919-1	2	30	6	5	60	Parallel	Infinite	20	Stag.	96	8	X	2.86	3600
919-2	2	30	6	5	60	Parallel	Infinite	20	Stag.	96	8	X	2.86	5000
919-3	2	30	6	5	60	Parallel	Infinite	20	Stag.	96	10	X	2.86	5000

Model ID	Geometry									Cross-section		CF detail		Mat'l
	n_{span}	L/d ratio	s_g [ft]	n_{girder}	Support skew [deg]; Layout		R [ft]	s_{cf} [ft]	CF layout	d_w [in]	t_{deck} [in]	CF type	A_{cf} [in^2]	E_c [ksi]
919-4	2	30	6	5	60	Parallel	Infinite	20	Stag.	96	8	K	2.86	5000
919-5	2	30	6	5	60	Parallel	Infinite	20	Stag.	96	8	X	4.79	5000
920-1	2	30	6	5	60	Parallel	Infinite	30	Stag.	96	8	X	2.86	5000
921-1	2	30	6	5	60	Parallel	1500	20	Cont.	96	8	X	2.86	3600
921-2	2	30	6	5	60	Parallel	1500	20	Cont.	96	8	X	2.86	5000
921-3	2	30	6	5	60	Parallel	1500	20	Cont.	96	10	X	2.86	5000
921-4	2	30	6	5	60	Parallel	1500	20	Cont.	96	8	K	2.86	5000
921-5	2	30	6	5	60	Parallel	1500	20	Cont.	96	8	X	4.79	5000
922-1	2	30	6	5	60	Parallel	1500	30	Cont.	96	8	X	2.86	5000
923-1	2	30	6	5	60	Parallel	750	20	Cont.	96	8	X	2.86	3600
923-2	2	30	6	5	60	Parallel	750	20	Cont.	96	8	X	2.86	5000
923-3	2	30	6	5	60	Parallel	750	20	Cont.	96	10	X	2.86	5000
923-4	2	30	6	5	60	Parallel	750	20	Cont.	96	8	K	2.86	5000
923-5	2	30	6	5	60	Parallel	750	20	Cont.	96	8	X	4.79	5000
924-1	2	30	6	5	60	Parallel	750	30	Cont.	96	8	X	2.86	5000
925-1	2	30	6	5	60	Trap.	Infinite	20	Cont.	96	8	X	2.86	3600
925-2	2	30	6	5	60	Trap.	Infinite	20	Cont.	96	8	X	2.86	5000
925-3	2	30	6	5	60	Trap.	Infinite	20	Cont.	96	10	X	2.86	5000
925-4	2	30	6	5	60	Trap.	Infinite	20	Cont.	96	8	K	2.86	5000
925-5	2	30	6	5	60	Trap.	Infinite	20	Cont.	96	8	X	4.79	5000
926-1	2	30	6	5	60	Trap.	Infinite	30	Cont.	96	8	X	2.86	5000
927-1	2	30	6	5	60	Trap.	Infinite	20	Stag.	96	8	X	2.86	3600
927-2	2	30	6	5	60	Trap.	Infinite	20	Stag.	96	8	X	2.86	5000
927-3	2	30	6	5	60	Trap.	Infinite	20	Stag.	96	10	X	2.86	5000
927-4	2	30	6	5	60	Trap.	Infinite	20	Stag.	96	8	K	2.86	5000
927-5	2	30	6	5	60	Trap.	Infinite	20	Stag.	96	8	X	4.79	5000
928-1	2	30	6	5	60	Trap.	Infinite	30	Stag.	96	8	X	2.86	5000
929-1	2	30	6	5	60	Trap.	1500	20	Cont.	96	8	X	2.86	3600
929-2	2	30	6	5	60	Trap.	1500	20	Cont.	96	8	X	2.86	5000
929-3	2	30	6	5	60	Trap.	1500	20	Cont.	96	10	X	2.86	5000
929-4	2	30	6	5	60	Trap.	1500	20	Cont.	96	8	K	2.86	5000
929-5	2	30	6	5	60	Trap.	1500	20	Cont.	96	8	X	4.79	5000
930-1	2	30	6	5	60	Trap.	1500	30	Cont.	96	8	X	2.86	5000
931-1	2	30	6	5	60	Trap.	750	20	Cont.	96	8	X	2.86	3600
931-2	2	30	6	5	60	Trap.	750	20	Cont.	96	8	X	2.86	5000
931-3	2	30	6	5	60	Trap.	750	20	Cont.	96	10	X	2.86	5000
931-4	2	30	6	5	60	Trap.	750	20	Cont.	96	8	K	2.86	5000
931-5	2	30	6	5	60	Trap.	750	20	Cont.	96	8	X	4.79	5000
932-1	2	30	6	5	60	Trap.	750	30	Cont.	96	8	X	2.86	5000
933-1	2	30	6	7	0	Parallel	Infinite	20	Cont.	96	8	X	2.86	3600
933-2	2	30	6	7	0	Parallel	Infinite	20	Cont.	96	8	X	2.86	5000
933-3	2	30	6	7	0	Parallel	Infinite	20	Cont.	96	10	X	2.86	5000
933-4	2	30	6	7	0	Parallel	Infinite	20	Cont.	96	8	K	2.86	5000
933-5	2	30	6	7	0	Parallel	Infinite	20	Cont.	96	8	X	4.79	5000
934-1	2	30	6	7	0	Parallel	Infinite	30	Cont.	96	8	X	2.86	5000
935-1	2	30	6	7	0	Parallel	1500	20	Cont.	96	8	X	2.86	3600
935-2	2	30	6	7	0	Parallel	1500	20	Cont.	96	8	X	2.86	5000
935-3	2	30	6	7	0	Parallel	1500	20	Cont.	96	10	X	2.86	5000
935-4	2	30	6	7	0	Parallel	1500	20	Cont.	96	8	K	2.86	5000
935-5	2	30	6	7	0	Parallel	1500	20	Cont.	96	8	X	4.79	5000
936-1	2	30	6	7	0	Parallel	1500	30	Cont.	96	8	X	2.86	5000
937-1	2	30	6	7	0	Parallel	750	20	Cont.	96	8	X	2.86	3600
937-2	2	30	6	7	0	Parallel	750	20	Cont.	96	8	X	2.86	5000
937-3	2	30	6	7	0	Parallel	750	20	Cont.	96	10	X	2.86	5000
937-4	2	30	6	7	0	Parallel	750	20	Cont.	96	8	K	2.86	5000
937-5	2	30	6	7	0	Parallel	750	20	Cont.	96	8	X	4.79	5000
938-1	2	30	6	7	0	Parallel	750	30	Cont.	96	8	X	2.86	5000
939-1	2	30	6	7	30	Parallel	Infinite	20	Cont.	96	8	X	2.86	3600
939-2	2	30	6	7	30	Parallel	Infinite	20	Cont.	96	8	X	2.86	5000
939-3	2	30	6	7	30	Parallel	Infinite	20	Cont.	96	10	X	2.86	5000
939-4	2	30	6	7	30	Parallel	Infinite	20	Cont.	96	8	K	2.86	5000
939-5	2	30	6	7	30	Parallel	Infinite	20	Cont.	96	8	X	4.79	5000
940-1	2	30	6	7	30	Parallel	Infinite	30	Cont.	96	8	X	2.86	5000
941-1	2	30	6	7	30	Parallel	1500	20	Cont.	96	8	X	2.86	3600
941-2	2	30	6	7	30	Parallel	1500	20	Cont.	96	8	X	2.86	5000
941-3	2	30	6	7	30	Parallel	1500	20	Cont.	96	10	X	2.86	5000
941-4	2	30	6	7	30	Parallel	1500	20	Cont.	96	8	K	2.86	5000
941-5	2	30	6	7	30	Parallel	1500	20	Cont.	96	8	X	4.79	5000
942-1	2	30	6	7	30	Parallel	1500	30	Cont.	96	8	X	2.86	5000
943-1	2	30	6	7	30	Parallel	750	20	Cont.	96	8	X	2.86	3600
943-2	2	30	6	7	30	Parallel	750	20	Cont.	96	8	X	2.86	5000
943-3	2	30	6	7	30	Parallel	750	20	Cont.	96	10	X	2.86	5000
943-4	2	30	6	7	30	Parallel	750	20	Cont.	96	8	K	2.86	5000
943-5	2	30	6	7	30	Parallel	750	20	Cont.	96	8	X	4.79	5000
944-1	2	30	6	7	30	Parallel	750	30	Cont.	96	8	X	2.86	5000
945-1	2	30	6	7	60	Parallel	Infinite	20	Cont.	96	8	X	2.86	3600
945-2	2	30	6	7	60	Parallel	Infinite	20	Cont.	96	8	X	2.86	5000
945-3	2	30	6	7	60	Parallel	Infinite	20	Cont.	96	10	X	2.86	5000
945-4	2	30	6	7	60	Parallel	Infinite	20	Cont.	96	8	K	2.86	5000

Model ID	Geometry									Cross-section		CF detail		Mat'l
	n_{span}	L/d ratio	s_g [ft]	n_{girder}	Support skew [deg]; Layout		R [ft]	s_{cf} [ft]	CF layout	d_w [in]	t_{deck} [in]	CF type	A_{cf} [in^2]	E_c [ksi]
945-5	2	30	6	7	60	Parallel	Infinite	20	Cont.	96	8	X	4.79	5000
946-1	2	30	6	7	60	Parallel	Infinite	30	Cont.	96	8	X	2.86	5000
947-1	2	30	6	7	60	Parallel	Infinite	20	Stag.	96	8	X	2.86	3600
947-2	2	30	6	7	60	Parallel	Infinite	20	Stag.	96	8	X	2.86	5000
947-3	2	30	6	7	60	Parallel	Infinite	20	Stag.	96	10	X	2.86	5000
947-4	2	30	6	7	60	Parallel	Infinite	20	Stag.	96	8	K	2.86	5000
947-5	2	30	6	7	60	Parallel	Infinite	20	Stag.	96	8	X	4.79	5000
948-1	2	30	6	7	60	Parallel	Infinite	30	Stag.	96	8	X	2.86	5000
949-1	2	30	6	7	60	Parallel	1500	20	Cont.	96	8	X	2.86	3600
949-2	2	30	6	7	60	Parallel	1500	20	Cont.	96	8	X	2.86	5000
949-3	2	30	6	7	60	Parallel	1500	20	Cont.	96	10	X	2.86	5000
949-4	2	30	6	7	60	Parallel	1500	20	Cont.	96	8	K	2.86	5000
949-5	2	30	6	7	60	Parallel	1500	20	Cont.	96	8	X	4.79	5000
950-1	2	30	6	7	60	Parallel	1500	30	Cont.	96	8	X	2.86	5000
951-1	2	30	6	7	60	Parallel	750	20	Cont.	96	8	X	2.86	3600
951-2	2	30	6	7	60	Parallel	750	20	Cont.	96	8	X	2.86	5000
951-3	2	30	6	7	60	Parallel	750	20	Cont.	96	10	X	2.86	5000
951-4	2	30	6	7	60	Parallel	750	20	Cont.	96	8	K	2.86	5000
951-5	2	30	6	7	60	Parallel	750	20	Cont.	96	8	X	4.79	5000
952-1	2	30	6	7	60	Parallel	750	30	Cont.	96	8	X	2.86	5000
953-1	2	30	6	7	60	Trap.	Infinite	20	Cont.	96	8	X	2.86	3600
953-2	2	30	6	7	60	Trap.	Infinite	20	Cont.	96	8	X	2.86	5000
953-3	2	30	6	7	60	Trap.	Infinite	20	Cont.	96	10	X	2.86	5000
953-4	2	30	6	7	60	Trap.	Infinite	20	Cont.	96	8	K	2.86	5000
953-5	2	30	6	7	60	Trap.	Infinite	20	Cont.	96	8	X	4.79	5000
954-1	2	30	6	7	60	Trap.	Infinite	30	Cont.	96	8	X	2.86	5000
955-1	2	30	6	7	60	Trap.	Infinite	20	Stag.	96	8	X	2.86	3600
955-2	2	30	6	7	60	Trap.	Infinite	20	Stag.	96	8	X	2.86	5000
955-3	2	30	6	7	60	Trap.	Infinite	20	Stag.	96	10	X	2.86	5000
955-4	2	30	6	7	60	Trap.	Infinite	20	Stag.	96	8	K	2.86	5000
955-5	2	30	6	7	60	Trap.	Infinite	20	Stag.	96	8	X	4.79	5000
956-1	2	30	6	7	60	Trap.	Infinite	30	Stag.	96	8	X	2.86	5000
957-1	2	30	6	7	60	Trap.	1500	20	Cont.	96	8	X	2.86	3600
957-2	2	30	6	7	60	Trap.	1500	20	Cont.	96	8	X	2.86	5000
957-3	2	30	6	7	60	Trap.	1500	20	Cont.	96	10	X	2.86	5000
957-4	2	30	6	7	60	Trap.	1500	20	Cont.	96	8	K	2.86	5000
957-5	2	30	6	7	60	Trap.	1500	20	Cont.	96	8	X	4.79	5000
958-1	2	30	6	7	60	Trap.	1500	30	Cont.	96	8	X	2.86	5000
959-1	2	30	6	7	60	Trap.	750	20	Cont.	96	8	X	2.86	3600
959-2	2	30	6	7	60	Trap.	750	20	Cont.	96	8	X	2.86	5000
959-3	2	30	6	7	60	Trap.	750	20	Cont.	96	10	X	2.86	5000
959-4	2	30	6	7	60	Trap.	750	20	Cont.	96	8	K	2.86	5000
959-5	2	30	6	7	60	Trap.	750	20	Cont.	96	8	X	4.79	5000
960-1	2	30	6	7	60	Trap.	750	30	Cont.	96	8	X	2.86	5000
961-1	2	30	8	3	0	Parallel	Infinite	20	Cont.	96	8	X	2.86	3600
961-2	2	30	8	3	0	Parallel	Infinite	20	Cont.	96	8	X	2.86	5000
961-3	2	30	8	3	0	Parallel	Infinite	20	Cont.	96	10	X	2.86	5000
961-4	2	30	8	3	0	Parallel	Infinite	20	Cont.	96	8	K	2.86	5000
961-5	2	30	8	3	0	Parallel	Infinite	20	Cont.	96	8	X	4.79	5000
962-1	2	30	8	3	0	Parallel	Infinite	30	Cont.	96	8	X	2.86	5000
963-1	2	30	8	3	0	Parallel	1500	20	Cont.	96	8	X	2.86	3600
963-2	2	30	8	3	0	Parallel	1500	20	Cont.	96	8	X	2.86	5000
963-3	2	30	8	3	0	Parallel	1500	20	Cont.	96	10	X	2.86	5000
963-4	2	30	8	3	0	Parallel	1500	20	Cont.	96	8	K	2.86	5000
963-5	2	30	8	3	0	Parallel	1500	20	Cont.	96	8	X	4.79	5000
964-1	2	30	8	3	0	Parallel	1500	30	Cont.	96	8	X	2.86	5000
965-1	2	30	8	3	0	Parallel	750	20	Cont.	96	8	X	2.86	3600
965-2	2	30	8	3	0	Parallel	750	20	Cont.	96	8	X	2.86	5000
965-3	2	30	8	3	0	Parallel	750	20	Cont.	96	10	X	2.86	5000
965-4	2	30	8	3	0	Parallel	750	20	Cont.	96	8	K	2.86	5000
965-5	2	30	8	3	0	Parallel	750	20	Cont.	96	8	X	4.79	5000
966-1	2	30	8	3	0	Parallel	750	30	Cont.	96	8	X	2.86	5000
967-1	2	30	8	3	30	Parallel	Infinite	20	Cont.	96	8	X	2.86	3600
967-2	2	30	8	3	30	Parallel	Infinite	20	Cont.	96	8	X	2.86	5000
967-3	2	30	8	3	30	Parallel	Infinite	20	Cont.	96	10	X	2.86	5000
967-4	2	30	8	3	30	Parallel	Infinite	20	Cont.	96	8	K	2.86	5000
967-5	2	30	8	3	30	Parallel	Infinite	20	Cont.	96	8	X	4.79	5000
968-1	2	30	8	3	30	Parallel	Infinite	30	Cont.	96	8	X	2.86	5000
969-1	2	30	8	3	30	Parallel	1500	20	Cont.	96	8	X	2.86	3600
969-2	2	30	8	3	30	Parallel	1500	20	Cont.	96	8	X	2.86	5000
969-3	2	30	8	3	30	Parallel	1500	20	Cont.	96	10	X	2.86	5000
969-4	2	30	8	3	30	Parallel	1500	20	Cont.	96	8	K	2.86	5000
969-5	2	30	8	3	30	Parallel	1500	20	Cont.	96	8	X	4.79	5000
970-1	2	30	8	3	30	Parallel	1500	30	Cont.	96	8	X	2.86	5000
971-1	2	30	8	3	30	Parallel	750	20	Cont.	96	8	X	2.86	3600
971-2	2	30	8	3	30	Parallel	750	20	Cont.	96	8	X	2.86	5000
971-3	2	30	8	3	30	Parallel	750	20	Cont.	96	10	X	2.86	5000
971-4	2	30	8	3	30	Parallel	750	20	Cont.	96	8	K	2.86	5000
971-5	2	30	8	3	30	Parallel	750	20	Cont.	96	8	X	4.79	5000

Model ID	Geometry									Cross-section		CF detail		Mat'l
	n_{span}	L/d ratio	s_g [ft]	n_{girder}	Support skew [deg]; Layout		R [ft]	s_{cf} [ft]	CF layout	d_w [in]	t_{deck} [in]	CF type	A_{cf} [in^2]	E_c [ksi]
972-1	2	30	8	3	30	Parallel	750	30	Cont.	96	8	X	2.86	5000
973-1	2	30	8	3	60	Parallel	Infinite	20	Cont.	96	8	X	2.86	3600
973-2	2	30	8	3	60	Parallel	Infinite	20	Cont.	96	8	X	2.86	5000
973-3	2	30	8	3	60	Parallel	Infinite	20	Cont.	96	10	X	2.86	5000
973-4	2	30	8	3	60	Parallel	Infinite	20	Cont.	96	8	K	2.86	5000
973-5	2	30	8	3	60	Parallel	Infinite	20	Cont.	96	8	X	4.79	5000
974-1	2	30	8	3	60	Parallel	Infinite	30	Cont.	96	8	X	2.86	5000
975-1	2	30	8	3	60	Parallel	Infinite	20	Stag.	96	8	X	2.86	3600
975-2	2	30	8	3	60	Parallel	Infinite	20	Stag.	96	8	X	2.86	5000
975-3	2	30	8	3	60	Parallel	Infinite	20	Stag.	96	10	X	2.86	5000
975-4	2	30	8	3	60	Parallel	Infinite	20	Stag.	96	8	K	2.86	5000
975-5	2	30	8	3	60	Parallel	Infinite	20	Stag.	96	8	X	4.79	5000
976-1	2	30	8	3	60	Parallel	Infinite	30	Stag.	96	8	X	2.86	5000
977-1	2	30	8	3	60	Parallel	1500	20	Cont.	96	8	X	2.86	3600
977-2	2	30	8	3	60	Parallel	1500	20	Cont.	96	8	X	2.86	5000
977-3	2	30	8	3	60	Parallel	1500	20	Cont.	96	10	X	2.86	5000
977-4	2	30	8	3	60	Parallel	1500	20	Cont.	96	8	K	2.86	5000
977-5	2	30	8	3	60	Parallel	1500	20	Cont.	96	8	X	4.79	5000
978-1	2	30	8	3	60	Parallel	1500	30	Cont.	96	8	X	2.86	5000
979-1	2	30	8	3	60	Parallel	750	20	Cont.	96	8	X	2.86	3600
979-2	2	30	8	3	60	Parallel	750	20	Cont.	96	8	X	2.86	5000
979-3	2	30	8	3	60	Parallel	750	20	Cont.	96	10	X	2.86	5000
979-4	2	30	8	3	60	Parallel	750	20	Cont.	96	8	K	2.86	5000
979-5	2	30	8	3	60	Parallel	750	20	Cont.	96	8	X	4.79	5000
980-1	2	30	8	3	60	Parallel	750	30	Cont.	96	8	X	2.86	5000
981-1	2	30	8	3	60	Trap.	Infinite	20	Cont.	96	8	X	2.86	3600
981-2	2	30	8	3	60	Trap.	Infinite	20	Cont.	96	8	X	2.86	5000
981-3	2	30	8	3	60	Trap.	Infinite	20	Cont.	96	10	X	2.86	5000
981-4	2	30	8	3	60	Trap.	Infinite	20	Cont.	96	8	K	2.86	5000
981-5	2	30	8	3	60	Trap.	Infinite	20	Cont.	96	8	X	4.79	5000
982-1	2	30	8	3	60	Trap.	Infinite	30	Cont.	96	8	X	2.86	5000
983-1	2	30	8	3	60	Trap.	Infinite	20	Stag.	96	8	X	2.86	3600
983-2	2	30	8	3	60	Trap.	Infinite	20	Stag.	96	8	X	2.86	5000
983-3	2	30	8	3	60	Trap.	Infinite	20	Stag.	96	10	X	2.86	5000
983-4	2	30	8	3	60	Trap.	Infinite	20	Stag.	96	8	K	2.86	5000
983-5	2	30	8	3	60	Trap.	Infinite	20	Stag.	96	8	X	4.79	5000
984-1	2	30	8	3	60	Trap.	Infinite	30	Stag.	96	8	X	2.86	5000
985-1	2	30	8	3	60	Trap.	1500	20	Cont.	96	8	X	2.86	3600
985-2	2	30	8	3	60	Trap.	1500	20	Cont.	96	8	X	2.86	5000
985-3	2	30	8	3	60	Trap.	1500	20	Cont.	96	10	X	2.86	5000
985-4	2	30	8	3	60	Trap.	1500	20	Cont.	96	8	K	2.86	5000
985-5	2	30	8	3	60	Trap.	1500	20	Cont.	96	8	X	4.79	5000
986-1	2	30	8	3	60	Trap.	1500	30	Cont.	96	8	X	2.86	5000
987-1	2	30	8	3	60	Trap.	750	20	Cont.	96	8	X	2.86	3600
987-2	2	30	8	3	60	Trap.	750	20	Cont.	96	8	X	2.86	5000
987-3	2	30	8	3	60	Trap.	750	20	Cont.	96	10	X	2.86	5000
987-4	2	30	8	3	60	Trap.	750	20	Cont.	96	8	K	2.86	5000
987-5	2	30	8	3	60	Trap.	750	20	Cont.	96	8	X	4.79	5000
988-1	2	30	8	3	60	Trap.	750	30	Cont.	96	8	X	2.86	5000
989-1	2	30	8	5	0	Parallel	Infinite	20	Cont.	96	8	X	2.86	3600
989-2	2	30	8	5	0	Parallel	Infinite	20	Cont.	96	8	X	2.86	5000
989-3	2	30	8	5	0	Parallel	Infinite	20	Cont.	96	10	X	2.86	5000
989-4	2	30	8	5	0	Parallel	Infinite	20	Cont.	96	8	K	2.86	5000
989-5	2	30	8	5	0	Parallel	Infinite	20	Cont.	96	8	X	4.79	5000
990-1	2	30	8	5	0	Parallel	Infinite	30	Cont.	96	8	X	2.86	5000
991-1	2	30	8	5	0	Parallel	1500	20	Cont.	96	8	X	2.86	3600
991-2	2	30	8	5	0	Parallel	1500	20	Cont.	96	8	X	2.86	5000
991-3	2	30	8	5	0	Parallel	1500	20	Cont.	96	10	X	2.86	5000
991-4	2	30	8	5	0	Parallel	1500	20	Cont.	96	8	K	2.86	5000
991-5	2	30	8	5	0	Parallel	1500	20	Cont.	96	8	X	4.79	5000
992-1	2	30	8	5	0	Parallel	1500	30	Cont.	96	8	X	2.86	5000
993-1	2	30	8	5	0	Parallel	750	20	Cont.	96	8	X	2.86	3600
993-2	2	30	8	5	0	Parallel	750	20	Cont.	96	8	X	2.86	5000
993-3	2	30	8	5	0	Parallel	750	20	Cont.	96	10	X	2.86	5000
993-4	2	30	8	5	0	Parallel	750	20	Cont.	96	8	K	2.86	5000
993-5	2	30	8	5	0	Parallel	750	20	Cont.	96	8	X	4.79	5000
994-1	2	30	8	5	0	Parallel	750	30	Cont.	96	8	X	2.86	5000
995-1	2	30	8	5	30	Parallel	Infinite	20	Cont.	96	8	X	2.86	3600
995-2	2	30	8	5	30	Parallel	Infinite	20	Cont.	96	8	X	2.86	5000
995-3	2	30	8	5	30	Parallel	Infinite	20	Cont.	96	10	X	2.86	5000
995-4	2	30	8	5	30	Parallel	Infinite	20	Cont.	96	8	K	2.86	5000
995-5	2	30	8	5	30	Parallel	Infinite	20	Cont.	96	8	X	4.79	5000
996-1	2	30	8	5	30	Parallel	Infinite	30	Cont.	96	8	X	2.86	5000
997-1	2	30	8	5	30	Parallel	1500	20	Cont.	96	8	X	2.86	3600
997-2	2	30	8	5	30	Parallel	1500	20	Cont.	96	8	X	2.86	5000
997-3	2	30	8	5	30	Parallel	1500	20	Cont.	96	10	X	2.86	5000
997-4	2	30	8	5	30	Parallel	1500	20	Cont.	96	8	K	2.86	5000
997-5	2	30	8	5	30	Parallel	1500	20	Cont.	96	8	X	4.79	5000
998-1	2	30	8	5	30	Parallel	1500	30	Cont.	96	8	X	2.86	5000

Model ID	Geometry									Cross-section		CF detail		Mat'l
	n_{span}	L/d ratio	s_g [ft]	n_{girder}	Support skew [deg]; Layout		R [ft]	s_{cf} [ft]	CF layout	d_w [in]	t_{deck} [in]	CF type	A_{cf} [in^2]	E_c [ksi]
999-1	2	30	8	5	30	Parallel	750	20	Cont.	96	8	X	2.86	3600
999-2	2	30	8	5	30	Parallel	750	20	Cont.	96	8	X	2.86	5000
999-3	2	30	8	5	30	Parallel	750	20	Cont.	96	10	X	2.86	5000
999-4	2	30	8	5	30	Parallel	750	20	Cont.	96	8	K	2.86	5000
999-5	2	30	8	5	30	Parallel	750	20	Cont.	96	8	X	4.79	5000
1000-1	2	30	8	5	30	Parallel	750	30	Cont.	96	8	X	2.86	5000
1001-1	2	30	8	5	60	Parallel	Infinite	20	Cont.	96	8	X	2.86	3600
1001-2	2	30	8	5	60	Parallel	Infinite	20	Cont.	96	8	X	2.86	5000
1001-3	2	30	8	5	60	Parallel	Infinite	20	Cont.	96	10	X	2.86	5000
1001-4	2	30	8	5	60	Parallel	Infinite	20	Cont.	96	8	K	2.86	5000
1001-5	2	30	8	5	60	Parallel	Infinite	20	Cont.	96	8	X	4.79	5000
1002-1	2	30	8	5	60	Parallel	Infinite	30	Cont.	96	8	X	2.86	5000
1003-1	2	30	8	5	60	Parallel	Infinite	20	Stag.	96	8	X	2.86	3600
1003-2	2	30	8	5	60	Parallel	Infinite	20	Stag.	96	8	X	2.86	5000
1003-3	2	30	8	5	60	Parallel	Infinite	20	Stag.	96	10	X	2.86	5000
1003-4	2	30	8	5	60	Parallel	Infinite	20	Stag.	96	8	K	2.86	5000
1003-5	2	30	8	5	60	Parallel	Infinite	20	Stag.	96	8	X	4.79	5000
1004-1	2	30	8	5	60	Parallel	Infinite	30	Stag.	96	8	X	2.86	5000
1005-1	2	30	8	5	60	Parallel	1500	20	Cont.	96	8	X	2.86	3600
1005-2	2	30	8	5	60	Parallel	1500	20	Cont.	96	8	X	2.86	5000
1005-3	2	30	8	5	60	Parallel	1500	20	Cont.	96	10	X	2.86	5000
1005-4	2	30	8	5	60	Parallel	1500	20	Cont.	96	8	K	2.86	5000
1005-5	2	30	8	5	60	Parallel	1500	20	Cont.	96	8	X	4.79	5000
1006-1	2	30	8	5	60	Parallel	1500	30	Cont.	96	8	X	2.86	5000
1007-1	2	30	8	5	60	Parallel	750	20	Cont.	96	8	X	2.86	3600
1007-2	2	30	8	5	60	Parallel	750	20	Cont.	96	8	X	2.86	5000
1007-3	2	30	8	5	60	Parallel	750	20	Cont.	96	10	X	2.86	5000
1007-4	2	30	8	5	60	Parallel	750	20	Cont.	96	8	K	2.86	5000
1007-5	2	30	8	5	60	Parallel	750	20	Cont.	96	8	X	4.79	5000
1008-1	2	30	8	5	60	Parallel	750	30	Cont.	96	8	X	2.86	5000
1009-1	2	30	8	5	60	Trap.	Infinite	20	Cont.	96	8	X	2.86	3600
1009-2	2	30	8	5	60	Trap.	Infinite	20	Cont.	96	8	X	2.86	5000
1009-3	2	30	8	5	60	Trap.	Infinite	20	Cont.	96	10	X	2.86	5000
1009-4	2	30	8	5	60	Trap.	Infinite	20	Cont.	96	8	K	2.86	5000
1009-5	2	30	8	5	60	Trap.	Infinite	20	Cont.	96	8	X	4.79	5000
1010-1	2	30	8	5	60	Trap.	Infinite	30	Cont.	96	8	X	2.86	5000
1011-1	2	30	8	5	60	Trap.	Infinite	20	Stag.	96	8	X	2.86	3600
1011-2	2	30	8	5	60	Trap.	Infinite	20	Stag.	96	8	X	2.86	5000
1011-3	2	30	8	5	60	Trap.	Infinite	20	Stag.	96	10	X	2.86	5000
1011-4	2	30	8	5	60	Trap.	Infinite	20	Stag.	96	8	K	2.86	5000
1011-5	2	30	8	5	60	Trap.	Infinite	20	Stag.	96	8	X	4.79	5000
1012-1	2	30	8	5	60	Trap.	Infinite	30	Stag.	96	8	X	2.86	5000
1013-1	2	30	8	5	60	Trap.	1500	20	Cont.	96	8	X	2.86	3600
1013-2	2	30	8	5	60	Trap.	1500	20	Cont.	96	8	X	2.86	5000
1013-3	2	30	8	5	60	Trap.	1500	20	Cont.	96	10	X	2.86	5000
1013-4	2	30	8	5	60	Trap.	1500	20	Cont.	96	8	K	2.86	5000
1013-5	2	30	8	5	60	Trap.	1500	20	Cont.	96	8	X	4.79	5000
1014-1	2	30	8	5	60	Trap.	1500	30	Cont.	96	8	X	2.86	5000
1015-1	2	30	8	5	60	Trap.	750	20	Cont.	96	8	X	2.86	3600
1015-2	2	30	8	5	60	Trap.	750	20	Cont.	96	8	X	2.86	5000
1015-3	2	30	8	5	60	Trap.	750	20	Cont.	96	10	X	2.86	5000
1015-4	2	30	8	5	60	Trap.	750	20	Cont.	96	8	K	2.86	5000
1015-5	2	30	8	5	60	Trap.	750	20	Cont.	96	8	X	4.79	5000
1016-1	2	30	8	5	60	Trap.	750	30	Cont.	96	8	X	2.86	5000
1017-1	2	30	8	7	0	Parallel	Infinite	20	Cont.	96	8	X	2.86	3600
1017-2	2	30	8	7	0	Parallel	Infinite	20	Cont.	96	8	X	2.86	5000
1017-3	2	30	8	7	0	Parallel	Infinite	20	Cont.	96	10	X	2.86	5000
1017-4	2	30	8	7	0	Parallel	Infinite	20	Cont.	96	8	K	2.86	5000
1017-5	2	30	8	7	0	Parallel	Infinite	20	Cont.	96	8	X	4.79	5000
1018-1	2	30	8	7	0	Parallel	Infinite	30	Cont.	96	8	X	2.86	5000
1019-1	2	30	8	7	0	Parallel	1500	20	Cont.	96	8	X	2.86	3600
1019-2	2	30	8	7	0	Parallel	1500	20	Cont.	96	8	X	2.86	5000
1019-3	2	30	8	7	0	Parallel	1500	20	Cont.	96	10	X	2.86	5000
1019-4	2	30	8	7	0	Parallel	1500	20	Cont.	96	8	K	2.86	5000
1019-5	2	30	8	7	0	Parallel	1500	20	Cont.	96	8	X	4.79	5000
1020-1	2	30	8	7	0	Parallel	1500	30	Cont.	96	8	X	2.86	5000
1021-1	2	30	8	7	0	Parallel	750	20	Cont.	96	8	X	2.86	3600
1021-2	2	30	8	7	0	Parallel	750	20	Cont.	96	8	X	2.86	5000
1021-3	2	30	8	7	0	Parallel	750	20	Cont.	96	10	X	2.86	5000
1021-4	2	30	8	7	0	Parallel	750	20	Cont.	96	8	K	2.86	5000
1021-5	2	30	8	7	0	Parallel	750	20	Cont.	96	8	X	4.79	5000
1022-1	2	30	8	7	0	Parallel	750	30	Cont.	96	8	X	2.86	5000
1023-1	2	30	8	7	30	Parallel	Infinite	20	Cont.	96	8	X	2.86	3600
1023-2	2	30	8	7	30	Parallel	Infinite	20	Cont.	96	8	X	2.86	5000
1023-3	2	30	8	7	30	Parallel	Infinite	20	Cont.	96	10	X	2.86	5000
1023-4	2	30	8	7	30	Parallel	Infinite	20	Cont.	96	8	K	2.86	5000
1023-5	2	30	8	7	30	Parallel	Infinite	20	Cont.	96	8	X	4.79	5000
1024-1	2	30	8	7	30	Parallel	Infinite	30	Cont.	96	8	X	2.86	5000
1025-1	2	30	8	7	30	Parallel	1500	20	Cont.	96	8	X	2.86	3600

Model ID	Geometry									Cross-section		CF detail		Mat'l
	n_{span}	L/d ratio	s_g [ft]	n_{girder}	Support skew [deg]; Layout		R [ft]	s_{cf} [ft]	CF layout	d_w [in]	t_{deck} [in]	CF type	A_{cf} [in^2]	E_c [ksi]
1025-2	2	30	8	7	30	Parallel	1500	20	Cont.	96	8	X	2.86	5000
1025-3	2	30	8	7	30	Parallel	1500	20	Cont.	96	10	X	2.86	5000
1025-4	2	30	8	7	30	Parallel	1500	20	Cont.	96	8	K	2.86	5000
1025-5	2	30	8	7	30	Parallel	1500	20	Cont.	96	8	X	4.79	5000
1026-1	2	30	8	7	30	Parallel	1500	30	Cont.	96	8	X	2.86	5000
1027-1	2	30	8	7	30	Parallel	750	20	Cont.	96	8	X	2.86	3600
1027-2	2	30	8	7	30	Parallel	750	20	Cont.	96	8	X	2.86	5000
1027-3	2	30	8	7	30	Parallel	750	20	Cont.	96	10	X	2.86	5000
1027-4	2	30	8	7	30	Parallel	750	20	Cont.	96	8	K	2.86	5000
1027-5	2	30	8	7	30	Parallel	750	20	Cont.	96	8	X	4.79	5000
1028-1	2	30	8	7	30	Parallel	750	30	Cont.	96	8	X	2.86	5000
1029-1	2	30	8	7	60	Parallel	Infinite	20	Cont.	96	8	X	2.86	3600
1029-2	2	30	8	7	60	Parallel	Infinite	20	Cont.	96	8	X	2.86	5000
1029-3	2	30	8	7	60	Parallel	Infinite	20	Cont.	96	10	X	2.86	5000
1029-4	2	30	8	7	60	Parallel	Infinite	20	Cont.	96	8	K	2.86	5000
1029-5	2	30	8	7	60	Parallel	Infinite	20	Cont.	96	8	X	4.79	5000
1030-1	2	30	8	7	60	Parallel	Infinite	30	Cont.	96	8	X	2.86	5000
1031-1	2	30	8	7	60	Parallel	Infinite	20	Stag.	96	8	X	2.86	3600
1031-2	2	30	8	7	60	Parallel	Infinite	20	Stag.	96	8	X	2.86	5000
1031-3	2	30	8	7	60	Parallel	Infinite	20	Stag.	96	10	X	2.86	5000
1031-4	2	30	8	7	60	Parallel	Infinite	20	Stag.	96	8	K	2.86	5000
1031-5	2	30	8	7	60	Parallel	Infinite	20	Stag.	96	8	X	4.79	5000
1032-1	2	30	8	7	60	Parallel	Infinite	30	Stag.	96	8	X	2.86	5000
1033-1	2	30	8	7	60	Parallel	1500	20	Cont.	96	8	X	2.86	3600
1033-2	2	30	8	7	60	Parallel	1500	20	Cont.	96	8	X	2.86	5000
1033-3	2	30	8	7	60	Parallel	1500	20	Cont.	96	10	X	2.86	5000
1033-4	2	30	8	7	60	Parallel	1500	20	Cont.	96	8	K	2.86	5000
1033-5	2	30	8	7	60	Parallel	1500	20	Cont.	96	8	X	4.79	5000
1034-1	2	30	8	7	60	Parallel	1500	30	Cont.	96	8	X	2.86	5000
1035-1	2	30	8	7	60	Parallel	750	20	Cont.	96	8	X	2.86	3600
1035-2	2	30	8	7	60	Parallel	750	20	Cont.	96	8	X	2.86	5000
1035-3	2	30	8	7	60	Parallel	750	20	Cont.	96	10	X	2.86	5000
1035-4	2	30	8	7	60	Parallel	750	20	Cont.	96	8	K	2.86	5000
1035-5	2	30	8	7	60	Parallel	750	20	Cont.	96	8	X	4.79	5000
1036-1	2	30	8	7	60	Parallel	750	30	Cont.	96	8	X	2.86	5000
1037-1	2	30	8	7	60	Trap.	Infinite	20	Cont.	96	8	X	2.86	3600
1037-2	2	30	8	7	60	Trap.	Infinite	20	Cont.	96	8	X	2.86	5000
1037-3	2	30	8	7	60	Trap.	Infinite	20	Cont.	96	10	X	2.86	5000
1037-4	2	30	8	7	60	Trap.	Infinite	20	Cont.	96	8	K	2.86	5000
1037-5	2	30	8	7	60	Trap.	Infinite	20	Cont.	96	8	X	4.79	5000
1038-1	2	30	8	7	60	Trap.	Infinite	30	Cont.	96	8	X	2.86	5000
1039-1	2	30	8	7	60	Trap.	Infinite	20	Stag.	96	8	X	2.86	3600
1039-2	2	30	8	7	60	Trap.	Infinite	20	Stag.	96	8	X	2.86	5000
1039-3	2	30	8	7	60	Trap.	Infinite	20	Stag.	96	10	X	2.86	5000
1039-4	2	30	8	7	60	Trap.	Infinite	20	Stag.	96	8	K	2.86	5000
1039-5	2	30	8	7	60	Trap.	Infinite	20	Stag.	96	8	X	4.79	5000
1040-1	2	30	8	7	60	Trap.	Infinite	30	Stag.	96	8	X	2.86	5000
1041-1	2	30	8	7	60	Trap.	1500	20	Cont.	96	8	X	2.86	3600
1041-2	2	30	8	7	60	Trap.	1500	20	Cont.	96	8	X	2.86	5000
1041-3	2	30	8	7	60	Trap.	1500	20	Cont.	96	10	X	2.86	5000
1041-4	2	30	8	7	60	Trap.	1500	20	Cont.	96	8	K	2.86	5000
1041-5	2	30	8	7	60	Trap.	1500	20	Cont.	96	8	X	4.79	5000
1042-1	2	30	8	7	60	Trap.	1500	30	Cont.	96	8	X	2.86	5000
1043-1	2	30	8	7	60	Trap.	750	20	Cont.	96	8	X	2.86	3600
1043-2	2	30	8	7	60	Trap.	750	20	Cont.	96	8	X	2.86	5000
1043-3	2	30	8	7	60	Trap.	750	20	Cont.	96	10	X	2.86	5000
1043-4	2	30	8	7	60	Trap.	750	20	Cont.	96	8	K	2.86	5000
1043-5	2	30	8	7	60	Trap.	750	20	Cont.	96	8	X	4.79	5000
1044-1	2	30	8	7	60	Trap.	750	30	Cont.	96	8	X	2.86	5000
1045-1	2	30	10	3	0	Parallel	Infinite	20	Cont.	96	8	X	2.86	3600
1045-2	2	30	10	3	0	Parallel	Infinite	20	Cont.	96	8	X	2.86	5000
1045-3	2	30	10	3	0	Parallel	Infinite	20	Cont.	96	10	X	2.86	5000
1045-4	2	30	10	3	0	Parallel	Infinite	20	Cont.	96	8	K	2.86	5000
1045-5	2	30	10	3	0	Parallel	Infinite	20	Cont.	96	8	X	4.79	5000
1046-1	2	30	10	3	0	Parallel	Infinite	30	Cont.	96	8	X	2.86	5000
1047-1	2	30	10	3	0	Parallel	1500	20	Cont.	96	8	X	2.86	3600
1047-2	2	30	10	3	0	Parallel	1500	20	Cont.	96	8	X	2.86	5000
1047-3	2	30	10	3	0	Parallel	1500	20	Cont.	96	10	X	2.86	5000
1047-4	2	30	10	3	0	Parallel	1500	20	Cont.	96	8	K	2.86	5000
1047-5	2	30	10	3	0	Parallel	1500	20	Cont.	96	8	X	4.79	5000
1048-1	2	30	10	3	0	Parallel	1500	30	Cont.	96	8	X	2.86	5000
1049-1	2	30	10	3	0	Parallel	750	20	Cont.	96	8	X	2.86	3600
1049-2	2	30	10	3	0	Parallel	750	20	Cont.	96	8	X	2.86	5000
1049-3	2	30	10	3	0	Parallel	750	20	Cont.	96	10	X	2.86	5000
1049-4	2	30	10	3	0	Parallel	750	20	Cont.	96	8	K	2.86	5000
1049-5	2	30	10	3	0	Parallel	750	20	Cont.	96	8	X	4.79	5000
1050-1	2	30	10	3	0	Parallel	750	30	Cont.	96	8	X	2.86	5000
1051-1	2	30	10	3	30	Parallel	Infinite	20	Cont.	96	8	X	2.86	3600
1051-2	2	30	10	3	30	Parallel	Infinite	20	Cont.	96	8	X	2.86	5000

Model ID	Geometry									Cross-section		CF detail		Mat'l
	n_{span}	L/d ratio	s_g [ft]	n_{girder}	Support skew [deg];	Layout	R [ft]	s_{cf} [ft]	CF layout	d_w [in]	t_{deck} [in]	CF type	A_{cf} [in^2]	E_c [ksi]
1051-3	2	30	10	3	30	Parallel	Infinite	20	Cont.	96	10	X	2.86	5000
1051-4	2	30	10	3	30	Parallel	Infinite	20	Cont.	96	8	K	2.86	5000
1051-5	2	30	10	3	30	Parallel	Infinite	20	Cont.	96	8	X	4.79	5000
1052-1	2	30	10	3	30	Parallel	Infinite	30	Cont.	96	8	X	2.86	5000
1053-1	2	30	10	3	30	Parallel	1500	20	Cont.	96	8	X	2.86	3600
1053-2	2	30	10	3	30	Parallel	1500	20	Cont.	96	8	X	2.86	5000
1053-3	2	30	10	3	30	Parallel	1500	20	Cont.	96	10	X	2.86	5000
1053-4	2	30	10	3	30	Parallel	1500	20	Cont.	96	8	K	2.86	5000
1053-5	2	30	10	3	30	Parallel	1500	20	Cont.	96	8	X	4.79	5000
1054-1	2	30	10	3	30	Parallel	1500	30	Cont.	96	8	X	2.86	5000
1055-1	2	30	10	3	30	Parallel	750	20	Cont.	96	8	X	2.86	3600
1055-2	2	30	10	3	30	Parallel	750	20	Cont.	96	8	X	2.86	5000
1055-3	2	30	10	3	30	Parallel	750	20	Cont.	96	10	X	2.86	5000
1055-4	2	30	10	3	30	Parallel	750	20	Cont.	96	8	K	2.86	5000
1055-5	2	30	10	3	30	Parallel	750	20	Cont.	96	8	X	4.79	5000
1056-1	2	30	10	3	30	Parallel	750	30	Cont.	96	8	X	2.86	5000
1057-1	2	30	10	3	60	Parallel	Infinite	20	Cont.	96	8	X	2.86	3600
1057-2	2	30	10	3	60	Parallel	Infinite	20	Cont.	96	8	X	2.86	5000
1057-3	2	30	10	3	60	Parallel	Infinite	20	Cont.	96	10	X	2.86	5000
1057-4	2	30	10	3	60	Parallel	Infinite	20	Cont.	96	8	K	2.86	5000
1057-5	2	30	10	3	60	Parallel	Infinite	20	Cont.	96	8	X	4.79	5000
1058-1	2	30	10	3	60	Parallel	Infinite	30	Cont.	96	8	X	2.86	5000
1059-1	2	30	10	3	60	Parallel	Infinite	20	Stag.	96	8	X	2.86	3600
1059-2	2	30	10	3	60	Parallel	Infinite	20	Stag.	96	8	X	2.86	5000
1059-3	2	30	10	3	60	Parallel	Infinite	20	Stag.	96	10	X	2.86	5000
1059-4	2	30	10	3	60	Parallel	Infinite	20	Stag.	96	8	K	2.86	5000
1059-5	2	30	10	3	60	Parallel	Infinite	20	Stag.	96	8	X	4.79	5000
1060-1	2	30	10	3	60	Parallel	Infinite	30	Stag.	96	8	X	2.86	5000
1061-1	2	30	10	3	60	Parallel	1500	20	Cont.	96	8	X	2.86	3600
1061-2	2	30	10	3	60	Parallel	1500	20	Cont.	96	8	X	2.86	5000
1061-3	2	30	10	3	60	Parallel	1500	20	Cont.	96	10	X	2.86	5000
1061-4	2	30	10	3	60	Parallel	1500	20	Cont.	96	8	K	2.86	5000
1061-5	2	30	10	3	60	Parallel	1500	20	Cont.	96	8	X	4.79	5000
1062-1	2	30	10	3	60	Parallel	1500	30	Cont.	96	8	X	2.86	5000
1063-1	2	30	10	3	60	Parallel	750	20	Cont.	96	8	X	2.86	3600
1063-2	2	30	10	3	60	Parallel	750	20	Cont.	96	8	X	2.86	5000
1063-3	2	30	10	3	60	Parallel	750	20	Cont.	96	10	X	2.86	5000
1063-4	2	30	10	3	60	Parallel	750	20	Cont.	96	8	K	2.86	5000
1063-5	2	30	10	3	60	Parallel	750	20	Cont.	96	8	X	4.79	5000
1064-1	2	30	10	3	60	Parallel	750	30	Cont.	96	8	X	2.86	5000
1065-1	2	30	10	3	60	Trap.	Infinite	20	Cont.	96	8	X	2.86	3600
1065-2	2	30	10	3	60	Trap.	Infinite	20	Cont.	96	8	X	2.86	5000
1065-3	2	30	10	3	60	Trap.	Infinite	20	Cont.	96	10	X	2.86	5000
1065-4	2	30	10	3	60	Trap.	Infinite	20	Cont.	96	8	K	2.86	5000
1065-5	2	30	10	3	60	Trap.	Infinite	20	Cont.	96	8	X	4.79	5000
1066-1	2	30	10	3	60	Trap.	Infinite	30	Cont.	96	8	X	2.86	5000
1067-1	2	30	10	3	60	Trap.	Infinite	20	Stag.	96	8	X	2.86	3600
1067-2	2	30	10	3	60	Trap.	Infinite	20	Stag.	96	8	X	2.86	5000
1067-3	2	30	10	3	60	Trap.	Infinite	20	Stag.	96	10	X	2.86	5000
1067-4	2	30	10	3	60	Trap.	Infinite	20	Stag.	96	8	K	2.86	5000
1067-5	2	30	10	3	60	Trap.	Infinite	20	Stag.	96	8	X	4.79	5000
1068-1	2	30	10	3	60	Trap.	Infinite	30	Stag.	96	8	X	2.86	5000
1069-1	2	30	10	3	60	Trap.	1500	20	Cont.	96	8	X	2.86	3600
1069-2	2	30	10	3	60	Trap.	1500	20	Cont.	96	8	X	2.86	5000
1069-3	2	30	10	3	60	Trap.	1500	20	Cont.	96	10	X	2.86	5000
1069-4	2	30	10	3	60	Trap.	1500	20	Cont.	96	8	K	2.86	5000
1069-5	2	30	10	3	60	Trap.	1500	20	Cont.	96	8	X	4.79	5000
1070-1	2	30	10	3	60	Trap.	1500	30	Cont.	96	8	X	2.86	5000
1071-1	2	30	10	3	60	Trap.	750	20	Cont.	96	8	X	2.86	3600
1071-2	2	30	10	3	60	Trap.	750	20	Cont.	96	8	X	2.86	5000
1071-3	2	30	10	3	60	Trap.	750	20	Cont.	96	10	X	2.86	5000
1071-4	2	30	10	3	60	Trap.	750	20	Cont.	96	8	K	2.86	5000
1071-5	2	30	10	3	60	Trap.	750	20	Cont.	96	8	X	4.79	5000
1072-1	2	30	10	3	60	Trap.	750	30	Cont.	96	8	X	2.86	5000
1073-1	2	30	10	5	0	Parallel	Infinite	20	Cont.	96	8	X	2.86	3600
1073-2	2	30	10	5	0	Parallel	Infinite	20	Cont.	96	8	X	2.86	5000
1073-3	2	30	10	5	0	Parallel	Infinite	20	Cont.	96	10	X	2.86	5000
1073-4	2	30	10	5	0	Parallel	Infinite	20	Cont.	96	8	K	2.86	5000
1073-5	2	30	10	5	0	Parallel	Infinite	20	Cont.	96	8	X	4.79	5000
1074-1	2	30	10	5	0	Parallel	Infinite	30	Cont.	96	8	X	2.86	5000
1075-1	2	30	10	5	0	Parallel	1500	20	Cont.	96	8	X	2.86	3600
1075-2	2	30	10	5	0	Parallel	1500	20	Cont.	96	8	X	2.86	5000
1075-3	2	30	10	5	0	Parallel	1500	20	Cont.	96	10	X	2.86	5000
1075-4	2	30	10	5	0	Parallel	1500	20	Cont.	96	8	K	2.86	5000
1075-5	2	30	10	5	0	Parallel	1500	20	Cont.	96	8	X	4.79	5000
1076-1	2	30	10	5	0	Parallel	1500	30	Cont.	96	8	X	2.86	5000
1077-1	2	30	10	5	0	Parallel	750	20	Cont.	96	8	X	2.86	3600
1077-2	2	30	10	5	0	Parallel	750	20	Cont.	96	8	X	2.86	5000
1077-3	2	30	10	5	0	Parallel	750	20	Cont.	96	10	X	2.86	5000

Model ID	Geometry									Cross-section		CF detail		Mat'l
	n_{span}	L/d ratio	s_g [ft]	n_{girder}	Support skew [deg]; Layout		R [ft]	s_{cf} [ft]	CF layout	d_w [in]	t_{deck} [in]	CF type	A_{cf} [in^2]	E_c [ksi]
1077-4	2	30	10	5	0	Parallel	750	20	Cont.	96	8	K	2.86	5000
1077-5	2	30	10	5	0	Parallel	750	20	Cont.	96	8	X	4.79	5000
1078-1	2	30	10	5	0	Parallel	750	30	Cont.	96	8	X	2.86	5000
1079-1	2	30	10	5	30	Parallel	Infinite	20	Cont.	96	8	X	2.86	3600
1079-2	2	30	10	5	30	Parallel	Infinite	20	Cont.	96	8	X	2.86	5000
1079-3	2	30	10	5	30	Parallel	Infinite	20	Cont.	96	10	X	2.86	5000
1079-4	2	30	10	5	30	Parallel	Infinite	20	Cont.	96	8	K	2.86	5000
1079-5	2	30	10	5	30	Parallel	Infinite	20	Cont.	96	8	X	4.79	5000
1080-1	2	30	10	5	30	Parallel	Infinite	30	Cont.	96	8	X	2.86	5000
1081-1	2	30	10	5	30	Parallel	1500	20	Cont.	96	8	X	2.86	3600
1081-2	2	30	10	5	30	Parallel	1500	20	Cont.	96	8	X	2.86	5000
1081-3	2	30	10	5	30	Parallel	1500	20	Cont.	96	10	X	2.86	5000
1081-4	2	30	10	5	30	Parallel	1500	20	Cont.	96	8	K	2.86	5000
1081-5	2	30	10	5	30	Parallel	1500	20	Cont.	96	8	X	4.79	5000
1082-1	2	30	10	5	30	Parallel	1500	30	Cont.	96	8	X	2.86	5000
1083-1	2	30	10	5	30	Parallel	750	20	Cont.	96	8	X	2.86	3600
1083-2	2	30	10	5	30	Parallel	750	20	Cont.	96	8	X	2.86	5000
1083-3	2	30	10	5	30	Parallel	750	20	Cont.	96	10	X	2.86	5000
1083-4	2	30	10	5	30	Parallel	750	20	Cont.	96	8	K	2.86	5000
1083-5	2	30	10	5	30	Parallel	750	20	Cont.	96	8	X	4.79	5000
1084-1	2	30	10	5	30	Parallel	750	30	Cont.	96	8	X	2.86	5000
1085-1	2	30	10	5	60	Parallel	Infinite	20	Cont.	96	8	X	2.86	3600
1085-2	2	30	10	5	60	Parallel	Infinite	20	Cont.	96	8	X	2.86	5000
1085-3	2	30	10	5	60	Parallel	Infinite	20	Cont.	96	10	X	2.86	5000
1085-4	2	30	10	5	60	Parallel	Infinite	20	Cont.	96	8	K	2.86	5000
1085-5	2	30	10	5	60	Parallel	Infinite	20	Cont.	96	8	X	4.79	5000
1086-1	2	30	10	5	60	Parallel	Infinite	30	Cont.	96	8	X	2.86	5000
1087-1	2	30	10	5	60	Parallel	Infinite	20	Stag.	96	8	X	2.86	3600
1087-2	2	30	10	5	60	Parallel	Infinite	20	Stag.	96	8	X	2.86	5000
1087-3	2	30	10	5	60	Parallel	Infinite	20	Stag.	96	10	X	2.86	5000
1087-4	2	30	10	5	60	Parallel	Infinite	20	Stag.	96	8	K	2.86	5000
1087-5	2	30	10	5	60	Parallel	Infinite	20	Stag.	96	8	X	4.79	5000
1088-1	2	30	10	5	60	Parallel	Infinite	30	Stag.	96	8	X	2.86	5000
1089-1	2	30	10	5	60	Parallel	1500	20	Cont.	96	8	X	2.86	3600
1089-2	2	30	10	5	60	Parallel	1500	20	Cont.	96	8	X	2.86	5000
1089-3	2	30	10	5	60	Parallel	1500	20	Cont.	96	10	X	2.86	5000
1089-4	2	30	10	5	60	Parallel	1500	20	Cont.	96	8	K	2.86	5000
1089-5	2	30	10	5	60	Parallel	1500	20	Cont.	96	8	X	4.79	5000
1090-1	2	30	10	5	60	Parallel	1500	30	Cont.	96	8	X	2.86	5000
1091-1	2	30	10	5	60	Parallel	750	20	Cont.	96	8	X	2.86	3600
1091-2	2	30	10	5	60	Parallel	750	20	Cont.	96	8	X	2.86	5000
1091-3	2	30	10	5	60	Parallel	750	20	Cont.	96	10	X	2.86	5000
1091-4	2	30	10	5	60	Parallel	750	20	Cont.	96	8	K	2.86	5000
1091-5	2	30	10	5	60	Parallel	750	20	Cont.	96	8	X	4.79	5000
1092-1	2	30	10	5	60	Parallel	750	30	Cont.	96	8	X	2.86	5000
1093-1	2	30	10	5	60	Trap.	Infinite	20	Cont.	96	8	X	2.86	3600
1093-2	2	30	10	5	60	Trap.	Infinite	20	Cont.	96	8	X	2.86	5000
1093-3	2	30	10	5	60	Trap.	Infinite	20	Cont.	96	10	X	2.86	5000
1093-4	2	30	10	5	60	Trap.	Infinite	20	Cont.	96	8	K	2.86	5000
1093-5	2	30	10	5	60	Trap.	Infinite	20	Cont.	96	8	X	4.79	5000
1094-1	2	30	10	5	60	Trap.	Infinite	30	Cont.	96	8	X	2.86	5000
1095-1	2	30	10	5	60	Trap.	Infinite	20	Stag.	96	8	X	2.86	3600
1095-2	2	30	10	5	60	Trap.	Infinite	20	Stag.	96	8	X	2.86	5000
1095-3	2	30	10	5	60	Trap.	Infinite	20	Stag.	96	10	X	2.86	5000
1095-4	2	30	10	5	60	Trap.	Infinite	20	Stag.	96	8	K	2.86	5000
1095-5	2	30	10	5	60	Trap.	Infinite	20	Stag.	96	8	X	4.79	5000
1096-1	2	30	10	5	60	Trap.	Infinite	30	Stag.	96	8	X	2.86	5000
1097-1	2	30	10	5	60	Trap.	1500	20	Cont.	96	8	X	2.86	3600
1097-2	2	30	10	5	60	Trap.	1500	20	Cont.	96	8	X	2.86	5000
1097-3	2	30	10	5	60	Trap.	1500	20	Cont.	96	10	X	2.86	5000
1097-4	2	30	10	5	60	Trap.	1500	20	Cont.	96	8	K	2.86	5000
1097-5	2	30	10	5	60	Trap.	1500	20	Cont.	96	8	X	4.79	5000
1098-1	2	30	10	5	60	Trap.	1500	30	Cont.	96	8	X	2.86	5000
1099-1	2	30	10	5	60	Trap.	750	20	Cont.	96	8	X	2.86	3600
1099-2	2	30	10	5	60	Trap.	750	20	Cont.	96	8	X	2.86	5000
1099-3	2	30	10	5	60	Trap.	750	20	Cont.	96	10	X	2.86	5000
1099-4	2	30	10	5	60	Trap.	750	20	Cont.	96	8	K	2.86	5000
1099-5	2	30	10	5	60	Trap.	750	20	Cont.	96	8	X	4.79	5000
1100-1	2	30	10	5	60	Trap.	750	30	Cont.	96	8	X	2.86	5000
1101-1	2	30	10	7	0	Parallel	Infinite	20	Cont.	96	8	X	2.86	3600
1101-2	2	30	10	7	0	Parallel	Infinite	20	Cont.	96	8	X	2.86	5000
1101-3	2	30	10	7	0	Parallel	Infinite	20	Cont.	96	10	X	2.86	5000
1101-4	2	30	10	7	0	Parallel	Infinite	20	Cont.	96	8	K	2.86	5000
1101-5	2	30	10	7	0	Parallel	Infinite	20	Cont.	96	8	X	4.79	5000
1102-1	2	30	10	7	0	Parallel	Infinite	30	Cont.	96	8	X	2.86	5000
1103-1	2	30	10	7	0	Parallel	1500	20	Cont.	96	8	X	2.86	3600
1103-2	2	30	10	7	0	Parallel	1500	20	Cont.	96	8	X	2.86	5000
1103-3	2	30	10	7	0	Parallel	1500	20	Cont.	96	10	X	2.86	5000
1103-4	2	30	10	7	0	Parallel	1500	20	Cont.	96	8	K	2.86	5000

Model ID	Geometry									Cross-section		CF detail		Mat'l
	n_{span}	L/d ratio	s_g [ft]	n_{girder}	Support skew [deg]; Layout		R [ft]	s_{cf} [ft]	CF layout	d_w [in]	t_{deck} [in]	CF type	A_{cf} [in^2]	E_c [ksi]
1103-5	2	30	10	7	0	Parallel	1500	20	Cont.	96	8	X	4.79	5000
1104-1	2	30	10	7	0	Parallel	1500	30	Cont.	96	8	X	2.86	5000
1105-1	2	30	10	7	0	Parallel	750	20	Cont.	96	8	X	2.86	3600
1105-2	2	30	10	7	0	Parallel	750	20	Cont.	96	8	X	2.86	5000
1105-3	2	30	10	7	0	Parallel	750	20	Cont.	96	10	X	2.86	5000
1105-4	2	30	10	7	0	Parallel	750	20	Cont.	96	8	K	2.86	5000
1105-5	2	30	10	7	0	Parallel	750	20	Cont.	96	8	X	4.79	5000
1106-1	2	30	10	7	0	Parallel	750	30	Cont.	96	8	X	2.86	5000
1107-1	2	30	10	7	30	Parallel	Infinite	20	Cont.	96	8	X	2.86	3600
1107-2	2	30	10	7	30	Parallel	Infinite	20	Cont.	96	8	X	2.86	5000
1107-3	2	30	10	7	30	Parallel	Infinite	20	Cont.	96	10	X	2.86	5000
1107-4	2	30	10	7	30	Parallel	Infinite	20	Cont.	96	8	K	2.86	5000
1107-5	2	30	10	7	30	Parallel	Infinite	20	Cont.	96	8	X	4.79	5000
1108-1	2	30	10	7	30	Parallel	Infinite	30	Cont.	96	8	X	2.86	5000
1109-1	2	30	10	7	30	Parallel	1500	20	Cont.	96	8	X	2.86	3600
1109-2	2	30	10	7	30	Parallel	1500	20	Cont.	96	8	X	2.86	5000
1109-3	2	30	10	7	30	Parallel	1500	20	Cont.	96	10	X	2.86	5000
1109-4	2	30	10	7	30	Parallel	1500	20	Cont.	96	8	K	2.86	5000
1109-5	2	30	10	7	30	Parallel	1500	20	Cont.	96	8	X	4.79	5000
1110-1	2	30	10	7	30	Parallel	1500	30	Cont.	96	8	X	2.86	5000
1111-1	2	30	10	7	30	Parallel	750	20	Cont.	96	8	X	2.86	3600
1111-2	2	30	10	7	30	Parallel	750	20	Cont.	96	8	X	2.86	5000
1111-3	2	30	10	7	30	Parallel	750	20	Cont.	96	10	X	2.86	5000
1111-4	2	30	10	7	30	Parallel	750	20	Cont.	96	8	K	2.86	5000
1111-5	2	30	10	7	30	Parallel	750	20	Cont.	96	8	X	4.79	5000
1112-1	2	30	10	7	30	Parallel	750	30	Cont.	96	8	X	2.86	5000
1113-1	2	30	10	7	60	Parallel	Infinite	20	Cont.	96	8	X	2.86	3600
1113-2	2	30	10	7	60	Parallel	Infinite	20	Cont.	96	8	X	2.86	5000
1113-3	2	30	10	7	60	Parallel	Infinite	20	Cont.	96	10	X	2.86	5000
1113-4	2	30	10	7	60	Parallel	Infinite	20	Cont.	96	8	K	2.86	5000
1113-5	2	30	10	7	60	Parallel	Infinite	20	Cont.	96	8	X	4.79	5000
1114-1	2	30	10	7	60	Parallel	Infinite	30	Cont.	96	8	X	2.86	5000
1115-1	2	30	10	7	60	Parallel	Infinite	20	Stag.	96	8	X	2.86	3600
1115-2	2	30	10	7	60	Parallel	Infinite	20	Stag.	96	8	X	2.86	5000
1115-3	2	30	10	7	60	Parallel	Infinite	20	Stag.	96	10	X	2.86	5000
1115-4	2	30	10	7	60	Parallel	Infinite	20	Stag.	96	8	K	2.86	5000
1115-5	2	30	10	7	60	Parallel	Infinite	20	Stag.	96	8	X	4.79	5000
1116-1	2	30	10	7	60	Parallel	Infinite	30	Stag.	96	8	X	2.86	5000
1117-1	2	30	10	7	60	Parallel	1500	20	Cont.	96	8	X	2.86	3600
1117-2	2	30	10	7	60	Parallel	1500	20	Cont.	96	8	X	2.86	5000
1117-3	2	30	10	7	60	Parallel	1500	20	Cont.	96	10	X	2.86	5000
1117-4	2	30	10	7	60	Parallel	1500	20	Cont.	96	8	K	2.86	5000
1117-5	2	30	10	7	60	Parallel	1500	20	Cont.	96	8	X	4.79	5000
1118-1	2	30	10	7	60	Parallel	1500	30	Cont.	96	8	X	2.86	5000
1119-1	2	30	10	7	60	Parallel	750	20	Cont.	96	8	X	2.86	3600
1119-2	2	30	10	7	60	Parallel	750	20	Cont.	96	8	X	2.86	5000
1119-3	2	30	10	7	60	Parallel	750	20	Cont.	96	10	X	2.86	5000
1119-4	2	30	10	7	60	Parallel	750	20	Cont.	96	8	K	2.86	5000
1119-5	2	30	10	7	60	Parallel	750	20	Cont.	96	8	X	4.79	5000
1120-1	2	30	10	7	60	Parallel	750	30	Cont.	96	8	X	2.86	5000
1121-1	2	30	10	7	60	Trap.	Infinite	20	Cont.	96	8	X	2.86	3600
1121-2	2	30	10	7	60	Trap.	Infinite	20	Cont.	96	8	X	2.86	5000
1121-3	2	30	10	7	60	Trap.	Infinite	20	Cont.	96	10	X	2.86	5000
1121-4	2	30	10	7	60	Trap.	Infinite	20	Cont.	96	8	K	2.86	5000
1121-5	2	30	10	7	60	Trap.	Infinite	20	Cont.	96	8	X	4.79	5000
1122-1	2	30	10	7	60	Trap.	Infinite	30	Cont.	96	8	X	2.86	5000
1123-1	2	30	10	7	60	Trap.	Infinite	20	Stag.	96	8	X	2.86	3600
1123-2	2	30	10	7	60	Trap.	Infinite	20	Stag.	96	8	X	2.86	5000
1123-3	2	30	10	7	60	Trap.	Infinite	20	Stag.	96	10	X	2.86	5000
1123-4	2	30	10	7	60	Trap.	Infinite	20	Stag.	96	8	K	2.86	5000
1123-5	2	30	10	7	60	Trap.	Infinite	20	Stag.	96	8	X	4.79	5000
1124-1	2	30	10	7	60	Trap.	Infinite	30	Stag.	96	8	X	2.86	5000
1125-1	2	30	10	7	60	Trap.	1500	20	Cont.	96	8	X	2.86	3600
1125-2	2	30	10	7	60	Trap.	1500	20	Cont.	96	8	X	2.86	5000
1125-3	2	30	10	7	60	Trap.	1500	20	Cont.	96	10	X	2.86	5000
1125-4	2	30	10	7	60	Trap.	1500	20	Cont.	96	8	K	2.86	5000
1125-5	2	30	10	7	60	Trap.	1500	20	Cont.	96	8	X	4.79	5000
1126-1	2	30	10	7	60	Trap.	1500	30	Cont.	96	8	X	2.86	5000
1127-1	2	30	10	7	60	Trap.	750	20	Cont.	96	8	X	2.86	3600
1127-2	2	30	10	7	60	Trap.	750	20	Cont.	96	8	X	2.86	5000
1127-3	2	30	10	7	60	Trap.	750	20	Cont.	96	10	X	2.86	5000
1127-4	2	30	10	7	60	Trap.	750	20	Cont.	96	8	K	2.86	5000
1127-5	2	30	10	7	60	Trap.	750	20	Cont.	96	8	X	4.79	5000
1128-1	2	30	10	7	60	Trap.	750	30	Cont.	96	8	X	2.86	5000
1129-1	2	35	6	3	0	Parallel	Infinite	20	Cont.	72	8	X	2.86	3600
1129-2	2	35	6	3	0	Parallel	Infinite	20	Cont.	72	8	X	2.86	5000
1129-3	2	35	6	3	0	Parallel	Infinite	20	Cont.	72	10	X	2.86	5000
1129-4	2	35	6	3	0	Parallel	Infinite	20	Cont.	72	8	K	2.86	5000
1129-5	2	35	6	3	0	Parallel	Infinite	20	Cont.	72	8	X	4.79	5000

Model ID	Geometry									Cross-section		CF detail		Mat'l
	n_{span}	L/d ratio	s_g [ft]	n_{girder}	Support skew [deg]; Layout		R [ft]	s_{cf} [ft]	CF layout	d_w [in]	t_{deck} [in]	CF type	A_{cf} [in^2]	E_c [ksi]
1130-1	2	35	6	3	0	Parallel	Infinite	30	Cont.	72	8	X	2.86	5000
1131-1	2	35	6	3	30	Parallel	Infinite	20	Cont.	72	8	X	2.86	3600
1131-2	2	35	6	3	30	Parallel	Infinite	20	Cont.	72	8	X	2.86	5000
1131-3	2	35	6	3	30	Parallel	Infinite	20	Cont.	72	10	X	2.86	5000
1131-4	2	35	6	3	30	Parallel	Infinite	20	Cont.	72	8	K	2.86	5000
1131-5	2	35	6	3	30	Parallel	Infinite	20	Cont.	72	8	X	4.79	5000
1132-1	2	35	6	3	30	Parallel	Infinite	30	Cont.	72	8	X	2.86	5000
1133-1	2	35	6	3	60	Parallel	Infinite	20	Cont.	72	8	X	2.86	3600
1133-2	2	35	6	3	60	Parallel	Infinite	20	Cont.	72	8	X	2.86	5000
1133-3	2	35	6	3	60	Parallel	Infinite	20	Cont.	72	10	X	2.86	5000
1133-4	2	35	6	3	60	Parallel	Infinite	20	Cont.	72	8	K	2.86	5000
1133-5	2	35	6	3	60	Parallel	Infinite	20	Cont.	72	8	X	4.79	5000
1134-1	2	35	6	3	60	Parallel	Infinite	30	Cont.	72	8	X	2.86	5000
1135-1	2	35	6	3	60	Parallel	Infinite	20	Stag.	72	8	X	2.86	3600
1135-2	2	35	6	3	60	Parallel	Infinite	20	Stag.	72	8	X	2.86	5000
1135-3	2	35	6	3	60	Parallel	Infinite	20	Stag.	72	10	X	2.86	5000
1135-4	2	35	6	3	60	Parallel	Infinite	20	Stag.	72	8	K	2.86	5000
1135-5	2	35	6	3	60	Parallel	Infinite	20	Stag.	72	8	X	4.79	5000
1136-1	2	35	6	3	60	Parallel	Infinite	30	Stag.	72	8	X	2.86	5000
1137-1	2	35	6	3	60	Trap.	Infinite	20	Cont.	72	8	X	2.86	3600
1137-2	2	35	6	3	60	Trap.	Infinite	20	Cont.	72	8	X	2.86	5000
1137-3	2	35	6	3	60	Trap.	Infinite	20	Cont.	72	10	X	2.86	5000
1137-4	2	35	6	3	60	Trap.	Infinite	20	Cont.	72	8	K	2.86	5000
1137-5	2	35	6	3	60	Trap.	Infinite	20	Cont.	72	8	X	4.79	5000
1138-1	2	35	6	3	60	Trap.	Infinite	30	Cont.	72	8	X	2.86	5000
1139-1	2	35	6	3	60	Trap.	Infinite	20	Stag.	72	8	X	2.86	3600
1139-2	2	35	6	3	60	Trap.	Infinite	20	Stag.	72	8	X	2.86	5000
1139-3	2	35	6	3	60	Trap.	Infinite	20	Stag.	72	10	X	2.86	5000
1139-4	2	35	6	3	60	Trap.	Infinite	20	Stag.	72	8	K	2.86	5000
1139-5	2	35	6	3	60	Trap.	Infinite	20	Stag.	72	8	X	4.79	5000
1140-1	2	35	6	3	60	Trap.	Infinite	30	Stag.	72	8	X	2.86	5000
1141-1	2	35	6	5	0	Parallel	Infinite	20	Cont.	72	8	X	2.86	3600
1141-2	2	35	6	5	0	Parallel	Infinite	20	Cont.	72	8	X	2.86	5000
1141-3	2	35	6	5	0	Parallel	Infinite	20	Cont.	72	10	X	2.86	5000
1141-4	2	35	6	5	0	Parallel	Infinite	20	Cont.	72	8	K	2.86	5000
1141-5	2	35	6	5	0	Parallel	Infinite	20	Cont.	72	8	X	4.79	5000
1142-1	2	35	6	5	0	Parallel	Infinite	30	Cont.	72	8	X	2.86	5000
1143-1	2	35	6	5	30	Parallel	Infinite	20	Cont.	72	8	X	2.86	3600
1143-2	2	35	6	5	30	Parallel	Infinite	20	Cont.	72	8	X	2.86	5000
1143-3	2	35	6	5	30	Parallel	Infinite	20	Cont.	72	10	X	2.86	5000
1143-4	2	35	6	5	30	Parallel	Infinite	20	Cont.	72	8	K	2.86	5000
1143-5	2	35	6	5	30	Parallel	Infinite	20	Cont.	72	8	X	4.79	5000
1144-1	2	35	6	5	30	Parallel	Infinite	30	Cont.	72	8	X	2.86	5000
1145-1	2	35	6	5	60	Parallel	Infinite	20	Cont.	72	8	X	2.86	3600
1145-2	2	35	6	5	60	Parallel	Infinite	20	Cont.	72	8	X	2.86	5000
1145-3	2	35	6	5	60	Parallel	Infinite	20	Cont.	72	10	X	2.86	5000
1145-4	2	35	6	5	60	Parallel	Infinite	20	Cont.	72	8	K	2.86	5000
1145-5	2	35	6	5	60	Parallel	Infinite	20	Cont.	72	8	X	4.79	5000
1146-1	2	35	6	5	60	Parallel	Infinite	30	Cont.	72	8	X	2.86	5000
1147-1	2	35	6	5	60	Parallel	Infinite	20	Stag.	72	8	X	2.86	3600
1147-2	2	35	6	5	60	Parallel	Infinite	20	Stag.	72	8	X	2.86	5000
1147-3	2	35	6	5	60	Parallel	Infinite	20	Stag.	72	10	X	2.86	5000
1147-4	2	35	6	5	60	Parallel	Infinite	20	Stag.	72	8	K	2.86	5000
1147-5	2	35	6	5	60	Parallel	Infinite	20	Stag.	72	8	X	4.79	5000
1148-1	2	35	6	5	60	Parallel	Infinite	30	Stag.	72	8	X	2.86	5000
1149-1	2	35	6	5	60	Trap.	Infinite	20	Cont.	72	8	X	2.86	3600
1149-2	2	35	6	5	60	Trap.	Infinite	20	Cont.	72	8	X	2.86	5000
1149-3	2	35	6	5	60	Trap.	Infinite	20	Cont.	72	10	X	2.86	5000
1149-4	2	35	6	5	60	Trap.	Infinite	20	Cont.	72	8	K	2.86	5000
1149-5	2	35	6	5	60	Trap.	Infinite	20	Cont.	72	8	X	4.79	5000
1150-1	2	35	6	5	60	Trap.	Infinite	30	Cont.	72	8	X	2.86	5000
1151-1	2	35	6	5	60	Trap.	Infinite	20	Stag.	72	8	X	2.86	3600
1151-2	2	35	6	5	60	Trap.	Infinite	20	Stag.	72	8	X	2.86	5000
1151-3	2	35	6	5	60	Trap.	Infinite	20	Stag.	72	10	X	2.86	5000
1151-4	2	35	6	5	60	Trap.	Infinite	20	Stag.	72	8	K	2.86	5000
1151-5	2	35	6	5	60	Trap.	Infinite	20	Stag.	72	8	X	4.79	5000
1152-1	2	35	6	5	60	Trap.	Infinite	30	Stag.	72	8	X	2.86	5000
1153-1	2	35	6	7	0	Parallel	Infinite	20	Cont.	72	8	X	2.86	3600
1153-2	2	35	6	7	0	Parallel	Infinite	20	Cont.	72	8	X	2.86	5000
1153-3	2	35	6	7	0	Parallel	Infinite	20	Cont.	72	10	X	2.86	5000
1153-4	2	35	6	7	0	Parallel	Infinite	20	Cont.	72	8	K	2.86	5000
1153-5	2	35	6	7	0	Parallel	Infinite	20	Cont.	72	8	X	4.79	5000
1154-1	2	35	6	7	0	Parallel	Infinite	30	Cont.	72	8	X	2.86	5000
1155-1	2	35	6	7	30	Parallel	Infinite	20	Cont.	72	8	X	2.86	3600
1155-2	2	35	6	7	30	Parallel	Infinite	20	Cont.	72	8	X	2.86	5000
1155-3	2	35	6	7	30	Parallel	Infinite	20	Cont.	72	10	X	2.86	5000
1155-4	2	35	6	7	30	Parallel	Infinite	20	Cont.	72	8	K	2.86	5000
1155-5	2	35	6	7	30	Parallel	Infinite	20	Cont.	72	8	X	4.79	5000
1156-1	2	35	6	7	30	Parallel	Infinite	30	Cont.	72	8	X	2.86	5000

Model ID	Geometry									Cross-section		CF detail		Mat'l
	n_{span}	L/d ratio	s_g [ft]	n_{girder}	Support skew [deg]; Layout		R [ft]	s_{cf} [ft]	CF layout	d_w [in]	t_{deck} [in]	CF type	A_{cf} [in^2]	E_c [ksi]
1157-1	2	35	6	7	60	Parallel	Infinite	20	Cont.	72	8	X	2.86	3600
1157-2	2	35	6	7	60	Parallel	Infinite	20	Cont.	72	8	X	2.86	5000
1157-3	2	35	6	7	60	Parallel	Infinite	20	Cont.	72	10	X	2.86	5000
1157-4	2	35	6	7	60	Parallel	Infinite	20	Cont.	72	8	K	2.86	5000
1157-5	2	35	6	7	60	Parallel	Infinite	20	Cont.	72	8	X	4.79	5000
1158-1	2	35	6	7	60	Parallel	Infinite	30	Cont.	72	8	X	2.86	5000
1159-1	2	35	6	7	60	Parallel	Infinite	20	Stag.	72	8	X	2.86	3600
1159-2	2	35	6	7	60	Parallel	Infinite	20	Stag.	72	8	X	2.86	5000
1159-3	2	35	6	7	60	Parallel	Infinite	20	Stag.	72	10	X	2.86	5000
1159-4	2	35	6	7	60	Parallel	Infinite	20	Stag.	72	8	K	2.86	5000
1159-5	2	35	6	7	60	Parallel	Infinite	20	Stag.	72	8	X	4.79	5000
1160-1	2	35	6	7	60	Parallel	Infinite	30	Stag.	72	8	X	2.86	5000
1161-1	2	35	6	7	60	Trap.	Infinite	20	Cont.	72	8	X	2.86	3600
1161-2	2	35	6	7	60	Trap.	Infinite	20	Cont.	72	8	X	2.86	5000
1161-3	2	35	6	7	60	Trap.	Infinite	20	Cont.	72	10	X	2.86	5000
1161-4	2	35	6	7	60	Trap.	Infinite	20	Cont.	72	8	K	2.86	5000
1161-5	2	35	6	7	60	Trap.	Infinite	20	Cont.	72	8	X	4.79	5000
1162-1	2	35	6	7	60	Trap.	Infinite	30	Cont.	72	8	X	2.86	5000
1163-1	2	35	6	7	60	Trap.	Infinite	20	Stag.	72	8	X	2.86	3600
1163-2	2	35	6	7	60	Trap.	Infinite	20	Stag.	72	8	X	2.86	5000
1163-3	2	35	6	7	60	Trap.	Infinite	20	Stag.	72	10	X	2.86	5000
1163-4	2	35	6	7	60	Trap.	Infinite	20	Stag.	72	8	K	2.86	5000
1163-5	2	35	6	7	60	Trap.	Infinite	20	Stag.	72	8	X	4.79	5000
1164-1	2	35	6	7	60	Trap.	Infinite	30	Stag.	72	8	X	2.86	5000
1165-1	2	35	8	3	0	Parallel	Infinite	20	Cont.	72	8	X	2.86	3600
1165-2	2	35	8	3	0	Parallel	Infinite	20	Cont.	72	8	X	2.86	5000
1165-3	2	35	8	3	0	Parallel	Infinite	20	Cont.	72	10	X	2.86	5000
1165-4	2	35	8	3	0	Parallel	Infinite	20	Cont.	72	8	K	2.86	5000
1165-5	2	35	8	3	0	Parallel	Infinite	20	Cont.	72	8	X	4.79	5000
1166-1	2	35	8	3	0	Parallel	Infinite	30	Cont.	72	8	X	2.86	5000
1167-1	2	35	8	3	30	Parallel	Infinite	20	Cont.	72	8	X	2.86	3600
1167-2	2	35	8	3	30	Parallel	Infinite	20	Cont.	72	8	X	2.86	5000
1167-3	2	35	8	3	30	Parallel	Infinite	20	Cont.	72	10	X	2.86	5000
1167-4	2	35	8	3	30	Parallel	Infinite	20	Cont.	72	8	K	2.86	5000
1167-5	2	35	8	3	30	Parallel	Infinite	20	Cont.	72	8	X	4.79	5000
1168-1	2	35	8	3	30	Parallel	Infinite	30	Cont.	72	8	X	2.86	5000
1169-1	2	35	8	3	60	Parallel	Infinite	20	Cont.	72	8	X	2.86	3600
1169-2	2	35	8	3	60	Parallel	Infinite	20	Cont.	72	8	X	2.86	5000
1169-3	2	35	8	3	60	Parallel	Infinite	20	Cont.	72	10	X	2.86	5000
1169-4	2	35	8	3	60	Parallel	Infinite	20	Cont.	72	8	K	2.86	5000
1169-5	2	35	8	3	60	Parallel	Infinite	20	Cont.	72	8	X	4.79	5000
1170-1	2	35	8	3	60	Parallel	Infinite	30	Cont.	72	8	X	2.86	5000
1171-1	2	35	8	3	60	Parallel	Infinite	20	Stag.	72	8	X	2.86	3600
1171-2	2	35	8	3	60	Parallel	Infinite	20	Stag.	72	8	X	2.86	5000
1171-3	2	35	8	3	60	Parallel	Infinite	20	Stag.	72	10	X	2.86	5000
1171-4	2	35	8	3	60	Parallel	Infinite	20	Stag.	72	8	K	2.86	5000
1171-5	2	35	8	3	60	Parallel	Infinite	20	Stag.	72	8	X	4.79	5000
1172-1	2	35	8	3	60	Parallel	Infinite	30	Stag.	72	8	X	2.86	5000
1173-1	2	35	8	3	60	Trap.	Infinite	20	Cont.	72	8	X	2.86	3600
1173-2	2	35	8	3	60	Trap.	Infinite	20	Cont.	72	8	X	2.86	5000
1173-3	2	35	8	3	60	Trap.	Infinite	20	Cont.	72	10	X	2.86	5000
1173-4	2	35	8	3	60	Trap.	Infinite	20	Cont.	72	8	K	2.86	5000
1173-5	2	35	8	3	60	Trap.	Infinite	20	Cont.	72	8	X	4.79	5000
1174-1	2	35	8	3	60	Trap.	Infinite	30	Cont.	72	8	X	2.86	5000
1175-1	2	35	8	3	60	Trap.	Infinite	20	Stag.	72	8	X	2.86	3600
1175-2	2	35	8	3	60	Trap.	Infinite	20	Stag.	72	8	X	2.86	5000
1175-3	2	35	8	3	60	Trap.	Infinite	20	Stag.	72	10	X	2.86	5000
1175-4	2	35	8	3	60	Trap.	Infinite	20	Stag.	72	8	K	2.86	5000
1175-5	2	35	8	3	60	Trap.	Infinite	20	Stag.	72	8	X	4.79	5000
1176-1	2	35	8	3	60	Trap.	Infinite	30	Stag.	72	8	X	2.86	5000
1177-1	2	35	8	5	0	Parallel	Infinite	20	Cont.	72	8	X	2.86	3600
1177-2	2	35	8	5	0	Parallel	Infinite	20	Cont.	72	8	X	2.86	5000
1177-3	2	35	8	5	0	Parallel	Infinite	20	Cont.	72	10	X	2.86	5000
1177-4	2	35	8	5	0	Parallel	Infinite	20	Cont.	72	8	K	2.86	5000
1177-5	2	35	8	5	0	Parallel	Infinite	20	Cont.	72	8	X	4.79	5000
1178-1	2	35	8	5	0	Parallel	Infinite	30	Cont.	72	8	X	2.86	5000
1179-1	2	35	8	5	30	Parallel	Infinite	20	Cont.	72	8	X	2.86	3600
1179-2	2	35	8	5	30	Parallel	Infinite	20	Cont.	72	8	X	2.86	5000
1179-3	2	35	8	5	30	Parallel	Infinite	20	Cont.	72	10	X	2.86	5000
1179-4	2	35	8	5	30	Parallel	Infinite	20	Cont.	72	8	K	2.86	5000
1179-5	2	35	8	5	30	Parallel	Infinite	20	Cont.	72	8	X	4.79	5000
1180-1	2	35	8	5	30	Parallel	Infinite	30	Cont.	72	8	X	2.86	5000
1181-1	2	35	8	5	60	Parallel	Infinite	20	Cont.	72	8	X	2.86	3600
1181-2	2	35	8	5	60	Parallel	Infinite	20	Cont.	72	8	X	2.86	5000
1181-3	2	35	8	5	60	Parallel	Infinite	20	Cont.	72	10	X	2.86	5000
1181-4	2	35	8	5	60	Parallel	Infinite	20	Cont.	72	8	K	2.86	5000
1181-5	2	35	8	5	60	Parallel	Infinite	20	Cont.	72	8	X	4.79	5000
1182-1	2	35	8	5	60	Parallel	Infinite	30	Cont.	72	8	X	2.86	5000
1183-1	2	35	8	5	60	Parallel	Infinite	20	Stag.	72	8	X	2.86	3600

Model ID	Geometry									Cross-section		CF detail		Mat'l
	n_{span}	L/d ratio	s_g [ft]	n_{girder}	Support skew [deg]; Layout		R [ft]	s_{cf} [ft]	CF layout	d_w [in]	t_{deck} [in]	CF type	A_{cf} [in^2]	E_c [ksi]
1183-2	2	35	8	5	60	Parallel	Infinite	20	Stag.	72	8	X	2.86	5000
1183-3	2	35	8	5	60	Parallel	Infinite	20	Stag.	72	10	X	2.86	5000
1183-4	2	35	8	5	60	Parallel	Infinite	20	Stag.	72	8	K	2.86	5000
1183-5	2	35	8	5	60	Parallel	Infinite	20	Stag.	72	8	X	4.79	5000
1184-1	2	35	8	5	60	Parallel	Infinite	30	Stag.	72	8	X	2.86	5000
1185-1	2	35	8	5	60	Trap.	Infinite	20	Cont.	72	8	X	2.86	3600
1185-2	2	35	8	5	60	Trap.	Infinite	20	Cont.	72	8	X	2.86	5000
1185-3	2	35	8	5	60	Trap.	Infinite	20	Cont.	72	10	X	2.86	5000
1185-4	2	35	8	5	60	Trap.	Infinite	20	Cont.	72	8	K	2.86	5000
1185-5	2	35	8	5	60	Trap.	Infinite	20	Cont.	72	8	X	4.79	5000
1186-1	2	35	8	5	60	Trap.	Infinite	30	Cont.	72	8	X	2.86	5000
1187-1	2	35	8	5	60	Trap.	Infinite	20	Stag.	72	8	X	2.86	3600
1187-2	2	35	8	5	60	Trap.	Infinite	20	Stag.	72	8	X	2.86	5000
1187-3	2	35	8	5	60	Trap.	Infinite	20	Stag.	72	10	X	2.86	5000
1187-4	2	35	8	5	60	Trap.	Infinite	20	Stag.	72	8	K	2.86	5000
1187-5	2	35	8	5	60	Trap.	Infinite	20	Stag.	72	8	X	4.79	5000
1188-1	2	35	8	5	60	Trap.	Infinite	30	Stag.	72	8	X	2.86	5000
1189-1	2	35	8	7	0	Parallel	Infinite	20	Cont.	72	8	X	2.86	3600
1189-2	2	35	8	7	0	Parallel	Infinite	20	Cont.	72	8	X	2.86	5000
1189-3	2	35	8	7	0	Parallel	Infinite	20	Cont.	72	10	X	2.86	5000
1189-4	2	35	8	7	0	Parallel	Infinite	20	Cont.	72	8	K	2.86	5000
1189-5	2	35	8	7	0	Parallel	Infinite	20	Cont.	72	8	X	4.79	5000
1190-1	2	35	8	7	0	Parallel	Infinite	30	Cont.	72	8	X	2.86	5000
1191-1	2	35	8	7	30	Parallel	Infinite	20	Cont.	72	8	X	2.86	3600
1191-2	2	35	8	7	30	Parallel	Infinite	20	Cont.	72	8	X	2.86	5000
1191-3	2	35	8	7	30	Parallel	Infinite	20	Cont.	72	10	X	2.86	5000
1191-4	2	35	8	7	30	Parallel	Infinite	20	Cont.	72	8	K	2.86	5000
1191-5	2	35	8	7	30	Parallel	Infinite	20	Cont.	72	8	X	4.79	5000
1192-1	2	35	8	7	30	Parallel	Infinite	30	Cont.	72	8	X	2.86	5000
1193-1	2	35	8	7	60	Parallel	Infinite	20	Cont.	72	8	X	2.86	3600
1193-2	2	35	8	7	60	Parallel	Infinite	20	Cont.	72	8	X	2.86	5000
1193-3	2	35	8	7	60	Parallel	Infinite	20	Cont.	72	10	X	2.86	5000
1193-4	2	35	8	7	60	Parallel	Infinite	20	Cont.	72	8	K	2.86	5000
1193-5	2	35	8	7	60	Parallel	Infinite	20	Cont.	72	8	X	4.79	5000
1194-1	2	35	8	7	60	Parallel	Infinite	30	Cont.	72	8	X	2.86	5000
1195-1	2	35	8	7	60	Parallel	Infinite	20	Stag.	72	8	X	2.86	3600
1195-2	2	35	8	7	60	Parallel	Infinite	20	Stag.	72	8	X	2.86	5000
1195-3	2	35	8	7	60	Parallel	Infinite	20	Stag.	72	10	X	2.86	5000
1195-4	2	35	8	7	60	Parallel	Infinite	20	Stag.	72	8	K	2.86	5000
1195-5	2	35	8	7	60	Parallel	Infinite	20	Stag.	72	8	X	4.79	5000
1196-1	2	35	8	7	60	Parallel	Infinite	30	Stag.	72	8	X	2.86	5000
1197-1	2	35	8	7	60	Trap.	Infinite	20	Cont.	72	8	X	2.86	3600
1197-2	2	35	8	7	60	Trap.	Infinite	20	Cont.	72	8	X	2.86	5000
1197-3	2	35	8	7	60	Trap.	Infinite	20	Cont.	72	10	X	2.86	5000
1197-4	2	35	8	7	60	Trap.	Infinite	20	Cont.	72	8	K	2.86	5000
1197-5	2	35	8	7	60	Trap.	Infinite	20	Cont.	72	8	X	4.79	5000
1198-1	2	35	8	7	60	Trap.	Infinite	30	Cont.	72	8	X	2.86	5000
1199-1	2	35	8	7	60	Trap.	Infinite	20	Stag.	72	8	X	2.86	3600
1199-2	2	35	8	7	60	Trap.	Infinite	20	Stag.	72	8	X	2.86	5000
1199-3	2	35	8	7	60	Trap.	Infinite	20	Stag.	72	10	X	2.86	5000
1199-4	2	35	8	7	60	Trap.	Infinite	20	Stag.	72	8	K	2.86	5000
1199-5	2	35	8	7	60	Trap.	Infinite	20	Stag.	72	8	X	4.79	5000
1200-1	2	35	8	7	60	Trap.	Infinite	30	Stag.	72	8	X	2.86	5000
1201-1	2	35	10	3	0	Parallel	Infinite	20	Cont.	72	8	X	2.86	3600
1201-2	2	35	10	3	0	Parallel	Infinite	20	Cont.	72	8	X	2.86	5000
1201-3	2	35	10	3	0	Parallel	Infinite	20	Cont.	72	10	X	2.86	5000
1201-4	2	35	10	3	0	Parallel	Infinite	20	Cont.	72	8	K	2.86	5000
1201-5	2	35	10	3	0	Parallel	Infinite	20	Cont.	72	8	X	4.79	5000
1202-1	2	35	10	3	0	Parallel	Infinite	30	Cont.	72	8	X	2.86	5000
1203-1	2	35	10	3	30	Parallel	Infinite	20	Cont.	72	8	X	2.86	3600
1203-2	2	35	10	3	30	Parallel	Infinite	20	Cont.	72	8	X	2.86	5000
1203-3	2	35	10	3	30	Parallel	Infinite	20	Cont.	72	10	X	2.86	5000
1203-4	2	35	10	3	30	Parallel	Infinite	20	Cont.	72	8	K	2.86	5000
1203-5	2	35	10	3	30	Parallel	Infinite	20	Cont.	72	8	X	4.79	5000
1204-1	2	35	10	3	30	Parallel	Infinite	30	Cont.	72	8	X	2.86	5000
1205-1	2	35	10	3	60	Parallel	Infinite	20	Cont.	72	8	X	2.86	3600
1205-2	2	35	10	3	60	Parallel	Infinite	20	Cont.	72	8	X	2.86	5000
1205-3	2	35	10	3	60	Parallel	Infinite	20	Cont.	72	10	X	2.86	5000
1205-4	2	35	10	3	60	Parallel	Infinite	20	Cont.	72	8	K	2.86	5000
1205-5	2	35	10	3	60	Parallel	Infinite	20	Cont.	72	8	X	4.79	5000
1206-1	2	35	10	3	60	Parallel	Infinite	30	Cont.	72	8	X	2.86	5000
1207-1	2	35	10	3	60	Parallel	Infinite	20	Stag.	72	8	X	2.86	3600
1207-2	2	35	10	3	60	Parallel	Infinite	20	Stag.	72	8	X	2.86	5000
1207-3	2	35	10	3	60	Parallel	Infinite	20	Stag.	72	10	X	2.86	5000
1207-4	2	35	10	3	60	Parallel	Infinite	20	Stag.	72	8	K	2.86	5000
1207-5	2	35	10	3	60	Parallel	Infinite	20	Stag.	72	8	X	4.79	5000
1208-1	2	35	10	3	60	Parallel	Infinite	30	Stag.	72	8	X	2.86	5000
1209-1	2	35	10	3	60	Trap.	Infinite	20	Cont.	72	8	X	2.86	3600
1209-2	2	35	10	3	60	Trap.	Infinite	20	Cont.	72	8	X	2.86	5000

Model ID	Geometry									Cross-section		CF detail		Mat'l
	n_{span}	L/d ratio	s_g [ft]	n_{girder}	Support skew [deg]; Layout		R [ft]	s_{cf} [ft]	CF layout	d_w [in]	t_{deck} [in]	CF type	A_{cf} [in^2]	E_c [ksi]
1209-3	2	35	10	3	60	Trap.	Infinite	20	Cont.	72	10	X	2.86	5000
1209-4	2	35	10	3	60	Trap.	Infinite	20	Cont.	72	8	K	2.86	5000
1209-5	2	35	10	3	60	Trap.	Infinite	20	Cont.	72	8	X	4.79	5000
1210-1	2	35	10	3	60	Trap.	Infinite	30	Cont.	72	8	X	2.86	5000
1211-1	2	35	10	3	60	Trap.	Infinite	20	Stag.	72	8	X	2.86	3600
1211-2	2	35	10	3	60	Trap.	Infinite	20	Stag.	72	8	X	2.86	5000
1211-3	2	35	10	3	60	Trap.	Infinite	20	Stag.	72	10	X	2.86	5000
1211-4	2	35	10	3	60	Trap.	Infinite	20	Stag.	72	8	K	2.86	5000
1211-5	2	35	10	3	60	Trap.	Infinite	20	Stag.	72	8	X	4.79	5000
1212-1	2	35	10	3	60	Trap.	Infinite	30	Stag.	72	8	X	2.86	5000
1213-1	2	35	10	5	0	Parallel	Infinite	20	Cont.	72	8	X	2.86	3600
1213-2	2	35	10	5	0	Parallel	Infinite	20	Cont.	72	8	X	2.86	5000
1213-3	2	35	10	5	0	Parallel	Infinite	20	Cont.	72	10	X	2.86	5000
1213-4	2	35	10	5	0	Parallel	Infinite	20	Cont.	72	8	K	2.86	5000
1213-5	2	35	10	5	0	Parallel	Infinite	20	Cont.	72	8	X	4.79	5000
1214-1	2	35	10	5	0	Parallel	Infinite	30	Cont.	72	8	X	2.86	5000
1215-1	2	35	10	5	30	Parallel	Infinite	20	Cont.	72	8	X	2.86	3600
1215-2	2	35	10	5	30	Parallel	Infinite	20	Cont.	72	8	X	2.86	5000
1215-3	2	35	10	5	30	Parallel	Infinite	20	Cont.	72	10	X	2.86	5000
1215-4	2	35	10	5	30	Parallel	Infinite	20	Cont.	72	8	K	2.86	5000
1215-5	2	35	10	5	30	Parallel	Infinite	20	Cont.	72	8	X	4.79	5000
1216-1	2	35	10	5	30	Parallel	Infinite	30	Cont.	72	8	X	2.86	5000
1217-1	2	35	10	5	60	Parallel	Infinite	20	Cont.	72	8	X	2.86	3600
1217-2	2	35	10	5	60	Parallel	Infinite	20	Cont.	72	8	X	2.86	5000
1217-3	2	35	10	5	60	Parallel	Infinite	20	Cont.	72	10	X	2.86	5000
1217-4	2	35	10	5	60	Parallel	Infinite	20	Cont.	72	8	K	2.86	5000
1217-5	2	35	10	5	60	Parallel	Infinite	20	Cont.	72	8	X	4.79	5000
1218-1	2	35	10	5	60	Parallel	Infinite	30	Cont.	72	8	X	2.86	5000
1219-1	2	35	10	5	60	Parallel	Infinite	20	Stag.	72	8	X	2.86	3600
1219-2	2	35	10	5	60	Parallel	Infinite	20	Stag.	72	8	X	2.86	5000
1219-3	2	35	10	5	60	Parallel	Infinite	20	Stag.	72	10	X	2.86	5000
1219-4	2	35	10	5	60	Parallel	Infinite	20	Stag.	72	8	K	2.86	5000
1219-5	2	35	10	5	60	Parallel	Infinite	20	Stag.	72	8	X	4.79	5000
1220-1	2	35	10	5	60	Parallel	Infinite	30	Stag.	72	8	X	2.86	5000
1221-1	2	35	10	5	60	Trap.	Infinite	20	Cont.	72	8	X	2.86	3600
1221-2	2	35	10	5	60	Trap.	Infinite	20	Cont.	72	8	X	2.86	5000
1221-3	2	35	10	5	60	Trap.	Infinite	20	Cont.	72	10	X	2.86	5000
1221-4	2	35	10	5	60	Trap.	Infinite	20	Cont.	72	8	K	2.86	5000
1221-5	2	35	10	5	60	Trap.	Infinite	20	Cont.	72	8	X	4.79	5000
1222-1	2	35	10	5	60	Trap.	Infinite	30	Cont.	72	8	X	2.86	5000
1223-1	2	35	10	5	60	Trap.	Infinite	20	Stag.	72	8	X	2.86	3600
1223-2	2	35	10	5	60	Trap.	Infinite	20	Stag.	72	8	X	2.86	5000
1223-3	2	35	10	5	60	Trap.	Infinite	20	Stag.	72	10	X	2.86	5000
1223-4	2	35	10	5	60	Trap.	Infinite	20	Stag.	72	8	K	2.86	5000
1223-5	2	35	10	5	60	Trap.	Infinite	20	Stag.	72	8	X	4.79	5000
1224-1	2	35	10	5	60	Trap.	Infinite	30	Stag.	72	8	X	2.86	5000
1225-1	2	35	10	7	0	Parallel	Infinite	20	Cont.	72	8	X	2.86	3600
1225-2	2	35	10	7	0	Parallel	Infinite	20	Cont.	72	8	X	2.86	5000
1225-3	2	35	10	7	0	Parallel	Infinite	20	Cont.	72	10	X	2.86	5000
1225-4	2	35	10	7	0	Parallel	Infinite	20	Cont.	72	8	K	2.86	5000
1225-5	2	35	10	7	0	Parallel	Infinite	20	Cont.	72	8	X	4.79	5000
1226-1	2	35	10	7	0	Parallel	Infinite	30	Cont.	72	8	X	2.86	5000
1227-1	2	35	10	7	30	Parallel	Infinite	20	Cont.	72	8	X	2.86	3600
1227-2	2	35	10	7	30	Parallel	Infinite	20	Cont.	72	8	X	2.86	5000
1227-3	2	35	10	7	30	Parallel	Infinite	20	Cont.	72	10	X	2.86	5000
1227-4	2	35	10	7	30	Parallel	Infinite	20	Cont.	72	8	K	2.86	5000
1227-5	2	35	10	7	30	Parallel	Infinite	20	Cont.	72	8	X	4.79	5000
1228-1	2	35	10	7	30	Parallel	Infinite	30	Cont.	72	8	X	2.86	5000
1229-1	2	35	10	7	60	Parallel	Infinite	20	Cont.	72	8	X	2.86	3600
1229-2	2	35	10	7	60	Parallel	Infinite	20	Cont.	72	8	X	2.86	5000
1229-3	2	35	10	7	60	Parallel	Infinite	20	Cont.	72	10	X	2.86	5000
1229-4	2	35	10	7	60	Parallel	Infinite	20	Cont.	72	8	K	2.86	5000
1229-5	2	35	10	7	60	Parallel	Infinite	20	Cont.	72	8	X	4.79	5000
1230-1	2	35	10	7	60	Parallel	Infinite	30	Cont.	72	8	X	2.86	5000
1231-1	2	35	10	7	60	Parallel	Infinite	20	Stag.	72	8	X	2.86	3600
1231-2	2	35	10	7	60	Parallel	Infinite	20	Stag.	72	8	X	2.86	5000
1231-3	2	35	10	7	60	Parallel	Infinite	20	Stag.	72	10	X	2.86	5000
1231-4	2	35	10	7	60	Parallel	Infinite	20	Stag.	72	8	K	2.86	5000
1231-5	2	35	10	7	60	Parallel	Infinite	20	Stag.	72	8	X	4.79	5000
1232-1	2	35	10	7	60	Parallel	Infinite	30	Stag.	72	8	X	2.86	5000
1233-1	2	35	10	7	60	Trap.	Infinite	20	Cont.	72	8	X	2.86	3600
1233-2	2	35	10	7	60	Trap.	Infinite	20	Cont.	72	8	X	2.86	5000
1233-3	2	35	10	7	60	Trap.	Infinite	20	Cont.	72	10	X	2.86	5000
1233-4	2	35	10	7	60	Trap.	Infinite	20	Cont.	72	8	K	2.86	5000
1233-5	2	35	10	7	60	Trap.	Infinite	20	Cont.	72	8	X	4.79	5000
1234-1	2	35	10	7	60	Trap.	Infinite	30	Cont.	72	8	X	2.86	5000
1235-1	2	35	10	7	60	Trap.	Infinite	20	Stag.	72	8	X	2.86	3600
1235-2	2	35	10	7	60	Trap.	Infinite	20	Stag.	72	8	X	2.86	5000
1235-3	2	35	10	7	60	Trap.	Infinite	20	Stag.	72	10	X	2.86	5000

Model ID	Geometry									Cross-section		CF detail		Mat'l
	n_{span}	L/d ratio	s_g [ft]	n_{girder}	Support skew [deg]; Layout		R [ft]	s_{cf} [ft]	CF layout	d_w [in]	t_{deck} [in]	CF type	A_{cf} [in^2]	E_c [ksi]
1235-4	2	35	10	7	60	Trap.	Infinite	20	Stag.	72	8	K	2.86	5000
1235-5	2	35	10	7	60	Trap.	Infinite	20	Stag.	72	8	X	4.79	5000
1236-1	2	35	10	7	60	Trap.	Infinite	30	Stag.	72	8	X	2.86	5000
1237-1	2	35	6	3	0	Parallel	Infinite	20	Cont.	96	8	X	2.86	3600
1237-2	2	35	6	3	0	Parallel	Infinite	20	Cont.	96	8	X	2.86	5000
1237-3	2	35	6	3	0	Parallel	Infinite	20	Cont.	96	10	X	2.86	5000
1237-4	2	35	6	3	0	Parallel	Infinite	20	Cont.	96	8	K	2.86	5000
1237-5	2	35	6	3	0	Parallel	Infinite	20	Cont.	96	8	X	4.79	5000
1238-1	2	35	6	3	0	Parallel	Infinite	30	Cont.	96	8	X	2.86	5000
1239-1	2	35	6	3	30	Parallel	Infinite	20	Cont.	96	8	X	2.86	3600
1239-2	2	35	6	3	30	Parallel	Infinite	20	Cont.	96	8	X	2.86	5000
1239-3	2	35	6	3	30	Parallel	Infinite	20	Cont.	96	10	X	2.86	5000
1239-4	2	35	6	3	30	Parallel	Infinite	20	Cont.	96	8	K	2.86	5000
1239-5	2	35	6	3	30	Parallel	Infinite	20	Cont.	96	8	X	4.79	5000
1240-1	2	35	6	3	30	Parallel	Infinite	30	Cont.	96	8	X	2.86	5000
1241-1	2	35	6	3	60	Parallel	Infinite	20	Cont.	96	8	X	2.86	3600
1241-2	2	35	6	3	60	Parallel	Infinite	20	Cont.	96	8	X	2.86	5000
1241-3	2	35	6	3	60	Parallel	Infinite	20	Cont.	96	10	X	2.86	5000
1241-4	2	35	6	3	60	Parallel	Infinite	20	Cont.	96	8	K	2.86	5000
1241-5	2	35	6	3	60	Parallel	Infinite	20	Cont.	96	8	X	4.79	5000
1242-1	2	35	6	3	60	Parallel	Infinite	30	Cont.	96	8	X	2.86	5000
1243-1	2	35	6	3	60	Parallel	Infinite	20	Stag.	96	8	X	2.86	3600
1243-2	2	35	6	3	60	Parallel	Infinite	20	Stag.	96	8	X	2.86	5000
1243-3	2	35	6	3	60	Parallel	Infinite	20	Stag.	96	10	X	2.86	5000
1243-4	2	35	6	3	60	Parallel	Infinite	20	Stag.	96	8	K	2.86	5000
1243-5	2	35	6	3	60	Parallel	Infinite	20	Stag.	96	8	X	4.79	5000
1244-1	2	35	6	3	60	Parallel	Infinite	30	Stag.	96	8	X	2.86	5000
1245-1	2	35	6	3	60	Trap.	Infinite	20	Cont.	96	8	X	2.86	3600
1245-2	2	35	6	3	60	Trap.	Infinite	20	Cont.	96	8	X	2.86	5000
1245-3	2	35	6	3	60	Trap.	Infinite	20	Cont.	96	10	X	2.86	5000
1245-4	2	35	6	3	60	Trap.	Infinite	20	Cont.	96	8	K	2.86	5000
1245-5	2	35	6	3	60	Trap.	Infinite	20	Cont.	96	8	X	4.79	5000
1246-1	2	35	6	3	60	Trap.	Infinite	30	Cont.	96	8	X	2.86	5000
1247-1	2	35	6	3	60	Trap.	Infinite	20	Stag.	96	8	X	2.86	3600
1247-2	2	35	6	3	60	Trap.	Infinite	20	Stag.	96	8	X	2.86	5000
1247-3	2	35	6	3	60	Trap.	Infinite	20	Stag.	96	10	X	2.86	5000
1247-4	2	35	6	3	60	Trap.	Infinite	20	Stag.	96	8	K	2.86	5000
1247-5	2	35	6	3	60	Trap.	Infinite	20	Stag.	96	8	X	4.79	5000
1248-1	2	35	6	3	60	Trap.	Infinite	30	Stag.	96	8	X	2.86	5000
1249-1	2	35	6	5	0	Parallel	Infinite	20	Cont.	96	8	X	2.86	3600
1249-2	2	35	6	5	0	Parallel	Infinite	20	Cont.	96	8	X	2.86	5000
1249-3	2	35	6	5	0	Parallel	Infinite	20	Cont.	96	10	X	2.86	5000
1249-4	2	35	6	5	0	Parallel	Infinite	20	Cont.	96	8	K	2.86	5000
1249-5	2	35	6	5	0	Parallel	Infinite	20	Cont.	96	8	X	4.79	5000
1250-1	2	35	6	5	0	Parallel	Infinite	30	Cont.	96	8	X	2.86	5000
1251-1	2	35	6	5	30	Parallel	Infinite	20	Cont.	96	8	X	2.86	3600
1251-2	2	35	6	5	30	Parallel	Infinite	20	Cont.	96	8	X	2.86	5000
1251-3	2	35	6	5	30	Parallel	Infinite	20	Cont.	96	10	X	2.86	5000
1251-4	2	35	6	5	30	Parallel	Infinite	20	Cont.	96	8	K	2.86	5000
1251-5	2	35	6	5	30	Parallel	Infinite	20	Cont.	96	8	X	4.79	5000
1252-1	2	35	6	5	30	Parallel	Infinite	30	Cont.	96	8	X	2.86	5000
1253-1	2	35	6	5	60	Parallel	Infinite	20	Cont.	96	8	X	2.86	3600
1253-2	2	35	6	5	60	Parallel	Infinite	20	Cont.	96	8	X	2.86	5000
1253-3	2	35	6	5	60	Parallel	Infinite	20	Cont.	96	10	X	2.86	5000
1253-4	2	35	6	5	60	Parallel	Infinite	20	Cont.	96	8	K	2.86	5000
1253-5	2	35	6	5	60	Parallel	Infinite	20	Cont.	96	8	X	4.79	5000
1254-1	2	35	6	5	60	Parallel	Infinite	30	Cont.	96	8	X	2.86	5000
1255-1	2	35	6	5	60	Parallel	Infinite	20	Stag.	96	8	X	2.86	3600
1255-2	2	35	6	5	60	Parallel	Infinite	20	Stag.	96	8	X	2.86	5000
1255-3	2	35	6	5	60	Parallel	Infinite	20	Stag.	96	10	X	2.86	5000
1255-4	2	35	6	5	60	Parallel	Infinite	20	Stag.	96	8	K	2.86	5000
1255-5	2	35	6	5	60	Parallel	Infinite	20	Stag.	96	8	X	4.79	5000
1256-1	2	35	6	5	60	Parallel	Infinite	30	Stag.	96	8	X	2.86	5000
1257-1	2	35	6	5	60	Trap.	Infinite	20	Cont.	96	8	X	2.86	3600
1257-2	2	35	6	5	60	Trap.	Infinite	20	Cont.	96	8	X	2.86	5000
1257-3	2	35	6	5	60	Trap.	Infinite	20	Cont.	96	10	X	2.86	5000
1257-4	2	35	6	5	60	Trap.	Infinite	20	Cont.	96	8	K	2.86	5000
1257-5	2	35	6	5	60	Trap.	Infinite	20	Cont.	96	8	X	4.79	5000
1258-1	2	35	6	5	60	Trap.	Infinite	30	Cont.	96	8	X	2.86	5000
1259-1	2	35	6	5	60	Trap.	Infinite	20	Stag.	96	8	X	2.86	3600
1259-2	2	35	6	5	60	Trap.	Infinite	20	Stag.	96	8	X	2.86	5000
1259-3	2	35	6	5	60	Trap.	Infinite	20	Stag.	96	10	X	2.86	5000
1259-4	2	35	6	5	60	Trap.	Infinite	20	Stag.	96	8	K	2.86	5000
1259-5	2	35	6	5	60	Trap.	Infinite	20	Stag.	96	8	X	4.79	5000
1260-1	2	35	6	5	60	Trap.	Infinite	30	Stag.	96	8	X	2.86	5000
1261-1	2	35	6	7	0	Parallel	Infinite	20	Cont.	96	8	X	2.86	3600
1261-2	2	35	6	7	0	Parallel	Infinite	20	Cont.	96	8	X	2.86	5000
1261-3	2	35	6	7	0	Parallel	Infinite	20	Cont.	96	10	X	2.86	5000
1261-4	2	35	6	7	0	Parallel	Infinite	20	Cont.	96	8	K	2.86	5000

Model ID	Geometry									Cross-section		CF detail		Mat'l
	n_{span}	L/d ratio	s_g [ft]	n_{girder}	Support skew [deg]; Layout		R [ft]	s_{cf} [ft]	CF layout	d_w [in]	t_{deck} [in]	CF type	A_{cf} [in^2]	E_c [ksi]
1261-5	2	35	6	7	0	Parallel	Infinite	20	Cont.	96	8	X	4.79	5000
1262-1	2	35	6	7	0	Parallel	Infinite	30	Cont.	96	8	X	2.86	5000
1263-1	2	35	6	7	30	Parallel	Infinite	20	Cont.	96	8	X	2.86	3600
1263-2	2	35	6	7	30	Parallel	Infinite	20	Cont.	96	8	X	2.86	5000
1263-3	2	35	6	7	30	Parallel	Infinite	20	Cont.	96	10	X	2.86	5000
1263-4	2	35	6	7	30	Parallel	Infinite	20	Cont.	96	8	K	2.86	5000
1263-5	2	35	6	7	30	Parallel	Infinite	20	Cont.	96	8	X	4.79	5000
1264-1	2	35	6	7	30	Parallel	Infinite	30	Cont.	96	8	X	2.86	5000
1265-1	2	35	6	7	60	Parallel	Infinite	20	Cont.	96	8	X	2.86	3600
1265-2	2	35	6	7	60	Parallel	Infinite	20	Cont.	96	8	X	2.86	5000
1265-3	2	35	6	7	60	Parallel	Infinite	20	Cont.	96	10	X	2.86	5000
1265-4	2	35	6	7	60	Parallel	Infinite	20	Cont.	96	8	K	2.86	5000
1265-5	2	35	6	7	60	Parallel	Infinite	20	Cont.	96	8	X	4.79	5000
1266-1	2	35	6	7	60	Parallel	Infinite	30	Cont.	96	8	X	2.86	5000
1267-1	2	35	6	7	60	Parallel	Infinite	20	Stag.	96	8	X	2.86	3600
1267-2	2	35	6	7	60	Parallel	Infinite	20	Stag.	96	8	X	2.86	5000
1267-3	2	35	6	7	60	Parallel	Infinite	20	Stag.	96	10	X	2.86	5000
1267-4	2	35	6	7	60	Parallel	Infinite	20	Stag.	96	8	K	2.86	5000
1267-5	2	35	6	7	60	Parallel	Infinite	20	Stag.	96	8	X	4.79	5000
1268-1	2	35	6	7	60	Parallel	Infinite	30	Stag.	96	8	X	2.86	5000
1269-1	2	35	6	7	60	Trap.	Infinite	20	Cont.	96	8	X	2.86	3600
1269-2	2	35	6	7	60	Trap.	Infinite	20	Cont.	96	8	X	2.86	5000
1269-3	2	35	6	7	60	Trap.	Infinite	20	Cont.	96	10	X	2.86	5000
1269-4	2	35	6	7	60	Trap.	Infinite	20	Cont.	96	8	K	2.86	5000
1269-5	2	35	6	7	60	Trap.	Infinite	20	Cont.	96	8	X	4.79	5000
1270-1	2	35	6	7	60	Trap.	Infinite	30	Cont.	96	8	X	2.86	5000
1271-1	2	35	6	7	60	Trap.	Infinite	20	Stag.	96	8	X	2.86	3600
1271-2	2	35	6	7	60	Trap.	Infinite	20	Stag.	96	8	X	2.86	5000
1271-3	2	35	6	7	60	Trap.	Infinite	20	Stag.	96	10	X	2.86	5000
1271-4	2	35	6	7	60	Trap.	Infinite	20	Stag.	96	8	K	2.86	5000
1271-5	2	35	6	7	60	Trap.	Infinite	20	Stag.	96	8	X	4.79	5000
1272-1	2	35	6	7	60	Trap.	Infinite	30	Stag.	96	8	X	2.86	5000
1273-1	2	35	8	3	0	Parallel	Infinite	20	Cont.	96	8	X	2.86	3600
1273-2	2	35	8	3	0	Parallel	Infinite	20	Cont.	96	8	X	2.86	5000
1273-3	2	35	8	3	0	Parallel	Infinite	20	Cont.	96	10	X	2.86	5000
1273-4	2	35	8	3	0	Parallel	Infinite	20	Cont.	96	8	K	2.86	5000
1273-5	2	35	8	3	0	Parallel	Infinite	20	Cont.	96	8	X	4.79	5000
1274-1	2	35	8	3	0	Parallel	Infinite	30	Cont.	96	8	X	2.86	5000
1275-1	2	35	8	3	30	Parallel	Infinite	20	Cont.	96	8	X	2.86	3600
1275-2	2	35	8	3	30	Parallel	Infinite	20	Cont.	96	8	X	2.86	5000
1275-3	2	35	8	3	30	Parallel	Infinite	20	Cont.	96	10	X	2.86	5000
1275-4	2	35	8	3	30	Parallel	Infinite	20	Cont.	96	8	K	2.86	5000
1275-5	2	35	8	3	30	Parallel	Infinite	20	Cont.	96	8	X	4.79	5000
1276-1	2	35	8	3	30	Parallel	Infinite	30	Cont.	96	8	X	2.86	5000
1277-1	2	35	8	3	60	Parallel	Infinite	20	Cont.	96	8	X	2.86	3600
1277-2	2	35	8	3	60	Parallel	Infinite	20	Cont.	96	8	X	2.86	5000
1277-3	2	35	8	3	60	Parallel	Infinite	20	Cont.	96	10	X	2.86	5000
1277-4	2	35	8	3	60	Parallel	Infinite	20	Cont.	96	8	K	2.86	5000
1277-5	2	35	8	3	60	Parallel	Infinite	20	Cont.	96	8	X	4.79	5000
1278-1	2	35	8	3	60	Parallel	Infinite	30	Cont.	96	8	X	2.86	5000
1279-1	2	35	8	3	60	Parallel	Infinite	20	Stag.	96	8	X	2.86	3600
1279-2	2	35	8	3	60	Parallel	Infinite	20	Stag.	96	8	X	2.86	5000
1279-3	2	35	8	3	60	Parallel	Infinite	20	Stag.	96	10	X	2.86	5000
1279-4	2	35	8	3	60	Parallel	Infinite	20	Stag.	96	8	K	2.86	5000
1279-5	2	35	8	3	60	Parallel	Infinite	20	Stag.	96	8	X	4.79	5000
1280-1	2	35	8	3	60	Parallel	Infinite	30	Stag.	96	8	X	2.86	5000
1281-1	2	35	8	3	60	Trap.	Infinite	20	Cont.	96	8	X	2.86	3600
1281-2	2	35	8	3	60	Trap.	Infinite	20	Cont.	96	8	X	2.86	5000
1281-3	2	35	8	3	60	Trap.	Infinite	20	Cont.	96	10	X	2.86	5000
1281-4	2	35	8	3	60	Trap.	Infinite	20	Cont.	96	8	K	2.86	5000
1281-5	2	35	8	3	60	Trap.	Infinite	20	Cont.	96	8	X	4.79	5000
1282-1	2	35	8	3	60	Trap.	Infinite	30	Cont.	96	8	X	2.86	5000
1283-1	2	35	8	3	60	Trap.	Infinite	20	Stag.	96	8	X	2.86	3600
1283-2	2	35	8	3	60	Trap.	Infinite	20	Stag.	96	8	X	2.86	5000
1283-3	2	35	8	3	60	Trap.	Infinite	20	Stag.	96	10	X	2.86	5000
1283-4	2	35	8	3	60	Trap.	Infinite	20	Stag.	96	8	K	2.86	5000
1283-5	2	35	8	3	60	Trap.	Infinite	20	Stag.	96	8	X	4.79	5000
1284-1	2	35	8	3	60	Trap.	Infinite	30	Stag.	96	8	X	2.86	5000
1285-1	2	35	8	5	0	Parallel	Infinite	20	Cont.	96	8	X	2.86	3600
1285-2	2	35	8	5	0	Parallel	Infinite	20	Cont.	96	8	X	2.86	5000
1285-3	2	35	8	5	0	Parallel	Infinite	20	Cont.	96	10	X	2.86	5000
1285-4	2	35	8	5	0	Parallel	Infinite	20	Cont.	96	8	K	2.86	5000
1285-5	2	35	8	5	0	Parallel	Infinite	20	Cont.	96	8	X	4.79	5000
1286-1	2	35	8	5	0	Parallel	Infinite	30	Cont.	96	8	X	2.86	5000
1287-1	2	35	8	5	30	Parallel	Infinite	20	Cont.	96	8	X	2.86	3600
1287-2	2	35	8	5	30	Parallel	Infinite	20	Cont.	96	8	X	2.86	5000
1287-3	2	35	8	5	30	Parallel	Infinite	20	Cont.	96	10	X	2.86	5000
1287-4	2	35	8	5	30	Parallel	Infinite	20	Cont.	96	8	K	2.86	5000
1287-5	2	35	8	5	30	Parallel	Infinite	20	Cont.	96	8	X	4.79	5000

Model ID	Geometry									Cross-section		CF detail		Mat'l
	n_{span}	L/d ratio	s_g [ft]	n_{girder}	Support skew [deg]; Layout		R [ft]	s_{cf} [ft]	CF layout	d_w [in]	t_{deck} [in]	CF type	A_{cf} [in^2]	E_c [ksi]
1288-1	2	35	8	5	30	Parallel	Infinite	30	Cont.	96	8	X	2.86	5000
1289-1	2	35	8	5	60	Parallel	Infinite	20	Cont.	96	8	X	2.86	3600
1289-2	2	35	8	5	60	Parallel	Infinite	20	Cont.	96	8	X	2.86	5000
1289-3	2	35	8	5	60	Parallel	Infinite	20	Cont.	96	10	X	2.86	5000
1289-4	2	35	8	5	60	Parallel	Infinite	20	Cont.	96	8	K	2.86	5000
1289-5	2	35	8	5	60	Parallel	Infinite	20	Cont.	96	8	X	4.79	5000
1290-1	2	35	8	5	60	Parallel	Infinite	30	Cont.	96	8	X	2.86	5000
1291-1	2	35	8	5	60	Parallel	Infinite	20	Stag.	96	8	X	2.86	3600
1291-2	2	35	8	5	60	Parallel	Infinite	20	Stag.	96	8	X	2.86	5000
1291-3	2	35	8	5	60	Parallel	Infinite	20	Stag.	96	10	X	2.86	5000
1291-4	2	35	8	5	60	Parallel	Infinite	20	Stag.	96	8	K	2.86	5000
1291-5	2	35	8	5	60	Parallel	Infinite	20	Stag.	96	8	X	4.79	5000
1292-1	2	35	8	5	60	Parallel	Infinite	30	Stag.	96	8	X	2.86	5000
1293-1	2	35	8	5	60	Trap.	Infinite	20	Cont.	96	8	X	2.86	3600
1293-2	2	35	8	5	60	Trap.	Infinite	20	Cont.	96	8	X	2.86	5000
1293-3	2	35	8	5	60	Trap.	Infinite	20	Cont.	96	10	X	2.86	5000
1293-4	2	35	8	5	60	Trap.	Infinite	20	Cont.	96	8	K	2.86	5000
1293-5	2	35	8	5	60	Trap.	Infinite	20	Cont.	96	8	X	4.79	5000
1294-1	2	35	8	5	60	Trap.	Infinite	30	Cont.	96	8	X	2.86	5000
1295-1	2	35	8	5	60	Trap.	Infinite	20	Stag.	96	8	X	2.86	3600
1295-2	2	35	8	5	60	Trap.	Infinite	20	Stag.	96	8	X	2.86	5000
1295-3	2	35	8	5	60	Trap.	Infinite	20	Stag.	96	10	X	2.86	5000
1295-4	2	35	8	5	60	Trap.	Infinite	20	Stag.	96	8	K	2.86	5000
1295-5	2	35	8	5	60	Trap.	Infinite	20	Stag.	96	8	X	4.79	5000
1296-1	2	35	8	5	60	Trap.	Infinite	30	Stag.	96	8	X	2.86	5000
1297-1	2	35	8	7	0	Parallel	Infinite	20	Cont.	96	8	X	2.86	3600
1297-2	2	35	8	7	0	Parallel	Infinite	20	Cont.	96	8	X	2.86	5000
1297-3	2	35	8	7	0	Parallel	Infinite	20	Cont.	96	10	X	2.86	5000
1297-4	2	35	8	7	0	Parallel	Infinite	20	Cont.	96	8	K	2.86	5000
1297-5	2	35	8	7	0	Parallel	Infinite	20	Cont.	96	8	X	4.79	5000
1298-1	2	35	8	7	0	Parallel	Infinite	30	Cont.	96	8	X	2.86	5000
1299-1	2	35	8	7	30	Parallel	Infinite	20	Cont.	96	8	X	2.86	3600
1299-2	2	35	8	7	30	Parallel	Infinite	20	Cont.	96	8	X	2.86	5000
1299-3	2	35	8	7	30	Parallel	Infinite	20	Cont.	96	10	X	2.86	5000
1299-4	2	35	8	7	30	Parallel	Infinite	20	Cont.	96	8	K	2.86	5000
1299-5	2	35	8	7	30	Parallel	Infinite	20	Cont.	96	8	X	4.79	5000
1300-1	2	35	8	7	30	Parallel	Infinite	30	Cont.	96	8	X	2.86	5000
1301-1	2	35	8	7	60	Parallel	Infinite	20	Cont.	96	8	X	2.86	3600
1301-2	2	35	8	7	60	Parallel	Infinite	20	Cont.	96	8	X	2.86	5000
1301-3	2	35	8	7	60	Parallel	Infinite	20	Cont.	96	10	X	2.86	5000
1301-4	2	35	8	7	60	Parallel	Infinite	20	Cont.	96	8	K	2.86	5000
1301-5	2	35	8	7	60	Parallel	Infinite	20	Cont.	96	8	X	4.79	5000
1302-1	2	35	8	7	60	Parallel	Infinite	30	Cont.	96	8	X	2.86	5000
1303-1	2	35	8	7	60	Parallel	Infinite	20	Stag.	96	8	X	2.86	3600
1303-2	2	35	8	7	60	Parallel	Infinite	20	Stag.	96	8	X	2.86	5000
1303-3	2	35	8	7	60	Parallel	Infinite	20	Stag.	96	10	X	2.86	5000
1303-4	2	35	8	7	60	Parallel	Infinite	20	Stag.	96	8	K	2.86	5000
1303-5	2	35	8	7	60	Parallel	Infinite	20	Stag.	96	8	X	4.79	5000
1304-1	2	35	8	7	60	Parallel	Infinite	30	Stag.	96	8	X	2.86	5000
1305-1	2	35	8	7	60	Trap.	Infinite	20	Cont.	96	8	X	2.86	3600
1305-2	2	35	8	7	60	Trap.	Infinite	20	Cont.	96	8	X	2.86	5000
1305-3	2	35	8	7	60	Trap.	Infinite	20	Cont.	96	10	X	2.86	5000
1305-4	2	35	8	7	60	Trap.	Infinite	20	Cont.	96	8	K	2.86	5000
1305-5	2	35	8	7	60	Trap.	Infinite	20	Cont.	96	8	X	4.79	5000
1306-1	2	35	8	7	60	Trap.	Infinite	30	Cont.	96	8	X	2.86	5000
1307-1	2	35	8	7	60	Trap.	Infinite	20	Stag.	96	8	X	2.86	3600
1307-2	2	35	8	7	60	Trap.	Infinite	20	Stag.	96	8	X	2.86	5000
1307-3	2	35	8	7	60	Trap.	Infinite	20	Stag.	96	10	X	2.86	5000
1307-4	2	35	8	7	60	Trap.	Infinite	20	Stag.	96	8	K	2.86	5000
1307-5	2	35	8	7	60	Trap.	Infinite	20	Stag.	96	8	X	4.79	5000
1308-1	2	35	8	7	60	Trap.	Infinite	30	Stag.	96	8	X	2.86	5000
1309-1	2	35	10	3	0	Parallel	Infinite	20	Cont.	96	8	X	2.86	3600
1309-2	2	35	10	3	0	Parallel	Infinite	20	Cont.	96	8	X	2.86	5000
1309-3	2	35	10	3	0	Parallel	Infinite	20	Cont.	96	10	X	2.86	5000
1309-4	2	35	10	3	0	Parallel	Infinite	20	Cont.	96	8	K	2.86	5000
1309-5	2	35	10	3	0	Parallel	Infinite	20	Cont.	96	8	X	4.79	5000
1310-1	2	35	10	3	0	Parallel	Infinite	30	Cont.	96	8	X	2.86	5000
1311-1	2	35	10	3	30	Parallel	Infinite	20	Cont.	96	8	X	2.86	3600
1311-2	2	35	10	3	30	Parallel	Infinite	20	Cont.	96	8	X	2.86	5000
1311-3	2	35	10	3	30	Parallel	Infinite	20	Cont.	96	10	X	2.86	5000
1311-4	2	35	10	3	30	Parallel	Infinite	20	Cont.	96	8	K	2.86	5000
1311-5	2	35	10	3	30	Parallel	Infinite	20	Cont.	96	8	X	4.79	5000
1312-1	2	35	10	3	30	Parallel	Infinite	30	Cont.	96	8	X	2.86	5000
1313-1	2	35	10	3	60	Parallel	Infinite	20	Cont.	96	8	X	2.86	3600
1313-2	2	35	10	3	60	Parallel	Infinite	20	Cont.	96	8	X	2.86	5000
1313-3	2	35	10	3	60	Parallel	Infinite	20	Cont.	96	10	X	2.86	5000
1313-4	2	35	10	3	60	Parallel	Infinite	20	Cont.	96	8	K	2.86	5000
1313-5	2	35	10	3	60	Parallel	Infinite	20	Cont.	96	8	X	4.79	5000
1314-1	2	35	10	3	60	Parallel	Infinite	30	Cont.	96	8	X	2.86	5000

Model ID	Geometry									Cross-section		CF detail		Mat'l
	n_{span}	L/d ratio	s_g [ft]	n_{girder}	Support skew [deg]; Layout		R [ft]	s_{cf} [ft]	CF layout	d_w [in]	t_{deck} [in]	CF type	A_{cf} [in^2]	E_c [ksi]
1315-1	2	35	10	3	60	Parallel	Infinite	20	Stag.	96	8	X	2.86	3600
1315-2	2	35	10	3	60	Parallel	Infinite	20	Stag.	96	8	X	2.86	5000
1315-3	2	35	10	3	60	Parallel	Infinite	20	Stag.	96	10	X	2.86	5000
1315-4	2	35	10	3	60	Parallel	Infinite	20	Stag.	96	8	K	2.86	5000
1315-5	2	35	10	3	60	Parallel	Infinite	20	Stag.	96	8	X	4.79	5000
1316-1	2	35	10	3	60	Parallel	Infinite	30	Stag.	96	8	X	2.86	5000
1317-1	2	35	10	3	60	Trap.	Infinite	20	Cont.	96	8	X	2.86	3600
1317-2	2	35	10	3	60	Trap.	Infinite	20	Cont.	96	8	X	2.86	5000
1317-3	2	35	10	3	60	Trap.	Infinite	20	Cont.	96	10	X	2.86	5000
1317-4	2	35	10	3	60	Trap.	Infinite	20	Cont.	96	8	K	2.86	5000
1317-5	2	35	10	3	60	Trap.	Infinite	20	Cont.	96	8	X	4.79	5000
1318-1	2	35	10	3	60	Trap.	Infinite	30	Cont.	96	8	X	2.86	5000
1319-1	2	35	10	3	60	Trap.	Infinite	20	Stag.	96	8	X	2.86	3600
1319-2	2	35	10	3	60	Trap.	Infinite	20	Stag.	96	8	X	2.86	5000
1319-3	2	35	10	3	60	Trap.	Infinite	20	Stag.	96	10	X	2.86	5000
1319-4	2	35	10	3	60	Trap.	Infinite	20	Stag.	96	8	K	2.86	5000
1319-5	2	35	10	3	60	Trap.	Infinite	20	Stag.	96	8	X	4.79	5000
1320-1	2	35	10	3	60	Trap.	Infinite	30	Stag.	96	8	X	2.86	5000
1321-1	2	35	10	5	0	Parallel	Infinite	20	Cont.	96	8	X	2.86	3600
1321-2	2	35	10	5	0	Parallel	Infinite	20	Cont.	96	8	X	2.86	5000
1321-3	2	35	10	5	0	Parallel	Infinite	20	Cont.	96	10	X	2.86	5000
1321-4	2	35	10	5	0	Parallel	Infinite	20	Cont.	96	8	K	2.86	5000
1321-5	2	35	10	5	0	Parallel	Infinite	20	Cont.	96	8	X	4.79	5000
1322-1	2	35	10	5	0	Parallel	Infinite	30	Cont.	96	8	X	2.86	5000
1323-1	2	35	10	5	30	Parallel	Infinite	20	Cont.	96	8	X	2.86	3600
1323-2	2	35	10	5	30	Parallel	Infinite	20	Cont.	96	8	X	2.86	5000
1323-3	2	35	10	5	30	Parallel	Infinite	20	Cont.	96	10	X	2.86	5000
1323-4	2	35	10	5	30	Parallel	Infinite	20	Cont.	96	8	K	2.86	5000
1323-5	2	35	10	5	30	Parallel	Infinite	20	Cont.	96	8	X	4.79	5000
1324-1	2	35	10	5	30	Parallel	Infinite	30	Cont.	96	8	X	2.86	5000
1325-1	2	35	10	5	60	Parallel	Infinite	20	Cont.	96	8	X	2.86	3600
1325-2	2	35	10	5	60	Parallel	Infinite	20	Cont.	96	8	X	2.86	5000
1325-3	2	35	10	5	60	Parallel	Infinite	20	Cont.	96	10	X	2.86	5000
1325-4	2	35	10	5	60	Parallel	Infinite	20	Cont.	96	8	K	2.86	5000
1325-5	2	35	10	5	60	Parallel	Infinite	20	Cont.	96	8	X	4.79	5000
1326-1	2	35	10	5	60	Parallel	Infinite	30	Cont.	96	8	X	2.86	5000
1327-1	2	35	10	5	60	Parallel	Infinite	20	Stag.	96	8	X	2.86	3600
1327-2	2	35	10	5	60	Parallel	Infinite	20	Stag.	96	8	X	2.86	5000
1327-3	2	35	10	5	60	Parallel	Infinite	20	Stag.	96	10	X	2.86	5000
1327-4	2	35	10	5	60	Parallel	Infinite	20	Stag.	96	8	K	2.86	5000
1327-5	2	35	10	5	60	Parallel	Infinite	20	Stag.	96	8	X	4.79	5000
1328-1	2	35	10	5	60	Parallel	Infinite	30	Stag.	96	8	X	2.86	5000
1329-1	2	35	10	5	60	Trap.	Infinite	20	Cont.	96	8	X	2.86	3600
1329-2	2	35	10	5	60	Trap.	Infinite	20	Cont.	96	8	X	2.86	5000
1329-3	2	35	10	5	60	Trap.	Infinite	20	Cont.	96	10	X	2.86	5000
1329-4	2	35	10	5	60	Trap.	Infinite	20	Cont.	96	8	K	2.86	5000
1329-5	2	35	10	5	60	Trap.	Infinite	20	Cont.	96	8	X	4.79	5000
1330-1	2	35	10	5	60	Trap.	Infinite	30	Cont.	96	8	X	2.86	5000
1331-1	2	35	10	5	60	Trap.	Infinite	20	Stag.	96	8	X	2.86	3600
1331-2	2	35	10	5	60	Trap.	Infinite	20	Stag.	96	8	X	2.86	5000
1331-3	2	35	10	5	60	Trap.	Infinite	20	Stag.	96	10	X	2.86	5000
1331-4	2	35	10	5	60	Trap.	Infinite	20	Stag.	96	8	K	2.86	5000
1331-5	2	35	10	5	60	Trap.	Infinite	20	Stag.	96	8	X	4.79	5000
1332-1	2	35	10	5	60	Trap.	Infinite	30	Stag.	96	8	X	2.86	5000
1333-1	2	35	10	7	0	Parallel	Infinite	20	Cont.	96	8	X	2.86	3600
1333-2	2	35	10	7	0	Parallel	Infinite	20	Cont.	96	8	X	2.86	5000
1333-3	2	35	10	7	0	Parallel	Infinite	20	Cont.	96	10	X	2.86	5000
1333-4	2	35	10	7	0	Parallel	Infinite	20	Cont.	96	8	K	2.86	5000
1333-5	2	35	10	7	0	Parallel	Infinite	20	Cont.	96	8	X	4.79	5000
1334-1	2	35	10	7	0	Parallel	Infinite	30	Cont.	96	8	X	2.86	5000
1335-1	2	35	10	7	30	Parallel	Infinite	20	Cont.	96	8	X	2.86	3600
1335-2	2	35	10	7	30	Parallel	Infinite	20	Cont.	96	8	X	2.86	5000
1335-3	2	35	10	7	30	Parallel	Infinite	20	Cont.	96	10	X	2.86	5000
1335-4	2	35	10	7	30	Parallel	Infinite	20	Cont.	96	8	K	2.86	5000
1335-5	2	35	10	7	30	Parallel	Infinite	20	Cont.	96	8	X	4.79	5000
1336-1	2	35	10	7	30	Parallel	Infinite	30	Cont.	96	8	X	2.86	5000
1337-1	2	35	10	7	60	Parallel	Infinite	20	Cont.	96	8	X	2.86	3600
1337-2	2	35	10	7	60	Parallel	Infinite	20	Cont.	96	8	X	2.86	5000
1337-3	2	35	10	7	60	Parallel	Infinite	20	Cont.	96	10	X	2.86	5000
1337-4	2	35	10	7	60	Parallel	Infinite	20	Cont.	96	8	K	2.86	5000
1337-5	2	35	10	7	60	Parallel	Infinite	20	Cont.	96	8	X	4.79	5000
1338-1	2	35	10	7	60	Parallel	Infinite	30	Cont.	96	8	X	2.86	5000
1339-1	2	35	10	7	60	Parallel	Infinite	20	Stag.	96	8	X	2.86	3600
1339-2	2	35	10	7	60	Parallel	Infinite	20	Stag.	96	8	X	2.86	5000
1339-3	2	35	10	7	60	Parallel	Infinite	20	Stag.	96	10	X	2.86	5000
1339-4	2	35	10	7	60	Parallel	Infinite	20	Stag.	96	8	K	2.86	5000
1339-5	2	35	10	7	60	Parallel	Infinite	20	Stag.	96	8	X	4.79	5000
1340-1	2	35	10	7	60	Parallel	Infinite	30	Stag.	96	8	X	2.86	5000
1341-1	2	35	10	7	60	Trap.	Infinite	20	Cont.	96	8	X	2.86	3600

Model ID	Geometry									Cross-section		CF detail		Mat'l
	n_{span}	L/d ratio	s_g [ft]	n_{girder}	Support skew [deg]; Layout		R [ft]	s_{cf} [ft]	CF layout	d_w [in]	t_{deck} [in]	CF type	A_{cf} [in^2]	E_c [ksi]
1341-2	2	35	10	7	60	Trap.	Infinite	20	Cont.	96	8	X	2.86	5000
1341-3	2	35	10	7	60	Trap.	Infinite	20	Cont.	96	10	X	2.86	5000
1341-4	2	35	10	7	60	Trap.	Infinite	20	Cont.	96	8	K	2.86	5000
1341-5	2	35	10	7	60	Trap.	Infinite	20	Cont.	96	8	X	4.79	5000
1342-1	2	35	10	7	60	Trap.	Infinite	30	Cont.	96	8	X	2.86	5000
1343-1	2	35	10	7	60	Trap.	Infinite	20	Stag.	96	8	X	2.86	3600
1343-2	2	35	10	7	60	Trap.	Infinite	20	Stag.	96	8	X	2.86	5000
1343-3	2	35	10	7	60	Trap.	Infinite	20	Stag.	96	10	X	2.86	5000
1343-4	2	35	10	7	60	Trap.	Infinite	20	Stag.	96	8	K	2.86	5000
1343-5	2	35	10	7	60	Trap.	Infinite	20	Stag.	96	8	X	4.79	5000
1344-1	2	35	10	7	60	Trap.	Infinite	30	Stag.	96	8	X	2.86	5000
1345-1	3	25	6	3	0	Parallel	1500	20	Cont.	72	8	X	2.86	5000
1345-2	3	25	6	3	0	Parallel	1500	20	Cont.	72	8	X	4.79	5000
1346-1	3	25	6	3	0	Parallel	750	20	Cont.	72	8	X	2.86	5000
1346-2	3	25	6	3	0	Parallel	750	20	Cont.	72	8	X	4.79	5000
1347-1	3	25	6	5	0	Parallel	1500	20	Cont.	72	8	X	2.86	5000
1347-2	3	25	6	5	0	Parallel	1500	20	Cont.	72	8	X	4.79	5000
1348-1	3	25	6	5	0	Parallel	750	20	Cont.	72	8	X	2.86	5000
1348-2	3	25	6	5	0	Parallel	750	20	Cont.	72	8	X	4.79	5000
1349-1	3	25	8	3	0	Parallel	1500	20	Cont.	72	8	X	2.86	5000
1349-2	3	25	8	3	0	Parallel	1500	20	Cont.	72	8	X	4.79	5000
1350-1	3	25	8	3	0	Parallel	750	20	Cont.	72	8	X	2.86	5000
1350-2	3	25	8	3	0	Parallel	750	20	Cont.	72	8	X	4.79	5000
1351-1	3	25	8	5	0	Parallel	1500	20	Cont.	72	8	X	2.86	5000
1351-2	3	25	8	5	0	Parallel	1500	20	Cont.	72	8	X	4.79	5000
1352-1	3	25	8	5	0	Parallel	750	20	Cont.	72	8	X	2.86	5000
1352-2	3	25	8	5	0	Parallel	750	20	Cont.	72	8	X	4.79	5000
1353-1	3	25	10	3	0	Parallel	1500	20	Cont.	72	8	X	2.86	5000
1353-2	3	25	10	3	0	Parallel	1500	20	Cont.	72	8	X	4.79	5000
1354-1	3	25	10	3	0	Parallel	750	20	Cont.	72	8	X	2.86	5000
1354-2	3	25	10	3	0	Parallel	750	20	Cont.	72	8	X	4.79	5000
1355-1	3	25	10	5	0	Parallel	1500	20	Cont.	72	8	X	2.86	5000
1355-2	3	25	10	5	0	Parallel	1500	20	Cont.	72	8	X	4.79	5000
1356-1	3	25	10	5	0	Parallel	750	20	Cont.	72	8	X	2.86	5000
1356-2	3	25	10	5	0	Parallel	750	20	Cont.	72	8	X	4.79	5000
1357-1	3	25	6	3	0	Parallel	1500	20	Cont.	96	8	X	2.86	5000
1357-2	3	25	6	3	0	Parallel	1500	20	Cont.	96	8	X	4.79	5000
1358-1	3	25	6	3	0	Parallel	750	20	Cont.	96	8	X	2.86	5000
1358-2	3	25	6	3	0	Parallel	750	20	Cont.	96	8	X	4.79	5000
1359-1	3	25	6	5	0	Parallel	1500	20	Cont.	96	8	X	2.86	5000
1359-2	3	25	6	5	0	Parallel	1500	20	Cont.	96	8	X	4.79	5000
1360-1	3	25	6	5	0	Parallel	750	20	Cont.	96	8	X	2.86	5000
1360-2	3	25	6	5	0	Parallel	750	20	Cont.	96	8	X	4.79	5000
1361-1	3	25	8	3	0	Parallel	1500	20	Cont.	96	8	X	2.86	5000
1361-2	3	25	8	3	0	Parallel	1500	20	Cont.	96	8	X	4.79	5000
1362-1	3	25	8	3	0	Parallel	750	20	Cont.	96	8	X	2.86	5000
1362-2	3	25	8	3	0	Parallel	750	20	Cont.	96	8	X	4.79	5000
1363-1	3	25	8	5	0	Parallel	1500	20	Cont.	96	8	X	2.86	5000
1363-2	3	25	8	5	0	Parallel	1500	20	Cont.	96	8	X	4.79	5000
1364-1	3	25	8	5	0	Parallel	750	20	Cont.	96	8	X	2.86	5000
1364-2	3	25	8	5	0	Parallel	750	20	Cont.	96	8	X	4.79	5000
1365-1	3	25	10	3	0	Parallel	1500	20	Cont.	96	8	X	2.86	5000
1365-2	3	25	10	3	0	Parallel	1500	20	Cont.	96	8	X	4.79	5000
1366-1	3	25	10	3	0	Parallel	750	20	Cont.	96	8	X	2.86	5000
1366-2	3	25	10	3	0	Parallel	750	20	Cont.	96	8	X	4.79	5000
1367-1	3	25	10	5	0	Parallel	1500	20	Cont.	96	8	X	2.86	5000
1367-2	3	25	10	5	0	Parallel	1500	20	Cont.	96	8	X	4.79	5000
1368-1	3	25	10	5	0	Parallel	750	20	Cont.	96	8	X	2.86	5000
1368-2	3	25	10	5	0	Parallel	750	20	Cont.	96	8	X	4.79	5000
1369-1	3	30	6	3	0	Parallel	Infinite	20	Cont.	72	8	X	2.86	5000
1369-2	3	30	6	3	0	Parallel	Infinite	20	Cont.	72	8	X	4.79	5000
1370-1	3	30	6	5	0	Parallel	Infinite	20	Cont.	72	8	X	2.86	5000
1370-2	3	30	6	5	0	Parallel	Infinite	20	Cont.	72	8	X	4.79	5000
1371-1	3	30	8	3	0	Parallel	Infinite	20	Cont.	72	8	X	2.86	5000
1371-2	3	30	8	3	0	Parallel	Infinite	20	Cont.	72	8	X	4.79	5000
1372-1	3	30	8	5	0	Parallel	Infinite	20	Cont.	72	8	X	2.86	5000
1372-2	3	30	8	5	0	Parallel	Infinite	20	Cont.	72	8	X	4.79	5000
1373-1	3	30	10	3	0	Parallel	Infinite	20	Cont.	72	8	X	2.86	5000
1373-2	3	30	10	3	0	Parallel	Infinite	20	Cont.	72	8	X	4.79	5000
1374-1	3	30	10	5	0	Parallel	Infinite	20	Cont.	72	8	X	2.86	5000
1374-2	3	30	10	5	0	Parallel	Infinite	20	Cont.	72	8	X	4.79	5000
1375-1	3	30	6	3	0	Parallel	Infinite	20	Cont.	96	8	X	2.86	5000
1375-2	3	30	6	3	0	Parallel	Infinite	20	Cont.	96	8	X	4.79	5000
1376-1	3	30	6	5	0	Parallel	Infinite	20	Cont.	96	8	X	2.86	5000
1376-2	3	30	6	5	0	Parallel	Infinite	20	Cont.	96	8	X	4.79	5000
1377-1	3	30	8	3	0	Parallel	Infinite	20	Cont.	96	8	X	2.86	5000
1377-2	3	30	8	3	0	Parallel	Infinite	20	Cont.	96	8	X	4.79	5000
1378-1	3	30	8	5	0	Parallel	Infinite	20	Cont.	96	8	X	2.86	5000
1378-2	3	30	8	5	0	Parallel	Infinite	20	Cont.	96	8	X	4.79	5000

Model ID	Geometry									Cross-section		CF detail		Mat'l
	n_{span}	L/d ratio	s_g [ft]	n_{girder}	Support skew [deg]; Layout		R [ft]	s_{cf} [ft]	CF layout	d_w [in]	t_{deck} [in]	CF type	A_{cf} [in^2]	E_c [ksi]
1379-1	3	30	10	3	0	Parallel	Infinite	20	Cont.	96	8	X	2.86	5000
1379-2	3	30	10	3	0	Parallel	Infinite	20	Cont.	96	8	X	4.79	5000
1380-1	3	30	10	5	0	Parallel	Infinite	20	Cont.	96	8	X	2.86	5000
1380-2	3	30	10	5	0	Parallel	Infinite	20	Cont.	96	8	X	4.79	5000